

**UC Davis**

**UC Davis Electronic Theses and Dissertations**

**Title**

Characterization of the Photodynamics of Photoswitches: A Study of a Photomagnetic Molecular Photoswitch, Phytochromes, Cyanobacteriochromes, and a Cellular Retinoic Acid Binding Protein II Rhodopsin Mimic

**Permalink**

<https://escholarship.org/uc/item/2268h589>

**Author**

Jenkins, Adam

**Publication Date**

2021

Peer reviewed|Thesis/dissertation

**Characterization of the Photodynamics of Photoswitches: A Study of a  
Photomagnetic Molecular Photoswitch, Phytochromes,  
Cyanobacteriochromes, and a Cellular Retinoic Acid Binding Protein  
II Rhodopsin Mimic**

By

ADAM JOSEPH JENKINS  
DISSERTATION

Submitted in partial satisfaction of the requirements for the degree of

DOCTOR OF PHILOSOPHY

in

Chemistry

in the

OFFICE OF GRADUATE STUDIES

of the

UNIVERSITY OF CALIFORNIA

DAVIS

Approved:

---

Delmar S. Larsen, PhD, Chair

---

James B. Ames, PhD

---

David B. Goodin, PhD

Committee in Charge

2021

Copyright © 2021 by Adam Jenkins

**Dedicated to my Family and Friends**

## Acknowledgments

First, I want to thank my mother, Uncle John, and Aunt Lisa for always being supportive and helpful before, during, and now after my graduate career. Next, I want to thank my friends, (In particular: Dr. Leland Gee, Dr. Nakul Mishra, Dr. Cindy Pham, Matt Owen, Eugene Ogorodnik, Crystal Moon, Zefan Hurely, Charlie Sievers, and the Dancing Crew) for all the support over the years. Without the support of all these individuals, I would not have been able to complete a Ph.D. in physical chemistry.

Furthermore, this work would not have been possible without the guidance and expertise of several individuals that deserve to be named. First, I thank my advisor, Professor Delmar S. Larsen for all his support and guidance over the course of my graduate career and for providing me the opportunity to learn ultrafast optical spectroscopy and global analysis methods. Next, I would like to acknowledge the efforts of all my collaborators: Professor Natia Frank, Professor J. Clark Lagarias, Dr. Nathan C. Rockwell, Ms. Shelley S. Martin, Professor Babak Borhan, Professor James H. Geiger, Dr. Alireza Ghanbarpour, Professor Massimo Olivucci, Dr. Madushanka Manathunga, Professor Igor Schapiro, and Dr. Adyito Rao. Without them, I would not have been able to study the photoinduced dynamics of various systems ranging from relatively small photomagnetic photoswitches to several classes of larger photoreceptor proteins.

Lastly, I would like to thank my lab mates (Dr. Jack Fuzell, and Dr. Julia S. Kirpich) for all their support and advice after joining the lab. I also want to thank my senpai, Dr. L. Tyler Mix, for taking the time to initially train me in ultrafast transient absorption spectroscopy and how to analyze the resulting data using global analysis methods.

# Table of Contents

<b>Acknowledgments .....</b>	<b>iii</b>
<b>Table of Contents .....</b>	<b>iv</b>
<b>Table of Figures.....</b>	<b>xiv</b>
<b>Table of Tables .....</b>	<b>xxv</b>
<b>Table of Equations .....</b>	<b>xxvii</b>
<b>Abstract.....</b>	<b>xxviii</b>
<b>Chapter 1. Introduction to Photoswitches .....</b>	<b>1</b>
<b>Chapter 2. Investigated Photoswitches .....</b>	<b>16</b>
Molecular Photoswitches .....	16
Spiropyran & Spirooxazine.....	16
Biological Photoreceptors.....	19
Phytochrome Superfamily .....	20
Opsins & Semisynthetic Human Cellular Retinoic Acid Binding Protein II Rhodopsin	
Mimics .....	34
<b>Chapter 3. Methods and Experimental Protocols .....</b>	<b>41</b>
Molecular Photoswitch and Photomagnetic Molecular Photoswitch Sample Preparation...	42
Phytochrome and Cyanobacteriochrome Sample Preparation.....	43
hCRABPII Rhodopsin Mimic Sample Preparation .....	44
Broadband Transient Absorption Spectroscopy .....	46
Ultrafast Transient Absorption Spectroscopy.....	50

Long-Time Transient Absorption Spectroscopy.....	58
Cryokinetic UV-Vis Absorption Spectroscopy .....	59
Origin of Signals.....	63
Global Analysis.....	64
Singular Value Decomposition Analysis for Spectral Decomposition.....	69
<b>Chapter 4. Ultrafast Spintronics: Dynamics of the Photoisomerization-Induced Spin- Charge Excited-State (PISCES) Mechanism in Spirooxazine-Based Photomagnetic</b>	
<b>Materials .....</b>	<b>72</b>
Abstract.....	72
Introduction.....	73
APSO and CoAPSO Ultrafast Dynamics .....	77
Results and Discussion .....	80
Closing Comments.....	85
Associated Content .....	87
Supporting Information (pg. 263).....	87
Funding .....	87
Acknowledgments.....	87
<b>Chapter 5. Conservation and Diversity in the Secondary Forward Photodynamics of Red/Green Cyanobacteriochromes.....</b>	<b>88</b>
Abstract.....	88
Introduction.....	89
Material and Methods .....	93
CBCR Purification and Characterization.....	93

Transient Signals.....	94
Results.....	96
Global Analysis.....	104
Discussion.....	111
Productive Photodynamics.....	111
Nonproductive Photodynamics.....	114
Concluding Comments.....	118
Associated Content .....	120
Supporting Information (pg. 273).....	120
Accession Codes .....	120
Funding .....	120
Acknowledgments.....	120
<b>Chapter 6. Conservation and Diversity in the Primary Reverse Photodynamics of</b>	
<b>Red/Green Cyanobacteriochromes.....</b>	<b>121</b>
Abstract.....	121
Introduction.....	122
Materials and Methods.....	126
Results.....	127
Global Analysis.....	132
Class I <sub>R</sub> sensors .....	133
Class II <sub>R</sub> sensors.....	136
Class III <sub>R</sub> sensors .....	137
Correlations.....	139



Discussion .....	141
Excited-State Evolution .....	143
Ground-State Photocycle Evolution .....	149
Efficiency of secondary interconversions and thermal shunts that restore the $^{15}\text{E}_g$ state .....	152
Associated Content .....	154
Supporting Information (pg. 282).....	154
Accession Codes .....	154
Funding.....	154
Acknowledgments.....	154

## **Chapter 7. Conservation and Diversity in the Secondary Reverse Photodynamics of**

<b>Red/Green Cyanobacteriochromes.....</b>	<b>155</b>
Abstract.....	155
Introduction.....	156
Materials and Methods.....	163
Sample Preparation .....	163
Transient Signals.....	163
Global Analysis.....	163
Results.....	164
Wild-Type Red/Green CBCR Secondary Reverse Dynamics.....	165
WT vs $\beta$ 2FV NpR6012g4 Secondary Reverse Dynamics.....	168
Global Analysis.....	170
Wild-Type Canonical Red/Green CBCRs.....	170

Photointermediate Shunts. ....	171
Meta-G Red Shifted of $^{15}\text{ZPr}$ . ....	173
Inhomogeneity of Primary Reverse Class III <sub>R</sub> Domains. ....	174
WT vs $\beta$ 2FV NpR6012g4. ....	175
Discussion.....	177
Photointermediate Shunts. ....	179
Meta-G Red Shifted of $^{15}\text{ZPr}$ . ....	182
Concluding Comments.....	184
Associated Content .....	185
Supporting Information (pg. 304).....	185
Accession Codes .....	185
Funding.....	185
Acknowledgments.....	185

**Chapter 8. Comparison of the Forward and Reverse Secondary Photodynamics of the Bacterial Phytochrome Cph1 and the Canonical Red/Green Cyanobacteriochrome**

<b>NpR6012g4.....</b>	<b>186</b>
Abstract.....	186
Introduction.....	187
Experimental.....	194
Sample Preparation. ....	194
Room Temperature Transient Absorption Spectroscopy.....	195
Cryokinetic UV-Vis Spectroscopy. ....	195
Global Analysis.....	196

Results.....	197
Forward Room-Temperature TA Dynamics.....	197
Forward Cryokinetics.....	199
Reverse Room-Temperature TA Dynamics.....	204
Reverse Cryokinetics.....	207
Discussion.....	210
Forward Dynamics.....	210
Reverse Dynamics.....	215
Conclusion.....	219
Associated Content.....	220
Supporting Information (pg. 334).....	220
Accession Codes.....	220
Funding.....	220
Acknowledgments.....	220
<b>Chapter 9. Extending Cyanobacteriochrome Photoswitching into the Far-Red.....</b>	<b>221</b>
Abstract.....	221
Introduction.....	222
Anacy_2551g3 Primary Forward Dynamics.....	226
Results and Discussion.....	229
WT vs. S917P:Q918P: A Model for Increased Fluorescence and Photointermediate	
Quantum Yield.....	233
Concluding Comments.....	233
Associated Content.....	235

Supporting Information (pg. 366).....	235
Accession Codes .....	235
Funding .....	235
Acknowledgments.....	235
<b>Chapter 10. Computational and Spectroscopic Characterization of the Photocycle of an Artificial Rhodopsin .....</b>	<b>236</b>
Abstract.....	236
Introduction.....	237
M2 <sub>15C</sub> -PSB and M2 <sub>AT</sub> -USB QM/MM models.....	240
M2 <sub>15C</sub> -PSB to M2 <sub>AT</sub> -USB conversion .....	241
M2 <sub>AT</sub> -USB to M2 <sub>15C</sub> -PSB conversion .....	248
Proposed M2 photocycle mechanism .....	254
Is M2 a good model system to study the factors effecting rhodopsin photoisomerization?.....	256
Conclusions.....	257
Associated Content .....	259
Supporting Information (pg. 386).....	259
Funding .....	259
Acknowledgments.....	259
<b>Copyright Information .....</b>	<b>260</b>
<b>Appendices.....</b>	<b>262</b>
Chapter 4. Supporting Information for “Ultrafast Spintronics: Dynamics of the Photoisomerization-Induced Spin-Charge Excited State (PISCES) Mechanism in Spirooxazine-based Photomagnetic Materials” .....	262

A4.1: Experimental Procedures .....	262
A4.2: Sample Preparation .....	263
A4.3: Ultrafast Transient Spectra for APSO and CoAPSO .....	264
A4.4: Possible Ring Closure Mechanisms.....	265
A4.5: Quantum Yield Estimations for APSO and CoAPSO .....	265
A4.6: APSO and CoAPSO Transient Green to UV Comparison .....	267
A4.7: Global Analysis of APSO and CoAPSO .....	268
A4.8: EADS Analysis of APSO and CoAPSO.....	269
Chapter 5. Supporting information for “Conservation and Diversity in the Secondary Forward Photodynamics of Red/Green Cyanobacteriochromes” .....	272
A5.1: Supplemental Secondary Forward Dynamics of Red/Green CBCRs .....	272
A5.2: Supplemental Abbreviated Red/Green CBCR Amino Acid Alignments .....	278
Chapter 6. Supporting Information For “Conservation and Diversity in the Primary Reverse Photodynamics of the Canonical Red/Green Cyanobacteriochrome Family” .....	281
A6.1: Supplemental Methods.....	281
A6.1.1 Estimating Quantum Yield by Comparing Raw Signals. ....	281
A6.1.2 Target Model Construction. ....	282
A6.1.3 Quantum Yield Estimations from Target Modeling. ....	283
A6.2: Supplemental Red/Green CBCR Primary Reverse Dynamics.....	285
A6.3: Supplementary Discussion on Red/Green CBCR Structures.....	296
A6.4: Supplemental Tables for the Primary Reverse Dynamics of Red/Green CBCRs	300
Chapter 7. Supporting Information for “Conservation and Diversity in the Secondary Reverse Photodynamics of the Canonical Red/Green Cyanobacteriochrome Family” .....	303

A7.1: Wild-Type Red/Green CBCRs Spectra and Dynamics .....	304
A7.2: Wild-Type Reverse Dynamics Non-Conserved Feature.....	314
A7.3: Wild-Type Amino Acid Sequence Alignments .....	318
A7.4: Wild-Type Red/Green CBCR Structures.....	320
A7.5: $\beta$ 2FV NpR6012g4.....	323
A7.5.1: Forward Dynamics.....	325
A7.5.2: Reverse Dynamics .....	328
A7.5.3: WT and $\beta$ 2FV Photocycles.....	330
A7.5.4: Forward $\beta$ 2FV NpR6012g4 Dynamics Discussion .....	330
Chapter 8. Supporting Information for “Comparative Secondary Photodynamics of the Red/Far-Red Phytochrome Cph1 and the Red/Green Cyanobacteriochrome NpR6012g4” .....	333
A8.1: Background Information.....	333
A8.1.1: Additional Background Information for Figure A8.1 .....	334
A8.2: Supplemental Cph1 $\Delta$ and NpR6012g4 Room Temperature Dynamics.....	336
A8.3: Cph1 $\Delta$ Forward Cryokinetics .....	341
A8.4: NpR6012g4 Forward Cryokinetics .....	348
A8.5: Cph1 $\Delta$ Reverse Cryokinetics .....	352
A8.6: NpR6012g4 Reverse Cryokinetics.....	358
Chapter 9. Supporting Information for “Extending the Photoswitching Activity to the Far- red for Cyanobacteriochromes” .....	365
A9.1: Supplemental Methods.....	365
A9.1.1 Sample Preparation. ....	365

A9.1.2 Dual Excitation Interweaved Spectroscopy. ....	365
A9.1.3 Global Analysis.....	367
A9.1.4 Computational Methodology. ....	368
A9.2: Structural Information.....	370
A9.3: Ultrafast Dynamics .....	371
A9.4: Sequential Global Analysis.....	376
A9.5: Target Model Construction.....	381
A9.6: QM/MM Vertical Excitation Energies.....	384
Chapter 10. Supporting Information for “Computational and Spectroscopic Characterization of the Photocycle of an Artificial Rhodopsin” .....	385
10.1: Computational Methods.....	385
A10.1.1: ASEC-FEG protocol. ....	387
A10.1.2: Generation of the initial conditions.....	390
A10.1.3: Comparison of M215C-PSB model against crystallographic structure. ....	391
A10.2: Experimental Methods .....	393
A10.2.1: Sample Preparation. ....	393
A10.2.2: Ultrafast Transient Broadband Absorption Spectroscopy. ....	393
A10.2.3: Cryokinetic UV-Vis Spectroscopy. ....	394
A10.2.4: Protein Expression, Purification, and Characterization. ....	394
A10.4: Supporting experimental results for M2 <sub>15C</sub> -PSB isomerization.....	397
A10.5: Supporting experimental results for M2 <sub>AT</sub> -USB isomerization.....	401
A10.6: Energy profiles along the reaction paths leading to Kink CIs. ....	405
A10.7: Geometric parameters of excited state optimized M2 <sub>AT</sub> -USB structures. ....	407

A10.8: Proposed proton transfer mechanisms. ....	408
A10.9: Impact of electronic state mixing on the photoisomerization of M2 <sub>15C</sub> -PSB. ....	409
<b>References</b> .....	<b>412</b>

## Table of Figures

<b>Figure 1.1:</b> Generic Photocycle and Potential Energy Surface of a Photoswitch.....	4
<b>Figure 1.2:</b> Biological Signaling Mechanism Example.....	7
<b>Figure 1.3:</b> Applications of Photoreceptors.....	10
<b>Figure 1.4:</b> Photoswitches Studied in this Dissertation.....	12
<b>Figure 2.1:</b> Spiropyran and Spirooxazine Components.....	17
<b>Figure 2.2:</b> Spiropyran Photocycle.....	18
<b>Figure 2.3:</b> Positive and Negative Spirooxazine Photoswitches.....	19
<b>Figure 2.4:</b> <sup>15ZP</sup> and <sup>15EP</sup> Conformations of 15-anti Phycocyanobilin.....	20
<b>Figure 2.5:</b> Structures of Several Bilin Chromophores.....	22
<b>Figure 2.6:</b> Representative Structure and Spectra for a Tri-Domain Phytochrome.....	24
<b>Figure 2.7:</b> Representative Structure and Spectra for a Bi-Domain Phytochrome.....	25
<b>Figure 2.8:</b> Representative Structure and Diverse Photoactivity of CBCRs.....	26
<b>Figure 2.9:</b> Red/Green CBCR Generalized Photocycle.....	29
<b>Figure 2.10:</b> Comparison of the dark adapted and Signaling States of NpR6012g4.....	32
<b>Figure 2.11:</b> Correlating Excited State Kinetic Heterogeneity to Tyr Rotamers in NpR6012g4.....	34
<b>Figure 2.12:</b> Microbial and Animal Retinal Chromophores.....	36
<b>Figure 2.13:</b> Microbial Rhodopsin Photocycle.....	37
<b>Figure 2.14:</b> Animal Rhodopsin Photocycle modified from Ernst et al.....	38



<b>Figure 2.15</b> Microbial Rhodopsin Diverse Photoactivity .....	40
<b>Figure 3.1:</b> Model Timescale of a Red/Green CBCR Potential Energy Surface .....	47
<b>Figure 3.2:</b> Typical Pump-Probe Experimental Set-Up.....	49
<b>Figure 3.3:</b> NpR6012g4 Example of Primary Transient Absorption Data .....	50
<b>Figure 3.4:</b> Spectra-Physics Spitfire Pro Laser Set-up .....	51
<b>Figure 3.5:</b> Pump-probe Spectroscopy Experimental Set-up.....	53
<b>Figure 3.6:</b> Home-Built NOPA Line.....	54
<b>Figure 3.7:</b> Images of Superfluorescence, Pump Pulse, and Broadband Probe-Pulse Used in the Study of Primary Dynamics.....	56
<b>Figure 3.8:</b> Phase Matching Condition for Nonlinear Optics .....	57
<b>Figure 3.9:</b> NpR6012g4 Example of Secondary Transient Absorption Data .....	59
<b>Figure 3.10:</b> Experimental Scheme for Cryokinetic UV-Vis Spectroscopy .....	60
<b>Figure 3.11</b> NpR6012g4 Example of Cryokinetic Difference Spectra .....	62
<b>Figure 3.12:</b> Model “Temperature-Scale” of a Red/Green CBCR Potential Energy Surface .....	63
<b>Figure 3.13:</b> Representative Ultrafast Difference Spectrum Decomposition at a Single Time Point .....	64
<b>Figure 3.14:</b> Some Possible Models for a Four-Compartment System .....	65
<b>Figure 3.15:</b> Example of Sequential Analysis using the primary forward dynamics of NpR6012g4 .....	67
<b>Figure 3.16:</b> Representative target analysis for primary forward dynamics of NpR6012g4.....	68
<b>Figure 3.17:</b> $^{15}\text{EP}_g$ Signaling State Basis Set for NpR6012g4.....	70
<b>Figure 3.18:</b> Simulated and Experimental $^{15}\text{EP}_g$ Signaling State Spectra Comparison of NpR6012g4.....	71

<b>Figure 4.1:</b> Photoisomerization-Induced Spin-Charge Excited-State Process.....	75
<b>Figure 4.2:</b> APSO and CoAPSO Static Dark-Adapted State Spectra .....	76
<b>Figure 4.3:</b> APSO and CoAPSO Transient Absorption and Kinetics.....	79
<b>Figure 4.4:</b> APSO and CoAPSO EADS .....	80
<b>Figure 4.5:</b> Generalized ring-closing reaction diagram for APSO/CoAPSO .....	82
<b>Figure 4.6:</b> Dynamics at the MLCT Band .....	84
<b>Figure 5.1:</b> Canonical Red/Green CBCR Photocycle.....	91
<b>Figure 5.2:</b> Representative Canonical Red/Green CBCR and Chromophore Structure and Static Absorbance Spectra .....	98
<b>Figure 5.3:</b> Red/Green CBCRs Secondary Forward Transient Difference Spectra.....	100
<b>Figure 5.4:</b> Red/Green CBCRs Secondary Forward Kinetics.....	103
<b>Figure 5.5:</b> Excitation Wavelength Influence on the Forward Dynamics .....	104
<b>Figure 5.6:</b> Red/Green CBCRs Secondary Forward Mechanism .....	107
<b>Figure 5.7:</b> Red/Green CBCRs Secondary Forward EADS .....	109
<b>Figure 5.8:</b> Comparison of the Orange Absorbance of the Dark-Adapted State .....	115
<b>Figure 5.9:</b> Trp655 and Asp657 Structural Heterogeneity of the $^{15}ZP_r$ state .....	117
<b>Figure 6.1:</b> Dark-adapted and Signaling State Chromophore Configurations and Static Spectra .....	125
<b>Figure 6.2:</b> Representative Red/Green CBCRs Primary Reverse Dynamics TA Spectra .....	129
<b>Figure 6.3:</b> Representative Red/Green CBCRs Primary Reverse Kinetic Traces .....	132
<b>Figure 6.4:</b> Representative Red/Green CBCRs Primary Reverse Target Models .....	135
<b>Figure 6.5:</b> Representative Red/Green CBCRs Primary Reverse Dynamics SADS .....	137
<b>Figure 6.6:</b> Overlap of Class III <sub>R</sub> Photointermediates with the Static Difference Spectrum.....	139

<b>Figure 6.7:</b> Red/Green CBCRs Primary Reverse Dynamics Correlation Plots .....	141
<b>Figure 6.8:</b> Composite Photocycle of Red/Green CBCRs .....	143
<b>Figure 6.9:</b> Partial Amino Acid Sequence Alignment .....	147
<b>Figure 6.10:</b> <sup>15</sup> EP <sub>g</sub> Signaling State Hydrogen Bonding Network .....	149
<b>Figure 7.1:</b> Red/Green CBCR Chromophore Photocycle .....	157
<b>Figure 7.2:</b> Representative Red/Green CBCR Parental State Spectra .....	158
<b>Figure 7.3:</b> Generalized Conserved Red/Green CBCR Photocycle .....	159
<b>Figure 7.4:</b> Representative Red/Green CBCR Secondary Reverse Transient Difference Spectra .....	166
<b>Figure 7.5:</b> Representative Red/Green CBCR Secondary Reverse Kinetic Traces .....	168
<b>Figure 7.6:</b> WT and β2FV NpR6012g4 Secondary Reverse Dynamics .....	169
<b>Figure 7.7:</b> Representative Red/Green CBCR Secondary Reverse EADS .....	172
<b>Figure 7.8:</b> Target Analysis of the Reverse Dynamics of NpF21564g6 .....	174
<b>Figure 7.9:</b> WT and β2FV NpR6012g4 Secondary reverse EADS .....	176
<b>Figure 7.10:</b> Red/Green CBCR Composite Photocycle .....	178
<b>Figure 7.11:</b> Proposed Molecular Level Explanations of Non-Conserved Features .....	181
<b>Figure 8.1:</b> Structural Comparison of the <sup>15</sup> ZP <sub>r</sub> Dark-adapted States of Cph1Δ and NpR65012g4 .....	189
<b>Figure 8.2:</b> Chromophore and Spectral Comparison of the Dark-Adapted and Light-Adapted States of Cph1Δ and NpR65012g4 .....	191
<b>Figure 8.3:</b> Current Simplified Photocycle of Cph1Δ .....	193
<b>Figure 8.4:</b> Room-Temperature TA Dynamics of the Secondary Forward Reaction of Cph1Δ and NpR6012g4 .....	198

<b>Figure 8.5:</b> Cryokinetics of the Secondary Forward Reaction of Cph1 $\Delta$ and NpR6012g4.....	201
<b>Figure 8.6:</b> Room-Temperature TA and Cryokinetics EADS Comparison of the Secondary Forward Reaction of Cph1 $\Delta$ and NpR6012g4.....	203
<b>Figure 8.7:</b> Room-Temperature TA Dynamics of the Secondary Reverse Reaction of Cph1 $\Delta$ and NpR6012g4.....	205
<b>Figure 8.8:</b> Room-Temperature TA EADS of the Secondary Forward Reaction of Cph1 $\Delta$ and NpR6012g4.....	207
<b>Figure 8.9:</b> Cryokinetics of the Secondary Reverse Reaction of Cph1 $\Delta$ and NpR6012g4 .....	208
<b>Figure 8.10:</b> Terminal Cryokinetics of the Secondary Reverse Reaction of Cph1 $\Delta$ .....	210
<b>Figure 8.11:</b> Forward Photocycle of Cph1 $\Delta$ and NpR6012g4 and Forward PES of Cph1 $\Delta$ .....	213
<b>Figure 8.12:</b> Reverse Photocycle of Cph1 $\Delta$ and NpR6012g4 and Reverse PES of Cph1 $\Delta$ .....	216
<b>Figure 9.1:</b> WT and S917P:Q918P Anacy_2551g3 Parental State Spectra.....	223
<b>Figure 9.2:</b> WT Anacy_2551g3 <sup>15</sup> ZP <sub>f</sub> Dark-Adapted State Structure and Possible Chromophore Tautomers .....	225
<b>Figure 9.3:</b> WT and S917P:Q918P Anacy_2551g3 Primary Forward Transient Difference Spectra .....	228
<b>Figure 9.4:</b> WT and S917P:Q918P Anacy_2551g3 Primary Forward Kinetic Traces.....	229
<b>Figure 9.5:</b> WT Anacy_2551g3 Target Model and SADS .....	231
<b>Figure 10.1:</b> Ground state Absorbance Spectra of M2 <sub>AT</sub> -USB and M2 <sub>15C</sub> -PSB .....	241
<b>Figure 10.2:</b> Primary Photodynamics of the M2 <sub>15C</sub> -PSB Reaction .....	242
<b>Figure 10.3:</b> Cryokinetic SAS of the M2 <sub>15C</sub> -PSB Reaction.....	243
<b>Figure 10.4:</b> Select Dihedral Evolution Trajectories of the M2 <sub>15C</sub> -PSB reaction.....	245
<b>Figure 10.5:</b> M2 <sub>15C</sub> -PSB Reaction PES .....	247

<b>Figure 10.6:</b> Primary Photodynamics the M2 <sub>AT</sub> -USB Reaction .....	249
<b>Figure 10.7:</b> Cryokinetic SAS of the M2 <sub>AT</sub> -USB Reaction .....	250
<b>Figure 10.8:</b> CASSCF and CASPT2 energies of the M2 <sub>AT</sub> -USB Reaction.....	252
<b>Figure 10.9:</b> M2 <sub>AT</sub> -USB Reaction PES.....	254
<b>Figure 10.10:</b> Proposed M2 Photocycle.....	256
<b>Figure A4.1:</b> PMC and SO forms of APSO.....	263
<b>Figure A4.2:</b> Transient Absorption of APSO and CoAPSO in the visible region.....	264
<b>Figure A4.3:</b> Possible Thermal Isomerization Pathways for SO to PMC Forms .....	265
<b>Figure A4.4:</b> APSO and CoAPSO Quantum Yield Estimations .....	266
<b>Figure A4.5:</b> APSO and CoAPSO Green to UV Dynamics Comparison.....	267
<b>Figure A4.6:</b> APSO and CoAPSO Concentration Profiles and EADS.....	268
<b>Figure A4.7:</b> APSO and CoAPSO Sequential Models .....	269
<b>Figure A5.1:</b> Red/Green CBCR Static Absorbance Spectra.....	272
<b>Figure A5.2:</b> Red/Green CBCR Secondary Forward Transient Absorption Spectra .....	273
<b>Figure A5.3:</b> Primary and Secondary Forward 1 ms Transient Absorbance Spectra .....	274
<b>Figure A5.4:</b> Sequential Model.....	275
<b>Figure A5.5:</b> Secondary Forward Red/Green CBCR EADS .....	275
<b>Figure A5.6:</b> Secondary Forward Red/Green CBCR DADS.....	276
<b>Figure A5.7:</b> Secondary Forward Red/Green CBCR Concentration Profiles .....	277
<b>Figure A5.8:</b> Red/Green CBCR Amino Acid Sequence Alignment Near the Asp Motif. ....	278
<b>Figure A5.9:</b> Red/Green CBCR Parial Amino Acid Sequence .....	279
<b>Figure A5.10:</b> Red/Green CBCR Partial Amino Acid Sequence Near Selectively <sup>15</sup> ZP <sub>o</sub> Selectively Conserved Residue.....	280

<b>Figure A6.1:</b> Remaining Red/Green CBCR Ground State Absorption Spectra .....	285
<b>Figure A6.2:</b> Remaining Red/Green CBCR Primary Reverse Transient Absorption Difference Spectra.....	286
<b>Figure A6.3:</b> Remaining Red/Green CBCR Primary Reverse Transient Absorption Difference Spectra at Later Times .....	287
<b>Figure A6.4:</b> Remaining Red/Green CBCR Primary Reverse Kinetics .....	287
<b>Figure A6.5:</b> Remaining Red/Green CBCR Primary Reverse Kinetics Focused on Later Times .....	288
<b>Figure A6.6:</b> Red/Green CBCR Lumi-G <sub>o</sub> Quantum Yield Estimation Using Raw Spectra.....	289
<b>Figure A6.7:</b> Red/Green CBCR Primary Reverse EADS.....	290
<b>Figure A6.8:</b> Red/Green CBCR Primary Reverse EADS Decomposition .....	291
<b>Figure A6.9:</b> Red/Green CBCR Primary Reverse Target Models.....	292
<b>Figure A6.10:</b> Remaining Red/Green CBCR Primary Reverse SADS .....	293
<b>Figure A6.11:</b> Remaining Red/Green CBCR Primary Reverse Concentration Curves.....	293
<b>Figure A6.12:</b> NpR1597g4 Photointermediate and Static Difference Spectra Comparison.....	294
<b>Figure A6.13:</b> Remaining Red/Green CBCR SADS Lumi-G <sub>o</sub> Quantum Yield Estimates.....	294
<b>Figure A6.14:</b> Representative Red/Green CBCR SADS Lumi-G <sub>o</sub> Quantum Yield Estimates .	295
<b>Figure A6.15:</b> Resolved PCB Chromophore Conformation Comparison .....	297
<b>Figure A6.16:</b> Resolved Positions of Analogous Alanine Residues in the Dark-Adapted and Signaling State Structures .....	298
<b>Figure A6.17:</b> Resolved Signaling State Structures of Red/Green CBCRs Focusing on the Chromophore Pocket .....	299
<b>Figure A6.18:</b> NpR6012g4 and Slr1393g3 Full Sequence Alignment .....	299

<b>Figure A7.1:</b> Red/Green CBCRs Ground State Absorption. ....	304
<b>Figure A7.2:</b> Red/Green CBCR Secondary Reverse Transient Absorption Difference Spectra	305
<b>Figure A7.3:</b> Red/Green CBCR Secondary Reverse Kinetic Traces.....	306
<b>Figure A7.4:</b> Sequential Model.....	307
<b>Figure A7.5:</b> Red/Green CBCR Secondary Reverse Dynamics EADS.....	309
<b>Figure A7.6:</b> Red/Green CBCR Secondary Reverse Dynamics Concentration Profiles .....	310
<b>Figure A7.7:</b> Red/Green CBCR Secondary Reverse Dynamics Normalized EADS.....	311
<b>Figure A7.8:</b> Red/Green CBCR Primary and Secondary Reverse Dynamics Comparison.....	312
<b>Figure A7.9:</b> Primary and Secondary NpR4776g3 Meta-G <sub>r</sub> Comparison .....	314
<b>Figure A7.10:</b> Reverse Meta-G <sub>r</sub> and Forward Lumi-R <sub>f</sub> Spectral Comparison .....	315
<b>Figure A7.11:</b> Primary and Secondary Reverse Kinetics Comparison.....	316
<b>Figure A7.12:</b> Red/Green CBCR Amino Acid Sequence Alignment Separated by Shunting ..	318
<b>Figure A7.13:</b> Red/Green CBCR Amino Acid Sequence Alignment Separated by Meta-G <sub>r</sub> Red Shifted of <sup>15</sup> ZP <sub>r</sub> .....	319
<b>Figure A7.14:</b> Proposed Chromophore Isomerization for Red/Green CBCRs.....	320
<b>Figure A7.15:</b> Chromophore Overlap of Red/Green CBCR with Resolved Structures. ....	321
<b>Figure A7.16:</b> Signaling State Structural Comparison of NpR6012g4 and Slr13963g3. ....	322
<b>Figure A7.17:</b> Ground State Absorption Comparison of NpR6012g4 and Slr13963g3.....	323
<b>Figure A7.18:</b> Location of β2FV in NpR6012g4 .....	324
<b>Figure A7.19:</b> Secondary Forward Dynamics of WT and β2FV NpR6012g4 .....	325
<b>Figure A7.20:</b> Secondary Forward Sequential Analysis of WT and β2FV NpR6012g4 .....	326
<b>Figure A7.21:</b> Secondary Forward Target Analysis of WT and β2FV NpR6012g4.....	327
<b>Figure A7.22:</b> WT and β2FV NpR6012g4 Secondary Reverse SADS Comparison.....	328

<b>Figure A7.23:</b> WT and $\beta$ 2FV NpR6012g4 Secondary Forward and Reverse Transient Difference Spectra.....	329
<b>Figure A7.24:</b> WT and $\beta$ 2FV NpR6012g4 Photocycles.....	330
<b>Figure A8.1:</b> Cph1 $\Delta$ and NpR6012g4 Sequence Alignment. ....	333
<b>Figure A8.2:</b> Current Model Mechanisms of the Forward and Reverse Reaction of Cph1 $\Delta$ . ...	334
<b>Figure A8.3:</b> Current Model Mechanisms of the Forward and Reverse Reaction of NpR6012g4. .....	335
<b>Figure A8.4:</b> Forward and Reverse Reaction EADS of Cph1 and NpR6012g4.....	336
<b>Figure A8.5:</b> Cph1 $\Delta$ and NpR6012g4 Primary Forward Kinetics Comparison .....	337
<b>Figure A8.6:</b> Secondary Forward Cph1 $\Delta$ TA Difference Spectra (20-40 $\mu$ s) .....	337
<b>Figure A8.7:</b> Secondary Forward and Reverse Cph1 $\Delta$ TA Difference Spectra (2-10 ms).....	338
<b>Figure A8.8:</b> Secondary Forward Room Temperature TA EADS of Cph1 $\Delta$ . ....	339
<b>Figure A8.9:</b> Primary and Secondary Forward Cph1 $\Delta$ TA spectra Comparison.....	339
<b>Figure A8.10:</b> Cryokinetics Experiment Flowchart.....	341
<b>Figure A8.11:</b> Temperature Dependence of the parental States of Cph1 $\Delta$ .....	342
<b>Figure A8.12:</b> Forward Cryokinetics of Cph1 $\Delta$ from 160 K to 180 K.....	343
<b>Figure A8.13:</b> Forward Cryokinetics of Cph1 $\Delta$ from 190 K to 210 K.....	344
<b>Figure A8.14:</b> Forward Cryokinetics of Cph1 $\Delta$ from 220 K to 240 K.....	345
<b>Figure A8.15:</b> Forward Cryokinetics of Cph1 $\Delta$ from 250 K to 270 K.....	346
<b>Figure A8.16:</b> Forward Cryokinetics of NpR6012g4 from 150 K to 160 K. ....	348
<b>Figure A8.17:</b> Forward Cryokinetics of NpR6012g4 from 170 K to 190 K. ....	349
<b>Figure A8.18:</b> Forward Cryokinetics of NpR6012g4 from 200 K to 275 K. ....	350
<b>Figure A8.19:</b> Reverse Cryokinetics of Cph1 $\Delta$ from 160 K to 180 K.....	352



<b>Figure A8.20:</b> Reverse Cryokinetics of Cph1 $\Delta$ from 190 K to 210 K.....	353
<b>Figure A8.21:</b> Reverse Cryokinetics of Cph1 $\Delta$ from 220 K to 240 K.....	354
<b>Figure A8.22:</b> Reverse Cryokinetics of Cph1 $\Delta$ from 250 K to 270 K.....	355
<b>Figure A8.23:</b> Reverse Cryokinetics of Cph1 $\Delta$ from 280 K to 290 K.....	356
<b>Figure A8.24:</b> Reverse Cryokinetics of NpR6012g4 from 150 K to 170 K. ....	358
<b>Figure A8.25:</b> Reverse Cryokinetics of NpR6012g4 from 180 K to 200 K. ....	359
<b>Figure A8.26:</b> Reverse Cryokinetics of NpR6012g4 from 210 K to 230 K. ....	360
<b>Figure A8.27:</b> Reverse Cryokinetics of NpR6012g4 from 150 K to 170 K. ....	361
<b>Figure A8.28:</b> Terminal Reverse Cryokinetics of NpR6012g4 from 260 K to 280 K. ....	361
<b>Figure A8.29:</b> Comparison of the Reverse Cryokinetics of Cph1 $\Delta$ and NpR6012g4 .....	363
<b>Figure A8.30:</b> Photocycle of Cph1 $\Delta$ .....	364
<b>Figure A9.1:</b> Dual Excitation Wavelength Interleaved (DEWI) Spectroscopy Schematic. ....	366
<b>Figure A9.2:</b> PCB Chromophore Comparison of a Red/Green and Far-Red CBCR.....	370
<b>Figure A9.3:</b> Classical Chromophore Photocycle.....	371
<b>Figure A9.4:</b> Anacy_2551g3 Primary Forward Difference Spectra .....	371
<b>Figure A9.5:</b> WT Anacy_2551g3 Visible Probe DEWI Results .....	372
<b>Figure A9.6:</b> WT Anacy_2551g3 NIR Probe DEWI Results.....	373
<b>Figure A9.7:</b> S917P:Q918P Anacy_2551g3 Visible Probe DEWI Results.....	374
<b>Figure A9.8:</b> S917P:Q918P Anacy_2551g3 NIR Probe DEWI Results .....	375
<b>Figure A9.9:</b> Forward Quantum Yield Estimation for WT and S917P:Q918P Anacy_2551g3	376
<b>Figure A9.10:</b> Sequential Model.....	377
<b>Figure A9.11:</b> WT Anacy_2551g3 EADS and Concentration Profiles.....	379
<b>Figure A9.12:</b> WT Anacy_2551g3 Difference of EADS .....	380

<b>Figure A9.13:</b> S917P:Q918P Anacy_2551g3 EADS and Concentration Profiles.....	380
<b>Figure A9.14:</b> S917P:Q918P Anacy_2551g3 SADS.....	383
<b>Figure A9.15:</b> WT and S917PQ918P $^{15}\text{ZP}_{\text{fr}}^*$ Lifetime Comparison.....	383
<b>Figure A10.1:</b> Initial Conditions for M2 <sub>15C</sub> -PSB and M2 <sub>AT</sub> -USB.....	387
<b>Figure A10.2:</b> ASEC Protocol.....	389
<b>Figure A10.3:</b> QM/MM setup.....	391
<b>Figure A10.4:</b> Evolution of CASSCF (dashed) and CASPT2 energies (solid) along the isomerization of M2 <sub>15C</sub> -PSB around C13=C14 double bond.....	392
<b>Figure A10.5:</b> Cryokinetic Experimental Schematic.....	395
<b>Figure A10.6:</b> M2 <sub>15C</sub> -PSB Cryokinetics at Select Temperatures.....	397
<b>Figure A10.7:</b> M2 <sub>15C</sub> -PSB Cryokinetics Between 170 and 200 K.....	398
<b>Figure A10.8:</b> M2 <sub>15C</sub> -PSB Cryokinetics Between 210 and 240 K.....	399
<b>Figure A10.9:</b> Comparison of the 650 and 710 nm kinetics of M2 <sub>15C</sub> -PSB.....	401
<b>Figure A10.10:</b> M2 <sub>AT</sub> -USB Cryokinetics Between 170 and 190 K.....	401
<b>Figure A10.11:</b> M2 <sub>AT</sub> -USB Cryokinetics Between 200 and 240 K.....	402
<b>Figure A10.12:</b> M2 <sub>AT</sub> -USB Cryokinetics at 250 and 260 K.....	403
<b>Figure A10.13:</b> Evolution of CASSCF (dashed) and CASPT2 energies (solid) along the isomerization of M2 <sub>AT</sub> -USB around C15=N double bond.....	405
<b>Figure A10.14:</b> Evolution of CASSCF (dashed) and CASPT2 energies (solid) along the isomerization of M2 <sub>AT</sub> -USB around C11=C12 and C13=C14 double bonds.....	406
<b>Figure A10.15:</b> M2 <sub>AT</sub> -USB Optimized Geometric Parameters.....	407
<b>Figure A10.16:</b> Proposed Deprotonation Pathways for M2.....	408

<b>Figure A10.17:</b> CASPT2 and CASSCF Energies and Mulliken charges along a representative M2 <sub>15C</sub> -PSB trajectory .....	409
--	-----

## Table of Tables

<b>Table 1.1:</b> Common Molecular Photoswitches .....	6
<b>Table 1.2:</b> Classes of Biological Photoreceptors .....	8
<b>Table 2.1:</b> List of Phytochromes and CBCR with reported Photodynamics .....	30
<b>Table 5.1:</b> Secondary Forward EADS Timescales.....	108
<b>Table 6.1:</b> Resolved Red/Green CBCR D-ring Dihedral and Ring Tilt Angles .....	151
<b>Table 9.1:</b> Plausible Chromophore Tautomers Hybrid QM/MM Vertical Energies.....	232
<b>Table A4.1:</b> APSO EADS Assignments .....	270
<b>Table A4.2:</b> CoAPSO EADS Assignments .....	271
<b>Table A5.1:</b> Amino Acids at Locations With Known Importance .....	279
<b>Table A6.1:</b> Global Analysis Excited State Parameters.....	300
<b>Table A6.2:</b> Global Analysis Photointermediate Parameters.....	301
<b>Table A6.3:</b> Photointermediate Quantum Yield Estimates and electronic absorption spectral properties.....	302
<b>Table A6.4:</b> Distances between the Chromophore and Adjacent Residues .....	302
<b>Table A7.1:</b> Red/Green CBCR Secondary Reverse Global Analysis Parameters .....	308
<b>Table A7.2:</b> Primary and Secondary Reverse Dynamics Excitation Wavelengths.....	312
<b>Table A7.3:</b> Comparison of the Primary and secondary Reverse Dynamics.....	313
<b>Table A7.4:</b> Reverse Meta-G <sub>r/f</sub> and Forward Lumi-R <sub>f</sub> Comparison .....	314

<b>Table A7.5:</b> Comparison of Various Reverse Dynamics Features in canonical red/green CBCRs .....	317
<b>Table A7.6:</b> Comparison of Reverse EADS Absorption and Non-Conserved Features in canonical red/green CBCRs .....	317
<b>Table A7.7:</b> Red/Green CBCR Chromophore Dihedral and Tilt Angles .....	320
<b>Table A7.8:</b> Average Chromophore Dihedral and Tilt Angles in NpR6012g4 .....	321
<b>Table A7.9:</b> Distances of Residues Closest to the Chromophore in the $^{15}E_p$ State.....	322
<b>Table A7.10:</b> WT and $\beta$ 2FV Forward Dynamics Sequential Model Parameters .....	326
<b>Table A8.1:</b> Experimental Parameters .....	336
<b>Table A8.2:</b> Cph1 $\Delta$ Forward and Reverse Room-Temp TA Observations .....	340
<b>Table A8.3:</b> Cph1 $\Delta$ Forward Cryokinetics Observations .....	347
<b>Table A8.4:</b> NpR6012g4 Forward Cryokinetics Observations.....	351
<b>Table A8.5:</b> Cph1 $\Delta$ Reverse Cryokinetics Observations .....	357
<b>Table A8.6:</b> NpR6012g4 Reverse Cryokinetics Observations.....	362
<b>Table A9.1:</b> DEWI Experimental Parameters for the Forward Dynamics of WT and S917P:Q918P Anacy_2551g3 .....	367
<b>Table A9.2:</b> Chromophore Structural Information for the $^{15}ZP_{fr}$ Dark-Adapted State of Anacy_2551g3.....	370
<b>Table A9.3:</b> Lumi-FR QY estimation from scaling of the transient spectra in Figure A9.9. ....	376
<b>Table A9.4:</b> Sequential Model Parameters for WT and S917P:Q918P Anacy_2551g3.....	378
<b>Table A9.5:</b> Target Model Parameters for WT and S917P:Q918P Anacy_2551g3 .....	382
<b>Table A9.6:</b> QM/MM Ground State and Excited State Vertical Excitation Energies of Four Probable Chromophore Tautomers.....	384

**Table A10.1.** Cryokinetic observations and interpretations for the M2<sub>15C</sub>-PSB Reaction..... 400

**Table A10.2.** Cryokinetic observations and interpretations for the M2<sub>AT</sub>-PUSB Reaction..... 404

## **Table of Equations**

**Equation 3.1:** Transient Difference Spectra Generation ..... 48

**Equation 3.2:** Phase Matching Condition..... 57

**Equation 3.3:** Separation of Spectral and Time Domains by Global Analysis ..... 65

**Equation 3.4:** Solutions of First Order Difference Equations Used in Global Analysis ..... 65

**Equation 3.5:** Global Analysis Connectivity Matrix ..... 66

**Equation 3.6:** Singular Value Decomposition..... 69

**Equation 3.7:** Determination of Concentration of Spectral Eigenvectors ..... 69

## Abstract

Photoreceptors play essential roles in initiating a wide array of biological responses based on external light conditions. Photoreceptors have been shown to be involved in phototropism, shade avoidance, seed germination, vision, and chromic acclimation. These photosensitive proteins initiate these various responses by reversibly photoconverting between a thermally stable dark-adapted state and a meta-stable light-adapted state when a covalently bound chromophore absorbs a photon of light. The chromophore causes the large-scale reorganization of the protein by undergoing a structural or electronic change. Since photoreceptors have evolved to initiate various biological responses as well as improve the efficiency of photosynthesis via chromatic acclimation (converting higher energy light to lower energy light that can be used for photosynthesis), they are also of interest to serve as a basis for designing novel fluorescent probes for medicinal imaging applications or optogenetic tools to selectively initiate and control biological functions in living tissue and study neural circuits at a more fundamental level.

To better understand biological signal transduction and establish the practicality of these photoreceptors for the application outlined above, a molecular level understanding of these photoreceptors is of paramount importance. Key to developing a molecular level understanding of these photoinduced events is the characterization of the photoreceptor forward and reverse reactions with time and temperature dependent spectroscopic techniques. These experiments track changes in the absorption spectra due to the photoreaction, which allows for a mapping of the underlying mechanism and estimations of transient properties (e.g., timescale, energy barriers, quantum efficiencies). Photoreceptors are especially well suited for being studied by time-resolved techniques since the reaction is initiated at a known time point (i.e., photoexcitation). The

analysis of the resulting time-dependent data sets reveals complex mechanisms, including ground state inhomogeneity, unproductive pathways, and estimation of the quantum efficiencies. Cryokinetic UV-Vis spectroscopy complements the room-temperature primary and secondary transient absorption spectroscopic results as well as isolates quickly evolving intermediates difficult to resolve at room temperature.

In the first part of this dissertation a brief overview to photoswitches, including select molecular photoswitches and biological photoreceptors, is provided and followed by a description of the experimental protocols used in the subsequent chapters. The second part of this dissertation is a collection of studies on the photoinduced dynamics of: i) a synthetic cobalt-dioxolene based photomagnetic molecular photoswitch and ii) several biological photoreceptors including comparative studies on the forward and reverse dynamics of several red/green cyanobacteriochromes (CBCRs) isolated from *Nostoc punctiforme*, a comparison of the secondary forward and reverse dynamics of the photosensory core of cyanobacterial phytochrome 1 (Cph1 $\Delta$ ) isolated from *Synechocystis sp.* PCC 6803 and the canonical red/green CBCR NpR6012g4 isolated from *Nostoc punctiforme*, primary forward dynamics of a wild-type and mutated far-red/x CBCR isolated from *Anabaena cylindrica* PCC 7122, and the photocycle of a novel semisynthetic rhodopsin mimic.

# Chapter 1. Introduction to Photoswitches

A central goal of chemistry is the development of a molecular-level understanding of the dynamics of chemical reactions. If we can develop a fundamental understanding of a chemical reaction, then we can guide the reaction to be more efficient and selective, develop new reactions from the bottom up, and generate new products. The overall mechanism of a chemical reaction can be multifaceted and involve several elementary steps and intermediate populations that connect the starting reactant to the terminal product. Furthermore, a reaction mechanism may not be a sequential evolution originating from the reactant(s) but may incorporate branches that leads to the generation of different product species as well as decay back to the reactant. If we can understand the nature of all the species generated, we may be able to manipulate the environment or the reaction itself to preferentially generate a particular product of interest.

Developing a molecular-level understanding of a reaction requires identifying the underlying mechanism. This requires the isolation and identification of each intermediate population and product as well as the timescale of the evolution of every elementary step. The identification of intermediate and product species typically involves characterization of not only the chemical composition, but the overall geometric and electronic structures of the population as well. This can be done using various spectroscopic methods such as UV-Vis absorption, FTIR, Raman, and X-ray based spectroscopies. In addition to the identity of the population, one would also need to know how the populations evolve in time: does the population exhibit a sequential or branching mechanism, does the species decay, etc. Once a base mechanism is established one can then test how the manipulation of a different parameter such as the identity of a reactant, reactant concentration, solvent, pH, pressure, wavelength or intensity of light, or temperature influences



the mechanism and through trial and error establish optimal parameters for increasing the yield of a product of interest. For example, one could try modulating the temperature of the reaction to manipulate the equilibrium constant and reaction kinetics to prefer the product forming pathway, increase the pressure so that molecules are more likely to collide and prefer the side of the reaction with fewer gaseous species, or substitute a relatively large reactant that shields the reaction site to a smaller one in the hopes of making the reaction more likely to occur.

While most chemical reactions use thermal energy to overcome barriers in their reaction mechanisms, light-activated photoreactions are capable of being initiated by the absorption of externally applied photons. These light-activated processes make these systems unique since most molecules do not undergo any reactions when absorbing light and primarily fluoresce. The use of photon energy results in the generation of high-energy populations that cannot be accessed thermally and leads to the opening of new reaction channels that would otherwise be inaccessible. These reactions typically involve modification of the electronic configuration of a molecule and results in the breaking or formation of bonds, intramolecular or intermolecular charge transfer, or ionization of the molecule.<sup>1-5</sup> This modification of the electronic structure can also lead to the generation of typically unproducibile products such as relatively small cyclic organic compounds.<sup>6,</sup>

7

Of particular interest are the light-initiated reactions of photoswitches which are unique compared to other photoinduced reactions since they are bidirectional and reversibly convert between a thermally stable dark-adapted state and a meta-stable light-adapted state.<sup>8-16</sup> Photoswitches utilize

several mechanisms to convert between the dark-adapted and light-adapted states such as trans/cis isomerization, dimerization, bond formation or breakage, and proton/ligand transfer. The mechanism of these photoconversions is typically a multi-stepped process where each step has an energy barrier that must be overcome either via absorption of a photon or the presence of enough thermal energy (Figure 1.1). Upon photoexcitation of the dark-adapted state, an electronically excited dark-adapted state is populated that can either decay back to the dark-adapted ground state or populate a primary intermediate population ( $I_{d1}$ ). This primary intermediate population then evolves through a series of secondary intermediate populations ( $I_{d2} - I_{dn}$ ) on unique timescales ( $k_{dn}$ ) before generating the light-adapted state photoproduct. While the reverse dynamics originating from the light-adapted state can be similarly photoactivated and progress through typically unique  $I_l$  intermediates, it can also thermally revert back to the dark-adapted state when the thermal energy is greater than the potential energy barrier through a currently not well understood dark-reversion mechanism. Once we fundamentally understand the dynamics of these photoconversions, we can then hope to design photoswitches to have desirable traits such as preferred absorbance wavelengths and increased photoproduct yields.

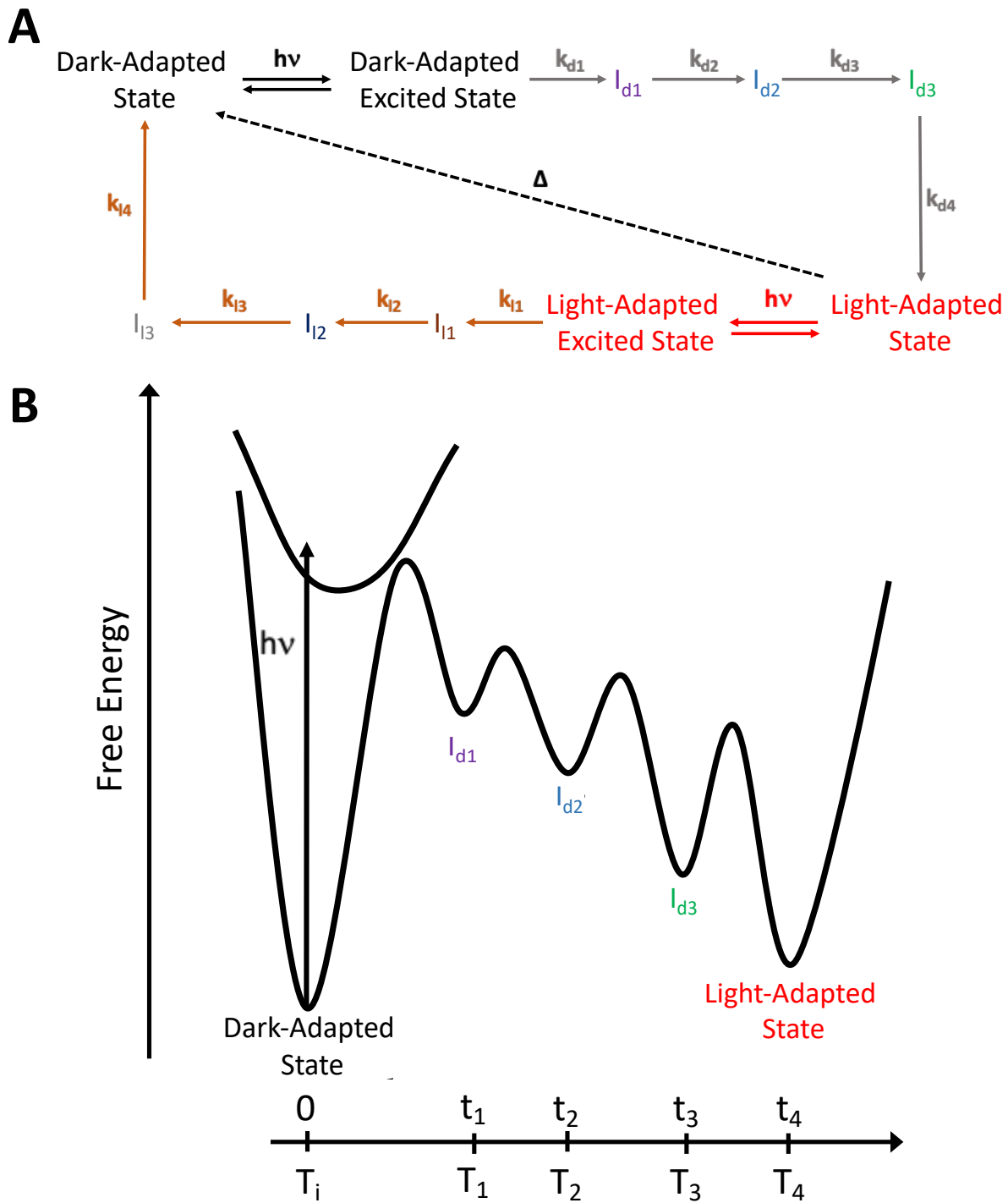


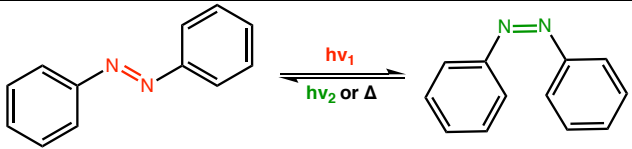
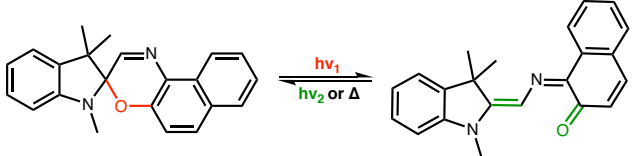
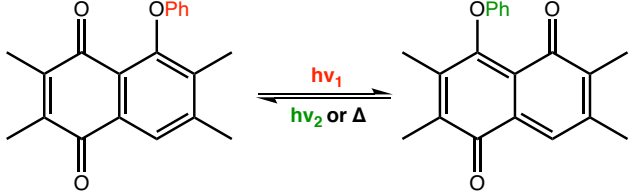
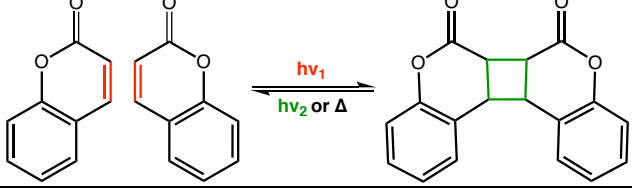
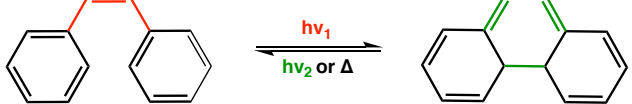
**Figure 1.1:** Generic Photocycle and Potential Energy Surface of a Photoswitch

Generic (A) photocycle and (B) forward reaction potential energy surface of a photoswitch showing unique timescales and thermal energy barriers of several intermediate populations.

Examples of photoswitches are molecular photoswitches which are typically relatively small, highly conjugated organic molecules.<sup>8-16</sup> There are several classes of molecular photoswitches that are initially sorted by the photoinduced reaction mechanism. While trans/cis isomerization as observed in azobenzene is common (Table 1.1),<sup>8-10</sup> other photoinduced reactions that involve forming and breaking bonds have also been observed such as ring opening/closing as observed in spirooxazines,<sup>12, 14</sup> ligand transfer as observed in quinones,<sup>15</sup> dimerization as observed in coumarin,<sup>13</sup> and cyclization as observed in stilbene.<sup>11</sup> Since the photoreaction causes a change in geometry, polarity, or charge distribution, the dark-adapted and light-adapted states as well as the transient intermediate populations typically have unique absorption spectra which allows for the mapping of the photocycle spectroscopically. While the generic mechanism in Figure 1.1 is simplified and does not show more complicated dynamics such as branching, unproductive-subpopulations, intermediate shunts, or the coevolution of subpopulations, transient and temperature resolved optical studies coupled with multi-variable data analysis methods is capable of extracting the spectra of the underlying populations and the timescales of their evolution. A more thorough overview of spiropyran and spirooxazine is provided in Chapter 2 and the dynamics of a spirooxazine photoswitch is explored in Chapter 4.

**Table 1.1:** Common Molecular Photoswitches

Common molecular photoswitches with their mechanism and representative sample.

Mechanism	Photoswitches	Example
<i>trans/cis</i> Isomerization	Azobenzenes, <sup>8-10</sup> Stilbenes, <sup>10</sup> Acylhydrazones, <sup>10</sup> Hemithioindigo <sup>10</sup>	
Ring Closure/Opening	Diarylethenes, <sup>10</sup> Spiropyran/ Spirooxazines <sup>12, 14</sup>	
Proton/Ligand Transfer	Quinone, <sup>15</sup> Silylideneaniline <sup>16</sup>	
Dimerization	Coumarins <sup>13</sup>	
Cyclization	Stilbene <sup>11</sup>	

In addition to synthetic molecular photoswitches, biological photoswitches termed photoreceptors have been found in all forms of life (archaea, bacteria, and eukaryotes) where they illicit an array of homeostatic responses based on external light conditions. Examples includes but is not limited to, human vision,<sup>17</sup> seed germination<sup>18</sup> and shade avoidance<sup>19</sup> in plants,<sup>19-21</sup> as well as phototaxis<sup>22-24</sup> and chromatic acclimation<sup>25, 26</sup> in bacteria. For a biological organism to respond to external light conditions, they evolved a typically reversible photoactivated system which uses a carefully structured protein that covalently binds a light-sensitive chromophore. Upon resonant illumination, the chromophore undergoes a change that results in converting the protein conformation between

a thermally stable dark-adapted state and a meta-stable light-adapted state. As we will see in later chapters (5-9), the photoconversion mechanisms of photoreceptors are more complicated due to the heterogeneous nature of the protein scaffold.<sup>27-29</sup> Population of the light-adapted state typically causes further changes in a coupled output domain which in turn initiates a signal cascade that ultimately results in a vast array of biological responses (Figure 1.2).

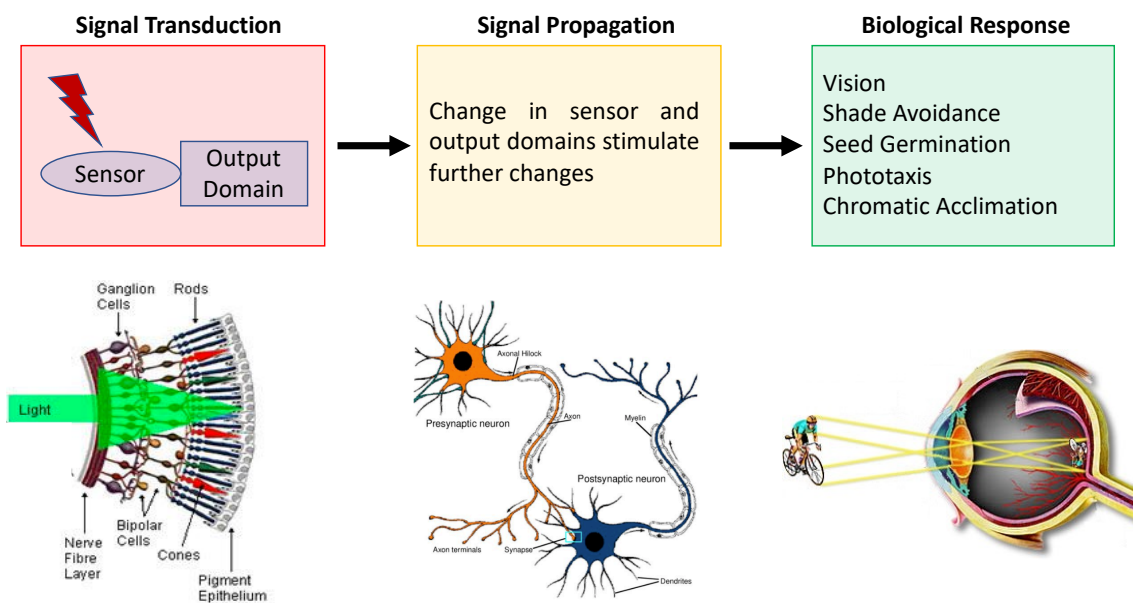


**Figure 1.2:** Biological Signaling Mechanism Example

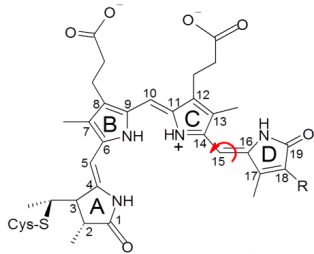
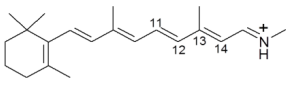
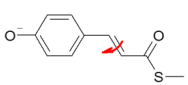
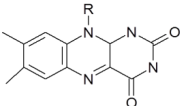
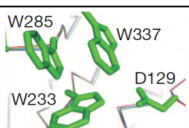
Example of a biological signaling mechanisms adapted from Montgomery<sup>30</sup> and using vision as an example.

There are several different classes of photoreceptors that are initially separated into different families based on the identity of the embedded chromophore (Table 1.2). There are five main identified chromophore classes: i) linear-tetrapyrrole (bilin), ii) retinal, iii) coumaric acid, iv) flavin, and v) tryptophan pyramid. Upon absorption, these biological chromophores have been reported to undergo photoisomerization (tetrapyrrole, retinal, and coumaric acid), bond formation

or breakage, electron or proton transfer (flavin), and homodimer dissociation (tryptophan pyramid).<sup>31</sup> Within these classes there is further diversity such as the conjugation length of the bilin chromophores used in the linear-tetrapyrrole based phytochrome family and the location of the isomerization event in the retinal based rhodopsin family. The diversity of both phytochromes and rhodopsin is discussed further in Chapter 2.

**Table 1.2:** Classes of Biological Photoreceptors

Classes of photoreceptors with the five typical chromophores and their respective photochemistry. This table is adapted from Van der Horst et al.<sup>31</sup> and is courtesy of Dr. Peter Kim.

Classes	Chromophores	Photosensor Family	Photochemistry
Tetrapyrrole		Phytochromes and Cyanobacteriochromes	Z/E isomerization
Retinal		Rhodopsins	Z/E isomerization
Coumaric Acid		Xanthopsins	Z/E isomerization
Flavin		Cryptochromes Phototropin BLUF Domains	Cysteine Adduct Electron Transfer Proton Transfer
Tryptophan Pyramid		UVR8	Homodimer Dissociation

In addition to being interesting for the development of an understanding of chemical reactions and photoinduced biological signal transduction, photoreceptors can be utilized in a vast array of applications due to their inherent spatial and temporal control coupled with the photoinduced changes in geometry and charge distribution (Figure 1.3). Examples of applications includes but is not limited to: chemical sensors,<sup>32, 33</sup> data storage and processing,<sup>34</sup> solar energy storage,<sup>35-37</sup> supramolecular chemistry,<sup>38, 39</sup> transistors,<sup>40, 41</sup> drug and chemical release,<sup>42</sup> molecular machines (Figure 1.3B),<sup>43</sup> fluorescent probes,<sup>44-47</sup> and optogenetic tools.<sup>44, 47</sup> For example, since the two states of molecular photoswitches may have different redox potentials, they can be used to modulate the charge and spin states of transition metal complexes (Figure 1.3A). This could result in a complex that can use external light to control the spin and charge state of the transition metal, leading to a molecular photomagnetic complex that could be incorporated into a spintronic device for data storage and processing purposes. This method is not only advantageous for ease of incorporation to current electronics given the availability of visible LEDs, but could also result in an elongated photoinduced spin state lifetimes since the lifetime would now depend on the stability of the light-adapted state of the photoswitch rather than the excited state of the transition metal complex.<sup>48</sup> Strategies for designing such photomagnetic complexes using Cr(III) or Fe(III) and spiropyran have been previously reported.<sup>49</sup> Furthermore, since biological photoreceptors have evolved to initiate various biological responses, they are of interest to serve as the basis for the development of optogenetics tools which can be used to control biological responses in living tissue and study neural circuits at a more selective and fundamental level.<sup>50-53</sup> To date, optogenetic tools have been used to control various biological functions such as neuron activation and deactivation (Figure 1.3C),<sup>54, 55</sup> messenger molecules,<sup>56</sup> DNA transcription,<sup>57</sup> and gene expression.<sup>50</sup> While we have been focused on the generation of the photoproduct up to now, if the



primary photoinduced event was inhibited, a highly fluorescent tool could be generated and used in medicinal imaging applications (Figure 1.3D).<sup>44-47</sup>

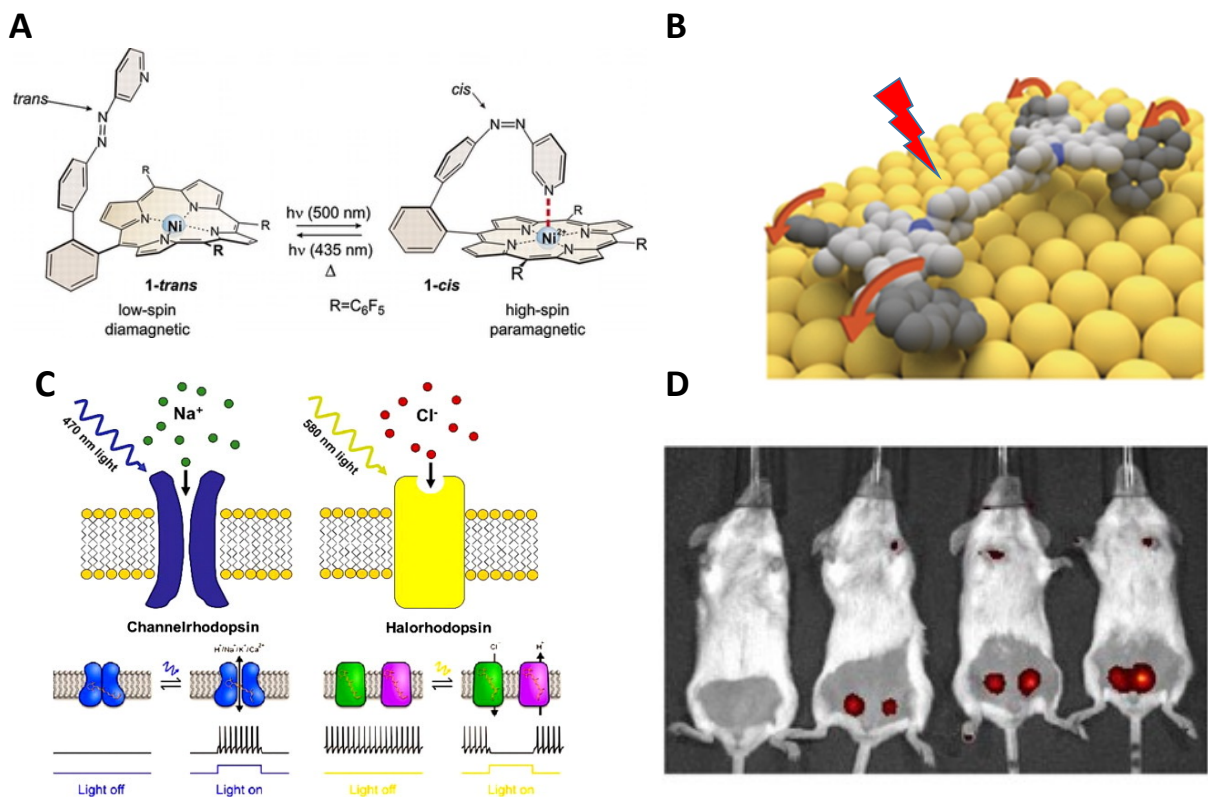


**Figure 1.3:** Applications of Photoreceptors

Photoreceptor applications: (A) photo-modulation of charge and spin states,<sup>58</sup> magnetic modulation (B) molecular motors,<sup>43</sup> (C) control of the action potential of a neuron via optogenetic tools,<sup>54</sup> and (D) tumor imaging using a fluorescent probe.<sup>46</sup>

For the development of photoreceptors for the applications outlined above as well as a fundamental understanding of photoinduced chemical reactions and biological signal transduction, a molecular-level understanding of the photoinduced dynamics is of the utmost importance. Fortunately, the reaction dynamics of photoswitches are particularly well suited for being characterized by time

and temperature resolved absorption spectroscopies since i) the reaction is initiated at a well-defined time point (photoexcitation) and ii) the dark-adapted and light-adapted states as well as the intermediate populations typically have unique spectral features, kinetics, and energy barriers. While the resulting time and temperature dependent spectra may be a superposition of various populations, multi-variable data analysis methods (i.e., global analysis and singular value decomposition analysis) can be used to separate the spectral and variable (time and temperatures) domains and extract variable independent spectra and concentration profiles as well as provide approximations for the quantum yield of the reaction. A more thorough explanation of the spectroscopic techniques and data analysis methods utilized in this dissertation is provided in Chapter 3.

Using time and temperature resolved optical spectroscopies coupled with multi-variable data analysis methods, I studied the dynamics of three diverse classes of photoswitches (Figure 1.4): i. a spirooxazine-cobalt-dioxolene photomagnetic complex (Chapter 4),<sup>59</sup> ii. cyanobacteriochromes (CBCRs; Chapters 5-9)<sup>27-29</sup> and the photosensory core of cyanobacterial phytochrome 1 (Cph1 $\Delta$ ; Chapters 9), and a semisynthetic rhodopsin mimic (M2; Chapter 10).<sup>60</sup> These studies resolved molecular level explanations for not only the overall photocycle, but for spectral tuning and modulation of the quantum efficiencies via protein-chromophore and ligand-metal interactions.

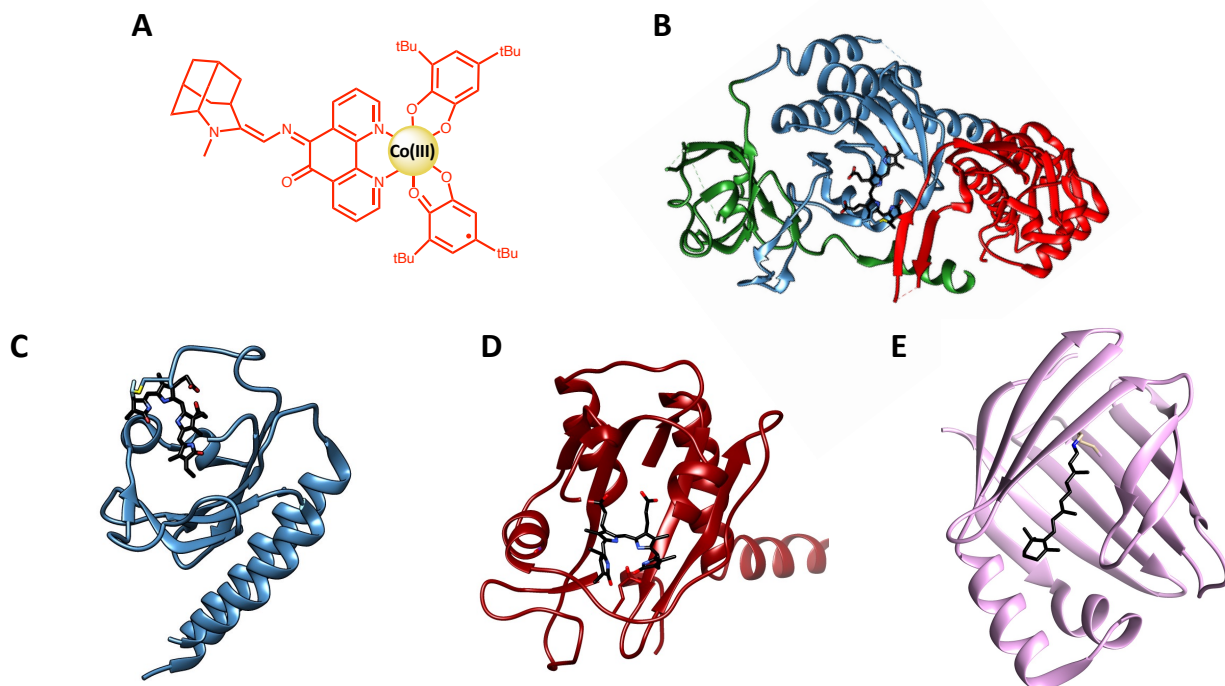


**Figure 1.4:** Photoswitches Studied in this Dissertation

Photoswitches studied in this dissertation: (A) Photomagnetic photoswitch (CoAPSO; Chapter 4), (B) cyanobacterial phytochrome (Cph1; PDB: 2VEA; Chapter 8), (C) canonical red/green cyanobacteriochromes (NpR6012g4 and many others; PDB: 6BHN; Chapters 5-8), (D) far-red cyanobacteriochrome (Anacy\_2551g3; PDB: 6UVB; Chapter 9), and (E) semisymmetric rhodopsin mimic (M2; PDB: 4YFP; Chapter 10).

Similar to the iron and chromium/spiroopyran complexes mentioned earlier, the Frank Lab generated a photomagnetic photoswitch by ligating a negative spirooxazine photoswitch (discussed in the next chapter) which undergoes a photoinduced ring closure reaction (Figure 2.3) to cobalt-dioxolene.<sup>48</sup> The dark-adapted ring-opened *trans-low-spin (ls)*-Co(III) state reversibly photoconverted to the light-adapted ring-closed *high spin (hs)*-Co(II) state upon green light illumination, resulting in a substantial increase in the magnetization of the complex. The intramolecular charge transfer was associated with increased  $\pi$ -backbonding of the ring-closed

form that lowered the reduction potential of Co(III). This additional electron destabilized the low-spin conformation and resulted in a spin-forbidden  $d \rightarrow d$  transition and resulted in the formation of a high spin species. The photoinduced dynamics of both the negative spirooxazine and the photomagnetic complex are explored in detail in Chapter 4 and revealed that ring closure was not necessary for generation of hs-Co(II) and that excited state relaxation on the same timescale of isomerization was sufficient.<sup>59</sup>

The main focus of this dissertation is on the photoinduced dynamics of biological photoreceptors. While a more in-depth overview of the bilin-based phytochrome superfamily is provided in the next chapter, the cyanobacteriochrome (CBCR) family will be briefly introduced here. Phytochromes are tri-domain (PAS-GAF-PHY)<sup>61</sup> photoreceptors that were originally discovered in plants and were associated with seed germination and shade avoidance.<sup>62</sup> Later, they were discovered to also be present in algae, bacteria, and fungi.<sup>19-21</sup> While phytochromes have been known for about 70 years, in the last couple decades or so, a new class of photoreceptors termed cyanobacteriochromes were discovered that only require a single GAF domain to both linearly bind the bilin chromophore and have reversible photoconversion spanning the near ultraviolet to the far-red spectral regions. This diverse photoactivity is the result of the utilization of bilin chromophores with different conjugation lengths<sup>63-65</sup> as well as the incorporation of unique protein-chromophore interactions<sup>64, 66-68</sup> (discussed in the next chapter). Given this great diversity in photoactivity and mechanisms, several subfamilies of CBCRs have been identified, including the canonical red/green,<sup>69</sup> noncanonical red/green,<sup>70</sup> noncanonical orange/green,<sup>69</sup> green/red,<sup>71</sup> insert-cysteine,<sup>68, 72</sup> DXCF,<sup>68</sup> and far-red/x<sup>63, 65</sup> CBCRs. The photodynamics of i) nearly a dozen canonical red/green CBCRs are compared in Chapters 5-7, ii) the photosensory core of

cyanobacterial phytochrome 1 (Cph1 $\Delta$ ) and a red/green CBCR are compared in Chapter 8, and iii) a wild-type and double mutant of a far-red CBCR are compared in Chapter 9. These studies resolved that the forward and reverse dynamics of red/green CBCRs consisted of selectively conserved mechanisms of monotonic and non-monotonic spectral evolution respectively (Chapters 5-7).<sup>27,28</sup> This indicates that the reverse reaction is unique and not simply the reverse of the forward reaction. Interestingly, the initial phase forward dynamics of the Cph1 $\Delta$  (Chapter 8) was in full agreement with these red/green CBCRs, indicating that Cph1 $\Delta$  may be more like red/green CBCRs than canonical phytochromes.<sup>73</sup> Furthermore, protein tuning of the chromophore excited state was observed in the reverse dynamics where fluorescence or photointermediate population were preferred when a residue near the bilin chromophore was tyrosine or histidine, respectively.<sup>28</sup> While the ultrafast reverse dynamics (Chapter 6) suggested that red/green CBCRs with relatively blue shifted light-adapted spectra were more efficient,<sup>28</sup> the secondary dynamics (Chapter 7) revealed that they actually had lower photoproduct quantum yields due to the presence of photointermediate shunts. Assuming that the features resolved in these multi-CBCR studies holds true, then biological tools inspired by red/green CBCRs could be developed where fluorescence could be optimized by using or generating single mutants that have tyrosine near the bilin C10 and photoproduct quantum yield could be optimized by using red/green CBCRs with relatively red-shifted light-adapted spectra and wild-type or single mutant red/green CBCRs with a tyrosine near the bilin C10.

While several biological photoreceptors are naturally reversible, some retinal-based rhodopsin photoreceptors (i.e., those utilized in human vision) are not and require enzymes to reconstitute the biologically active dark-adapted state. This irreversibility makes the development of a

molecular level understanding of the underlying mechanism and determination of various properties such as quantum efficiency and spectral tuning difficult to ascertain and verify. One way to overcome these limitations is by developing photo-reversible semisynthetic analogues that mimics the behavior of natural rhodopsins. A couple photo-reversible rhodopsin mimics have recently been developed by using cellular retinoic acid binding protein II (CRABPII) as a base.<sup>74-</sup>

<sup>76</sup> To ascertain if these mimics hold the potential to be use as a basis to more easily study protein-retinol chromophore interactions comparable to native systems, the photocycle of one of these mimics (M2) was determined using time and temperature resolved spectroscopies coupled with global analysis and hybrid quantum mechanics /molecular mechanics methods (Chapter 10). These studies on M2 indicated that semisynthetic analogues of rhodopsin using CRABPII could be generated and used to study protein-chromophore interactions dictating the photodynamics of natural rhodopsins due to the incorporation of dynamics observed in bacteriorhodopsin and microbial rhodopsin (Chapter 10).<sup>60</sup>

## Chapter 2. Investigated Photoswitches

A brief overview of the three photoswitch classes investigated in this dissertation was discussed in Chapter 1. Here a more comprehensive overview of each class is provided.

### *Molecular Photoswitches*

While there are several different classes of molecular photoswitches as outlined in the previous chapter, only spiropyran and spirooxazine will be discussed in this chapter since the only molecular photoswitch in this study is spirooxazine.

### *Spiropyran & Spirooxazine*

Spiropyran and spirooxazine are related molecular photoswitches that both undergo identical reversible photoconversions typically between a ring-closed dark-adapted state that typically absorbs UV radiation and a ring-open light adapted state that typically absorbs visible radiation (Table 1.1). This red shift in absorbance in the ring open state is due to an increase in conjugation that preferentially stabilizes the excited state. While both spiropyrans and spirooxazines incorporate an indoline ring, spiropyran utilizes a chromoene ring whereas spirooxazine utilizes an oxazine ring (Figure 2.1); the difference being an additional nitrogen in oxazine.<sup>12, 14, 77</sup> In addition to the structural similarities, spiropyrans and spirooxazines also unsurprisingly have similar spectral features and photocycles.<sup>14, 78</sup> The main difference is that spirooxazines exhibit greater light fatigue, going over 10,000 cycles, whereas spiropyrans degrades between 100-1000 cycles. This fatigue is due to the zwitterion open ring intermediate that is vulnerable to reactions with the environment, such as oxidation.

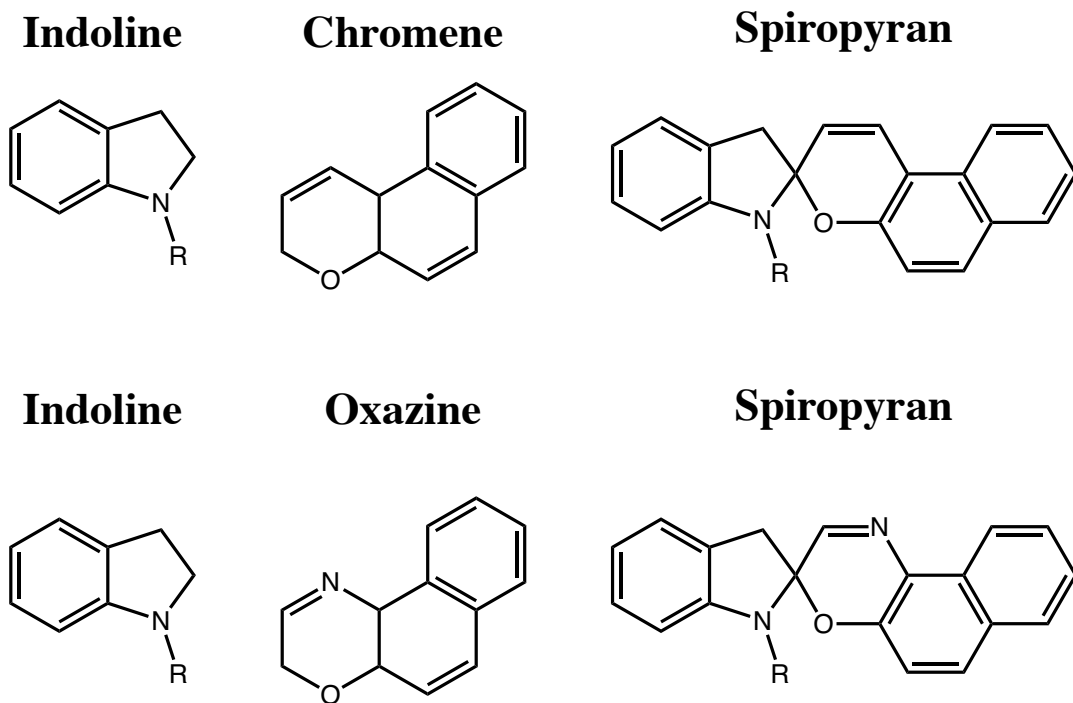


**Figure 2.1:** Spiropyran and Spirooxazine Components

Indoline and chromene or oxazine building blocks for spiropyran and spirooxazines, respectively

To better understand how molecular photoswitches function in the hopes of designing improved photoswitches for an array of applications, the characterization of the ultrafast dynamics is of paramount importance. The ultrafast dynamics of the ring opening and closing reactions of spiropyrans<sup>79-82</sup> and the ring opening reaction of spirooxazines<sup>83-96</sup> have been extensively reported. The ultrafast dynamics of ring closing reaction of spirooxazines is less studied with only a single study reported to date.<sup>97</sup> The ring opening mechanism of spiropyrans begins with the cleavage of the C<sub>indoline</sub> - O<sub>chromene</sub> bond, creating a *cis*-MC photointermediate that has been observed using transient absorption spectroscopy (Figure 2.2).<sup>78</sup> This *cis*-MC photointermediate can be represented as either a heterolytic cleavage of the C<sub>indoline</sub> - O<sub>chromene</sub> bond or as a 6 $\pi$  electrocyclic ring opening that creates a zwitterionic intermediate with a positively charged carbon and



negatively charged oxygen.<sup>78</sup> An isomerization event then occurs at the C<sub>indolone</sub> - C<sub>chromene</sub> ring, generating the *trans*-MC photoproduct. Interestingly, this photoreaction can also be initiated using two photon absorption of NIR radiation that allows for longer wavelength excitation that has higher tissue penetration, lower photoswitch degradation. The reverse ring-closing reaction is less studied but believed to be essentially the opposite of the forward reaction. In addition to being photoactivated, the reverse reaction can occur spontaneously at a high enough temperature.

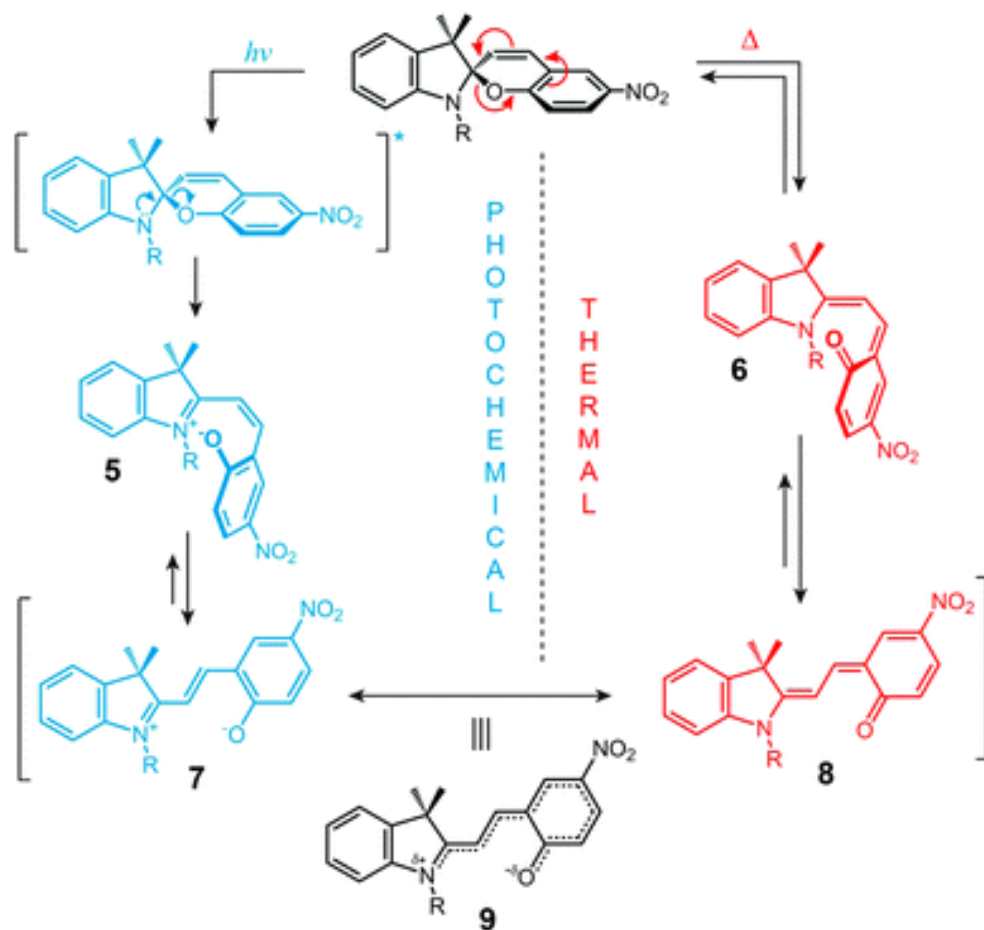


**Figure 2.2:** Spiropyran Photocycle

Spiropyran photocycle, created by Klajn.<sup>78</sup>

While the ring closed and ring open confirmations are typically the dark-adapted and light-adapted states respectively for spirooxazine systems, a negative spirooxazine with an open trans-MC dark-adapted state and a ring closed SO light adapted state was generated by adding an azahomoadamantyl group that destabilizes the closed form by overlapping the p-orbital of a nitrogen with the antibonding orbital of the C-O bond (Figure 2.3).<sup>98</sup> The ultrafast dynamics of this negative spirooxazine in conjunction with a photomagnetic spirooxazine cobalt dioxolene complex is explored in detail in Chapter 4.<sup>59</sup>

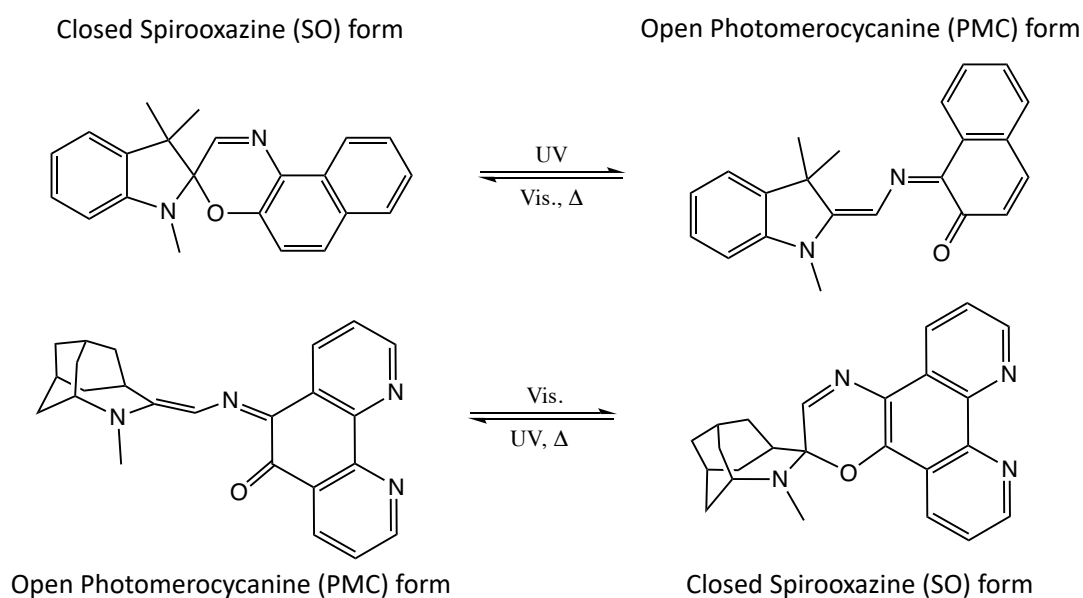


**Figure 2.3:** Positive and Negative Spirooxazine Photoswitches

Positive and Negative Spirooxazine Photoswitches

### ***Biological Photoreceptors***

While there are several different classes of biological photoreceptors as outlined in the previous chapter, only the phytochromes and rhodopsins families will be discussed here since the other families are not a part of this dissertation.

### Phytochrome Superfamily

Phytochromes are linear-tetrapyrrole (bilin)-based photoreceptors first discovered in plants where they dictate seed germination and shade avoidance by measuring the ration of red to far-red light.<sup>62</sup> Since their discovery, phytochromes were discovered to be extensively present in biological systems, appearing in algae, bacteria, and fungi as well.<sup>19-21</sup> Phytochromes measure the ratio of red to far-red light by covalently binding a heme derived linear tetrapyrrole (verdin or bilin) chromophore which reversibly photoconverts the protein between a thermally stable, red absorbing dark-adapted state with the 15Z, 15-anti conformation ( $^{15Z}P_r$ ) of the chromophore and a meta-stable far-red signaling state with the 15E, 15-anti conformation ( $^{15E}P_{fr}$ ) of the chromophore (Figure 2.4).<sup>61</sup>

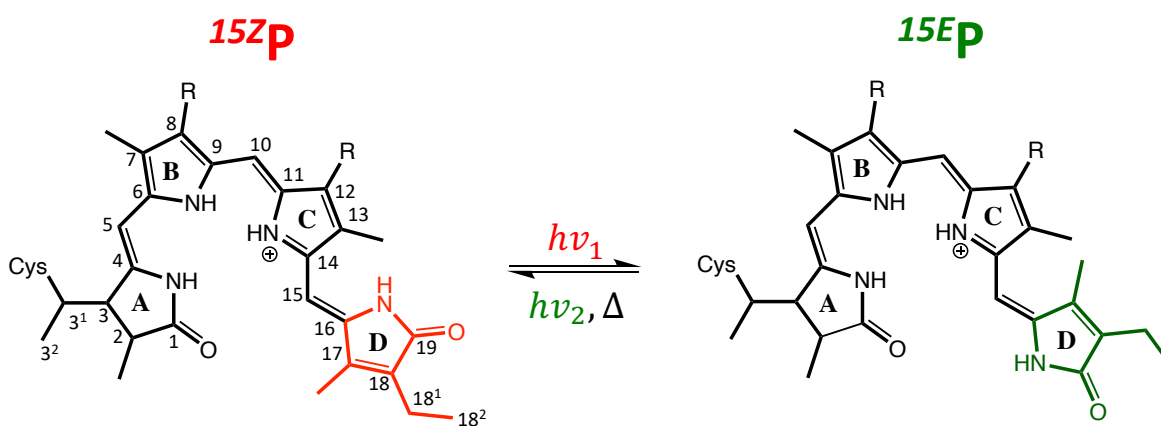


**Figure 2.4:**  $^{15Z}P$  and  $^{15E}P$  Conformations of 15-anti Phycocyanobilin

Comparison of the structures of phycocyanobilin (PCB) bilin chromophore is the  $^{15Z}P$  dark adapted (left) and  $^{15E}P$  signaling (right) states.

There are several different linear tetrapyrrole chromophores that could be bound by the highly conserved cysteine residue at either the 3<sup>1</sup> or 3<sup>2</sup> position of the chromophore. The conjugated of

the linear tetrapyrroles widely varies and accounts in part for the spectral tuning of the phytohormone superfamily. The most conjugated linear tetrapyrrole is the parental biliverdin (BV) and upon single C=C saturation can populate phytochromobilin (PΦB), 15, 16 or 18<sup>1</sup>, 18<sup>2</sup>-dihydrobiliverdin (15, 16 or 18<sup>1</sup>, 18<sup>2</sup>-DHBV), as seen in Figure 2.5. From the structures 15, 16-DHBV would restrict the conjugation the most out of the three as well as result in a photoinactive photoreceptor since there would no longer be 15E/15Z isomers. These linear-tetrapyrroles can be further saturated to generate phycoviolobin (PVB), phycoerythobilin (PEB) and phycocyanobilin (PCB) which would result in further blue shifted absorbance. It should also be noted that not all linear tetrapyrroles are typically present in biological systems. For instance 18<sup>1</sup>, 18<sup>2</sup>-DHBV is an intermediate in PCB production and has only been observed as the primary chromophore in a single protein.<sup>65</sup>

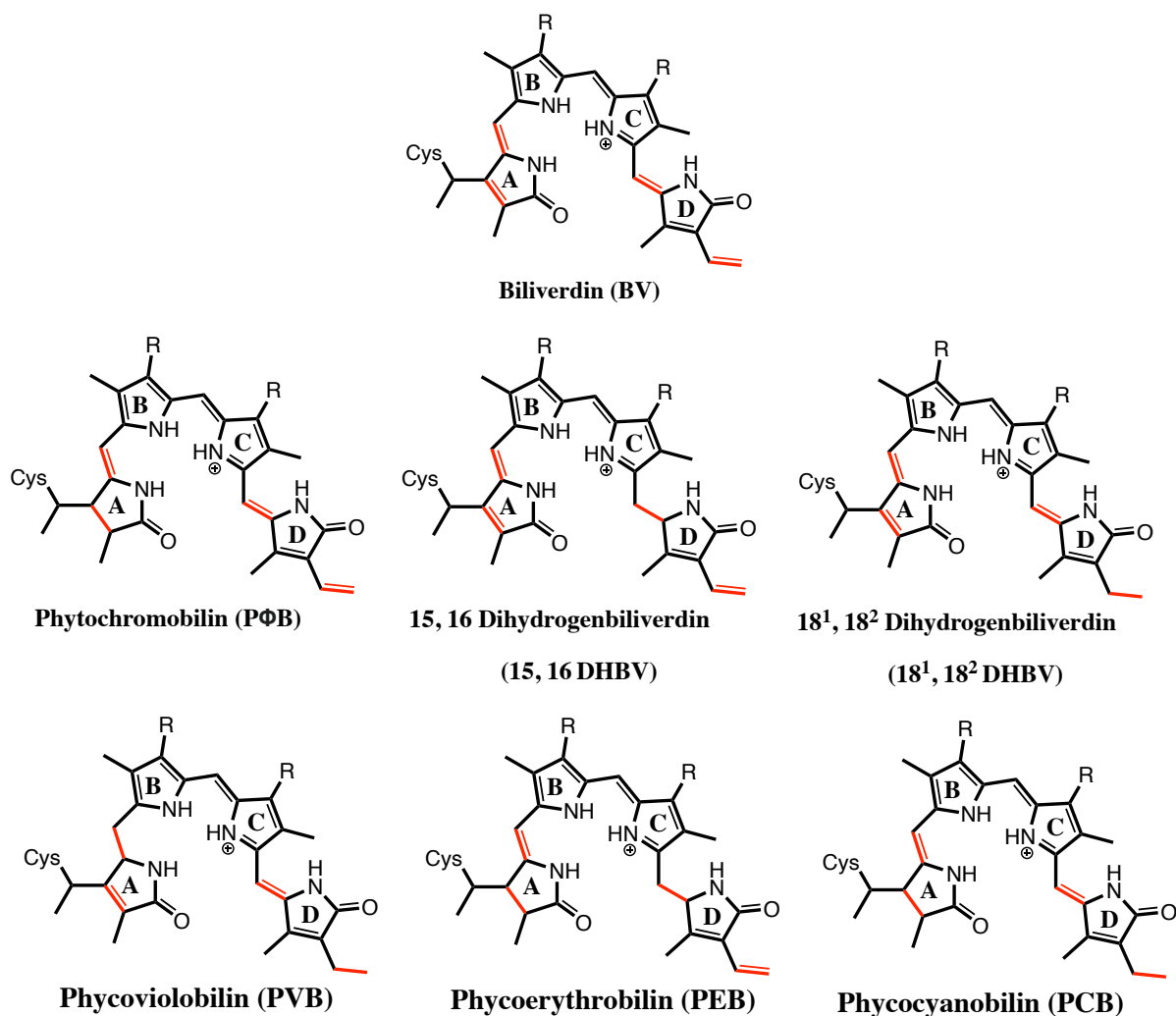


**Figure 2.5:** Structures of Several Bilin Chromophores

Structures of the Z-conformation of a few bilin chromophores where the differences of the chromophores are highlighted in red.

Within the phytochrome superfamily, there are three families which includes tri-domain, bi-domain, and uni-domain photoreceptors. The tri-domain phytochromes are composed of PAS, GAF, and PHY domains, where all three are required to bind and tailor the bilin chromophore to have reversible photoconversion between a red absorbing dark-adapted state and a far-red absorbing light-adapted state (Figure 2.6). The GAF and PHY domains are of particular

importance since the GAF domain covalently binds the linear-tetrapyrrole chromophore through highly conserved cysteine residue and the PHY domain has been shown to be essential for stabilizing the far-red absorbance by interacting with the chromophore through a salt bridge.<sup>99</sup> Within the tri-domain phytochrome family there are three subfamilies: (i) canonical plant phytochromes, (ii) bacteriophytochromes and (iii) bacterial phytochromes.

- (i) Canonical plant phytochromes typically bind the PΦB chromophore (Figure 2.5) and have red/far-red photocycles. A representative canonical plant phytochrome is oat PhyA, which was extensively studied in the 80s.
- (ii) Bacterial phytochromes (which includes cyanobacterial phytochromes [Cphs]) are found in bacteria and typically bind the PCB chromophore (Figure 2.5). One of the most studied bacterial phytochrome is cyanobacterial phytochrome 1 (Cph1) from the cyanobacterium *Synechocystis* sp. PCC6803. Cph1 has a reported structure for the full photosensory core in the <sup>15</sup>ZP<sub>r</sub> dark adapted state<sup>61</sup> and several primary dynamic studies published.<sup>100-104</sup> The secondary forward and reverse dynamics of Cph1 are discussed in detail in Chapter 8.
- (iii) Bacteriophytochromes, such as DrBphP from *Deinococcus radiodurans*, typically bind the highly conjugated BV chromophore (Figure 2.5) which results in the red shifting the photocycle of bacterial phytochromes into far-red to NIR spectral region. The lower energy excitation of bacteriophytochromes makes them attractive candidates for *in vivo* fluorescent probes due to deeper tissue penetration. As with Cph1, a structure of the photosensory module of DrBphP in the dark-adapted state has also been reported.<sup>105</sup>

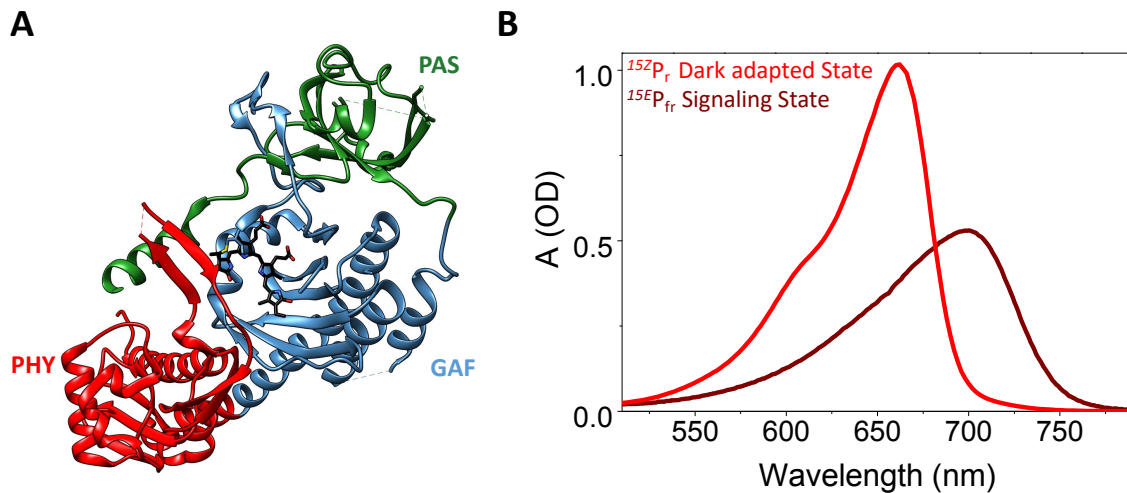


**Figure 2.6:** Representative Structure and Spectra for a Tri-Domain Phytochrome  
 Representative (A)  $^{15Z}P_r$  dark-adapted state structure (2VEA) and (B)  $^{15Z}P_r$  dark-adapted and  $^{15E}P_r$  light-adapted spectra of cyanobacterial phytochrome 1 (Cph1).

Similar to the tri-domain phytochromes, bi-domain phytochromes, aka PAS-less unknotted phytochromes, also have red/far-red photocycles, but only require GAF and PHY domains (Figure 2.7). PAS-less phytochromes include the PCB utilizing Cph1 from *Synechoccus OSB* and Cph2 from *Synechocystis* sp. PCC6803.<sup>106</sup> As with the tri-domain phytochromes, the bilin chromophore is covalently bound in the GAF domain via a highly conserved cysteine residue and the tongue of the PHY domain is responsible for generating the far-red absorbance (Figure 2.7A).

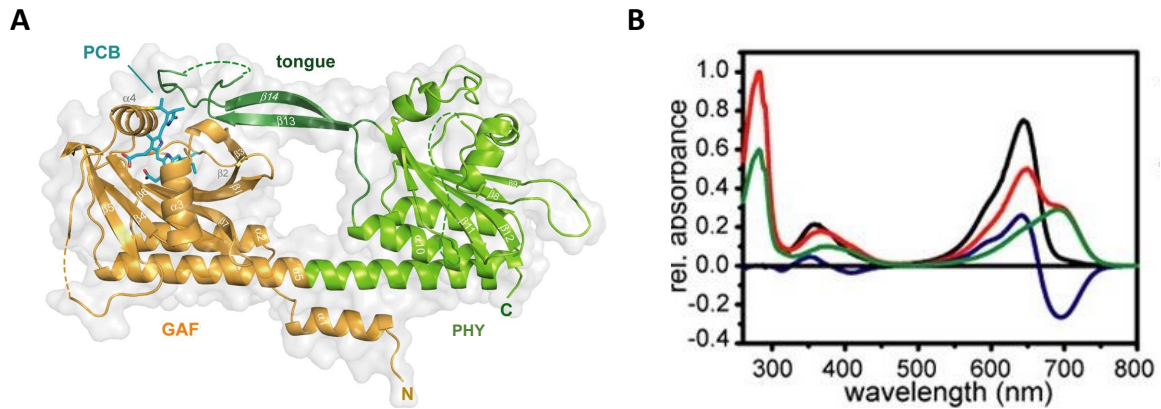


**Figure 2.7:** Representative Structure and Spectra for a Bi-Domain Phytochrome  
 Representative (A)  $^{15Z}P_r$  dark-adapted state structure (4BWI) and (B)  $^{15Z}P_r$  dark-adapted and  $^{15E}P_{fr}$  light-adapted spectra of cyanobacterial phytochrome 2 (Cph2) modified from Anders et al.<sup>107</sup> In the spectra, the black, red, and green spectra correspond to  $^{15Z}P_r$ ,  $^{15E}P_{fr}$ , and  $^{15Z}P_r - ^{15E}P_{fr}$ , respectively.

Single domain phytochromes or cyanobacteriochromes (CBCRs) are bilin-based photoreceptors distantly related to plant phytochromes that only require a single GAF domain to covalently bind a linear tetrapyrrole chromophore via a highly conserved cysteine residue as well as exhibit reversible and diverse photoactivity spanning the near ultraviolet (NUV) to the far-red spectral regions (Figure 2.8). While most phenotypes of CBCRs have yet to be determined, some CBCRs have been reported to be involved in phototaxis<sup>22-24</sup> and chromatic acclimation<sup>25, 26</sup> to improve the efficiency of photosynthesis. The diverse photoactivity of CBCRs coupled with their relatively small size (100-200 amino acids) and resolved phenotypes has made them attractive candidates to serve as a basis for the development of novel biological tools. Given this great diversity in photoactivity and mechanisms, several subfamilies of CBCRs have been identified, including the canonical red/green (NpR6012g4),<sup>69</sup> noncanonical red/green (NpR3784),<sup>70</sup> noncanonical orange/green (NpF2164g7),<sup>69</sup> green/red (RcaE),<sup>71</sup> insert-cysteine (NpF2164g3),<sup>68, 72</sup> DXCF



(Tlr0924),<sup>68</sup> and far-red/x (Anacy\_2551g3)<sup>63, 65</sup> CBCRs. Using NpR6012g4 from *Nostoc punctiforme* as an example, the CBCR domain nomenclature typically follows: Np is the bacteria that the CBCR is isolated from (*Nostoc punctiforme*), R is the directionality of the DNA and can be right (R), left (L), forward (F), or backward (B); 6012 is the gene number; and g# represents that it is the #th tandem CBCR domain.

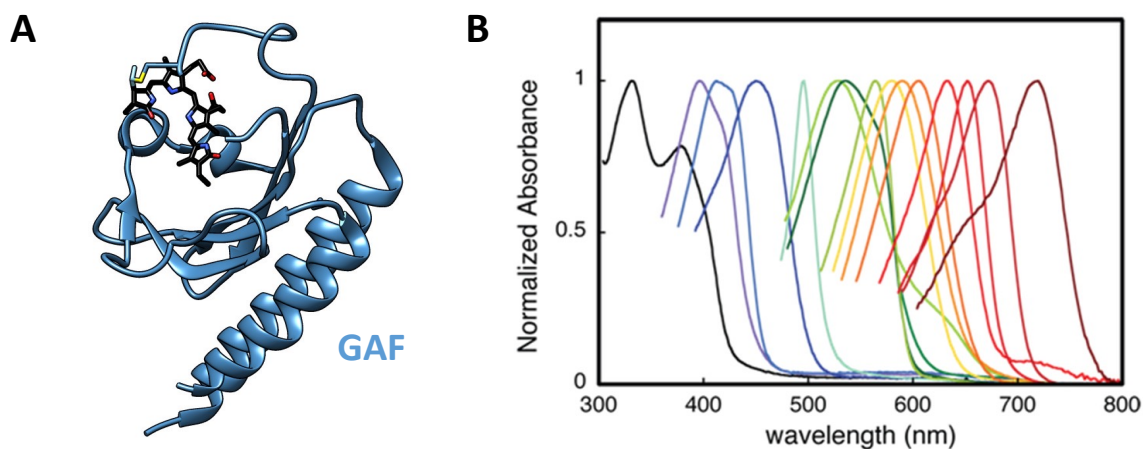


**Figure 2.8:** Representative Structure and Diverse Photoactivity of CBCRs

Representative (A) <sup>152</sup>P<sub>r</sub> dark-adapted state structure (6GHN) of NpR6012g4 and (B) spectral comparison of several CBCR domains, emphasizing the great photoactivity diverse of the CBCR family. Figure courtesy the Lagarias Lab.

The CBCR family owes its great spectral diversity to the utilization of different bilin chromophores with varying conjugation length (Figure 2.5) and diverse photoinduced chemistry including changes in the structural conformation, protonation state, and number of cysteine linkages to the chromophore. While the CBCRs studied in this dissertation typically utilize the phycocyanobilin (PCB; Figure 2.5) chromophore, other bilin chromophores with altered conjugation lengths such as phycoviolobin (PVB),<sup>64</sup> biliverdin (BV) and 18<sup>1</sup>, 18<sup>2</sup>- dihydrogenbiliverdin (DHBV)<sup>63, 65</sup> have also been reported (Figure 2.5). Diversity in the PCB chromophore has also been reported where

solution NMR spectroscopy resolved that NpR6012g4, a red/green CBCR, has the chromophore in a relatively planar 15Z, 15-anti conformation in the red absorbing dark-adapted state and a severely distorted 15E,15-anti conformation in the light adapted state.<sup>108</sup> In contrast, the green absorbing dark-adapted state of RcaE ( $^{15Z}P_g$ ) was attributed to chromophore deprotonation at either the B or C-ring nitrogen group and the red absorbing light-adapted state ( $^{15E}P_r$ ) was reported to be fully protonated and adopt a more cyclic all-syn conformation.<sup>109</sup> The all-syn chromophore conformation may be present in the dark-adapted state as well for RcaE and was also observed in the far-red absorbing dark-adapted state ( $^{15Z}P_{fr}$ ) of Anacy\_2551g3<sup>67</sup> where it is believed to stabilize unique protein-chromophore interactions that are responsible for generating the far-red absorbance. Lastly, CBCRs with significantly blue-shifted absorbance between the near-UV to blue spectral regions the absorbance were reported to typically have dual cysteine linkages to the C10 of the bilin of the chromophore that breaks the conjugation between the B and C rings.<sup>66, 110</sup> Two CBCR families that utilize secondary cysteine linkages have been identified where the DXCF family converts PCB to PVB and has a conserved Asp-Xaa-Cys-Phe (DXCF)<sup>64, 66, 68</sup> motif and a secondary linkage to the chromophore occurring in either the dark-adapted or light-adapted state and the insert-cysteine that does not produce PVB, occurs only in the dark-adapted state, and has the secondary cysteine located in an insertion in the protein fold.<sup>68</sup>

The mechanism of the reversible photoconversion of CBCRs between a thermally stable dark-adapted state and a meta-stable light-adapted state is multifaceted and involves multiple transient intermediate populations. Given the complexity of the photoconversion pathways, an overview of the nomenclature outlined by Gottlieb et al.<sup>111</sup> as well as a simplified photocycle model for red/green CBCRs (Figure 2.9) is provided below. The parental dark-adapted and light-adapted

states are symbolized by a capital “P” and has the chromophore conformation (typically 15Z for the dark-adapted state and 15E for the light-adapted state) in the preceding superscript and wavelength region of absorbance (i.e., ‘r’ for ‘red’) in the following subscript ( $^{15Z}P_r$ ). Upon photoexcitation of the dark-adapted  $^{15Z}P_r$  state, the resulting  $^{15Z}P_r^*$  excited state can either decay back to the ground state via radiant or non-radiant pathways<sup>112</sup> or populate the initial Lumi- $R_f$  photointermediate where ‘R’ is the wavelength region of the starting parental state absorbance and ‘f’ is the wavelength region of the Lumi intermediate absorbance. Ultrafast IR and UV-Vis studies indicate that this process occurs on the ps-ns timescale and suggesting that Lumi- $R_f$  has the isomerized chromophore.<sup>113</sup> This change in the chromophore structure initiates further change in the protein structure, resulting in the population of several secondary Meta- $R_x$  intermediates until the protein structure has the form of the light-adapted ( $^{15E}P_g$ ) state.<sup>108</sup> While this process also applies to the reverse reaction, the dark-adapted state can also recover thermally via the currently not well understood mechanism of dark reversion.

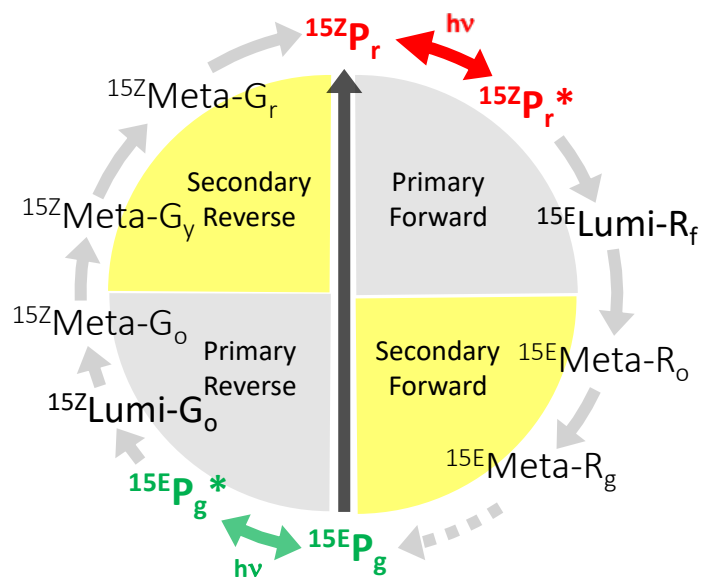


**Figure 2.9:** Red/Green CBCR Generalized Photocycle

Generalized red/green photocycle. The central black arrow going from  $^{15E}P_g$  to  $^{15Z}P_r$  represents dark reversion from the light state to the dark state.

The photodynamics of several phytochromes and CBCRs has been reported as outlined in Table 2.1. In this body of work, the photodynamics of a cyanobacterial phytochrome as well as several red/green and far-red/x CBCRs will be discussed in detail in Chapters 5-9.

**Table 2.1:** List of Phytochromes and CBCR with reported Photodynamics  
A list of phytochrome subfamilies that have representatives with reported photodynamics.  
Original table courtesy of Dr. Julia S. Kirpich.

Phytochrome Family		Organism	Protein
I Plant Phytochrome		Oat	PhyA <sup>114-125</sup>
		Pea	Phy <sup>126-131</sup>
		Maize	Phy <sup>132</sup>
		Cucumber	Phy <sup>132, 133</sup>
		Potato	PhyA <sup>134</sup>
		Potato	PhyB <sup>134</sup>
II Cyanobacterial Phytochrome I (also called Cphs)		<i>Synechocystis</i> sp. strain PCC 6803	Cph1 <sup>73, 101-104, 113, 135-150</sup>
		<i>Tolypothrix</i> PCC7601	CphA <sup>124</sup>
		<i>Calothrix</i> sp. PCC7601 ( <i>Fremyella diplosiphon</i> )	CphA <sup>151, 152</sup>
		<i>Calothrix</i> sp. PCC7601 ( <i>Fremyella diplosiphon</i> )	CphB <sup>152</sup>
III Bacteriophytochrome		<i>Agrobacterium fabrum</i> C58	Agp1 (or AtBphP1) <sup>153-156</sup>
		<i>Agrobacterium fabrum</i> C58	Agp2 (or AtBphP2) <sup>157</sup>
		<i>Deinococcus radiodurans</i>	DrBphP <sup>158, 159</sup>
		<i>Deinococcus radiodurans</i>	DrCBD <sup>160, 161</sup>
		<i>Rhodopseudomonas palustris</i>	BphP1-FP <sup>162</sup>
		<i>Rhodopseudomonas palustris</i>	iRFP670 <sup>162</sup>
		<i>Rhodopseudomonas palustris</i>	iRFP682 <sup>162</sup>
		<i>Stigmatella aurantiaca</i>	SaBphP1 <sup>163</sup>
		<i>Rhodopseudomonas palustris</i>	iRFP702 <sup>164</sup>
		<i>Rhodopseudomonas palustris</i>	iRFP713 <sup>164</sup>
		<i>Rhodopseudomonas palustris</i>	iRFP720 <sup>164</sup>
		<i>Agrobacterium tumefaciens</i> C58	PAiRFP1 <sup>46</sup>
		<i>Agrobacterium tumefaciens</i> C58	PAiRFP2 <sup>46</sup>
		<i>Rhodopseudomonas palustris</i>	RpBphP2 <sup>99, 165, 166</sup>
		<i>Rhodopseudomonas palustris</i>	RpBphP3 <sup>112, 167, 168</sup>
	<i>Pseudomonas aeruginosa</i>	PaBphP <sup>165, 169, 170</sup>	
IV PAS-less 'Knotless' Phytochromes		<i>Synechocystis</i> sp. strain PCC 6803	Cph2 <sup>107, 171-173</sup>
		<i>Synechococcus</i> sp. OS-A and OS-B'	SyBCph1 (OS-B') <sup>174, 175</sup>
V Cyanobacteriochromes	Canonical red/green	<i>Nostoc punctiforme</i>	NpF2164g5 <sup>176</sup>
		<i>Anabaena</i> sp. PCC 7120	AnPixJg2 <sup>29, 177, 178</sup>
		<i>Nostoc punctiforme</i>	NpAF142g2 <sup>27, 28, 176, 179</sup>
		<i>Nostoc punctiforme</i>	NpF2164g4 <sup>27, 28, 176, 179</sup>
		<i>Nostoc punctiforme</i>	NpF2164g6 <sup>27, 28, 176, 179, 180</sup>
		<i>Nostoc punctiforme</i>	NpF2854g3 <sup>27, 28, 176, 179</sup>
		<i>Nostoc punctiforme</i>	NpR1597g4 <sup>27, 28, 176, 179, 181</sup>
		<i>Nostoc punctiforme</i>	NpR4776g2 <sup>27, 176, 179</sup>
		<i>Nostoc punctiforme</i>	NpR4776g3 <sup>27, 28, 176, 179</sup>
		<i>Nostoc punctiforme</i>	NpR5113g2 <sup>28, 176, 181</sup>
	<i>Nostoc punctiforme</i>	NpR6012g4 <sup>27, 28, 73, 179, 181-184</sup>	
	Orange/green	<i>Synechocystis</i> sp. PCC6803	Slr1393 <sup>185, 186</sup>
	Non-canonical red/green	<i>Nostoc punctiforme</i>	NpF2164g7 <sup>187</sup>
	Green/red	<i>Fremyella diplosiphon</i>	RcaE <sup>181, 190-192</sup>
	Far/red CBCRs	<i>Anabaena cylindrica</i> PCC 7122	Anacy 2551g3*
		<i>Leptolyngbya</i> sp. JSC-1	JSC1 58120g3β**
		<i>Synechocystis</i> sp. PCC 6803	Syn7502 01757**
		<i>Synechocystis</i> sp. PCC 6803	Syn7437 1656**
	DXCF	<i>Thermosynechococcus elongatus</i>	Thr0924 <sup>193-195</sup>
	<i>Oscillatoria acuminata</i> PCC 6304	Oscil6304 2705 <sup>196</sup>	
Insert-cys	<i>Nostoc punctiforme</i>	NpF2164g3 <sup>111</sup>	
DXCF + Insert-Cus	<i>Moorea producens</i>	LYNGBM3L 56870 g6**	

Dynamics are in preparation and either \*discussed or \*\*not in this dissertation

Since this dissertation focuses on the canonical red/green CBCRs, a short overview of relevant information not discussed in detail in the canonical red/green CBCRs chapters (5-8) is given below. To date, the red/green CBCR, NpR6012g4 is the most studied CBCR with several dynamic studies<sup>39, 169-171, 173-176</sup> as well as ten possible structures for both the dark-adapted and light-adapted states resolved via solution NMR.<sup>108</sup> Ames and co-workers reported that the red absorbing dark-adapted state of NpR6012g4 has a 15Z, 15-anti chromophore conformation and that the green absorbing signaling state has a 15E, 15-anti chromophore conformation coupled with severe structural deformation of the D-ring (Figure 2.10). This increase in structural deformation is believed to be the cause of the green absorbance of the light-adapted state and was attributed by Rockwell et al. to two highly conserved phenylamine residues.<sup>197</sup> This topic is discussed in great detail in Chapters 5-8.

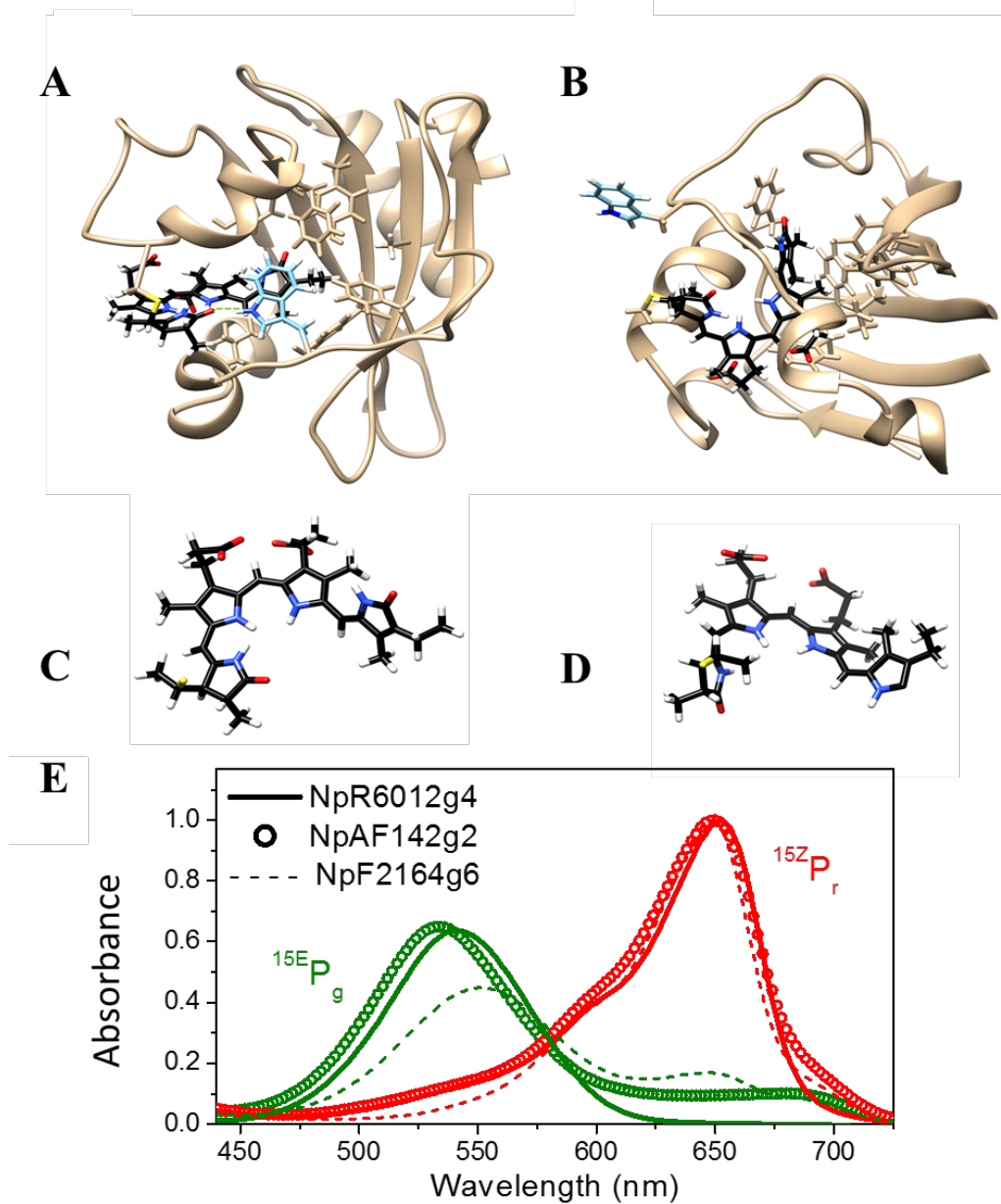


**Figure 2.10:** Comparison of the dark adapted and Signaling States of NpR6012g4  
 The dark-adapted (6BHN) and signaling (6BHO) state structures of NpR6012g4 are compared in A and B. This figure was adopted from Jenkins et al.<sup>27</sup>

The secondary (1 ns – 1 ms) forward and both the primary (150 fs – 10) and secondary reverse dynamics are extensively discussed in Chapters 4-6. In the primary forward dynamics of NpR6012g4, Kim et al.<sup>182</sup> resolved excited state heterogeneity that was later suggested by Kirpich

et al.<sup>29</sup> to be associated with the three rotamers of Tyr624 (Figure 2.11) where: (i) 50% of the solution NMR structures had Tyr624 perpendicular to the D-ring of the chromophore where it would inhibit the isomerization event and result in the unproductive excited state population. (ii) 30% of the structures have Tyr624 pointing away from the chromophore where there would be unimpeded D-ring isomerization and was associated with the faster evolving productive excited state population. (iii) 20% of the structures had the Tyr624 residue pointing to and in parallel to the D-ring of the chromophore which may restrict the D-ring isomerization and was associated with the slower evolving excited state subpopulation. Interestingly, Kim et al.<sup>184</sup> resolved that not only the excited state populations evolves into the Lumi-R<sub>f</sub> photointermediate and that a reactive GSI was in part responsible for the relatively large forward quantum efficiency of NpR6012g4. Later, these reactive GSI were later reported by Chang et al.<sup>180</sup> to not be a conserved feature in the forward reaction of high yielding CBCRs. In a multi-domain study, Gottlieb et al. resolved that on the primary timescale (150 fs – 8 ns) multi-phasic excited state evolution is a conserved mechanism of the forward reaction of red/green CBCRs and that there were three unique classes separated based on the kinetics where Class-I<sub>F</sub> resolved no Lumi-R intermediate population, Class-II<sub>F</sub> involved the population of a red shifted Lumi-R<sub>f</sub>, as observed in NpR6012g4, and Class-III<sub>F</sub> resolved the evolution of a Lumi-R<sub>f</sub> intermediate to a blue shifted Meta-R<sub>o</sub> intermediate. As discussed in depth in Chapter 4, this blue shifting extends into the secondary forward dynamics where a nearly conserved mechanism of monotonic blue-shifting from Lumi-R<sub>f</sub> to the <sup>15E</sup>P<sub>g</sub> signaling state was observed.<sup>27</sup> The multi-CBCR study also resolved a positive correlation between <sup>15Z</sup>P<sub>r</sub> peak wavelength and Lumi-R<sub>f</sub> quantum yield which may be due to differing hydrogen bonding networks resolved and associated with the fluorescent and photoactive <sup>15Z</sup>P<sub>r</sub> subpopulations in the related bacterial phytochrome Cph1 by Kirpich et al.<sup>100</sup>



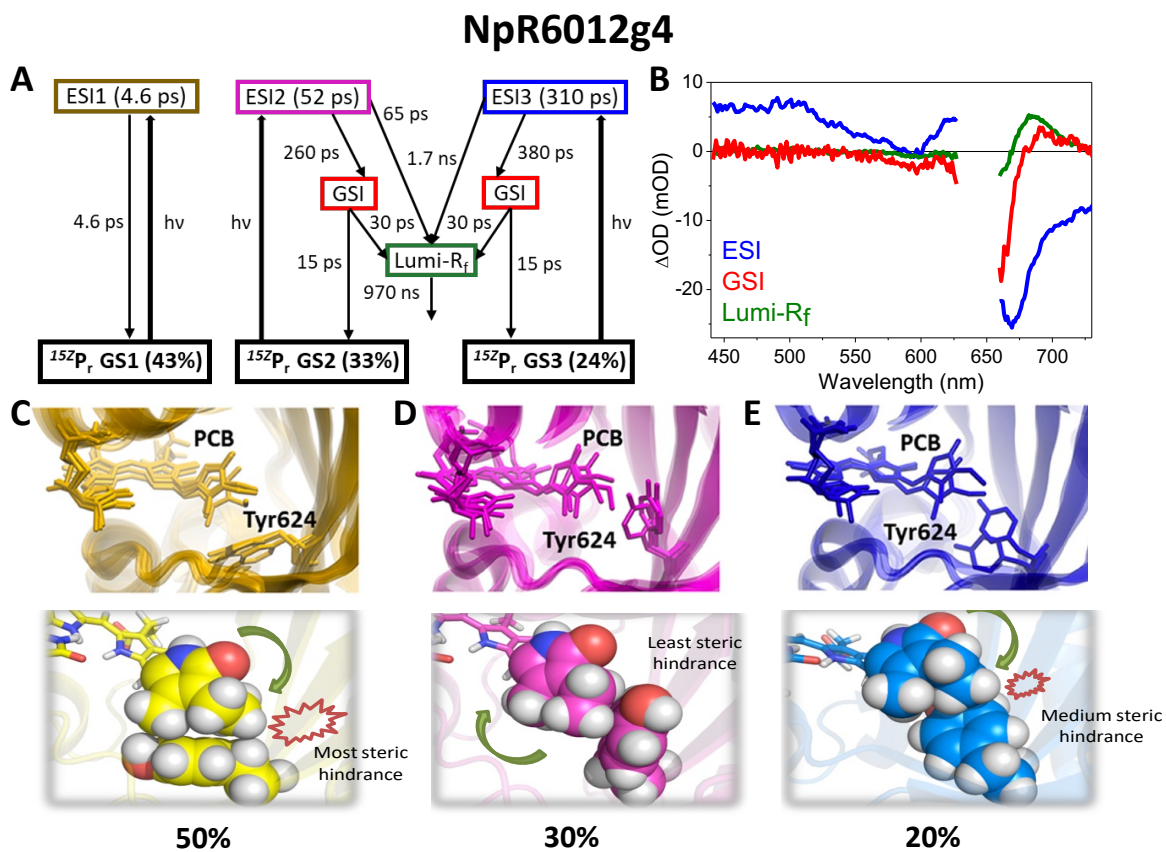


**Figure 2.11:** Correlating Excited State Kinetic Heterogeneity to Tyr Rotamers in NpR6012g4

(A, B) Target model and resulting SADS for the primary dynamics of NpR6012g4 proposed by Kim et al.<sup>182, 184</sup> displaying heterogeneous evolution of spectrally homogeneous  $^{15Z}P_r^*$  populations that were correlated to (C-E) Tyr624 rotamers by Kirpich et al.<sup>29</sup> This figure was adapted from Kirpich et al.<sup>29</sup>

### *Opsins & Semisynthetic Human Cellular Retinoic Acid Binding Protein II Rhodopsin Mimics*

Opsins are a class of photoreceptor proteins that utilize a retinal chromophore (Table 1.2, Figure 2.12) and is broken down into two types: Type I (microbial or bacterial opsins) and Type II (animal opsins). Despite Type I and Type II opsins having negligible sequence similarities, both utilize a seven-transmembrane helix structure (7TM) that has both the C terminus located outside of the cell and the N terminus located inside of the protein.<sup>198, 199</sup> The retinal chromophore is bound to

the protein through a Schiff-base (RSB) linkage to a conserved Lys residue in the middle of the seventh transmembrane crossing (TM7). Rhodopsins are of inherent interest because they have been reported to be highly efficient biological processes and have been incorporated into photogate ion pumps, ion channels, and light sensors in bacteria<sup>198</sup> as well as vision and maintenance of the circadian clock in animals.<sup>199</sup> Given the high efficiency, wavelength tuneability, and resolved phenotypes of rhodopsin photoreceptors, they have already been implemented as optogenetic tools to study neural circuits and to control the firing and deactivation of neuron cells.<sup>52-55, 200-204</sup>

While both microbial and animal rhodopsins utilize the  $\beta$ -carotene derived retinal chromophore to under photoconversion between the thermally stable dark-adapted state and a meta-stable light-adapted state, they undergo different photoinduced isomerization mechanisms. Microbial rhodopsins involve an isomerization reaction at the C13=C14 double bond and has the all-*trans*-retinal configuration in the dark-adapted state and 13-*cis*-retinal configuration in the light-adapted state (Figure 2.12). In contrast, animal rhodopsins have the isomerization reaction at C11=C12 double bond and has the 11-*cis*-retinal configuration in the dark-adapted state and all-*trans*-retinal configuration in the light-adapted state.<sup>205</sup> While both microbial and animal rhodopsins typically have a protonated Schiff base in the dark-adapted states, the light-adapted state of animal rhodopsins typically have a deprotonated Schiff base where as microbial rhodopsins remain protonated.

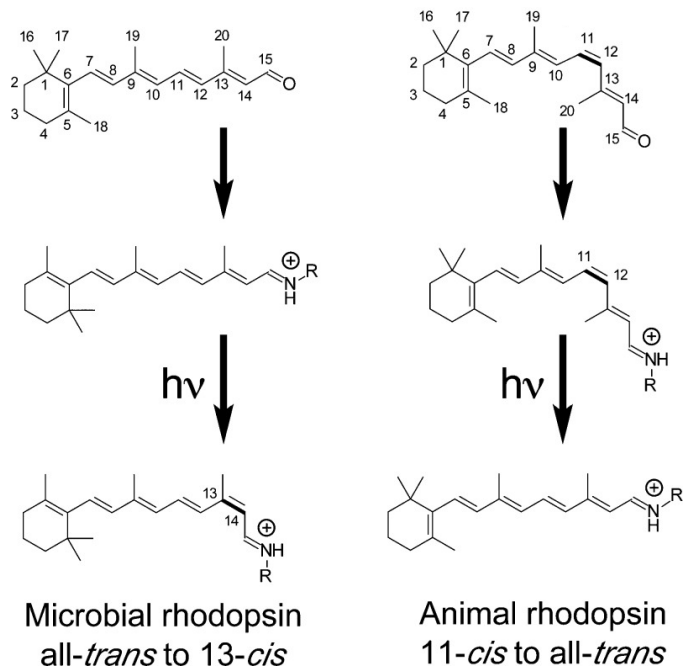


**Figure 2.12:** Microbial and Animal Retinal Chromophores

Microbial and Animal Retinal Chromophores modified from Ernst et al.<sup>205</sup>

An example of a microbial rhodopsin photocycle using channelrhodopsin-2 (ChR2) as a representative system is provided in Figure 2.13. The photoisomerization around the C13=C14 double bond in microbial rhodopsins typically occurs on a femtosecond to picosecond timescale and results in the population of the initial photointermediate, P500. P500 exhibits a slight red shift compared to the ground state due to restructuring of the protein to prepare for the deprotonation step that results in P390. P390 evolves to P520 that is believed to involve a re-protonation and restructuring of the chromophore that results in the initiating of biological responses. The reverse photoreaction is reported to be simpler than the forward and involved a single photointermediate, Des480, before populating the dark-adapted state (D470).

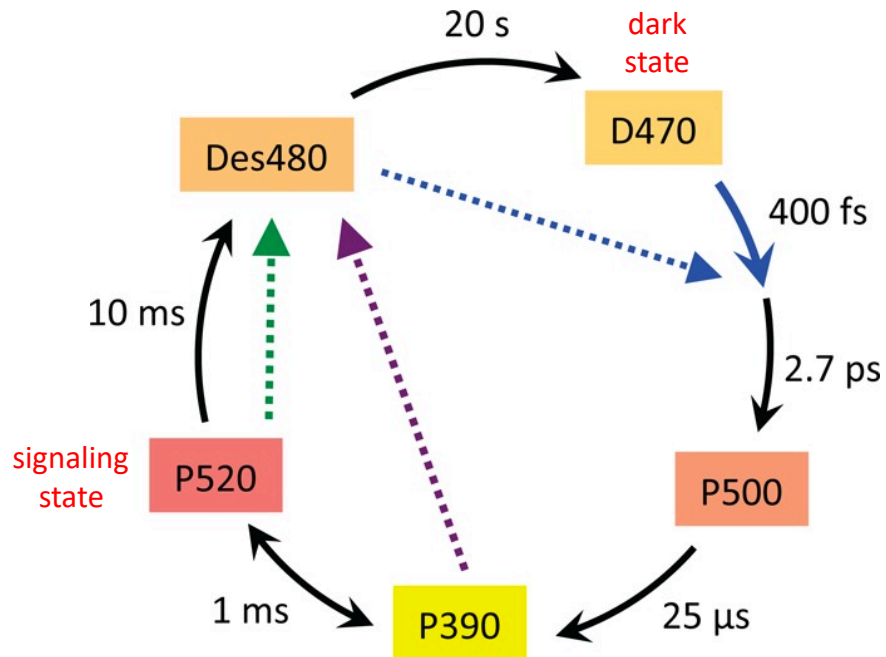


**Figure 2.13:** Microbial Rhodopsin Photocycle

Example of a microbial rhodopsin photocycle using bacteriorhodopsin modified from Ernst et al.<sup>205</sup>

As with microbial rhodopsins, the initial photoisomerization reaction of a representative animal rhodopsin, bovine rhodopsin, is completed on a femtosecond timescale. Upon photoisomerization to all-*trans*-retinol, bovine rhodopsin progresses through a mechanism of nonmonotonic spectral evolution where a primary intermediate (photorhodopsin) red shifted of the dark-adapted state evolves through a series of monotonic blue shifted intermediates on the ns to μs timescale. The evolution of meta I to the Meta II signaling state involves large structural changes and a deprotonation event. Meta II acts as an agonist-bound active receptor that catalyzes GDP/GTP, initiating a signaling cascade.

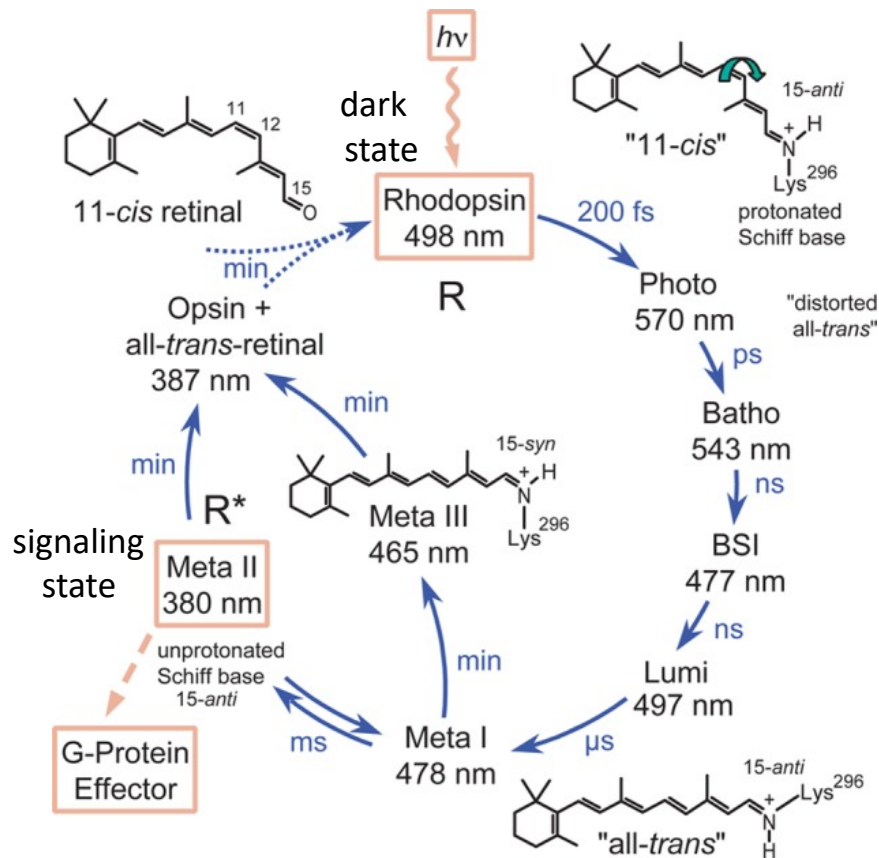


**Figure 2.14** Animal Rhodopsin Photocycle modified from Ernst et al.

Example of an animal rhodopsin photocycle using bovine rhodopsin modified from Ernst et al.<sup>205</sup>

While microbial rhodopsin (Type 1) has established reversible photoconversion, it is not conserved in animal rhodopsin (Type II), which requires the all-*trans* retinal chromophore to unbind from the opsin and be converted back to 11-*cis*-retinal externally. Initially retinal is reduced to retinol by retinol dehydrogenase and transported outside of opsin and to adjacent retinal pigment epithelial cells (RPE). In the RPE three steps are accomplished: (i) esterification of the chromophore to is accomplished by lecithin/retinol acyltransferase. (ii) all-*trans*-retinol is converted to 11-*cis*-retinol by retinoid isomerohydrolase (RPE65). (iii) The 11-*cis*-retinol is converted to then 11-*cis*-retinal by 11-*cis*-RDH.<sup>205, 206</sup> This irreversibility of the photoinduced dynamics of animal rhodopsin has

made the collection and replication of dynamic data on these systems more complicated and sensitive.

One important aspect of rhodopsins is the wavelength tuneability that allows for diverse photosensitivity to an array of wavelengths and selective excitation such as color vision (blue,  $\lambda_{\max} = \sim 425$  nm; green,  $\lambda_{\max} = \sim 530$  nm; red,  $\lambda_{\max} = \sim 560$  nm) and vision in dim light (rhodopsins,  $\lambda_{\max} = \sim 500$  nm). Given that these opsins all utilize the same chromophore implies that this spectral diversity arises from interactions of the chromophore with the protein. A few factors of wavelength have been identified, such as (i) protonation state of the chromophore, (ii) chromophore and protein electrostatic interactions. While deprotonation of the chromophore typically results in a blue shifting in the chromophore absorbance, chromophore and protein electrostatic interaction are more varying and typically incorporate the counteranions of the retinol chromophore since the retinal chromophore is protonated in the ground state. In the excited state, there is great charge transfer character to the  $\beta$ -ionone ring, resulting in a neutralization of the Schiff base. Interaction between counteranions and the protonated positive Schiff base stabilizes the ground state relative to the excited state. If the counteranions are near the  $\beta$ -ionone ring, then the excited state would be stabilized relatively to the ground state, red shifting the absorbance. It has been reported for bacteriorhodopsin that Asp85 and Asp212 are typically deprotonated and are effective counterions to the protonated Schiff base. These electrostatic interactions between these negatively charged amino acids and  $\pi$ -electrons destabilized the energy of the electronic excited state, blue shifting the absorbance.<sup>207</sup> It is believed that isolation between the chromophore and protein results in a red shift of absorbance since counteranions perturbs the delocalization of the positive charge of the polyene.<sup>208</sup>

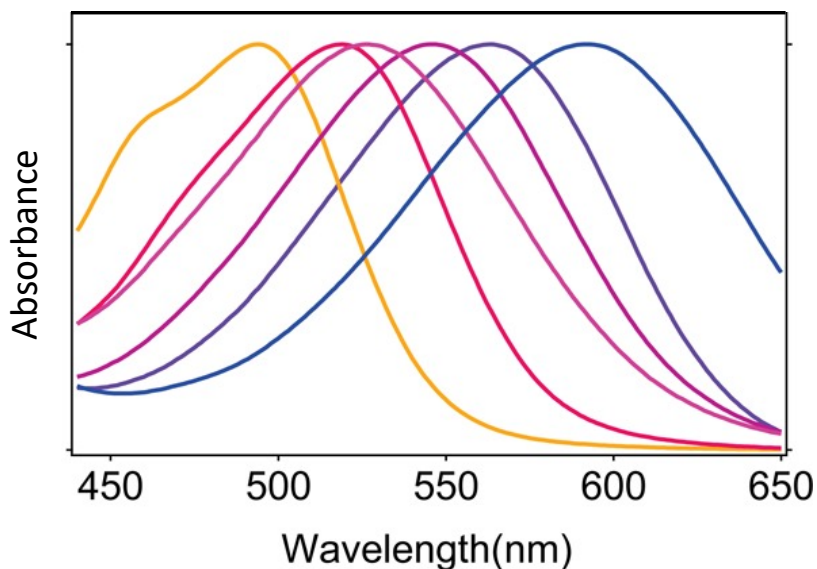


**Figure 2.15** Microbial Rhodopsin Diverse Photoactivity

Microbial rhodopsin diverse photoactivity modified from Ernst et al.<sup>205</sup>

To better understand wavelength tuning and develop novel optogenetic tools, rhodopsin mimics using modified human cellular retinoic acid binding protein II (hCRABPII) were generated and shown to have reversible photoconversion.<sup>74-76</sup> One of these mimics, was a triple mutant of CRAPBII (KLE CRABPII),<sup>76</sup> which was characterized using quantum mechanics/molecular mechanics (QM/MM) and ultrafast transient absorption spectroscopy.<sup>209</sup> These CRAPBII mimics differ from natural rhodopsins, by being much smaller and allowing for hydration of the chromophore pocket.<sup>209</sup> Since these artificial rhodopsins are photo-reversible, they provide an opportunity to more easily study the biological basis of wavelength tuning and the underlying photo-mechanisms of retinal incorporating photoreceptors. Both of these topics are explored more in depth in Chapter 10 where the photocycle of an octomutant of CRABPII was explored using spectroscopic and computational methods.

## Chapter 3. Methods and Experimental Protocols

The molecular photoswitch and photomagnetic photoswitch were synthesized by the Frank Lab at University of Victoria, all phytochrome and cyanobacteriochrome (CBCR) samples were prepared by the Lagarias Lab at UC Davis, and the hCRABPII rhodopsin mimic were prepared by the Geiger and Borhan Labs at Michigan State University. These collaborations allowed the Larsen Lab to study all these systems using transient absorption and cryokinetic spectroscopies to identify mechanisms and elucidate protein-chromophore interactions that result in various phenomena such as wavelength tuning and manipulation of the efficiencies of the various photoinduced pathways. The experiments presented here would not have been possible without the efforts of Ms. Aiko and Prof. Frank of the Frank Lab, Ms. Shelley S. Martin, Dr. Nathan Rockwell, and Prof. J. Clark Lagarias of the Lagarias Lab and Dr. Alireza Ghanbarpour and Prof. James H. Geiger of the Geiger Lab.

To engineer tools with desired traits, such as high photoproduct quantum yield for the use as spintronic or optogenetic tools or high fluorescence for use as fluorescent probes, a molecular level understanding of the underlying dynamics of these photoswitching systems is of paramount importance. The dynamics of these photoswitches were characterized using transient absorption (TA) and cryokinetic UV-vis absorption spectroscopies coupled with global analysis methods, where ultrafast (150 fs – 10 ns) TA spectroscopy yielded information of the excited state dynamics that dictates initial efficiencies of the various pathways and long-time (1 ns – 1 ms) TA and cryokinetic UV-Vis absorption spectroscopies gave mechanistic information of the progression of the initial photointermediates captured in the ultrafast dynamics to the generation of the photoproduct.



### ***Molecular Photoswitch and Photomagnetic Molecular Photoswitch Sample Preparation***

The molecular photoswitch (APSO) and photomagnetic molecular photoswitch (CoAPSO) samples were prepared by the Frank Lab at University of Victoria as outlined below.<sup>48, 98</sup> APSO synthesis was conducted initially under inert conditions using traditional Schlenk techniques and finished in an aerobic environment. Triethylamine (280  $\mu$ L, 1.2 equiv.) was added to a chilled solution of 4,5-Dimethyl-4-azahomoadamant-4-enium iodide (454 mg, 1.5 mmol) and dimethylformamide and the resulting mixture was stirred for 30 min. Afterwards, 5-Hydroxy-6-nitroso-1,10-phenanthroline (335 mg, 1.5 mmol) and molecular sieves (4Å) were added, and the mixture was allowed to warm to 22 °C prior to being heated to 65°C for 3 hr. Over the course of the heating the color of the solution became purple and once the heating time was up the solution was allowed to cool to room temperature. The solvent was then removed *in vacuo* and the purple solid was taken up in CH<sub>2</sub>Cl<sub>2</sub> (60 mL), filtered, washed with two aliquots of 10 mL of water, and dried over MgSO<sub>4</sub>. The solvent was removed *in vacuo* and the APSO was pre-purified by column chromatography (neutral Al<sub>2</sub>O<sub>3</sub>, CH<sub>2</sub>Cl<sub>2</sub> eluent) before recrystallization from acetone over 12 hrs. This resulted in green crystals which were isolated, washed with cold ethyl acetate, and dried under vacuum.

APSO was then also used for the synthesis of CoAPSO where 33 mg (0.95 equiv.) was slowly added over the course of five minutes to [Co(3,5-DTBSQ)<sub>2</sub>(py)<sub>2</sub>] (60 mg, 0.09 mmol, 1.00 equiv.). The resulting solution was stirred for 8 hrs. and then left for 12 hrs. Fine purple needles were generated and isolated by filtration, washed with diethyl ether (2 x 5 mL) and pentane (2 x 5 mL) and dried *in vacuo*. While the resulting purple microcrystalline solid is stable in air and can be handled under aerobic conditions, as soon as it is dissolved it is highly oxygen sensitive. Seeing as

such, dried pellets were shipped to UC Davis for the ultrafast dynamics studies and dissolved in degassed toluene in a N<sub>2</sub> glove box to give an approximate maximum absorbance of 0.5 OD at the pathlength of the cuvette. The cuvette was capped prior to removal from the glovebox and sealed with black wax immediately upon removal. The APSO samples used in the ultrafast dynamics study was prepared in the same manner.

### ***Phytochrome and Cyanobacteriochrome Sample Preparation***

All the phytochrome and cyanobacteriochrome samples were prepared by the Lagarias Lab at University of California, Davis. While the procedure is outlined elsewhere,<sup>63, 65, 69, 210-212</sup> a brief overview modified from Kim et al.<sup>101</sup> is given below. For cyanobacterial phytochrome 1 (Cph1), *Escherichia coli* strain LMG194 (Invitrogen) was co-transformed with two plasmids, pBAD-Cph1(N514)-CBD and pPL-PCB to allow for production of holo-Cph1 *in vivo*. Transformed cells were selected on rich medium (RM) plates containing 100 mg/mL ampicillin and 50 mg/mL kanamycin. An individual colony was cultured overnight in RM (AMP50 KAN25) and inoculated with 1:500 ratio in 100 mL of RM. Upon reaching the desired optical density of 0.5 OD at 600 nm, the culture was transferred to 900 mL of LB (Luria-Bertani medium) containing 50 mg/mL ampicillin, 25 mg/mL kanamycin, and 1 mM isopropyl β-D-1-thiogalactopyranoside for a total expression of 6 L. After 1 h at 37 °C and in a shaker -incubator (Innova 4340 from New Brunswick Scientific) with shaking at 250RPM, arabinose was added to a final concentration of 0.002% (w/v) followed by incubation for 1 h prior to reducing the temperature to 20 °C for 16 h. Subsequently, cells were harvested by centrifugation at 5,000 ×g for 10 min and stored at –80 °C. The pellet was resuspended at 1 g wet weight per 4 mL of lysis buffer A [25 mM Hepes-Na (pH 8.0), 500 mM NaCl, 1 mM EDTA] plus 0.1% (v/v) Triton X-100. Cells were lysed by two passes through a

microfluidizer (M-110Y) at 15,000 psi, and all subsequent steps were carried out at 4 °C. Crude lysate was clarified by centrifugation (35,000 rpm, Ti-60 Beckman, 30 min) and applied to a 30-mL chitin column (New England Biolabs), which was washed thoroughly with buffer-A at 1 mL/min. Intein-mediated cleavage was induced by flushing the column with 1 bed volume of elution buffer (buffer A + 1 mM dithiothreitol). Fractions containing Cph1(N514) were pooled and concentrated in Amicon spin prep columns (10,000-kDa cut-off) and dialyzed against 1 L of buffer B [25 mM Tes-KOH (pH 8.0), 25 mM KCl, 10% glycerol] overnight at 4°.

The CBCRs studied in this body of work (Chapters 4-8) were generation as outlined by Rockwell et al. <sup>63, 69</sup> where a DNA region coding for each GAF domain was amplified by PCR from *N. punctiforme* genomic DNA using appropriate primers, followed by cloning into the unique *Nco* I and *Sma* I sites of pBAD-Cph1-CBD.<sup>213</sup> Co-expression with PCB biosynthetic machinery in *E. coli* followed a published procedure,<sup>214</sup> and purification of GAF domains as intein-chitin binding domain (intein-CBD) fusions followed the procedure employed for *Synechocystis* Cph1.<sup>213</sup> After lysis, ultracentrifugation, and binding to chitin resin (NEB) in accordance with the manufacturer's instructions, intein cleavage was initiated by addition of DTT to the column, followed by overnight incubation at 4 °C. Peak fractions were pooled and dialyzed against TKKG buffer (25 mM TES-KOH pH 7.8, 100 mM KCl, 10% (v/v) glycerol) overnight prior to freezing in liquid nitrogen and storage at -80°C. Absorbance spectra were acquired at 25 °C on a Cary 50 spectrometer.

### ***hCRABPII Rhodopsin Mimic Sample Preparation***

The hCRABPII mimics were prepared by the Geiger lab at Michigan State University using the following protocol. The hCRABPII variants were expressed using BL21 (DE3) pLysE *E. coli*

competent cells (50  $\mu$ L) for gene transformation. The sample was held 30 minutes in ice. After heat-shock at 42  $^{\circ}$ C for 45 seconds, 950  $\mu$ L of LB was added to the sample. The sample and agar plate containing ampicillin (100  $\mu$ g/mL) were kept at 37  $^{\circ}$ C for 30 minutes. Then 100  $\mu$ L of the solution was streaked on LB agar plate and incubated at 37  $^{\circ}$ C overnight. To inoculate 1 L of LB with ampicillin (100  $\mu$ g/mL) a single colony was used. After the cell culture was grown at 37  $^{\circ}$ C while shaking for 8 h, (OD~0.9) the overexpression was started by adding 1 mL of 1M IPTG solution into 1 L cell culture (overall concentration 1.0 mM of IPTG). The solution was shaken at 19  $^{\circ}$ C for 36 hours.<sup>74, 75</sup>

Following expression, the next step was to isolate and purify the samples. This was accomplished by collecting the cells by centrifuging for 20 min at 5,000 rpm (4  $^{\circ}$ C). The supernatant was discarded, and the cells were resuspended in 60 mL of Tris buffer (10 mM Tris•HCl, pH=8.0). Then ultrasonication was used to lyse the cells (Power 60%, 1 min x 3), and the sonicated mixture centrifuged at 16  $^{\circ}$ C (10,000 rpm, 20 min). Next the purification was performed at 4  $^{\circ}$ C by ion exchange chromatography using Q Sepharose<sup>TM</sup>, Fast Flow resin. The protein was bound to the column by gravity flow, the column washed with 50 mL of 10 mM tris. HCl buffer. The bound protein was then eluted with 10 mM Tris, 150 mM NaCl, pH = 8.0, the pure fractions desalted using EMD Millipore centriprep centrifugal units (cutoffs:10 KDa) with 10 mM Tris pH=8.0 buffer, three times, and loaded on a second anion exchange column (15Q, GE Health Sciences, BioLogic DuoFlow system). The same Source Q program as mentioned previously was used for the purification.<sup>74</sup>

For both the ultrafast dynamics and cryokinetic UV-Vis studies, the samples were prepared in 150

mM NaCl, 10 mM Tris-HCl (pH=8.0). For both ultrafast and cryokinetic experiments, the concentration of retinal was kept at 0.5 equivalent of protein concentration in all experiments. The concentrations of proteins were calculated according to the extinction coefficient reported previously for M2 and M3.<sup>75</sup> The concentration of samples was calculated with regards to meet the optimal OD for ultrafast (0.5 in 0.2mm cuvette) and cryokinetics (OD=0.5 in 1mm cuvette) experiments measured by Cary 100 Bio Win UV UV-Vis spectrophotometer (Varian Instruments). The PSB has absorptions corresponding to  $\lambda_{\max} > 450$  nm, while deprotonated imine peaks (SB) appear at  $\lambda_{\max} \sim 368$  nm. The unbound retinal absorbs at  $\lambda_{\max} \sim 380$  nm. *All-trans* retinal extinction coefficient in ethanol is  $48,000 \text{ M}^{-1}\text{cm}^{-1}$  at 380 nm. For the ultrafast experiments, approximately 1mL of photoreceptor samples were concentrated to give  $\sim 0.5$  OD absorbance at a path length of 1 mm.

### ***Broadband Transient Absorption Spectroscopy***

Time resolved absorbance spectroscopy is a powerful tool that can map photoinduced reactions by measuring changes in the absorption bands of the chromophore, molecular photoswitch, transition metal complex, etc. The mechanisms of light activated photoswitches are particularly optimal for being studied by transient absorption spectroscopies since the reaction is initiated at a well-defined timepoint (arrival of the pump pulse) and the populations typically have unique spectral signatures. Using the forward dynamics of a canonical red/green CBCR as an example (Figure 3.1), after photoexcitation of the  $^{15}\text{ZP}_r$  dark-adapted state, a  $^{15}\text{ZP}_r^*$  is generated that partially populates a primary Lumi- $\text{R}_f$  photointermediate with absorbance red shifted of  $^{15}\text{ZP}_r$  on a sub-nanosecond timescale. This Lumi- $\text{R}_f$  intermediate then evolved through a series secondary Meta-R intermediate that have sequentially longer-lived intermediates and continually blue-shifted

absorbance prior to populating the  $^{15E}P_g$  light-adapted state. Given the expansive timescale of the photoreaction (~hundreds of femtoseconds to a few milliseconds), two different experimental set ups were used to measure what we termed the primary (~150 fs – 8 ns) and secondary (~550 ps – 1 ms) timescales.

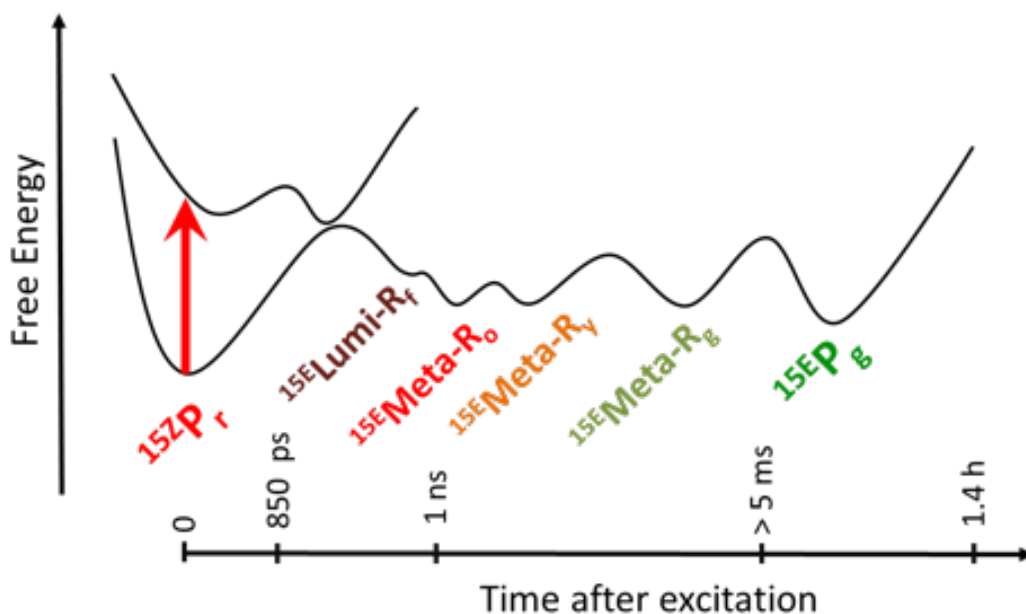


**Figure 3.1:** Model Timescale of a Red/Green CBCR Potential Energy Surface  
Model potential energy surface (PES) being mapped in the time domain.

While the primary and secondary broadband transient absorption spectroscopies presented extensively in this dissertation utilized different equipment and optical set-ups, the fundamentals are neigh identical. Considering these facts, an overview of the traditional pump-probe version of transient absorption spectroscopy will be given first and will be followed by the individual experimental protocols. In pump-probe spectroscopy, a broadband probe pulse and a pump pulse are initially spatially and temporally overlapped at the sample (Figure 3.2). While the generation

of these pulses will be discussed in detail in the subsequent chapters, the pump pulse would ideally be at a slightly higher wavelength than the wavelength of max absorbance of the sample to optimize the likelihood of having a clean bleach. The pump and probe pulses approach the sample at an angle so that the pump pulse would be blocked by an iris to limit pump scatter while the probe pulse passes through the center of the iris and is dispersed onto a photodiode array by a diffraction grating. To measure the spectra at different delays after excitation from the pump pulse, the timing of either one of the pulses needs to be tunable, allowing for the measuring of spectra at well-defined pump-probe delay times and the mapping of the photocycle (Figure 3.1). Since the work in this dissertation is on reversible photoswitches, the sample is illuminated with a light emitting diode (LED) resonant with the desired photoproduct prior to excitation to push as much of the population into the starting state prior to excitation as possible. Furthermore, the probe pulse operates at double the frequency of the pump pulse so that a clean reference spectrum can be taken before each post-excited spectrum so that reliable difference spectra can be calculated for ease of interpretation where

$$\Delta Abs(\lambda, t) = Abs(\lambda, t)_{pumped} - Abs(\lambda, t)_{unpumped} = -\log_{10} \left( \frac{I(\lambda, t)_{pumped}}{I(\lambda, t)_{unpumped}} \right)$$

**Equation 3.1:** Transient Difference Spectra Generation

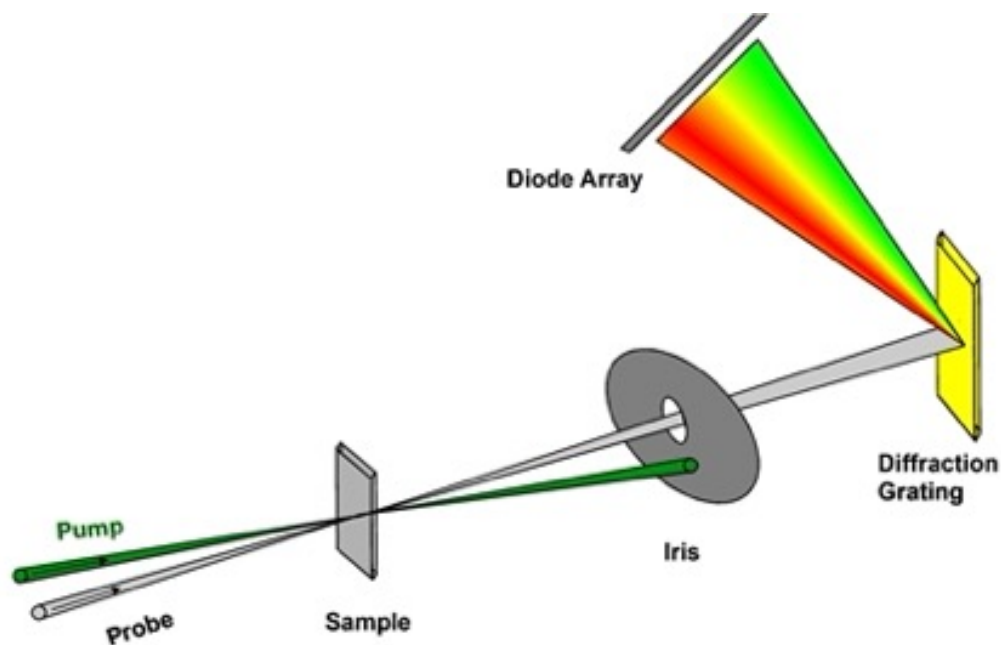


**Figure 3.2:** Typical Pump-Probe Experimental Set-Up

Typical Pump-Probe experimental set-up where the pump and probe beams intersect at the sample and the probe beam is blocked and the probe beam is dispersed on a photodiode array by a diffraction grating.

In this dissertation, two types of sample ‘holders’ were used. Since most of the samples were not air sensitive, they were in a closed-circuit flow cell constructed of silica tubing and a 2 mm quartz cuvette. The solution flowed at a rate of approximately 10-20 mL/min to ensure that fresh sample was excited and probed with each set of pulses. For air sensitive samples, 0.25 to 0.5 mm quartz cuvettes with caps were put in nitrogen glove box and sealed with black wax upon removal. These sample cuvettes were then placed on a motorized stage that translated the cuvette in an oval pattern so that fresh sample was being excited and probed at each set of pulses as well as to keep the sample at room temperature. It should also be noted that the air-sensitive sample holder set up removes the ability to push the population into the desired state with an external LED since it is not possible to remove the LED light from the probe region. Since population cannot be forced



back, this experimental set up is limited to samples that either quickly decay back to the dark-adapted state or have photoproduct bands that are not resonant with the excitation wavelength.

An example of the resulting transient difference spectra and kinetics using the primary forward dynamics of NpR6012g4 is given below in Figure 3.3. The origin of these signals will be discussed in a later section in this chapter, but for now it can be easily seen that there are unique spectral signatures that evolve in time, showcasing that this technique allows one to study photoinduced dynamics as outlined in Figure 3.1.

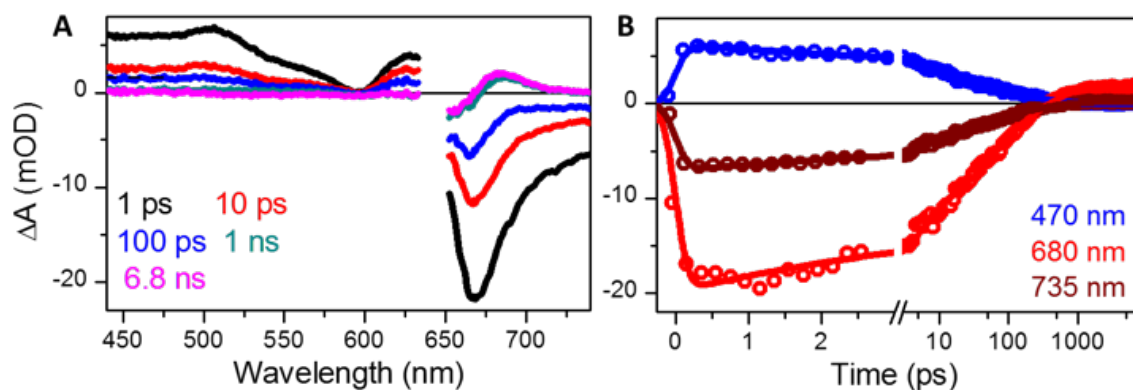


**Figure 3.3:** NpR6012g4 Example of Primary Transient Absorption Data

Example of primary transient absorption difference spectra and kinetics using the primary forward dynamics of NpR6012g4.

### *Ultrafast Transient Absorption Spectroscopy*

To generate the ultrafast pulses for the primary transient absorption experiments, an amplified Ti:Sapphire laser system that outputs 2.5 mJ pulses at a central wavelength of 800 nm with a bandwidth at 40 nm and pulse width of 40 fs at a rate of 1 KHz was used. To accomplish this, two pump lasers, a seed laser and an amplifier were utilized (Figure 3.4). To generate femtosecond

pulses, ~4 W of the second harmonic (532 nm) of a continuous wave (CW) Nd:YAG laser (Spectra Physics, Millennia Pro) was used to pump a Ti:Sapphire (Ti:Al<sub>2</sub>O<sub>3</sub>) based oscillator (Spectra-Physics, Tsunami). To remove the randomly dispersed phases of several longitudinal within the optical cavity of the Tsunami, an acousto-optic modulator is used to generate phase-locking (aka mode-locking) that results in the longitudinal modes becoming in phase with a separation in time of double the cavity length divided by the speed of light. If the laser cavity is stable, it will remain in (passive) mode-locking when the driving rf pulse is removed through passive Kerr lensing. The Tsunami outputs ~400 mW at 800 nm with a bandwidth of 40 nm and pulse-width of 30 fs at rate of 80 MHz. The output of the tsunami is then magnified in a Nd:YLF (Empower; Spectra Physics) pumped, Ti:Sapphire based amplifier (Spitfire Pro; Spectra Physics) through chirped pulse amplification. Chirped pulse amplification ensures that the Ti:Sapphire crystal in the amplifier is not damaged due to the concentration of all the photons in a small space by at the essentially the same time by increase the pulse-width of the seed laser via group velocity dispersion.

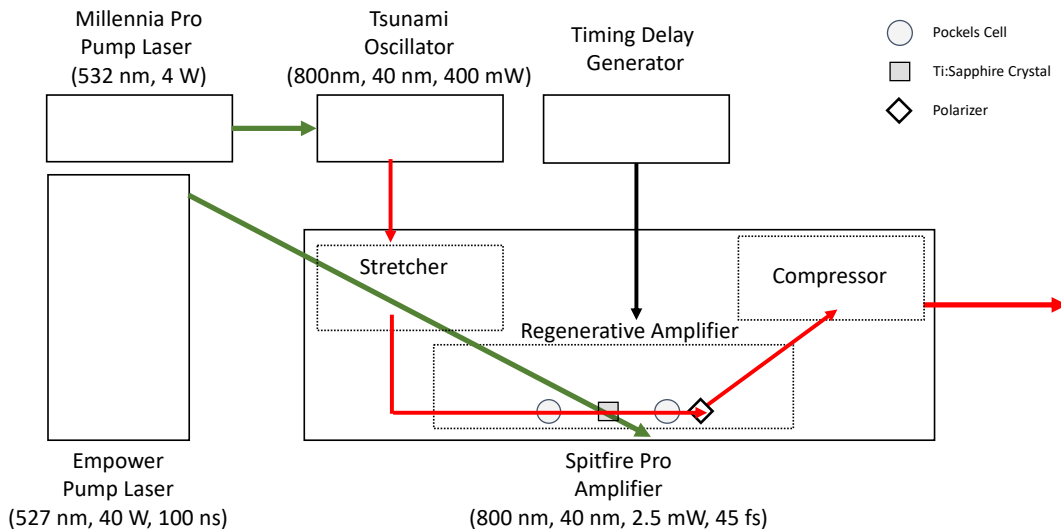


**Figure 3.4:** Spectra-Physics Spitfire Pro Laser Set-up

Spectra-Physics Spitfire Pro Laser Set-up.

The output of the ultrafast Ti:Sapphire laser system was used for the transient absorption spectroscopic techniques such as pump-probe (Figure 3.5). The laser output was split into two beams where one generates the broadband probe pulses and the other generates the pump pulses used to excite the sample. The broadband probe pulse was generated via nonlinear optical effects<sup>215, 216</sup> by passing the 800 nm fundamental through a slowly translating CaF<sub>2</sub> crystal. Once the white light is generated, it is passed through two parabolic mirrors, where the first collimates the beam and the second focusses the probe light at the sample and directs it into the spectrograph (Oriel MS 127i) where the first order diffraction is detected using a 256-pixel photodiode array (Hamamatsu S3901 and C7884). To measure spectra at different time relative to the pump pulse, the fundamental that generates the broadband probe pulse transverses a computer-controlled delay stage with a 0.1  $\mu\text{m}$  (0.33 fs) resolution and an upper temporal limit of  $\sim 8$  ns. To have a clean reference spectrum, every other pump pulse is blocked by a chopper synched to the laser and revolving at 500 Hz. Lastly, the pump pulse is set at the magic angle ( $54.7^\circ$ ) with respect to the probe light to remove anisotropic effects due to preferentially excited rotational dynamics using a Berek polarizer and is directed away from the spectrograph as well as blocked by an iris as to not contaminate the signal. An example of the transient difference spectra and kinetics that can be resolved using ultrafast transient absorption spectroscopy is given above (Figure 3.3). In addition to pump-probe experiments, more sophisticated three pulse experiments such as pump-dump-probe and dual excitation wavelength interweave (DEWI) spectroscopies could also be performed. Pump-dump-probe spectroscopy allows for studying possible ground state evolution as observed in the forward reaction of NpR6012g4.<sup>184</sup> DEWI is a powerful technique for studying excitation wavelength dependence of the photoinduced dynamics by measuring two pump-probe data sets at different excitation wavelengths near simultaneously as exemplified in the forward dynamics of

RcaE<sup>190</sup> and Cph1.<sup>100</sup> DEWI spectroscopy was used in to study the far-red CBCRs presented in Chapters 8 An experimental schematic having the third pulse and additional chopper is provided in the appendix (Figure A9.1).

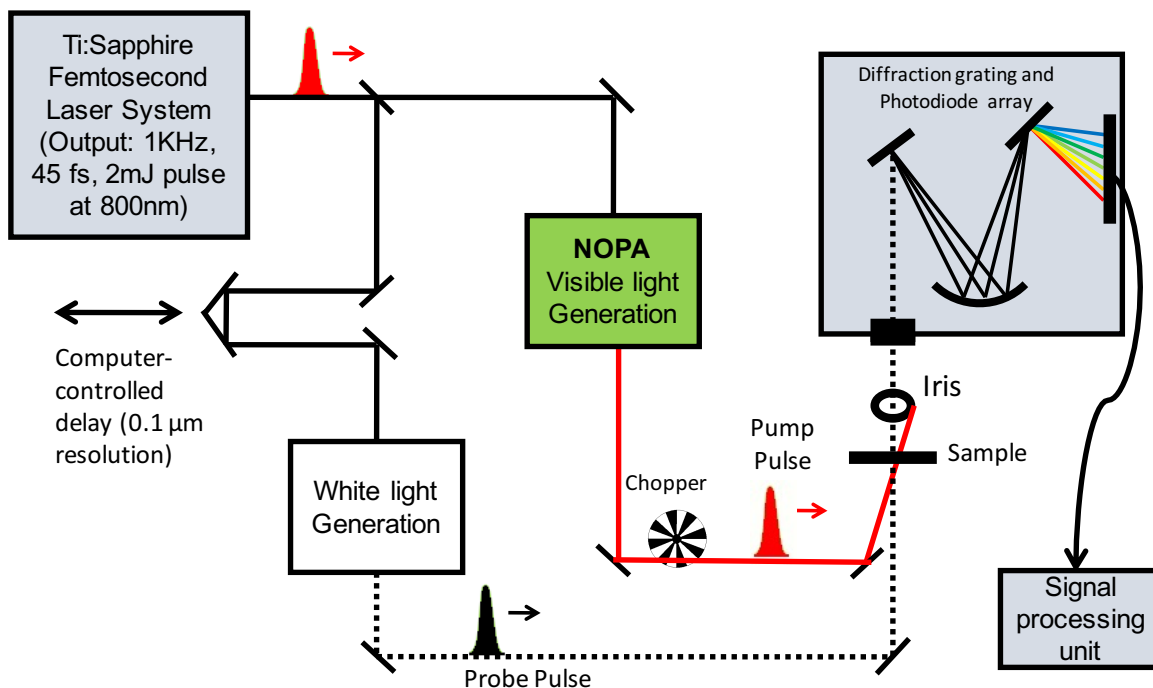


**Figure 3.5:** Pump-probe Spectroscopy Experimental Set-up

Pump-probe spectroscopy experimental set-up.

The pump or excitation pulses between  $\sim 500\text{-}730$  nm were generated using home-built noncollinear optical parametric amplifiers (NOPAs). A diagram of a single NOPA line can be found in Figure 3.6. To generate the excitation pulse, the 800 nm fundamental is split into a white light seed pulse and a 400 nm pump pulse. The white light seed is generated by passing the 800 nm fundamental of the laser through a neutral density (ND) filter and a YAG crystal to generate a white light supercontinuum. To generate the 400 nm pump pulse, sum harmonic generation (SHG) of the laser fundamental is accomplished by passing the 800 nm beam through a 2 x 2 x 1 mm

BBO crystal that has been cut at  $29.2^\circ$  and held perpendicular to the incoming beam. The BBO crystal is also rotated in such a manner that the polarization of the 400 nm pump line polarization is rotated  $90^\circ$  to that of the 800 nm fundamental, which is required to take advantage of the birefringent nature of the BBO crystal used for enhancement of the seed pulse.

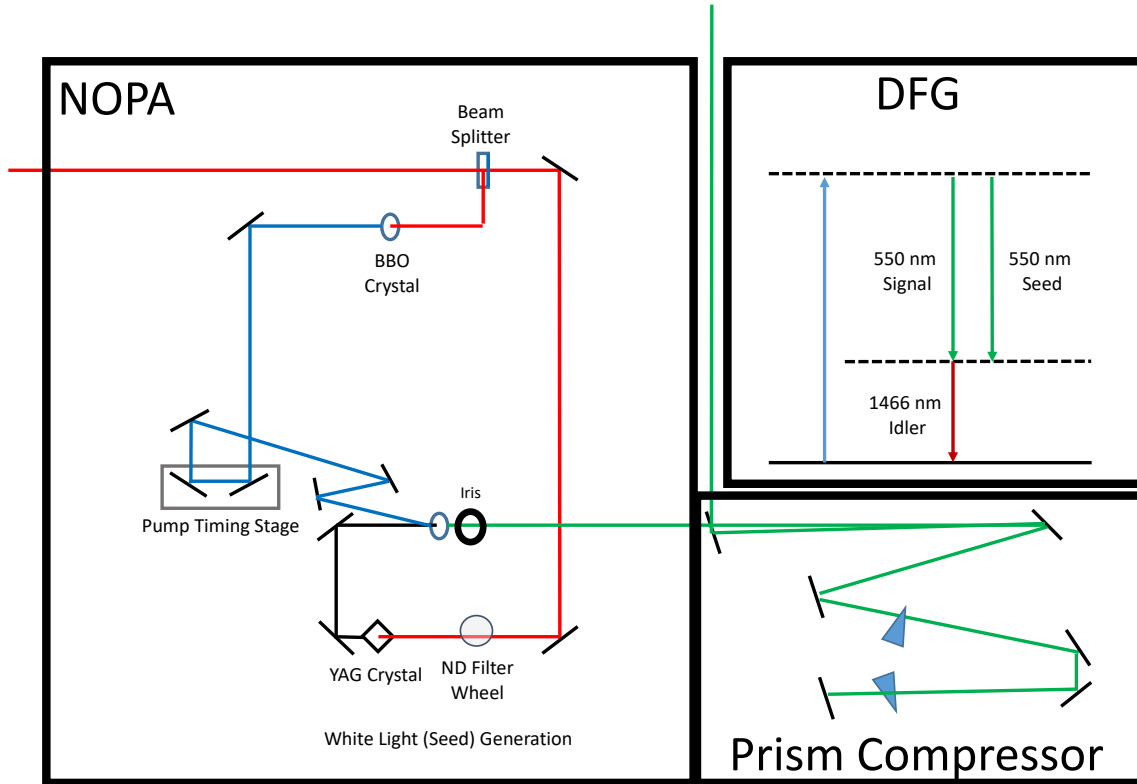


**Figure 3.6:** Home-Built NOPA Line

Home-built NOPA Line for generating pump pulses. Except for white light (black line), the wavelengths of light are color coded to match the corresponding visible light color.

The seed pulse is then amplified by the pump pulses via difference frequency generation (DFG) by using a BBO crystal cut at  $32^\circ$ . When just the 400 nm pump pulse travels through the BBO crystal the 400 nm light generates a large density of uncorrelated excitons that can spontaneously decay into two photons (signal and idler) of lower energy, resulting in the amplification of quantum

noise.<sup>217-219</sup> The greatest emission is when in addition to energy ( $\omega_{pump} = \omega_{signal} + \omega_{idler}$ ), momentum is also conserved which is accomplished when the wavevectors of the signal ( $k_{signal}$ ) and idler ( $k_{idler}$ ) sum to the pump wavevector ( $k_{pump}$ ).<sup>220</sup> Since there are an infinite number of unique signal-idler pairs that satisfies these conditions and they can be emitted in any plane in the direction of  $k_{pump}$ , a broad, non-monochromatic cone of fluorescence (Figure 3.7; left) termed superfluorescence is generated. While the excitons were initially uncorrelated, they later correlate via their electromagnetic radiation field,<sup>217, 218</sup> resulting in superfluorescence having a relative short lifetime. Given the angle of the pump pulse and the optical axis, where the higher energy light could be closer to the pump and the lower energy light is further away from the pump. While those familiar with prisms may be surprised that the superfluorescence cone can have lower energy light emitted at a larger angle, it is not unexpected due to the requirement that energy and angular momenta must be conserved (Figure 3.8). An overview of how these angles between the crystal and pump ( $\theta_m$ ) and the pump and seed ( $\alpha$ ) can be calculated can be found in reference 219.

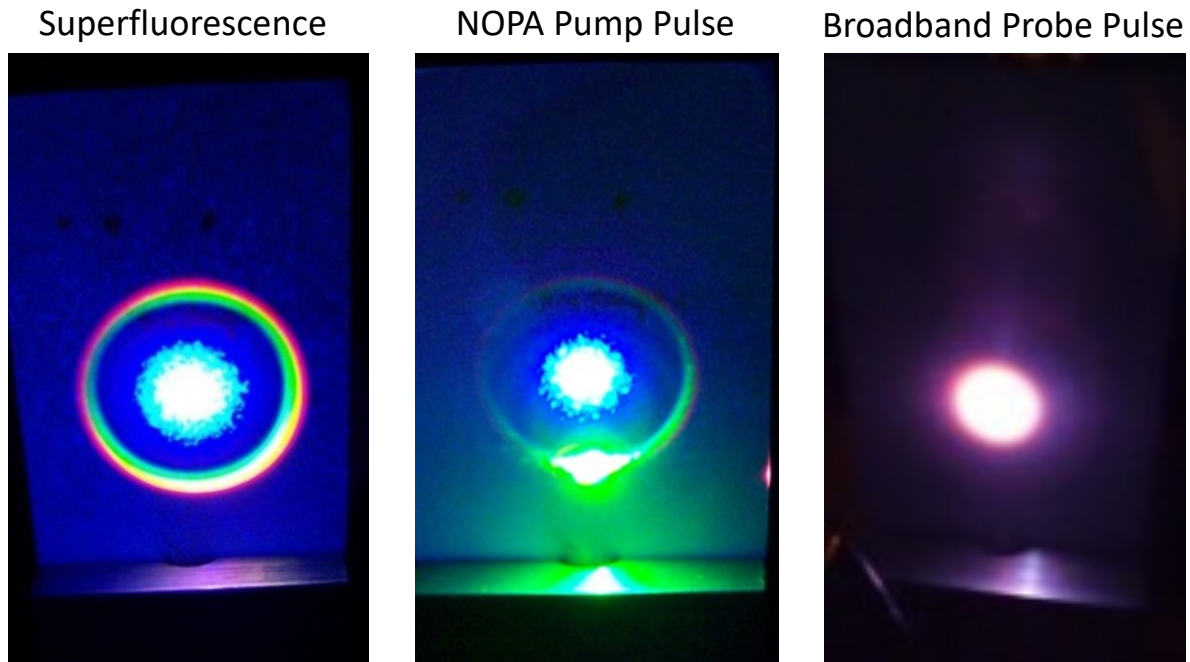


**Figure 3.7:** Images of Superfluorescence, Pump Pulse, and Broadband Probe-Pulse Used in the Study of Primary Dynamics

(left) superfluorescence used to enhance the seed pulse for generation of the (middle) pump pulse and broadband probe pulse generate in  $\text{CaF}_2$ . Images are courtesy Dr. Tyler L. Mix.

The probability of the wavelength and directionality of the superfluorescence changes upon the addition of a temporally and spatially overlapped seed pulse. The seed pulse interacts with the excitons in the crystal generated by the pump pulse, drastically increasing the probability that the exciton will generate the same wavelength as the seed pulse and in the same direction, resulting in the amplification of the seed pulse (Figure 3.7; middle). For this amplification of the seed pulse to occur, four criteria have to be met: the superfluorescence cone and seed pulses must be 1) spatially and 2) temporally overlapped at the BBO crystal, 3) the pump and seed pulses must have their polarizations perpendicular and 4) the pump and seed have to be phased matched to satisfy the conservation of angular momentum. In addition to overlapping the excitons within the crystal, the spatial overlap also dictates which wavelength of light in the white light seed will be amplified.

The polarizations of the pulses are also required to take advantage of the birefringent nature of the BBO crystal to prevent walk-off between the pump and seed pulses. The phase matching condition corresponds to the conservation of momentum and requires that

$$\hbar\mathbf{k}_{pump} + \hbar\mathbf{k}_{seed} = \hbar\mathbf{k}_{signal} + \hbar\mathbf{k}_{idler}$$

**Equation 3.2:** Phase Matching Condition

(as seen in Figure 3.8) where  $\mathbf{k}$  is the wavevector and  $\hbar$  is the reduced Plank's constant

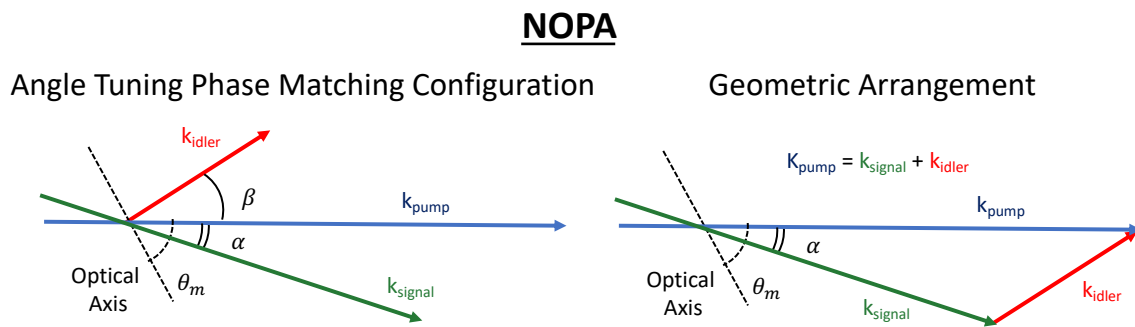


**Figure 3.8:** Phase Matching Condition for Nonlinear Optics

Path of pump and seed beam in NOPA recreated from of Manzoni et al.<sup>219</sup>

After the generation of the excitation pulses in the NOPA line, a prism compressor is utilized to minimize the instrument response time via shortening the pulse width of the excitation pulse. As seen in Figure 3.6, a prism compressor is composed of two prisms and an array of mirrors. The initial prism is used to separate the various spectral components spatially by spectral dispersion and the second prism is oriented in a manner where the longer wavelengths traverse through a great length in the prism than the shorter wavelengths so that even though longer wavelengths interact with the prism less, they are delayed more than the shorter wavelengths in order to



counterbalance the positive chirp impressed by the previous optics. This ultimately results in the compression of the excitation pulse. The light going into the first prism is set at the Brewster angle with respect to the prism surface to remove or at least minimize the amount of light being reflected instead of transmitted. Following the prism compressor, the pump light is passed through a chopper synched to the output of the laser and revolving at a frequency of 500 Hz to block every other pulse so that a reference spectrum could be obtained prior to the excited spectrum so that a difference spectrum can be obtained. Images of the superfluorescence and pump pulse that occurs in the NOPA and the CaF<sub>2</sub> derived broadband probe pulse are given below (Figure 3.7).

### ***Long-Time Transient Absorption Spectroscopy***

While irreplaceable in studying the excited state dynamics that initially set the fluorescent and photoproduct quantum efficiencies, if one desires to study the full photocycle of a photoreceptor, a delay time of greater than ~10 ns is required. Similar to the ultrafast transient absorption set up, the Ti:Sapphire laser (Spectra-physics, Spitfire) was used to generate a broadband pulse by passing ~1  $\mu$ J of the 800 nm fundamental through a slowly translating 10 mm CaF<sub>2</sub> crystal. These probe pulses were imaged via a spectrograph (Oriel Instruments 77480) onto a 512 pixel silicon diode array (Hamamatsu C7884-8L003). The ultrafast and long-time transient absorption set-ups largely differs in the source of the excitation pulse and the generation of the delay between the pump and probe pulses. Since it is not practical to make a delay stage that could result in a ms delay time, an external 500 Hz Q-switched Nd-YAG laser (Pulselas-A-532-300) that was frequency doubled to 532 nm using a 5 mm thick potassium dihydrogen phosphate crystal and had a pulse-width of ~ 550 ps was electronically delayed with respect to the ultrafast Ti:Sapphire laser. Since the delay between the pump and probe pulses are electronically controlled, the upper probe

time limit is set by the flow rate of the sample which was decreased to  $\sim 20\text{-}30$  mL/min and resulted in the first 1 ms being unaffected by the flow conditions. Given the instrument response of the long-time set-up being  $\sim 550$  ps and the upper temporal limit of the ultrafast set up being  $\sim 8$  ns allows for 8 ns of comparison between the primary and secondary dynamics, and as seen in Chapters 5-7 they are in good agreement.

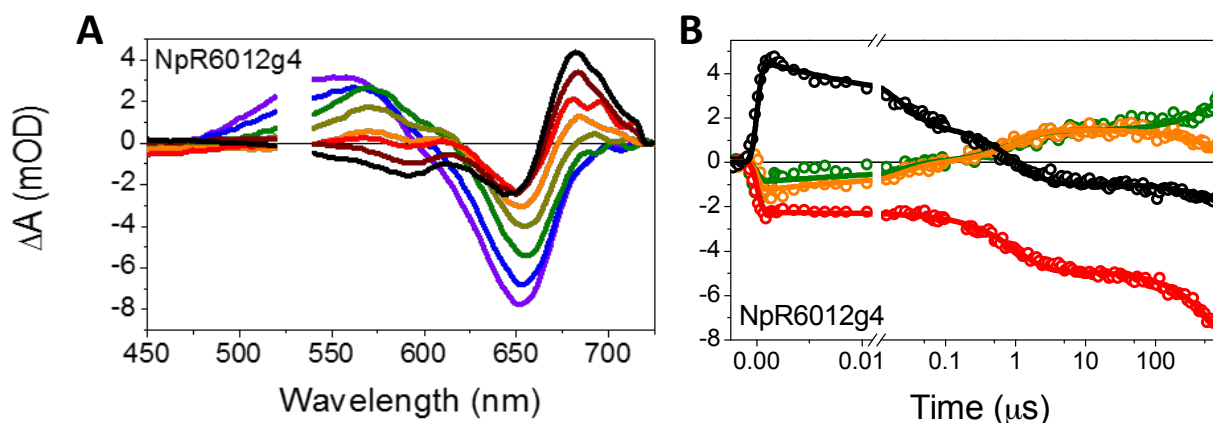


**Figure 3.9:** NpR6012g4 Example of Secondary Transient Absorption Data

Example of secondary transient absorption difference spectra and kinetics using the primary forward dynamics of NpR6012g4.

### *Cryokinetic UV-Vis Absorption Spectroscopy*

To determine photoinduced mechanisms, cryokinetic UV-Vis spectroscopy was performed in addition to the room-temperature primary and secondary transient absorption TA spectroscopy. Cryokinetic UV-Vis spectroscopy was performed by placing an Oxford Instruments Optistat DN liquid nitrogen cryostat into a Shimadzu UV-1700 UV-Vis spectrometer. To prevent condensation, the sample chamber of the cryostat was flushed with nitrogen gas for approximately five minutes before putting the sample in. Typically, cryokinetics are collected from approximately room temperature (290 K) to 170 K by steps of 10 K. The terminal temperature of 170 K was chosen

since the glycerol-buffer solvent cracks around 160 K, resulting in extra noise due to the scattering of light. If cryokinetics is desired at lower temperatures and the glycerol/buffer mixture must be used as the cryo-solvent, then, a secondary experiment can be performed between 80 and 160 K. A temperature and illumination scheme of a typical cryokinetic experiment can be found below in Figure 3.10.

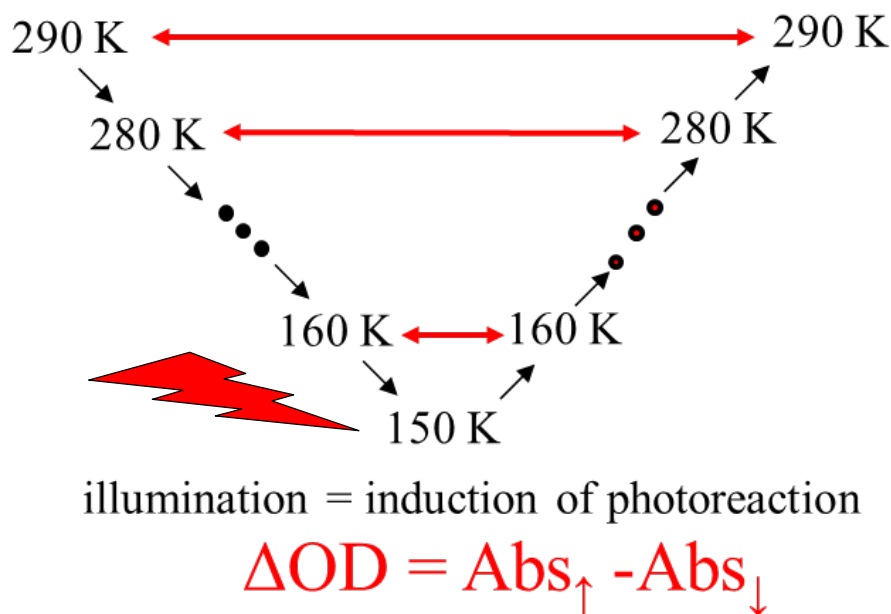


**Figure 3.10:** Experimental Scheme for Cryokinetic UV-Vis Spectroscopy  
 Temperature and illumination experimental scheme for typical cryokinetic UV-Vis experiment.

Initially, the sample is illuminated with light resonant with the terminal photoproduct to push population into the initial state and remove contamination from the other reaction direction dynamics. After pre-illuminating the sample, reference spectra are obtained every 3 minutes for approximately 30 minutes to capture a ‘true’ reference spectrum at each temperature of interest. While collecting the data, kinetic plots at the peaks of interest (typically main absorption peak of

the chromophore or where the difference spectra are changing) can be plotted to ensure that the curve has leveled off, suggesting that the population of the states of the sample has equilibrated at the new temperature. At the terminal temperature (~170 K), light corresponding to the state that is to be excited is shined onto the sample to initiate the photochemistry. This is done incrementally and with checking the difference spectra with respect to the reference until a difference spectrum with decent intensity is achieved (~30 mOD). Once the illumination is completed, the UV-Vis spectra are collected at each temperature every 3 minutes until the kinetics of peaks of interest (photoproduct(s) and bleach) have leveled off. It is important to measure absorbance spectra past where the kinetics have leveled off since this may allow for determination of the Gibbs Free Energy of the intermediates via transition-state theory or assuming Arrhenius kinetics. This highlights why coarsely working up the data and analysis of the difference spectra and kinetics at time points and wavelengths of interest while collecting both room-temperature transient absorption and cryokinetic dynamics is important to ensure that enough focus is being placed at the wavelengths, times, and temperatures of interest. Typically, the 170 K is already finished due to the trapping of the photogenerated intermediate population. Example cryokinetic difference spectra at select temperature for the forward reaction of NpR6012g4 is given in Figure 3.11.

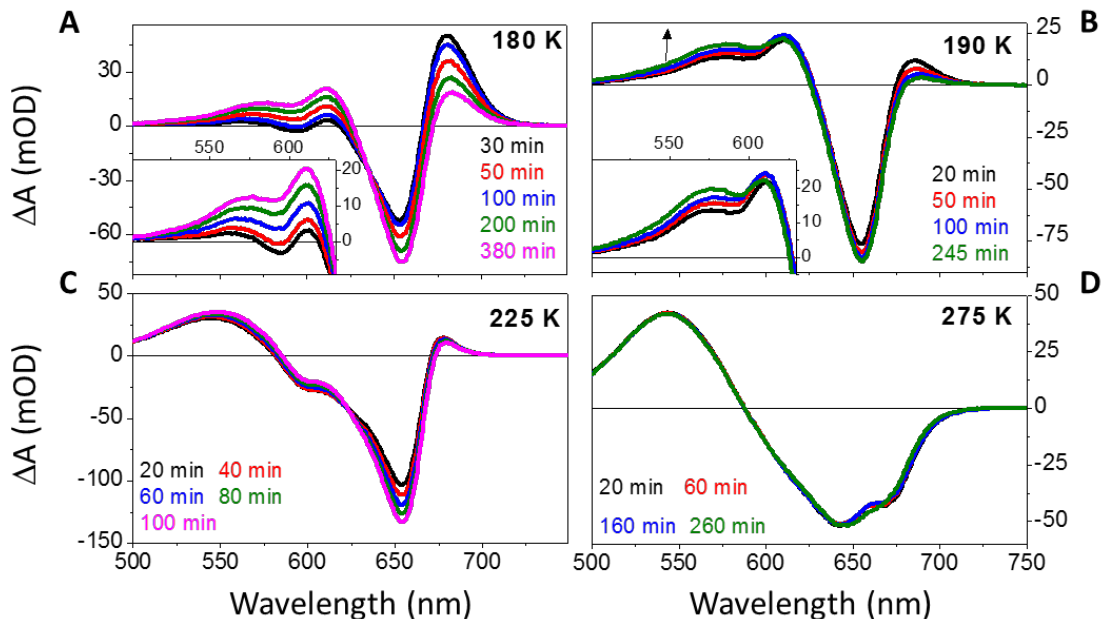


**Figure 3.11** NpR6012g4 Example of Cryokinetic Difference Spectra

Example Cryokinetic data for the forward dynamics of NpR6012g4. Modified from Jenkins et al.<sup>73</sup>

Analogous to room temperature transient absorption spectroscopy, there are clearly resolved unique spectral features that evolve with temperature, allowing for the mapping of a the photocycle. This occurs due to the stepwise increase in temperature that incrementally adds thermal energy to the system, allowing for the progression of the dynamics over larger energy barriers (Figure 3.12). Furthermore, cryokinetics is a powerful tool that can isolate quickly evolving populations not readily resolved at room temperature by removing the thermal energy required to get over the barrier. Furthermore, we resolved that cryokientics is a useful tool for verifying photoinduced reaction mechanisms and is a cost-effective way for groups or individuals interested in measuring dynamics without investing in an expensive laser apparatus.

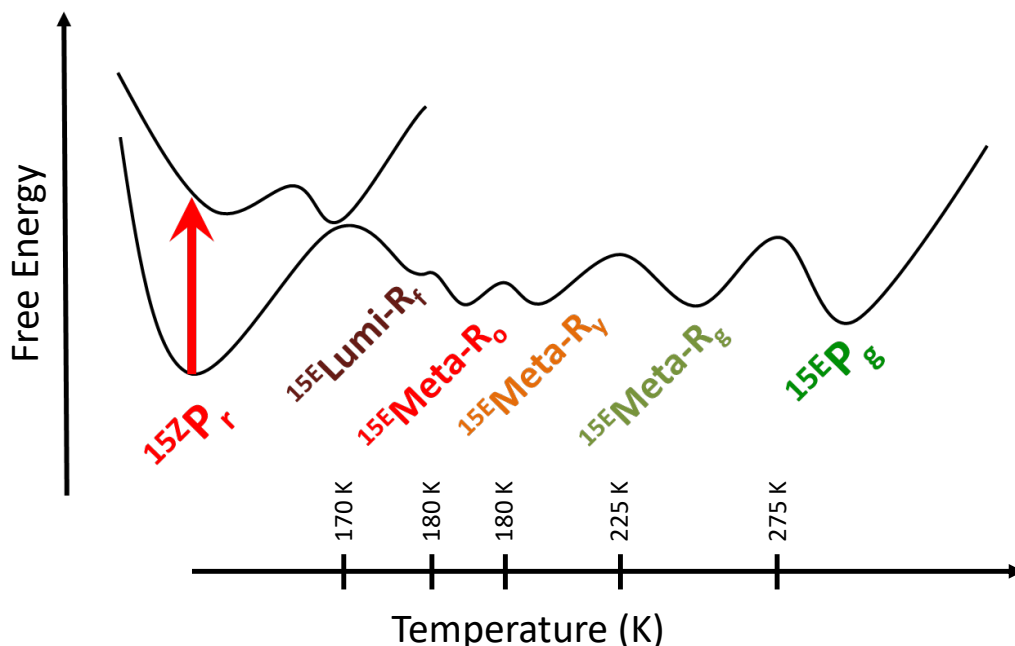


**Figure 3.12:** Model “Temperature-Scale” of a Red/Green CBCR Potential Energy Surface

Model potential energy surface (PES) being mapped in the temperature domain.

### *Origin of Signals*

Ultrafast difference spectra are typically a superposition of four signals that evolve with time: (i) negative ground state bleach (GSB) that is due to the loss of the initial population and typically matches the ground state absorption band, (ii) negative stimulated emission (SE) of the excited state population ( $S_m \rightarrow S_0$ ) which typically matches the fluorescence band, (iii) positive excited state absorption (ESA) due to further excitation of the excited population ( $S_m \rightarrow S_n$ ) and (iv) photointermediate absorption ( $S_a \rightarrow S_b$ ). Except for the typical removal of signals derived from the excited state population (SE and ESA), this spectral decomposition also applies TA dynamics on longer timescales and cryokinetic difference spectra.

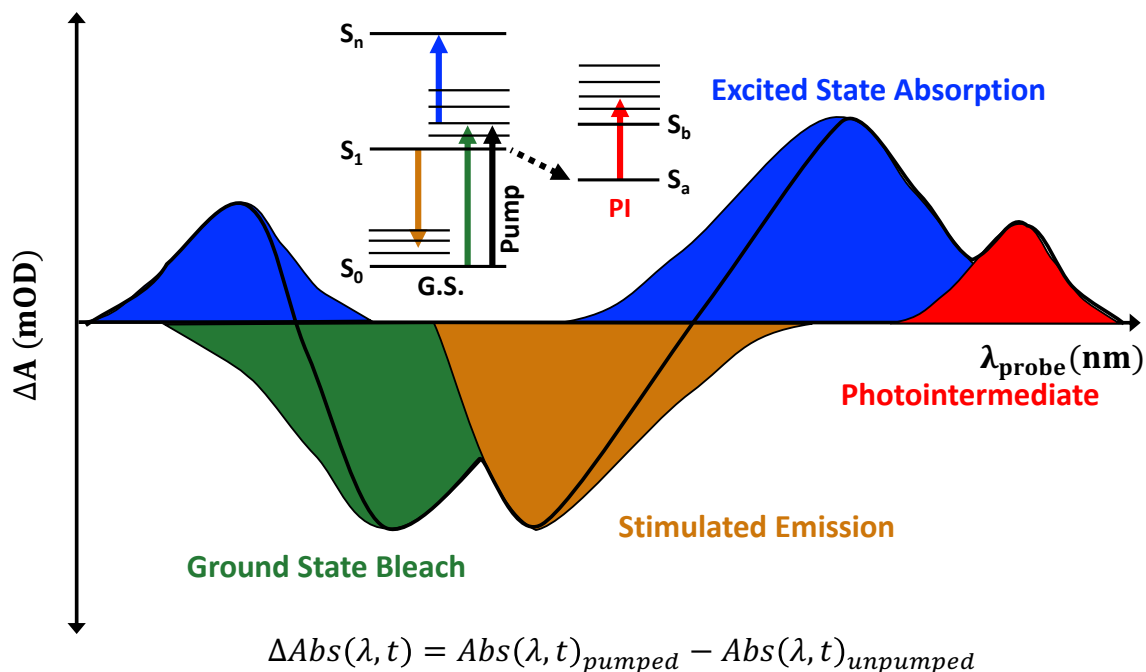


**Figure 3.13:** Representative Ultrafast Difference Spectrum Decomposition at a Single Time Point

Typical overlapping signals of an Ultrafast Difference Spectrum at a single time point. The overlapping signals are color code to the text in the figure and results in the black curve that represents the measured spectrum.

### ***Global Analysis***

Coupled with time resolved data, global analysis is a powerful tool that separates the time-dependent difference spectra into a linear combination of time-independent spectra weighted by a time dependent concentration profile. The difficulty of this analysis lies in determining the correct kinetic model that accurately describes the system. For example, Figure 3.14 illustrates how a four-component system can be modeled in several different ways: i. in parallel, ii. sequential, iii. bifurcation (i.e.,  $t_{12}$  and  $t_{14}$  or  $t_{23}$  and  $t_{24}$ ), and iv. trifurcation ( $t_{12}$ ,  $t_{13}$  and  $t_{14}$ ).

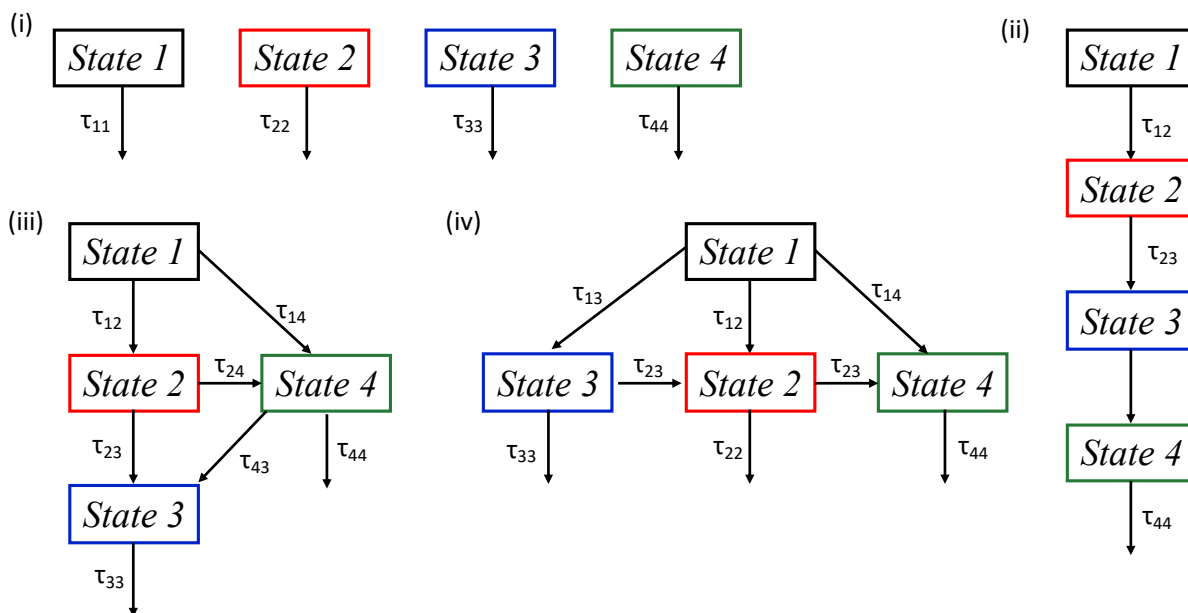


**Figure 3.14:** Some Possible Models for a Four-Compartment System

Some Possible Models for a Four-Compartment System. Note: that a system can have a model portrayed here but without all of the evolutions (i.e., a system can have model (iii) but without  $\tau_{24}$ ).

As mentioned above, global analysis results in the separation of the time-dependent transient spectra into sum of time-independent spectra  $[\mathcal{E}(\lambda)]$  weighted by a time-dependent concentration profile  $[C_n(t)]$ :

$$\Delta A(t, \lambda) = \sum_i^j C_i(t) \mathcal{E}_i(\lambda)$$

**Equation 3.3:** Separation of Spectral and Time Domains by Global Analysis

This is accomplished by fitting the data to the solutions of first order differential equations

$$\frac{dC_i}{dt} = A_i I(t) + \sum_{i,j} K_{i,j} C_j(t)$$

**Equation 3.4:** Solutions of First Order Difference Equations Used in Global Analysis



where  $A_i$  is a vector that contains the initial concentrations of the various subpopulations,  $I(t)$  is the temporal envelope of the pump pulse,  $K_{i,j}$  is a connectivity matrix (Equation 3.5) that contains the rate constants that describes the flow of population from the  $i^{\text{th}}$  population to the  $j^{\text{th}}$  population. First order differential equations are employed to fit the data since the reaction is assumed to be unimolecular.

$$K_{ij} = \begin{matrix} & K_{11} & K_{12} & \cdots & K_{1j} \\ K_{21} & & & & \\ \vdots & & & & \\ & K_{i1} & K_{i2} & \cdots & K_{ij} \end{matrix}$$

**Equation 3.5:** Global Analysis Connectivity Matrix

Initially, both transient absorption and cryokinetic data are fit with a sequential model where the population flows from one population to another sequentially ( $A \rightarrow B \rightarrow C \rightarrow \dots$ ) with consistently increasing lifetimes. When fitting the data, the fewest number of components that adequately fits the data are used. If the model represents the true underlying subpopulation, then species associated difference spectra (SADS) and their associated lifetimes are obtained. If the underlying dynamics are more complex or differ from the proposed model, the resulting spectra represent a linear combination of the SADS, and evolution associated difference spectra (EADS) are obtained along with the effective lifetimes of the various states. While a sequential approach is often sufficient to extract SADS for cryokinetics, this is not typically the case for the ultrafast dynamics which typically require more complex target models to isolate the underlying SADS. An example of sequential analysis using the ultrafast forward dynamics of NpR6012g4 as an example is presented below (Figure 3.15).

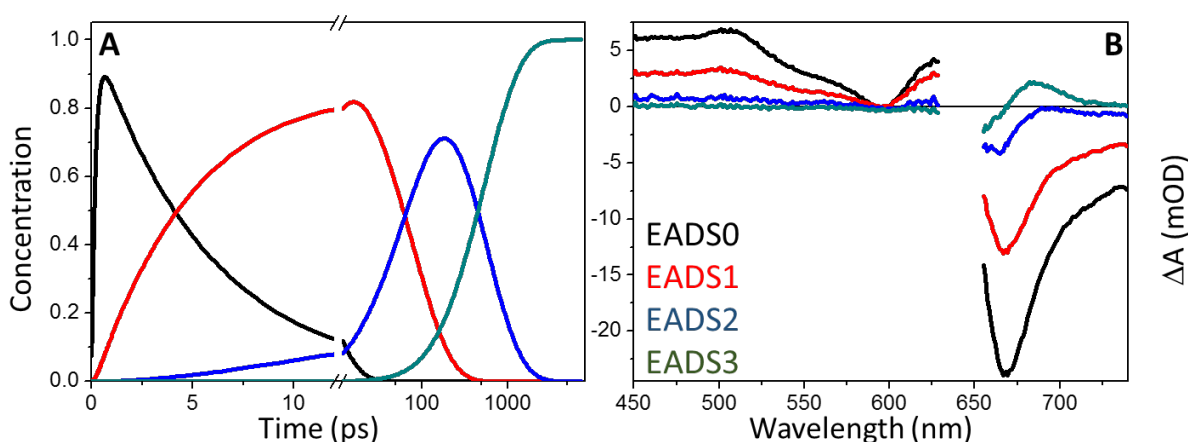


**Figure 3.15:** Example of Sequential Analysis using the primary forward dynamics of NpR6012g4

Representative concentration profiles and EADS obtained for the sequential analysis of the primary forward dynamics of NpR6012g4.

If the sequential model did not isolate the SADS, then more complicated target model is necessary that consist of coevolving subpopulations. As with the sequential model, the generation of the target model assumes a minimalistic approach when it comes to number of components and utilizes the observations from the raw transient spectra and kinetic traces of interest in junction with the EADS and effective lifetimes from the sequential approach. Using the primary forward dynamics of NpR6012g4 as an example, since there are features of similar excited state absorption and/or stimulated emission in the first two to three EADS indicates that there are at least two to three spectrally homogenous excited state populations. Furthermore, since the signal is comparable between ~650 and 730 nm in EADS0 and EADS1 indicates that the primary Lumi-R<sub>f</sub> intermediate is not generated by the faster evolving excited state subpopulation. The target model further differs from the sequential model since there are multiple starting populations whose initial concentrations all must sum to one. Since it is likely that the excited state populations have the same extinction coefficient, the starting concentrations of these compartments are adjusted to overlap the excited

state spectra while still summing to one. When taking all of these factors into account, the target model below was generated for the primary forward dynamics of NpR6012g4 and used to extract the corresponding SADS and concentration profiles (Figure 3.16).

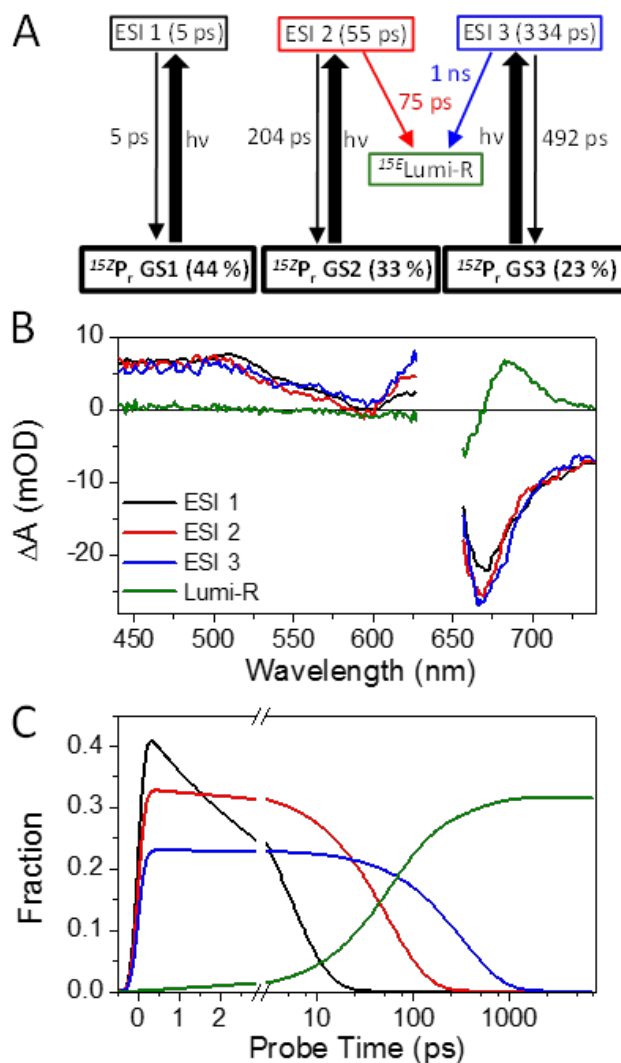


**Figure 3.16:** Representative target analysis for primary forward dynamics of NpR6012g4. Representative (A) target analysis and resulting (B) SADS and (C) concentration profiles for the forward primary dynamics of NpR6012g4 courtesy of Dr. Peter Kim.<sup>182</sup>

### ***Singular Value Decomposition Analysis for Spectral Decomposition***

To isolate the spectra of distinct populations from multidimensional data sets (i.e., such as time, temperature, pH dependent spectra) without imposing the bias of a kinetic model (i.e., first order associated with global analysis), singular value decomposition (SVD) analysis can be used. SVD analysis takes an M (wavelength) x N (variable) data matrix [D] and separates it into

$$[D] = [U][E][V]^t$$

**Equation 3.6:** Singular Value Decomposition

where [U] is a M x M matrix composed of spectral eigenvectors, [E] is a M x N singular values diagonal matrix and [V] is a N x N matrix of concentrations.

New eigenvectors (basis set) can then be generated by taking a linear combination of the basis set obtained from the SVD analysis. Generating eigenvectors requires an intuition of what the spectra should look like which is more straight forward for absorbance spectra than difference absorbance spectra since all absorbances will need to be positive. Since the experimental spectra has to be equal to the sum of the generated basis set weighted by the concentration of the subpopulations ([data] = [Basis Set][Conc.]; similar to Equation 3.3), the concentration of each basis set at parameter P can be determined by the following equation:<sup>221</sup>

$$[Conc.] = [Basis Set]^T * [Data] * inv([Basis Set]^T [Basis Set])$$

**Equation 3.7:** Determination of Concentration of Spectral Eigenvectors

The result of the SVD analysis of the temperature dependent spectra of the  $^{15}\text{E}_g$  signaling state of NpR6012g4 is presented in Figure 3.17.

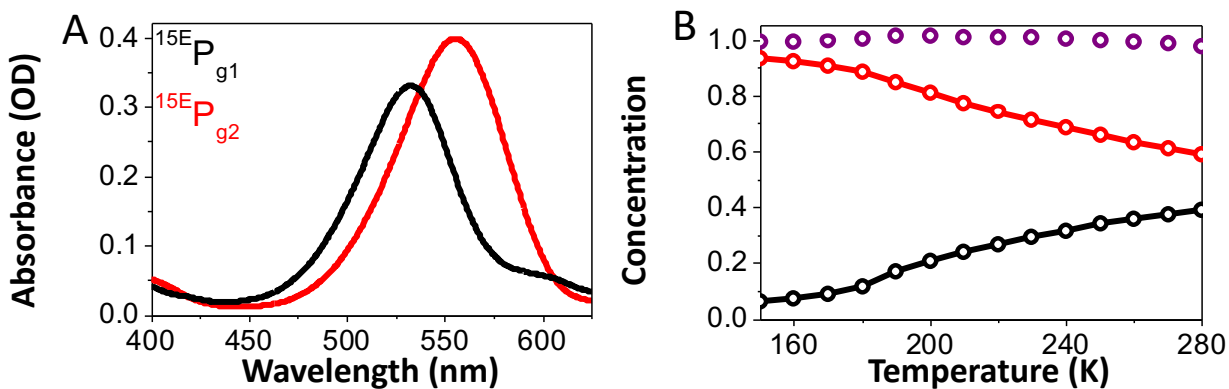


**Figure 3.17:**  $^{15}\text{E}_g$  Signaling State Basis Set for NpR6012g4

Representative (A) basis set and (B) concentration profiles from the SVD Analysis of the  $^{15}\text{E}_g$  signaling state of NpR6012g4.

To ensure a good fit of the basis set, a comparison of the experimental spectra and simulated spectra is required. If the simulated spectra are a good fit, then the basis set is a possible representation of the spectra of the subpopulations. The experimental spectra and simulated spectra using the basis set in Figure 3.17 at select temperatures for the  $^{15}\text{E}_g$  signaling state of NpR6012g4 are compared in Figure 3.18 showing a good fit.

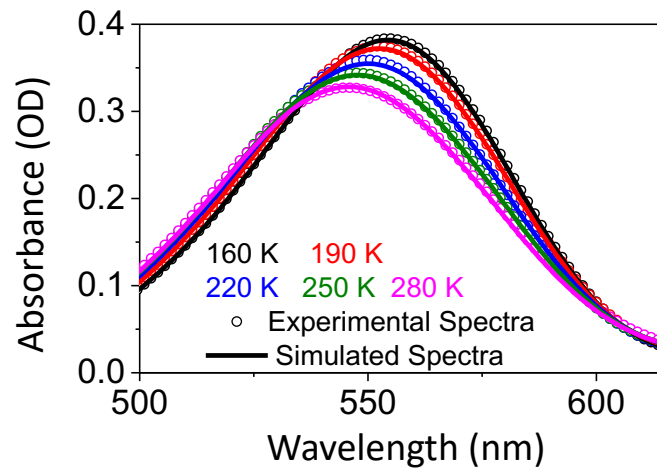


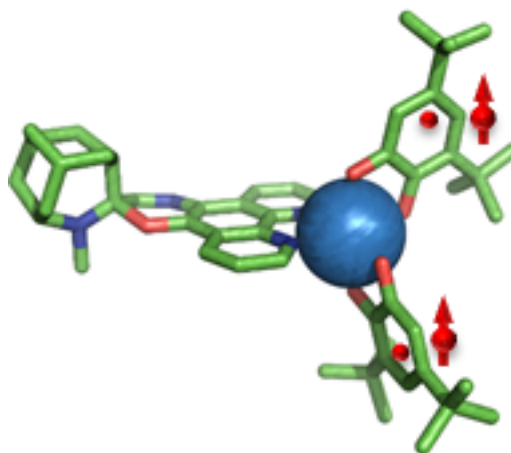
**Figure 3.18:** Simulated and Experimental  $^{15}\text{E}_g$  Signaling State Spectra Comparison of NpR6012g4

Comparison of the simulated and experimental  $^{15}\text{E}_g$  signaling state spectra of NpR6012g4.

# Chapter 4. Ultrafast Spintronics: Dynamics of the Photoisomerization-Induced Spin–Charge Excited-State (PISCES) Mechanism in Spirooxazine-Based Photomagnetic Materials

## *Abstract*

The optical control of spin state is of interest in the development of spintronic materials for data processing and storage technologies. Photomagnetic effects at the single molecule level have recently been observed in the thin film state at 300 K in photochromic cobalt dioxolenes. Visible light excitation leads to ring-closure of a photochromic spirooxazine bound to a cobalt dioxolene which leads to generation of a high magnetization state. The formation of the photomagnetic state occurs through a photoisomerization-induced spin-charge excited state process and is dictated by the spirooxazine ligand dynamics. Here, we report a mechanistic investigation by ultrafast spectroscopy in the UV-Vis region of the photochemical ring-closing process in the parent spirooxazine, azahomoadamantylphenanthroline spirooxazine and the photomagnetic spirooxazine cobalt-dioxolene complex. The cobalt appears to stabilize a PMC transient intermediate, presumably the TCC isomer, formed along the ground state potential energy surface. Structural changes associated with the TCC form induces formation of the high spin Co(II) form, suggesting that magnetization dynamics can occur along the excited state PES leading to ultrafast switching on the ps timescale. The ability of this system to undergo optically-induced spin state switching on the ps timescale in the solid state makes it a promising candidate for resistive nonvolatile memory technologies.



## ***Introduction***

The ever growing desire for improved methods of storing and processing data has led to intense research into quantum information processing technologies.<sup>222, 223</sup> Whereas conventional electronics utilize binary digits, quantum information processing relies on two-state quantum systems, such as photon polarization or electron spin, to form “qubits.” Entanglement and superposition of qubits leads to the generation of an infinite number of states, leading to an exponential increase in information storage and processing capabilities. Coherent population of spin states by optical excitation in organic materials provides an enticing strategy toward optical spin state manipulation.<sup>58, 224-234</sup>

We recently reported a novel strategy of generating photoinduced spin states through the coupling of ligand field switching to spin-coupled charge transfer in a class of electronically bistable cobalt complexes that incorporate a photochromic spirooxazine ligand.<sup>235</sup> A **Photoisomerization-Induced Spin-Charge Excited State (PISCES) process is observed that involves photo-induced switching of the spirooxazine ligand through steady-state irradiation with visible light (550 nm). The photoisomerization initiates a charge transfer spin transition process at the cobalt center, leading to a reversible increase in magnetization in both solution and organic thin films. The PISCES process enables optically induced and reversible changes in charge and spin states. Due to the unusually long lifetime (10 s) of the photoinduced charge/spin state at 300 K, the optically induced changes in oxidation and spin states can be directly observed for the first time by magnetometry and electronic absorption spectroscopy at ambient temperatures in the solid state.<sup>235</sup>**



The key to initiating the PISCES mechanism is the photoswitching (ring closing) reaction of a modified spirooxazine ligand between the open photomerocyanine (PMC) and ring-closed spirooxazine (SO) conformations (Figure A4.1). The PISCES process involves four primary metastable states (Figure 4.1). Photoexcitation of ground-state PMC-*ls*-Co(III) semiquinone form ( $S = 1/2$ ) of the complex (**1a**) leads to ring closure (**1b**). The SO form is a stronger  $\pi$  acceptor (by 0.3 eV) than the open PMC form and is predicted to stabilize the Co(II) state.<sup>236</sup> The change in ligand field is proposed to trigger a ligand-to-metal charge transfer/spin transition from a bound di-*tert*-butyl catecholate (DTBQ) ligand to the *ls*-Co (III) center to generate a SO-*hs*-Co(II) bis-semiquinone sextet state (**1c**) with a resultant increase in magnetization. The lifetime of the photoinduced magnetic state ( $\tau \sim 10$  s) appears to be dictated not by metal-centered excited states, which decay rapidly at room temperature (1-2 ns)<sup>237, 238</sup>, but by the lifetime of the SO metastable state of the photochromic ligand (**1c**  $\rightarrow$  **1d**).<sup>235</sup>

The principal advantages of the PISCES approach are that (i) the optical modulation of spin state originates at the single molecule level and can be controlled by the optical gating of the photochromic ligand, and (ii) because the photochrome can photoswitch in the solid state, the system can be incorporated into thin film device architectures.

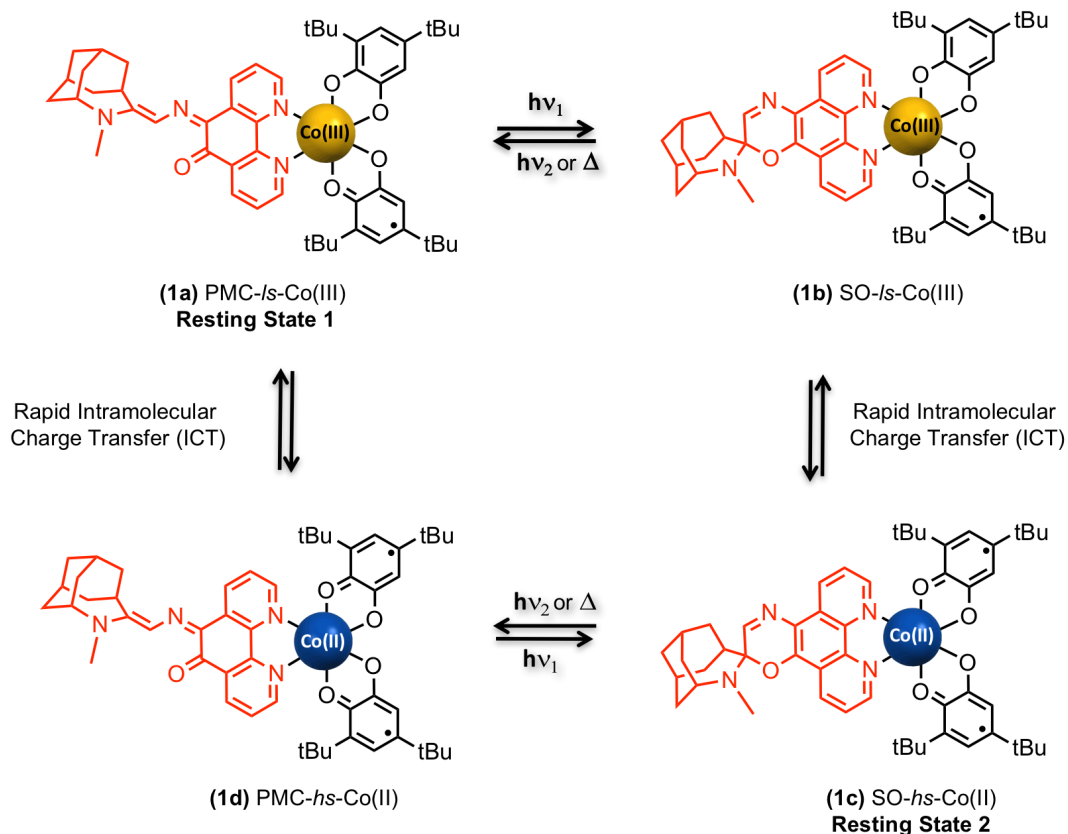


**Figure 4.1:** Photoisomerization-Induced Spin-Charge Excited-State Process

Generation of photomagnetic states of CoAPSO complex via a PISCES process. The APSO ligand is highlighted in red and the DTBQ ligands are in black. The cobalt metal is yellow and blue for the *low-spin* Co (III) and *high-spin* Co (II) oxidation states, respectively.

Due to the greater stability of the closed SO form of most spirooxazines, previous ultrafast dynamics studies focused on the light-induced ring-opening (SO  $\rightarrow$  PMC) reaction,<sup>83-96</sup> with the exception of Kumar et al.<sup>97</sup> who explored the ultrafast ring closing (PMC  $\rightarrow$  SO) photodynamics. Hence, the primary events underlying the PISCES mechanism of the modified spirooxazines species in Figure 4.1 are still unknown. Questions arise as to whether the potential energy surfaces of the photochrome excited states and metal-centered excited states cross, and whether there is electronic mixing between states. Additional unresolved questions include the role of vibrational excited (“hot”) ground state intermediates (GSIs), excited state evolution, and the nature of conical

intersections (CI) in the photodynamics of the spirooxazines. Here, we report a mechanistic investigation by ultrafast transient absorption (TA) spectroscopy of the primary photochemical ring-closing process in the parent spirooxazine, azahomoadamantylphenanthroline spirooxazine (APSO) and the spirooxazine cobalt-dioxolene complex (CoAPSO).

Figure 4.1A contrasts the ground state absorption spectra of APSO in the dark-adapted PMC (black curve) and light-adapted SO (red curve) conformations. As with other spirooxazines, the PMC state exhibits a strong  $\pi$ - $\pi^*$  transition near 550 nm, while the SO configuration absorbs in the ultraviolet around 330 nm.<sup>98, 235</sup> CoAPSO exhibits similar photoactivity with visible light illumination inducing the formation of the SO (and loss of the PMC) as indicated by decreasing 555 nm absorption (Figure 4.1B). However, the ring-closing dynamics of CoAPSO also results in an increase in the weak 700-800 nm transition (Figure 4.1B inset) that corresponds to a high-spin Co(II) MLCT band.<sup>235</sup>

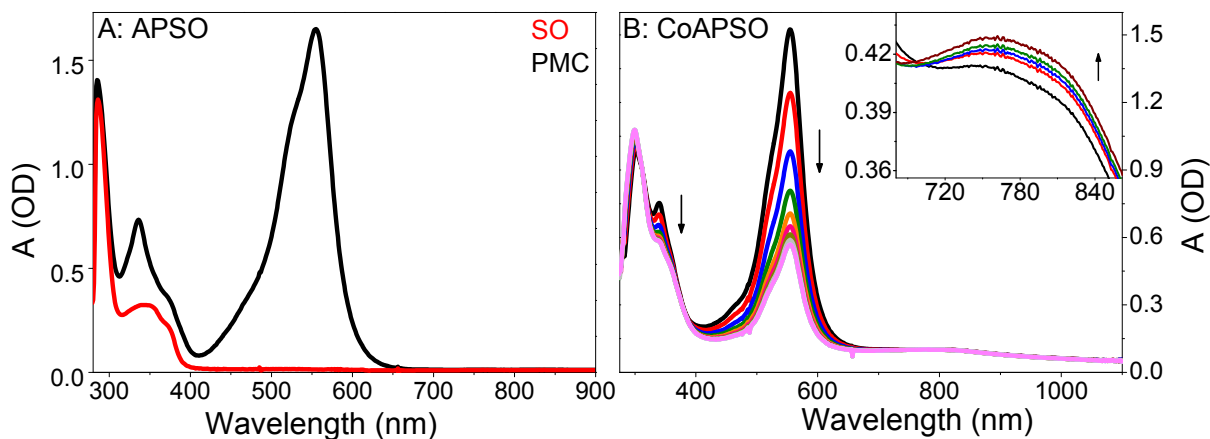


**Figure 4.2:** APSO and CoAPSO Static Dark-Adapted State Spectra

Normalized ground-state absorption spectrum for APSO (A) and CoAPSO (B) in toluene. (B) Steady state illumination of CoAPSO with 450-550 nm light, resulting in the conversion of the PMC to the SO given the decrease of the PMC  $\pi$ - $\pi^*$  band at 550 nm and increase of the *hs*-Co(II) MLCT band at 800 nm (inset).

The primary dynamics of ring closure reactions have been extensively studied in the related class of spiropyrans.<sup>79-82</sup> For spiropyran ring closure, both a singlet (py-BIPS, 6,8-dinitro BIPS, 6,8-dinitro BIPS/1'-(2-carboxyethyl) substituted derivative)<sup>79-81</sup> and a triplet<sup>82</sup> pathway have been proposed. The singlet pathway involves an initially vibrationally excited S<sub>1</sub> population that either directly evolves into the closed SO form<sup>79</sup> or relaxes to a hot GSI on the S<sub>0</sub> state of the PMC before evolving into the SO form.<sup>81</sup>

Kumar et al. reported the only ultrafast study of the ring closure excited-state dynamics of a spirooxazine chromophore, specifically 1,3-Dihydro-1,3,3-trimethylspiro[2H-indole-2,3'-[3H]phenanthr [9,10b](1,4)oxazine] (IPSO).<sup>97</sup> In contrast to APSO and CoAPSO, IPSO is like most spirooxazines with a closed SO configuration as the dark-adapted ground-state. Independently, Reguro and co-workers and Robb and co-workers studied the thermal and photoisomerization of the ring-closure reaction computationally of 2H-benzo[b][1,4]oxazine<sup>239</sup> and 3,4-dihydroquinoline chromophores,<sup>240</sup> respectively. In both systems, the photoreaction involved a trans-to-cis isomerization followed by a single-bond rotation prior to ring closure. However, it has also been proposed that thermal ring-closure reactions either proceed through a single-step rotation<sup>241</sup> or a two-step inversion pathways<sup>242</sup> (Figure A4.3).

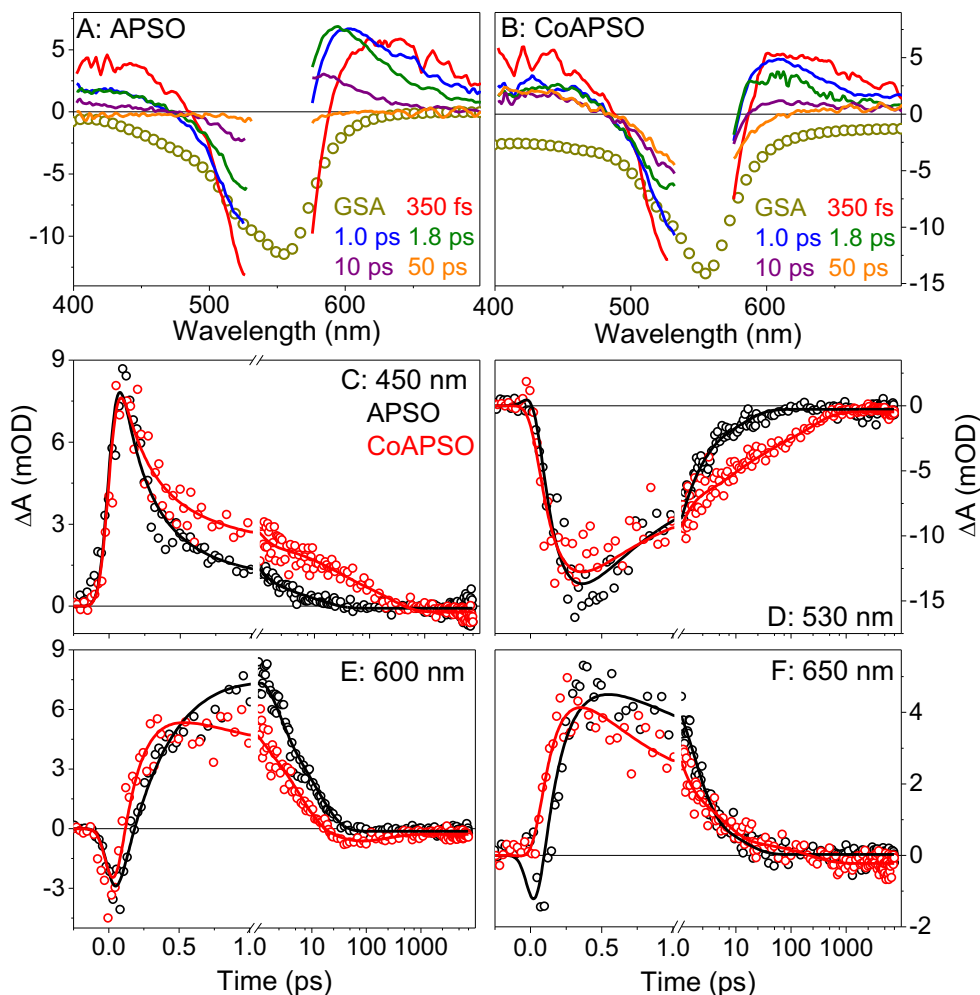
### ***APSO and CoAPSO Ultrafast Dynamics***

Figure 4.2 compares the visible TA signals for APSO and CoAPSO. The signals for both resemble the dynamics previously reported for IPSO with several key differences.<sup>97</sup> The TA spectra for both APSO and CoAPSO exhibit strong negative bleaches centered around 550 nm that are flanked by

positive absorptions (Figure 4.2A and Figure 4.2B). The red-flanked absorptions in both systems blue-shift on a  $\sim$ ps timescale, which is resolved as a growth in the 600-nm kinetics (Figure 4.2E and Figure 4.2F; black curves). Both blue flanking absorptions persist longer for CoAPSO than for APSO, while the red flanking absorptions decays more quickly to exposes negative bleach signals.

The APSO and CoAPSO kinetics are also multiphasic. In the 600 nm kinetics in Figure 4.2E and Figure 4.2F, there were short-lived decays ( $< 200$  fs) in the signals before a growth for both APSO and CoAPSO, respectively. This short-lived decay is observed in the initial TA spectra for APSO and CoAPSO, respectively (Figure A4.2). There was also a negative signal in the CoAPSO starting around 30 ps after the decay of the excited state absorption for the 600 nm kinetic trace (Figure 4.2E; black curve) that is also resolved in the 50 ps spectra around 600 nm (Figure 4.2B gold curve). This negative signal is likely the ground-state bleach since it overlaps the CoAPSO absorption spectrum (Figure 4.1), but does not appear in the APSO signals (Figure 4.2E).

Kumar et al. also observed a negligible quantum yield of ring closure in IPSO and suggested this originated from most of the excited-state population evolving through a non-productive “parasitic” conical intersection (CI) that quenched excited-state population back toward the PMC configuration rather than toward successful ring closure.<sup>97</sup> They proposed a four-state model according to which photogenerated PMC-S<sub>1</sub> population is rapidly (285 fs) quenched by a CI between the S<sub>1</sub>/S<sub>0</sub> surfaces to generate a hot PMC-S<sub>0</sub> GSI population that subsequently cools on 550 fs and 7.6 ps timescales.



**Figure 4.3:** APSO and CoAPSO Transient Absorption and Kinetics

Transient absorption (2A for APSO; 2B for CoAPSO) and kinetics (C-F; black curves: APSO; red curves: CoAPSO) for APSO and CoAPSO in the visible region. TA data is represented by open circles and the fit by solid lines obtained from the global analysis model in Figure A4.7. The transient spectra including the initial spectra are shown in more detail in Figure A4.2. The CoASPO signals were scaled two-fold to aid in comparison.

To aid in the interpretation of the multiphasic TA data for APCO and CoAPSO, the datasets were analyzed with a multi-compartment global analysis formalism<sup>221, 243</sup> that decomposes the data, via a postulated model, into *time-dependent* populations (i.e., concentration profiles) with *time-independent* spectra (Figures 4.4 and A4.6-A4.7). The TA datasets for both APSO and CoAPSO

were fit to a model involving the sequential evolution of multiple populations via unidirectional steps. The spectra extracted from these models are called Evolution Associated Difference Spectra (EADS) and reflect the spectra of transient populations of systems with sequential dynamics although may reflect coexisting populations. The TA datasets were fit to either a 5-population (APSO) or 6-population (CoAPSO) sequential model that fit the data well (Figure 4.3; solid curves) and the resulting EADS with estimated rate constants are qualitatively similar (Figure 4.4) to each other and to the IPSO signals reported by Kumar et al.<sup>97</sup> To interpret these EADS and kinetics, we adopt a multi-step mechanism based on potential energy surfaces calculated for the simpler ring-closing reaction of 2*H*-benzo[*b*][1,4]oxazine by Castro et al. (Figure 4.5).<sup>239</sup> From these surfaces we can correlate the non-adiabatic evolution of APSO (thick yellow lines) and CoAPSO (thick green lines) to the observed EADS in Figure 4.4.

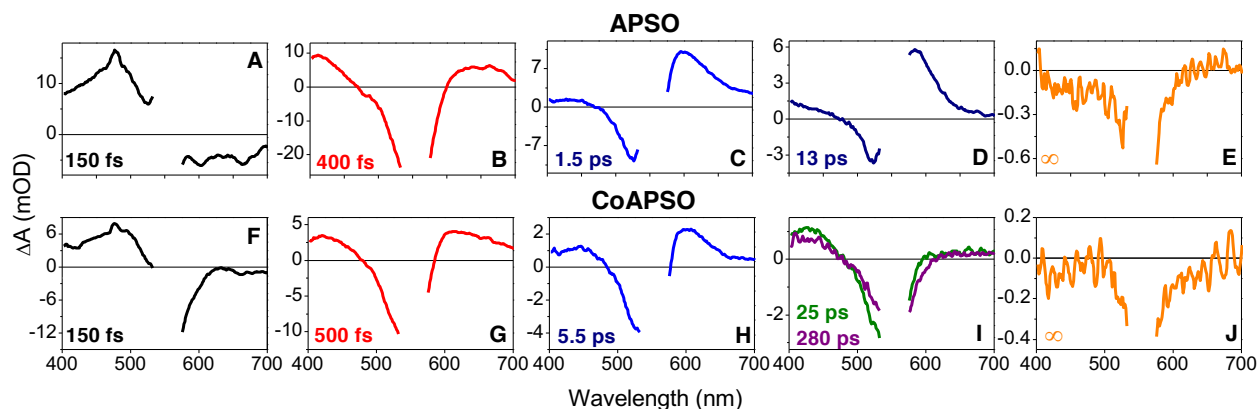


**Figure 4.4:** APSO and CoAPSO EADS

EADS for APSO (A-E) and CoAPSO (F-J) from the sequential model in Figure A4.7. Lifetimes are indicated in the legend. The 25 ps and 280 ps EADS for CoAPSO are overlapped in Figure 4.4I.

## ***Results and Discussion***

The Castro et al. study argues that the transition with the greatest oscillator strength for trans-PMC- $S_0$  of APSO is the  $S_0 \rightarrow S_3$  ( $\pi$ - $\pi^*$ ) transition (Figure 4.5; solid green arrow from point #0 to

point #1). The nascent excited-state trans-PMC-S<sub>3</sub> population (point 2) is observed in the TA data as the initial EADS (Figure 4.4A) and evolves along an isomerization coordinate on the S<sub>3</sub> surface before crossing two conical intersections with S<sub>2</sub> and S<sub>1</sub> surfaces. This rapidly quenches the S<sub>3</sub> population (~150 fs) to generate a vibrationally excited S<sub>1</sub> population (point 2) and as with hot populations, the EADS for this hot-PMC-S<sub>1</sub> population exhibits a broad, red-shifted absorption (Figure 4.4B). The hot-PMC-S<sub>1</sub> population is likely twisted along the isomerization coordinate that is expected to be initial intermediate in the ring-closing reaction.<sup>239,240</sup> The cooling and twisting dynamics (400-fs and 1.5 ps) of the hot-PMC-S<sub>1</sub> to generate the relaxed state (point 3) is resolved as a blue-shifting in the EADS (Figure 4.4C-D) of the red-flanked excited-state absorption (>600 nm) and is characteristic for the vibrational relaxation of similar rapidly-generated hot excited-state populations.<sup>244, 245</sup> Concurrent with vibrational relaxation is a partial population loss back to the original trans-PMC-S<sub>0</sub> population (point 0) is presumably facilitated by a CI between the S<sub>1</sub> and S<sub>0</sub> surfaces. After relaxation, the resulting relaxed-PMC-S<sub>1</sub> population evolves through a parasitic CI back to the original trans-PMC-S<sub>0</sub> population on a 13 ps timescale (Figure 4.4D). A weak portion of the population (Figure 4.4E) is successful in completing the ring-closing reaction (point 5) with an EADS that strongly resembles the bleach of the PMC form (Figure 4.2A; black curve). The yield for the ring-closure reaction is estimated at 2% from a simple comparison of the amplitude of initial and terminal bleaches (Figure A4.4C). However, it is unclear if this reaction occurs via an excited-state mechanism (e.g., point 3 → point 5) or a ground-state mechanism (point 3 → point 4 → point 5) since no clear cis-PMC-S<sub>0</sub> population is observed in the TA signals. Hence, neither productive pathway is included in Figure 4.5.



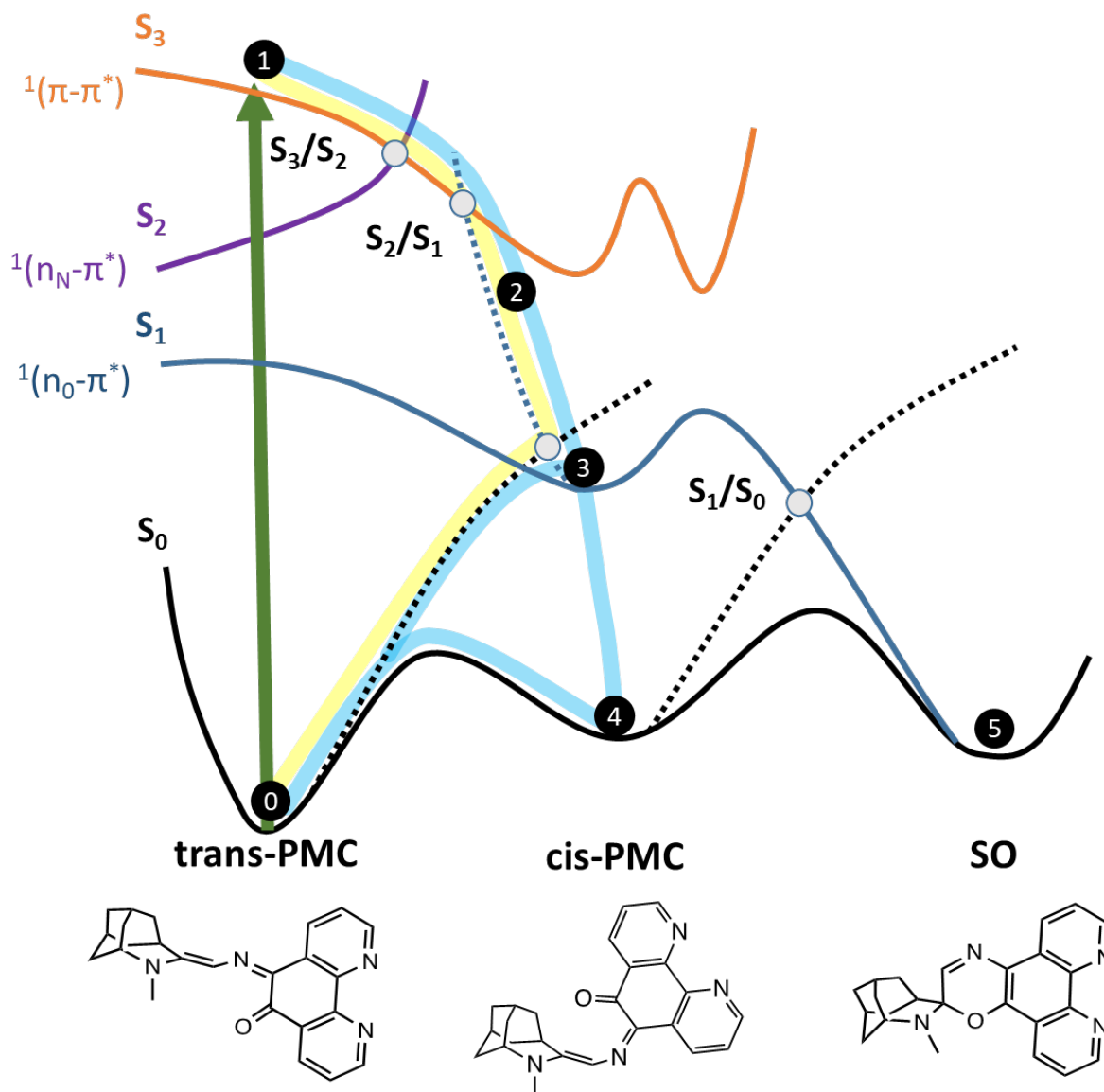


**Figure 4.5:** Generalized ring-closing reaction diagram for APSO/CoAPSO

Generalized ring-closing reaction diagram for APSO/CoAPSO based off of the potential energy surfaces calculated for *2H*-benzo[*b*][1,4]oxazine system calculated by Castro et al.<sup>239</sup> The reaction progress at the minima of the relevant electron surfaces are shown in solid lines while key non-minimized regions of the electronic surfaces are shown as dashed lines (where CIs are encountered). Key conical intersections are shown as grey filled circles. Structures for the trans-PMC, cis-PMC, and SO states are shown at the bottom. The thick transparent yellow and green lines indicate the APSO and CoAPSO evolutions, respectively. The pathways resulting in successful ring closure are not shown.

The EADS are qualitatively similar for APSO (Figure 4.4A-E) and CoAPSO (Figure 4.4F-J) suggesting similar evolution dynamics for the two systems (Figure 4.5; thick green and yellow curves). However, two important differences can be resolved: (1) the biphasic vibrational relaxation kinetics are distinctly slower in CoAPSO (500 fs vs. 400 fs and 5.5 ps vs. 1.5 ps) and (2) the relaxed-PMC-S<sub>1</sub> population decays more slowly (25 ps vs. 13 ps). For APSO, relaxed-PMC-S<sub>1</sub> decays directly into trans-PMC-S<sub>0</sub> (mostly) and for CoAPSO, relaxed-PMC-S<sub>1</sub> population coexists with a new population that is not observed in APSO and absorbs at 425 nm (Figure 4.4I; purple curve). This population is ascribed to the cis-PMC-S<sub>0</sub> (Figure 4.5; point 4) and persists on a 280 ps timescale before decaying back into trans-PMC-S<sub>0</sub>. A simple comparison of 500-fs and 280-fs EADS estimates that 17% of the excited-state population evolves into cis-PMC (Figure A4.4A). As with the terminal APSO EADS (Figure 4.4E), the terminal spectrum for CoAPSO (Figure 4.4J) strongly resembles the CoAPSO bleach (Figure 4.3); the yield for successful ring-closing is estimated at 4% (Figure A4.4B). As with APSO, it is unclear if the increased ring-closure reaction yield is due to manipulating the S<sub>1</sub> or S<sub>0</sub> surfaces. The long living cis-PMC-S<sub>0</sub> population would facilitate the ground-state evolution, while the longer-lived PMC-S<sub>1</sub> populations would also facilitate the excited-state mechanism.

The cobalt-benzoquinone components in CoAPSO stabilizes the cis-PMC-S<sub>0</sub> population (Figure 4.5; point 4) and the EADS for this population has an absorption peak around 425 nm (Figure 4.4I) with a weak, but resolvable, absorption that extends to the near IR (NIR). Figure 4.6 compares the kinetics of APSO and CoAPSO probed at 800 nm. The APSO near infra-red (NIR) signals are monophasic with a rapid rise and 400 fs decay attributed to the vibrational relaxation phase resolved in the visible TA data (Figure 4.4B); however, the subsequent structural dynamics are not

mirrored in the NIR kinetics. In contrast, the CoAPSO NIR signals are appreciably more complex (Figure 4.6B) with non-monotonic evolution and a long-living positive absorption. Since these data exhibit the same 280 ps kinetics resolved for the cis-PMC-S<sub>0</sub> population in the visible TA data (Figure 4.4I) then the terminal relaxation phase can be ascribed to decay of cis-PMC-S<sub>0</sub>. Its absence in the APSO signals (Figure 4.6A) further reinforces the interpretation of the visible TA data discussed above.

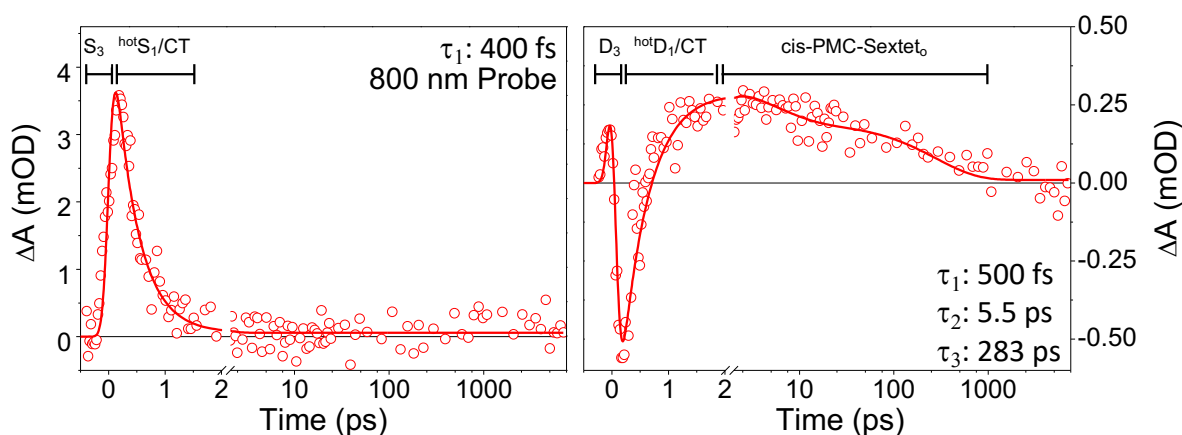


**Figure 4.6:** Dynamics at the MLCT Band

800-nm kinetics of APSO (A) and CoAPSO (B). Solid lines are global fits with the same sequential model and timescales used for the visible and UV spectral regions. The rate constants used for the fitting are given, with APSO requiring a single-component fit with a rate constant of 400 fs and CoAPSO requiring a three-compartment model with rate constants of 500 fs, 5.5 ps, and 280 ps (Figure A4.7).

Complexation of APSO to the electronically bistable cobalt dioxolene fragment leads to the appearance of a weak band in the 800 nm region assigned to a forbidden Co(II)-benzoquinone MLCT band of the CoAPSO complex (Figure 4.1B, inset). In the trans-PMC-S<sub>0</sub> state of CoAPSO, the absorbance of this band is weak due to a small population of the Co(II) form and dominant population of the PMC-Is-Co(III) form of the complex (Figure 4.1). The ligand-to-metal charge-

transfer intrinsic to the PISCES process (Figure 4.1) involves an electron transfer from the catecholate form of the DTBQ ligand to *ls*-Co-III, resulting in a broad 800-nm absorption assigned to a *hs*-Co(II)-semiquinone CT state, typically observed in the Co(II) state of the parent diimine cobalt dioxolenes.<sup>237, 238</sup> The observation of this CT band upon population of the *hs*-Co(II) state was initially postulated to occur after full ring closure. It is likely that the broad absorption of the *cis*-PMC-S<sub>0</sub> population of CoAPSO (Figure 4.4I) extends to the 800-nm probe kinetics (Figure 4.6B) and can be ascribed to this *hs*-Co(II) MLCT band. The <2 ps dynamics can be ascribed to the charge transfer from the catecholate to the *ls*-Co(III) metal center. Consequently, the full ring closure of the spirooxazine ligand is not necessary to induce the desired redox chemistry and induced spin state. A comparison with the conversion of the Co(II) mole fraction under steady state irradiation conditions reveals that the % Co(II) generated is close to the 17% estimated for population of the *cis*-PMC-S<sub>0</sub> state. Steady-state irradiation of a CoAPSO thin film (~300 nm) at 550 nm (5 mW/mm<sup>2</sup>) leads to formation of a photostationary state in 200s with a change in the Co(II) mole fraction of 21%, close to the 17% yield of *cis*-PMC-S<sub>0</sub> state population observed. A change of 21% mol fraction of Co(II) leads to a 37% change in magnetization per mol of substrate. This suggests that the PISCES process may be a generalized strategy to the optical gating of spin states in electronically bistable metal complexes, with a sufficient yield of photogenerated species for spin state detection.

### ***Closing Comments***

To conclude, the transient data suggests the formation of a meta-stable *cis* photo-intermediate that persists (~40 -100 ps) before evolving back into the original PMC state (Figure 4.5). It is unclear if this unstable photoproduct is the result of the double-bond or single-bond rotation, but the Co metal and accompanied ligands stabilize the primary *cis* intermediate so that its decay kinetics are clearly separate

from the excited-state populations that generate it. For both APSO and CoAPSO there is weak (2%-4%) ring-closure yield, with the primary path being relaxation back to the trans-PMC. This cis-PMC intermediate exhibits the spectroscopic signature of a spin-flip redox reaction, which suggesting the PISCE mechanisms for CoAPSO is operable with a picosecond photoswitching activity.

### *Associated Content*

#### *Supporting Information (pg. 262)*

The Supporting Information provides a description of the sample preparation, isomerization models, transient absorption experiment and global analysis, and assignment of the EADS signals. Supplemental transient figures and the quantum yield estimation are also provided.

#### *Funding*

This work was supported by the National Science Foundation to D.S.L. (CHE-1413739) and a National Science and Engineering Research Council (NSERC) Grant (RGPIN) to N.L.F.

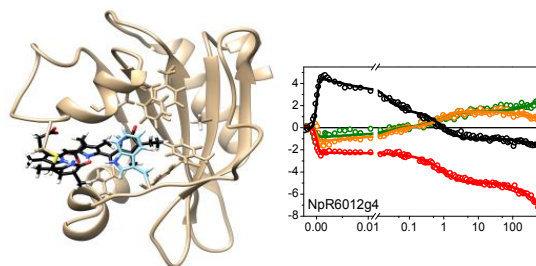
#### *Acknowledgments*

Dr. Mikas Vengris (Light Conversion Ltd.) is acknowledged for the donation of global and target analysis software.

# Chapter 5. Conservation and Diversity in the Secondary Forward Photodynamics of Red/Green Cyanobacteriochromes

## Abstract

Cyanobacteriochromes (CBCRs) are photosensitive proteins that are distantly related to the phytochrome family of photoreceptors that exhibit photoactivity initiated by the excited-state



photoisomerization of a covalently bound bilin chromophore. The canonical red-green sub-family is the most studied class of CBCRs studied to date. Recently, a comparative study of the ultrafast (100 fs – 10 ns) forward photodynamics of nine red/green photoswitching CBCR domains isolated from *Nostoc punctiforme* were reported. We extend this study by characterizing the secondary (10 ns -1 ms) forward photodynamics of eight red/green photoswitching CBCRs from *N. punctiforme* with broadband time-resolved absorption spectroscopy. We demonstrate that the dynamics of these representative red/green CBCRs can be separated into two coexisting pathways involving a photoactive pathway that is successful in generating the  $^{15E}P_g$  signaling state and an unsuccessful pathway that stalls after generating a meta-stable Lumi- $O_f$  intermediate. The photoactive pathway evolves through a similar mechanism that consist of a far-red absorbing Lumi- $R_f$  intermediate that ultimately generates the  $^{15E}P_g$  state via a succession of blue-shifting photointermediates. This suggests a steady deviation from planarity of the bilin chromophore during the dynamics. Only half of the characterized CBCRs exhibit the unproductive pathways due to photoexcitation of dark-adapted  $^{15Z}P_o$  sub-population.  $^{15Z}P_o$  is ascribed to the binding of the “lid-tryptophan” that fails to  $\pi$  stack to the D-ring of the bilin in the dark-adapted state and its presence can be identified via enhanced absorption of high-energy tail of the electronic absorption spectrum.

## ***Introduction***

Nature has optimized light sensitive proteins over many millennia to efficiently couple photon absorption into useful biological photoactivity and includes important processes such as photo-induced homeostasis and photosynthesis.<sup>31, 246, 247</sup> Although the mechanisms underlying photo-induced homeostasis activity differ greatly depending on the nature of the relevant photoreceptor protein that initiates the signaling cascade,<sup>248</sup> they typically involve small photoinduced structural change of an embedded chromophore (often isomerization, although other mechanisms like electron transfer and adduct formation also occur) within protein scaffolding to trigger a cascade of events that results in large scale structural rearrangements required to propagate signaling pathways.

Phytochromes, which are multidomain proteins that bind linear tetrapyrrole (bilin) chromophores and exhibit red (650-700 nm) and far-red (720-750 nm) sensitivity.<sup>248, 249</sup> These photoreceptors were initially discovered in plants and are responsible for light-induced responses such as shade avoidance and de-etiolation,<sup>250, 251</sup> but were subsequently discovered in algae, bacteria, cyanobacteria, and fungi.<sup>249, 252-254</sup> These broadly distributed photoactive proteins utilize different bilin chromophores depending on the organisms. For example, bacterial phytochromes use biliverdin-IX $\alpha$  (BV), while plant and cyanobacterial phytochromes utilize the more reduced phytychromobilin (P $\Phi$ B) and phycocyanobilin (PCB) chromophores, respectively.<sup>255</sup> Photoexcitation of the bilin chromophore in the P<sub>r</sub> dark-stable state of phytochrome (with its D-ring in a *15Z* configuration) initiates a photoisomerization reaction that generates a spectrally red-shifted primary Lumi-R intermediate (with its D-ring presumably adopting a *15E* configuration);



this is the first step in a series of intermediates that ultimately results in the formation of the terminal light-adapted  $P_{fr}$  photoproduct.

Cyanobacteriochromes (CBCRs) photoreceptors are distantly related to phytochromes in binding bilin chromophores, but differ in their domain structure, photoactivity, and photochemistry.<sup>246, 256</sup> A distinguishing feature of CBCRs is that isolated bilin-binding cGMP-specific phosphodiesterases, adenylyl cyclases and FhlA (GAF) domains exhibit reversible *in vitro* photoactivity; phytochromes require the flanking domains to exhibit similar activity.<sup>111, 176, 180, 184, 190, 195, 256</sup> The *in vivo* phenotypic roles of only very few CBCRs have been elucidated to date.<sup>257</sup> For example, the SyPixJ1 CBCR mediates positive phototaxis in *Synechocystis*<sup>258</sup> and NpCcaS in *Nostoc (N.) punctiforme* responds to changing ambient light conditions by modulating the expression of light harvesting antennae via a process known as complimentary chromatic adaptation (CCA).<sup>210, 259</sup> Furthermore, The hormogonia filaments of *N. punctiforme* were shown to require the NpF2161-2168 locus for the phototactic response.<sup>22</sup>

The canonical red/green family is the most extensively studied class of CBCRs with both primary<sup>176, 182-185</sup> (100 fs to 10 ns) and secondary<sup>177, 186, 187, 256, 260</sup> (10 ns to 10 ms) dynamics reported. However, many questions remain unanswered, especially finding the key to predicting the behavior within the family. Recently, Gottlieb et al. reported a wide-ranging study focusing on the diversity of primary forward reaction ( $^{15Z}P_r \rightarrow ^{15E}P_g$ ) photodynamics of nine red/green CBCR domains from *N. punctiforme* with ultrafast transient absorption spectroscopy.<sup>176</sup> These dynamics exhibit diverse kinetics and photocycle spectral dynamics, implicating the importance of protein structure in modulating the primary photoactivities of the conserved PCB chromophore. The

photodynamics of canonical red/green CBCRs were assigned to three classes (I, II and III) based on observation of zero, one, or two photoproducts within an  $\sim 10$  ns timescale.<sup>176</sup> The subsequent secondary (10 ns - 1 ms) dynamics track the evolution of these photoproduct(s) into the light-adapted state through to the formation of multiple transient intermediates (Figure 5.1). The primary forward dynamics consisted of  $^{15Z}P_r^*$  excited state and the primary  $^{15E}Lumi-R_f$  photointermediate and in some cases the next intermediate, while the secondary forward dynamics capture the evolution of  $^{15E}Lumi-R_f$  and the subsequent population to  $^{15E}P_g$ .<sup>108, 182</sup> The reverse dynamics complete the photocycle and involve the photoexcitation of the light-adapted  $^{15E}P_g$  population and the subsequent evolution to regenerate  $^{15Z}P_r$ .

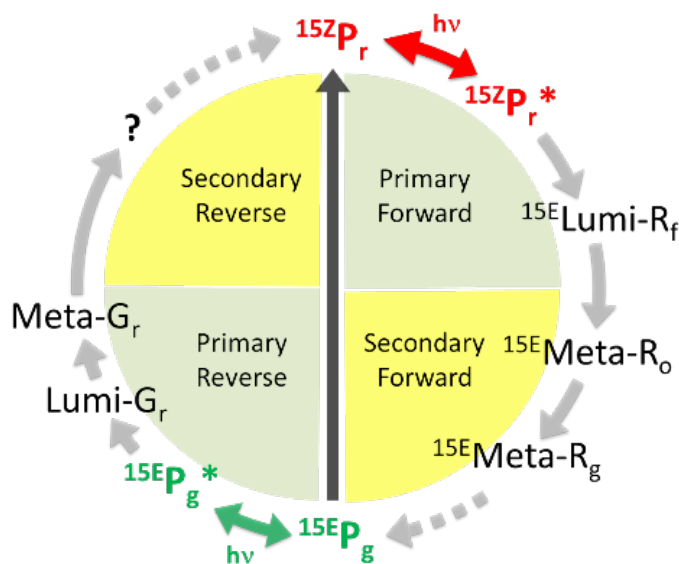


**Figure 5.1:** Canonical Red/Green CBCR Photocycle

Generalized red/green photocycle that comprised of the previously reported primary (150 fs – 8 ns) and secondary (550 ps – 1 ms) forward dynamics and primary reverse dynamics of NpR6012g4. The central black arrow going from  $^{15E}P_g$  to  $^{15Z}P_r$  represents dark reversion from the light state to the dark state.

The secondary dynamics for only a handful of CBCRs have been reported to date including NpF2164g3<sup>111</sup> and NpF2164g7<sup>187</sup> (B2J668), RcaE (Q47897),<sup>192</sup> NpR6012g4 (B2IU14),<sup>108</sup> AnPixJg2 (Q8YXY7),<sup>177</sup> NpR3784 (B2J457),<sup>188</sup> and Slr1393g3 (P73184).<sup>186</sup> The secondary forward dynamics of NpR6012g4 (red/green), NpF2164g7 (orange/green) and secondary reverse dynamics of RcaE (green/red) are unique among biliproteins since they exhibited heterogeneous dynamics beyond the primary dynamics timescale (>10 ns).<sup>187, 192</sup> The secondary forward dynamics of NpR6012g4 and secondary reverse dynamics of RcaE exhibited multiple spectrally heterogeneous Lumi photoproducts, where only one was photoactive in propagating to generate the light-adapted state. The secondary dynamics of NpR6012g4 was published alongside wildtype and mutant NpR6012g4 NMR data that correlated this spectral inhomogeneity to heterogeneous ground state structures.<sup>108</sup> The secondary forward dynamics of Slr1393g3 (red/green) resulted in the isolation of two intermediates before forming <sup>15E</sup>P<sub>g</sub> that differed from NpR6012g4 which exhibit a conserved mechanism of blue shifting intermediates, by having intermediates that are both blue shifted and red shifted of each other.<sup>186</sup>

These studies present a complex range of secondary dynamics in CBCRs including both homogeneous and inhomogeneous evolution, population merging (equilibration), shunting, and population collapsing. It is still unclear whether or not the secondary dynamics evolve through conserved mechanisms even for a specific sub-family. To address this, we collected the secondary dynamics (8 ns – 1 ms) using broadband transient absorption spectroscopy of eight red/green CBCR GAF domains isolated from *N. punctiforme*. This study complements the previous report of the primary dynamics (150 fs – 7.5 ns) of the same red-green CBCRs.<sup>176</sup>

## ***Material and Methods***

### *CBCR Purification and Characterization.*

The CBCRs GAF domains that were expressed were NpAF142g2, NpR1597g4, NpF2164g4, NpF2164g6, NpF2854g3, NpR4776g2, NpR4776g3, and NpR6012g4.<sup>176, 182-184</sup> The NpF2164g5 domain, explored in the Gottlieb et al. study,<sup>176</sup> was not characterized here since it is not a photoactive CBCR (i.e., does not generate a  $^{15}E_P_g$  state). Multiple sequence alignment of eight red/green GAF domains from *N. punctiforme* ATCC 29133 were performed using MUSCLE.<sup>261</sup> These sequences are aligned with the red/green CBCR domain AnPixJg2 (Q8YXY7), from *Anabaena* sp. PCC 7120 and the GAF domain of the phytochrome Cph1 (Q55168) from *Synechocystis* sp. PCC 6803 for comparison. A DNA region coding for each GAF domain was amplified by PCR from *N. punctiforme* genomic DNA using appropriate primers, followed by cloning into the unique *Nco* I and *Sma* I sites of pBAD-Cph1-CBD.<sup>213</sup> Co-expression with PCB biosynthetic machinery in *E. coli* followed a published procedure,<sup>214</sup> and purification of GAF domains as intein-chitin binding domain (intein-CBD) fusions followed the procedure employed for *Synechocystis* Cph1.<sup>213</sup> After lysis, ultracentrifugation, and binding to chitin resin (NEB) in accordance with the manufacturer's instructions, intein cleavage was initiated by addition of DTT to the column, followed by overnight incubation at 4 °C. Peak fractions were pooled and dialyzed against TKKG buffer (25 mM TES-KOH pH 7.8, 100 mM KCl, 10% (v/v) glycerol) overnight prior to freezing in liquid nitrogen and storage at -80°C. Absorbance spectra were acquired at 25 °C on a Cary 50 spectrometer.

### *Transient Signals.*

The dispersed secondary transient absorption setup was constructed from two separate laser systems. The probe beam was derived from an amplified Ti:sapphire laser system (Spectra Physics Spitfire Pro + Tsunami) operating at 1 kHz, which produced 2.25-mJ pulses of 800-nm fundamental output with a 40-fs Full Width at Half Maximum (FWHM) duration.<sup>262</sup> This pulse train was used to generate the dispersed white-light continuum probe (440 – 750 nm) by focusing the laser pulses into a slowly-translating thick (10 mm) CaF<sub>2</sub> crystal.

Excitation pulses were generated by an independent diode-pumped solid-state Nd:YAG laser (Alphas-A-532-300) with a fundamental 1064-nm output that was frequency-doubled to yield 532-nm pulses with a ~500-ps FWHM duration. The pump pulse train was set to 100 Hz electronically and locked to the ultrafast probe pulses with a pulse generator (Quantum Composers 9520) to produce difference spectra with respect to the non-pumped ground-state spectrum. The pump beam was electronically delayed with respect to the probe pulse. This allowed for up to ~10 ms of temporal separation although only the <1 ms dynamics were free of artifacts from the excited sample flowing out of the probe region. Pump pulses were linearly polarized at 54.7° (magic angle) with respect to probe pulses. The pump and probe pulse spot diameters at the sample were estimated at 200 μm and 50 μm, respectively, using a moveable razor blade. The greater pump pulse area minimizes artifact contributions to the signals due to varying spatial overlap between pump and probe beams, which was confirmed by monitoring changes in signal amplitude and spectral shape while dithering the pump beam with respect to the probe beam.

The temporal resolution of the experiment was estimated at  $\sim 550$  ps using the rise time of transient signals. Samples were continuously flowed in a closed circuit to ensure fresh sample for each excitation pulse (though more slowly than for ultrafast experiments to ensure the measurement of long-time intermediates) and were continuously illuminated prior to entering the cuvette with  $\sim 5$ -mW of green (532 nm) laser diode to maintain the CBCR in the  $^{15Z}P_r$  state during the experiment. The path length of the quartz cuvette was 2 mm and the samples were prepared with optical densities of 3-4 OD/cm (at the  $^{15Z}P_r$  peak absorption wavelength). All experiments were performed at room temperature (25 °C).

To explore the role of excitation wavelength on the observed dynamics, the 1 ms spectra from the secondary data (with 532 nm excitation pulses) were compared to the 1 ms transient spectra collected from ultrafast signals (with  $\sim 640$  nm excitation pulses),<sup>176</sup> which were collected by shifting the probe pulse slightly before ( $\sim 1$  ps) the pump pulse. To facilitate this, the sample flow rate is typically slowed down so that incomplete refreshing of new sample within the excitation laser volume in the flow cell. Under normal flow conditions, this pre-time zero signal (1 ms spectrum) is negligible. Subsequent “harmonic” dynamics (e.g., 4 ms) are not a major factor in these spectra, since the flow rate has completely refreshed (within the excitation volume) on this timescale.

While the 532-nm excitation pulses used to initiate the secondary dynamics in this study are off resonant with the  $^{15Z}P_r$  absorption spectrum of the CBCRs in this study, they are strongly resonant with the  $^{15E}P_g$  spectrum (Figure 5.2 and A5.1). Consequently, the measured raw signals consist of both forward ( $^{15Z}P_r \rightarrow ^{15E}P_g$ ) and reverse ( $^{15E}P_g \rightarrow ^{15Z}P_r$ ) reaction signals. To extract the

uncontaminated forward reaction signals, "clean" reverse reaction signals were first collected under continuous 630-laser diode illumination and 532 nm excitation (presented elsewhere) and were then subtracted from the mixed forward reaction signals to extract "true" forward reaction signals confirmed via the absence of bleach or photoproduct signals corresponding to the reverse dynamics. The raw signals can be found in Figure A5.2. For the rest of this paper, all references to transient signals are to the adjusted  $^{15Z}P_r$  data.

## **Results**

The secondary forward photodynamics were collected and analyzed for eight red/green CBCR domains from *N. punctiforme*: NpAF142g2, NpR1597g4, NpF2164g4, NpF2164g6, NpF2854g3, NpR4776g2, NpR4776g3, and NpR6012g4.<sup>176, 182-184</sup> Of these eight GAF domains, the dynamics of two representative CBCR domains (NpF2164g6 and NpAF142g2) are emphasized to exemplify the longtime forward reaction dynamics. The NMR structures of the dark ( $^{15Z}P_r$ ) and light ( $^{15Z}P_g$ ) states<sup>108</sup> of NpR6012g4 are compared in Figure 5.2A-D with corresponding ground-state absorption spectra for NpR6012g4, NpF2164g4, and NpAF142g2 contrasted Figure 5.2E. The spectral shapes of the  $^{15Z}P_r$  absorption bands (red curves) of all CBCRs are qualitatively similar with a shoulder near 600 nm (Figures 5.2E and A5.1).<sup>263</sup> In contrast, the light-adapted  $^{15E}P_g$  spectra (Figures 5.2E and A5.1; green curves) of almost all CBCRs are near Gaussian except for NpR1597g4 and NpR4776g2, where residual  $^{15Z}P_r$  absorbance was still observed (Figures 5.2E and A5.1; red curves). The nomenclature previously outlined by Gottlieb et al. will be used here where the parental states are abbreviated to  $^{15C}P_x$ , where "C" represents the E/Z conformation of the chromophore and "x" is the spectral region of maximal absorbance. The photointermediates are represented by Lumi- $X_a$  (initial photointermediate) or Meta- $X_a$  (all secondary intermediates)

where “X” was the spectral region of maximal absorption for the parental state that was excited and “a” is the spectral region of maximal absorption of the intermediate.<sup>111</sup> The secondary reverse dynamics are analyzed and discussed in detail elsewhere (manuscript in preparation).

The transient absorption (TA) spectra for all CBCRs domains at select delay times are contrasted in Figure 5.2. In general, TA spectra can be decomposed into a superposition of four overlapping signals:

- (1) negative ground state bleach signal from the loss of ground-state absorption (GSB);
- (2) negative stimulated emission (SE) signal attributed to excited-state  $^{15Z}P_r^*$  populations;
- (3) positive excited-state absorptions (ESA) from  $S_1 \rightarrow S_n$  transitions induced from excited-state  $^{15Z}P_r^*$  populations; and
- (4) positive photoproduct absorptions (e.g., Lumi-R<sub>f</sub>) ascribed to photogenerated ground-state intermediate(s).

Although well resolved in the Gottlieb et al. study,<sup>176</sup> the excited-state signals (SE and ESA) are poorly resolved in the secondary data presented here, due to the 550 ps instrument response (IRF).



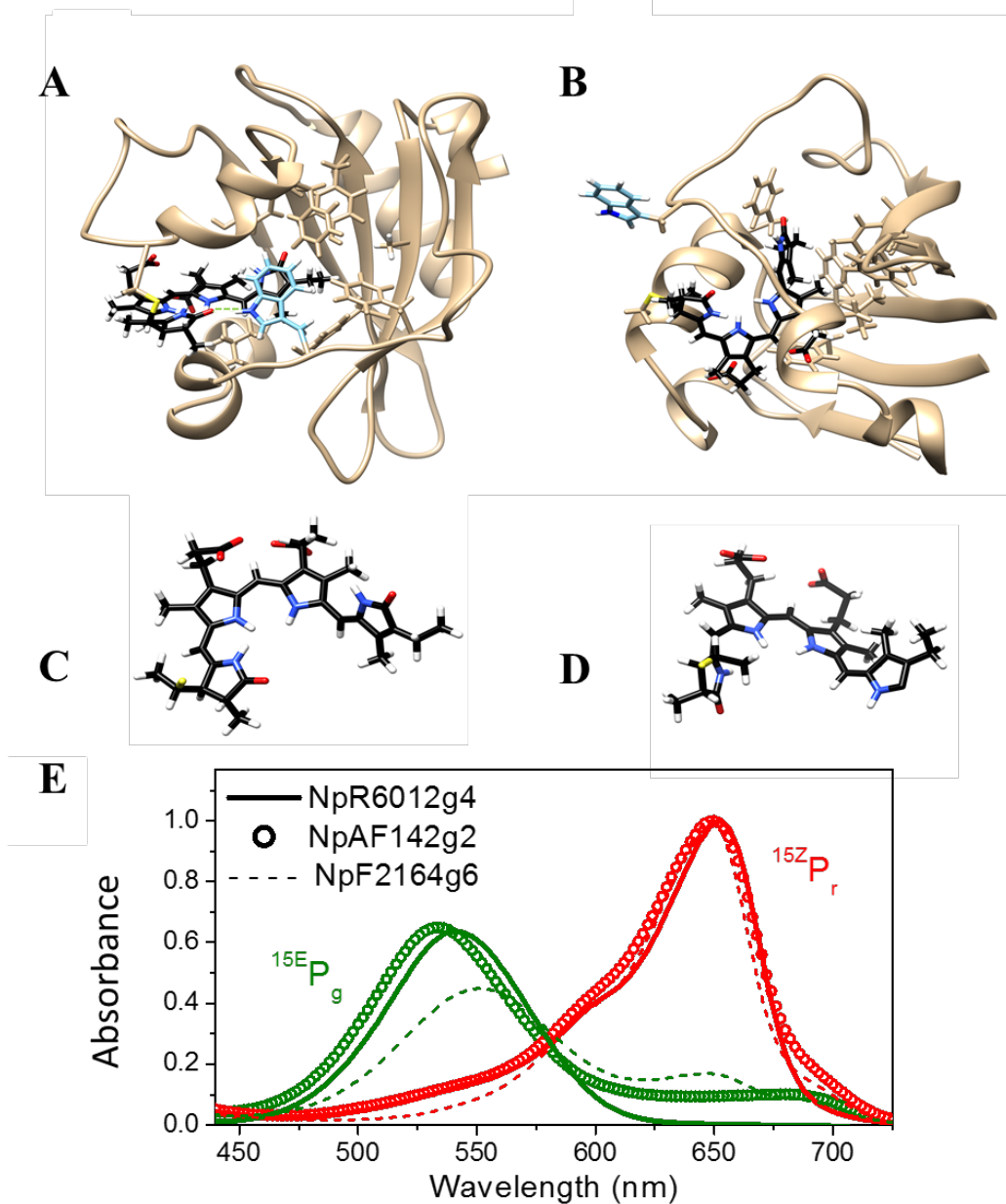


**Figure 5.2:** Representative Canonical Red/Green CBCR and Chromophore Structure and Static Absorbance Spectra

(A, B) NpR6012g4 protein structure around the dark (A; PDB 6BHN) and light (B; PDB 6BHO) states. Rings A through D of the bilin chromophore progress from left to right in alphabetical order. (C-D) Chromophore conformation in the dark-adapted and light-adapted states. Displacement of Trp655 away from the chromophore due to the isomerization event, causing the loss of the interactions between the chromophore and Trp655. (E) The static ground state absorbance of the dark (red) and light (green) states for NpR6012g4 (solid lines), NpFA142g2 (open circles), and NpF2164g6 (crossed curves).

The spectral evolution of the TA signals for nearly all the CBCRs follows similar pathways with monotonically blue-shifting intermediates from primary Lumi-R<sub>f</sub> (peaking around 675 nm) generated by the decay of the excited-state <sup>15</sup>ZP<sub>f</sub>\* populations to generate <sup>15</sup>EP<sub>g</sub> (peaking between 550-575 nm). These primary intermediates absorb in the yellow and orange regions of the spectrum (Figure 5.2A & C). The amplitude of the negative GSB increases as the Lumi-R<sub>f</sub> population with an overlapping positive absorption shifts to the subsequent Meta intermediates (Figure 5.1). On slower timescales, the absorption bands ascribed to the subsequent orange absorbing Meta-R<sub>o</sub> and yellow absorbing Meta-R<sub>y</sub> intermediates blue-shift to yield green-absorbing bands ascribed to Meta-R<sub>g</sub> populations that closely resembles <sup>15</sup>EP<sub>g</sub> (Figure 5.2E) spectrally. This indicates that these photoreactions are mostly completed on a <10 ms timescale (at least with respect to the bilin electronic absorption spectrum). The >1-ms TA difference spectra for all CBCR, where the excited sample progress to flow out of the excitation region, are compared in the Supporting Information (Figure A5.3).

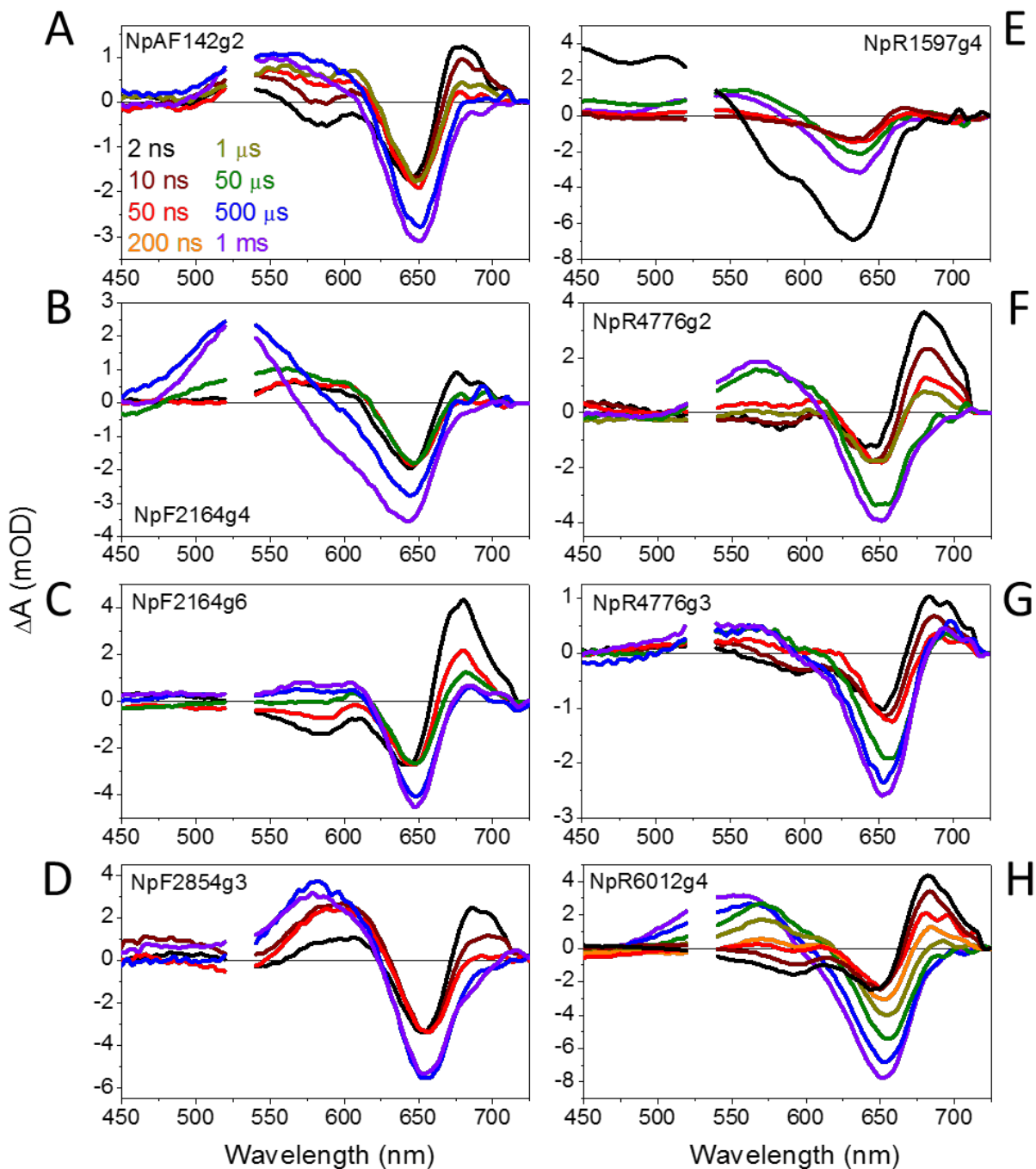


**Figure 5.3:** Red/Green CBCRs Secondary Forward Transient Difference Spectra

Transient absorption difference spectra for: (A) NpAF142g2, (B) NpF2164g4, (C) NpF2164g6, (D) NpF2854g3, (E) NpR1597g4, (F) NpR4776g2, (G) NpR4776g3, and (H) NpR6012g4. Spectra colors correspond to the probe times specified in the legend in panel A. Not all probe times are represented for each CBR. A narrow spectral window around the 532 nm excitation wavelength was excised due to pump scattering.

While the transient absorption (TA) of the CBCRs share similar spectral features, the kinetic traces in Figure 5.4 show key differences in the timescales. The traces clearly show the shared dynamic trends between the CBCRs:  $^{15E}$ Lumi- $R_f$  photoproduct (680 nm, black curve),  $^{15Z}P_r$  ground state bleach band (650 nm, red curve), and subsequent blue-shifted  $^{15E}$ Meta- $R_o$ ,  $^{15E}$ Meta- $R_y$ , and  $^{15E}$ Meta- $R_g$  photoproducts (590 nm, orange and 550 nm, green curves). For NpF2164g6, the primary Lumi- $R_f$  intermediate (black trace) decays within 1  $\mu$ s to generate the secondary Meta- $R_y$  intermediate (orange and green traces). NpAF142g2, NpF2164g6, and NpR4776g3 follow a similar progression, but with a primary Lumi- $R_f$  photoproduct (black trace) that persists for 50  $\mu$ s and 500  $\mu$ s, respectively (Figures 5.4A, C & G). Dissimilarities such as these are observed in the other CBCRs as well (Figure 5.4).

NpF2854g3 (Figure 5.4D) also exhibits dynamics starkly different from those of the other CBCRs. Gottlieb et al. reported that NpF2854g3 generates Meta- $R_o$  more quickly than the other CBCRs,<sup>176</sup> and a similar progression is observed in these secondary dynamics, as NpF2854g3 evolves into a positive band at 590 nm (orange data and curve) more quickly than any of the other CBCRs. The amplitude of the 590-nm trace for NpF2854g3 is reflected in the kinetic trace of the GSB (650 nm, red data and curve), suggesting the absorption band near 590 nm shifts back and forth, overlapping with the bleach band to different extents over time. This suggests that NpF2854g3 exhibits more complex structural rearrangements on this particular timescale than the other CBCRs, such as an equilibrium between a Meta- $R_o$  and a Meta- $R_y$  photointermediates that later coevolve to a Meta- $R_g$ . In addition to the more complex photodynamics exhibited of NpF2854g3 compared to the other CBCRs presented here, NpF2854g3 exhibited a weakening of the signal at all wavelengths on the same timescale (90 $\mu$ s – 1 ms; Figure 5.4D), suggesting that there is a shunt from the Meta- $R_g$

photointermediate back to the  $^{15}ZP_r$  ground state. NpF1597g4 had weaker absorbance in the far-red region and fast filling in of the bleach due to low Lumi- $R_f$  quantum yields as previously reported.<sup>176</sup>

In Figure 5.5, transient absorption difference spectra from the previous ultrafast study<sup>176</sup> are compared with those from the present study for the two representative CBCRs at probe times specified in the panels (2 ns, 7 ns, and 1 ms after excitation). The data are qualitatively similar, although with some important differences in the 550-620-nm region for both CBCRs, where the amplitudes of the 532 nm excitation signals are generally more negative than that of the red-excitation data. This indicates a loss of an absorbing population in that region for the green-excitation data, or a GSB near 600 nm (orange spectral region) belonging to a separate population not present after red excitation. Here the 1 ms data for both datasets for each CBCR exhibit similar spectra (Figure 5.5C and Figure 5.5F). These trends were also observed in the 2 ns and 1 ms spectra after 532 nm and 650 nm excitation of NpR6012g4. This may possibly be arising from a distinct ground-state subpopulation coexisting with  $^{15}ZP_r$  being preferentially excited by the 532-nm pulses, namely  $^{15}ZP_o$  which was previously reported Lim et al. for NpR6012g4.<sup>108</sup>

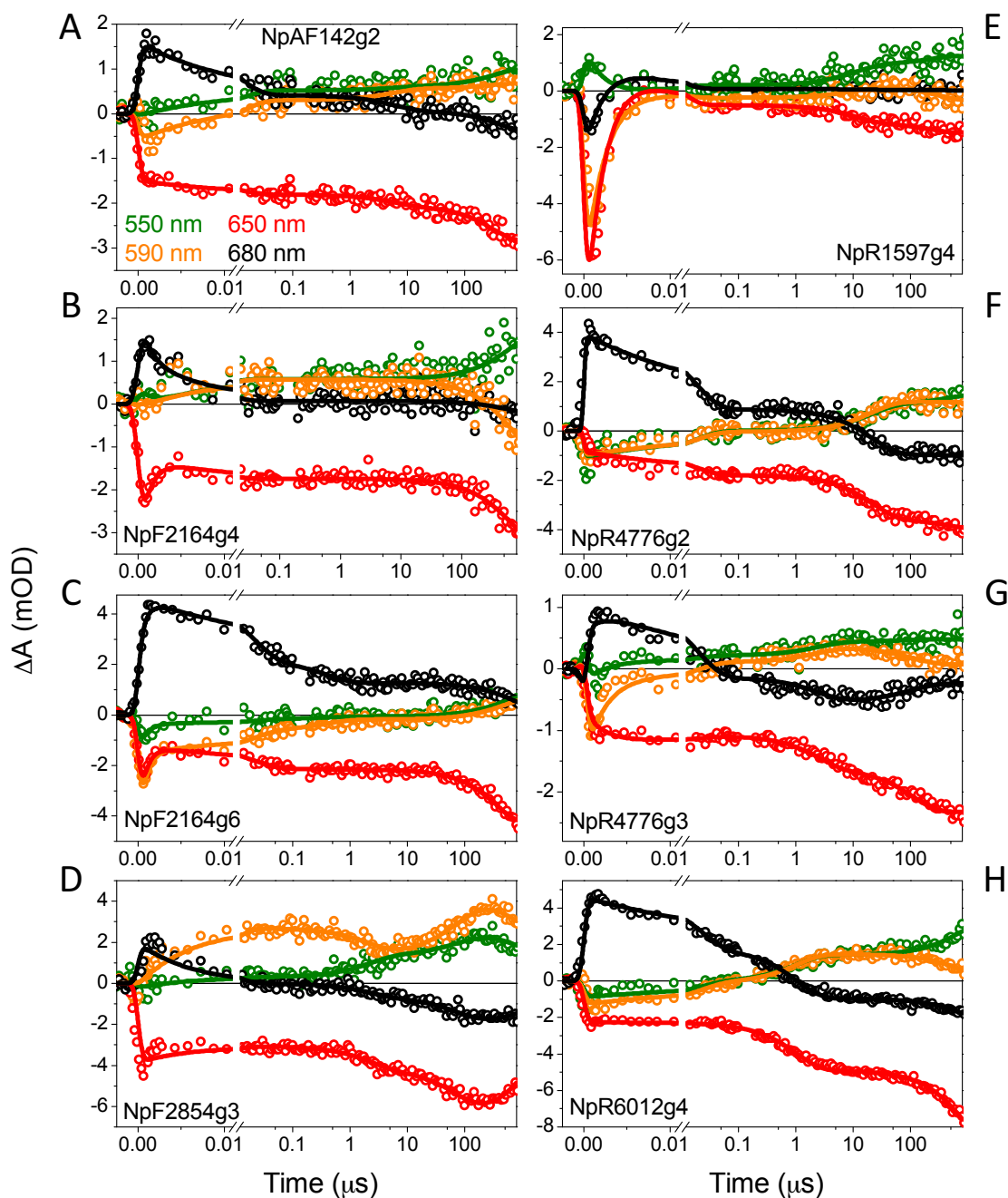


**Figure 5.4:** Red/Green CBCRs Secondary Forward Kinetics

Kinetic traces for: (A) NpAF142g2, (B) NpF2164g4, (C) NpF2164g6, (D) NpF2854g3, (E) NpR1597g4, (F) NpR4776g2, (G) NpR4776g3, and (H) NpR6012g4. Spectra colors correspond to the wavelengths specified in the legend in panel A. Data (open circles) are overlaid with fits (solid curves) extracted from the target model for each respective CBR (Figure 5.6: Red/Green CBCRs Secondary Forward Mechanism and Table 5.1).

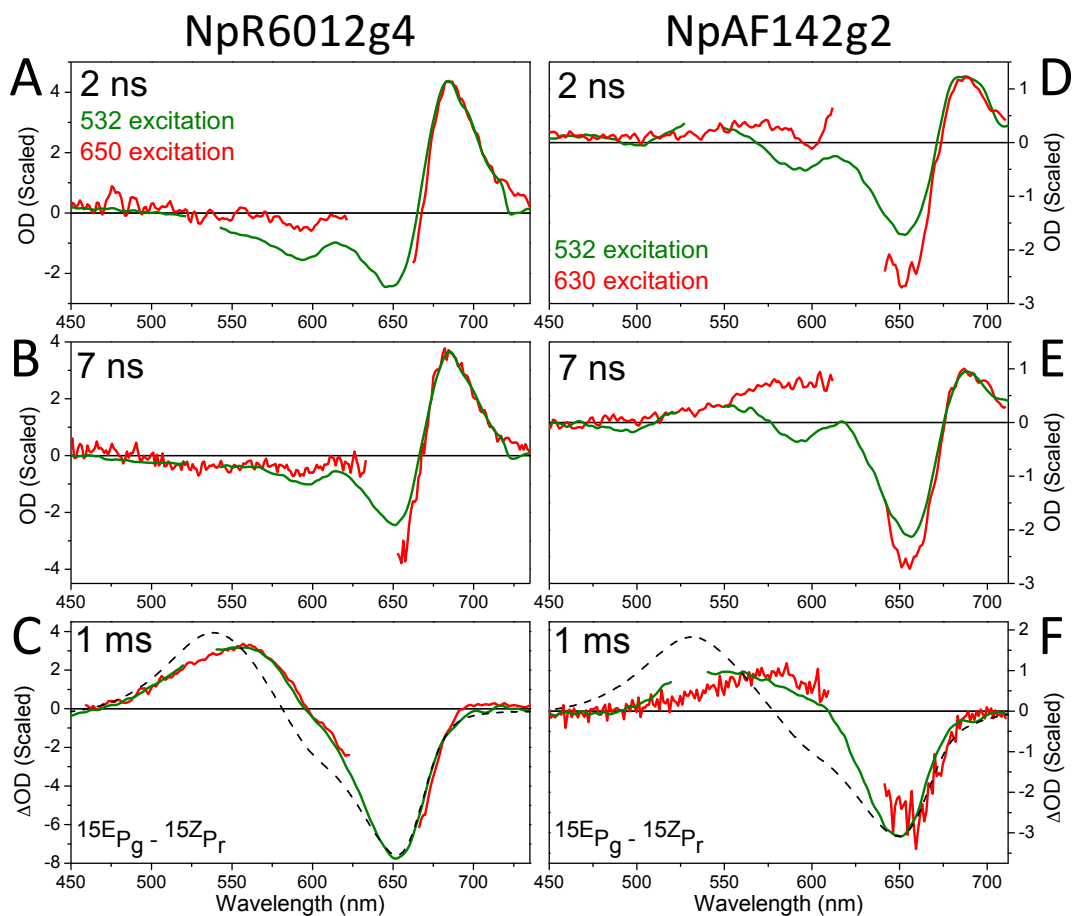


**Figure 5.5:** Excitation Wavelength Influence on the Forward Dynamics

Comparison of transient absorption difference spectra for NpR6012g4 and NpAF142g2 after 630-nm or 650-nm excitation (red curves) discussed in detail in primary forward photodynamics of red/green CBCRs survey with after 532-nm excitation (green curves) at 2 ns (A and D), 7 ns (B and E), and 1 ms (C and F).<sup>176</sup> For NpF2164g6 (A, B, and C), note the relative differences in amplitude near 600 nm in the bleach band in A and B. NpAF142g2 (D, E, and F) exhibits amplitude and signal differences in the bleach band and in the 550-600-nm region of the secondary photoproduct. Ground-state  $^{15}E_g - ^{15}Z_r$  difference spectra are overlaid with the 1 ms spectra (C and F, grey dashed curves).

### **Global Analysis**

Sequential models (state 1 → state 2 → state 3 → state 4, etc.) were initially used to fit the TA data (Figures 5.6 and A5.4; Table 5.1) resulting in evolution associated difference spectra (EADS)

of increasing lifetimes for each population in the sample. This approach is useful in identifying the underlying “apparent” (i.e., experimentally observed) timescales in the data, but does not necessarily decompose the apparent timescales into the microscopic timescales of co-evolving populations.<sup>221, 243</sup> This requires a more complex non-sequential target analysis to adequately address *a priori* knowledge to the system of interest.<sup>182, 195</sup> However, the sequential EADS analysis can be used to extract useful timescale information in the systems.<sup>182, 184</sup> In addition to the sequential model, a parallel model using the same time constants as the sequential model, and the result difference associated difference spectra (DADS) can be found in the supplemental information (Figure A5.6).

All TA signals were fit to sequential models consisting of up to five compartments (Figures A5.5 and A5.7). For several of the CBCRs, including the representative CBCRs, certain features of the forward reaction EADS indicate complex underlying dynamics after excitation involving multiple photoproduct populations that progress with strong spectral and temporal overlap. For example, in the case of NpR6012g4, EADS1 and EADS2 share a similar absorption band in the 670-720-nm region, albeit with differing amplitudes (Figure A5.5). On the same timescale, the 550-620-nm negative region in EADS1 decays to near zero in EADS2. This evolution indicates at least two separate populations are represented by EADS1 that decay on different timescales. The decay of the shorter lived state from  $P_0$  accounts for the decay of the negative signal between EADS1 and EADS2. This inhomogeneity was also readily apparent when comparing the 532 nm and 650 nm excitation spectra as selected times (Figure 5.5), which showed that the higher energy excitation resulted in a stronger positive absorption signal from 550 – 620 nm since the  $^{152}P_0$  state is preferentially excited with the 532 nm excitation pulse, but not the 650 nm. The existence of



another longer living population originating from  $P_r$  justifies the relative persistence of the positive absorption band near 680 nm in EADS2. Furthermore, while the positive band near 680 nm decays to ~50% of its original amplitude between EADS1 and EADS2, the same trend is not observed for the bleach band near 650 nm further indicating underlying heterogeneous dynamics. Similar trends are observed in the EADS for NpAF142g2 (Figure A5.5A), NpF2164g6 (Figure A5.5B), and NpR4776g2 (Figure A5.5C).

A generalized target model was constructed to fit the TA data of each CBCR (Figure 5.6) with corresponding EADS (Figure 5.7) and concentration profiles (Figure A5.7). Timescales for all CBCRs are listed in Table 5.1. Timescales and EADS for excited-state species ( $^{15}ZP_r^*$  and  $^{15}ZP_o^*$ ) are omitted from Table 5.1 and Figure 5.7, where applicable (see the Gottlieb et al.<sup>176</sup> for more details).

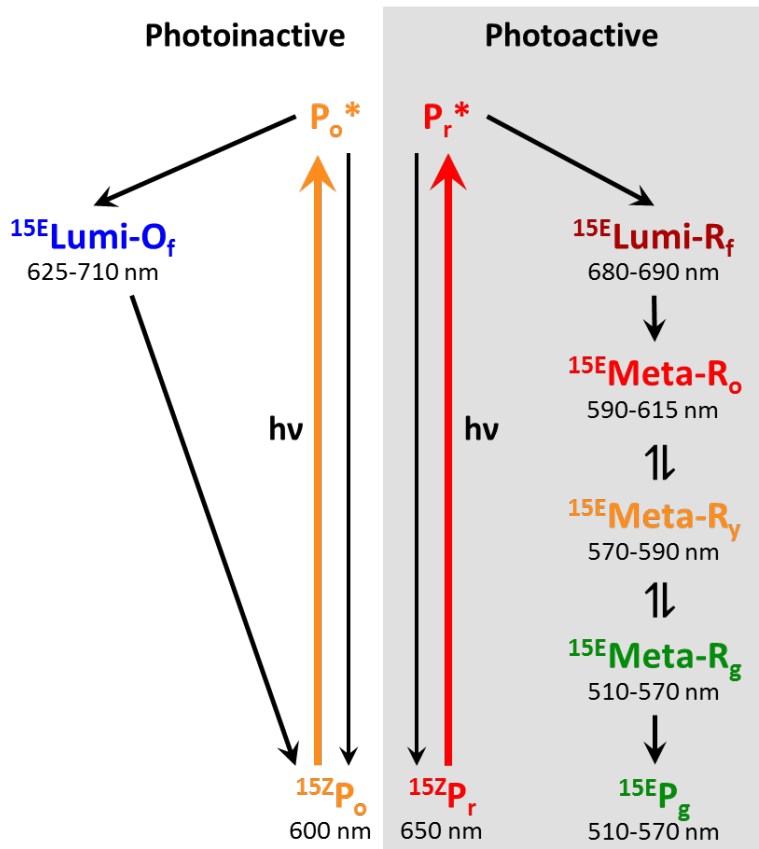


**Figure 5.6:** Red/Green CBCRs Secondary Forward Mechanism

General photocycle model and proposed reaction pathway for the forward reaction of the CBCRs in the present study at 532-nm excitation.  $^{15}ZP_o$  and  $^{15}ZP_r$  are initially activated by light to generate the primary  $^{15}E\text{Lumi-O}_f$  and  $^{15}E\text{Lumi-R}_f$  intermediates.  $^{15}ZP_r$  generates  $^{15}E\text{Lumi-R}_f$ , propagates the photocycle to eventually generate  $^{15}E P_g$ , while  $^{15}E\text{Lumi-O}_f$  decays back into the original  $^{15}ZP_o$  state. Labels for intermediates are color-coded to the EADS in Figure 5.7.

Not all CBCRs exhibit inhomogeneous dynamics, as several CBCRs show no apparent Lumi-O<sub>f</sub> photoproduct stemming from  $^{15}ZP_o$ . These CBCRs required only sequential EADS analyses to yield appropriate models and corresponding species associated difference spectrum (SADS) for microscopic populations, only utilizing the shaded region of the target model (Figure 5.6). The effectiveness of these models for describing the data is demonstrated via the excellent agreement

between the simulated kinetics traces and raw data in Figure 5.4. This target model differed significantly from the one used to fit the secondary forward dynamics for NpF2164g7 (orange/green), which proposed a more complex heterogeneous model.<sup>187</sup>

**Table 5.1:** Secondary Forward EADS Timescales

Timescales extracted from the sequential EADS analysis for the CBCRs in this study. The corresponding EADS are shown in Figure 5.7. \*Species exhibited unproductive Lumi-O<sub>f</sub> pathway. The percent of the population that evolves through these pathways are presented in the two far right columns. \*\*The final timescale contains phase attributed to the flow of the irradiated sample volume out of the probe volume.

Sample	Lumi-Of	EADS0	EADS1	EADS2	EADS3	% L-Of	%EADS
NpAF142g2*	7 $\mu$ s	11 ns	865 $\mu$ s	>3 ms**	-	21	79
NpF2164g4	NA	8 ns	825 $\mu$ s	>3 ms**	-	0	100
NpF2164g6*	45 ns	555 $\mu$ s	>3 ms**	-	-	67	33
NpF2854g3	NA	6 ns	2.2 $\mu$ s	80 $\mu$ s	2.8 ms**	0	100
NpR1597g4	NA	5.5 ns	8.5 $\mu$ s	220 $\mu$ s	>3 ms**	0	100
NpR4776g2*	16 ns	21 $\mu$ s	510 $\mu$ s	>3 ms**	-	77	23
NpR4776g3	NA	190 ns	2.5 $\mu$ s	110 $\mu$ s	>3 ms**	0	100
NpR6012g4*	21 ns	1 $\mu$ s	880 $\mu$ s	>3 ms**	-	60	40

The various spectral regions of the EADS or SADS of the eight CBCR domains compared in Figure 5.7, are highlighted with their respective color to help visualize the Lumi-O<sub>r</sub>, Lumi-R<sub>f</sub>, Meta-R<sub>o</sub>, Meta-R<sub>y</sub>, and Meta-R<sub>g</sub> spectra that compose the EADS and the trend of the evolution.

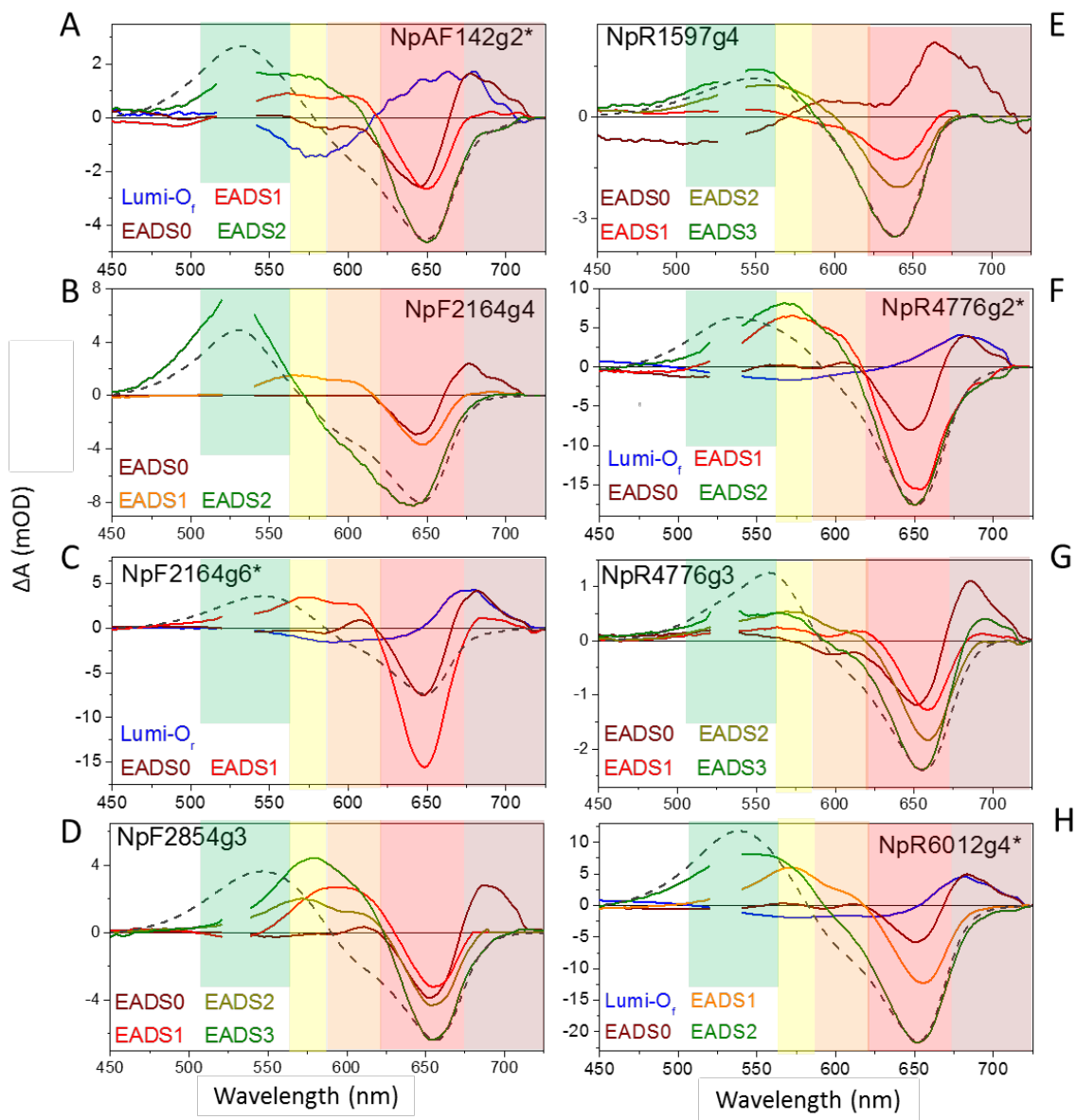


**Figure 5.7:** Red/Green CBCRs Secondary Forward EADS

Evolution associated difference spectra (EADS) for the eight CBCRs as extracted from the model in Figure 5.6 and kinetic parameters in Table 5.1. The  $^{15}E_g - ^{15}Z_P_r$  difference spectra scaled to coincide with other signals are plotted for comparison (dashed curves). The Lumi- $R_f$  population for NpR1597g4 (E, dark red curve) was poorly resolved due to its low yield and rapid lifetime. Excited-state SADS are not shown, if resolved. The different spectral regions of the EADS are highlighted to assist in visualizing the various intermediates where far-red is represented by wine and all the other visible wavelength regions are represented with their respective colors. Each sample that exhibited evidence of the photoinactive  $^{15}Z_P_o$  subpopulation are indicated with an asterisk in the panel label.

All eight studied CBCRs presented here followed a simple evolutionary mechanism within the ~1 ms probe window. Even though NpF2164g7 had a more complex heterogeneous model, the blue-shifting of the subsequent intermediates was also observed.<sup>187</sup> The secondary forward dynamics of NpF2164g6 ( $^{15Z}P_r \rightarrow ^{15E}P_g$ ) exhibit similar trends of the reverse reaction of RcaE ( $^{15E}P_r \rightarrow ^{15Z}P_g$ ), where there was a long lived Lumi state that evolved to a Meta state. NpF2164g6 had a Lumi decay constant of 556  $\mu$ s, compared to the 110  $\mu$ s decay constant of the RacE Lumi-R<sub>f</sub> state, making it the longest lived primary photoproduct to be resolved to date (Table 5.1).<sup>177, 186, 192</sup> NpR1597g4 exhibits an exceptionally longer-lived excited state (Figure 5.4E) than the other CBCRs, as evidenced by the traces up to 3-4 ns and the lack of a clear Lumi-R<sub>f</sub> photoproduct absorption near 680 nm (Figure 5.3E), also characterized in ultrafast signals.<sup>176, 190</sup> While NpR1597g4 does exhibit slight positive signals at 680 nm, the Lumi-R<sub>f</sub> spectrum extracted from the target model does not agree with those of the other CBCRs (Figure 5.7).<sup>176</sup> The Lumi-R<sub>f</sub> spectrum for NpR1597g4 shows negative signals in the blue and green regions, where the other CBCRs' Lumi-R<sub>f</sub> populations are near-zero. This discrepancy is likely due to the extraction of a low-yielding Lumi-R<sub>f</sub> photoproduct spectrum from the signals and not an accurate representation of the Lumi-R<sub>f</sub> spectrum.

Uniquely, NpR4776g3 deviated from this conserved mechanism of blue shifting intermediate observed in the 7 other CBCRs domains by exhibiting a far-red absorbing state that was populated after Meta-R<sub>g</sub> (Figure 5.7G; yellow and green curves). It is unclear what is causing this red-shifted state and is a matter of further investigation.

## ***Discussion***

The secondary (>10 ns) forward ( $^{15Z}P_r \rightarrow ^{15E}P_g$ ) broadband TA signals of eight red/green photoswitching CBCR GAF domains display the diversity in their secondary dynamics. While all CBCRs studied share similar ground-state absorption spectra (Figures 5.1 and A5.1), the previously reported primary (<10 ns) signals exhibited stark differences in photoproduct quantum yields, excited-state and photoproduct dynamics as well as revealed that there are at least three different classes: Class I characterized by no, or little Lumi formation, class II characterized by Lumi formation, but no apparent evolution to a Meta state on an ultrafast timescale (< 8 ns), and class III which did have Meta formation on the ultrafast timescale.<sup>176</sup> While these CBCRs share certain similarities beyond the ultrafast timescale, key differences in timescales are observed in the secondary time regime (>10 ns).

### *Productive Photodynamics.*

Most of the CBCRs exhibit similar multiphase evolution from excitation of  $^{15Z}P_r$  to generation of  $^{15E}P_g$ . From the kinetic traces in Figure 5.4, positive signals in the orange and green (590-520 nm) arise from Lumi- $R_f$  decay and are attributed to Meta-R populations. This monotonic evolution can be attributed to similar protein scaffolds near the chromophore during the reaction.<sup>177, 197</sup> Previously, Velazquez and coworkers suggested the importance of the Trp residue stacked onto the D-ring of the chromophore of AnPixJg2 in moderating the isomerization of the chromophore after photoexcitation.<sup>264</sup> This Trp would be expected to be a major component for many CBCRs in progressing the chromophore through the photocycle from  $^{15Z}P_r$  to  $^{15E}P_g$ , as this Trp is highly conserved in red/green photoswitching CBCRs.<sup>197</sup> Recently, Rockwell and coworkers argued against the importance of the conserved Trp through identification of two highly conserved

phenylalanine (Phe) residues essential for evolution of the  $^{15E}P_g$  ground-state.<sup>197</sup> These two Phe residues are conserved in six of the eight CBCRs in this paper. In the two outliers, NpR1597g4 incorporates methionine (Met) in the place of the helix Phe and NpR4776g3 incorporates tyrosine (Tyr) and isoleucine (Ile) in place of both the  $\beta 2$  and helix Phe residues, respectively (Table A5.1).<sup>15E</sup>The replacement of the two Phe residues in NpR4776g3 may be the cause of the observed Meta- $R_f$  state observed in NpR4776g3 where the chromophore becomes less structurally deformed due to a less rigid protein structure near the D-ring of the chromophore (Figure 5.1). This Meta- $R_f$  state evolved by two ms since it is not apparent in later transient difference spectra (Figure A5.3G).

In contrast to the monotonic evolution from Lumi- $R_f$  to  $^{15E}P_g$  observed in most red/green CBCRs, NpF2854g3 is more complex, exhibiting biphasic growth (Figure 5.4D; yellow curve), despite its conservation of the two aforementioned Phe residues.<sup>197</sup> The amplitude of the 590-nm kinetic trace for NpF2854g3 first peaks near 50 ns after excitation, only to reach a relative minimum at  $\sim 7 \mu s$ . The signal then increases, reaching maximum amplitude near 250  $\mu s$  and decaying past the 1 ms probe delay window. A similar non-monotonic trend is observed in the dynamics at the other wavelengths (Figure 5.4D), stemming from the overlap of multiple populations in those spectral regions. The kinetics for NpF2854g3 indicate the absorption maxima of secondary intermediates shift back and forth between 50 ns and the end of the probe delay window, not following the unidirectional evolution observed in the other CBCRs. The NpF2854g3 EADS in Figure 5.7D more clearly depict the shifting of the ground-state intermediate absorption bands. Like many of the CBCRs studied, NpF2854g3 generates a Lumi- $R_f$  photoproduct that absorbs near 680 nm and decays into Meta- $R_o$  near 600 nm. The Meta- $R_o$  band, then, blue-shifts to yield Meta- $R_y$ . Strikingly, the Meta- $R_y$  absorption band peaking at 570 nm red-shifts to yield an absorption band

of increased amplitude peaking near 580 nm. This new band, attributed to Meta-R<sub>y2</sub>, does not undergo any clear shifting within the 1 ms probe delay window, although the amplitude of the signal does decrease. Dynamics comparable to those described for NpF2854g3 were not observed for any other red/green CBCR. The 680 nm kinetic trace for NpR4776g3 also showed weak signs of a biphasic growth that was also apparent in the transient absorption spectra (Figure 5.4G) and Meta-R<sub>g</sub> EADS (Figure 5.7G; green curve), but this was attributed to contamination from the reverse reaction ( $^{15E}P_g \rightarrow ^{15Z}P_r$ ) that was not successfully removed from the adjusted data since the reverse reaction has positive absorption in this region around this time after excitation (Figure A5.1).

Similar dynamics to NpF2854g3 were detected in the secondary dynamics for the violet/orange NpF2164g3 CBCR in the reverse direction.<sup>111</sup> For NpF2164g3, the initial Lumi-O<sub>r</sub> photoproduct decays on a 9-ns timescale into Meta-O<sub>g</sub>. The photocycle and spectral sensitivity of NpF2164g3 are greatly influenced by the presence of a second Cys linkage at carbon 10 of the PCB chromophore.<sup>68, 111</sup> However, instead of blue-shifting further to generate  $^{15Z}P_v$ , Meta-O<sub>g</sub> decays on a 750-ns timescale to yield an orange-absorbing Meta-O<sub>r</sub> intermediate peaking near 650 nm. Furthermore, the 1 ms spectrum collected for NpF2164g3 exhibits a positive absorption peaking near 630 nm. This indicates the reverse reaction of NpF2164g3 is slow to generate  $^{15Z}P_v$  from  $^{15E}P_o$ , and that it progresses in a more complex pathway of intermediates, compared with many red/green CBCRs, including AnPixJg2.<sup>111, 177</sup> NpF2164g3 does not belong to the red/green photoswitching family and displays certain structural and spectroscopy discrepancies from these CBCRs, but arose within the red/green subfamily based upon evolutionary relationships.<sup>68, 69</sup> Moreover, NpF2164g3 also lacks the two Phe residues conserved in many of the red/green CBCRs.<sup>111, 197</sup> The effects of



structural residue modification on the photoactivity of NpF2164g3 have yet to be discovered.<sup>111</sup> The similarities shared between the forward reactions and sequences of the CBCR domains studied and mentioned here may indicate parallel evolutionary origin and function for several of these CBCRs. However, this study alone cannot fully address this hypothesis.

#### *Nonproductive Photodynamics.*

The comparison of dark adapted ground state spectra for all the domains studied here are compared (Figure 5.8A) revealed that all of the domains exhibit small, but non-zero absorption at 532 nm, making it possible to initiate forward reaction dynamics with 532-nm pump pulses.<sup>176</sup> Upon excitation with 532-nm pulses, NpAF142g2, NpF2164g6, NpR4776g2, and NpR6012g4 exhibited broader and slightly blue-shifted photoproduct absorption and a prominent 600-nm GSB (Figure 5.7). The four CBCRs that displayed Lumi-O<sub>r</sub> photoproducts, with the exception of NpF2164g6, generally exhibit greater positive absorption in the more blue shifted wavelengths in the static spectra (Figure 5.8D).

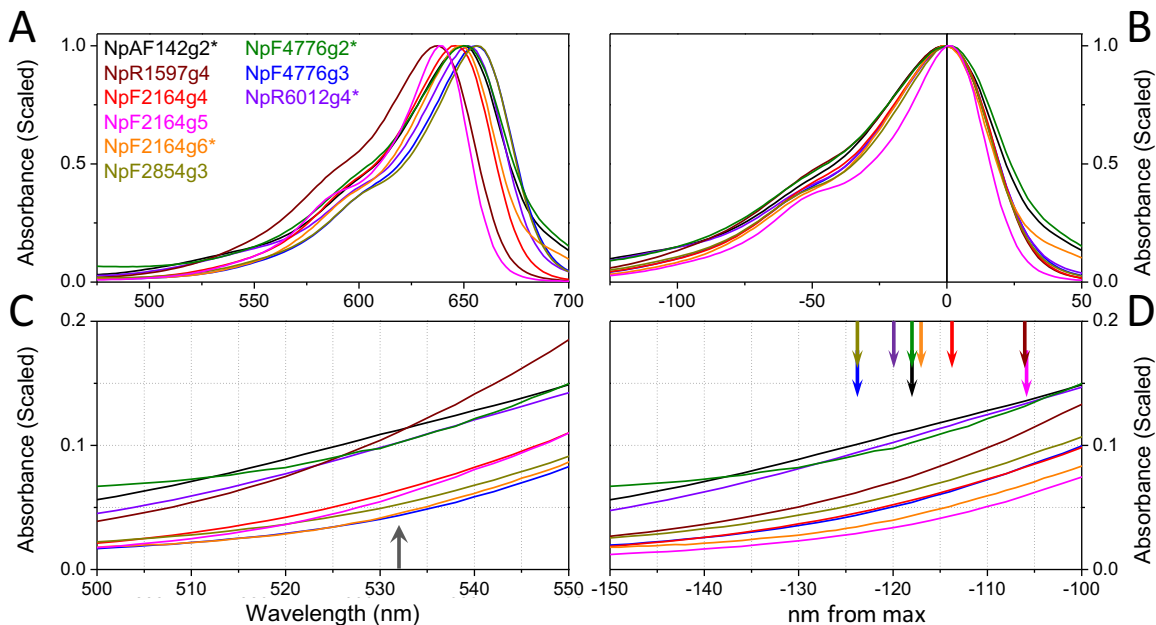


**Figure 5.8:** Comparison of the Orange Absorbance of the Dark-Adapted State (A)  $^{15Z}P_r$  ground-state absorption spectra for all CBCRs in this study, normalized at the wavelengths of maximum absorbance. The samples that exhibited the unproductive  $^{15Z}P_o$  state are indicated with an asterisk. (B) Absorption spectra from panel A, shifted to coalesce the wavelengths of maximum absorbance. (C) Spectra from panel A, focusing on the spectral region near the excitation wavelength (532 nm, grey arrow). (D) Shifted absorption spectra from panel B, focusing on the spectral region near the excitation wavelength (532 nm, represented by arrows color coded to match the legend in panel A).

The generalized target model for the red/green CBCRs is presented in Figure 5.6, which has been previously reported for NpR6012g4,<sup>108</sup> has the presence of photoinactive Lumi-O<sub>f</sub> and photoactive Lumi-R<sub>f</sub> subpopulations that arise due to an out or in orientation of Trp655 and horizontal or vertical orientations of the Asp657 residue (Figure 5.9), respectively. Ten percent of reported structures of NpR6012g4 incorporated an “out” Trp655 and “horizontal” Asp657 that resulted in the photoinactive orange absorbing subpopulation.<sup>108</sup> For the eight proteins, the sequence

alignment of every protein had a Trp and Asp residue at the corresponding locations of Trp655 and Asp657 in NpR6012g4, except for NpR1597g4, which had a valine (Val) and all had Asp (Figure A5.8).<sup>69</sup> This highly conserved sequence suggest that there may be similar lid Trp and horizontal/vertical Asp orientations for all these systems, but NMR or X-ray crystallography would need to be performed to confirm. Assuming that all of these proteins have Asp in this location suggest that the Asp in the proteins that do not exhibit the photoinactive Lumi-O<sub>f</sub> either does not have the vertical Asp orientation or the Asp does not interact with the chromophore.

Several CBCRs do not complete the photocycle within the 1 ms probe delay and several CBCRs only require the <sup>15</sup>ZP<sub>r</sub> signals (shaded region) to fit the data. NpR1597g4, NpF2164g4, NpF2854g3, and NpR4776g3 exhibit the sequential evolution of photoproduct species after excitation with no apparent Lumi-O<sub>f</sub> photoproduct dynamics. The remaining CBCRs (NpAF142g2, NpF2164g6, NpR4776g2, and NpR6012g4) exhibit multiphasic decay kinetics, which Lumi-O<sub>f</sub> spectra exhibiting broad and blue shifted bleach bands near 600 nm. The new photoproduct with blue-shifted features likely evolves from the excitation of the 600-nm P<sub>o</sub> subpopulation. Like NpF2164g7 and RcaE, half of the CBCRs presented here have inhomogeneity that persist to the Lumi state, suggesting that inhomogeneity lasting past the initial excited states may be a consistent trend for some CBCRs.<sup>187, 192</sup> Similar ground-state inhomogeneity and excitation-wavelength-dependences have been reported for CBCRs and related photoreceptor proteins.<sup>184, 191</sup> Keeping consistency with NpR6012g4, all of Lumi-O<sub>f</sub> states observed had shorter lifetimes than the Lumi-R<sub>f</sub> state and failed to evolve to a Meta state, except for NpAF142g2 which unproductive Lumi-O<sub>f</sub> state had a longer lifetime than the productive Lumi-R<sub>f</sub> state (Table 5.1).<sup>108</sup>

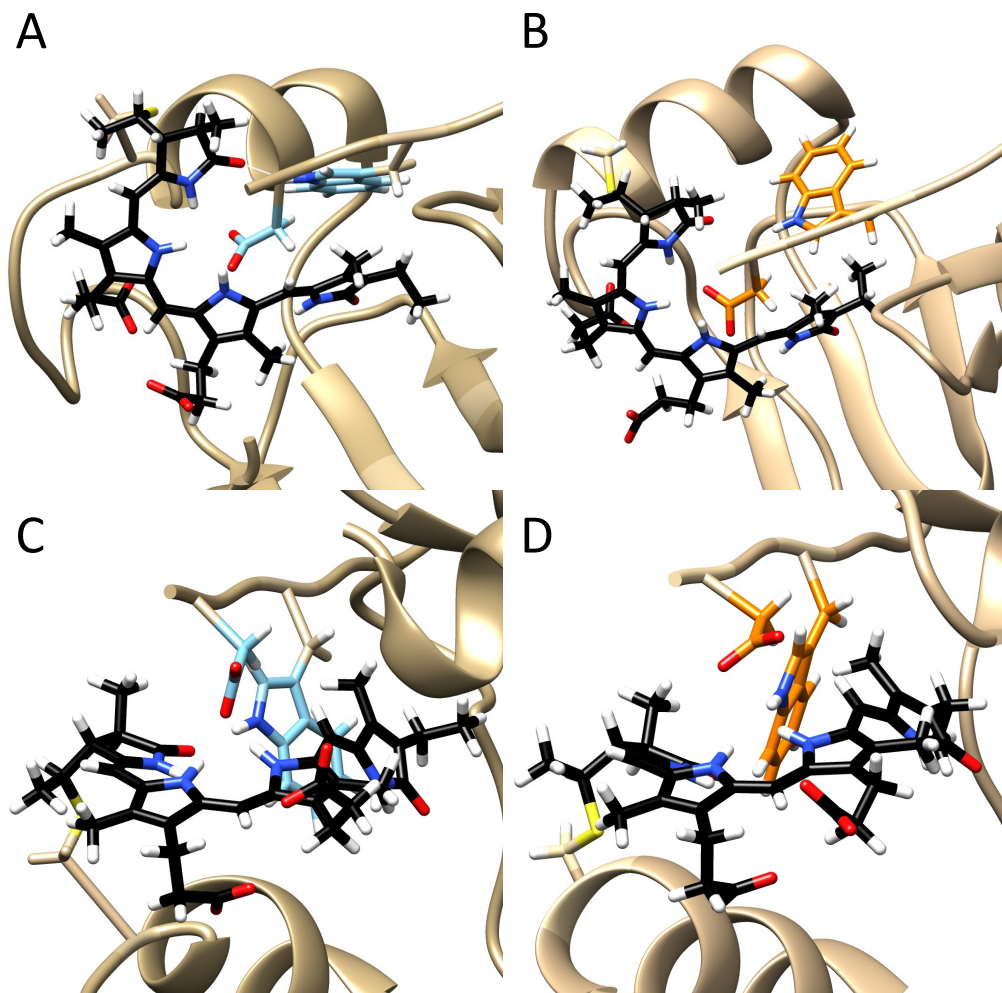


**Figure 5.9:** Trp655 and Asp657 Structural Heterogeneity of the  $^{15Z}P_r$  state

Structural heterogeneity of Trp655 and Asp657 of the  $^{15Z}P_r$  state (PDB: 6BHN) that results in the red absorbing (left column, blue amino acid residues) and orange absorbing (right column, orange amino acid residues) subpopulations. For the red absorbing subpopulation Trp655 overlaps with the D-ring (A) and H-bonds with the A-ring of the PCB chromophore and Asp657 is in a “vertical” orientation (C) that can also H-bond to the chromophore. In the orange absorbing subpopulation Trp655 is rotated away from the D-ring (B) and the Asp657 is in a “horizontal” configuration (D) that cannot H-bond to the chromophore.

NpR1597g4 had a Val in place of Trp, for the Trp/Asp requirements for the  $^{15Z}P_o$  subpopulation,<sup>108</sup> but since NpR1597g4 did not exhibit features associated with the  $^{15Z}P_o$  subpopulations this does

not shed much light on the amino acid residue requirements for the unproductive  $^{15Z}P_o$  subpopulation. Interestingly, given the amino acid sequences previously reported by Rockwell et al.<sup>69, 197</sup> (Figures A5.9 and A5.10), all of the domains that exhibited features of the unproductive  $^{15Z}P_o$  subpopulation incorporate a glycine residue (except for NpR6012g4) at T631 of NpR6012g4 and all the domains that did not exhibit features of the  $^{15Z}P_o$  subpopulation incorporate a serine residue at this location. To determine if the serine or glycine amino acid residue at this location is indicative of the presence or lack thereof, of the  $^{15Z}P_o$  subpopulation, further studies can probe the secondary dynamics of difference Red/Green CBCRs with reported serine or glycine amino acid residues at this location (Figure A5.10), such as AnPixJg2, AnPixJg3, AnpixJg4, NpR5113g2, etc.

### ***Concluding Comments***

The secondary photodynamics of several red/green photoswitching CBCRs from the cyanobacterial *N. punctiforme* were characterized with transient absorption spectroscopy from ns to ms. It was observed that all nine *N. punctiforme* CBCR samples had a consistent trend of blue shifting intermediates, suggesting that the evolution from Z-to-E is a smooth, sustained transition. Also, all of the samples other than NpR1597g4 and NpF477g3 had a continuous blue shift of each intermediate to a new color region whereas the final evolution for these two proteins remained in the same region (yellow). This consistent blue-shifting with evolution was also observed in NpF2164g7.<sup>187</sup> Similar to the ultrafast studies, the protein samples were classified into categories based on the nature of the photodynamics: CBCRs exhibiting or not exhibiting a Lumi-O<sub>f</sub> photoproduct. Considering that half of the CBCRs presented here had heterogeneity past the initial excited states suggest that heterogeneity persisting to the secondary photoproducts may be more common than originally thought. It is clear that the inhomogeneity present in the ultrafast dynamics

carries over to some degree into the secondary timescale.<sup>176</sup> The exact causes of the distinctions between the timescales of all the CBCRs, however, are not known and elucidation of this will require more extensive structural and spectroscopic studies.

### *Associated Content*

#### *Supporting Information (pg. 272)*

The Supporting Information provides ground state spectra, raw difference spectra, comparison of the 1 ms spectra collected from the primary and secondary dynamics, EADS concentration profiles, DADS, and abbreviated amino acid sequence alignments

#### *Accession Codes*

NpAF142g2 (B2JAQ4), NpR1597g4 (B2J0R5), NpF2164g4, NpF2164g6, NpF2164g7 (B2J668), NpF2854g3 (B2IVK2), NpR4776g2, NpR4776g3 (B2IZ18), NpR5113g2 (B2J261), and NpR6012g4 (B2IU14), RcaE (Q47897), Slr1393 (P73184), AnPixJg2 (Q8YXY7), Cph1 (Q55168)

#### *Funding*

This work was supported by a grant from the Chemical Sciences, Geosciences, and Biosciences Division, Office of Basic Energy Sciences, Office of Science, United States Department of Energy (DOE DE-FG02-09ER16117) to both J.C.L. and D.S.L.

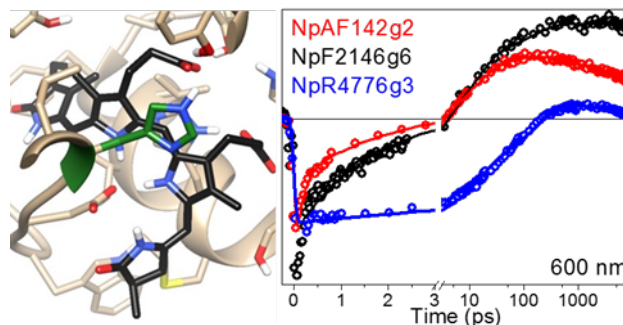
#### *Acknowledgments*

This work was supported by a grant from the Chemical Sciences, Geosciences, and Biosciences Division, Office of Basic Energy Sciences, Office of Science, United States Department of Energy (DOE DE-FG02-09ER16117) to both J.C.L. and D.S.L. Nathan C. Rockwell (University of California, Davis) is acknowledged for sample preparation and constructive discussions. Dr. Mikas Vengris (Light Conversion Ltd.) is also acknowledged for the donation of global and target analysis software.

# Chapter 6. Conservation and Diversity in the Primary Reverse Photodynamics of Red/Green Cyanobacteriochromes

## Abstract

In this report, we compare the femtosecond-nanosecond primary reverse photodynamics ( $^{15}E_p \rightarrow ^{15}Z_p$ ) of eight tetrapyrrole binding photoswitching cyanobacteriochromes in the canonical red/green family from the



cyanobacterium *Nostoc punctiforme*. Three characteristic classes were identified based on the diversity of excited-state and ground-state properties including lifetime, photocycle initiation quantum yield, photointermediate stability, spectra and temporal properties. We observed a correlation between excited-state lifetime and peak wavelength of the electronic absorption spectrum with higher-energy-absorbing representatives exhibiting both faster excited-state decay times and higher photoisomerization quantum yields. The latter was attributed to both increased structural restraints and differences in H-bonding networks that facilitate photoisomerization. All three classes exhibited primary Lumi-G<sub>0</sub> intermediates, with Class II<sub>R</sub> and III<sub>R</sub> representatives evolving to a secondary Meta-G photointermediate. Class II<sub>R</sub> Meta-G intermediates were orange absorbing, whereas Class III<sub>R</sub> Meta-G had structurally relaxed, red-absorbing chromophores that resemble their dark-adapted  $^{15}Z_p$  states. Differences in the reverse and forward reactions mechanisms are discussed within the context of structural constraints.



## ***Introduction***

Understanding the molecular-level mechanisms of how biological functions can be initiated by externally applied light is a major goal of modern biophysics and is key in designing novel photosensory proteins such as *in vivo* fluorescent probes for medical imaging<sup>265-268</sup> and optogenetic tools with novel light-activated responses.<sup>50, 269</sup> In most examples of such photoactive systems, the responses are initiated by the photoexcitation of a chromophore embedded within a protein scaffold. Consequently, one of the most important steps that dictates activity (i.e., efficiency, spectral properties, photochemistry and eventual photoactivity) is the excited-state evolution of the embedded chromophores after photoexcitation, which occurs on the femtosecond to nanosecond timescales.

A goal of optogenetics is to leverage photoproteins with tunable spectral properties to control biological function with the application of light. Modern optogenetic efforts have focused on either a rational designed (bottom-up) or reengineering (top-down) approaches. The latter approach involves the use of existing photoactive systems with known biological responses. An example of this approach is the photoactivation of individual neurons with modified channelrhodopsin and halorhodopsin constructs that operate as photo-gated sodium and potassium ion channels, respectively. Channelrhodopsin is activated by blue light and halorhodopsin is activated by yellow light thereby enabling selective ion transport in neurons via the ability to initiate and terminate action potentials with two colors of light.<sup>55, 201, 202</sup> The phytochrome superfamily of photosensory proteins is a class of bi-stable photoactive proteins that has been extensively exploited for optogenetic applications.<sup>270-278</sup>

Canonical phytochromes are multi-domain photoreceptors that utilize a linear tetrapyrrole (bilin) chromophore to detect red and far-red light by reversible photoisomerization reactions.<sup>249</sup> These systems were initially discovered in plants where they dictate plant growth in an effort of shade avoidance,<sup>20, 21</sup> and they were later discovered in other organisms including algae, bacteria, and fungi.<sup>246, 279, 280</sup> In cyanobacteria, similar photoswitches termed cyanobacteriochromes (CBCRs) that like phytochromes utilize bilin chromophores, but exhibit a wider spectral range of photoactivity that spans the near ultraviolet (UV) to the near infrared (NIR) spectral regions.<sup>63, 64, 68, 69, 110, 281-283</sup> Multiple CBCR families that have been identified include the blue-absorbing dual-Cys DXCF,<sup>66, 72, 110</sup> violet-absorbing insert-cysteine,<sup>68, 284</sup> green/red,<sup>285</sup> extended red/green,<sup>282, 69, 70, 197</sup> and multiple far-red<sup>63</sup> families. Here we will focus on canonical red/green CBCRs isolated from the cyanobacteria *Nostoc punctiforme*.<sup>69, 70, 197</sup> Members of this family possess conserved Phe residues that constrain the chromophore in their green-absorbing signaling state.<sup>69, 70, 197</sup>

Prototypical members of the red/green CBCR family incorporate phycocyanobilin (PCB) chromophores (Figure 6.1A). The largest CBCR family, red/green CBCRs account for a quarter of all characterized CBCRs and exhibit red-absorbing dark states ( $^{15Z}P_r$ ) that interconvert to green-absorbing photoproduct 'signaling' states upon light absorption ( $^{15E}P_g$ ; Figure 6.1A).<sup>69</sup> The diversity in the forward ( $^{15Z}P_r \rightarrow ^{15E}P_g$ ) primary (100 fs-8 ns)<sup>176</sup> and secondary (ns-ms)<sup>27</sup> photodynamics of several red/green CBCRs from *N. punctiforme* have been characterized with broadband transient absorption (TA) spectroscopy - the most well studied being NpR6012g4.<sup>29, 108, 182-184</sup> Forward and reverse photodynamics of the red/green CBCRs, AnPixJg2 from *Anabaena* sp. PCC 7120<sup>29, 177, 264</sup> and Slr1393g3 from *Synechocystis* PCC6803,<sup>185, 186</sup> have also been extensively studied. Given the strong diversity in the spectral and dynamic properties of the CBCR

superfamily, it is unclear that these three examples are fully representative of the red/green family as a whole. First seen in the secondary forward dynamics of NpR6012g4, an unproductive orange-absorbing subpopulation ( $^{15Z}P_o$ ) was also observed in the secondary dynamics of 4 out of 8 red/green CBCRs so far examined.<sup>27, 108</sup> Such comparative studies have provided insight into amino acids responsible for conserved and non-conserved dynamic features. Indeed, with the exception of NpR6012g4, all of the red/green CBCRs that afforded a  $^{15Z}P_o$  species incorporated glycine just outside of the protein binding pocket; whereas, all of the red/green CBCRs that lacked  $^{15Z}P_o$  species incorporated a serine at this location.<sup>108</sup> Such secondary forward dynamic studies also revealed that red/green CBCRs all afford a series of blue-shifted photointermediates before populating the  $^{15E}P_g$  signaling state - a result consistent with increasing out-of-plane twisting of their bilin chromophores.

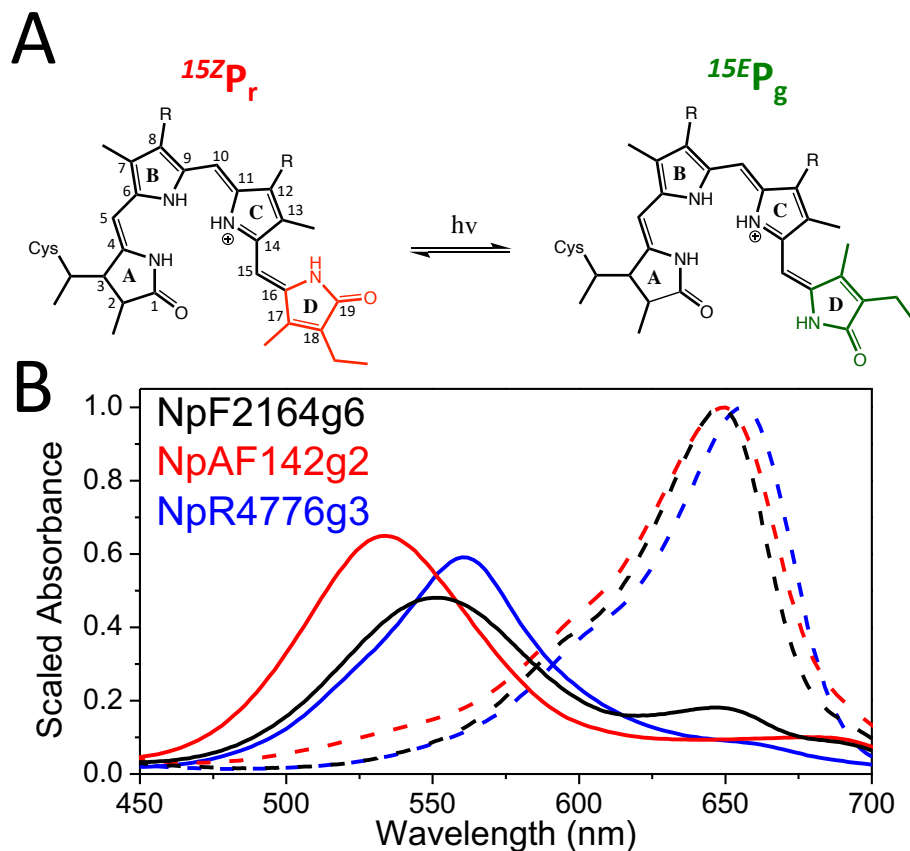


**Figure 6.1:** Dark-adapted and Signaling State Chromophore Configurations and Static Spectra  
 (A) PCB chromophore configurations in dark-adapted ( $^{15Z}P_r$ ) and signaling ( $^{15E}P_g$ ) states.  
 (B) Absorption spectra of  $^{15E}P_g$  (solid curves) and  $^{15Z}P_r$  (dashed curves) states of NpF2164g6 (black curves), NpAF142g2 (red curves), and NpR4776g3 (blue curves). All  $^{15E}P_g$  spectra are scaled to the corresponding normalized  $^{15Z}P_r$  absorption spectra.

Primary reverse dynamics of several red/green CBCRs, i.e. AnPixJg2 (Q8YXY7),<sup>29</sup> NpR6012g4,<sup>183</sup> NpR2164g6,<sup>180</sup> and Slr1393g3 (P73184),<sup>185</sup> have been examined. Such studies resolved a red-shifted Lumi- $G_o$  photointermediate that rapidly evolves to a blue-shifted Meta- $G_o$  species. Meta- $G_o$  subsequently evolves via a series of intermediates to eventually populated the  $^{15Z}P_r$  dark state on slower timescales. Here, we compare the primary reverse ( $^{15E}P_g \rightarrow ^{15Z}P_r$ ) photodynamics of NpR6012g4 (B2IU14) with seven other red/green CBCRs from *Nostoc punctiforme*: NpAF142g2 (B2JAQ4), NpR1597g4 (B2J0R5), NpF2164g4, NpF2164g6 (B2J668),

NpF2854g3 (B2IVK2), NpR4776g3 (B2IZ18), and NpR5113g2 (B2J261). Three classes were identified that were separated based on the kinetics and spectra of the photointermediates. The electronic absorption spectra for representatives of each class are compared in Figure 6.1B, with the remaining presented in the Supporting Information (Figure A6.1). Key dynamics were correlated with conserved amino acid residues, such as the rates of excited state and Lumi-G<sub>0</sub> dynamics and a selectively conserved histidine/tyrosine residue. The results also indicate that no one sample can be considered as representative of the canonical red/green CBCR family.

### ***Materials and Methods***

All experimental protocols, including CBCR preparation at a pH of 8 and experiment setups, were discussed in detail previously<sup>176, 182</sup> with two key differences: (1) the primary reverse  $^{15E}P_g \rightarrow ^{15Z}P_r$  dynamics were initiated with 530-545 nm ultrafast pulses with ~20-nm full-width at half maximum (FWHM) and (2) the actinic light used to maintain the probed CBCRs in the  $^{15E}P_g$  state was ~30 mW of 650-nm light from a laser diode. All other experimental parameters were unchanged.

Methodologies underlying the global analysis technique used to characterize these data were also outlined previously, including both sequential and target analyses of transient broadband datasets.<sup>176, 182</sup> Initially, nonbiased sequential models were used that result in extracted spectra and correlated apparent lifetimes. If these extracted spectra represent the true populations, then they are designated as Species Associated Difference Spectra (SADS) with associated lifetimes. If the extracted spectra are superpositions of the underlying populations, then they are designated as Evolution Associated Difference Spectra (EADS) with apparent lifetimes. If the sequential model did not extract SADS, then more complex multi-component target models are constructed using

the trends observed in the transient difference spectra and kinetics coupled with the EADS and apparent lifetimes. All of the CBCRs studied here were initially fitted with sequential models (Figures A6.7 and A6.8) before more complex target models were constructed as outlined in the SI.

To guide the target analysis, especially in estimating quantum yields of the primary photoisomerization event, NpR6012g4 was used as a reference based on the assumption that the excited state and photointermediate species for all red/green CBCRs would have comparable extinction coefficients. The excited-state ( $^{15}E_P_g^*$ ) SADS for each CBCR were scaled to that of NpR6012g4. This scaling factor was then used to adjust the Lumi-G<sub>0</sub> SADS and then the  $\Phi_{\text{Lumi-G}_0}$  was determined using the time constants to produce a Lumi-G<sub>0</sub> comparable to that of NpR6012g4 while still fitting the data.  $\Phi_{\text{Lumi-G}_0}$  values were then determined for the other CBCRs using the time constants extracted from the target global analysis (Figures A6.13 and A6.14). This approach previously was used to estimate  $\Phi_{\text{Lumi-Rf}}$  of 36% for the forward reaction of NpR6012g4 after 630 nm excitation with *Synechocystis* Cph1 as a reference and for the forward reaction of several canonical red/green CBCRs using NpR6012g4 as a reference.<sup>176, 182</sup>

## **Results**

The previous characterization of the primary forward dynamics of the same red/green CBCRs identified three classes that were based on the kinetic behavior of these photoproteins on the primary timescale (150 fs to 8 ns) rather than fundamental difference in the reaction dynamics.<sup>176</sup> Using the established nomenclature for these photoreceptors,<sup>69, 176</sup> Class I<sub>F</sub> sensors (forward reaction) exhibited no measurable photointermediate formation, Class II<sub>F</sub> sensors exhibited only

the primary Lumi-R<sub>f</sub> photointermediate in this timescale, and Class III<sub>F</sub> sensors exhibited both the primary Lumi-R<sub>f</sub> and secondary Meta-R<sub>o/y</sub> photointermediates.

Similarly, the behavior in the reverse dynamics of the CBCRs studied here also can be separated into three classes based on kinetics, number and spectra of the photointermediates observed within the primary timescale. The primary reverse classes were defined as follows:

- Class I<sub>R</sub> CBCRs (NpF2164g6)<sup>180</sup> exhibit a single orange-absorbing photointermediate population (Lumi-G<sub>o</sub>).
- Class II<sub>R</sub> CBCRs (NpAF142g2, NpF2164g4, NpF2854g3, NpR6012g4)<sup>183</sup>) exhibit Lumi-G<sub>o</sub> and the evolution to a blue-shifted Meta-G<sub>y</sub> population.
- Class III<sub>R</sub> CBCRs (NpR1597g4, NpR4776g3, NpR5113g2) exhibit Lumi-G<sub>o</sub> and the evolution to a red-shifted Meta-G<sub>r</sub> population.

A representative CBCR was selected from each class (Class I<sub>R</sub>: NpF2164g6, Class II<sub>R</sub>: NpAF142g2, and Class III<sub>R</sub>: NpR4776g3) to be discussed in detail below with other CBCRs being presented in the Supporting Information. The dynamics of NpF2164g6 were previously reported,<sup>180</sup> but the data presented here was newly collected and analyzed with minor differences in fitting parameters.

TA spectra for each representative red/green CBCR at specified delay times are contrasted in Figure 6.2. The spectra of the other red/green CBCRs can be found in Figures A6.2 and A6.3. The TA spectra are a superposition of multiple overlapping signals including: (1) negative ground-state bleach (GSB) signal that is indicative of loss of the ground-state absorption (GSA) and spans the

GSA spectral region; (2) the negative stimulated emission (SE;  $S_1 \rightarrow S_0$  transition) band that peaks near 630 nm in all of the red/green CBCRs characterized here; (3) the positive excited-state absorption (ESA;  $S_1 \rightarrow S_n$  transitions) that contributes a broad absorbance in the short and long wavelength regions of the spectra ( $\sim 400$ - $475$  nm and  $\sim 670$ - $750$  nm); and (4) positive Lumi-G photoproduct band(s) best resolved after the excited-state  $^{15}E_P_g^*$  population(s) have decayed.

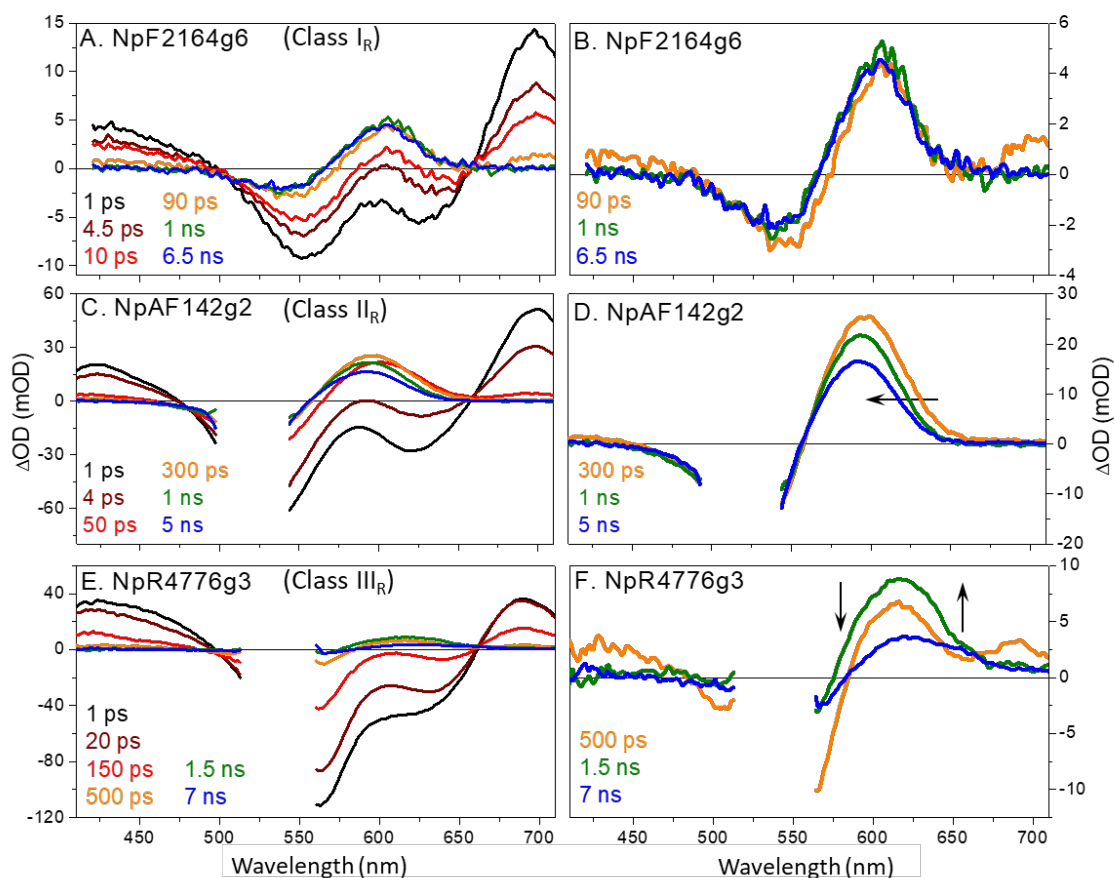


**Figure 6.2:** Representative Red/Green CBCRs Primary Reverse Dynamics TA Spectra  
 Transient absorption (TA) spectra for the reverse dynamics for representative CBCRs of each class: (A) NpF2164g6, (C) NpAF142G2, and (E) NpR4776g3 at delay time points specified in the legends. The long-time focused spectra for (B) NpF2164g6 (D) NpAF142G2 and (F) NpR4776g3 highlight the evolution of the primary photoproduct(s) for each CBCR.



The early-time TA signals directly track the excited-state  $^{15E}P_g^*$  dynamics. All characterized CBCRs share similar spectral properties with slight wavelength shifts and differences in relative signal amplitudes and decay dynamics (Figures 6.2 and A6.2-A6.5). After  $^{15E}P_g^*$  decayed, a single positive absorption band was observed at  $\sim 610$  nm (Figures 6.2 B, D & F). For the Class I<sub>R</sub> sensor NpF2164g6, this band did not shift or decay on the 8 ns timescale of this experiment. In contrast, the Class II<sub>R</sub> sensor NpAF142g2 exhibited a blue shifting behavior between 1 and 5 ns that was coupled with an overall decay of the signal (Figure 6.2D). The blue shifting behavior of the signal in NpAF142g2 is similar to that observed for NpR6012g4, which was ascribed to evolution of the initial Lumi-G<sub>o</sub> photointermediate to Meta-G<sub>y</sub>.<sup>183</sup> Given the smaller amplitude of the Meta-G<sub>y</sub> signal, we surmise that the Lumi-G<sub>o</sub> photointermediate either partially decays back to the initial  $^{15E}P_g$  state or Meta-G<sub>y</sub> has a smaller extinction coefficient than the ground state bleach. Finally, the Class III<sub>R</sub> sensor NpR4776g3 exhibited photoproduct absorption signals in the 550-625-nm region that were similar to those of NpF2164g6 and NpAF142g2. This implicated formation of a similar Lumi-G<sub>o</sub> intermediate, however a small growth at 650 nm also was observed between 500 ps and 1.5 ns, indicating co-evolution of a red-absorbing population (Figure 6.2F). The NpR5113g2 TA spectra also revealed formation of similar red-absorbing peak, albeit more slowly between 1 and 8 ns following a comparable conversion of Lumi-G<sub>o</sub> to a blue-shifted Meta-G<sub>y</sub> intermediate between 200 ps and 1 ns (Figure A6.3). The origin and identity of these red-absorbing bands are unclear from the raw TA signals and will be discussed further below.

Kinetic traces for representative Class I<sub>R</sub>, II<sub>R</sub> and III<sub>R</sub> sensors are compared in Figure 6.3 with the rest found in Figures A6.4 and A6.5. The 420 nm traces track the  $^{15E}P_g^*$  excited-state lifetimes (Figure 6.3, blue curves) which are inverted and mirrored by the GSB kinetic traces (Figure 6.3,

green curves). The  $> 1$  ns kinetic traces are enlarged to better display the evolution of ground state intermediates and products (Figures 6.3B, D & F). For NpF2164g6 (Class I<sub>R</sub>), a positive absorption at 600 nm that correlates to the Lumi-G<sub>0</sub> population persisted beyond the temporal window of these experiments (Figures 6.3A & B). For NpAF142g2, a Class II<sub>R</sub> sensor, growths in both the orange (590 nm) and red (630 nm) spectral regions were observed. In contrast with NpF2164g6, both of these NpAF142g2 intermediates began to decay prior to 1 ns with the 630 nm peak decaying more rapidly than the 590 nm peak (Figure 6.3E, red and dark red) - a result consistent with the blue shifting in the spectra of NpAF142g2. This blue shift preceded an overall decay in both signals between 1 and 8 ns possibly due to a shunt back to the  $^{15E}P_g$  ground state or to a reduced extinction coefficient of the subsequent Meta-G intermediate (Figure 6.2D). By comparison with the representative Class I<sub>R</sub> and II<sub>R</sub> sensors, the representative Class III<sub>R</sub> sensor NpR4776g3 exhibited comparable ESA and GSB absorption, albeit on a considerably slower timescale. Similar to Class I<sub>R</sub> and II<sub>R</sub> sensors, the orange to red absorption of NpR4776g3 attributed to Lumi-G<sub>0</sub> appeared as the  $^{15E}P_g^*$  absorption decayed. Unlike the Class I<sub>R</sub> and II<sub>R</sub> sensors, after Lumi-G<sub>0</sub> (610 nm trace) had decayed, a weak absorption appeared deeper in the red between 650-660 nm for NpR4776g3 (Figures 6.3E & F; dark red curves).

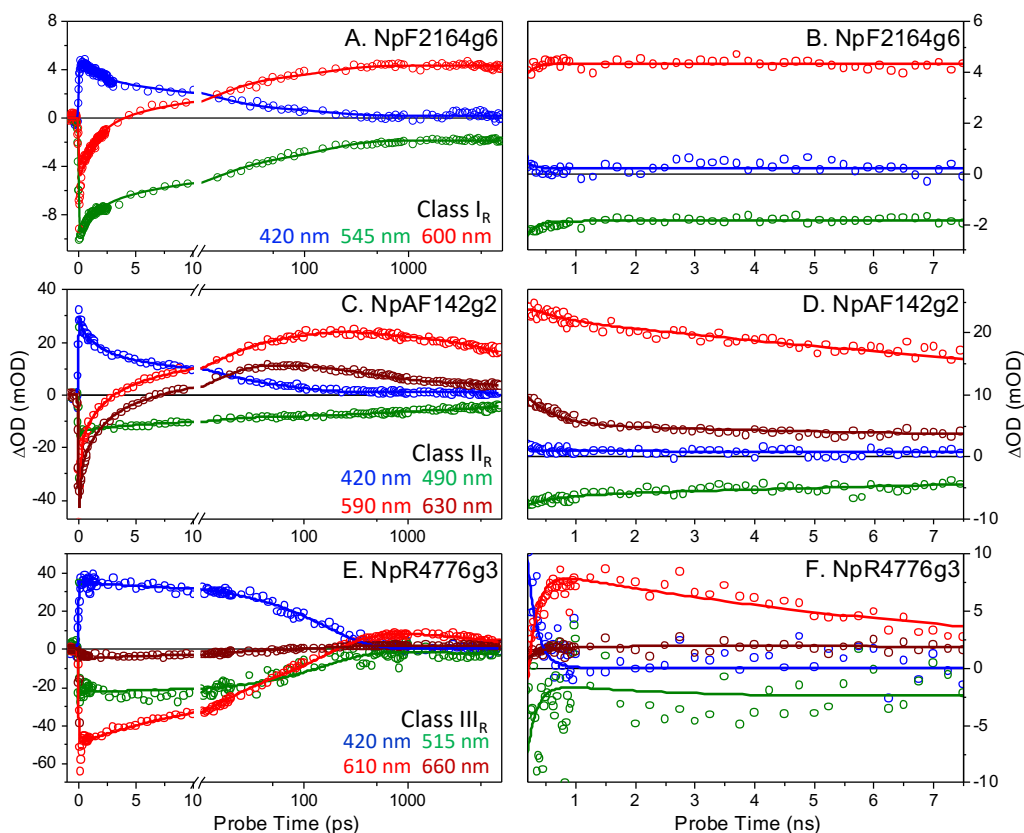


**Figure 6.3:** Representative Red/Green CBCRs Primary Reverse Kinetic Traces  
 Kinetic traces for the reverse reaction dynamics for (A, B) NpF2164g6, (C, D) NpAF142g2, and (E, F) NpR4776g3 at specific probe wavelengths indicated in the legends. The  $>1$  ns signals have been zoomed (B, D, and F) in to emphasize the evolution of photoproduct populations and the bleach bands at later probe delay times. Fits from target analysis (solid lines) for each CBCR are overlaid with raw data (open circles) for comparison and to evaluate goodness of fit.

### ***Global Analysis***

From the reverse TA spectra and kinetics, three reverse reaction categories were identified:

1. The Class I<sub>R</sub> sensor NpF2164g6<sup>180</sup> exhibits a single photointermediate (Lumi-G<sub>0</sub>) with no discernible evolution of additional photoproducts within the  $<8$  ns experimental timescale.
2. Class II<sub>R</sub> sensors NpAF142g2, NpF2164g4, NpF2854g3, and NpR6012g4<sup>183</sup> exhibit two photointermediates with Lumi-G<sub>0</sub> evolving into the blue-shifted Meta-G<sub>γ</sub>. Amongst the

four Class II<sub>R</sub> sensors, NpF2854g3 remains an outlier since its Meta-G photointermediate is even further blue shifted to the green region, where it overlaps with the bleach.<sup>27</sup> Class II<sub>R</sub> sensors represented here by NpAF142g2<sup>183</sup> includes the extensively studied NpR6012g4 and AnPixJg2<sup>29</sup> from *Anabaena sp.* PCC 7120.

3. Class III<sub>R</sub> sensors NpR1597g4, NpR4776g3, and NpR5113g2 exhibit Lumi-G<sub>o</sub> that subsequently evolves to a red-shifted population (620-670 nm) within the ~8-ns experimental time window. NpR4776g3 typifies this category whereas NpR5113g2 is an outlier by exhibiting additional Meta-G<sub>y</sub> and Meta-G<sub>o</sub> photointermediates between Lumi-G<sub>o</sub> and Meta-G<sub>r</sub> (Figures 6.6 and A6.10). Slr1393g3<sup>185</sup> from *Synechocystis sp.* also is a Class III<sub>R</sub> sensor.

#### *Class I<sub>R</sub> sensors*

The reverse reaction signals exhibit multi-exponential excited-state kinetics, which argues for the use of the inhomogeneous target models previously proposed for the reverse dynamics of other CBCRs.<sup>29, 111, 183, 189, 191, 195</sup> One can also model a homogeneous ground state that is excited into heterogenous excited states, but the heterogenous ground state model was preferred given the evidence for ground state inhomogeneity previously reported.<sup>108</sup> The parameters for the fits can be found in Tables A6.1 and A6.2. The target model for NpF2164g6 (Figure 6.4A) includes two productive ground-state populations (GS1, 35% and GS2, 34%) and a single unproductive population (GS2, 31%) that are simultaneously photoexcited to separate excited-state (<sup>15E</sup>P<sub>g</sub>\*) populations. The <sup>15E</sup>P<sub>g</sub>\*-I and <sup>15E</sup>P<sub>g</sub>\*-II populations exhibit branched decay pathways, both yielding Lumi-G<sub>o</sub> with different efficiencies, whereas <sup>15E</sup>P<sub>g</sub>\*-III decays back to the <sup>15E</sup>P<sub>g</sub> ground

state with no measurable Lumi-G<sub>0</sub> quantum yield. The model used for NpF2164g6 was identical to the one previously reported, albeit with differing time constants.<sup>180</sup>

The SADS associated with  $^{15E}P_g^*$ -I and  $^{15E}P_g^*$ -II of NpF2164g6 were near identical and locked together into the same spectrum (Figure 6.4A, blue curve) in the fitting. This is indicative of the structural similarities between the two populations. There were small differences in the  $^{15E}P_g^*$ -III SADS compared to  $^{15E}P_g^*$ -I and  $^{15E}P_g^*$ -II, particularly in the SE and ESA regions ranging from 550-700 nm (Figure 6.4A). The third SADS represents Lumi-G<sub>0</sub> and is similar to the raw spectral signals at longer probe times (Figure 6.2A & B). The discrepancies in the evolution and decay rates of  $^{15E}P_g^*$ -I and  $^{15E}P_g^*$ -II accounted for the observed multiphasic decay dynamics.

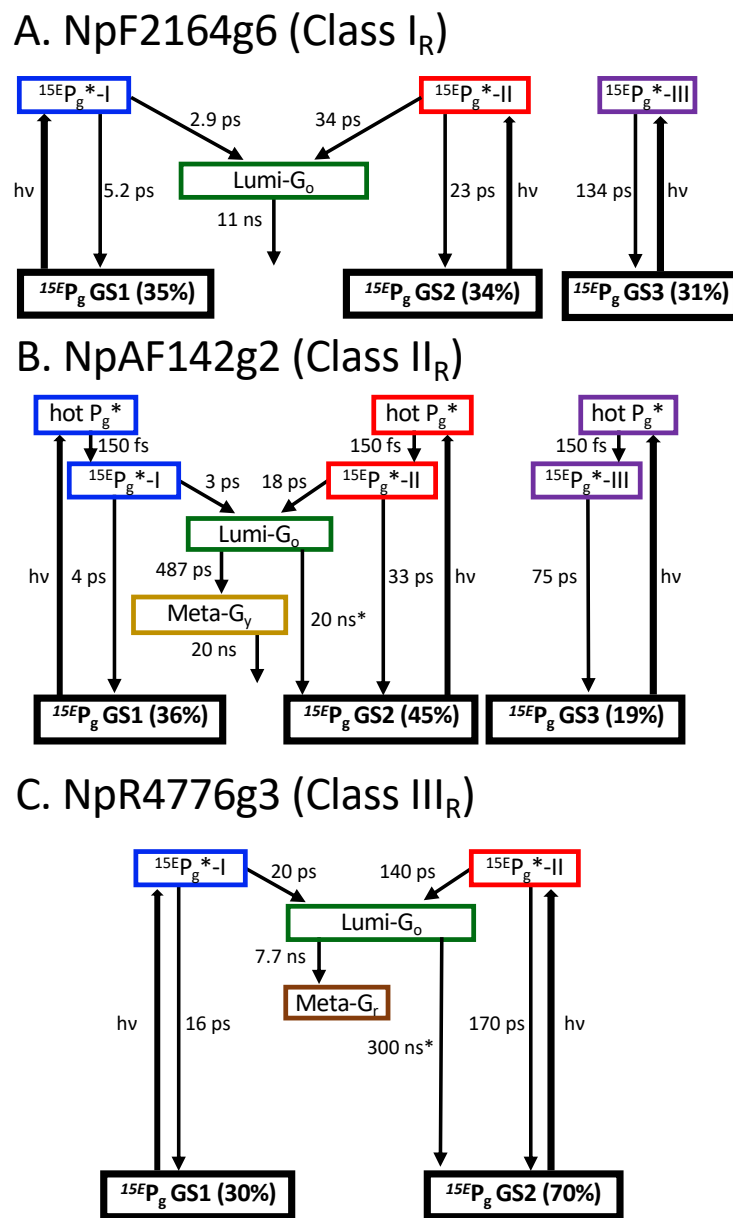


**Figure 6.4:** Representative Red/Green CBCRs Primary Reverse Target Models

Representative target models for (A) Class I<sub>R</sub> sensors exhibiting one Lumi-G<sub>o</sub> photoproduct within the ultrafast timescale (NpF2164g6), (B) Class II<sub>R</sub> sensors exhibiting Lumi-G<sub>o</sub> and Meta-G<sub>y</sub> photoproducts evolving sequentially within the ultrafast timescale (NpAF142g2), and (C) Class III<sub>R</sub> sensors exhibiting a red-shifted population within the ultrafast timescale (NpR4776g3). Population colors correspond to the SADS and concentration profiles in Figure 6.5. Time constants and ground-state occupancy levels are also found in Tables A6.1 and A6.2. \*Time constants correspond to a shunt. The target models for the non-representative CBCRs are in the SI (Figure A6.9).

### *Class II<sub>R</sub> sensors*

In contrast to NpF2164g6, the Class II<sub>R</sub> sensor NpAF142g2 exhibited initial <sup>hot</sup>P<sub>g</sub>\* excited-state populations from photoexcitation of co-existing ground-state populations - GS1, GS2 and GS3 (in a 36:45:19 ratio). These “hot” populations decayed quickly (~150-fs) to yield relaxed and independently evolving excited-state populations (<sup>15E</sup>P<sub>g</sub>\*-I, <sup>15E</sup>P<sub>g</sub>\*-II and <sup>15E</sup>P<sub>g</sub>\*-III) without generating any measurable Lumi-G<sub>o</sub> or refilling of the bleach. These non-productive, fast relaxation dynamics are common in many red/green CBCRs (e.g. Figure A6.10) and have been observed on comparable timescales in other systems.<sup>101, 104, 176, 182, 183, 191, 195, 286</sup> As with the Class I<sub>R</sub> sensors the target model for NpAF142g2 (Figure 6.4B) includes three <sup>15E</sup>P<sub>g</sub> ground-state populations each generating separate excited-state populations. The two shorter lived excited-state populations (<sup>15E</sup>P<sub>g</sub>\*-I and <sup>15E</sup>P<sub>g</sub>\*-II) were photoactive and generated Lumi-G<sub>o</sub> (Figures 6.4B and 6.5C) whereas the longer living excited-state population (<sup>15E</sup>P<sub>g</sub>\*-III) was photoinactive. In contrast to the Class I<sub>R</sub> sensor NpF2164g6, we observed evolution of Lumi-G<sub>o</sub> to Meta-G<sub>y</sub> that was accompanied by a blue-shifting of the spectra as well as a small decrease in the overall amplitude (Figure 6.5C).

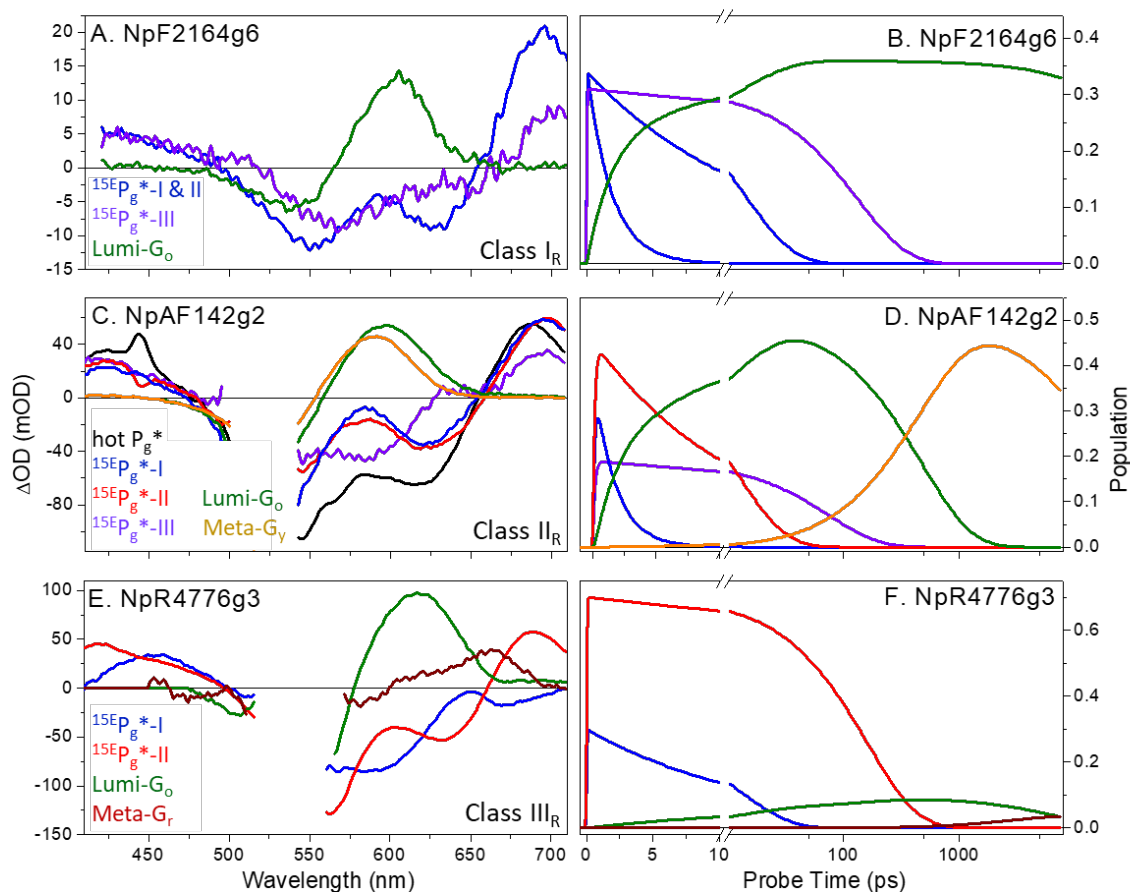


**Figure 6.5:** Representative Red/Green CBCRs Primary Reverse Dynamics SADS

Target analysis results of reverse reactions with multiple ground-state populations. SADS based on the target models in Figure 6.4 are compared for (A) NpF2164g6, (C) NpAF142g2, and (E) NpR4776g3. Concentration profiles are contrasted for (B) NpF2164g6, (D) NpAF142g2, and (F) NpR4776g3. Vibrationally excited (“hot”) populations are not shown in the concentration profiles. The SADS and concentration profiles for the non-representative CBCRs are in the SI (Figures A6.10 and A6.11).

### *Class III<sub>R</sub> sensors*

The target model in Figure 6.4C describing the representative Class III<sub>R</sub> sensor NpR4776g3 consists of two productive ground-state populations that generate distinct excited-state populations ( $^{15}E_p_g^*$ -I and  $^{15}E_p_g^*$ -II). There was no indication of a third unproductive population, as seen for



Class I<sub>R</sub> and II<sub>R</sub> sensors.<sup>183</sup> The spectral shape of the <sup>15E</sup>P<sub>g</sub>\*-I and <sup>15E</sup>P<sub>g</sub>\*-II SADS displayed the same overall spectral trend with a steady increase in the signal from ~ 550 to 700 nm, but had different minima and maxima along this curve (Figure 6.5E). As seen with other CBCRs, <sup>15E</sup>P<sub>g</sub>\*-I and <sup>15E</sup>P<sub>g</sub>\*-II both produced Lumi-G<sub>0</sub> with different efficiencies (vide infra) with some of each population decaying back to the <sup>15E</sup>P<sub>g</sub> ground state. Lumi-G<sub>0</sub> photointermediates of two of the Class III<sub>R</sub> sensors (NpR4776g3 and NpR1597g4) were red shifted relative to those of other red/green sensors reported here (Figure 6.6). Class III<sub>R</sub> Lumi-G<sub>0</sub> photointermediates subsequently evolved to red-absorbing populations. For NpR4776g3 and NpR1597g4, this red-absorbing Meta-G<sub>r</sub> population showed significant spectral overlap with the <sup>15Z</sup>P<sub>r</sub> - <sup>15E</sup>P<sub>g</sub> difference spectrum (Figure 6.6A and Figure A6.12). A similar red-absorbing (~650 nm) population was reported for Slr1393g3 on ultrafast timescales, but it was not ascertained whether this protein also exhibited a blue-shifted Meta intermediate due to the long living excited-state dynamics.<sup>185</sup> The Lumi-G<sub>0</sub> → Meta-G<sub>y</sub> transition occurred with a 100% yield for the Class II<sub>R</sub> sensor NpR6012g4.<sup>183</sup> However, branching mechanisms incorporating shunts were required for all Class III<sub>R</sub> sensors in order to properly fit the GSB recovery kinetics.

NpR5113g2 differed from the other Class III<sub>R</sub> sensors in that four photointermediates populations (Lumi-G<sub>0</sub>, Meta-G<sub>y</sub>, Meta-G<sub>o</sub>, and Meta-G<sub>r</sub>) were resolved, yielding a terminal red-absorbing population that was red-shifted relative to the <sup>15Z</sup>P<sub>r</sub> dark state (Figure 6.6B). Similar to Class II<sub>R</sub> sensors, NpR5113g2 exhibited an initial blue shift during the conversion of Lumi-G<sub>0</sub> to Meta-G<sub>y</sub> which was not observed in the other two Class III<sub>R</sub> sensors. In contrast to the Class II<sub>R</sub> sensors, NpR5113g2 exhibited a red shift to yield a mixture of Meta-G<sub>o</sub> and Meta-G<sub>r</sub> photointermediates populated on comparable timescales, given the dual peak nature of the terminal SADS (Figure

6.6B; red curve). The presence of a deep red-absorbing population was also observed in the cryokinetics of NpR5113g2 - a species that has also been observed in the secondary reverse dynamics of AnPixJg2.<sup>29, 181</sup>

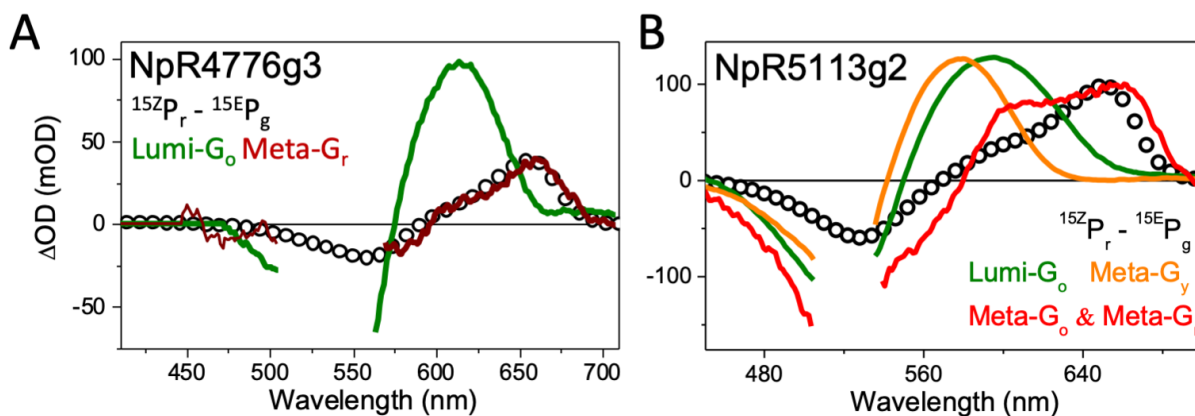


**Figure 6.6:** Overlap of Class III<sub>R</sub> Photointermediates with the Static Difference Spectrum  
 Overlap of Class III<sub>R</sub> photointermediates with the  $^{15Z}P_r - ^{15E}P_g$  difference spectra for (A) NpR4776g3 and (B) NpR5113g2. The comparison of the terminal photointermediates and the terminal state for NpR4776g3 (A, dark red curve) and NpR5113g2 (B, red curve) indicates that the chromophore has a similar conformation as the  $^{15Z}P_r$  dark state. For NpR5113g2, the terminal spectrum is a mixture of Meta-G<sub>o</sub> and Meta-G<sub>r</sub> photointermediates (B; red curve).

### Correlations

The previous characterization of the primary forward dynamics of these red/green CBCRs identified several correlations,<sup>176</sup> most notably (1) the negative correlation between the excited-state ( $^{15Z}P_r^*$ ) lifetime and  $\Phi_{Lumi-R}$  and (2) the positive correlation between the peak wavelength of  $^{15Z}P_r$  and  $\Phi_{Lumi-R}$ . The dynamic parameters of the reverse dynamics of the red/green CBCRs resolved here were plotted against each other to identify any possible underlying correlations in the reverse reaction (Figure 6.7). Four correlations were identified: (1) a negative correlation

between average excited-state ( $^{15E}P_g^*$ ) lifetime and  $\Phi_{\text{Lumi-G}_0}$ , (2) a negative correlation between  $^{15E}P_g$  peak wavelength and  $\Phi_{\text{Lumi-G}_0}$ , (3) a positive correlation between  $\Phi_{\text{Lumi-G}_0}$  (reverse reaction) and  $\Phi_{\text{Lumi-Rf}}$  (forward reaction), and (4) a positive correlation between excited-state lifetime ( $^{15E}P_g^*$ ) and  $^{15E}P_g$  peak wavelength (Figure 6.7). Interestingly, the reverse reaction exhibited a negative correlation between  $^{15E}P_g$  peak wavelength and  $\Phi_{\text{Lumi}}$  whereas the forward dynamics exhibited a positive correlation between  $^{15Z}P_r$  peak wavelength and  $\Phi_{\text{Lumi}}$ .<sup>176</sup>

The correlation plots also emphasized several Class features. Class III<sub>R</sub> sensors (excepting NpR5113g2) exhibited the longest average excited-state lifetimes and the average excited-state lifetime of NpAF142g2 was longer than the other Class II<sub>R</sub> CBCRs (Figure 6.7; blue dots and Table A6.1). The excited-state population(s) of Slr1393g3, a Class III<sub>R</sub> sensor, were longer lived and similar to NpR1597g4 (Figure A6.4).<sup>185</sup> Class III<sub>R</sub> sensors, NpAF142g2, and perhaps NpR2854g3 were modeled with intermediate shunts back to  $^{15E}P_g$  to fit the GSB recovery kinetics. Three of these, i.e., NpAF142g2, NpR1597g4, and NpR4776g3, also exhibited relatively slow Lumi-G<sub>0</sub> evolution (Figure A6.9). NpR5113g2 notably did not exhibit slower Lumi-G<sub>0</sub> dynamics, but instead progressed through a unique mechanism in relation to the other Class III<sub>R</sub> sensors (Figures 6.6 and 6.9). These discrepancies in the correlation plots result either from different protein environments surrounding the PCB chromophore, i.e., change in protonation or residues altering ionic reactions, in the initial dynamics, or from different interactions with more distant regions of the protein during the longer term dynamics (see subsequent discussion).

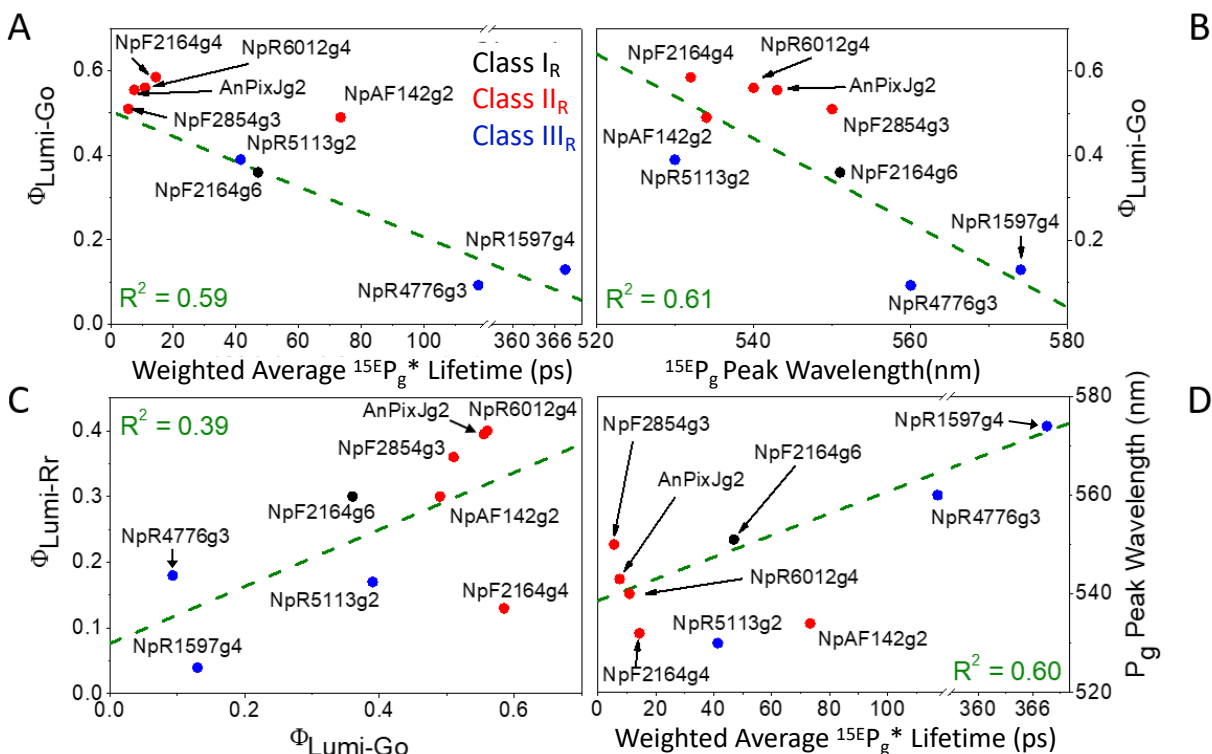


**Figure 6.7:** Red/Green CBCRs Primary Reverse Dynamics Correlation Plots

Correlation plots for (A) weighted  $^{15}E_g^*$  half-life vs  $\Phi_{Lumi-Go}$ , (B)  $^{15}E_g$  peak wavelength vs.  $\Phi_{Lumi-Go}$ , (C)  $\Phi_{Lumi-Go}$  vs.  $\Phi_{Lumi-Rr}$ , and (D) weighted  $^{15}E_g^*$  half-life vs.  $^{15}E_g$  peak wavelength. The classes are color coded as follows: Class I<sub>R</sub>: Black, Class II<sub>R</sub>: Red and Class III<sub>R</sub>: Blue. The linear correlation coefficients ( $R^2$ ) are given in green for each panel and shows that these are rough correlations due in part to the uniqueness of the Class III<sub>R</sub> sensors. It should be noted that an excitation wavelength dependence for  $\Phi_{Lumi-Go}$  has been reported for NpR6012g4.<sup>183</sup> Slr1393g3 was left out since it was not analyzed beyond a sequential model.<sup>185</sup>

## Discussion

While a range of primary forward dynamics were previous reported for ten red/green CBCRs from *N. punctiforme*,<sup>29, 176, 185</sup> their corresponding reverse dynamics exhibit a greater diversity of excited-state and ground-state kinetics, spectra, and mechanisms. It has been suggested previously that AnPixJg2, NpR6012g4, and Slr1393g3 may each be representative of the red/green CBCR

family. The range of reverse dynamics observed here makes it difficult to argue that any one CBCR is representative of the range of observed diversity for the canonical reg/green CBCR subfamily.

Figure 6.8 shows a simplified model of the full photocycle of these red/green CBCRs that includes both forward<sup>35, 36</sup> and reverse dynamics. For simplicity, ground-state shunts have been omitted. In contrast with the forward dynamics comprised by a sequence of monotonically evolving blue-shifting ground-state intermediates between the far-red-absorbing Lumi-R<sub>f</sub> intermediate and the <sup>15E</sup>P<sub>g</sub> signaling state, the reverse dynamics exhibit an initially recursive behavior with a blue-shifted intermediate evolving from the primary Lumi-G<sub>o</sub> intermediate prior to a red-shifting sequence of intermediates that regenerates the <sup>15Z</sup>P<sub>r</sub> dark state. While the complete analysis of the secondary reverse dynamics of these proteins will be published elsewhere,<sup>179</sup> the primary dynamics collected here provide a glimpse into the diversity of the canonical red/green CBCR family. Although the differing primary dynamics observed here likely are attributed to dissimilar protein residues near the chromophore, kinetic differences on longer time scales could also reflect changes involving regions outside the chromophore binding pocket.<sup>177, 197</sup>

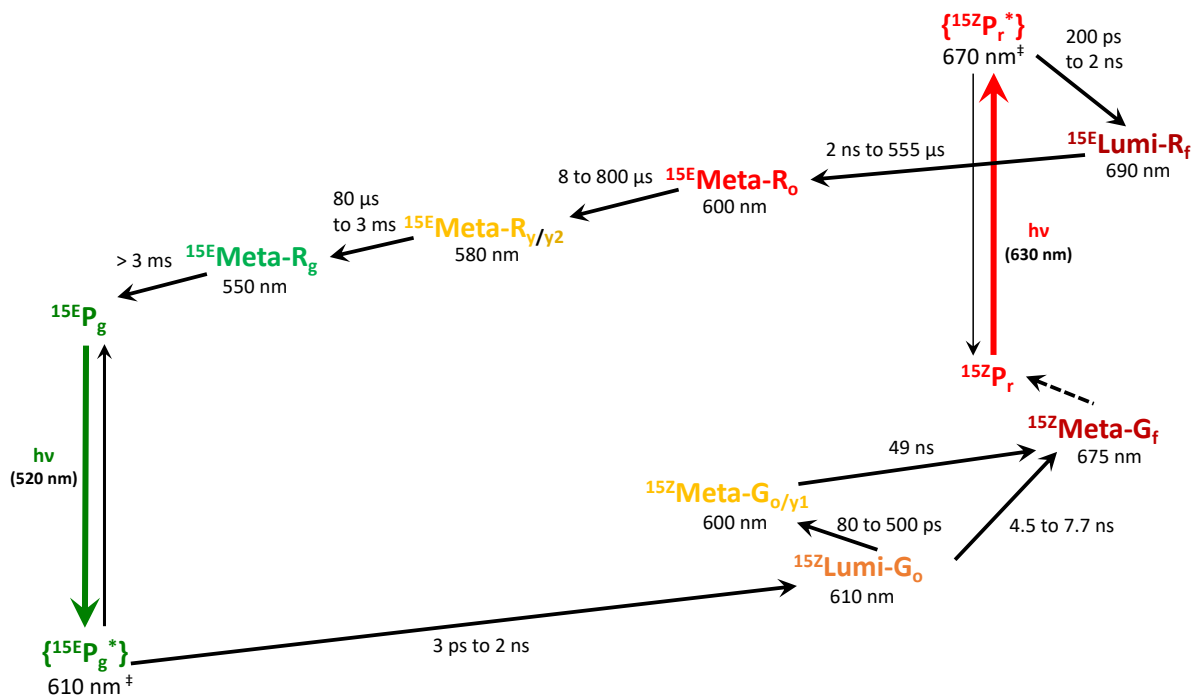


**Figure 6.8:** Composite Photocycle of Red/Green CBCRs

Composite photocycle of canonical red/green CBCRs. The dashed line represents the secondary reverse dynamics yet to be published and is not inclusive.<sup>179</sup> Excited states are placed within brackets to signify the multiple heterogenous excited-state populations that are present. †Fluorescence emission maxima representing relaxed excited state populations for AnPixJg2.<sup>177</sup> All of the lifetimes for the forward directions were obtained from previous studies.<sup>27, 176</sup>

### *Excited-State Evolution*

Red/green CBCRs of all three classes exhibited multi-phasic excited-state dynamics that were ascribed to the photoexcitation of multiple  $^{15E}P_g$  ground-state subpopulations. On average, the Class II<sub>R</sub> sensors exhibited the fastest  $^{15E}P_g^*$  excited-state lifetimes with an average of 11.7 ps (Figure 6.7A). The Class I<sub>R</sub> sensor (NpF2164g6) and Class III<sub>R</sub> sensors exhibited slower decay kinetics at 46 ps and 175 ps on average, respectively. As generally expected for photoactive proteins, the average quantum efficiency of Lumi-G<sub>o</sub> formation, i.e., 0.36 (Class I<sub>R</sub>), 0.54 (Class

II<sub>R</sub>) and 0.20 (Class III<sub>R</sub>), correlate well with their corresponding excited state decay rates (Figure 6.7A).

As observed with other studies of CBCR ultrafast dynamics,<sup>111, 183, 187</sup> not all photogenerated  $^{15E}P_g^*$  populations yielded a primary Lumi-G<sub>o</sub> photoproduct. The SADS of photoactive  $^{15E}P_g^*$  subpopulations typically share similar spectral properties whereas the non-photoactive  $^{15E}P_g^*$  populations often exhibit altered SADS features (Figures 6.5C and A6.10). We attribute small structural rearrangements of the surrounding protein environment to be the likely origin of the different sub-populations.<sup>112</sup> Such spectral dissimilarities between photoactive and non-photoactive populations implicate differences in the chromophore conformation that contribute to their distinct excited-state fates. The preferential excitement of the non-photoactive  $^{15E}P_g^*$  populations by longer wavelengths may be the origin of the observed trend that excitation pulses at shorter wavelengths result in larger quantum yields for NpR6012g4 and Slr1393g3.<sup>183, 185</sup>

Although spectrally inhomogeneous  $^{15E}P_g^*$  populations were not previously observed for NpR6012g4,<sup>183</sup> spectral inhomogeneity was observed for several red/green CBCRs studied here (Figures 6.5C and A6.10). The observation of unproductive  $^{15E}P_g^*$  sub-populations in one or more CBCRs in all the three classes suggests that inhomogeneity is a consistent trend for the reverse photoreaction of all three classes of red/green CBCRs. Such unproductive excited-state populations likely are present in the majority of photoactive biliproteins, as they have been reported in non-canonical red/green (NpR3784),<sup>189</sup> non-canonical orange/green (NpF2164g7),<sup>187</sup> green/red (RcaE),<sup>190, 191</sup> and insert-cysteine (NpF2164g3)<sup>111</sup> CBCRs. For the reverse reactions of NpF2164g3<sup>111</sup> and NpF2164g7<sup>187</sup> as well as both forward and reverse reactions of RcaE<sup>190, 191</sup> the

spectra of photoinactive and photoactive excited-state populations were indistinguishable. For the forward reaction of NpF2164g3,<sup>111</sup> NpF2164g6 (canonical red/green),<sup>176</sup> and NpF2164g7,<sup>187</sup> varying degrees of excited-state spectral inhomogeneity were observed.

The observed correlation between longer excited-state lifetime and decreased photocycle quantum yield (Figure 6.7) was expected and also consistent with a similar trend for the forward reactions of the same CBCRs<sup>176</sup> and those of other photoreactive systems.<sup>137, 287-289</sup> The negative correlation between initial parental state peak wavelength and quantum efficiency of the reverse primary photoreaction (Figure 6.7)<sup>176</sup> also supports the conclusion that red/green CBCRs with the most distorted  $^{15}E_{\text{P}_g}$  chromophores are the most photoactive. Based on the assumption that the CBCRs with blue-shifted  $^{15}E_{\text{P}_g}$  signaling states possess more distorted chromophores, this conclusion also is consistent with the larger Stokes shifts observed for the  $^{15}E_{\text{P}_g}$  signaling states than those for the  $^{15}Z_{\text{P}_r}$  dark states ( $\sim 2000 \text{ cm}^{-1}$  vs  $\sim 500 \text{ cm}^{-1}$ ; Figure 6.8). In contrast, the forward reaction had a positive correlation between initial parental state peak wavelength and quantum efficiency that may be associated with differences in the hydrogen bonding network and protonation of key amino acid residues as proposed for the  $^{15}Z_{\text{P}_r}$  state of Cph1.<sup>100</sup> Taken together, these results indicate that the forward and reverse reactions are mechanistically different.<sup>176, 177</sup>

The different dynamics of the three red/green CBCR classes can be explained by multiple structural features. These include differences in chromophore-contacting H-bonding networks,<sup>100, 157, 163</sup> D-ring dihedral angle, and conformations of amino acid residues near the D-ring.<sup>108</sup> The influence of a hydrogen bond network on the primary photodynamics is well known for phytochrome systems, such as Apg2 from *Agrobacterium fabrum*,<sup>157</sup> Cph1 from *Synechocystis* sp.



PCC6803,<sup>100</sup> and SaBphP1 from *Stigmatella aurantiaca*.<sup>163</sup> For example, Apg2 exhibited a lower Lumi quantum yield at higher pH, whereas the photosensory core of Cph1 (Cph1Δ) only yielded Lumi-R<sub>f</sub> at lower pHs. SaBphP1 also possessed a higher Lumi quantum yield when H-bonding to the D-ring was removed.<sup>163</sup> Spectral inhomogeneity ascribed to D-ring dihedral angle inhomogeneity and conformation of amino acid residues near the D-ring of the bilin has also been reported.<sup>108</sup> A similar influence of a hydrogen-bonding network on CBCR photochemistry is anticipated. This hypothesis has yet to be explored; however, H-bonding network heterogeneity may be responsible for the presence of photoactive and non-photoactive populations observed for red/green CBCRs.

Several conserved residues have been identified in the red/green CBCR subfamily to strongly influence photoactivity including mechanisms, kinetics, and quantum yields. Such residues are highlighted in the amino acid sequence alignment shown in Figure 6.9. Many of these residues are conserved in all three classes resolved here. Two conserved Phe residues were responsible for structurally deforming the chromophore in the signaling state<sup>197</sup> and different conformations of the conserved 'lid-Trp' and a highly conserved aspartic acid modulate the amount of photo-unproductive <sup>15Z</sup>P<sub>o</sub> subpopulations formed for the red/green CBCR NpR6102g.<sup>108</sup> With the exception of NpAF142g2, all Class I<sub>R</sub> and II<sub>R</sub> red/green CBCRs studied here possess a histidine (His) residue predicted to be located close to the bilin C10 position<sup>108</sup>; these include His659 in NpR6012g4 and His293 in AnPixJg2. Both of these His amino acid residue locations have been independently reported to have influence on the chromophore or dynamics, with the H659C mutant of NpR6012g4 introducing a secondary linkage to C10<sup>211</sup> and the H293Y mutant of AnPixJg2 dark reverting faster than the wild-type without significantly changing the absorbance spectra.<sup>290</sup> In all

Class III<sub>R</sub> CBCRs and NpAF142g2, a tyrosine (Tyr) residue is found at this location (Figure 6.9). Canonical red/green CBCRs that possess Tyr at this location exhibit slower excited-state dynamics and slower Lumi-G<sub>0</sub> evolution than those of Class I<sub>R</sub> and II<sub>R</sub> sensors (Figures 6.7 and A6.9; Table A6.2).

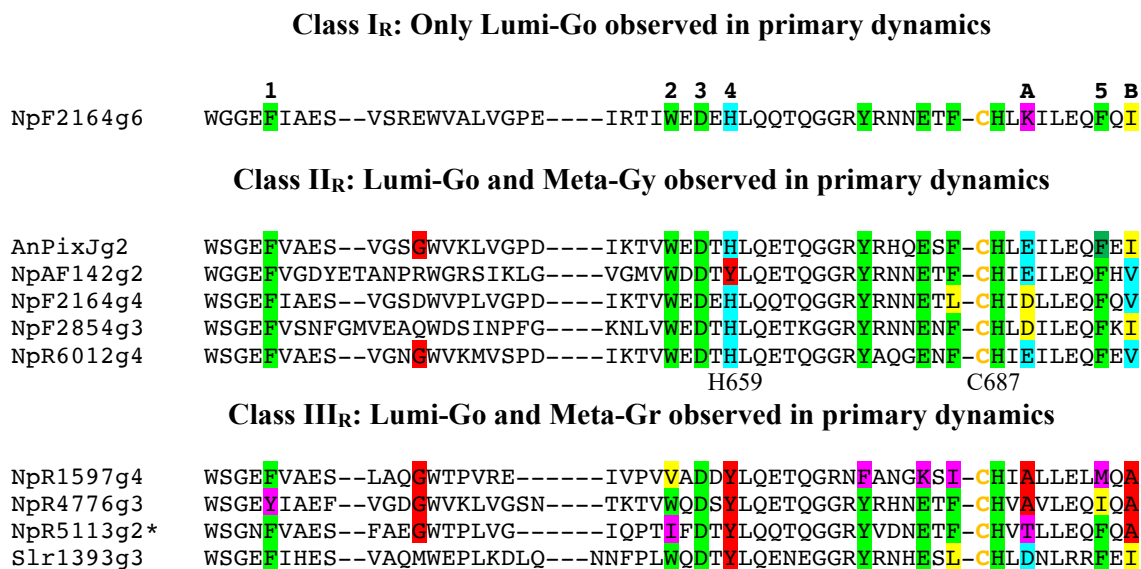


**Figure 6.9:** Partial Amino Acid Sequence Alignment

Partial amino acid sequence alignment of the red/green CBCRs presented here reported by Rockwell et al.<sup>69, 197</sup> The top row serves as a reference to the important columns where numbered columns correspond to (1) β2 Phe, (2) Lid-Trp, (3) Asp, (4) His near bilin C10 and (5) Helix Phe and letters correspond to residues not yet studied for their importance to photochemistry. Bold orange Cs represent the conserved, bilin-binding cysteine residue and omitted insertion sequences (removed for clarity) are indicated with dashes. For all three classes, the β2 and Helix Phes (associated with bilin deformation) and 'lid-Trp' and Asp residues (associated with the unproductive <sup>152</sup>P<sub>o</sub> species) were highly conserved. Residues highlighted in green are highly conserved among the three classes, in yellow are seen repeatedly, in pink are unique, in light blue are preferentially observed in Class II<sub>R</sub> and in red are preferentially observed in Class III<sub>R</sub>. \*Class III<sub>R</sub> red/green CBCR with Meta-G<sub>y</sub>.

The highly conserved histidine (H260) in the bacterial phytochrome Cph1 $\Delta$  was shown to modulate the excited-state dynamics via an  $\alpha$ -facial H-bonding network involving ordered waters, the C-ring propionate and the D-ring NH of the chromophore.<sup>100, 163</sup> Based on NMR studies, the corresponding His residue in NpR6012g4 (H688) does not engage in the same type of H-bonding network with the D-ring.<sup>108</sup> In Class I<sub>R</sub> and II<sub>R</sub> red-green CBCRs, a second histidine, i.e. H659 of Np6012g4 can participate in a  $\beta$ -facial H-bonding network that engages the bilin C-ring propionate sidechain in both photostates (Figure 6.10).<sup>108</sup> The corresponding His of AnPixJg2 (H263) is also located in position to form a similar H-bonding interaction, implicating a similar role in this protein; however this H-bonding interaction is not seen in the crystal structure of AnPixJg2.<sup>257</sup> The equivalent residue in Slr1393g3 (Y500) did not appear to be involved in a H-bonding network to the D-ring of the chromophore given the crystal structure ( $>3.5$  Å; Figure 6.10), making it unclear how the Tyr residue may influence the excited state evolution (Figures 6.7 and 6.9). Experiments to replace  $\beta$ -facial His with Tyr in Type I<sub>R</sub> and II<sub>R</sub> red/green CBCRs and to test the pH-dependence of the ultrafast kinetic behavior of both variants will be of interest to assess the role of this residue in tuning photochemistry and fluorescence quantum yields of canonical red/green CBCRs.

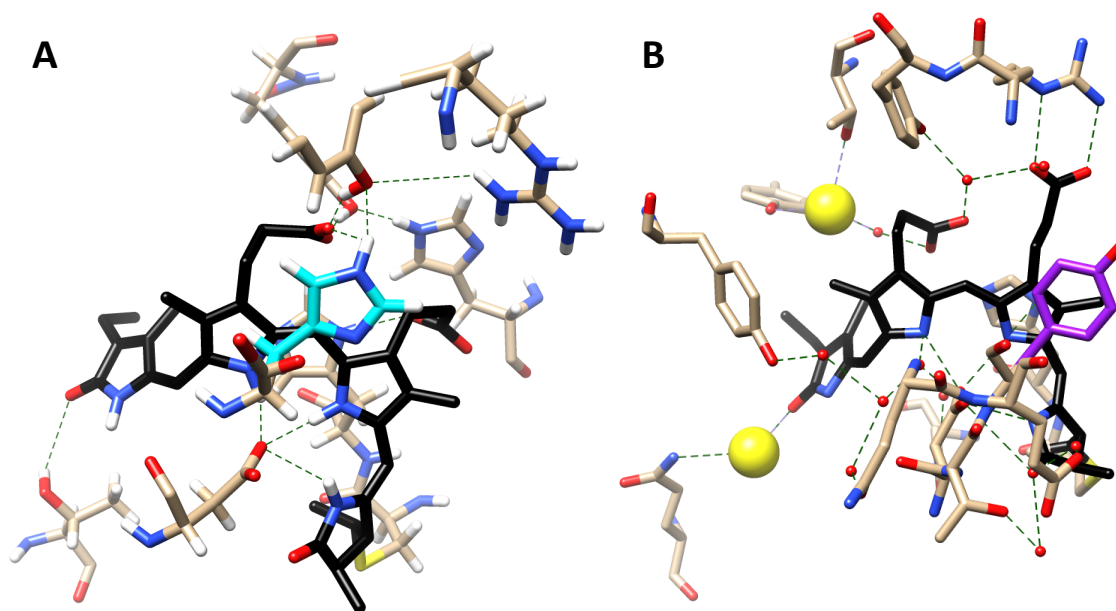


**Figure 6.10:**  $^{15}E_g$  Signaling State Hydrogen Bonding Network

Hydrogen bonding network (green dashed lines) of the  $^{15}E_g$  signaling state of (A) NpR6012g4 (PDB: 6BHO) and (B) Slr1393g3 (PDB: 5M82) assuming a maximum distance of 3.5 Å for a H-bond. Carbon atoms of the bilin chromophore A to D ring are colored black (from right to left), while carbon atoms of H659 (NpR6012g4) and Y500 (Slr1393g3), are colored cyan and purple, respectively. Carbon atoms of amino acids in the two proteins are colored tan. Water molecules (red dots) and sodium ions (yellow spheres) are shown for Slr1393g3 (PDB:5M82).

### *Ground-State Photocycle Evolution*

All CBCRs studied here exhibited a red-shifted primary Lumi- $G_o$  photointermediate on an ultrafast timescale which ultimately evolved into the dark-adapted  $^{15}ZP_r$  state on slower secondary ( $>10$  ns) timescales. Except for Class  $I_R$  sensors, Lumi- $G_o$  photointermediates evolved to secondary Meta- $G$  species on an ultrafast timescale. Class  $II_R$  sensors evolved to an orange-absorbing Meta- $G_o$  photointermediate on an average timescale of 470 ps, whereas Lumi- $G_o$  intermediates for the Class

III<sub>R</sub> sensors evolved to a red-absorbing Meta-G<sub>r</sub> species with non-unity quantum yields on a longer average timescale of 3 ns (Table A6.2).

Taken together, our studies show that the reverse dynamics of canonical red/green CBCRs are more complicated than their monotonic blue shifting forward dynamics.<sup>27</sup> Instead, the reverse reaction dynamics typically involved an initial blue shifting of a Lumi-G<sub>o</sub>-derived intermediates prior to later generation of red-shifted intermediates and <sup>15Z</sup>P<sub>r</sub> dark-state recovery on secondary (>10 ns) timescales (Figure 6.8).<sup>179</sup> Assuming structural deformation of the chromophore as the driving force behind the spectral shifting of the intermediates (and not charge transfer, protonation events, or hydration of the chromophore pocket), such non-monotonic evolution suggests that the Lumi-G<sub>o</sub> structurally deforms to generate a blue-shifted Meta intermediate analogous to the forward reaction. Unlike the forward reaction however, structural relaxation of these Meta intermediates (presumably by via planarization of the D-ring) follows to generate the red-shifted <sup>15Z</sup>P<sub>r</sub> dark state. Interestingly, comparison of the Nc-C14-C15-C16 dihedral angles of AnPixJg2,<sup>257</sup> NpR6012g4,<sup>108</sup> and Slr1393g3,<sup>291</sup> reveals that D-ring remains out-of-plane in both <sup>15Z</sup>P<sub>r</sub> and <sup>15E</sup>P<sub>g</sub> states (Table 6.1, Figure A6.15) despite their 150-180° rotation around C14-C15-C16-Nd dihedral bond (Figure 6.1A). Nevertheless, the D-ring tilt is larger in the <sup>15E</sup>P<sub>g</sub> state than the <sup>15Z</sup>P<sub>r</sub> state (Table 6.1), which likely accounts for the blue-shifted absorption maximum of the former.

**Table 6.1:** Resolved Red/Green CBCR D-ring Dihedral and Ring Tilt Angles

Dihedral angles and tilt angles of C/D rings for AnPixJg2,<sup>257</sup> NpR6012g4,<sup>108</sup> and Slr1393g3.<sup>291</sup> Atoms are labeled as in Figure 6.1A. The C/D ring tilt of AnPixJg2 was determined by measuring the angle between two planes defined by the C and D rings using Chimera.<sup>292</sup>

CBCR	Code	Nc-C14-C15-C16	C14-C15-C16-Nd	C/D Ring Tilt
Dark Adapted <sup>15Z</sup> P <sub>r</sub>				
AnPixJg2 <sup>257</sup>	3W2Z	-147.9°	27.0°	55.5°
NpR6012g4 <sup>108</sup>	6BHN	-132.4°±7.8°	359.4°±5.9°	49.0°±5.6°
Slr1393g3 <sup>291</sup>	5DFY	-155.6°	26.3°	48°
Light Adapted <sup>15E</sup> P <sub>g</sub>				
NpR6012g4 <sup>108</sup>	6BHO	-131.8°±14.3°	189.4°±17.6°	58.8°±4.8°
Slr1393g3 <sup>291</sup>	5M82	-109.8°	181.6°	62°

In the reverse reaction dynamics of some Class III<sub>R</sub> sensors, photointermediates are observed that are even more red-shifted than the final <sup>15Z</sup>P<sub>r</sub> photoproduct. One example is NpR5113g2 whose Meta-G<sub>r</sub> intermediate absorbs at longer wavelengths than its <sup>15Z</sup>P<sub>r</sub> dark state (Figure 6.6B).<sup>179, 187</sup> This “spectral overshooting” suggests the D-ring can adopt a more planar geometry immediately prior to forming <sup>15Z</sup>P<sub>r</sub> - an observation previously reported for other CBCRs.<sup>29, 179</sup> The Class III<sub>R</sub> sensor NpR4776g3 exhibits a partially populated (within 8 ns) red-absorbing species that strongly resembles the <sup>15Z</sup>P<sub>r</sub> absorption spectrum. We attribute this species to an intermediate subpopulation with a relaxed chromophore whose absorption spectrum resembles <sup>15Z</sup>P<sub>r</sub> that appears prior to the large-scale deformation needed to generate the <sup>15Z</sup>P<sub>r</sub> dark state. This may reflect the presence of smaller, less constraining amino acid residues near the chromophore. This hypothesis is consistent with the red-shifted Meta-G<sub>r</sub> photointermediate observed in NpR5113g2 (Figure 6.6B) and those of other Class III<sub>R</sub> sensors resolved here, i.e. NpR4776g3 and NpR1597g4. With the exception of Slr1393g3, the majority of the Class III<sub>R</sub> sensors possess alanine residues at two positions (labeled

A and B) that replace residues with larger sidechains in the Class I<sub>R</sub> and II<sub>R</sub> subfamilies (Figure 6.9). In future studies, we hope to examine the influence of residue exchange at these two positions as well as other amino acid substitutions (Figure 6.9, residues highlighted in red) on the secondary reverse photodynamics of the canonical red/green CBCR family. A structural comparison of the amino acid residues corresponding to these conserved alanine residues in Slr1393g3 and NpR6012g4 is presented in the SI (Figures A6.16-A6.18 and Table A6.4).

*Efficiency of secondary interconversions and thermal shunts that restore the <sup>15E</sup>P<sub>g</sub> state*

It is common to model subsequent photointermediate evolution from the primary Lumi photoproduct with unity quantum yields (i.e., non-branching unidirectional evolution). For the Tyr incorporating CBCRs (Class III<sub>R</sub> and NpAF142g2), we observed non-unity quantum yields for the evolution of Lumi-G<sub>o</sub> into Meta-G<sub>o</sub> (Figures 6.3, A6.4, A6.5, and A6.9). This can be accounted for by shunting of one or more of these intermediates back to the original ground state species. From analysis of the present data, we obtained estimates of 2.4% to 66.7% of the Lumi-G<sub>o</sub> population decaying back into the respective <sup>15E</sup>P<sub>g</sub> parental populations (Figure A6.9). We hypothesize that the CBCRs that exhibit shunts possess fewer constraining H-bonding interactions with the chromophore D-ring that increase the energy barrier between Lumi-G<sub>o</sub> and <sup>15E</sup>P<sub>g</sub>. Indeed, CBCRs that possess shunts exhibit on average longer Lumi-G<sub>o</sub> lifetimes than those that do not (2.3 ns vs 410 ps). Shunts in the photocycles of other bilin photoreceptors have been reported including the bacteriophytochromes SaBphP1 from *Stigmatella aurantiaca*,<sup>163</sup> and Apg1 and Apg2 from *Agrobacterium fabrum*.<sup>293, 294</sup> NpR6012g4 was also reported to have photointermediate shunts on the secondary timescale.<sup>29</sup> The structural basis for the occurrence of these shunt pathways are not presently known, but they likely involve residues close to the bilin chromophore that participate

in larger H-bonding networks. These networks also are expected to be influenced by solvent pH, temperature and sidechain orientations that contribute to the heterogeneity of both primary and secondary photoinduced protein dynamics. We intend to explore further the structural basis of these photointermediate shunts in the secondary reverse dynamics paper.<sup>179</sup>



## *Associated Content*

### *Supporting Information (pg. 281)*

The Supporting Information provides ground state spectra, difference spectra, kinetic traces, EADS, SADS, concentration curves, target models, global analysis parameters for the CBCRs not presented in the manuscript. Structures comparing the chromophore conformation in the dark adapted and signaling states of AnPixJg2, NpR6012g4, and Slr1393g3 are compared. Lastly, protein structures near the chromophore of the signaling state of NpR6012g4 and Slr1393g3 and their distances from the D-ring were compared.

### *Accession Codes*

NpAF142g2 (B2JAQ4), NpR1597g4 (B2J0R5), NpF2164g4, NpF2164g6, NpF2164g7 (B2J668), NpF2854g3 (B2IVK2), NpR4776g2, NpR4776g3 (B2IZ18), NpR5113g2 (B2J261), NpR6012g4 (B2IU14), RcaE (Q47897), Slr1393 (P73184), AnPixJg2 (Q8YXY7), and Cph1 (Q55168)

### *Funding*

This work was supported by a grant from the Chemical Sciences, Geosciences, and Biosciences Division, Office of Basic Energy Sciences, Office of Science, United States Department of Energy (DOE DE-FG02-09ER16117) to both J.C.L. and D.S.L.

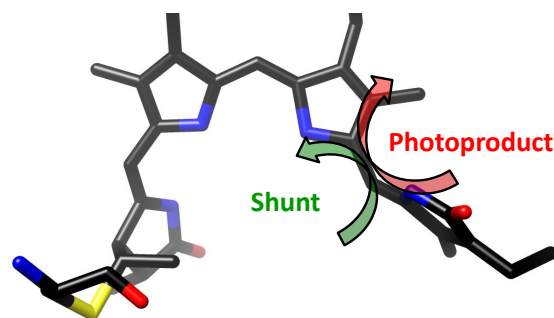
### *Acknowledgments*

Nathan C. Rockwell (University of California, Davis) is acknowledged for sample preparation and constructive discussions and Dr. Mikas Vengris (Light Conversion Ltd.) is acknowledged for the donation of global and target analysis software. Molecular graphics images were produced using the UCSF Chimera package from the Resource for Biocomputing, Visualization, and Informatics at the University of California, San Francisco (supported by NIH P41 RR-01081).

# Chapter 7. Conservation and Diversity in the Secondary Reverse Photodynamics of Red/Green Cyanobacteriochromes

## *Abstract*

Cyanobacteriochromes (CBCR) are linear-tetrapyrrole based photoreceptor proteins distantly related to phytochromes and are involved in various biological responses such as phototaxis and chromatic acclimation. To date the forward



and reverse primary dynamics and the secondary forward dynamics have been reported for several canonical red/green CBCRs isolated from *Nostoc punctiforme*. To finish the conserved photocycle, the secondary reverse dynamics of eight canonical red/green CBCR domains isolated from *Nostoc punctiforme* and one mutant ( $\beta$ 2FV NpR6012g4) were resolved and compared to three previously reported CBCRs here. The reverse dynamics of these domains resolved a conserved mechanistic backbone that consisted of non-monotonic spectral evolution consisting of a blue shifting phase that preceded a red shifting phase. This was in contrast with the forward dynamics which consisted of a nearly conserved mechanism of monotonic blue shifting, indicating that the reverse reaction is not simply the reverse of the forward reaction. Building on the conserved mechanism of non-monotonic spectral evolution, some non-conserved features such as the previously reported photointermediate shunts back to  $^{15}E_P_g$  and photointermediates red shifted of the  $^{15}Z_P_r$  photoproduct were observed. The underlying mechanism behind photointermediate shunts may involve an increase in the structural deformation of the chromophore along the D-ring isomerization coordinate which reverts the isomerization. The Meta-G intermediate red shifted of  $^{15}Z_P_r$  was attributed to a more spacious chromophore pocket that allowed for increased planarization of the D-ring.

## ***Introduction***

A current focus in modern biophysics is the development of light activated biological tools that are either highly fluorescent<sup>44-47</sup> to be used for medicinal imaging purposes or highly efficient to develop optogenetic tools to selectively control biological function in living tissue and study neural circuits at a more fundamental level.<sup>44, 47, 51, 52, 55, 201, 295</sup> A good starting point for both applications is biological photoreceptors since they have evolved to improve the efficiency of photosynthesis via chromatic acclimation<sup>26, 71, 259, 296</sup> and initiate various responses such as phototaxis or the opening of ion channels in response to external light conditions.<sup>44, 45, 47, 55, 201, 202</sup> Photoreceptors accomplish these functions by reversibly converting between a thermally stable dark-adapted state and meta-stable light-adapted state that typically have unique spectral and structural properties. To date, photoreceptors have been used as fluorescent probes to image tumors and as optogenetic tools to control the action potential of neurons, better map neural circuits and study neuroscience at a more fundamental level.<sup>44, 45, 47, 51-54, 200, 204, 295</sup>

An example of photoreceptors are phytochromes which are tri-domain (PAS-GAF-PHY) photosensory proteins that utilize linear tetrapyrrole (bilin) chromophores to reversibly photoconvert between a thermally stable, red absorbing ( $^{15Z}P_r$ ) dark-adapted and a meta-stable far-red absorbing ( $^{15E}P_{fr}$ ) light-adapted state (Figure 7.1). Phytochromes were originally discovered in plants where they regulate growth and seed germination,<sup>18, 19, 297</sup> but were later discovered in algae, bacteria, and fungi.<sup>246, 279</sup> More recently, a distantly related family of photosensory proteins found exclusively in cyanobacteria termed cyanobacteriochromes (CBCRs) were discovered that also incorporates a bilin chromophore but only required a single GAF domain to establish reversible photoconversion that spans the near UV to the far-red spectral regions.<sup>63, 64, 68, 69, 72, 110, 197, 283</sup> Given

the great spectral diversity of the CBCR family, multiple subfamilies of CBCRs have been identified such as red/green,<sup>69</sup> green/red,<sup>283</sup> DXCF,<sup>64, 72, 110</sup> insert-cystine,<sup>68</sup> and far-red/x CBCRs.<sup>63</sup> These families of CBCR owes their diverse photoactivity to the incorporation of chromophores with varying conjugation lengths<sup>65, 68, 69</sup> and unique photoinduced chemical responses that includes structural conformational changes,<sup>27, 108, 197</sup> protonation events,<sup>109, 192</sup> the forming or breakage of secondary cysteine linkages,<sup>68</sup> and unique protein-chromophore interactions.<sup>67</sup> While the majority of the phenotypes of CBCRs are unknown, it has been reported that some are involved in chromatic acclimation and phototaxis.<sup>22, 23, 45, 285</sup> These reported phenotypes coupled with the relatively small size and diverse photoactivity of CBCRs makes them promising candidates for serving as the basis for the development of novel biological tools. Some modified photoreceptors belonging to the phytochrome superfamily have already been tested *in vitro* and *in vivo* as fluorescent probes or as optogenetic tools.<sup>298-301</sup> To optimize photoreceptors for incorporation into biological tools, a molecular level understanding of the underlying mechanisms and efficiencies of the photoinduced reactions is required.

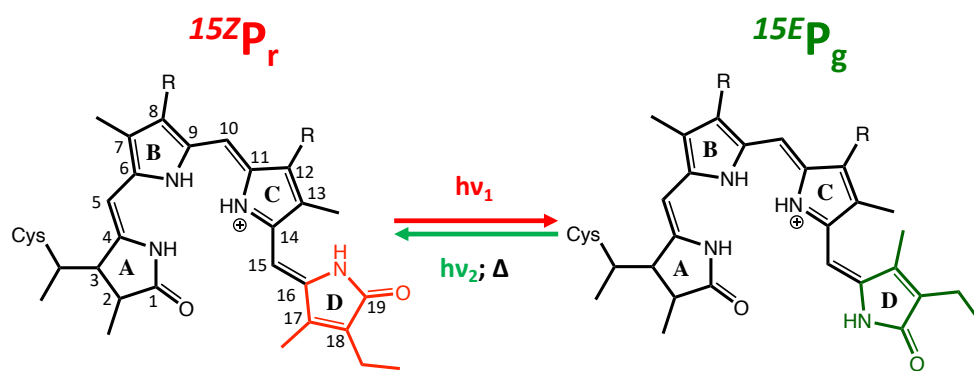


**Figure 7.1:** Red/Green CBCR Chromophore Photocycle

Molecular structures of the 15Z and 15E conformations of phycocyanobilin (PCB) in canonical red/green CBCRs.

The red/green family of CBCRs is the most extensively studied, with resolved structures for three domains<sup>108, 257, 291</sup> and several dynamics studies on numerous domains.<sup>27-29, 73, 176, 178, 180, 182-186, 264</sup> The crystal structures resolved that the phycocyanobilin (PCB) chromophore adopts a 15Z, 15-anti conformation in the thermally stable, red absorbing dark-adapted state ( $^{15Z}P_r$ ) and a 15E, 15-anti chromophore conformation in the meta-stable, green absorbing light-adapted state ( $^{15E}P_g$ ; Figure 7.1).<sup>108, 212</sup> These structures also support the hypothesis that two highly conserved phenylalanine (Phe) residues generates the green absorbance of the light-adapted state via structural deformation of the chromophore as proposed earlier by Rockwell et al.<sup>197</sup> based on the red shifting and broadening of the light adapted state when these phenylalanine residues were replaced with valine (Figure 7.2). Compared to WT NpR6012g4 and other red/green CBCRs from *Nostoc Punctiforme* (NpF2164g4, NpF2164g6, B2J668; and NpR4776g3, B2IZ18) (Figure 7.2 and Figure A7.17),  $\beta$ 2FV NpR6012g4 had similar  $^{15Z}P_r$  spectra, indicating that  $\beta$ 2FV do not play a significant role in the dark-adapted state absorbance.

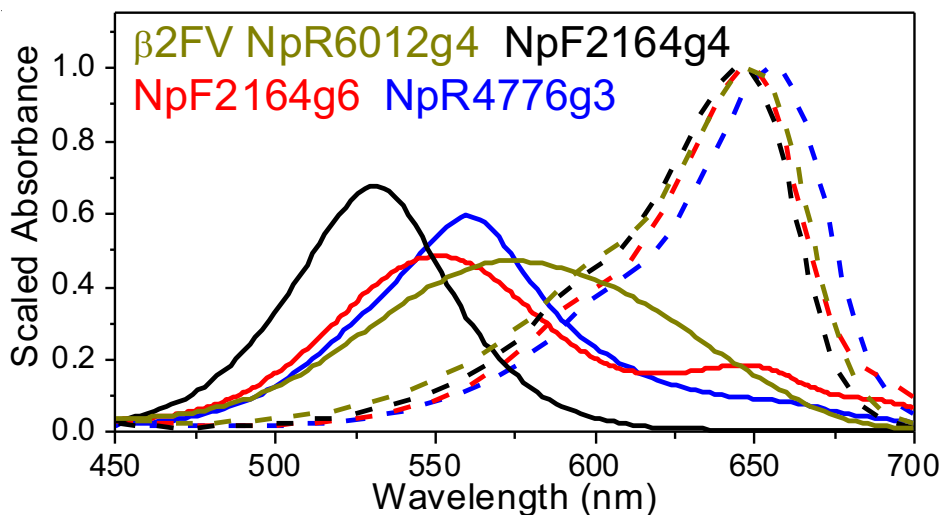


**Figure 7.2:** Representative Red/Green CBCR Parental State Spectra

Static absorption spectra of NpF2164g4 (black curves), NpF2164g6 (red curves), NpR4776g3 (red curves), and  $\beta$ 2FV NpR6012g4 (dark yellow) in the dark-adapted ( $^{15Z}P_r$ ; dashed curves) and light-adapted ( $^{15E}P_g$ ; solid curves) states.

To date, comparative studies of the primary (125 fs - 10 ns)<sup>176</sup> and secondary (10 ns – 1 ms)<sup>27</sup> dynamics of the forward reaction ( $^{15Z}P_r \rightarrow ^{15E}P_g$ ) and the primary dynamics of the reverse reaction ( $^{15E}P_g \rightarrow ^{15Z}P_r$ )<sup>28</sup> for several canonical red/green CBCR domains isolated from *Nostoc Punctiforme* have been reported. Using the nomenclature outlined by Gottlieb et al,<sup>111</sup> the forward dynamics resolved a nearly conserved mechanism of consistently blue shifted photointermediates from the initial Lumi-R<sub>f</sub> photointermediate to the  $^{15E}P_g$  photoproduct (Figure 7.3).<sup>27, 176</sup> This step-wise evolution is consistent with the structural deformation model where there is a continual increase of the distortion of the chromophore going from the initial Lumi-R<sub>f</sub> intermediate to the  $^{15E}P_g$  photoproduct.<sup>197, 212</sup> The primary reverse dynamics resolved three classes with different kinetic and spectral features where Class-I<sub>R</sub> consisted of a single photointermediate (Lumi-G<sub>0</sub>) red shifted of the light-adapted state and Class-II<sub>R</sub> and Class-III<sub>R</sub> resolved evolution of Lumi-G<sub>0</sub> to blue shifted and red shifted Meta-G intermediates, respectively.<sup>28</sup>

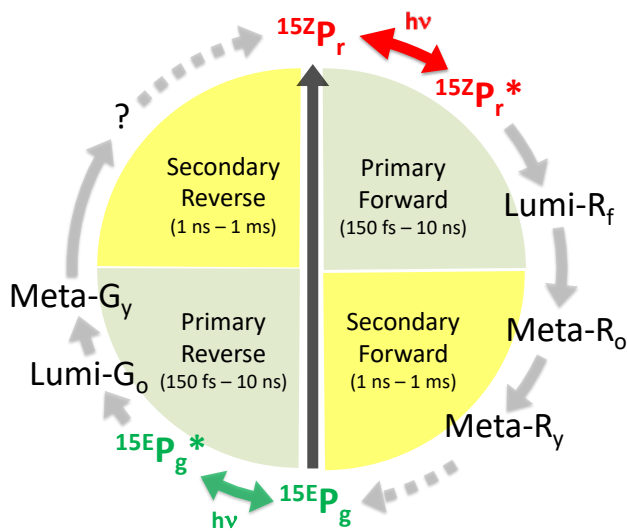


**Figure 7.3:** Generalized Conserved Red/Green CBCR Photocycle

Generalized conserved photocycle for red/green CBCRs to date.<sup>27, 28, 176</sup> The primary reverse dynamics resolved classes with different spectral features, but given the dynamics reported here, Class-II<sub>R</sub> was chosen for this scheme.

The strength of these multi-CBCR studies lies in the identification of conserved and non-conserved features as well as possible correlations. The primary dynamics studies resolved a positive correlation between shorter excited state lifetimes and initial photointermediate (Lumi) quantum yield in both directions, a positive correlation between  $^{15Z}P_r$  peak wavelengths and Lumi-R quantum yields in the forward reaction and a negative correlation between  $^{15E}P_g$  peak wavelengths and Lumi-G quantum yields in the reverse reaction.<sup>28, 176</sup> The positive correlation between  $^{15Z}P_r$  peak wavelengths and Lumi-R quantum yields may be associated with a difference in the hydrogen bonding networks as resolved in a related cyanobacterial phytochrome.<sup>73, 100, 176</sup> For the reverse reaction, the trend between  $^{15E}P_g$  peak wavelengths and Lumi-G quantum yields was associated with CBCRs with more deformed chromophores be more primed to isomerize.<sup>28</sup> Furthermore, the primary reverse dynamics<sup>28</sup> isolated four domains that exhibited relatively long excited state and Lumi-G<sub>0</sub> lifetimes as well as photointermediate shunts back to the initial  $^{15E}P_g$  parental state. These dynamics were correlated to the presence of a selectively conserved tyrosine residue near the bilin C10 that may have an altered hydrogen bonding network that inhibits the photoinduced D-ring isomerization.<sup>28</sup> The secondary forward dynamics study resolved that a previously reported unproductive subpopulation of the dark-adapted state ( $^{15E}P_o$ )<sup>108</sup> was present in half of the domains that were studied and the presence of this subpopulation was correlated to greater orange absorbance in the static  $^{15Z}P_r$  spectra.<sup>27, 108</sup> These possible metrics for identifying red/green CBCRs with larger quantum yields would be of interest for the engineering and incorporation of these CBCRs as biological tools.

Currently, the secondary reverse dynamics have been reported for three red/green CBCR domains: AnPixJg2 (Q8YXY7) from *Anabaena* sp. PCC 7120,<sup>29, 177, 264</sup> NpR6012g4 from *Nostoc*

*Punctiforme*,<sup>29, 73</sup> and Slr1393g3 from *Synechocystis* sp. PCC6803 (P73184).<sup>186</sup> The reverse dynamics of NpR6012g4 and AnpixJg2 have comparable photocycles consisting of non-monotonic spectral evolution, but NpR6012g4 exhibited three photointermediate shunts back to the  $^{15E}P_g$  state, one from Lumi-G<sub>o</sub>,<sup>73</sup> Meta-G<sub>o</sub>, and Meta-G<sub>y</sub>.<sup>29</sup> The presence of shunting indicates that Lumi quantum yields are an upper limit estimate of the efficiencies of these photoswitches and that secondary dynamics is required to determine the photoproduct yield. In addition to the photointermediate shunts in NpR6012g4, a weak far-red absorption that had a similar lifetime to Meta-G<sub>y</sub> was observed in AnpixJg2 that was attributed to a Meta-G<sub>f</sub> intermediate.<sup>29</sup> Similar photointermediate that absorbed deeper into the red than the dark-adapted state photoproduct was observed in the reverse reaction of NpR5113g2 (B2J261)<sup>28</sup> and an orange/green CBCR (NpF2164g7)<sup>187</sup> as well.

To date it is unclear if the reverse dynamics of the canonical red/green CBCRs utilize a nearly conserved mechanism like the forward dynamics<sup>27, 176</sup> or if there are different pathways as the primary reverse dynamics suggest.<sup>28</sup> It is also unknown if the shunts back to  $^{15E}P_g$  and the Meta-G<sub>f</sub> photointermediate red shifted of the  $^{15Z}P_r$  photoproduct reported by Kirpich et al.<sup>29</sup> are recurring features in the secondary reverse dynamics of red/green CBCRs or are unique to NpR6012g4 and AnPixJg2, respectively. Lastly, the influence that the conserved  $\beta 2$  Phe associated with the structural deformation of the light-adapted state has in the dynamics of these red/green CBCRs is also unclear. To ascertain the nature of the reverse dynamics of red/green CBCRs, the extent of the presence of shunting and Meta-G<sub>f</sub> photointermediates, and the influence that the highly conserved  $\beta 2$  has on the reverse dynamics of canonical red/green CBCRs, the secondary reverse dynamics of the previously resolved wild-type (WT) NpR6012g4,<sup>29</sup> AnPixJg2,<sup>29</sup> and Slr1393g3<sup>186</sup> were



compared with the  $\beta$ 2FV mutant of NpR6012g4 and nine WT CBCR domains isolated from *Nostoc Punctiforme*: NpAF142g2 (B2JAQ4), NpF2164g4, NpF2164g6, NpF2854g3 (B2IVK2), NpR1597g4 (B2J0R5), NpR4776g2, NpR4776g3, NpR5113g2. All these domains incorporate the PCB chromophore depicted in Figure 7.1, and the spectra of the parental states for all these photoreceptors can be found between Figure 7.2B and Figure A7.1. The  $\beta$ 2FV mutation did not impact the forward dynamics significantly (Supporting Information; SI) so only the reverse dynamics of  $\beta$ 2FV NpR6012g4 will be discussed here.

The reverse dynamics of the canonical red/green CBCR domains reported here coupled with the previously reported AnPixJg2,<sup>177, 264</sup> NpR6012g4,<sup>29, 73</sup> and Slr1393g3,<sup>185, 186</sup> resolved conserved and non-conserved features. A conserved mechanistic backbone consisting of non-monotonic spectral evolution where a blue shifting phase preceded a red-shifting phase was observed for every CBCR and the non-conserved photointermediate shunts and Mega-G photointermediate red shifted of the  $^{15Z}P_r$  photoproduct were resolved not to be unique to NpR6012g4 and AnPixJg2,<sup>29</sup> respectively. Interestingly, WT NpR6012g4 was reported to have photointermediate shunts but not a Meta-G red shifted of  $^{15Z}P_r$ , whereas  $\beta$ 2FV NpR6012g4 was observed to have the opposite trends. This reversal of the non-conserved trends between the WT and the mutant coupled with a weak correlation between  $^{15E}P_g$  and Meta-G photointermediate absorbance with shunting suggested that photointermediate shunts may be due to an increase in structural deformation of the chromophore along the D-ring isomerization coordinate that lowers the energy barrier between the intermediate and  $^{15E}P_g$ . The reversal of the non-conserved features between WT and  $\beta$ 2FV NpR6012g4 also indicates that the Meta-G<sub>f</sub> red shifted of  $^{15Z}P_r$  may be due to planarization of the chromophore beyond that of the dark-adapted state.

## ***Materials and Methods***

### *Sample Preparation*

The samples were prepared as previously described.<sup>68, 197</sup> Static absorption spectra were acquired at 25 °C on a Cary 50 modified to allow top-down illumination of the sample to initiate photochemistry,<sup>68</sup> using bandpass filters at 400±35 nm and 600±20 nm.

### *Transient Signals*

The instrumental setup for measuring the reverse secondary dynamics is identical to the forward secondary dynamics.<sup>27</sup> The only difference between the reverse dynamics presented here and the previously published forward secondary dynamics is that instead of a green LED to initially push population into the <sup>15</sup>ZP<sub>r</sub> dark-adapted state prior to the pump and probe pulses, a red LED was used to initially push population into the <sup>15</sup>E<sub>g</sub> light-adapted state.

### *Global Analysis*

All datasets were analyzed with global analysis methods that fit the data to multi-component models to ultimately separate the transient spectra into a linear combination of time-independent spectra that are weighted by a time-dependent convolution profile as determined by the equation below<sup>221, 243</sup>

$$\frac{dc_i}{dt} = A_i I(t) + \sum_{i,j} K_{ij} c_i(t)$$

where  $A_i$  is the initial concentration of the  $i^{\text{th}}$  population,  $I(t)$  is a gaussian function to fit the instrument response,  $K_{ij}$  is a connectivity matrix that describes how the  $i^{\text{th}}$  population is connected to every  $j^{\text{th}}$  population, and  $c_i(t)$  is the concentration of the  $i^{\text{th}}$  population at time  $t$ . More details of

the application of this analysis to other CBCRs are presented elsewhere.<sup>180, 183, 195</sup>

Initially, an unbiased sequential model ( $A \rightarrow B \rightarrow C \dots$ ; Figure A7.4) where population flows from one population to another linearly with consistently increasing time constants was used to fit each data set. If the postulated model correctly represents the underlying photodynamics of the sample, then the extracted time-independent spectra are Species-Associated-Difference-Spectra (SADS) and represent the true difference spectra of the constituent populations and their associated lifetimes are attained. If the model is incorrect, then the extracted spectra are Evolution-Associated-Difference-Spectra (EADS) and are superpositions of SADS and apparent lifetimes are obtained. While the sequential EADS do not normally represent the true spectra of the constituent species, this approach is useful in estimating the number of distinct kinetic species and their apparent lifetimes.<sup>180, 195</sup> This extracted information can then be used to construct more sophisticated target models to extract SADS. With the exception of NpF2164g6, the secondary reverse photodynamics presented here were not analyzed past the sequential EADS approach because there were no clear features of branching mechanisms or inhomogeneous dynamics. All models presented here demonstrate excellent fit to the data (Figures 7.5, 7.6, and A7.3; solid curves), indicating that the models are viable.

### ***Results***

Out of the eight WT domains characterized here, the dynamics of NpF2164g4, NpF2164g6, and NpR4776g3 were chosen to be representative and are discussed in detail. The previously reported secondary reverse dynamics of WT NpR6012g4<sup>29, 73</sup> are compared to that of  $\beta$ 2FV NpR6012g4 in the mutant section and the remaining WT dynamics are in the SI.

*Wild-Type Red/Green CBCR Secondary Reverse Dynamics.*

Transient difference spectra of NpF2164g4, NpF2164g6, and NpR4776g3 are compared in Figure 7.4 and the remaining WT can be found in Figure A7.2. All these domains exhibited ground state bleach (GSB) between ~525-550 nm and initial photointermediate bands between ~550-650 nm. As time progressed, there was an initial decrease in the overall signal and blue shifting of the spectra (Figure 7.4; ~10 ns to 1  $\mu$ s) that preceded a consistent red shifting (Figure 7.4; ~100  $\mu$ s to 1 ms). The decrease in signal during the blue shifting was due to increased spectral overlap between the intermediates and bleach as well as photointermediate shunt back to  $^{15E}P_g$  for a few domains.<sup>29, 73</sup> The spectral width of the photointermediate bands also displayed tendencies to become broader with increasing probe times. Interestingly, NpF2164g6 and NpR4776g3 exhibited a minor loss of far-red positive absorption between 100 and 1000  $\mu$ s, suggesting the presence of a transient population red shifted of the  $^{15Z}P_r$  photoproduct (Figures 7.4B, C & H; magenta to dark yellow curves). Similar far-red dynamics was previously resolved for AnpJg2 by Kirpich et al..<sup>29</sup>

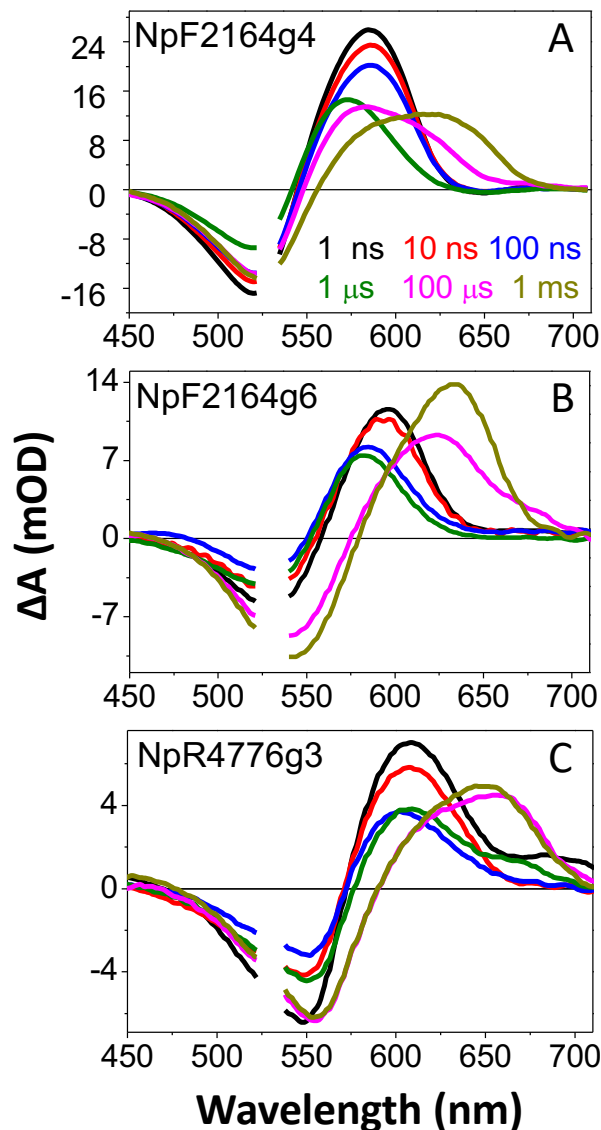


**Figure 7.4:** Representative Red/Green CBCR Secondary Reverse Transient Difference Spectra  
 Selected transient difference spectra of (A) NpF2164g4, (B) NpF2164g6, and (C) NpR4776g3 at select probe times as outlined in the legend of panel A.

This non-monotonic spectral evolution that consisted of a blue shifting phase preceding a red shifting phase is more readily observed in the select kinetic traces (Figures 7.5, 7.6, and A7.3). The kinetic trace at 510 nm (Figure 7.5A) tracks the GSB evolution where initially the GSB was being filled up to  $\sim 0.1 \mu\text{s}$  and was then revealed to be larger around  $100 \mu\text{s}$ . This filling of the bleach

up to  $\sim 1 \mu\text{s}$  was concurrent with the decay at 600 nm (Figure 7.5D) as well as the growth at 550 nm (Figure 7.5B) and was ascribed to the evolution of the first resolved photointermediate to a secondary blue shifted intermediate that more strongly overlaps the GSB. The absorbance at 600 nm for NpF2164g6 started decaying prior to NpF2164g4 (Figure 7.5D;  $\sim 0.01 \mu\text{s}$  vs  $\sim 0.5 \mu\text{s}$ ) despite the primary reverse dynamics revealing that NpF2164g6 has a longer initial photointermediate (Lumi-G<sub>0</sub>) lifetime than NpF2164g4.<sup>28</sup> This was attributed to the 600 nm kinetics for NpF2164g4 tracking the evolution of a secondary intermediate (Meta-G<sub>y</sub>) and not Lumi-G<sub>0</sub> (Figure A7.8).

This blue shifting phase was followed by a red shifting phase as seen in the kinetics between 600 and 685 nm (Figure 7.5D-F) where a revealing of the bleach was synchronized with a growth in the red spectral region was observed beyond  $\sim 1 \mu\text{s}$ . While nearly every domain exhibited either continuous growth or a plateau in the red to far-red region, the kinetics of NpF2164g6 exhibited a clear decay in the 685 nm kinetic trace at  $\sim 110 \mu\text{s}$  (Figure 7.5). A comparable decay in the far-red region was also weakly observed in NpR4776g3 (Figure 7.5F inset) and was consistent with the blue shifting of the difference spectra after 100  $\mu\text{s}$  (Figures 7.4B & C). These dynamics indicates the presence of a transient population with absorbance red shifted of  $^{15Z}\text{P}_r$  and were also weakly observed in AnPixJg2.<sup>28</sup>

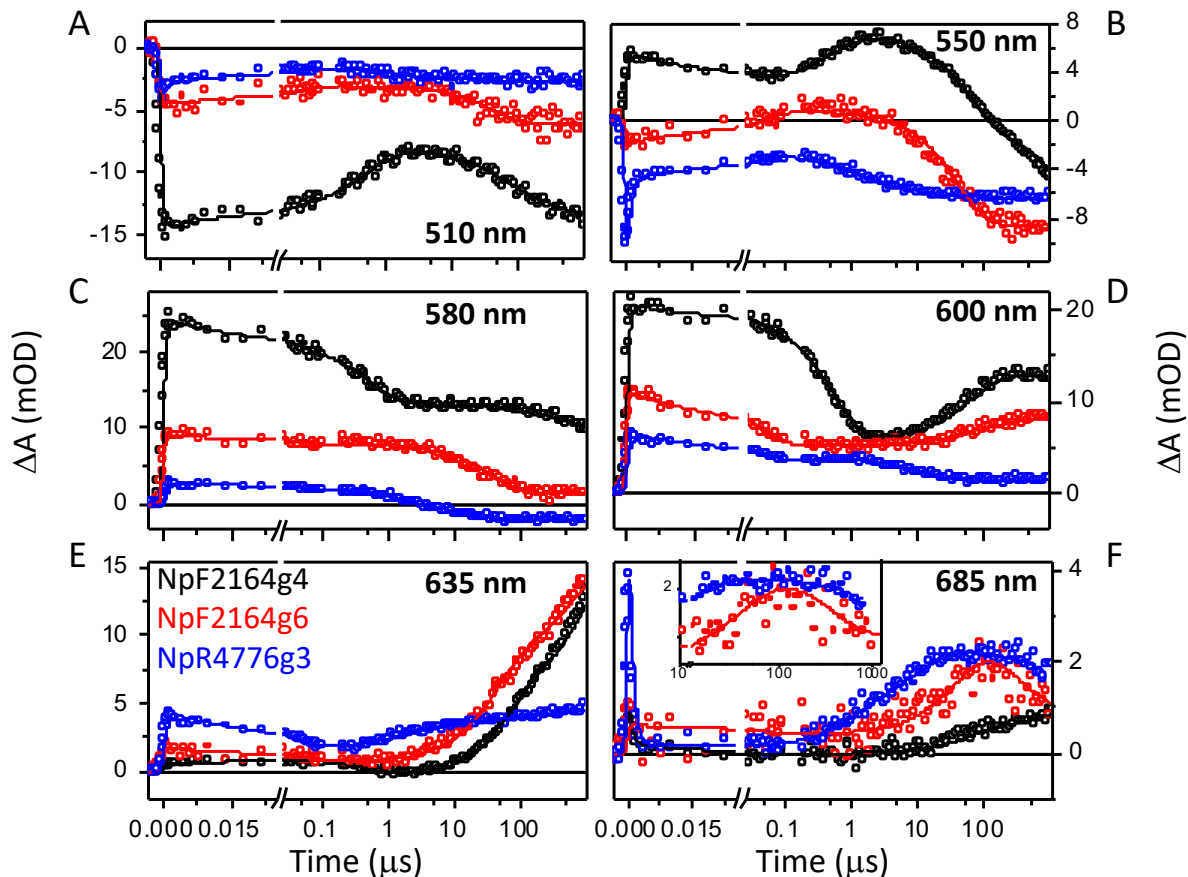


**Figure 7.5:** Representative Red/Green CBCR Secondary Reverse Kinetic Traces

Selected kinetic traces (open circles: data; solid curves: fit) of NpF2164g4 (black curves), NpF2164g6 (red curves), and NpR4776g3 (blue curves). Fits to the data were obtained via either sequential (NpF2164g4 and NpR4776g3) or branched target (NpF2164g6; Figure 7.8) models. The > 1-ms kinetics are not shown due to the excited sample migration outside of the probe region and NpR4776g3 was limited to ~800  $\mu\text{s}$  to better fit the decay at 685 nm (F, blue curve).

*WT vs  $\beta 2FV$  NpR6012g4 Secondary Reverse Dynamics.*

The secondary reverse dynamics of NpR6012g4 have been reported to consist of non-monotonic spectral evolution where the Lumi- $G_o$  (575 nm, Figure 7.6E) blue shifts through Meta- $G_o$  and Meta- $G_y$  (1-100  $\mu\text{s}$ ; Figure 7.6A) before red shifting to Meta- $G_r$  (>100  $\mu\text{s}$ ; Figure 7.6G) and

eventually  $^{15Z}P_r$ .<sup>29, 73</sup> All of the photointermediate populations except for Meta- $G_r$  were reported to be meta-stable and have shunts back to the  $^{15E}P_g$  state.

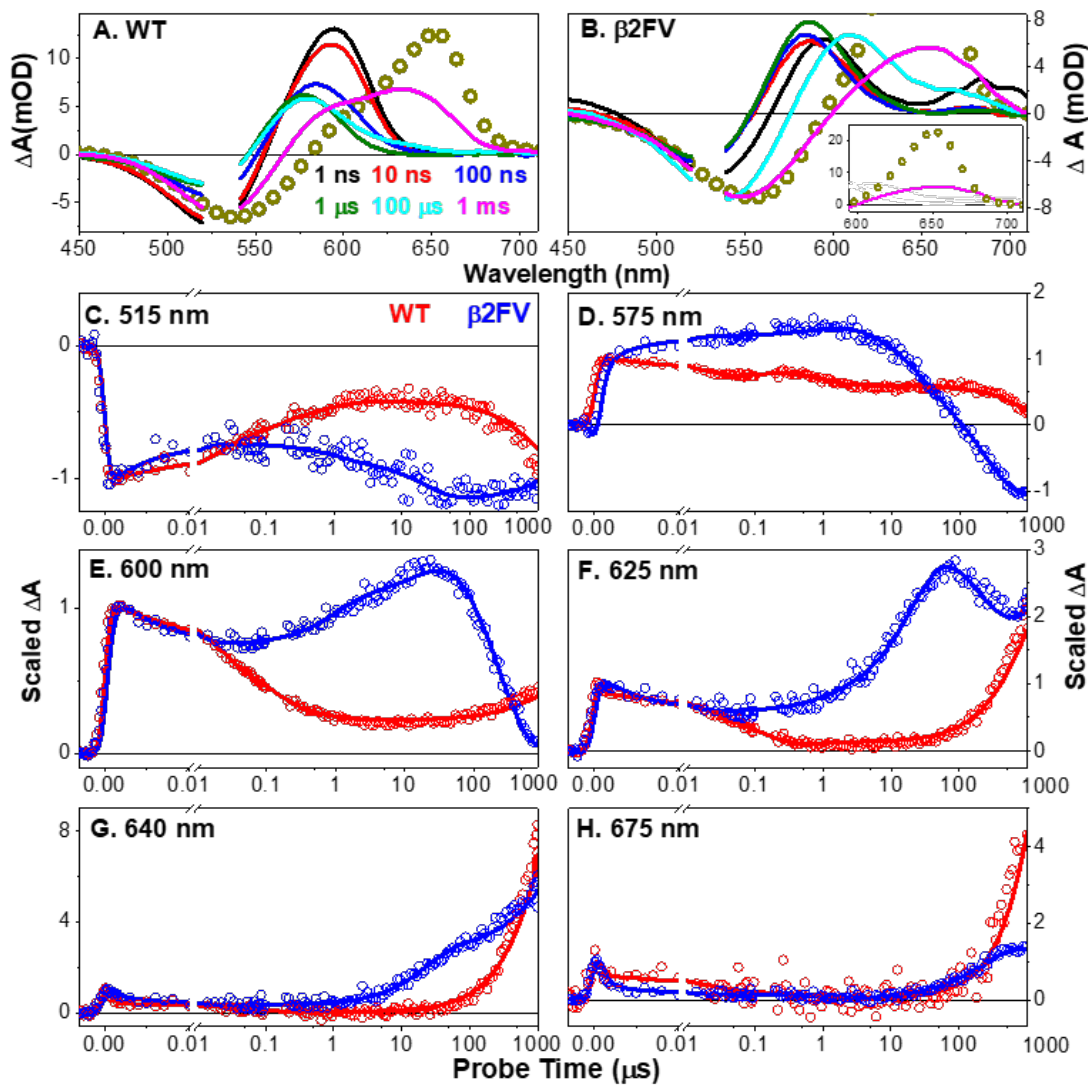


**Figure 7.6:** WT and  $\beta 2FV$  NpR6012g4 Secondary Reverse Dynamics

(A-B) Transient absorption spectra at selected probe times and (C-H) kinetic traces at select wavelengths for the secondary reverse reaction of WT (red) and  $\beta 2FV$  (blue) NpR6012g4. The ground-state  $^{15Z}P_r - ^{15E}P_g$  difference absorption spectra (unfilled golden circles) are added to panels A and B to serve as a visual aid. For direct comparison of the WT and mutant kinetics, the fit (solid curves) and data (unfilled circles) for each kinetic trace was normalized at the signal minimum (or maximum) shortly after time zero.



The reverse dynamics of  $\beta$ 2FV NpR6012g4 exhibited comparable non-monotonic spectral evolution to the WT but had two distinctly different spectral features. Unlike the WT,  $\beta$ 2FV NpR6012g4 did not have comparable signal decay during the blue-shifting phase, suggesting that the mutation did not have photointermediate shunts (Figures 7.6A & B). Secondly, the transient difference spectra of  $\beta$ 2FV NpR6012g4 exhibited positive absorbance red shifted of  $^{15Z}P_r$  (Figure 7.6B). This is consistent with the non-monophasic kinetics observed at 625 nm (Figure 7.6F) where a decay was observed starting around 80  $\mu$ s (Figures 7.6E & F) preceded a secondary growth starting at  $\sim$ 700  $\mu$ s. These dynamics suggest that there is a Meta intermediate red shifted of  $^{15Z}P_r$  present in  $\beta$ 2FV NpR6012g4 and not the WT. While a red shifted Meta was not observed in WT NpR6012g4, similar red shifted intermediates were observed in other canonical red/green CBCR domains reported here (Figures 7.4-7.6 and A7.10) as well as previously reported in AnPixJg2.<sup>29</sup> It should also be noted that  $\beta$ 2FV NpR6012g4 exhibited features of a long living excited state population in the 675 nm kinetic trace up to  $\sim$ 2.5 ns (Figure 7.6H; blue curve) and in the 1 ns spectra (Figure 7.6B).

### ***Global Analysis***

#### *Wild-Type Canonical Red/Green CBCRs.*

Consistent with the transient difference spectra and kinetics, the evolution of the photointermediates extracted from the sequential analysis exhibited nonmonotonic spectral evolution consisting of a blue shifting phase that preceded a red shifting phase and eventual population of the  $^{15Z}P_r$  photoproduct (Figures 7.7 and A7.5). A comparison of the secondary reverse dynamics EADS and primary reverse dynamics SADS indicated that for half of the domains (NpAF142g2, NpF2164g6, NpF2854g3, and NpR4776g3) the first EADS extracted in

the secondary dynamics was Lumi-G<sub>o</sub>, but for the other half (NpF2164g4, NpR1597g4, NpR5113g2, and NpR6012g4) the first photointermediate resolved was the first Meta-G photointermediate (Figure A7.8). This is not surprising given the previously reported Lumi-G<sub>o</sub> lifetimes.<sup>28</sup> On top of this mechanistic backbone of non-monotonic spectral evolution, non-conserved features such as the previously reported ground state photointermediate shunts and Meta-G photointermediate red shifted of <sup>15Z</sup>P<sub>r</sub> were also observed (Figures 7.7C & E, A7.5-A7.8, and A7.10).<sup>28, 29, 73</sup>

#### *Photointermediate Shunts.*

Similar to a previous study on NpR6012g4,<sup>29</sup> some of the reverse dynamics of the CBCRs studied here (NpAF142g2, NpF2164g4, NpF2854g3, NpR4776g2, NpR4776g3, and NpR5113g2) exhibited a clear decrease in the amplitude of the orange to red positive absorbance and a concurrent filling of the bleach (Figures 7.7, A7.5, and A7.7). The photointermediate bands of NpF2854g3 and NpR5113g2 exhibited only a decay with no discernable spectral shifting between EADS2 and EADS3, whereas NpR4776g3 and NpF2164g4 exhibited a blue and red shift of the positive band respectively (Figures 7.7, A7.5, and A7.6). This loss of amplitude can be explained by two mechanisms: photointermediate shunts back to <sup>15E</sup>P<sub>g</sub> or evolution to a Meta-G<sub>g</sub> intermediate that strongly overlaps the bleach. Previously for NpR6012g4, these spectral features were associated with photointermediate shunts due to the statical unlikelihood of an intermediate having the same absorbance band as the light-adapted state.<sup>29, 73</sup> The presence of shunts would also be consistent with, the primary reverse study,<sup>28</sup> where four of the domains (NpAF142g2, NpF2854g3, NpR4776g3, NpR5113g2) required a Lumi-G<sub>o</sub> shunt to adequately fit the GSB recovery kinetics.

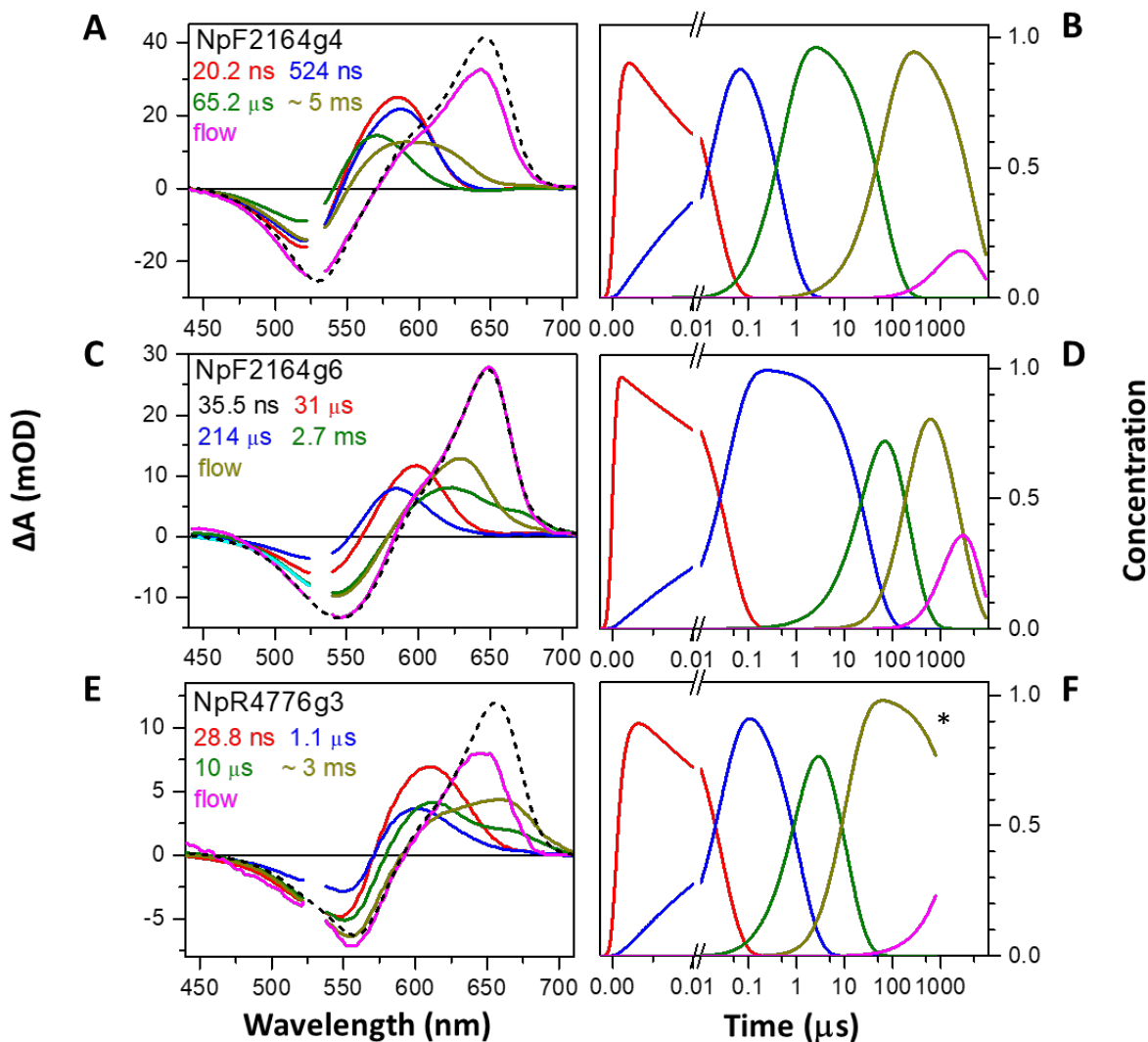


**Figure 7.7:** Representative Red/Green CBCR Secondary Reverse EADS and concentration profiles (right column) for (A) NpF2164g4, (B) NpF2164g6, and (C) NpR4776g43. Both (C) NpF2164g6 and (E) NpR4776g3 resolved a photointermediate red shifted of the  $^{152}\text{P}_r$  photoproduct. \*NpR4776g3 was cut to  $\sim 850 \mu\text{s}$  to better fit the decay kinetics near 685 nm (Figure 7.5), but the sequential analysis for the full 10 ms can be found in the SI (Figure A7.5).

Interestingly, when NpF2164g4 exhibited a decay in the signal between EADS2 and EADS3 (Figure 7.7A), there was a red shift in absorbance. With this red shift in absorbance, one would expect to observe a revealing of the bleach and a growth in the positive amplitude due to less spectral overlap of the intermediate and the bleach. This spectral trend can be interpreted as either

a photointermediate shunt or as the presence of two spectrally heterogeneous photointermediate populations that are populated on the same timescale and the slightly blue shifted population is shorter lived and evolves into a population that strongly overlaps the bleach. Given the simplicity and difference in the terminal spectral intensity compared to the initial intermediate in relation to the other domains (Figures 7.4, 7.7, and A7.5), the photointermediate shunt explanation was preferred.

#### *Meta-G Red Shifted of $^{15Z}P_r$ .*

Photointermediates red shifted of the  $^{15Z}P_r$  photoproduct have been reported in previous studies on the reverse dynamics of NpR5113g2,<sup>28</sup> weakly for AnPixJg2,<sup>29, 177</sup> and the noncanonical orange/green CBCR, NpF2164g7.<sup>187</sup> Here, five domains (NpF2164g6, NpR4776g3, NpR5113g2,  $\beta$ 2FV NpR6012g4, and maybe NpAF142g2) exhibited spectral features of photointermediates with absorbance red shifted of  $^{15Z}P_r$  (Figure 7.7C, green curve; Figure 7.7E, dark yellow curve; Figure A7.5H, dark yellow; Figure 7.7B, magenta; Figure A7.5A; dark yellow and magenta curves; Figure A7.10). For all of the red/green CBCRs other than NpF2164g6, a sequential approach was sufficient since the last resolved photointermediate was the Meta-G population red shifted of  $^{15Z}P_r$  (Figures A7.5-A7.8). The 635 and 685 nm kinetic traces of NpF2164g6 (Figure 7.5) resolved that the far-red absorbing photointermediate was populated after and evolved before Meta-G<sub>r</sub> and indicates that there is a bifurcation of the dynamics. This bifurcation was used in the target global analysis of NpF2164g6 which extracted red and far-red absorbing photointermediates and their respective time constants (Figure 7.8).

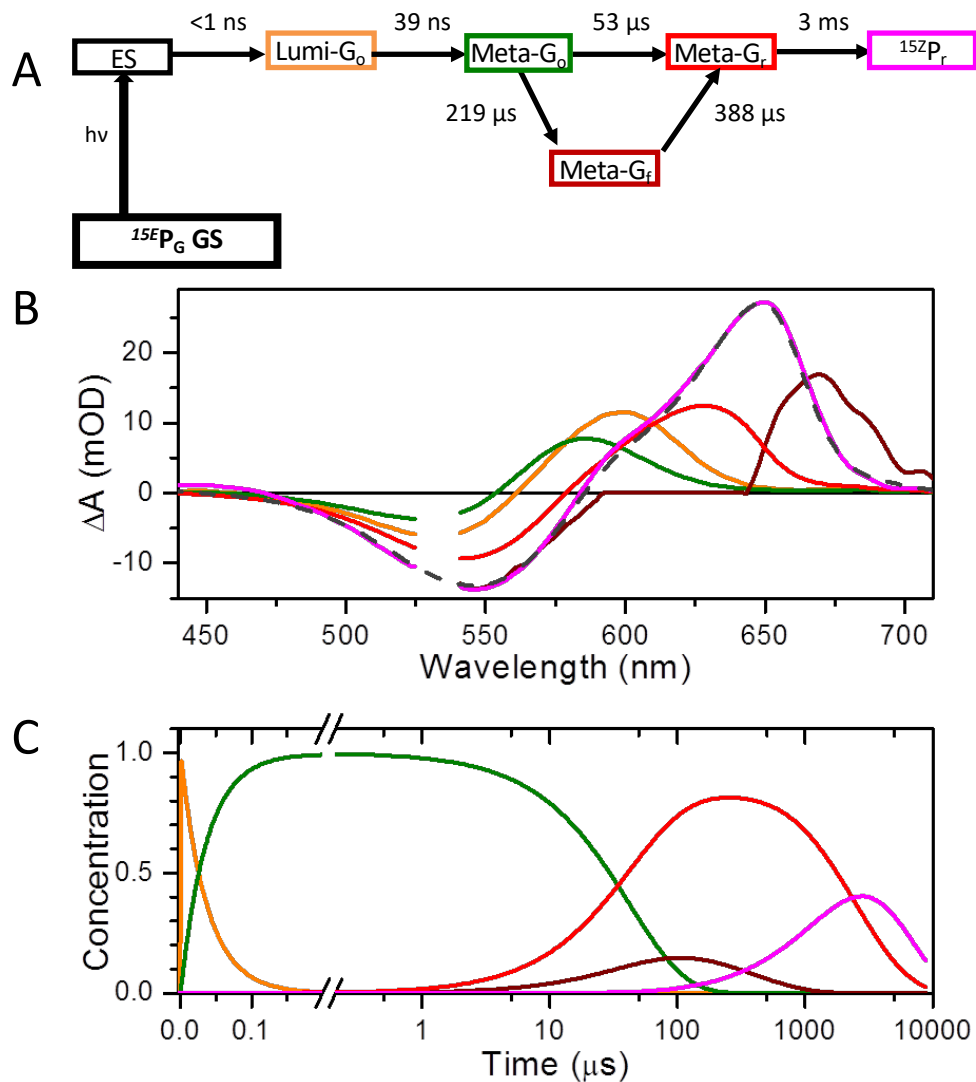


**Figure 7.8:** Target Analysis of the Reverse Dynamics of NpF21564g6

(A) Proposed branching model of NpF2164g6 with the resulting (B) SADS and (C) concentration profiles that depicts the population of Meta-G<sub>f</sub> after and evolution before Meta-G<sub>r</sub>.

*Inhomogeneity of Primary Reverse Class III<sub>R</sub> Domains.*

The global analysis of the primary reverse dynamics of NpR4776g3 and NpR5113g2 extracted populations that are spectrally comparable to  $^{15Z}P_r$  and Meta-G<sub>r</sub> on an ultrafast timescale (Figures A7.8 and A7.9).<sup>28</sup> These red absorbing populations in the primary dynamics of these domains were

not resolved on the same timescale in the secondary dynamics. This was associated with kinetic inhomogeneity that was resolved due to different ground state subpopulations being excited by the different excitation pulses (Table A7.2). The presence of ground state inhomogeneity of the  $^{15}E_g$  light-adapted state is also supported by temperature dependent ground state absorbance spectra.<sup>181</sup>

#### *WT vs $\beta$ 2FV NpR6012g4.*

The forward dynamics of  $\beta$ 2FV NpR6012g4 were comparable to that of the previously published WT NpR6012g4 as discussed in the SI. The main discrepancies in the forward dynamics were that the photoproduct of  $\beta$ 2FV NpR6012g4 absorbed in the yellow spectral region rather than the green spectral region and the respective timescales (Figures A7.17, 719-7.21, and Table A7.10). This suggests that the mutation altered the photoproduct absorption and the timescale of the evolution but did not change the underlying mechanism of the forward reaction. It is unclear how the  $\beta$ 2FV mutation affected the primary forward or reverse dynamics of NpR6012g4 and is a matter that can be investigated further elsewhere.

Unlike the forward reaction, there were differences in the dynamics of secondary reverse reaction of WT and  $\beta$ 2FV NpR6012g4. The sequential analysis of the secondary reverse dynamics of WT and  $\beta$ 2FV NpR6012g4 are compared in Figure 7.9, where both WT and  $\beta$ 2FV require a seven-compartment sequential model to fully fit the measured signals. Compared to WT,  $\beta$ 2FV NpR6012g4 incorporated more photointermediates in the red-shifting phase of the dynamics, fewer photointermediates in the blue shifting phase and a less of a drastic decrease in the overall amplitude in the blue shifting phase (Figures 7.9A & B). The lack of a decrease in amplitude during

the blue shifting phase suggest that unlike the WT,  $\beta$ 2FV NpR6012g4 does not have resolved photointermediate shunts. This is consistent with the faster intermediate evolution observed in the mutant that suggest that there is smaller energy barrier between the photointermediates. Interestingly, EADS6 of  $\beta$ 2FV NpR6012g4 was red shifted of the  $^{15}\text{Z}_\text{P}$  photoproduct. While this feature was not observed in WT NpR6012g4 (Figures 7.4-7.7), it was observed in several canonical red/green CBCRs (Figures 7.7, A7.5-A7.7, and A7.10).<sup>29</sup>

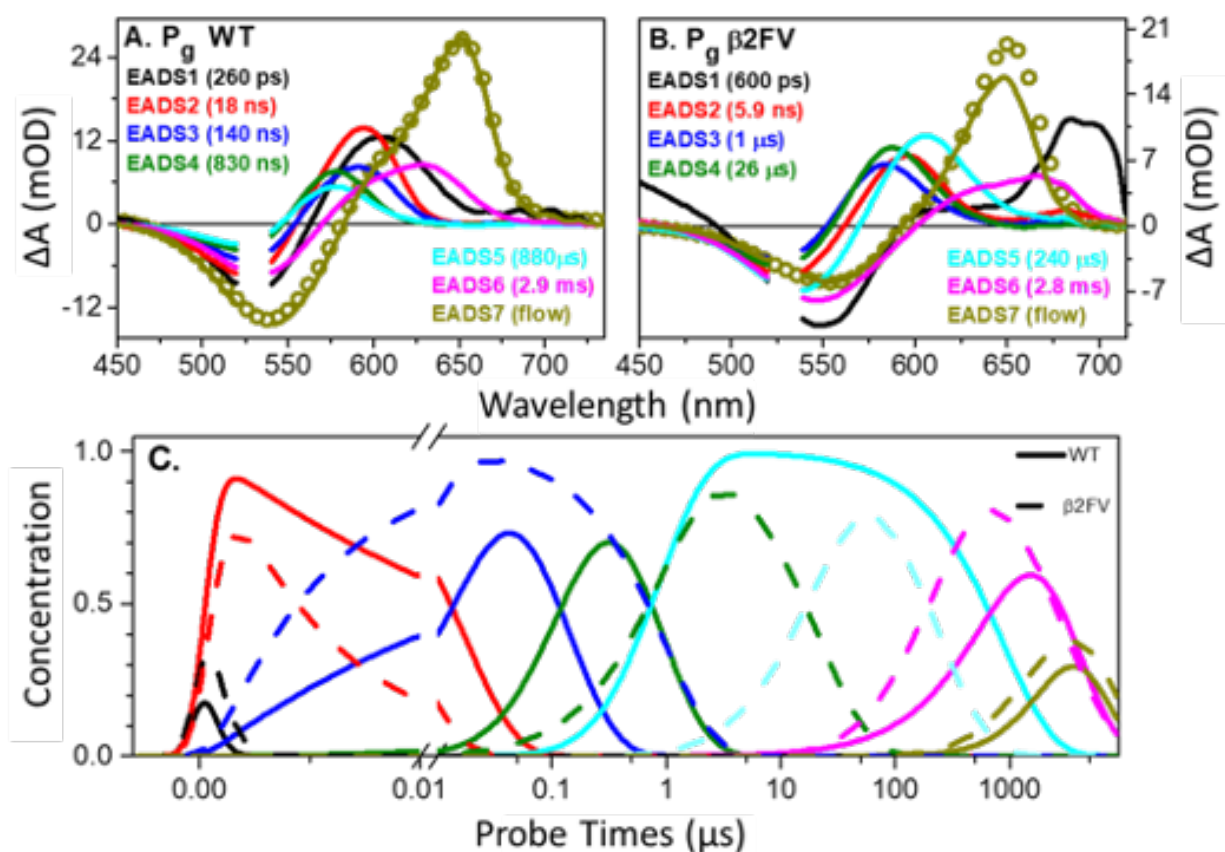


**Figure 7.9:** WT and  $\beta$ 2FV NpR6012g4 Secondary reverse EADS

EADS of (A) WT and (B)  $\beta$ 2FV NpR6012g4. (C) Comparison of the concentration profiles of WT (solid curves) and  $\beta$ 2FV (dashed curves) NpR6012g4 which shows that the reverse reaction evolves faster in  $\beta$ 2FV NpR6012g4. EADS1 for  $\beta$ 2FV was attributed to a long-lived excited state population.

## ***Discussion***

Despite the spectral and temporal differences in the classes resolved in the primary reverse dynamics,<sup>28</sup> the reverse secondary dynamics of the eight WT red/green CBCR domains from *Nostoc punctiforme* coupled with the previously reported primary reverse dynamics<sup>28, 183, 185</sup> and secondary reverse dynamics of NpR6012g4,<sup>29</sup> AnPixJg2<sup>29, 177</sup> and Slr1393g3,<sup>186</sup> revealed a conserved mechanistic backbone where nonmonotonic spectral evolution consisting of a blue shifting phase that preceded a red shifting phase (Figure 7.10). This non-monotonic spectral evolution following the initial Lumi intermediate was in stark contrast to the monotonic spectral evolution that was observed in the forward reaction (Figure 7.10), indicating that the two reaction directions proceed through unique pathways and that the reverse direction is not simply the reverse of the forward reaction. Given this and the similarities of the red shifted Meta-G<sub>r</sub> of the reverse reaction of select CBCRs and the Lumi-R<sub>f</sub> of the forward reaction,<sup>176</sup> suggest that both reaction directions, involves either a counter-clockwise or clockwise rotation looking down the D-ring. A counter-clockwise rotation would be consistent with the D-ring isomerization traveling the path of least resistance with the methyl and amine groups of the D-ring moving away from the methyl group of the C-ring for the forward and reverse reactions respectively (Figures A7.14 and A7.15). While non-monotonic spectral evolution following the initial photointermediate was not observed in the forward direction of canonical red/green CBCRs,<sup>27, 176</sup> it was observed in the reverse dynamics Violet/Orange insert-cysteine CBCR, NpF2164g3,<sup>111</sup> and the orange/green CBCR, NpF2164g7,<sup>187</sup> suggesting a shared reaction paradigm that extends beyond the red/green CBCRs and that non-monotonic evolution may be a consistent trend of the reverse dynamics of CBCRs.



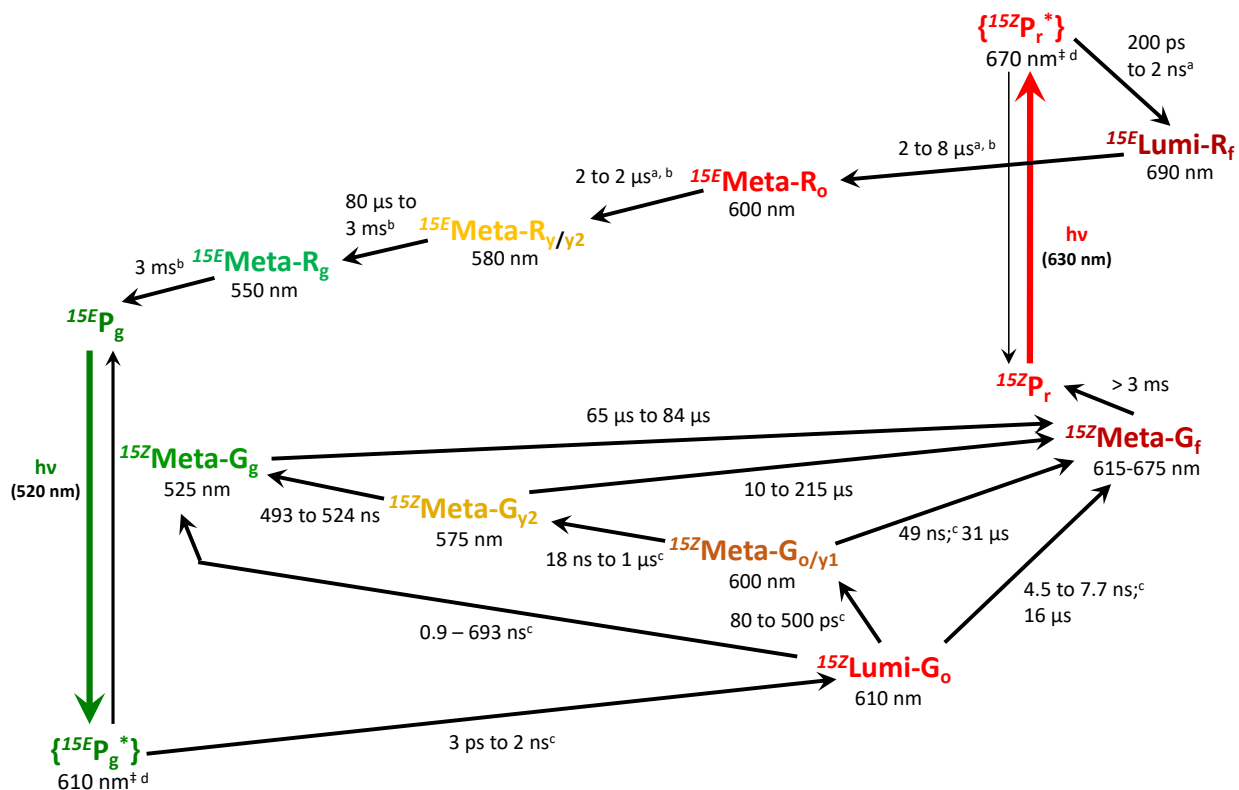


**Figure 7.10: Red/Green CBCR Composite Photocycle**

Composite photocycle of the red/green CBCRs. Excited states are in brackets to signify the multiple heterogeneous excited state population resolved in the primary dynamics.<sup>28, 176</sup> The double dagger near the excited state populations indicates the fluorescence emission maxima representing relaxed excited-state populations for AnPixJg2.<sup>177</sup> Note that some features such as shunts and equilibria were left out for simplicity. Figure citations: a,<sup>176, 182</sup> b,<sup>27, 183</sup> c,<sup>28</sup> d.<sup>177</sup>

The primary dynamics identified five domains (NpF2164g6, NpAF142g2, NpR1597g4, NpR4776g3, and NpR5113g2) that exhibited slower evolution of the excited state and Lumi-G intermediate that did not extend to the Meta-G intermediates.<sup>28</sup> Four of these domains (NpAF142g2, NpR1597g4, NpR4776g3, and NpR5113g2) had a selectively conserved Tyr residues near C10 of the bilin and was suggested to manipulate the hydrogen bonding network to inhibit the photoinduced D-ring isomerization event. Comparing the lifetimes from the sequential

(Figure A7.6 and Table A7.1) analysis suggests that the Tyr influence is only on the initial dynamics and impacts the efficiencies of these photoreceptors and that the strength of the H-bonding responsible for the intermediate tertiary structure is responsible for the secondary dynamic timescales. This would be consistent with the restructuring of the GAF domain playing a larger role in these longer dynamics than the chromophore and adjacent amino acid residues. Interestingly, the slowest evolving CBCR in the primary dynamics (NpF2164g6), which had a His residue in place of Tyr near the bilin C10, was also the slowest evolving CBCR on the secondary timescale, suggesting that the tertiary protein structure of NpF2164g6 may have increased protein-protein interaction compared to the other CBCRs.

Upon the mechanistic backbone of non-monotonic spectral evolution, there were two non-conserved features: photointermediate shunts back to the  $^{15E}P_g$  parental state and Meta-G photointermediates red shifted of  $^{15Z}P_r$  (Figures A7.5-A7.7 and A7.10). As discussed in the next two sections, while comparison of these non-conserved features with spectral absorbance, lifetimes, and amino acid sequence alignments resolved only a weak correlation between blue shifted  $^{15E}P_g$  and intermediate spectra and the presence of shunts (Tables A7.5 and A7.6), the comparison of WT and  $\beta$ 2FV NpR6012g4 suggest that these features are reliant on the size of the chromophore pocket, particularly near the D-ring.

#### *Photointermediate Shunts.*

Photointermediate shunts back to the starting parental state has been previously reported for a few bilin based photoreceptors, such as the bacteriophytochromes Apg1<sup>293</sup> and Apg2<sup>293, 294</sup> from *Agrobacterium fabrum*, SaBphP1 from *Stigmatella aurantiaca*,<sup>163</sup> and the canonical red/green

CBCR NpR6012g4<sup>29, 73</sup> where anywhere between 30 to 60% of the intermediate population decays back to the starting state. In addition to NpR6012g4, the primary reverse dynamics of several canonical red/green CBCRs resolved that all the domains that incorporated a Tyr near the bilin C10 required incorporated Lumi-G<sub>o</sub> shunts in the modeling in order to fit the GSB recovery kinetics.<sup>28</sup> The incorporation of shunts in the reverse dynamics of several domains suggest that non-unity quantum yields are more commonplace than originally thought and that characterization of the photodynamics of these photoreceptors needs to be measured in both the primary and secondary timescales to get a more accurate estimation of the photoproduct quantum yield. Further multi-domain studies in the forward and reverse reaction of other CBCR families may be beneficial to observe if shunting is a trend of the CBCR family.

The presence of photointermediate shunts indicates that there is a relatively small energy barrier between the starting <sup>15E</sup>P<sub>g</sub> state and the photointermediate populations which may be correlated to structural deformation of the chromophore along the D-ring isomerization coordinate (Figure 7.11). This correlation would be consistent with the reduced blue shifting phase and removal of features associated with shunts in the β2FV mutant of NpR6012g4 that replaced a Phe associated with structurally deforming the chromophore<sup>197</sup> with Val (Figures 7.6, 7.9, and A7.18) as well as photointermediate shunts only being resolved in the blue shifting phase of the reverse dynamics (Figures 7.7, A7.5 and A7.6). A weak correlation between the presence of shunting and relatively blue shifted <sup>15E</sup>P<sub>g</sub> light-adapted state and intermediate absorbances (Tables A7.5 and A7.6) was also observed which suggest that more distorted chromophores have smaller energy barriers between the intermediates and <sup>15E</sup>P<sub>g</sub> and have shunting. If this trend of red/green CBCRs with relatively blue shifted <sup>15E</sup>P<sub>g</sub> spectra being correlated to shunts were to hold true, it would provide

a possible metric for identifying CBCRs with larger photoproduct quantum yields. While CBCRs with relatively red shifting light-adapted spectra may have larger photoproduct quantum yield due to then minimalization of the presence of shunts, there would however be a trade off with the initial Lumi-G<sub>0</sub> quantum since the primary dynamics resolved that red/green CBCRs with blue shifted light-adapted state spectra were more efficient.<sup>28</sup>

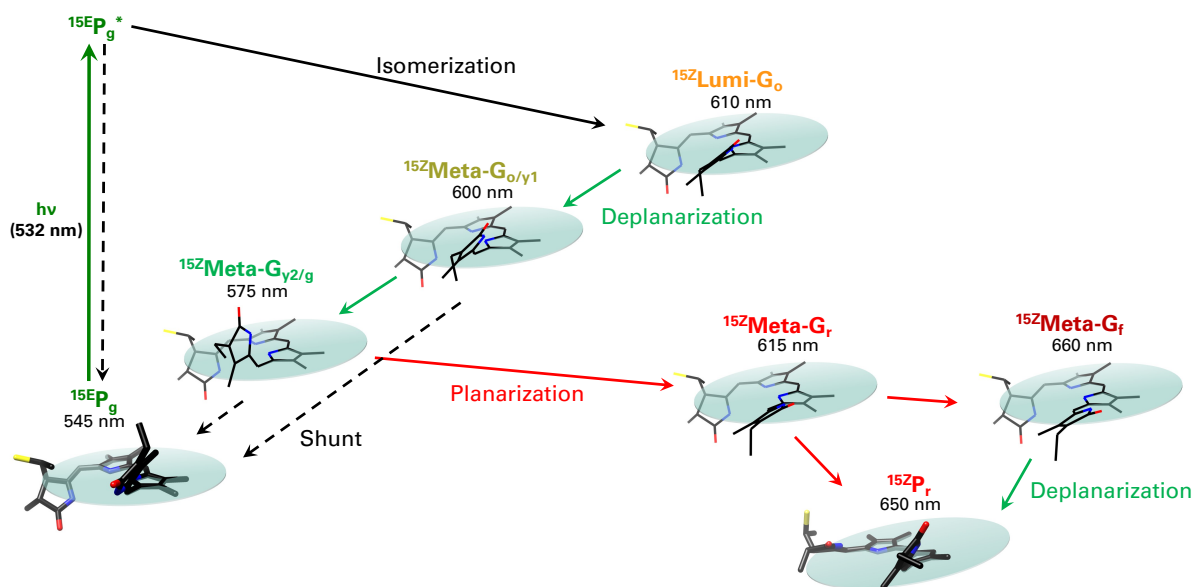


**Figure 7.11:** Proposed Molecular Level Explanations of Non-Conserved Features  
 Model of the proposed chromophore evolution in the reverse dynamics of canonical red/green CBCRs assuming structural deformation at the D-ring. Solid black, green, and red lines represent photoinduced isomerization, structural deformation, and planarization, respectively. The dashed black lines represent shunting. The light-adapted (6BHO) and dark-adapted (6BHN) state chromophores were generated using the resolved crystal structures of NpR6012g4.<sup>108</sup> The intermediates structures were generated in Chimera by initially isomerizing the  $^{15}E_g$  structure along the C15=C16 bond and then adjusting the C14, C15 dihedral angle for each intermediate based on the magnitude of the spectral shift. Deformation and planarization in other planes are possible, but this coordinate was chosen given the presence of shunts. The A-ring of the chromophore was ignored for the intermediate populations since it is expected to influence the spectra less compared to the D-ring due to reduced conjugation.

A model displaying the believed changes along the isomerization coordinate of the chromophore is proposed in Figure 7.11 where the blue shifting dynamics were correlated to increased structural deformation along the isomerization coordinate and resulted in the lowering of the energy barrier between the intermediate and the  $^{15E}P_g$  light-adapted state. It should be noted however, that the distortions can be in different planes of the D-ring as well as other locations of the chromophore, but the D-ring isomerization coordinate was preferred given the presence of photointermediate shunts. To support this hypothesis or develop a different one for the mechanism behind shunting in the reverse reaction of red/green CBCRs, high resolution structures of the intermediates would be required.

#### *Meta-G Red Shifted of $^{15Z}P_r$ .*

In addition to the nonmonotonic spectral evolution and shunting, a few domains (AnPixJg2,<sup>29</sup> NpF2164g6, NpR4776g3, NpR5113g2,<sup>28</sup>  $\beta$ 2FV NpR6012g4, and maybe NpAF142g2) exhibited evidence of a Meta-G photointermediate red shifted of  $^{15Z}P_r$  that was reminiscent of Lumi-R<sub>f</sub> from the forward reaction (Figure A7.10) and was interpreted as a bifurcation of the dynamics, as readily observed in NpF2164g6 (Figure 7.8). Since a transient population red shifted of the photoproduct was observed in  $\beta$ 2FV NpR6012g4 and not the WT (Figure 7.9), suggest that this intermediate could result from a larger chromophore pocket near the D-ring (Figure A7.18) that would allow for additional planarization. While an increase in planarization along the D-ring isomerization coordinate is given in Figure 7.11, an increase in planarization between the A and B rings is also possible. Usurpingly, nearly all of the Class III<sub>R</sub> domains that were suggested to have smaller amino acid residues near the D-ring of the chromophore in the primary dynamics,<sup>28</sup> also exhibited red shifted Meta-G<sub>r</sub> intermediates in the secondary dynamics resolved here. An intermediate that

is more planar than the dark-adapted state photoproduct is also consistent with the resolved  $^{15Z}P_r$  dark-adapted state structures of AnPixJg2,<sup>257</sup> NpR6012g4,<sup>108</sup> and Slr1393g3<sup>291</sup> which all have non-planar chromophore configurations (Table A7.7 and Figure A7.15).

Interestingly, there was not a correlation between  $^{15Z}P_r$  absorbance, and the presence of this red shifted Meta-G<sub>r</sub> photointermediate (Tables A7.5 and A7.6), since one may think that the relatively red shifted  $^{15Z}P_r$  dark-adapted states would likely have larger chromophore pockets that would allow the chromophore to planarize further (Table A7.7 and Figure A7.15). This lack of a correlation between the  $^{15Z}P_r$  dark-adapted state absorption and the presence of the red shifted Meta-G<sub>r</sub> is consistent with possible ground state absorption manipulation via structural deformation and H-bonding networks as previously reported for a cyanobacterial phytochrome and suggested to be present in red/green CBCRs.<sup>28, 100, 302</sup>

Some domains incorporated both the Meta-G red shifted of  $^{15Z}P_r$  and shunts, indicating that the chromophore pocket size near the D-ring throughout the evolution of the reaction plays a more significant role rather than specific amino acid residue(s). This is supported by the amino acid sequence alignment that did not isolate any selectively conserved amino acid residues when separating the domains by the presence of ground state intermediate shunts or red shifted Meta-G<sub>r</sub> intermediates (Figures A7.12 and A7.13). After initiating the reverse dynamics, the significant residues are likely near the D-ring of the chromophore in the starting conformation as previously reported,<sup>28</sup> but as the reaction progresses, restructuring of the protein could change the residues nearest to the D-ring as well as the distances of said residues.

### ***Concluding Comments***

This paper completes the initial survey of the primary and secondary photodynamics of red/green CBCRs isolated from *Nostoc punctiforme*. In contrast to the forward dynamics, the secondary reverse domains resolved a conserved mechanism of nonmonotonic spectral evolution that consisted of a blue shifting phase that preceded a red shifting phase. Comparable trends were also observed in the V/O photoswitch from NpF2164g3, suggesting a conserved mechanism in the reverse reaction of CBCRs that extends past the nine R/G photoswitches presented here.<sup>111</sup> Beyond the conserved nonmonotonic evolution backbone, previously reported photointermediate shunts and Meta-G photointermediates red shifted of the  $^{15Z}P_r$  photoproduct were observed in several of the domains reported here suggesting that they are somewhat prevalent. The photointermediate shunts may be due to an increase of the structural deformation of the chromophore along the D-ring isomerization coordinate and results in a decrease in the energy barrier between the photointermediate and  $^{15E}P_g$ . The Meta-G photointermediates red shifted of  $^{15Z}P_r$  were reminiscent of the Lumi-R<sub>f</sub> photointermediate of the forward reaction and were correlated to a larger chromophore pocket that allowed for further planarization of the chromophore.

### *Associated Content*

*Supporting Information (pg. 303)*

### *Accession Codes*

NpAF142g2 (B2JAQ4), NpR1597g4 (B2J0R5), NpF2164g4, NpF2164g6, NpF2164g7 (B2J668), NpF2854g3 (B2IVK2), NpR4776g2, NpR4776g3 (B2IZ18), NpR5113g2 (B2J261), NpR6012g4 (B2IU14), Slr1393 (P73184), and AnPixJg2 (Q8YXY7)

### *Funding*

This work was supported by a grant from the Chemical Sciences, Geosciences, and Biosciences Division, Office of Basic Energy Sciences, Office of Science, United States Department of Energy (DOE DE-FG02-09ER16117) to both J.C.L. and D.S.L.

### *Acknowledgments*

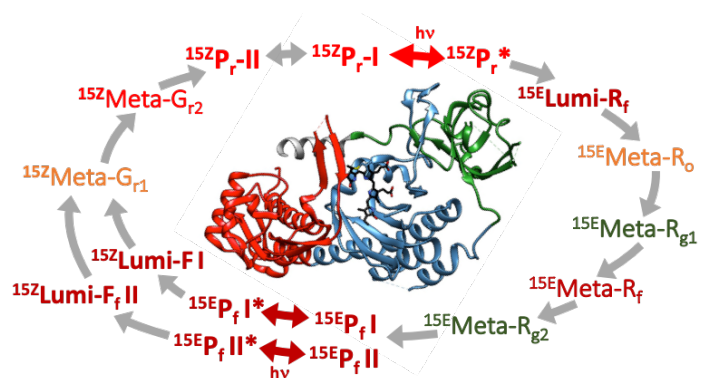
This work was supported by a grant from the Chemical Sciences, Geosciences, and Biosciences Division, Office of Basic Energy Sciences, Office of Science, United States Department of Energy (DOE DE-FG02-09ER16117) to both J.C.L. and D.S.L. Nathan C. Rockwell (University of California, Davis) is acknowledged for sample preparation and constructive discussions. Dr. Mikas Vengris (Light Conversion Ltd.) is also acknowledged for the donation of global and target analysis software. Molecular graphics images were produced using the UCSF Chimera package from the Resource for Biocomputing, Visualization, and Informatics at the University of California, San Francisco (supported by NIH P41 RR-01081).



# Chapter 8. Comparison of the Forward and Reverse Secondary Photodynamics of the Bacterial Phytochrome Cph1 and the Canonical Red/Green Cyanobacteriochrome NpR6012g4

## Abstract

The forward and reverse photodynamics of the photosensory core of the red/far-red cyanobacterial phytochrome Cph1 (Cph1 $\Delta$ ) from *Synechocystis* sp. PCC 6803 and the canonical red/green cyanobacteriochrome NpR6012g4 from



*Nostoc punctiforme* were compared using room temperature transient absorption and cryokinetic UV-Vis absorption spectroscopies coupled with global analysis methods. We resolved monotonic evolution from the initial Lumi-R<sub>f</sub> intermediate to a green-absorbing intermediate Meta-R<sub>g</sub> in the forward <sup>15Z</sup>P<sub>r</sub> to <sup>15E</sup>P<sub>fr</sub> photoconversion pathway for the photosensory module of Cph1 (Cph1 $\Delta$ ). The presence of this strongly blue-shifted Meta-R<sub>g</sub> species, which precedes the appearance of the previously reported Meta-R<sub>b</sub> species, suggests that the initial phase of the forward photoconversion pathway for Cph1 $\Delta$  differs from that of other phytochromes. Surprisingly, the forward photodynamics of the red/green cyanobacteriochrome NpR6012g4 are remarkably similar with this initial phase of Cph1 $\Delta$ 's forward photoconversion process, including the presence of a previously unresolved Meta-R<sub>o</sub> intermediate detected here by cryokinetic measurements. The reverse photoconversion pathway of Cph1 $\Delta$  also shares similar transient spectral intermediates with those of NpR6012g4. These studies suggest that, except for its inability to form a far-red-light-absorbing <sup>15E</sup>P<sub>fr</sub> photoproduct, the initial forward and reverse photoconversion pathways of the red/green cyanobacteriochromes are mechanistically similar to those of Cph1 $\Delta$ .

## ***Introduction***

It is well known that biological systems have diverse responses to external light conditions ranging from seed germination and shade avoidance in plants<sup>19-21</sup> to phototaxis in bacteria.<sup>22, 23</sup> To initiate these light activated functions, biological systems have evolved sophisticated photosensory proteins termed photoreceptors that reversibly photoconvert between a thermally stable dark-adapted state and a meta-stable light adapted state. While photoreceptors have been known for a long time, there is still much left unknown about the underlying mechanism of biological signal transduction. Furthermore, if we can develop a molecular level understand of these light activated events, we may be able to design novel biological tools based on photoreceptors to serve as florescent probes<sup>44-47</sup> for medicinal imaging applications or optogenetic tools to control biological activity in living tissue and study neural circuits at a more selective and fundamental level.<sup>44, 47, 51, 52, 55, 201, 295</sup>

One family of photoreceptors are the linear tetrapyrrole (bilin)-based phytochromes that have red/far-red (R/FR) photocycles and were first discovered in plants where they regulate various processes such as shade avoidance and seed germination.<sup>19-21</sup> Later, phytochromes were discovered to be widely distributed in bacteria, fungi and other photosynthetic eukaryotes.<sup>246, 279, 280</sup> Prototypical phytochromes possess a conserved 'photosensory' module consisting of PAS, GAF, and PHY domains (Figure 8.1), all of which participate in tailoring the bilin chromophore environment for reversible R/FR light sensing. By contrast with the prototypical phytochrome family, the bilin-binding GAF domains of cyanobacteriochromes (CBCRs) are sufficient for reversible two-color light sensing by this distantly related photoreceptor family that are found exclusively in cyanobacteria (Figure 8.1). Many critical chromophore-contacting protein residues

found in the GAF domains of phytochromes are also present in CBCR GAF domains, which similarly constrain their bilin chromophores (Figure A8.1).<sup>45, 72</sup> While phytochromes are typically red/far-red photoswitches, CBCRs exhibit a broader range of light sensing, encompassing the entire visible spectrum and extending into the near-ultraviolet and near-infrared regions.<sup>63, 64, 68, 69, 110, 281-283</sup> The broader light-sensing range of CBCRs mainly reflects amino acid substitutions within the GAF domain that significantly extend or restrict the  $\pi$ -conjugation of the bilin chromophore. Many cyanobacteria possess both bacterial phytochromes and CBCRs that covalently bind the same chromophore precursor, phycocyanobilin (PCB; Figure 8.2), via a highly conserved GAF-domain cysteine residue as exemplified by the photosensory core of cyanobacterial phytochrome 1 from *Synechocystis* sp. PCC 6803 (Cph1 $\Delta$ ; Q55168) and the fourth GAF domain of the CBCR NpR6012 from *Nostoc Punctiforme* (NpR6012g4; B2IU14).

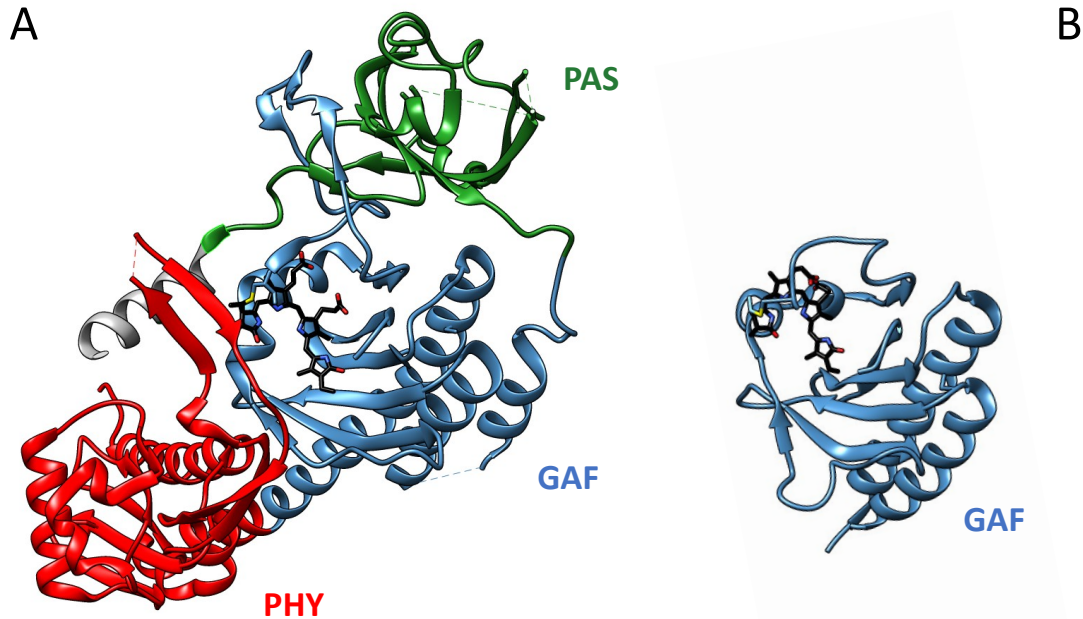


**Figure 8.1:** Structural Comparison of the  $^{15Z}P_r$  Dark-adapted States of Cph1 $\Delta$  and NpR65012g4 Structures of the PAS-GAF-PHY photosensory region of the red/far-red cyanobacterial phytochrome 1 (Cph1 $\Delta$ )<sup>61</sup> from the cyanobacterium *Synechocystis* sp. PCC6803 (A; 2VEA), and of the GAF4 domain of the canonical red/green cyanobacteriochrome NpR6012 (NpR6012g4)<sup>108</sup> from the cyanobacterium *Nostoc punctiforme* (B; 6BHN). The PAS, GAF, and PHY domains are color coded green, blue, and red, respectively.

Interestingly, the  $^{15Z}P_r$  dark-adapted states of Cph1 $\Delta$  and NpR6012g4 are comparable, with both photoreceptors possessing comparable red absorbance maxima, which reflects similar chromophore-protein interactions (Figures 8.1 and A8.1), while the photoproduct states absorption maxima differ by almost 200 nm, i.e.,  $^{15E}P_g$  for NpR6012g4 and  $^{15E}P_{fr}$  for Cph1 $\Delta$  (Figure 8.2). Furthermore, the  $^{15Z}P_r$  dark-adapted states of both Cph1 $\Delta$  and NpR6012g4 consist of structurally and spectrally heterogeneous subpopulations.<sup>101 100, 302 176</sup> Dynamic studies on the ultrafast forward dynamics of Cph1 $\Delta$  have resolved a relatively red-shifted photoactive ( $^{15Z}P_r$ -I) subpopulation and

a relatively blue-shifted fluorescent ( $^{15Z}P_{r-II}$ ) subpopulation.<sup>101</sup> These two subpopulations were attributed to distinct hydrogen bonding networks that were dependent on the protonation state of His260.<sup>100, 302</sup> Heterogeneous hydrogen bonding networks may also be present in canonical red/green CBCRs and could explain the positive correlation between  $^{15Z}P_r$  absorbance and Lumi- $R_{fr}$  quantum yields resolved by Gottlieb et al.<sup>176</sup> In addition to heterogeneous hydrogen bonding networks, an orange-absorbing  $^{15Z}P_o$  subpopulation possessing unique orientations of highly conserved Trp and Asp acid residues also has been observed in several red/green CBCRs, including NpR6012g4.<sup>27, 108</sup> Unlike the fluorescent  $^{15Z}P_{r-II}$  subpopulation of Cph1 $\Delta$ , this  $^{15Z}P_o$  subpopulation of red/green CBCRs yielded an unstable red-shifted Lumi- $O_f$  intermediate upon photoactivation that only decayed back to  $^{15Z}P_o$ .

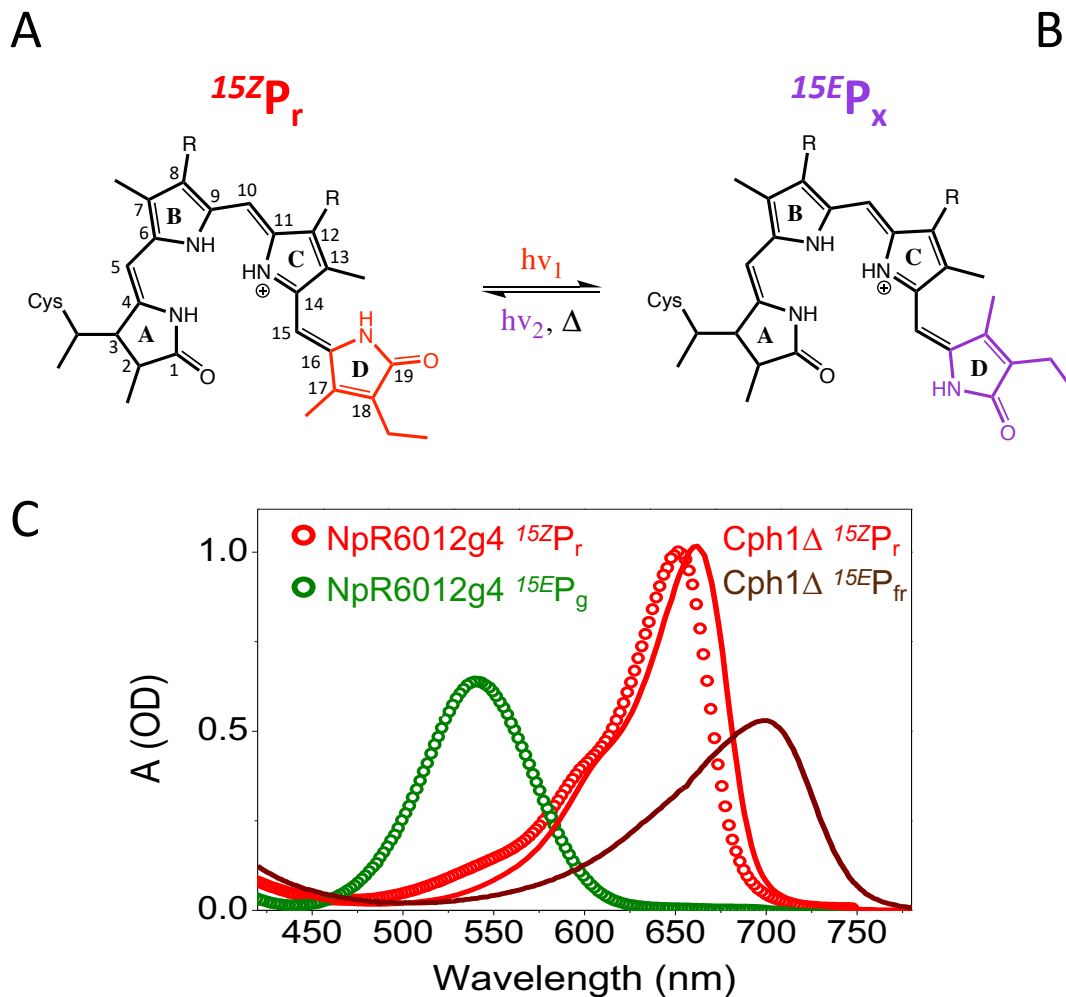


**Figure 8.2:** Chromophore and Spectral Comparison of the Dark-Adapted and Light-Adapted States of Cph1Δ and NpR6012g4

PCB dark adapted (A;  $^{15Z}P_r$ ) and signaling state (B;  $^{15E}P_x$ ) chromophore conformation structures. The subscript 'x' is used in place for 'f' and 'g' for Cph1Δ and NpR6012g4, respectively. (C) Absorption spectra of the dark-adapted and 'lit' photoproduct states of Cph1Δ (solid lines) and NpR6012g4 (open circles). The lit photoproduct states were scaled by the normalization factor of the dark-adapted states.

While the GAF domain structures of the dark-adapted states of the two proteins are similar, the lack of a photoproduct state structure for Cph1 $\Delta$  precludes understanding of the structural basis of the spectral differences between their photoproducts. Such spectral differences have been proposed to depend on both the PHY domain<sup>99</sup> that is missing from NpR6012g4 (Figure 8.1), and highly conserved phenylalanine (Phe) residues that are not present in Cph1 $\Delta$  (Figure A8.1).<sup>108, 197</sup> This indicates that the chromophore-protein interactions substantially differ in the photoproduct states of the two proteins.

Despite the primary (125 fs to 10 ns) and secondary (10 ns to >1 ms) forward dynamics<sup>100, 101, 104, 113, 123, 135, 137-140, 142, 302-305</sup> and primary reverse dynamics<sup>102, 103, 123</sup> having been extensively studied for Cph1 $\Delta$ , much is still to be learned about the Cph1 $\Delta$  photocycle (Figure 8.3 and Figure A8.2). Using the nomenclature outlined by Gottlieb et al.,<sup>111</sup> previous studies of the primary forward dynamics have resolved that the photo-productive pathways of Cph1 $\Delta$ <sup>100, 101, 104</sup> and NpR6012g4<sup>182</sup> possess comparable <sup>15Z</sup>P<sub>r</sub>\* excited state dynamics and red-shifted primary Lumi-R<sub>fr</sub> intermediates (Figures A8.4 and A8.5). The main difference in the primary forward dynamics of the two proteins was the larger Lumi-R<sub>fr</sub> quantum yield for NpR6012g4 (Figure A8.5) that is attributed to the presence of ‘second-chance’ photo-productive ground state intermediates (Figure 2.11).<sup>100, 101, 104, 184</sup> Secondary forward dynamics of Cph1 $\Delta$  also resolved a yellow-red intermediate attributed to a transient deprotonation event that subsequently evolved to the light-adapted state on a ms timescale.<sup>135</sup> This hypothesis gained further support by Hildebrandt and coworkers<sup>306</sup> using cryo-Raman spectroscopy and computational methods. Conflicting studies of transient deprotonation in the forward dynamics of phytochromes have been published for several phytochromes (discussed

further in the SI) and it has been noted that deprotonated PCB chromophores are typically much more blue shifted than those of the previously resolved Meta-R<sub>y</sub> intermediate.<sup>118, 128, 307-309</sup>

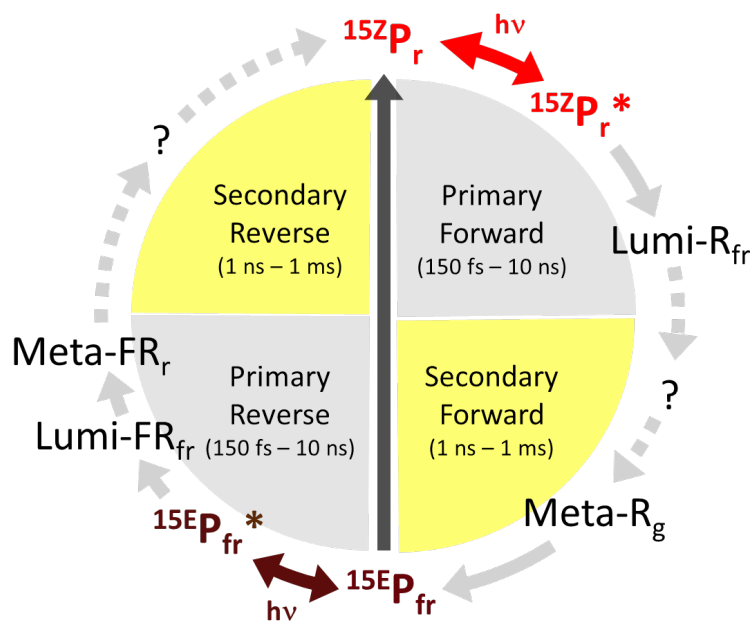


**Figure 8.3:** Current Simplified Photocycle of Cph1Δ

Currently resolved model of the photocycle of Cph1.<sup>101-104, 135</sup>

Given the limited spectral range and resolution in the ns to ms timescale for the forward dynamics of Cph1Δ,<sup>135, 153, 303</sup> it is not known whether the similarities of the primary forward dynamics of the two proteins extend through the evolution to secondary Meta-R intermediates, nor is it known how the initial Lumi-R<sub>fr</sub> eventually evolves to the previously resolved yellow-absorbing intermediate in Cph1Δ (Figure 8.3 and Figure A8.2). Moreover, the secondary reverse dynamics of Cph1Δ have yet been reported. Here, we compare the secondary forward and reverse dynamics of Cph1Δ and NpR6012g4<sup>27, 29, 108</sup> using transient absorption (TA) and global analysis



methodologies while also expanding on previous cryo-trapping spectroscopic measurements<sup>100, 101, 143</sup> to track the full photocycle. Coupled with cryokinetics, extension of the probe deeper into the blue spectral region, and increased resolution in the ns to ms, the TA dynamics presented here establish that the entire forward and reverse dynamic profiles of the Cph1 $\Delta$  and NpR6014g4 photocycles are remarkably similar, despite the striking difference in photoproduct absorption spectra. The forward dynamics resolved that Cph1 $\Delta$  does not behave like other phytochromes that typically have red absorbing intermediates and involves two unique epochs where Epoch I consisted of monotonic spectral evolution of several intermediates from Lumi-R<sub>fr</sub> to Meta-R<sub>g</sub>, identical to the forward dynamics of NpR6012g4, and Epoch II consisted of spectral non-monotonic evolution consistent with a transient deprotonation event. The reverse dynamics of Cph1 $\Delta$  was also similar to NpR6012g4 and consisted of spectral non-monotonic evolution and resolved that the fluorescent <sup>15</sup>ZP<sub>r</sub>-II subpopulation was populated prior to and evolved to the photoactive <sup>15</sup>ZP<sub>r</sub>-I subpopulation.

## ***Experimental***

### *Sample Preparation.*

Cph1 $\Delta$ <sup>140</sup> and NpR6012g4<sup>182</sup> samples were prepared as previously described for the room temperature transient absorption (TA) dynamics. For the cryokinetic measurements, samples were prepared in a similar manner but differed by adjusting the solvent to a 67% glycerol and 33% buffer solution.

### *Room Temperature Transient Absorption Spectroscopy.*

The experimental design for collecting pump-probe signals has been previously reported in detail.<sup>27, 188, 189</sup> Briefly, the broadband probe pulse was generated by focusing the 800 nm fundamental of a Ti:Sapphire amplified laser system (SpectraPhysics Spitfire Pro) through a slowly translating 10 mm thick CaF<sub>2</sub> crystal. The photodynamics for both the forward and reverse reactions were initiated by using the second harmonic (532 nm) of an independent Q-switched diode-pumped solid-state YAG laser (Pulselas-A532-300) operating at 15–20 μJ per pulse at 1 kHz and pulse width of 500 ps. The pump beam was electronically delayed with respect to the probe pulse, which allowed for up to ~10 ms of temporal separation although only the <1 ms dynamics were free of artifacts from the excited sample flowing out of the probe region. Fresh sample enriched in the desired state for each excitation pulse was generated by continuously flowing the sample in a closed circuit and continuously illuminating the sample with a 650 nm LED for the reverse reaction of Cph1Δ and NpR6012g4, and either a 725 nm LED or a 526 nm LED for the forward reaction of Cph1Δ and NpR6012g4, respectively. Supplemental data for room temperature TA measurements can be found in Tables A8.1 & A8.2 and Figures A8.4-A8.9.

### *Cryokinetic UV-Vis Spectroscopy.*

Cryokinetic measurements were performed using an Oxford Instruments Optistat DN liquid nitrogen cryostat placed in the beam path of a Shimadzu 1700 UV–Vis spectrometer. Cryokinetic signals were collected from 160 to 290 K for Cph1Δ and 150 to 275 K for NpR6012g4 in 10 K steps. Prior to data collection, samples were illuminated with laser diodes resonant with the terminal photoproduct, as outlined above, to push as much of the population as possible to the starting parental state population. Reference spectra were then recorded every 3 min for 27 min to

capture a true reference spectrum at each temperature. At the lowest temperature, samples were illuminated with red (forward reaction) or green/far-red (reverse reaction; NpR6012g4/Cph1Δ) laser diodes to initiate the photocycle. After illumination, spectra were collected every 3 min for various lengths of time before increasing the temperature. This incremental increase in temperature allows for the mapping of the photocycle by observing changes in the absorption spectra due to the evolution of populations once enough thermal energy is available to get over subsequent energy barriers. This ability to trap intermediates have proved useful in resolving rapidly evolving intermediates that are difficult to capture in room-temperature transient measurements. The differences between the terminal reference spectra and each illuminated spectrum at the same temperature were calculated for ease of interpretation. A flowchart depicting the cryokinetic measurement process is available in Figure A8.10. Since wavelength dependent dynamics and efficiencies has been reported,<sup>183, 185</sup> a table comparing the excitation wavelengths for the TA and cryokinetic measurements is provided in the SI (Table A8.1). Additional supplemental data for cryokinetic measurements can be found in Tables A8.3-A8.6 and Figures A8.11-A8.29.

### *Global Analysis.*

Coupled with time resolved spectroscopic data, global analysis is a powerful tool that separates the time dependent spectra into a linear combination of time-independent spectra that are weighted by a time-dependent concentration profile.<sup>221, 243</sup> Based on the model prescribed, the data is fit to a linear combination of the solutions to first order differential equations with the form:

$$\frac{dn_i}{dt} = A_i I(t) + \sum_{i,j} K_{i,j} n_j(t) \quad (1)$$

where  $n_i$  represents the  $i^{\text{th}}$  microscopic population of interest,  $A_i$  is the initial occupancy of the  $i^{\text{th}}$  population,  $I(t)$  is the pump pulse temporal envelope, and  $K_{i,j}$  is the connectivity matrix that is composed of the rate constants describing the flow from the  $i^{\text{th}}$  population in to the  $j^{\text{th}}$  population.

Initially, data are fit to a sequential model ( $A \rightarrow B \rightarrow C \dots$ ) with consistently increasing lifetimes. If the postulated model extracted the spectra of the true subpopulations, then species associated difference spectra (SADS) and the associated lifetimes are obtained. If the true subpopulations were not extracted, then evolution associated difference spectra (EADS) and the associated apparent lifetimes were obtained. If EADS were based on the postulated model, then more complicated target models with coevolving subpopulations are required to extract the SADS. Other than the previously reported secondary forward dynamics of NpR6012g4,<sup>27, 29, 108</sup> none of the data presented here was analyzed past a sequential model and all of the models fit the kinetics well.

## **Results**

### *Forward Room-Temperature TA Dynamics.*

Few of the signals previously reported for the primary dynamics of Cph1 $\Delta$ <sup>100-104</sup> and NpR6012g4<sup>182, 183</sup> were observed in the secondary dynamics because these signals would occur prior to the instrument response. These populations would either be unlikely to be trapped (i.e., excited state dynamics, <sup>15</sup>ZP<sub>r</sub>-II fluorescence) or would be low yielding (i.e. <sup>15</sup>ZP<sub>o</sub> isomerization) at cryo-temperatures and excitation wavelengths. While the room-temperature primary and secondary forward TA dynamics of NpR6012g4 have already been published,<sup>29, 108</sup> we include some of this data along with new data for Cph1 $\Delta$  data here for comparative purposes (Figure 8.4). As described previously, the secondary forward dynamics of NpR6012g4 consist of monotonic

spectral evolution from the initial red-shifted Lumi-R<sub>fr</sub> intermediate to <sup>15</sup>E P<sub>g</sub> (Figure A8.3).<sup>108, 182</sup> This mechanism is consistent with a gradual increase in the structural deformation of the chromophore<sup>197</sup> and was later revealed to be conserved in the forward dynamics of canonical red/green CBCRs family and not unique to NpR6012g4.<sup>27</sup>

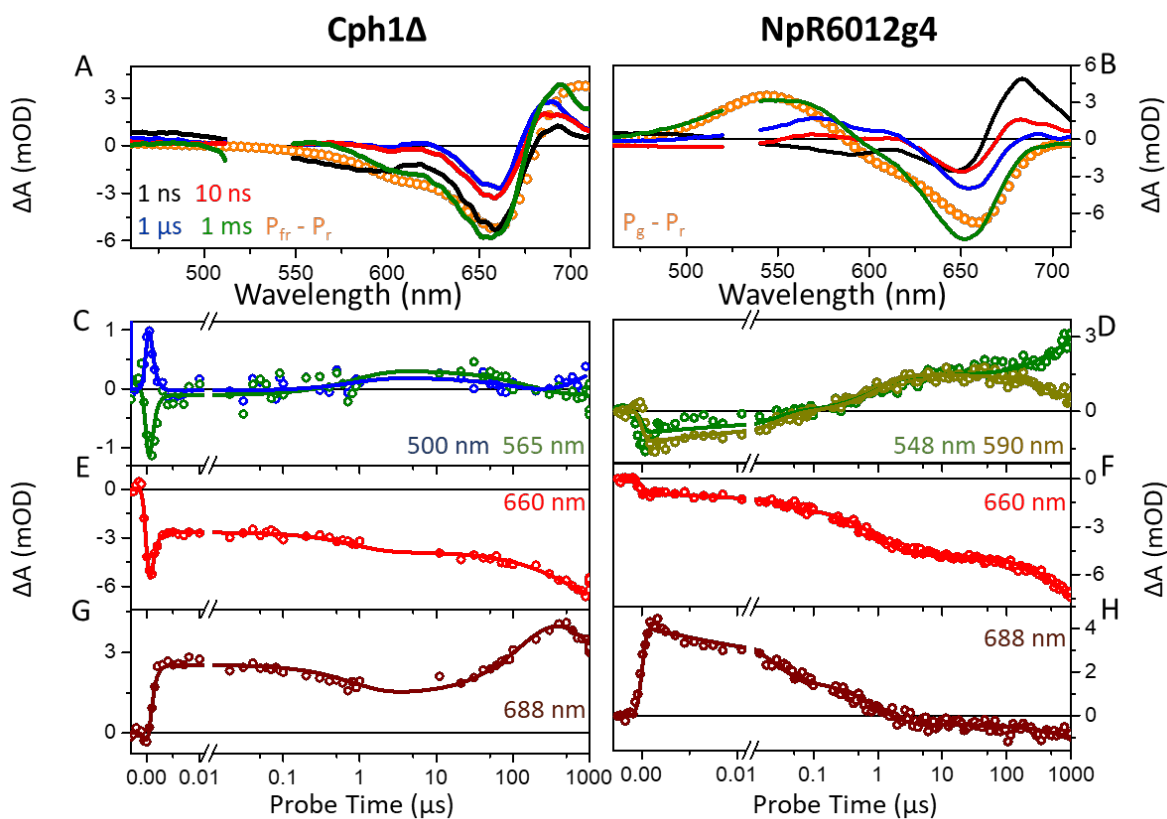


**Figure 8.4:** Room-Temperature TA Dynamics of the Secondary Forward Reaction of Cph1Δ and NpR6012g4

Comparison of the room temperature secondary forward TA dynamics of Cph1Δ (left) and NpR6012g4 (right)<sup>27, 108</sup> after 532 nm excitation. Panels A and B contrast the transient spectra of Cph1Δ and NpR6012g4, where NpR6012g4 is color coded to the legend in A. Panels C-H compares the kinetics of Cph1Δ and NpR6012g4 at selected wavelengths where the open circle represent the data and the solid lines represent the fits from global analysis. The green and blue absorbance spectra are more readily observed in Figure A8.6.

Building on previous studies, we resolved two distinct phases for the forward secondary dynamics of Cph1 $\Delta$ ,<sup>100, 101, 104</sup> in which monotonic evolution to shorter wavelengths, as was observed for NpR6012g4, preceded non-monotonic spectral evolution. Consistent with previous Cph1 $\Delta$  studies, we initially observed a negative signal around 660 nm and positive absorption in the far red, i.e., near 690 nm (Figure 8.4A, black curve). Such 1 ns signals were attributed to ground state bleach (GSB) and to formation of the primary Lumi-R<sub>f</sub> intermediate, respectively. On the ns to hundreds of  $\mu$ s timescale, Cph1 $\Delta$  exhibited the appearance of blue-shifted intermediates, e.g. the 688 nm kinetic trace (Figure 8.4G) resolves a clear signal decay up to 1  $\mu$ s that coincides with signal growth at 565 nm (Figure 8.4C; green curve) that is very similar with those observed for NpR6012g4 (Figure 8.4D&F). Also similar to NpR6012g4, a positive absorbance that strongly overlaps the bleach evolves on the  $\mu$ s timescale for Cph1 $\Delta$  (Figure 8.4A), implicating the presence of a Meta-R<sub>f</sub> intermediate which evolves to Meta-R<sub>g1</sub> (Figure A8.6). Meta-R<sub>g1</sub> persisted for a few hundred  $\mu$ s prior to evolving to a far-red absorbing Meta-R<sub>f</sub> population not seen in NpR6012g4 that strongly overlapped the absorption of the Lumi-R<sub>f</sub> intermediate (Figure 8.4C&G). Decay of this Meta-R<sub>f</sub> signal subsequently occurred with a timescale of  $\sim$  830  $\mu$ s, coincident with the growth of a previously resolved green-absorbing Meta-R<sub>g2</sub> intermediate<sup>135</sup> with a peak at 505 nm (Figure 8.4C [blue curve] and Figure A8.6).). The evolution of some of this Meta-R<sub>f</sub> population to a secondary green-absorbing population for Cph1 $\Delta$  was also captured in the normalized 2 to 9 ns difference spectra (Figure A8.7A) and in the cryokinetics (Figure 8.5) as discussed below.

#### *Forward Cryokinetics.*

Forward cryokinetics were next collected on both photoreceptors to track the complete forward photoconversion pathway and to isolate intermediates not well resolved by TA measurements.

Cryokinetic spectra at select temperatures for Cph1 $\Delta$  and NpR6012g4 are shown in Figure 8.5 and are compared with TA measurements in Figure 8.6. Spectra, kinetics, EADS and a table of the observed features at every temperature for Cph1 $\Delta$  (Figures A8.12-A8.15; Table A8.3) and NpR6012g4 (Figures A8.16-A8.18; Table A8.4) can be found in the supplemental information (SI). For the most part, both photoreceptors yielded similar intermediates. In agreement with the TA dynamics, monotonic spectral evolution from Lumi-R<sub>fr</sub> to Meta-R<sub>g</sub> was initially observed for both photoreceptors. At 190 K (Figure 8.5D) however, NpR6012g4 exhibited near constant orange absorbance while the far-red and yellow absorbances were decreasing and increasing, respectively. This suggests that there is a previously unresolved Meta-R<sub>o</sub> photointermediate being populated from Lumi-R<sub>fr</sub> as fast as it is evolving to Meta-R<sub>y</sub>.

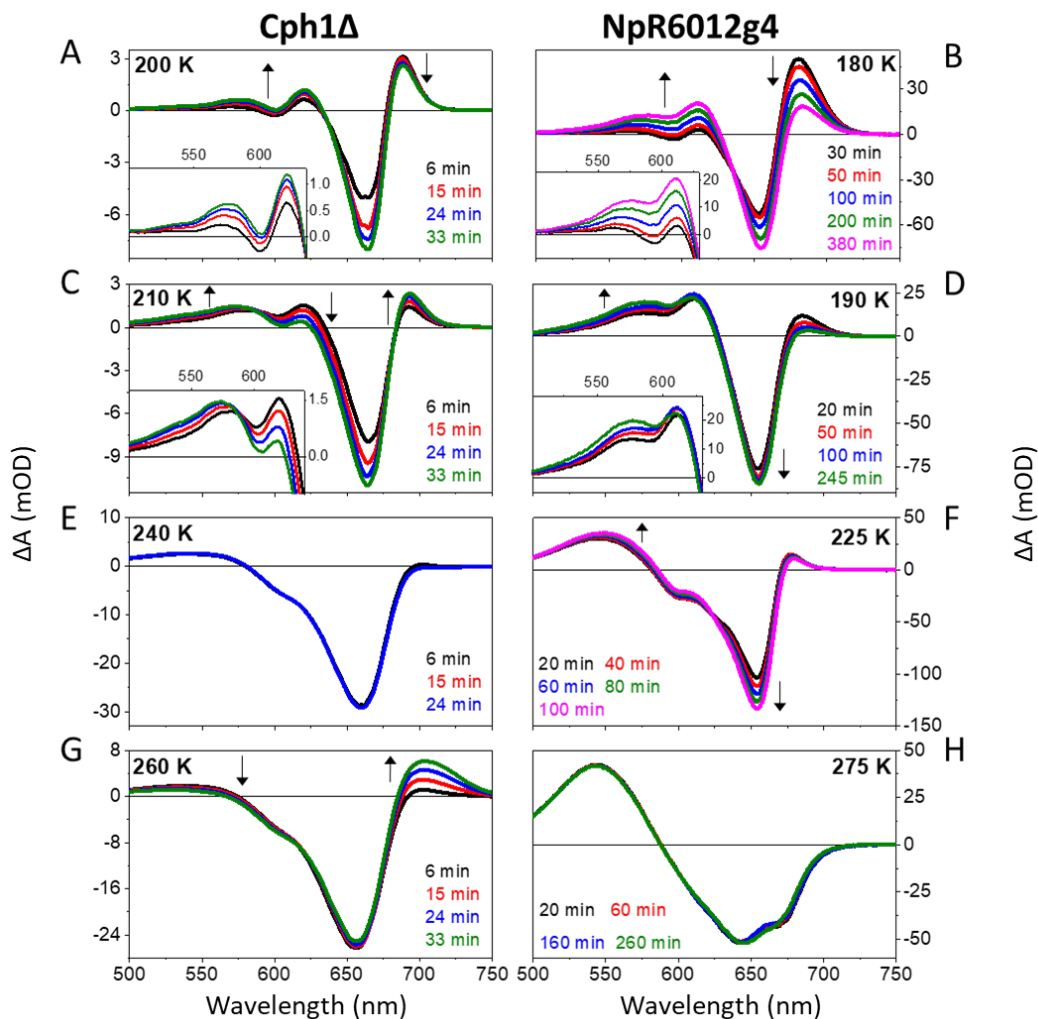


**Figure 8.5:** Cryokinetics of the Secondary Forward Reaction of Cph1 $\Delta$  and NpR6012g4. Comparison of the forward cryokinetic spectra of Cph1 $\Delta$  (left column) and NpR6012g4 (right column) at select temperatures that captures the dynamics of the photoreceptor. These temperatures were chosen since they offered the greatest spectral evolution clarity. The temperatures chosen for Cph1 $\Delta$  and NpR6012g4 differed slightly due to differences in the thermodynamic properties of these intermediate populations.

While the monotonic blue-shifting dynamics terminate with the population of the  $^{15E}P_g$  signaling state for NpR6012g4 (Figure 8.5H), the appearance of  $^{15E}Meta-R_{g1}$  in Cph1 $\Delta$  marked the beginning of the non-monotonic spectral evolution. At 210 K, a significant red shift from Meta- $R_{g1}$  to Meta-



$R_f$  was observed for Cph1 $\Delta$  (Figure 8.5C). The further growth of the green absorption at 210 K was attributed to continued evolution of Meta- $R_o$  to Meta- $R_{g1}$ . This sequential model was preferred over a branching model, since the former is consistent with what was observed in the TA data (Figure 8.4). At 240 K, Meta- $R_f$  could evolve to Meta- $R_{g2}$  that is further blue shifted than Meta- $R_{g1}$  (Figure 8.5C&E). The presence of two unique green absorbing intermediates is consistent with the observed TA dynamics at 504 nm and 565 nm (Figure 8.4C). When a high enough temperature was reached (260 K), growth of a broad far-red absorbance that matched the absorbance of  $^{15E}P_{fr}$  was observed, indicating the completion of the forward photoreaction of Cph1 $\Delta$  (Figure 8.5G).

Comparison of the room temperature TA and cryokinetic EADS for NpR6012g4 indicates that the same dynamics were extracted in both experiments given the excellent spectral overlap of the photointermediates and  $^{15E}P_g$  EADS (Figures 8.6B,D,&F). The comparison of the EADS for NpR6012g4 also emphasizes that the Meta- $R_y$  EADS of NpR6012g4 (Figure 8.6D; blue solid line and open circles) is a mixture of Meta- $R_y$  and Meta- $R_o$  photointermediates (Figure 8.5D). The photoinactive Lumi- $O_f$  observed in the room temperature dynamics was not resolved in the cryokinetics (Figure 8.6B) presumably due to a high energy barrier between  $^{15Z}P_o$  and Lumi- $O_f$  and low quantum yield of Lumi- $O_f$  after ~650 nm excitation.

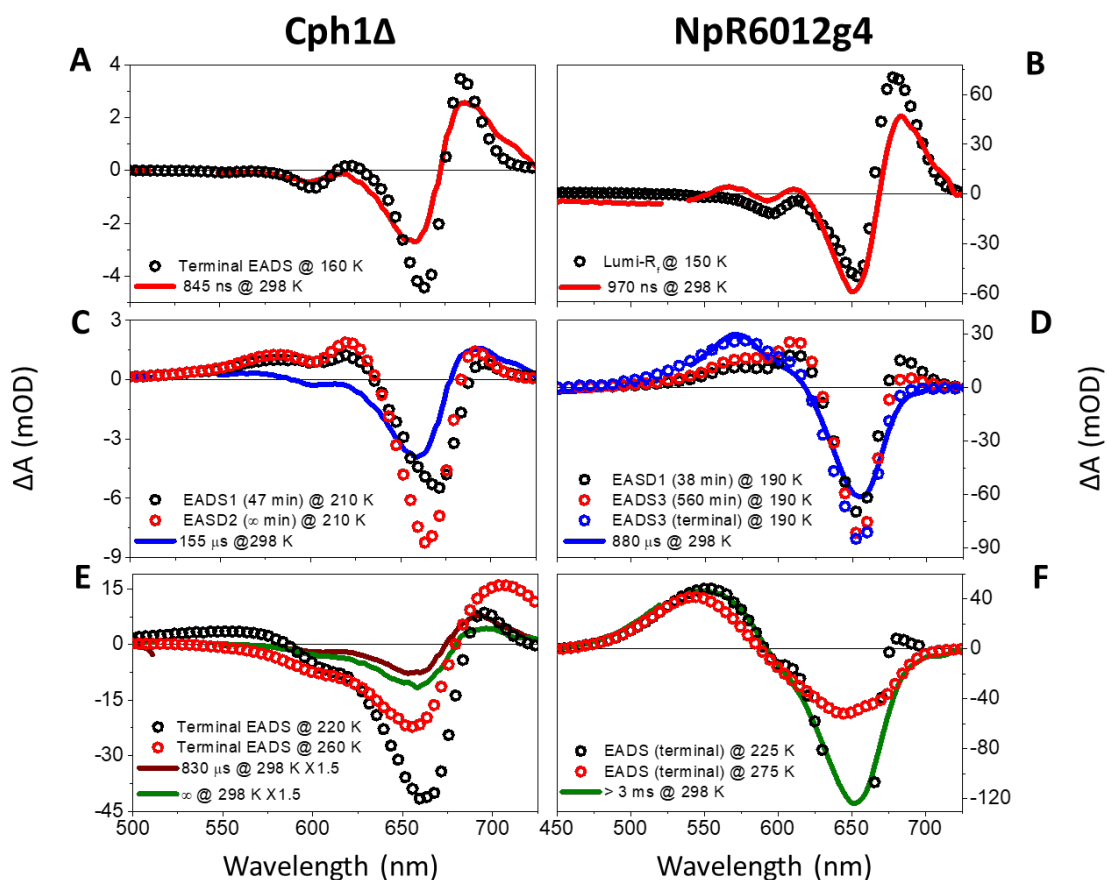


**Figure 8.6:** Room-Temperature TA and Cryokinetics EADS Comparison of the Secondary Forward Reaction of Cph1 $\Delta$  and NpR6012g4

Comparison of the forward room-temperature TA and cryokinetic EADS of the photointermediates for Cph1 $\Delta$  (left column) and NpR6012g4 (right column). The evolution of Meta-R<sub>f</sub> to Meta-R<sub>g2</sub> for Cph1 $\Delta$  at room temperature is more readily observed in Figure A8.8. Note that the Lumi-O<sub>f</sub> intermediate of NpR6012g4 was left out for simplicity.<sup>27, 108</sup>

While the TA and cryokinetic EADS were comparable for NpR6012g4, this was observed only for the Lumi-R<sub>f</sub> EADS (Figure 8.6A) for Cph1 $\Delta$ . Meta-R<sub>o</sub>, Meta-R<sub>g1</sub>, and Meta-R<sub>f</sub> EADS for Cph1 $\Delta$  differ from those of NpR6012g4 (Figure 8.6C) due in part to a difference in populations of these three photointermediates, temperature dependence of the parental states (Figure A8.11) that may also extend to the intermediates, and a relatively low energy barrier between Meta-R<sub>o</sub> and

Meta-R<sub>g1</sub> (Figures 8.4 and 8.5B). Data shown in Figure 8.6E depict the Meta-R<sub>f</sub> to Meta-R<sub>g2</sub> evolution where there is a decrease in the far-red absorbance and an increase in the green absorbance. This evolution is more readily observed when the green spectral region was emphasized (Figure A8.8) and continued in the flow region (2 to 9 ms) of the TA measurement (Figure A8.7A).

#### *Reverse Room-Temperature TA Dynamics.*

While the room-temperature secondary reverse dynamics of NpR6012g4 have already been published,<sup>29</sup> it is presented here for comparison with the Cph1Δ data. Unlike the forward dynamics, the reverse dynamics of NpR6012g4 had a trend of non-monotonic spectral evolution following Lumi-G<sub>0</sub> where a blue-shifting phase preceded a red-shifting phase (Figure 8.7 and Figure A8.3).<sup>29</sup> Interestingly, the two Meta-G intermediates resolved in the blue-shifting phase were both metastable and partially decayed back to the <sup>15</sup>E<sub>g</sub> state. Non-monotonic spectral evolution in the reverse reactions of canonical red/green CBCRs is not unique to NpR6012g4 and appears to be a conserved mechanism.<sup>179</sup> While the monotonic evolution of the intermediate populations in the forward dynamics was attributed to a gradual increase of the structural deformation of the chromophore due to two highly conserved phenylalanine residues,<sup>27, 108, 197</sup> a molecular level explanation for the reverse dynamics remains to be addressed in a future paper.<sup>179</sup>

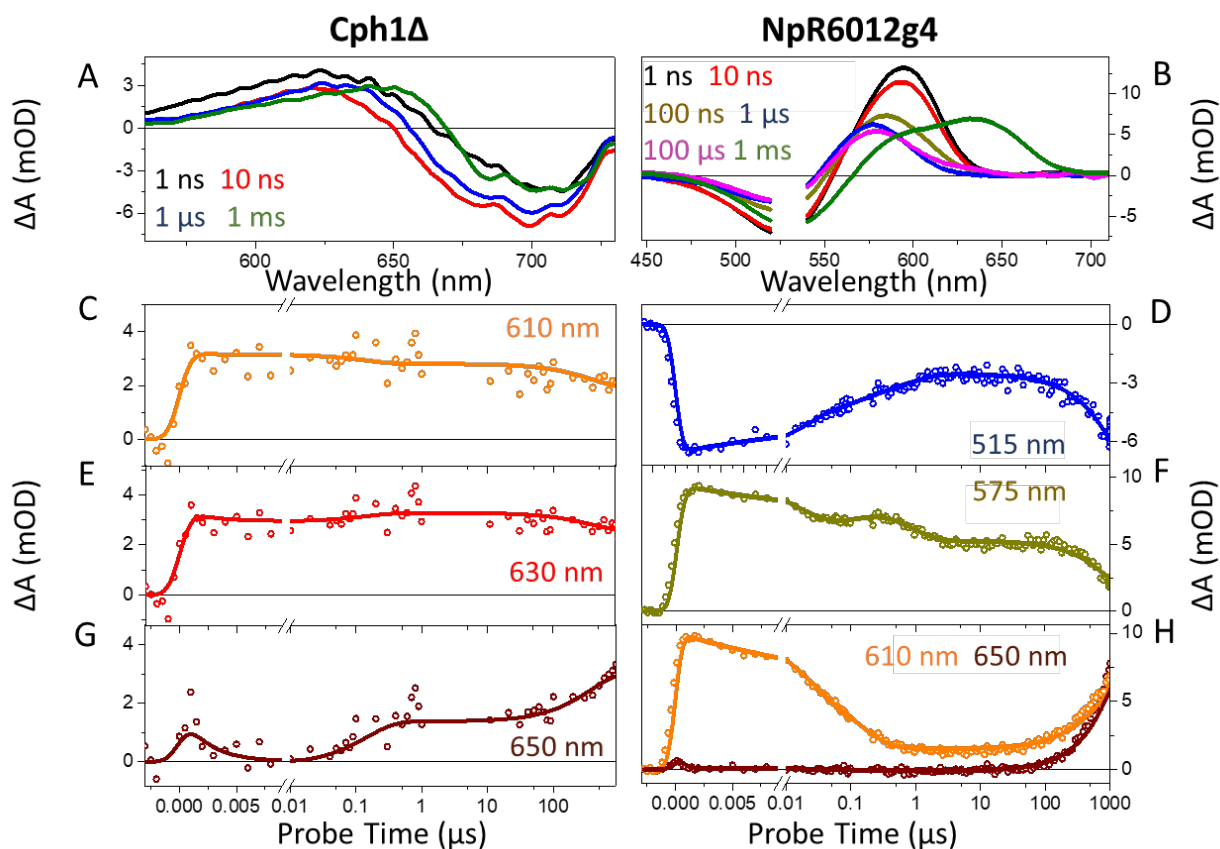


**Figure 8.7:** Room-Temperature TA Dynamics of the Secondary Reverse Reaction of Cph1 $\Delta$  and NpR6012g4

Comparison of the room temperature secondary reverse TA dynamics of Cph1 $\Delta$  (left column) and NpR6012g4 (right column).<sup>29</sup> Transient spectra at select times (A, B) and kinetic traces at select wavelengths (C-H) were chosen that highlights the dynamics. For the kinetic traces, the open circles represent the data and the solid lines represent the fit from global analysis.

Similar to NpR6012g4, the reverse TA dynamics of Cph1 $\Delta$  was also observed to progress through a non-monotonic spectral evolution mechanism that also consisted of a blue-shifting phase that preceded a red-shifting phase. The secondary reverse dynamics of Cph1 $\Delta$  exhibited initial loss of absorption in the red shoulder, resulting in a small blue shift and decrease in overall amplitude from 1 ns to 10 ns (Figure 8.7A; black to red curve). This was followed by a small red shift at 1

$\mu\text{s}$  (Figure 8.7A; blue curve) and a larger red shift at 1 ms (Figure 8.7A; green curve). The smaller red shift was also observed in the kinetics between 0.01 and 1  $\mu\text{s}$  where the 610 nm trace (Figure 8.7C) depicts a decrease in absorption while there is a small increase at 630 nm (Figure 8.7E). The second and slightly larger red shift was also captured in the  $> 10 \mu\text{s}$  kinetics when a decay at 630 nm (Figure 8.7E) and a concurrent growth at 650 nm (Figure 8.7G) occurred. Beyond the 1 ms used in the global analysis, the 2 to 9 ms normalized difference spectra of Cph1 $\Delta$  depicted a continued red shifting and growth in the overall amplitude (Figure A8.7B). Cph1 $\Delta$  differed from NpR6012g4 whose blue shifting of the initial Meta photointermediates was more substantial and a decrease in the overall amplitude was associated with shunting.<sup>29</sup> A table summarizing the room temperature reverse dynamics of Cph1 $\Delta$  can be found in the SI (Table A8.2).

The sequential analysis of the reverse room temperature TA dynamics of Cph1 $\Delta$  resolved that, unlike the reverse dynamics of NpR6012g4,<sup>29</sup> there is only a single evolution in the blue-shifting phase and at least three resolvable evolutions in the red-shifting phase of Cph1 $\Delta$  (Figure 8.8). The single blue-shifting evolution in Cph1 $\Delta$  had the same spectral trends and time constant as the evolution of Lumi-FR<sub>fr</sub> to Meta-FR<sub>r</sub> previously reported in the ultrafast dynamics by Kim et al.<sup>102</sup> This coupled with the strong spectral overlap of the 1-5 ns and 1 ms spectra from the primary and secondary dynamics (Figure A8.9), indicates that the initial blue-shifting phase in the secondary reverse dynamics of Cph1 $\Delta$  is due to continued evolution of Lumi-FR<sub>fr</sub>. Following the initial blue shifting, a less pronounced red shifting on a 145 ns timescale was observed that was followed by a more substantial red shift on a 375  $\mu\text{s}$  timescale (Figure 8.8A). The terminal EADS spectrum was blue shifted relative to the  $^{15Z}\text{P}_r - ^{15E}\text{P}_{fr}$  difference spectrum and appeared intermediate between the absorbance of the photoactive  $^{15Z}\text{P}_r\text{-I}$  and fluorescent  $^{15Z}\text{P}_r\text{-II}$  subpopulations,<sup>100, 101</sup>

suggesting that it may have a different distribution of the  $^{15Z}P_r$ -I and  $^{15Z}P_r$ -II subpopulations. Having a higher concentration of  $^{15Z}P_r$ -II would effectively blue shift the spectrum as observed and indicates that the two parental subpopulations have yet to reach equilibrium on the 1 ms timescale (Figure 8.8A).

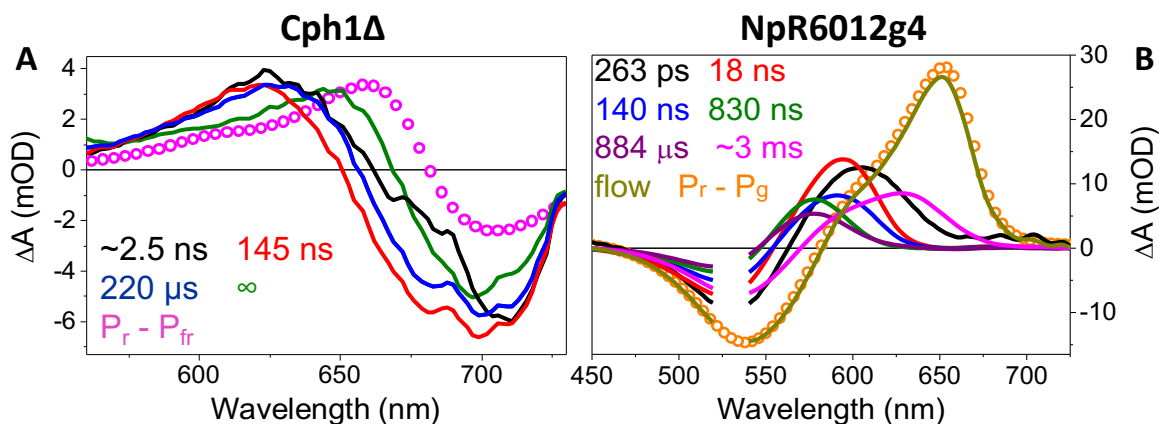


**Figure 8.8:** Room-Temperature TA EADS of the Secondary Forward Reaction of Cph1Δ and NpR6012g4

Comparison of the room temperature secondary reverse EADS of Cph1Δ (left) and NpR6012g4 (right)<sup>29</sup> (i.e., sequential models). The EADS (solid lines) are compared to the dark and light state difference spectra (open circles).

### *Reverse Cryokinetics.*

The reverse cryokinetics of Cph1Δ and NpR6012g4 were also measured and resolved intermediates not observed at room temperature due to temporal limitations of the TA measurements. The results of these measurements at select temperatures are compared in Figure 8.9. The data and EADS at all measured temperatures for the reverse reaction of both Cph1Δ and NpR6012g4 and corresponding tables of observations can be found in the SI (Figures A4.19-A8.28, Tables A8.5 and A8.6). These measurements show that the reverse cryokinetics of NpR6012g4 exhibited the same non-monotonic spectral evolution as the room temperature TA

dynamics (Figures 8.7B, 8.8B, and A8.3) plus two unresolved features. Upon excitation, NpR6012g4 initially exhibited a decrease in the nascent red-absorbing species and a filling of the bleach between 150 and 170 K (Figure A8.24), suggesting that, like Meta-G<sub>0</sub> and Meta-G<sub>y</sub>,<sup>29</sup> Lumi-G<sub>0</sub> also exhibits a pathway back to <sup>15E</sup>P<sub>g</sub>. The cryokinetics also isolated an extremely blue-shifted intermediate at 180 K that absorbs on the other side of the bleach (Figure 8.9B).

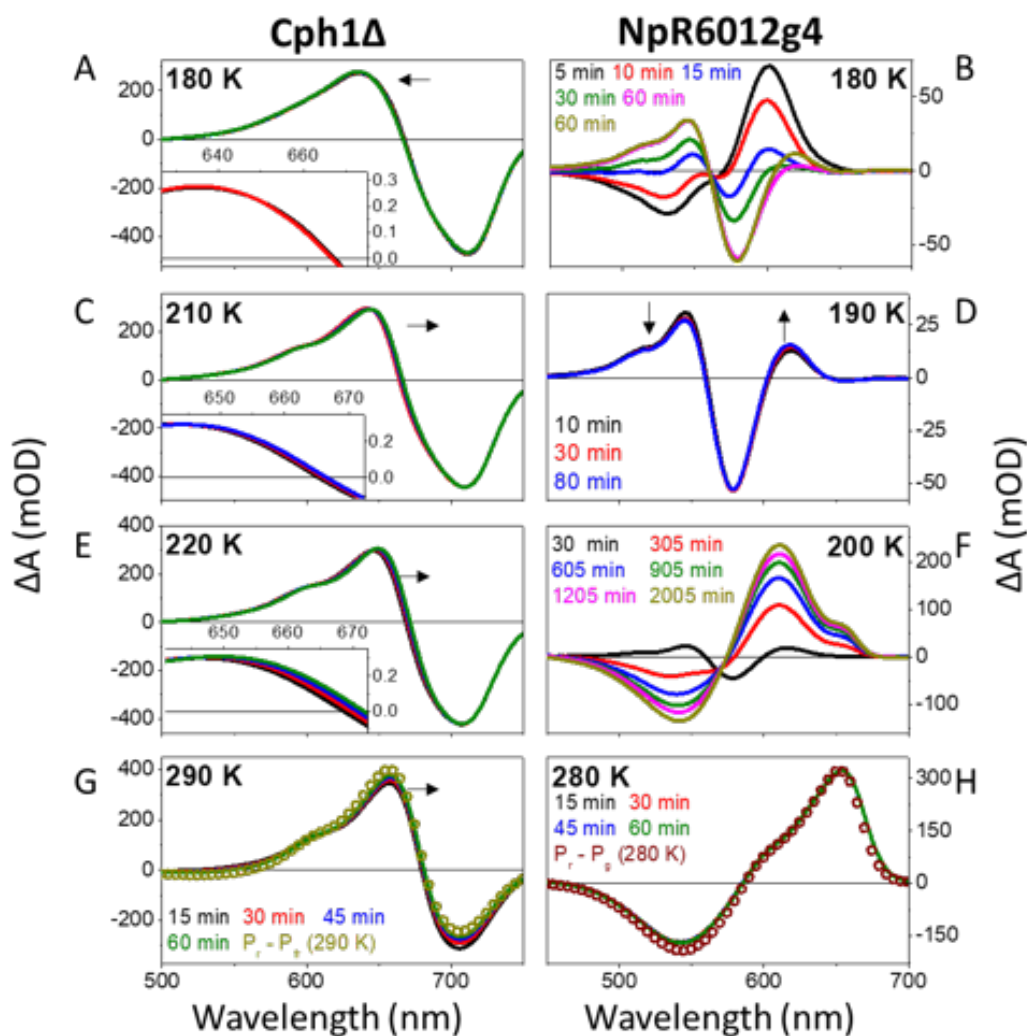


**Figure 8.9:** Cryokinetics of the Secondary Reverse Reaction of Cph1Δ and NpR6012g4  
Reverse cryokinetic spectra of Cph1Δ (left column) and NpR6012g4 (right column) at select temperatures that captures the dynamics of the photoreceptor. All of Cph1Δ are color coded to the legend in G. The initial blue shifting for Cph1Δ is better resolved in the EADS (Figure 8.10).

As with NpR6012g4, the reverse cryokinetics of Cph1Δ resolved intermediates not captured by the room-temperature TA measurements. Upon excitation at 160 K and warming to 180 K, the cryokinetic difference spectra of Cph1Δ exhibits a blue-shifting of a near-gaussian peak red-shifted of the GSB (Figures 8.9A, 8.10A, and A8.17A). The similarities of the cryokinetics with the TA dynamics (Figure 8.8A) suggest that the blue shifting of the positive absorption band (Figure 8.10A) is due to the loss of residual Lumi-FR<sub>fr</sub>. As with the room temperature TA dynamics, this blue shift preceded a smaller red shift seen at 210 K (Figure 8.9C) and a larger secondary red shift seen at 220 K (Figure 8.9E). Finally, warming to 290 K led to further red shifting of the spectra accompanied by a growth in the absorption which was attributed to population of the photoproduct given its resemblance of the  $^{15E}P_{fr} - ^{15Z}P_r$  difference spectrum (Figure 8.9G).

To establish where in the photocycle the spectrally heterogeneous  $^{15Z}P_r$ -I and  $^{15Z}P_r$ -II dark-adapted state subpopulations (Figure A8.11) were generated,<sup>100, 101, 302</sup> a comparison of the terminal EADS focusing on the positive absorption at all temperatures accompanied by  $^{15E}P_{fr} - ^{15Z}P_r$  difference spectra at select temperatures can be found in Figure 8.10. As discussed above, an initial blue shift in the spectra was observed between 160 and 180 K and was attributed to evolution of Lumi-FR<sub>fr</sub> to Meta-FR<sub>r1</sub>. The initial blue shift was followed by a relatively smaller red shift between at 210 K and a relatively larger red shift at 220 K. The comparison of the terminal EADS and ground state difference spectra at 220 K (Figure 8.10B) suggests that the smaller red shift at 210 K was attributed to a Meta-FR<sub>r2</sub> population and the larger red shift at 220 K was attributed to the fluorescent  $^{15Z}P_r$ -II subpopulation. This assignment is consistent with the room temperature TA dynamics (Figure 8.8). Since the terminal EADS matched the  $^{15Z}P_r - ^{15E}P_{fr}$  difference spectrum of Cph1Δ in glycerol at 290 K and nearly that determined at 250 K (Figure 8.10C&D), these data



suggest that the intermediate conversions between 220 and 290 K reflect population of the photoactive  $^{15Z}P_r$ -I subpopulation and its subsequent equilibration with  $^{15Z}P_r$ -II.

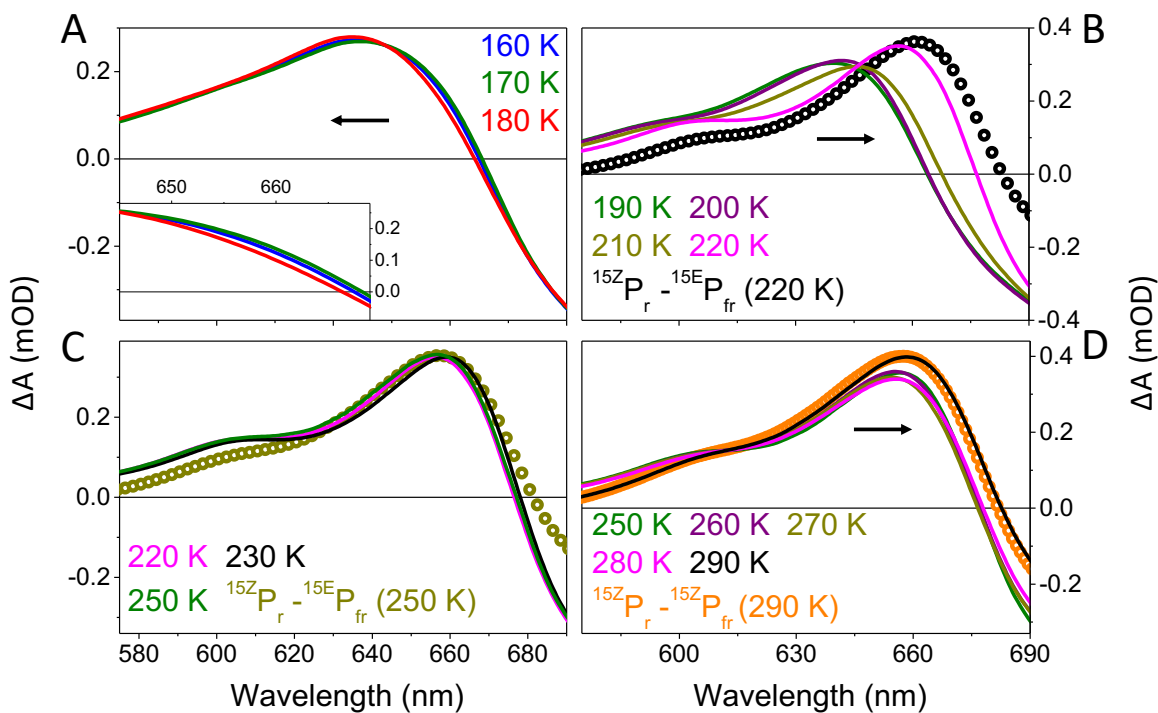


**Figure 8.10:** Terminal Cryokinetics of the Secondary Reverse Reaction of Cph1Δ

Terminal EADS (solid curves) for the reverse cryokinetics of Cph1Δ at select temperatures that captures the dynamics. The temperatures were separated to emphasize the dynamic features and ground state difference spectra (open circles) were added at a few temperatures due to the temperature dependence of the spectra (Figure A8.11).

## Discussion

### Forward Dynamics.

Building on previous studies by Kim et al.,<sup>101, 104</sup> van Thor et al.,<sup>135</sup> and Heyes et al.,<sup>303</sup> we resolved that the forward photodynamics of Cph1Δ consists of monotonic blue shifting, similar to that

observed in NpR6012g4, and subsequent non-monotonic spectral evolution. The differences in the direction of the spectral evolution coupled with the differences in the magnitude of the spectral shifts (Figures 8.4-8.6) suggest that there are two epochs in the forward dynamics of Cph1 $\Delta$  that underlie distinct mechanisms. This is demonstrated in a model potential energy surface (PES) and mechanism for Cph1 $\Delta$  (Figure 8.11) where epoch I is characterized by monotonic blue shifting from Lumi-R<sub>fr</sub> to Meta-R<sub>gl</sub> with relatively small spectral shifting and epoch II consists of non-monotonic spectral evolution with relatively large spectral shifts.

Both epochs of Cph1 $\Delta$  and NpR6012g4 all exhibited blue-shifted intermediates that absorb in the green spectral region in the forward reaction. There are multiple origins of such blue-shifted intermediates which includes: (i) deprotonation of the PCB chromophore,<sup>69, 135, 153, 306</sup> (ii) structural deformation, i.e. 'trapped twist' as assumed for NpR6012g4,<sup>197</sup> (iii) hydration of the chromophore pocket,<sup>264</sup> and (iv) charge transfer.<sup>310</sup> Charge transfer from the chromophore to a neighboring amino acid residue is possible, but an oxidized chromophore species has not been observed experimentally in phytochromes. Using resonance Raman and molecular dynamics simulations, Escobar et al.<sup>264</sup> originally postulated that hydration of the chromophore pocket following translation of a lid-Trp was the cause of the green-absorbing signaling state of AnPixJg2. The mechanism for the green absorbance was later replaced with structural deformation of the chromophore by studying mutations of conserved Phe residues of NpR6012g4 and NpR5113g2 by Rockwell et al.<sup>197</sup> and the resolved dark-adapted and signaling state structures of NpR6012g4 by Lim et al.<sup>108</sup> Since differential hydration of the chromophore pocket is likely not taking place in the single GAF domain photoreceptors, it is even less likely in a phytochrome that has a chromophore pocket even more protected from solvent. Given that epoch I of Cph1 $\Delta$  exhibited

comparable monotonic blue shifting to NpR6012g4 (Figures 8.4-8.6 and 8.11) and other red/green CBCRs, these data insinuate that Meta-R<sub>g1</sub> of Cph1Δ is likely associated with structural deformation of the chromophore.<sup>27, 29, 108, 197</sup> The dynamics observed in epoch II of Cph1Δ differed greatly from those of epoch I by consisting of relatively large non-monotonic spectral evolution. This observation, coupled with the evidence that Meta-R<sub>g2</sub> displayed similar lifetimes as the blue-shifted intermediate resolved by van Thor et al,<sup>135</sup> suggest that Meta-R<sub>g2</sub> arises from deprotonation of the chromophore. Transient deprotonation of the chromophore in the forward dynamics of Cph1Δ was further supported by cryo-Raman measurements and quantum chemical calculations by Hildebrandt and coworkers.<sup>306</sup> Transient deprotonation has been previously proposed for Cph1Δ and other bacteriophytochromes.<sup>135, 153, 306, 311, 312</sup> It is unclear which amino acid residues are associated with the transient deprotonation, but the subsequent protonation event may be due to the highly conserved His260, the freed side chain of Asp-207,<sup>61, 99, 304, 313</sup> or possibly one of the propionic acid sidechains of the bilin chromophore. Whether or not the PHY domain protonation dynamics assist the evolution to <sup>15E</sup>P<sub>fr</sub> and signal generation is presently not clear.

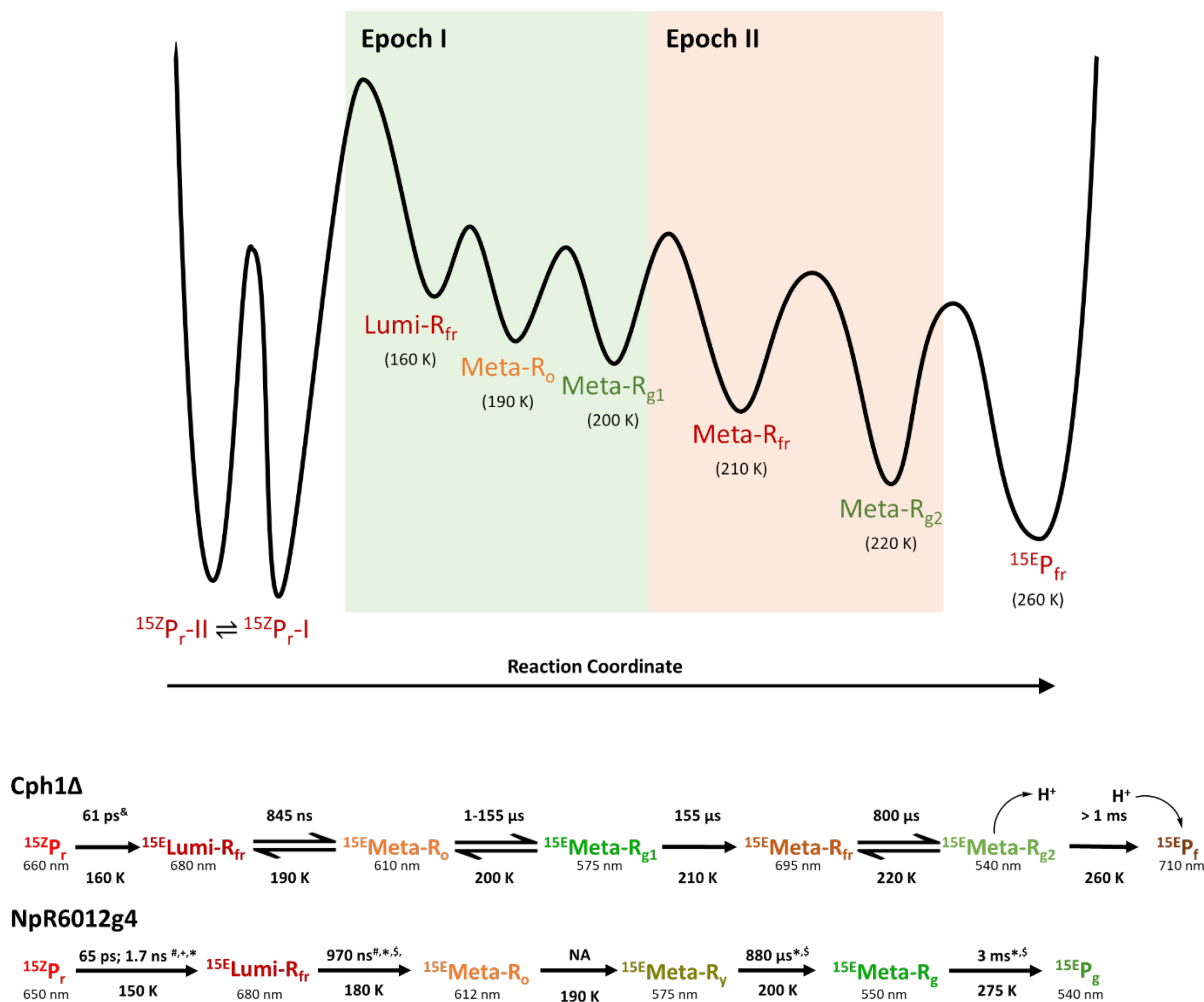


**Figure 8.11:** Forward Photocycle of Cph1Δ and NpR6012g4 and Forward PES of Cph1Δ (Top) Model PES for the forward reaction of Cph1Δ that depicts the two unique phases of the Cph1Δ forward dynamics. (Bottom) Comparison of the model forward mechanisms for Cph1Δ<sup>100, 101, 135</sup> and NpR6012g4.<sup>27, 29, 108, 176, 182, 184</sup> Note that the times and temperatures are associated with further propagation of the reaction and not the reverse reaction when equilibria were observed. The non-productive subpopulations of Cph1Δ and NpR6012g4 are not shown in the photocycles for simplicity.<sup>27, 108</sup>

The similarities in the forward dynamics of epoch I of Cph1Δ and NpR6012g4 suggest that they have similar origins (Figures 8.4-8.6 and 8.11). Since NpR6012g4 consists of only a single GAF domain, epoch I of Cph1Δ are likely due to changes in the GAF domain as Cph1Δ evolves from

its dark-adapted state to its light-adapted state. It also is not overly surprising that the GAF domain of NpR6012g4 and Cph1Δ would exhibit similar dynamics in the forward direction given their comparable  $^{15Z}P_r$  dark-adapted state spectra (Figure 8.2) and the similarities of their GAF domain sequences (Figure A8.1). Given the parallels of the forward dynamics presented here suggests that the forward photocycle of the bacterial phytochrome Cph1Δ may be more similar to the canonical red/green cyanobacteriochromes than to those of plant and bacterial phytochromes where the reported intermediates typically remain in the red to far-red spectral window.<sup>151, 153, 314, 315</sup>

While Cph1Δ and NpR6012g4 have near identical forward dynamics initially, they deviate after the population of the initial green-absorbing intermediate (Meta-R<sub>g1</sub> or Meta-R<sub>g</sub>). In NpR6012g4, subsequent intermediates continue to blue shift ultimately to match the spectra of the  $^{15E}P_g$  signaling state, whereas in Cph1Δ, these epoch I intermediates evolve via epoch II which consists of non-monotonically spectral evolution (Figures 8.4-8.6 and 8.11). Epoch II of Cph1Δ begins when Meta-R<sub>g1</sub> substantially red shifts upon forming Meta-R<sub>f</sub> before evolving to a second green-absorbing intermediate Meta-R<sub>g2</sub> that eventually red shifts upon forming the far-red absorbing  $^{15E}P_{fr}$  photoproduct.

Considering the evidence that a Meta-R<sub>f</sub> intermediate was present in the PAS-less Cph2 domain,<sup>171</sup> but not in NpR6012g4, and the evidence that the dynamics associated with this intermediate was on the same timescale as the structural evolution of the PHY domain,<sup>304</sup> we conclude that Meta-R<sub>f</sub> intermediate in Cph1Δ arises from formation of new PHY domain-chromophore interactions which stabilize the  $^{15E}P_{fr}$  signaling state.<sup>99</sup> Several changes in the PHY domain occur during

conversion of the dark-adapted state to the signaling state. These include formation of a salt bridge between the B-ring with Arg-254 and/or Arg-222, H-bonding of the D-ring carbonyl with Asp-207 and Tyr-263, or H-bonding between the C-ring with Thr-274 and Ser-272 through a water molecule as described by Essen et al.<sup>61</sup> A similar red shifting after Meta-R<sub>g</sub> was observed in the secondary forward dynamics of canonical red/green CBCR NpR4776g3, but it is unlikely to originate from the same dynamics since NpR4776g3 lacks both the PAS and PHY domains found in Cph1Δ.<sup>27</sup>

#### *Reverse Dynamics.*

The secondary reverse dynamics of both NpR6012g4 and Cph1Δ share non-monotonic spectral evolution consisting of an initial blue-shifting phase following the initial red-shifted Lumi primary photoproduct, which precedes a red-shifting phase and eventual population of the <sup>15</sup>ZP<sub>r</sub> photoproduct (Figures 8.7-8.10). A model PES for Cph1Δ and a comparison of the models for the reverse dynamics of Cph1Δ and NpR6012g4 is depicted in Figure 8.12. Unlike the forward reaction of Cph1Δ, the reverse reaction neither split into separate epochs nor exhibited features of extremely blue-shifted intermediates which could be associated with transient deprotonation events.

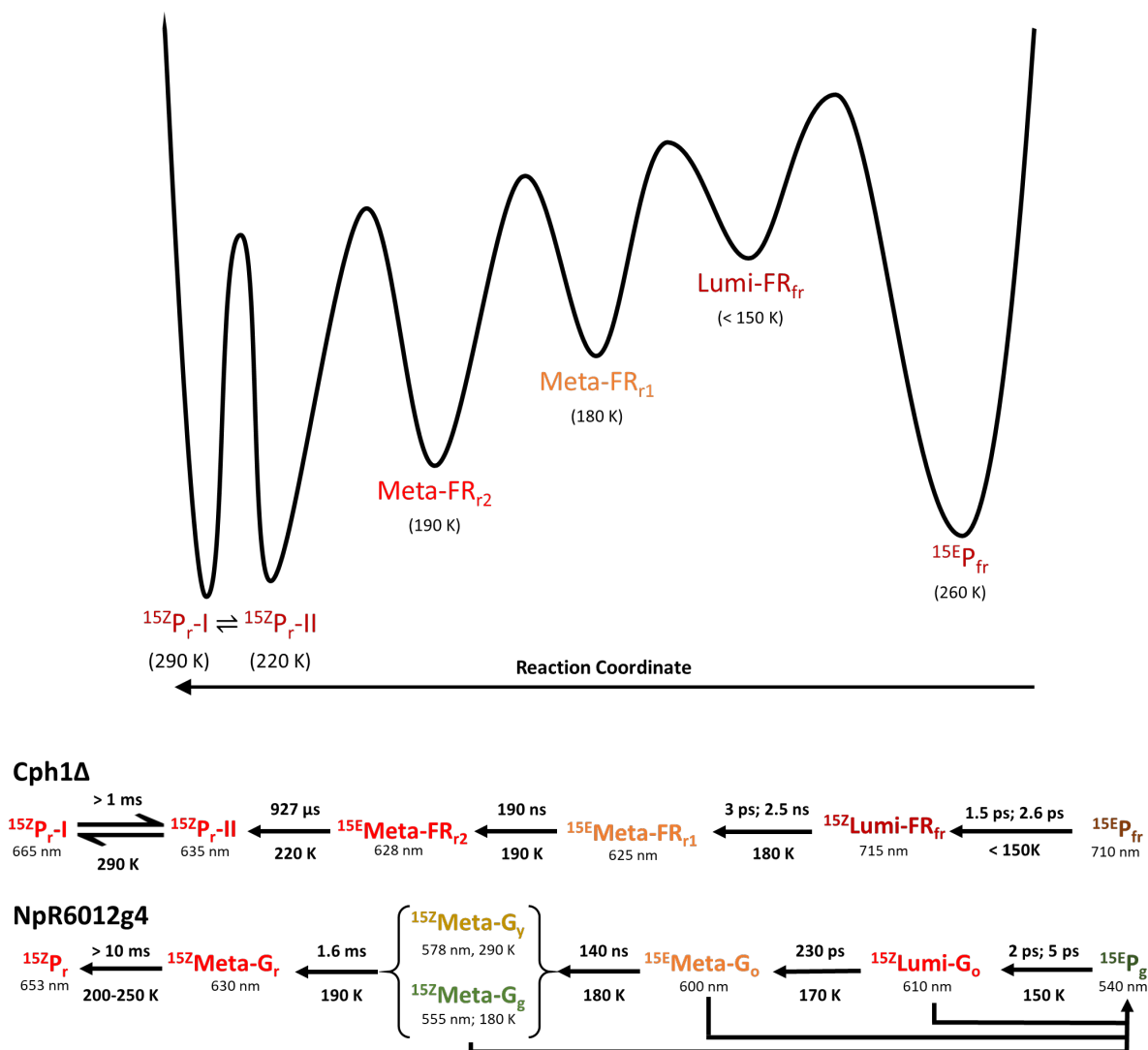


**Figure 8.12:** Reverse Photocycle of Cph1Δ and NpR6012g4 and Reverse PES of Cph1Δ

**Top)** Simplified model PES for the reverse reaction of Cph1Δ. **(Bottom)** Comparison of the model reverse mechanisms for Cph1Δ<sup>102</sup> and NpR6012g4.<sup>29, 179, 183</sup> Note that the times and temperatures are associated with further propagation of the reaction and not the reverse reaction when equilibria were observed.

While the secondary reverse TA dynamics and cryokinetics of NpR6012g4 consisted of non-monotonic evolution through meta-stable photointermediates, our cryokinetic analysis resolved

dynamics not observed in TA measurements (Figures 8.7-8.10 and 8.12). The cryokinetics of Lumi-G<sub>0</sub> and TA kinetics<sup>29</sup> of the first two Meta-G intermediates resolved a clear decay in the signal and filling of the bleach, which suggest that these photointermediates are meta-stable (Figures A8.24 and 8.8B) and that they partially decay back to the starting <sup>15</sup>E<sub>P<sub>g</sub></sub> state.<sup>29</sup> Interestingly, the cryokinetics of the reverse reaction of NpR6012g4 resolved extended blue shifting that was not observed in the room-temperature TA measurements (Figures 8.7 and 8.9). The room temperature TA dynamics revealed a yellow absorbing intermediate (Meta-G<sub>y</sub>) was populated from Meta-G<sub>0</sub>, whereas the cryokinetic analyses trapped a green absorbing intermediate (Meta-G<sub>g</sub>; Figures A8.24-8.28) at this point. Given the fact that neither of the parental states or any of the other intermediates experience this blue shift indicate that this is not a cryo-solvent or cooler temperature artifact. A plausible explanation for this blue shifting at 190 K is that the cooler temperatures allow for more severe structural deformation of the chromophore to take place before relaxing to Meta-G<sub>r</sub>. This would be consistent with the initial monotonic, stepwise blue shifting observed in the room temperature dynamics (Figures 8.7 and 8.9). Transient deprotonation is consistent with this extreme blue shifting as reported here for the forward reaction of Cph1Δ (Figures 8.4-8.6) and was proposed for the reverse dynamics of the red/green CBCR AnPixJg2 by cryo-Raman spectroscopy at 230 K.<sup>264</sup> At this temperature, evolution to the photoproduct was observed in the visible range of NpR6012g4. For this reason, NpR6012g4 could have smaller energy barriers between this intermediate and both the preceding and following populations by comparison with AnPixJg2. It should also be noted that, the room temperature dynamics of AnPixJg2 probed in the visible spectral region did not exhibit extreme blue shifting typically observed in deprotonation reactions,<sup>29, 177</sup> similar to NpR6012g4. This suggests that this extreme blue-shifted intermediate may be quickly evolving or not populated at room temperature.



Currently, it is not clear if the blue shifting is due to structural deformation or deprotonation of the chromophore. Future transient Raman or IR, and kinetic isotope studies will be useful to identify the underlying mechanisms.

Both Cph1 $\Delta$  and NpR6012g4 exhibit non-monotonic spectral evolution in the reverse dynamics. However, Cph1 $\Delta$  has a shorter blue-shifting phase and extended red-shifting phase compared to NpR6012g4 (Figures 8.7, 8.9, and A8.7B). For Cph1 $\Delta$ , there was only a single blue-shifted intermediate, resulting from evolution of residual Lumi-FR<sub>fr</sub>, whereas there were two blue-shifted intermediates for NpR6012g4 corresponding to the dual population of Meta-G<sub>o</sub> and Meta-G<sub>y</sub> photointermediates. Non-monotonic spectral evolution similar to that observed in Cph1 $\Delta$  has also been reported for the reverse dynamics of oat PhyA<sup>124, 316</sup> and CphA.<sup>124, 151</sup> Unlike red/green CBCRs, the blue shifting of the photointermediate in Cph1 $\Delta$  is likely to be attributable to the loss of interactions between the chromophore and the PHY domain rather than chromophore structural deformation. In Cph1 $\Delta$ , three populations were detected in the red-shifting epoch II phase where NpR6012g4 only had two. For both photoreceptors, the initial red shift was associated with the population of red-absorbing Meta photointermediates. Given the overlap with the ground state spectra, the second red shift was attributed to population of the fluorescent <sup>15Z</sup>P<sub>r-II</sub> parental subpopulation (Figures 8.7, 8.9, and 8.7B; 220 K, 220  $\mu$ s) in Cph1 $\Delta$  and the <sup>15Z</sup>P<sub>r</sub> parental state (Figures 8.7 and 8.9; 250 K, > 1ms) in NpR6012g4. The third red shift in Cph1 $\Delta$  was attributed to population of <sup>15Z</sup>P<sub>r-I</sub> and following equilibration of <sup>15Z</sup>P<sub>r-I</sub> and <sup>15Z</sup>P<sub>r-II</sub> (Figure 8.10). These red-shifting events can be described by structural relaxation of the chromophore to a more extended conformation since hydration was not observed in the forward reaction and the chromophore is already fully protonated. The evolution of the fluorescent <sup>15Z</sup>P<sub>r-II</sub> subpopulation to the photoactive

$^{15Z}P_r$ -I subpopulation supports the previously proposed model for the reverse dynamics of Cph1 $\Delta$  by Kim et al.<sup>102</sup> Given that the reverse dynamics are substantially different than the forward dynamics, we assert that there is no single path that connects the dark-adapted and signaling states, but rather there are unique mechanisms for the two pathways.

### ***Conclusion***

The secondary forward and reverse dynamics of Cph1 $\Delta$  and NpR6012g4 were compared, revealing similar photodynamics. The forward dynamics of Cph1 $\Delta$  revealed two epochs where the initial epoch I involves a monotonic blue shifting of photointermediates from the far-red to green spectral regions - in full agreement with those of NpR6012g4. This suggests that the restructuring of the GAF domain is the underlying mechanism of the blue shifting in both proteins. Epoch II was characterized by extreme, intermittent red- and blue-shifts within the far-red and green spectral regions. Such dynamics were concurrent with the refolding of the PHY domain and formation of new PHY-domain/chromophore interactions and possibly transient chromophore deprotonation events. The reverse dynamics of Cph1 $\Delta$  and NpR6012g4 were also similar, where a blue shifting of the intermediate(s) preceded a red shifting and eventual population the  $^{15Z}P_r$  parental state was observed. The cryokinetics of the reverse dynamics of Cph1 $\Delta$  also supports a previously published inhomogeneous model where there are photoactive ( $^{15Z}P_r$ -I) and fluorescent subpopulations ( $^{15Z}P_r$ -II) that are in equilibrium and that  $^{15Z}P_r$  -I is populated from  $^{15Z}P_r$ -II in the reverse reaction.

### *Associated Content*

*Supporting Information (pg. 333)*

### *Accession Codes*

Cph1 (Q55168) and NpR6012g4 (B2IU14)

### *Funding*

This work was supported by a grant from the Chemical Sciences, Geosciences, and Biosciences Division, Office of Basic Energy Sciences, Office of Science, United States Department of Energy (DOE DE-FG02-09ER16117) to both J.C.L. and D.S.L.

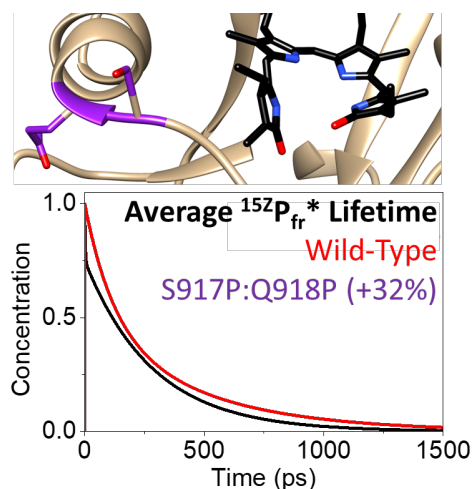
### *Acknowledgments*

This work was supported by a grant from the Chemical Sciences, Geosciences, and Biosciences Division, Office of Basic Energy Sciences, Office of Science, United States Department of Energy (DOE DE-FG02-09ER16117) to both J.C.L. and D.S.L. Nathan C. Rockwell (University of California, Davis) is acknowledged for sample preparation and constructive discussions. Dr. Mikas Vengris (Light Conversion Ltd.) is also acknowledged for the donation of global and target analysis software. Molecular graphics images were produced using the UCSF Chimera package from the Resource for Biocomputing, Visualization, and Informatics at the University of California, San Francisco (supported by NIH P41 RR-01081).

## Chapter 9. Extending Cyanobacteriochrome Photoswitching into the Far-Red

### *Abstract*

The identification or generation of relatively small far-red absorbing photoreceptor proteins is currently of great interest for the development of more easily detectable fluorescent probes for medicinal imaging and non-invasive optogenetic tools to selectively initiate and control biological responses in living tissue. Cyanobacteriochromes (CBCRs) are a class of relatively



small (~150 amino acid) photoreceptors with a newly reported family that has an unprecedented far-red absorbing dark-adapted state due to unique chromophore-protein interactions. To ascertain the nature of these far-red CBCRs and if they are a promising basis for further development of novel biological tools, we report the first ultrafast forward photodynamic study of a wild-type and mutated far-red CBCR (Anacy\_2551g3). The photodynamics resolved significant near-infrared (NIR) stimulated emission (SE) and the possible population of spectrally heterogeneous Lumi-FR photointermediates that were associated with chromophore tautomer heterogeneity. The mutation resulted in an ~32% elongated average excited state lifetime, suggesting an increase in SE, and an increase in the Lumi-FR quantum yield, providing a foundation for further engineering of these photoreceptors for the development of novel biological tools.

## ***Introduction***

Recently a lot of effort has been given to the development of NIR fluorescent probes and non-invasive optogenetic tools to control biological function in living tissue.<sup>44, 47, 50, 202</sup> The difficulty lies in the development of photostable biological tools that are either highly fluorescent or highly photoproduct yielding and absorb in the far-red due to deeper tissue penetration. Photoreceptor proteins are a good starting point for the development of novel biological tools since they have evolved to make photosynthesis more efficient via chromatic acclimation<sup>25, 26, 259, 285, 296</sup> and initiate an array of biological responses upon illumination.<sup>18, 19, 22, 24, 30</sup> One of the first classes of photoreceptors discovered were phytochromes which are tri-domain (PAS-GAF-PHY) linear tetrapyrrole (bilin)-based proteins originally found to dictate plant growth and shade avoidance by measuring the ratio of red to far-red light.<sup>20, 21</sup> Phytochromes were later discovered to be extensively present in various biological systems including algae, fungi, and bacteria.<sup>246, 279, 280</sup> Cyanobacteriochromes (CBCRs) are a related class of photoreceptors that were more recently discovered in cyanobacteria and while they also utilize a bilin chromophore, they only require a single GAF domain for reversible photoconversion spanning the near UV to far-red spectral regions.<sup>63, 64, 68, 69, 110, 281-283</sup> This wide-ranging spectral photosensitivity is the result of diverse chemical responses that includes protonation events<sup>285</sup> and secondary cysteine linkages,<sup>64, 68, 110</sup> as well as the incorporation of bilin chromophore with varied conjugation lengths.<sup>64, 65, 67, 68, 108, 109</sup> This diverse spectral photosensitivity of CBCRs coupled with their relatively small size and that they have evolved to improve the efficiency of photosynthesis via chromatic acclimation<sup>25, 26, 296</sup> and initiate various biological responses such as phototaxis<sup>22, 23</sup> makes CBCRs attractive candidates to serve as a basis for engineering novel biological tools. Despite all the positive attributes of CBCRs and that some members of the phytochrome superfamily having already been

extensively exploited for fluorescent imaging<sup>44-47</sup> and optogenetic applications,<sup>270, 271, 273-275</sup> the biological application of tools derived from CBCRs were limited until Rockwell et al. recently discovered a new family of CBCRs that is distantly related to the green/red family and have an unprecedented far-red absorbing dark-adapted state (Figure 9.1; black curves).<sup>63</sup>

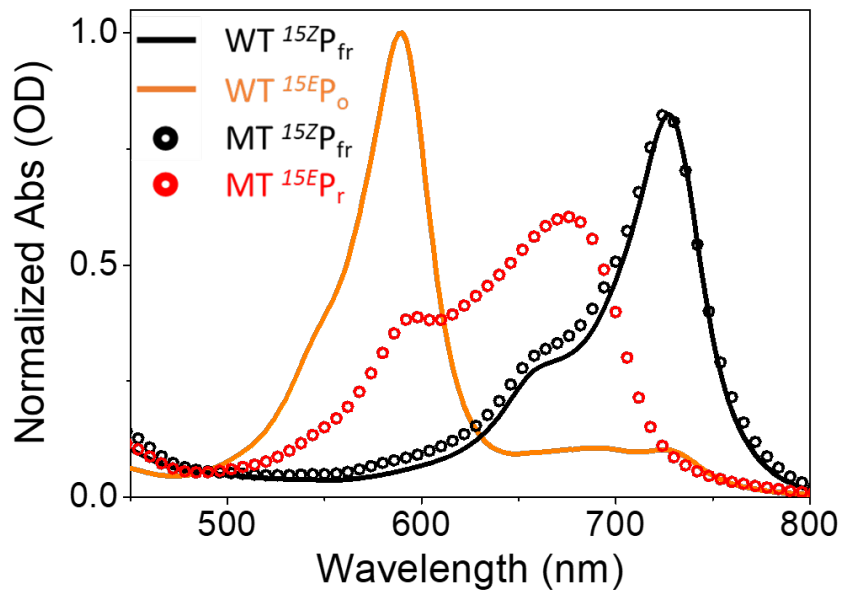


**Figure 9.1:** WT and S917P:Q918P Anacy\_2551g3 Parental State Spectra

UV-Vis spectrum of wild-type (WT; solid lines) and S917P:Q918P (MT; open circles) Anacy\_2551g3 in the  $^{15Z}P_{fr}$  dark-adapted (black curves) and  $^{15E}P_x$  light-adapted (orange and red curves) states. For the light-adapted state, 'x' is in place for 'o' and 'r' for the WT and MT, respectively. Both spectra for WT were scaled by the normalization factor for  $^{15E}P_o$  and both spectra for S917P:Q918P were scaled by the same factor that overlapped  $^{15Z}P_{fr}$  S917P:Q918P with  $^{15Z}P_{fr}$  WT.

Interestingly, some members of the far-red CBCR family incorporates the same phycocyanobilin (PCB) chromophore<sup>63</sup> as other CBCRs such as red/green<sup>108, 291</sup> and green/red CBCRs,<sup>109</sup>

suggesting that there may be unique chromophore-protein interactions in the far-red family that underlie this spectral sensitivity. To determine what these interactions could be, Bandara et al.<sup>67</sup> determined the structure of the  $^{15Z}P_{fr}$  dark-adapted state of Anacy\_2551g3 from *Anabaena cylindrica* PCC 7122 using X-ray crystallography (Figure 9.2A). The analysis of the structure suggested that the far-red absorbance could be due to a diprotonated-A-ring lactim and interactions between Glu914 and the NH group of the D-ring. These chromophore-protein interactions were stabilized by a cyclic 15Z, all-syn chromophore conformation (Figure 9.2 and Figure A9.2) which has only been resolved in the  $^{15E}P_r$  light-adapted state of RcaE from *Fremyella diplosiphon*,<sup>109</sup> a green/red CBCR, to date. While this tautomer was proposed to be the most probable for Anacy\_2551g3, many tautomers are possible (Figure 9.2B-E) that could initiate unique dynamics as observed in RcaE.<sup>190</sup> Furthermore, the presence of spectrally heterogeneous tautomers would be consistent with the shoulder blue shifted of the maxima in the  $^{15Z}P_{fr}$  dark-adapted spectrum of Anacy\_2551g3 (Figure 9.1) since comparable spectral features were observed in the spectra of the structurally heterogeneous  $^{15Z}P_r$  dark-adapted state of red/green CBCRs.<sup>27, 108</sup>

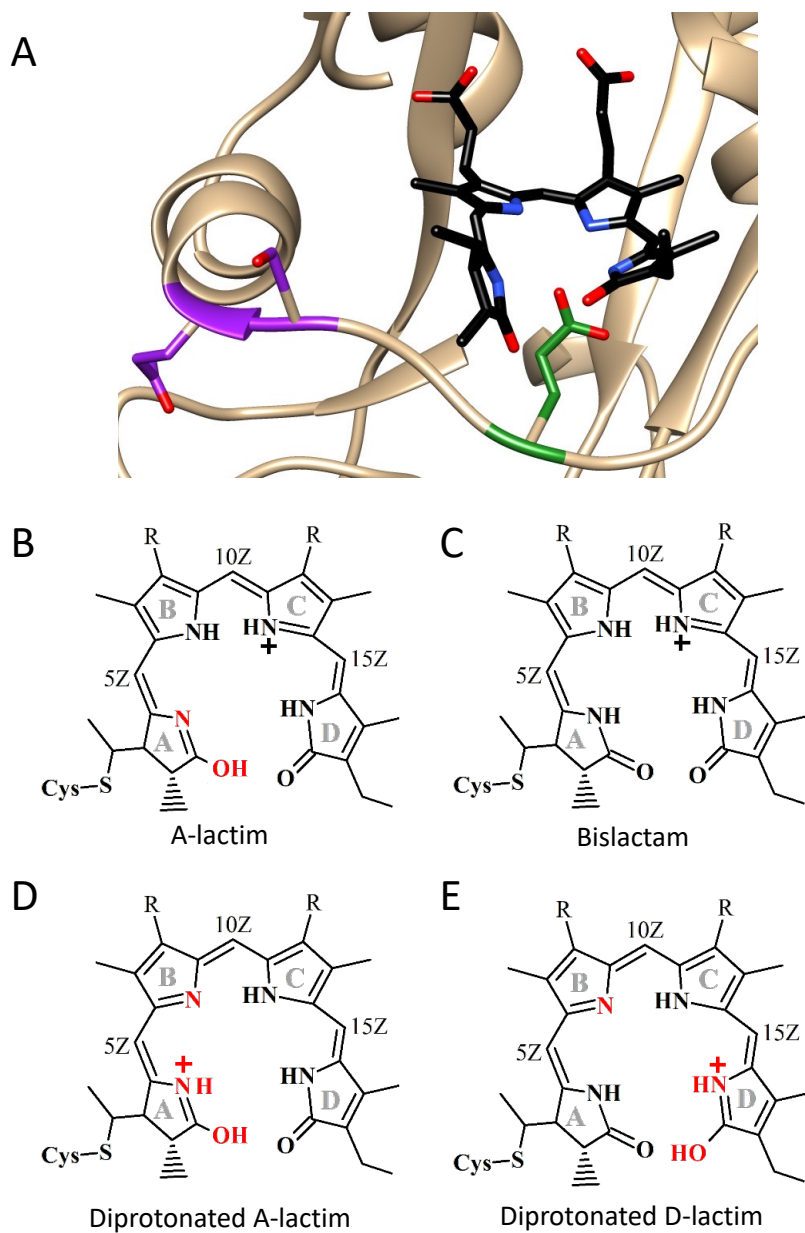


**Figure 9.2:** WT Anacy\_2551g3  $^{15}\text{ZP}_f$  Dark-Adapted State Structure and Possible Chromophore Tautomers

(A) Structure of the  $^{15}\text{ZP}_f$  dark adapted state of WT Anacy\_2551g3 (6UV8) that has a 15Z, all-syn chromophore conformation. The glutamate (Glu914) that interacts with the NH groups of the pyrrole rings and associated with generating the far-red absorbance in part is colored green. The residues replaced with proline in S917P:Q918P Anacy\_2551g3 are colored purple. Note that the protein ‘ribbon’ was reduced for ease of viewing the chromophore structure and placement of Glu914, Ser917, and Gln918. (B-E) Possible chromophore tautomers for WT Anacy\_2551g3.<sup>67</sup>



Given the unique chromophore conformation and proteins interactions as well as the likely presence of dark-adapted state tautomers in Anacy\_2551g3,<sup>67</sup> it is unclear how many unique intermediates are populated upon photoexcitation and if they are photoactive and populate the light-adapted state or decay back to the dark-adapted state as previously observed in other CBCRs.<sup>27, 29, 108, 190</sup> Determining the efficiencies of the fluorescent and photointermediate pathways as well as the stability of the photointermediate(s) is essential for ascertaining if this far-red family of CBCRs are a good basis for the development of novel biological tools. To address these uncertainties, we report the first study on the ultrafast forward dynamics of a representative of the far-red CBCR family, Anacy\_2551g3. Furthermore, a previously reported S917P:Q918P mutant of Anacy\_2551g3 that incorporated two prolines directly outside of a highly conserved Asp motif associated with spectral tuning and was inspired by the then believed photoinactive Oscil6304\_4080 from *Oscillatoria acuminata* PCC 6304 was also characterized to observe any changes in the primary forward dynamics.<sup>63, 67</sup> Interestingly, the mutation of Anacy\_2551g3 did not significantly influence the spectra of the dark-adapted state but had a profound impact on the light-adapted state spectra (Figure 9.1), significantly red shifting the maxima and creating a dual peak feature. The dual peaks suggested the presence of <sup>15E</sup>P<sub>o</sub> and <sup>15E</sup>P<sub>r</sub> subpopulations where the <sup>15E</sup>P<sub>o</sub> is preferred in wild-type (WT) and <sup>15E</sup>P<sub>r</sub> is preferred in S917P:Q918P.

### ***Anacy\_2551g3 Primary Forward Dynamics***

Since the dark-adapted state of Anacy\_2551g3 was suspected to be heterogeneous, ultrafast Dual Excitation Wavelength Interleaved (DEWI) pump-probe spectroscopy coupled with broadband detection in the visible (~475-730 nm) and NIR (~770-880 nm) spectral regions and global analysis methods were used to characterize the primary forward dynamics of WT and S917P:Q918P

Anacy\_2551g3. DEWI was preferred over more standard individual pump-probe measurements for studying the excitation energy dependence of the dynamics because the influence of sample degradation and light fluctuations are minimized by performing the pump-probe measurements near simultaneously. This technique was previously used to study the dynamics of the  $^{15Z}P_g$  tautomers of RcaE by Gottlieb et al.<sup>190</sup> and the heterogeneous H-bonding networks of the  $^{15Z}P_r$  subpopulations in the photosensory core of cyanobacterial phytochrome 1 from *Synechocystis* sp. PCC 6803 by Kirpich et al.<sup>100</sup> A description of DEWI spectroscopy and global analysis is provided in the Supplemental Information (SI). In order to focus on the forward dynamics in this letter, the reverse dynamics of these photoreceptors will be discussed elsewhere.<sup>317</sup>

Despite the likely presence of distinct  $^{15Z}P_{fr}$  ground state subpopulations in WT Anacy\_2551g3 given the dual peak feature in the fluorescence spectrum,<sup>63</sup> chromophore similarities to RcaE,<sup>190</sup> and dark-adapted spectral shape similarities to red/green CBCRs,<sup>27, 108</sup> the observed dynamics displayed no signs of excitation energy dependence (Figures A9.5-A9.8). This indicates that either both excitation wavelengths are initiating the same dynamics or that excited state tautomers equilibrate faster than the temporal resolution of the experiment. Due to the lack of significant differences in the transient data sets, only the 730 nm excitation data set is discussed here (Figures 9.3 and 9.4), while the additional data is in the SI (Figures A9.4-A9.8).

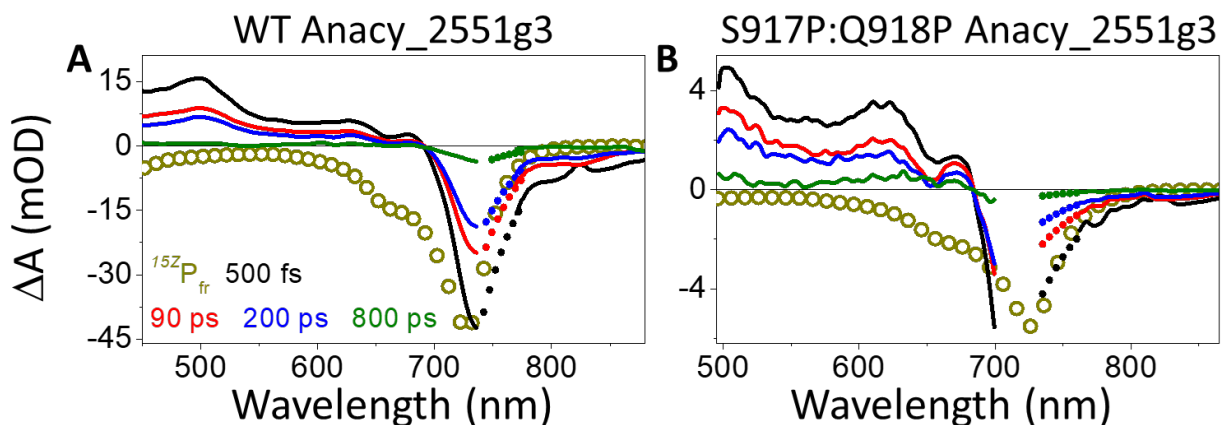


**Figure 9.3:** WT and S917P:Q918P Anacy\_2551g3 Primary Forward Transient Difference Spectra

Forward transient difference spectra of (A) WT and (B) S917P:Q918P Anacy\_2551g3 after 730 nm excitation and probed in the visible and NIR spectral regions. The transient NIR difference spectra were scaled such that they roughly match the inverted  $^{15Z}P_{fr}$  absorbance when the inverted  $^{15Z}P_{fr}$  absorbance was scaled to the visible bleach (dark yellow circles). The solid lines represent the collected difference spectra, and the dots were made by adding a gaussian function to the spectral gap. The  $\sim 820$  nm peaks were associated with second order diffraction of residual 410 nm from the noncollinear optical parametric amplifier.

Upon photoexcitation, WT and S918P:Q918P Anacy\_2551g3 exhibited  $^{15Z}P_{fr}^*$  excited state absorption blue shifted of a far-red ground state bleach (GSB) and stimulated emission (SE) in the near infrared (NIR) spectral region (Figures 9.3 and A9.4-A9.8). As  $^{15Z}P_{fr}^*$  decayed, long lived positive absorption was observed in the red ( $\sim 660$  nm; Figures 9.4A, 9.4B, and A9.4) and NIR (805 nm; Figures 9.4C&D) spectral regions, indicating the population of photointermediates. The NIR absorbance of an intermediate signifies a greater spectral shift between the GSB and initial intermediate than was observed in the forward reaction of other CBCRs<sup>28, 111, 176</sup> and is comparable to that of RcaE.<sup>190</sup>

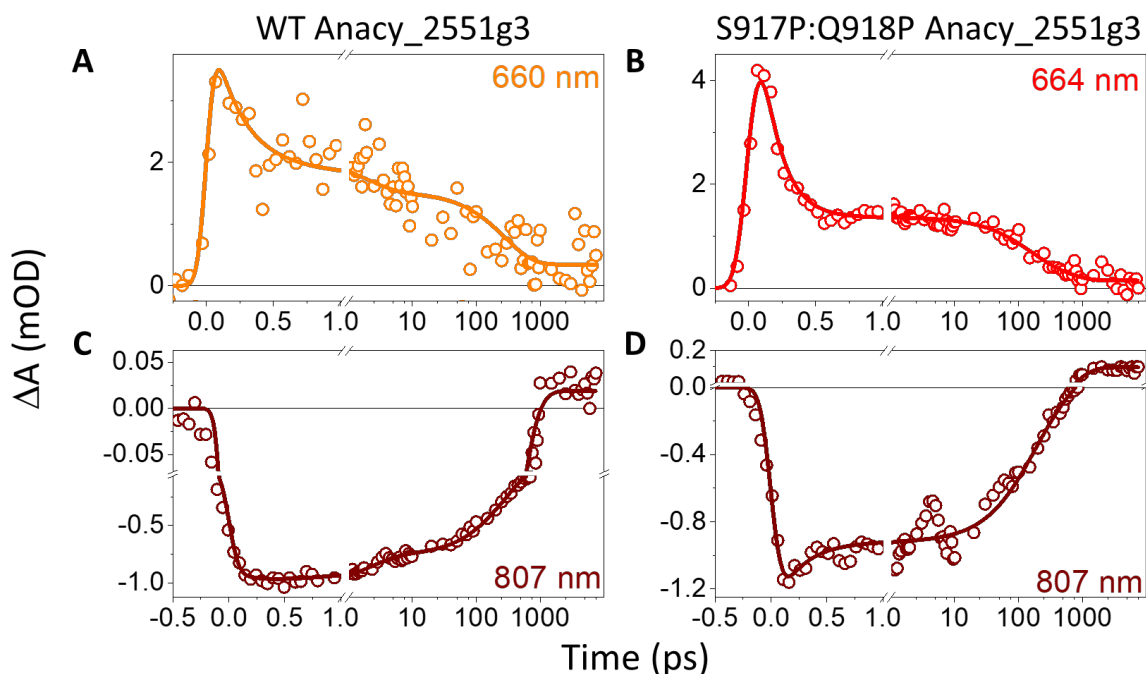


**Figure 9.4:** WT and S917P:Q918P Anacy\_2551g3 Primary Forward Kinetic Traces

Kinetic traces at select wavelengths of WT (A, C) and S917P:Q918P (D, E) Anacy\_2551g3 after 730 nm excitation. The 805 nm kinetics for both samples were normalized at the average SE maximum near 0.5 ps for ease of comparison. The open circles represent the data and the solid lines are the fit from the global analysis.

### ***Results and Discussion***

The sequential (Figures A9.10-A9.12; Table A9.4) and target (Figure 9.5 and Figure A9.14; Table A9.5) global analysis modeling of the visible and NIR dynamics (discussed in the SI) extracted two spectrally homogenous  $^{15}\text{ZP}_{\text{fr}}^*$  excited state subpopulations and long living positive absorbance bands in the red and NIR spectral regions at later times ( $>1000$  ps; Figure 9.5 and Figure A9.14). Since the two  $^{15}\text{ZP}_{\text{fr}}^*$  spectra were spectrally identical indicates that if different  $^{15}\text{ZP}_{\text{fr}}$  tautomers were excited, they would have equilibrated quicker than the temporal resolution of the experiment (Figure 9.5). While long lived positive red and NIR absorbances were extracted,

it is unclear how many distinct intermediates are present within the first 8 ns and how they are connected given the lack of a clear decay of the positive intermediate bands at 660 or 805 nm and the ambiguity of when the red-absorbing population was generated (Figure 9.4). Given the kinetics, one may conclude that there is a single intermediate that spans the red to NIR spectral regions. However, if one were to expect that Anacy\_2551g3 is to behave like other CBCRs they could conclude that there may be two separate intermediate populations since broad Lumi intermediates spanning ~200 nm have yet to be resolved.<sup>28, 111, 176, 190, 194</sup> If there are two spectrally heterogeneous intermediates, they could be populated sequentially where a primary NIR absorbing Lumi (Lumi-FR<sub>n</sub>) can evolve into a secondary red absorbing Meta (Lumi-FR<sub>n</sub> → Meta-FR<sub>r</sub>) or vice-versa, or in parallel (i.e., Lumi-FR<sub>n</sub> and Lumi-FR<sub>r</sub>). Since a decay in the kinetics at the photointermediate bands was not observed, it is possible that two spectrally heterogeneous Lumi-FR intermediates were populated directly from <sup>15Z</sup>P<sub>fr</sub>\*. Considering the likely presence of chromophore tautomers in the <sup>15Z</sup>P<sub>fr</sub> dark-adapted states of Anacy\_2551g3 and RcaE and that three spectrally heterogeneous Lumi-G intermediates were resolved in the forward dynamics of RcaE,<sup>190</sup> the observation of spectrally heterogeneous Lumi-FR populations in Anacy\_2551g3 would not be that surprising. To address these uncertainties, pump-dump-probe spectroscopy in the same time region and transient absorption spectroscopy beyond 8 ns could be performed.

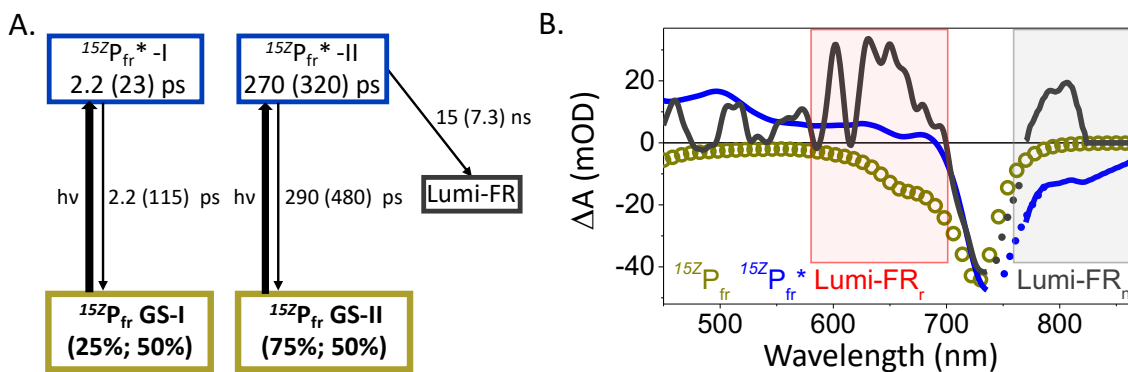


**Figure 9.5:** WT Anacy\_2551g3 Target Model and SADS

(A) Target models for the forward reactions of WT and S917P:Q918P (time constants in parenthesis) of Anacy\_2551g3 in the visible and NIR regions after 730 nm excitation. (B) WT Anacy\_2551g3 SADS spanning the visible and NIR spectral regions. SADS for S917P:Q918P Anacy\_2551g3 is available in the SI (Figure A9.14).

The generation of two coexisting, spectrally heterogeneous Lumi-FR intermediates that are either blue or red shifted of the GSB could be attributed to either unique tautomers being excited and having unique dynamics or excitation of a single tautomer with a bifurcation in the dynamics that results from fundamental changes of the chromophore. Since the  $^{15Z}P_{fr}$  dark-adapted ground state of Anacy\_2551g3 is likely composed of several different tautomers,<sup>67</sup> the vertical excitation energies of four probable chromophore tautomers were determined using the hybrid quantum mechanics/molecular mechanics (QM/MM) methodology described in the SI (Figure 9.2B-E; Table 9.1 and Table A9.6). The calculations resolved an  $\sim 100$  nm separation between the diprotonated lactim tautomers and either bislactam or A-lactim, suggesting that the red-absorbing intermediate may arise from a diprotonated lactim tautomer and that the NIR species may originate from either bislactam or A-lactim. The spectral separation of intermediates originating from these tautomers could then be amplified upon the isomerization of the chromophore to match the

experimental intermediate absorption bands through modification of the structural conformation of the chromophore, or manipulation of protein-chromophore interactions involving the A- or D-rings.<sup>67</sup> For example, loss of these interactions that generate and stabilize the far-red absorbance or an increase in the structural deformation of the chromophore could generate a relatively blue shifted Lumi-FR<sub>r</sub> intermediate and structural relaxation of the chromophore could generate a red shifted Lumi-FR<sub>n</sub> intermediate.

**Table 9.1:** Plausible Chromophore Tautomers Hybrid QM/MM Vertical Energies  
QM/MM vertical excitation energies using the ground state geometries of the four probable tautomers (Figure 9.2) in the <sup>15Z</sup>P<sub>f</sub> dark-adapted state.

Tautomer (Tautomer in Scheme 1)	GS nm (eV)
Bislactam (C)	660 (1.88)
A-Lactim (B)	675 (1.84)
Diprotonated A-Lactim (D)	566 (2.19)
Diprotonated D-Lactim (E)	571 (2.17)

The influence of protonation state of the chromophore on the photoinduced dynamics have been characterized for the phytochrome superfamily<sup>73, 112, 135, 190</sup> where transient deprotonation of the chromophore has been reported in phytochromes<sup>73, 135</sup> and was suggested to be the origin of the non-radiative deactivation pathway accounting for > 80% of the photoexcited molecules of RpBphP3 from *Rhodospseudomonas palustris*.<sup>112</sup> While both Lumi-FR intermediates resolved here are stable up to 8 ns, experiments on the longer timescales are required to establish the photo-productivity of the intermediates and track the mechanism through to the generation of the light adapted state.

### ***WT vs. S917P:Q918P: A Model for Increased Fluorescence and Photointermediate Quantum Yield***

The global analysis of WT and S917P:Q918P Anacy\_2551g3 resolved a doubling of the photointermediate quantum yield and extension of the average  $^{15}ZP_{fr}^*$  lifetime by ~32%, suggesting an increase in fluorescence, (Figures 9.5, A9.14, and A9.15; Table A9.5) that indicates that the mutant may be better suited than the WT for incorporation as fluorescent imaging or optogenetic tools. The underlying mechanism behind the longer lived  $^{15}ZP_{fr}^*$  and the increase in Lumi-FR quantum yield in S917P:Q918P Anacy\_2551g3 is currently unclear since the replaced residues were not near the D-ring of the chromophore nor removed a clear H-bonding network to the chromophore for WT Anacy\_2551g3 (Figure 9.2A) and a high-resolution structure of the  $^{15}ZP_{fr}$  dark-adapted state of S917P:Q918P Anacy\_2551g3 is not currently available. Given that the mutation introduced two prolines near the chromophore pocket and prolines have been known to influence the structure of proteins, a restructuring of the chromophore pocket and subsequent alteration of hydrogen bonding networks to relatively favor the unproductive subpopulation and facilitate the D-ring isomerization for the productive subpopulation is feasible and consistent with the global analysis (Figure 9.5A).

### ***Concluding Comments***

To conclude, we reported the first ultrafast forward dynamics on the recently discovered far-red/x CBCR family that have unique chromophore-protein interactions<sup>67</sup> and are of great interest for engineering more easily observed fluorescent probes for biological imaging and non-invasive optogenetic tools to control biological activity in living tissue. The ultrafast forward dynamics resolved significant SE in the NIR spectral region as well as two spectrally heterogeneous Lumi-



FR photointermediates that were attributed to different chromophore tautomers. The introduction of two proline residues right outside of a conserved Asp motif associated with spectral tuning lengthened the  $^{15Z}P_{fr}^*$  excited state lifetime by ~32% and nearly doubled the estimated Lumi-FR photointermediate quantum yield. This would be of interest for those wanting to engineer novel fluorescent imaging or optogenetic tools and suggest that this family of CBCRs are well suited for further development as biological tools.

### *Associated Content*

#### *Supporting Information (pg. 365)*

Experimental and theoretical methods, structural information, forward dynamics of WT and S917P:Q918P Anacy\_2551g3 at other excitation energy, discussion of sequential and target model global analysis, and QM/MM vertical excitation energies.

#### *Accession Codes*

Anacy\_2551g3 (K9ZI18) and RcaE (Q47897)

#### *Funding*

This work was supported by a grant from the Chemical Sciences, Geosciences, and Biosciences Division, Office of Basic Energy Sciences, Office of Science, United States Department of Energy (DOE DE-FG02-09ER16117) to both J.C.L. and D.S.L.

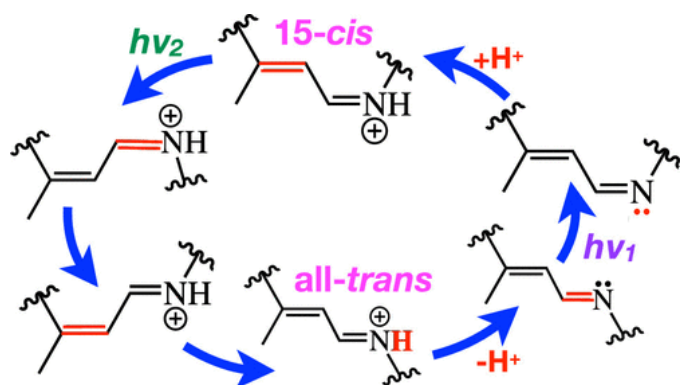
#### *Acknowledgments*

This work was supported by a grant from the Chemical Sciences, Geosciences, and Biosciences Division, Office of Basic Energy Sciences, Office of Science, United States Department of Energy (DOE DE-FG02-09ER16117) to both J.C.L. and D.S.L. Nathan C. Rockwell (University of California, Davis) is acknowledged for sample preparation and constructive discussions. Dr. Mikas Vengris (Light Conversion Ltd.) is also acknowledged for the donation of global and target analysis software. Molecular graphics images were produced using the UCSF Chimera package from the Resource for Biocomputing, Visualization, and Informatics at the University of California, San Francisco (supported by NIH P41 RR-01081).

# Chapter 10. Computational and Spectroscopic Characterization of the Photocycle of an Artificial Rhodopsin

## Abstract

The photocycle of a reversible photoisomerizing rhodopsin mimic (M2) is investigated. This system, based on the cellular retinoic acid binding protein, is structurally different from natural



rhodopsin systems, but exhibits a similar isomerization upon light irradiation. More specifically, M2 displays a 15-cis to all-trans conversion of retinal protonated Schiff base (rPSB) and all-trans to 15-cis isomerization of unprotonated Schiff base (rUSB). Here we use hybrid quantum mechanics/molecular mechanics (QM/MM) tools coupled with transient absorption and cryokinetic UV-vis spectroscopies to investigate these isomerization processes. The results suggest that primary rPSB photoisomerization of M2 occurs around the C13=C14 double bond within 2 ps following an aborted-bicycle pedal (ABP) isomerization mechanism similar to natural microbial rhodopsins. The rUSB isomerization is much slower and occurs within 48 ps around the C15=N double bond. Our findings reveal the possibility to engineer naturally occurring mechanistic features into artificial rhodopsins and also constitute a step toward understanding the photoisomerization of UV pigments. We conclude by reinforcing the idea that the presence of the retinal chromophore inside a tight protein cavity is not mandatory to exhibit ABP mechanism.

## ***Introduction***

Rhodopsins are a family of photoreceptor proteins found in all domains of life.<sup>205, 318, 319</sup> All members of the rhodopsin family exhibit a similar protein architecture consisting of a retinal chromophore (a retinal unprotonated (rUSB) or protonated Schiff base (rPSB)) located in a tight protein cavity formed by seven interconnected transmembrane  $\alpha$ -helices.<sup>318</sup> In the presence of light, rPSB undergoes a selective *cis*→*trans* or *trans*→*cis* double bond isomerization initiating crucial biological functions such as visual and non-visual functions in superior animals, ion transport, ion gating, phototaxis and gene expression in archaea and eubacteria.<sup>205</sup> The rPSB photoisomerization is one of the fastest and most efficient reactions in nature. For instance, in the dim-light visual pigment rhodopsin the isomerization is complete within 200 fs<sup>320, 321</sup> with a 0.65 quantum yield.<sup>287</sup> The rPSB isomerization in rhodopsin occurs inside a tight protein cavity through a unique space-saving mechanism called aborted-bicycle pedal (ABP) isomerization where two neighboring double bonds isomerize concertedly in opposite directions and one bond completes the isomerization and reaches the product while the other returns to the original configuration.<sup>322-</sup>

326

Recently, Geiger, Borhan and coworkers engineered the first artificial rhodopsin mimics that can reversibly photoisomerize.<sup>74</sup> A hexamutant (R111K:Y134F:T54V:R132Q: P39Y:R59Y) of a cytoplasmic protein called cellular retinoic acid binding protein II (CRABPII) (M2) was prepared by mutating CRABPII such that retinal reacts with a specific lysine residue inside the protein cavity to form a Schiff base linkage and react to light in a way similar to natural rhodopsins.<sup>74, 327,</sup>  
<sup>328</sup> Remarkably, M2 appears to display a photochromic cycle (from now on called photocycle) also observed in certain natural rhodopsins (e.g. in *Anabaena* sensory rhodopsin or in, so-called,

bistable rhodopsins such as melanopsin and jumping spider rhodopsin)<sup>329-331</sup> which has been investigated using UV spectroscopy and X-ray crystallography. In the thermodynamically favored form of M2 (M2<sub>AT</sub>-USB), the bound chromophore has the all-trans rUSB conformation. When irradiated with UV light (~360 nm), the chromophore isomerizes to the 15-*cis* rPSB conformation yielding a new protein form (M2<sub>15C</sub>-PSB). In the presence of green light (~550 nm) or heat, M2<sub>15C</sub>-PSB is transformed back to M2<sub>AT</sub>-USB. Such transformations can be repeated continuously, switching the system between the M2<sub>AT</sub>-USB and M2<sub>15C</sub>-PSB forms.

The molecular-level elucidation of the intermediate steps driving the M2 photocycle appears to be an important endeavor. This is key in identifying engineering rules allowing for the design and preparation of artificial light-responsive proteins mimicking natural systems. These can provide new molecular devices<sup>332-335</sup> functioning as sensors and actuators useful in bio-imaging and neuromedical science and, more generally, in synthetic biology.<sup>336</sup>

Due to the current absence of spectroscopic and theoretical studies, our present knowledge of the steps driving the M2 photocycles are, regrettably, highly incomplete. To date, only a single dynamic study on a triple mutant of CRABP-II has been reported.<sup>209</sup> In the present work we are particularly interested in the direct (all-*trans* to 15-*cis*) and reverse (15-*cis* to all-*trans*) photochemical steps. Indeed, (i) such photochemical steps have not been characterized in several aspects such as isomerization mechanism and time-scale and (ii) the following thermal steps, corresponding to successive conformational changes and connecting M2<sub>AT</sub>-USB to M2<sub>15C</sub>-PSB and *vice-versa* has also not been resolved.

The current information on M2 reveals several biomimetic features. In fact, (i) while the CRABPII is very different from opsin, the retinal chromophore isomerizes upon irradiation and it is somehow coupled with proton translocation as in certain microbial rhodopsins,<sup>205</sup> however (ii) the isomerization takes place around C15=N rather than the C11=C12 or C13=C14 bonds of natural rhodopsins. Thus, the investigation of the M2 photocycle will not only allow us to uncover the missing information mentioned above; but will also provide a model for studying how the protein/chromophore interactions affect the rhodopsin photoisomerization regioselectivity in general.

To address the issues above we have used a combined computational and experimental approach. More specifically, we use a sub-population of 20 initial conditions to simulate the light induced dynamics of M2<sub>15C</sub>-PSB and M2<sub>AT</sub>-USB for up to 0.8 ps via Tully's semi-classical trajectory computations at the state average CASSCF/6-31G\*/AMBER level of theory (see section SI1).<sup>337</sup> The construction of QM/MM models of both M2<sub>15C</sub>-PSB and M2<sub>AT</sub>-USB is performed using recently reported ASEC-FEG protocol<sup>338</sup> that involves geometry optimization on a free energy, rather than potential energy, surface. Such models are subsequently used to study the reaction timescales using semi-classical trajectories. In addition to the trajectories, the possible reaction paths for M2<sub>AT</sub>-USB photoisomerization around C11=C12, C13=C14 and C15=N bonds are mapped using relaxed scans. The results of simulations are compared against time resolved and temperature resolved dynamics. The sample preparation and experimental protocols are outlined in section S2. Ultrafast transient broadband absorption spectroscopy was performed at room temperature as previously described,<sup>262</sup> to ascertain the efficiency of these photoreactions. The M2<sub>15C</sub>-PSB and M2<sub>15C</sub>-PSB photodynamics were initiated with 565 nm and 400 nm, respectively.

Temperature and time resolved dynamics were measured using cryokinetic UV-Vis absorption spectroscopy as previously reported and outlined in the SI.<sup>339</sup> LEDs resonant with absorption bands of the starting populations were used to initiate the photoreaction and the cryogenic temperatures trap the resulting photointermediates. As the temperature of the sample is raised, the photointermediates evolve, allowing for the mapping of the photo-mechanism.

### ***M2<sub>15C</sub>-PSB and M2<sub>AT</sub>-USB QM/MM models***

The wavelength of the absorption maximum ( $\lambda_{\text{max}}$ ) of M2<sub>15C</sub>-PSB and M2<sub>AT</sub>-USB computed using the constructed QM/MM models were 499 nm (57.3 kcal/mol or 2.48 eV) and 345 nm (83.0 kcal/mol or 3.60 eV) respectively. These values are blue shifted by ca. 7 and 5 kcal/mol (0.30 and 0.22 eV) respectively relative to the observed values (see Figure 10.1) and, consistently, the values reported by Borhan, Geiger, and coworkers.<sup>74</sup> These values lie within the reported systematic error (7.5 kcal/mol or 0.33 eV) of the ASEC-FEG protocol which is expected to correctly reproduce trends in  $\lambda_{\text{max}}$  rather than in absolute values.<sup>338</sup> Furthermore, the visual comparison of computed model against the crystallographic structure indicated that the modeled and observed backbone are comparable with the exception of residues 55 to 60. As detailed in the supporting text, such backbone deviation appears to remove a potentially important  $\pi$ -stacking interaction between a tyrosine residue (TYR59) and the  $\beta$ -ionone region of the chromophore. The impact of such removal in our model has been directly tested and found not to significantly modify the vertical excitation energy nor the results of an excited state scan. Accordingly, the constructed models are assumed to be reliable enough for qualitative (i.e. mechanistic) studies reported in the following sections, mainly based on the comparison between experimental and computationally estimated  $\lambda_{\text{max}}$  and excited state lifetimes.

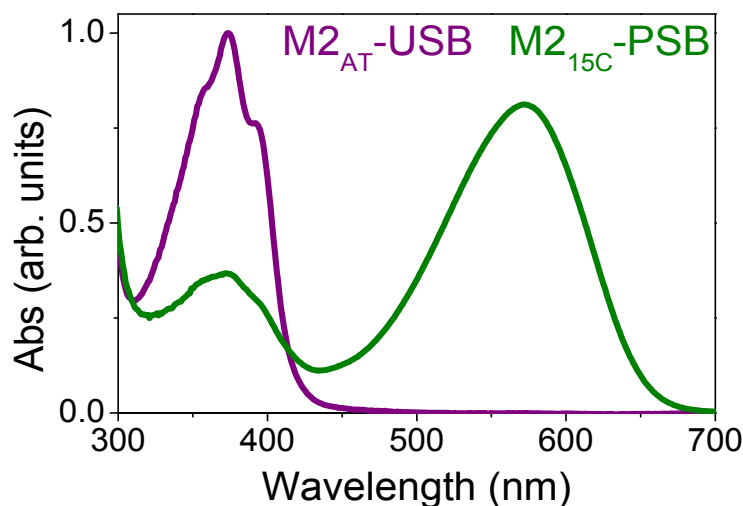


**Figure 10.1:** Ground state Absorbance Spectra of  $M2_{AT}$ -USB and  $M2_{15C}$ -PSB

Ground state absorption of the dark adapted  $M2_{AT}$ -USB (purple) and light adapted  $M2_{15C}$ -PSB (green) states. The  $M2_{15C}$ -PSB light state spectrum had contamination of the  $M2_{AT}$ -USB dark state as evident by the absorption in the UV region.

#### ***$M2_{15C}$ -PSB to $M2_{AT}$ -USB conversion***

The *15-cis* to *all-trans* reaction of  $M2_{15C}$ -PSB was characterized using ultrafast transient broadband absorption pump probe and cryokinetic spectroscopies. First, the ultrafast pump probe experiment conducted for  $M2_{15C}$ -PSB revealed that the decay of the excited state exhibited biphasic decay kinetics with two rate constants (400 fs and 5 ps, see Figure 10.2A). In the transient absorption spectra (Figure 10.2B) there is a negative signal between 575 and 625 nm that was ascribed to a ground state bleach given the overlap with the ground state absorption (GSA) and positive excited state absorption (ESA) at 475 nm. There also appears to be a longer-lived negative signal observed (compared to neighboring wavelength such as 650 nm) at 710 nm (Figure A10.9) and attributed to stimulated emission since it did not follow the GSA band (Figure 10.2B). The excited state decayed on two different timescales, where the majority (70%) of the excited state population decayed on a 400 fs timescale and a minority (30%) decayed on a 5 ps timescale



(Figures 10.2C and 10.2D). The ES population appears to relax back to the ground state, with no measurable long-lived photoproduct which points to a low quantum efficiency of the reaction.

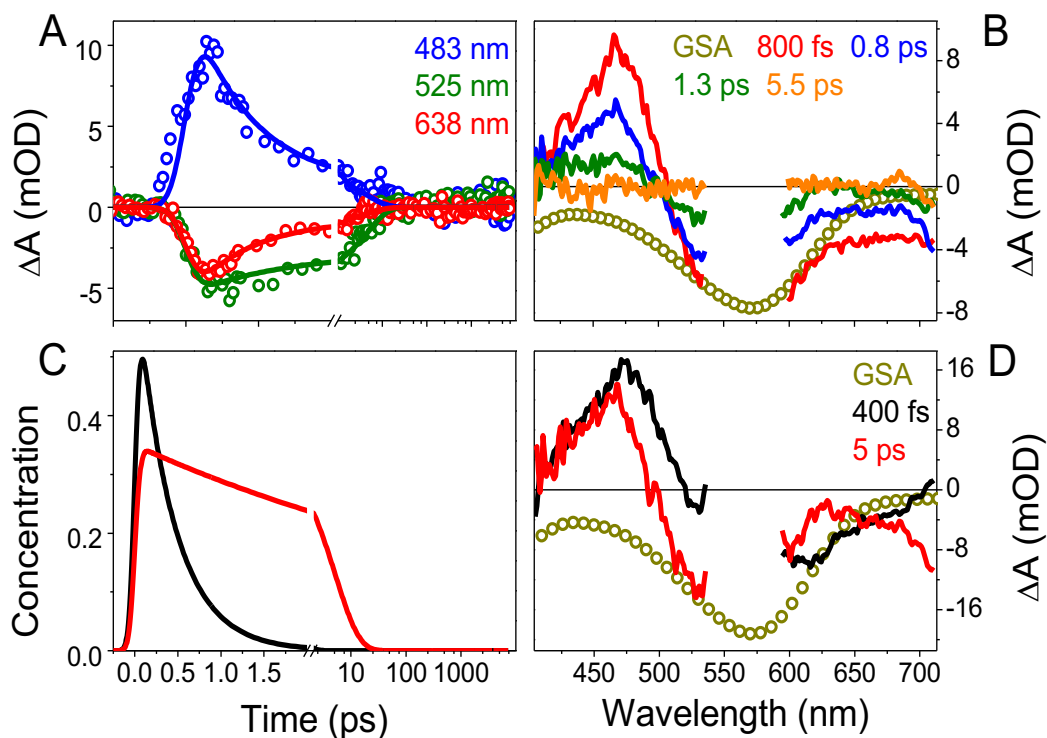


**Figure 10.2:** Primary Photodynamics of the M2<sub>15C</sub>-PSB Reaction

Photodynamics of M2<sub>15C</sub>-PSB after 565 nm excitation (A, B). In the kinetics (A), the data are represented by open circles and the fit is represented by solid lines. Global analysis of the same reaction using a parallel model where 70% of the population is in the faster state (C, D). GSA stands for ground state absorption and are represented by open golden circles. The resulting concentration profiles and EADS are color coded to the legend in D

The ultrafast studies were complemented with cryokinetic UV-Vis spectroscopy as described by Mix et al.<sup>339</sup> that resolved four distinct positive bands (Figures 10.3, A10.6-A10.8, and Table A10.1). The first cryotrapped intermediate (M2<sub>13C-15C</sub>-PSB) was characterized by a red-shifted absorption compared to the parental M2<sub>15C</sub>-PSB absorption at 560 nm. It was stable to ~180 K

whereby it evolves into a second intermediate ( $M2_{13C-15T-PSB}$ ), that peaks at  $\sim 550$  nm. This intermediate is stable to  $\sim 220$  K whereby it then evolves into the next intermediate ( $M2_{AT-PSB}$ ) which absorbed at an even lower energy of 574 nm.  $M2_{AT-PSB}$  persists to  $\sim 240$  K before evolving into the terminal state peaking at 340 nm, which strongly resembles the ground-state  $M2_{AT-USB}$  state (Figure A10.6). This final evolution step is ascribed to a proton transfer event that deprotonates the Schiff base of the chromophore and is responsible for the strong shift in the absorption spectrum from 574 nm to 340 nm. For these three intermediates, the ground state bleach was added to the difference spectra to produce species associated spectra (SAS) of the photointermediates (Figure 10.3).

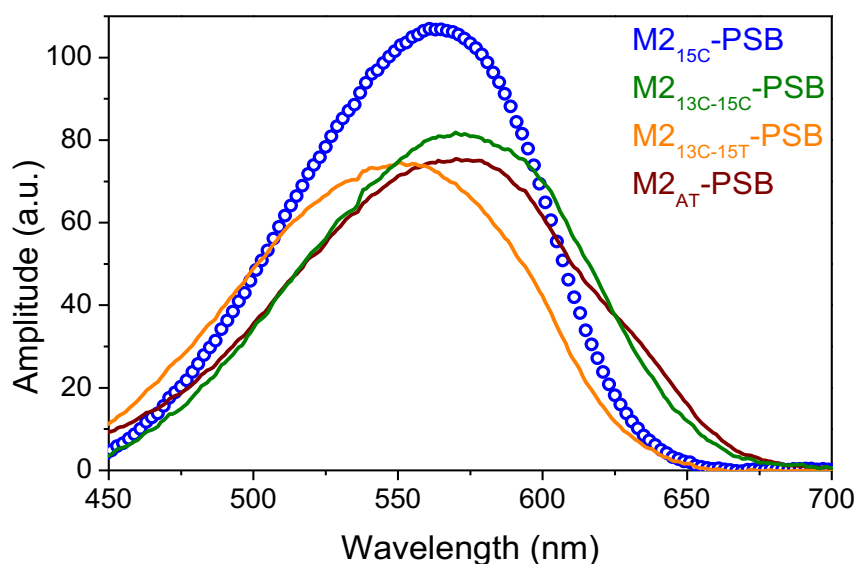


**Figure 10.3:** Cryokinetic SAS of the  $M2_{15C-PSB}$  Reaction

Species associated spectra (SAS) of the PSB intermediates obtained from adding the  $M2_{15C-PSB}$  bleach (at the same temperature) to the difference spectra (Figure A10.6). The  $M2_{15C-PSB}$  light state static spectra (blue curve) was taken from the 170 K reference spectra and  $M2_{13C-15C-PSB}$ ,  $M2_{13C-15T-PSB}$ , and  $M2_{AT-PSB}$  photointermediates were isolated at 190 K, 220 K, and 240 K, respectively.

The simulation of the photo-induced dynamics of M2<sub>15C</sub>-PSB at room temperature as the first step of the M2<sub>15C</sub>-PSB to M2<sub>AT</sub>-USB branch of the M2 photocycle is performed by randomly selected 20 initial conditions out of the generated 100 used to simulate the absorption band (see Figure 10.1 and A10.1B). Such initial conditions (see Figure A10.1A) were employed to propagate 20 trajectories starting from S<sub>1</sub> or S<sub>2</sub> (depending on the state displaying the larger initial oscillator strength and therefore transition probability). Within 0.8 ps, seven M2<sub>15C</sub>-PSB trajectories displayed isomerization and hopped to S<sub>0</sub> while the remaining trajectories remained significantly untwisted. Remarkably, none of the hopped trajectories isomerized around C15=N bond but instead five of them displayed C13=C14 twisting while the remaining two displayed C11=C12 twisting. Both trajectories that exhibited C11=C12 twisting formed, upon S<sub>0</sub> relaxation, the M2<sub>15C</sub>-PSB reactant and were therefore unproductive. However, the majority of trajectories that isomerized at C13=C14 formed 13-*cis*, 15-*cis* photoproduct. This is assigned to the first cryogenically trapped M2<sub>13C-15C</sub>-PSB and it is thus called using the same acronym.

All isomerizing trajectories followed the ABP isomerization mechanism similar to that of natural microbial rhodopsin such as bacteriorhodopsin. In fact, the isomerization around C12-C13=C14-C15 and C14-C15=N-C $\epsilon$  dihedrals take place concertedly in opposite directions. As illustrated in Figure 10.4, the twisting of C13=C14 and C15=N increases along the trajectories until the molecule hops to the ground state. Once the hop takes place, the C13=C14 twisting continues while the C14-C15=N-C $\epsilon$  dihedral reverts yielding a net C13=C14 isomerization and, therefore, to the above mentioned M2<sub>13C-15C</sub>-PSB intermediate (also see SI for a movie of a representative reactive trajectory).

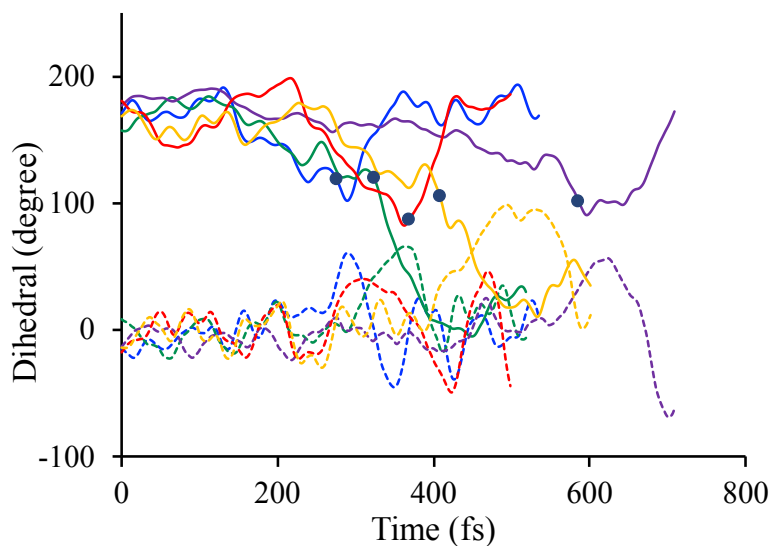


**Figure 10.4:** Select Dihedral Evolution Trajectories of the M2<sub>15C</sub>-PSB reaction  
Evolution of C12-C13=C14-C15 (solid) and C14-C15=N-C $\epsilon$  (dashed) dihedrals of the trajectories that displayed isomerization around C13=C14 double bond. Black spheres denote the hop times.

Since the above trajectory simulations indicate that M2<sub>15C</sub>-PSB isomerize around C13=C14 double bond leading to the 13-*cis*, 15-*cis* photoproduct we hypothesize, on the basis of the cryogenic data discussed above, that M2<sub>15C</sub>-PSB to M2<sub>AT</sub>-USB conversion takes place through at least two extra intermediates associated with a single chromophore change each. The second intermediate is predicted to be the 13-*cis*,15-*trans* chromophore isomer and is therefore called M2<sub>13C-15T</sub>-PSB for consistency with the cryogenic assignment. The third intermediate would feature a 13-*trans*,15-*trans* chromophore and it is called M2<sub>AT</sub>-PSB being assigned to the third cryogenic intermediate. QM/MM models for each intermediate were constructed using the ASEC-FEG protocol<sup>35</sup> leading to a prediction of their  $\lambda_{\max}$  values. When looking at these values, we concluded that the increased discrepancy from the experimental value of the corresponding cryogenically trapped intermediate, reflects the "distance" of the model from the initial x-ray crystallographic structure of M2<sub>15C</sub>-PSB (the only available template). In particular, while the primary photoproduct M2<sub>13C-15C</sub>-PSB display

a value close to the experiment, the more distant M2<sub>13C-15C</sub>-PSB and M2<sub>AT</sub>-PSB models deviate significantly suggesting a shortcoming with the modeling. This decrease in model accuracy can be tentatively attributed to the distant template structure. In fact, while the model of the first intermediate is constructed starting from a model constructed on the basis of an x-ray crystallographic structure, the model of the second intermediate is constructed by taking as a template the model of the first intermediate and it is thus not directly related to an experimental structure. Since the model of the third intermediate is constructed from the model of the second, the accuracy issue is further amplified. For this reason, the M2<sub>13C-15C</sub>-PSB and M2<sub>AT</sub>-PSB models are not considered in the following discussion.

Given the results of the cryokinetics and of the computation we propose the scheme reported in Figure 10.5 for the M2<sub>15C</sub>-PSB to M2<sub>AT</sub>-USB part of the M2 photocycle. The structure of the chromophore in M2<sub>13C-15C</sub>-PSB and M2<sub>AT</sub>-PSB is hypothetical and just follows the shortest possible sequential isomerization path from M2<sub>13C-15C</sub>-PSB to M2<sub>AT</sub>-PSB, again considering sequential single chemical changes in the chromophore.

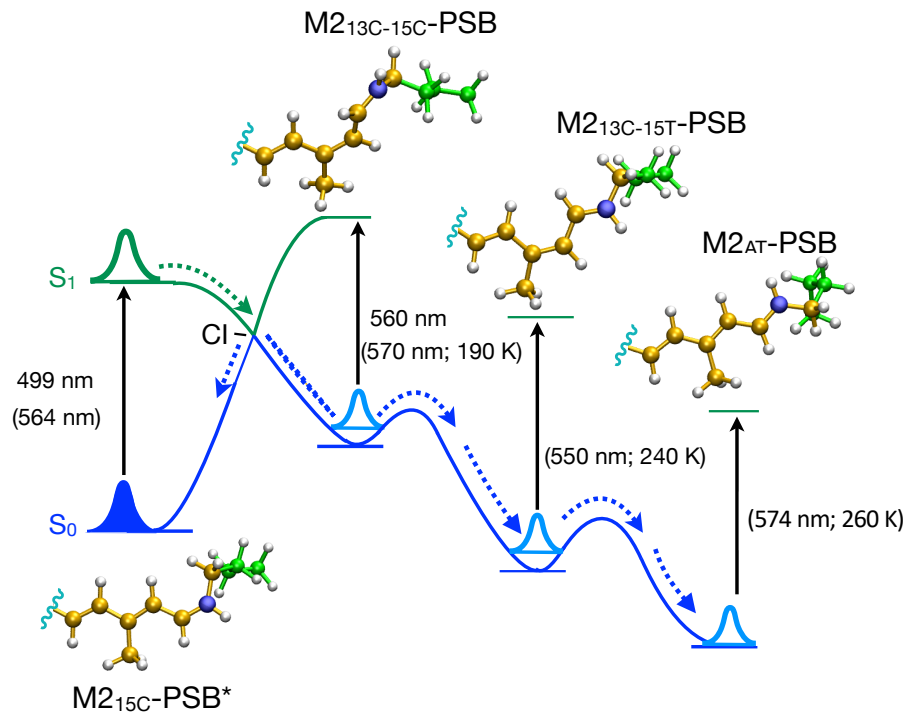


**Figure 10.5:** M2<sub>15C</sub>-PSB Reaction PES

Schematic representation of the PESs driving M2<sub>15C</sub>-PSB to M2<sub>AT</sub>-USB conversion. A population of M2<sub>15C</sub>-PSB molecules absorbing green light is promoted to S<sub>1</sub>. The excited population then relaxes and passes a canonical intersection (CI). A fraction of this population reaches the photoproduct form M2<sub>13C-15C</sub>-PSB. We hypothesize that this sub-population is further isomerized into M2<sub>13C-15T</sub>-PSB and finally, into M2<sub>AT</sub>-PSB. The last form undergoes a proton transfer resulting in M2<sub>AT</sub>-USB. Values in brackets are from the species associated spectra (Figure 10.3) from the cryokinetics experiments. \* denotes a model constructed from crystallographic structure. PDB ID: 4YFP

Comparison of computed and observed excited state lifetimes (400 ps from ultrafast measurements and theory; Figures 10.2 and 10.4) and the  $\lambda_{\text{max}}$  values (Figures 10.3 and 10.5) suggests that our description of the primary event is qualitatively correct. More specifically, the red shifting of the computationally predicted first intermediate agrees with the experimentally observed spectral trend, where the initial photointermediate absorption is red-shifted with respect to the reactant

absorption. The cryogenic data are then consistent with a blue-shifted secondary intermediate and a red-shifted tertiary intermediate, before blue-shifting to the  $M2_{AT}$ -USB dark state.

### ***$M2_{AT}$ -USB to $M2_{15C}$ -PSB conversion***

As with  $M2_{15C}$ -PSB dynamics, the dynamics of  $M2_{AT}$ -USB was characterized by ultrafast and cryokinetics experiments. The ultrafast transient absorption and kinetics of  $M2_{AT}$ -USB are displayed in Figure 10.6A, where primary observation is the decay of the excited state back to the ground state over 750 ps. In addition to the decay of the excited state, an evolution of a negative signal in the 575-642 nm (Figure 10.6A) region over  $\sim$ 300 ps is observed, but due to the location and broadness of the signal this is attributed to PSB contamination. In addition to the appearance of the negative signal for the 642 nm trace (Figure 10.6A, red curve), there is also a short lived (c.a.  $<$  200 fs) positive peak that spans from  $\sim$ 625 – 650 nm and is attributed to an early time artifact. The ultrafast dataset was fit with a sequential model and the resulting concentration profile and EADS are depicted in Figure 10.6C and Figure 10.6D, where the red and blue curves represent excited state absorption decay back to the ground state.

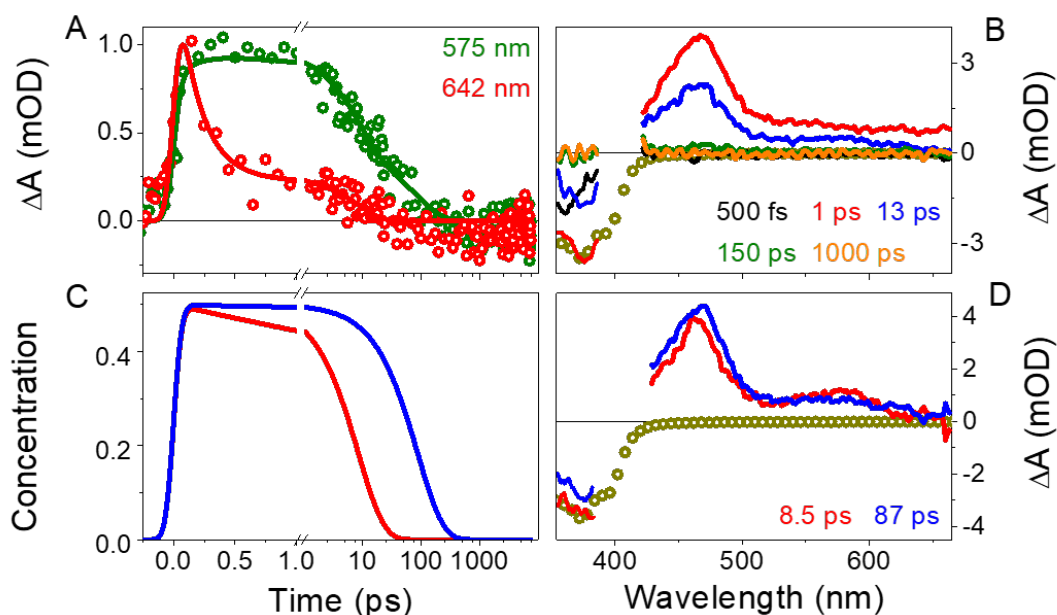


**Figure 10.6:** Primary Photodynamics of the M2<sub>AT</sub>-USB Reaction

Photodynamics of M2<sub>AT</sub>-USB after 400 nm excitation (A, B). The fits (A, solid lines) are the result of a parallel fitting. Concentration and EADS (C, D) from the fit are color coded to the legend in D. No photoproduct is resolved and only two excited-state populations with characteristic double peak features are observed.

The cryokinetics resolved a red shifted population that displayed red-shifted absorbance with respect to M2<sub>AT</sub>-USB and was attributed to M2<sub>15C</sub>-USB (Figures 10.7 and A10.10-A10.12, and Table A10.2). M2<sub>15C</sub>-USB decays back into M2<sub>AT</sub>-USB at 180 and 190 K, suggesting the presence of a shunt (Figure A10.10) and directly evolves into the M2<sub>15C</sub>-PSB photoproduct between 210 and 230 K (Figure A10.11). When a high enough temperature (240 K) was reached, a decay of the green absorbing band and a filling of the GSB was observed, suggesting dark conversion back to M2<sub>AT</sub>-USB (Figures A10.10-A10.12). This shows that M2<sub>AT</sub>-USB evolves to M2<sub>15C</sub>-PSB through a single intermediate that is followed by a protonation to the photoproduct. The M2<sub>15C</sub>-USB photointermediate was not observed in the room temperature dynamics due to the low quantum



efficiency of its formation. The  $M2_{15C}$ -PSB photoproduct is thermally stable up to 240 K where it thermally reconverts back to the deprotonated  $M2_{AT}$ -USB.

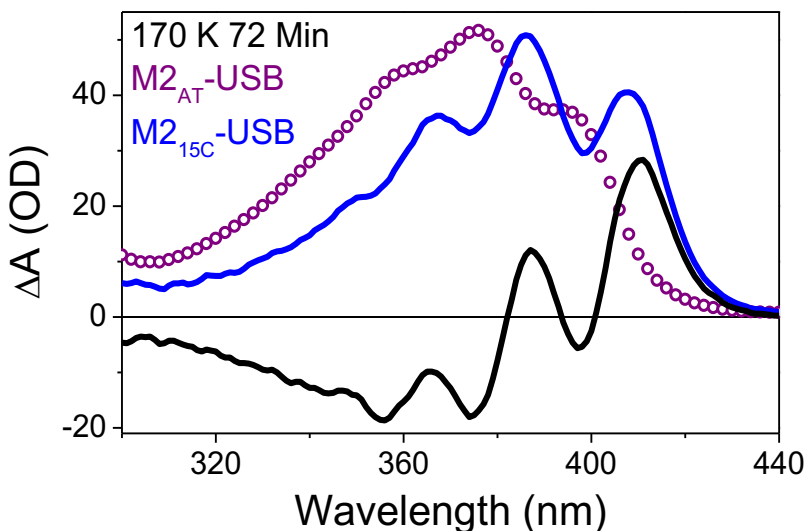


**Figure 10.7:** Cryokinetic SAS of the  $M2_{AT}$ -USB Reaction

$M2_{AT}$ -USB dark state static spectra (purple open circles curve), difference spectra (black curve) and species associated spectra (SAS; blue curve) of the  $M2_{15C}$ -USB intermediate at 170 K. The SAS was obtained from adding the  $M2_{AT}$ -USB bleach to the difference spectra.

In addition to the experimental results, the photoinduced dynamics of the  $M2_{AT}$ -USB to  $M2_{15C}$ -PSB branch of the M2 photocycle were studied by initiating  $M2_{AT}$ -USB trajectories on  $S_3$  or  $S_4$  at the 5-root-state-average CASSCF level due to their high oscillator strength. During the 0.8 ps simulation time, the majority of the trajectories hopped to  $S_3$  or  $S_2$  states but displayed no sign of isomerization possibly due to an encountered small barrier. For this reason, we then mapped the excited state isomerization path driven by the C15=N twist by computing a relaxed scan starting from the  $M2_{AT}$ -USB.

At this point, it is important to recall information on two important CIs related to the photoisomerization of conjugated polyene systems.<sup>340-342</sup> The first is a crossing between two states having 1A<sub>g</sub> and 1B<sub>u</sub> electronic structures (1B<sub>u</sub>/1A<sub>g</sub> crossing featuring a single 90° twisted C=C bond) and is found in cationic conjugated systems such as rPSB. The second, a crossing between 2A<sub>g</sub> and 1A<sub>g</sub> like states (2A<sub>g</sub>/1A<sub>g</sub> crossing, also called a (CH)<sub>3</sub>-kinked CI) is found in non-polar systems.<sup>342</sup>

Since rUSB is not a highly polar chromophore, we first assumed that a 2A<sub>g</sub>/1A<sub>g</sub> kinked CI, is more stable in comparison to 1B<sub>u</sub>/1A<sub>g</sub> CI and thus more accessible from the Franck-Condon (FC) point. Thus, we mapped the reaction path starting from the FC point and connecting it to a previously optimized 2A<sub>g</sub>/1A<sub>g</sub> CI. The computed path shows the existence of an S<sub>1</sub> minimum, but it also shows that reaching the CI from the minimum is impossible as this lies ~37 kcal/mol higher (see Figure A10.13). We then computed similar reaction paths for the isomerization around C11=C12 and C13=C14 double bonds. The results are reported in Figure A10.14. We then hypothesized that rUSB isomerizes around C15=N and that the reaction proceeds through a 1B<sub>u</sub>/1A<sub>g</sub> CI which was previously optimized. The computed reaction path is reported in Figure 10.8. The electronic states are labelled from S<sub>0</sub> to S<sub>5</sub> based on the order of the CASSCF energy at the FC region.

At the FC point, the computed oscillator strength maximum (2.3) corresponds to S<sub>0</sub>→S<sub>5</sub> transition at the CASSCF level. With the correction for dynamic electron correlation energy, the S<sub>5</sub> state becomes the lowest excited state at the CASPT2 level. The geometry optimization on S<sub>5</sub> resulted

in a minimum whose  $S_1$  and  $S_5$  CASPT2 energy order is switched. This indicates a crossing between the first two lowest excited states at the CASPT2 level. We then proceeded with a  $S_1$  geometry optimization which resulted in a  $S_1$  minimum located ca. 59 kcal/mol. This is assigned to the primary excited state photoproduct intermediate generated after photon absorption.

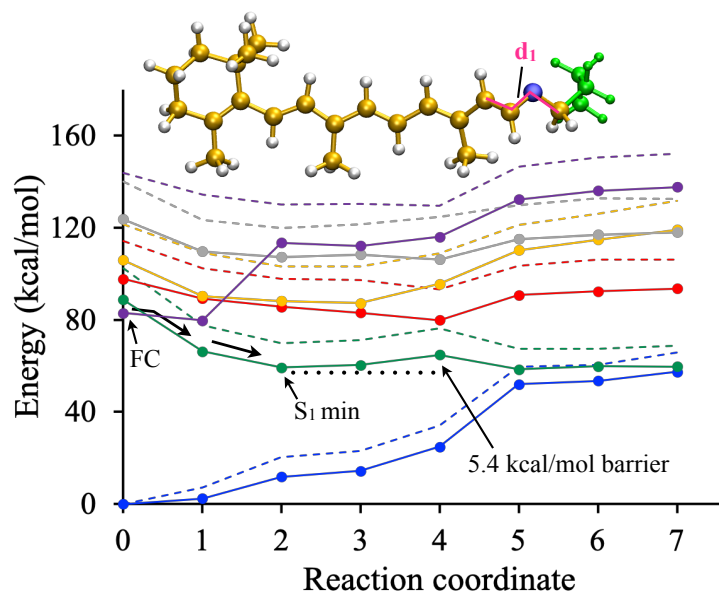


**Figure 10.8:** CASSCF and CASPT2 energies of the M2<sub>AT</sub>-USB Reaction

Evolution of CASSCF (dashed) and CASPT2 energies (solid) along the isomerization of M2<sub>AT</sub>-USB around C15=N double bond.  $S_0$  to  $S_5$  states are denoted by blue, green, red, yellow, grey and violet colors respectively. The points 3 to 7 of the reaction coordinate were obtained from a series of constraint geometry optimizations. More specifically, the geometry optimizations were carried out while keeping dihedral  $d_1$  (see USB structure on top) constrained at -160, -140, -120, -110 and -90 degrees respectively.

At this stage, it is important to mention that the above findings on rUSB isomerization display similarities to the information uncovered from the Siberian hamster cone pigments.<sup>343</sup> The calculations carried out at CASPT2//CASSCF/6-31G\* level in both studies indicate the following. First, at the FC point, the lowest energy 1B<sub>u</sub>-like state turns out to be the spectroscopically most

favorable state at the CASPT2 level. Second, there is a crossing between the lowest two excited states ( $2A_g/1B_u$  crossing) immediately after relaxation from the FC point. Third, once the molecule passes such a crossing it may reach a minimum on the lowest excited state; but the molecular structure of such a minimum does not exhibit inverted bond length alternation (BLA), which is essential for the double bond photoisomerization. However, we observe an expansion in the double bonds and a contraction in the single bonds when going from  $S_0$  optimized to  $S_1$  optimized structures (see Figure A10.15 for geometric parameters). This suggests that there is a barrier along the BLA coordinate. We computed the rest of the reaction path by constraining C14-C15=N-C $_{\epsilon}$  and computing a relaxed scan. The path shows a small ca. 5.4 kcal/mol energy barrier between  $S_1$  minimum and the  $S_0/S_1$  crossing which has a  $2A_g/1B_u$  CI structure.

Based on the above information, we propose the mechanistic scheme of Figure 10.9 for the  $M2_{AT}$ -USB to  $M2_{15C}$ -PSB conversion. Note that the calculated excited state barrier (the 5.4 kcal/mol seen in Figure 10.8; 1.6 ps excited state lifetime from Eyring equation), is consistent with the observed lifetime 8.5 ps (6.4 kcal/mol barrier from Eyring equation; 50% excited state population) excited state lifetime in  $M2_{AT}$ -USB ultrafast experiments.

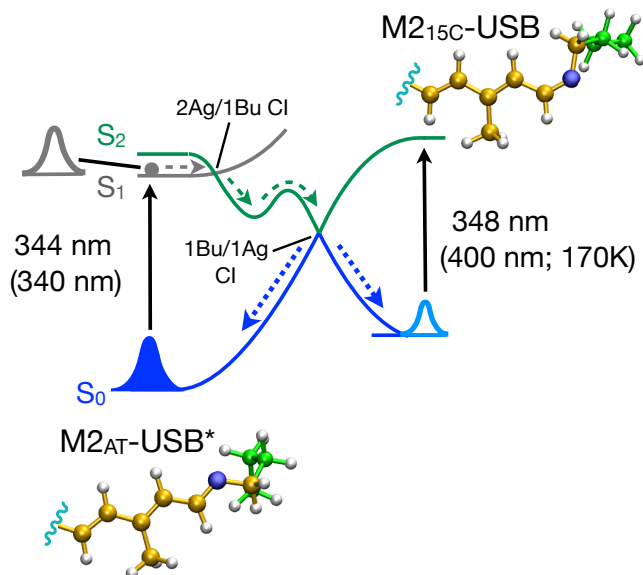


**Figure 10.9:** M2<sub>AT</sub>-USB Reaction PES

The proposed isomerization pathway for the M2<sub>AT</sub>-USB to M2<sub>15C</sub>-PSB conversion. A population of M2<sub>AT</sub>-USB absorbing a UV light pulse reaches the lowest excited state at the Frank-Condon (FC) region. It is then relaxed on the same state and crossed to the second excited state which is now lower in energy. The population is further relaxed on this state and reaches a minimum and proceeds towards a second CI and reaches the ground state photoproduct. It then undergoes the proton transfer and reaches the M2<sub>15C</sub>-PSB state. The wavelengths are in nm and the values reported in parenthesis are experimentally reported values extracted SAS for the M2<sub>15C</sub>-USB from the cryokinetics (Figure 10.7). \* denotes a model constructed from crystallographic structure. PDB ID: 4YFQ

### ***Proposed M2 photocycle mechanism***

According to the above results and to the assumed shortest possible, single chemical event, sequential isomerization hypothesis mentioned above, the molecular-level motion driving the M2 photocycle changes are proposed as follows (see Figure 10.10). The M2<sub>15C</sub>-PSB to M2<sub>13C-15C</sub>-PSB photoisomerization takes place via an ABP mechanism involving the C13=C14 and C15=N bonds. If we consider plane  $\beta$  which is defined by C14, C15 and H15 atoms and looking through the C14-C15 single bond in the direction of the  $\beta$ -ionone ring, the plane rotates in the clockwise direction.

This suggests that C13=C14 and C15=N double bonds twist in clockwise and counterclockwise directions respectively. After the isomerization, a M2<sub>AT</sub>-PSB intermediate is produced after two thermal steps (see Figure 10.5) indicated by the experimental investigations. At this stage, the deprotonation of the rPSB takes place. We examined the molecular structures that constitutes the M2<sub>AT</sub>-PSB ASEC configuration and noted a hydrogen bond network connecting the iminium hydrogen and a glutamate (GLU73 residue) located ca. 9 Å away from it. This network is also observed in the structure closest to the average (see Figure A10.16A). We propose that the proton translocation from rPSB to GLU73 takes place through such a network involving, according to our model, at least 3 water molecules during the M2<sub>AT</sub>-PSB to M2<sub>AT</sub>-USB conversion.

As discussed above, M2<sub>AT</sub>-USB then undergoes an isomerization around the C15=N bond in the presence of UV light and produces M2<sub>15C</sub>-USB directly. The corresponding atomic motion can be described similar to the M2<sub>15C</sub>-PSB case by considering a plane  $\gamma$  defined by C $\epsilon$ , N15 and the nitrogen lone pair. During M2<sub>AT</sub>-USB isomerization, the C15=N bond continues to twist in the counterclockwise direction while the C13=C14 bond undergoes a slight twist in the clockwise direction. The corresponding photoproduct regenerates the M2<sub>15C</sub>-PSB by obtaining a proton from the environment. We propose that a proton residing on the nearby glutamic acid residue (GLH73) is transferred to the Schiff base in this process. Moreover, we propose that such a transfer occurs through a H bond network that involves at least one water molecule (see Figure A10.16B).

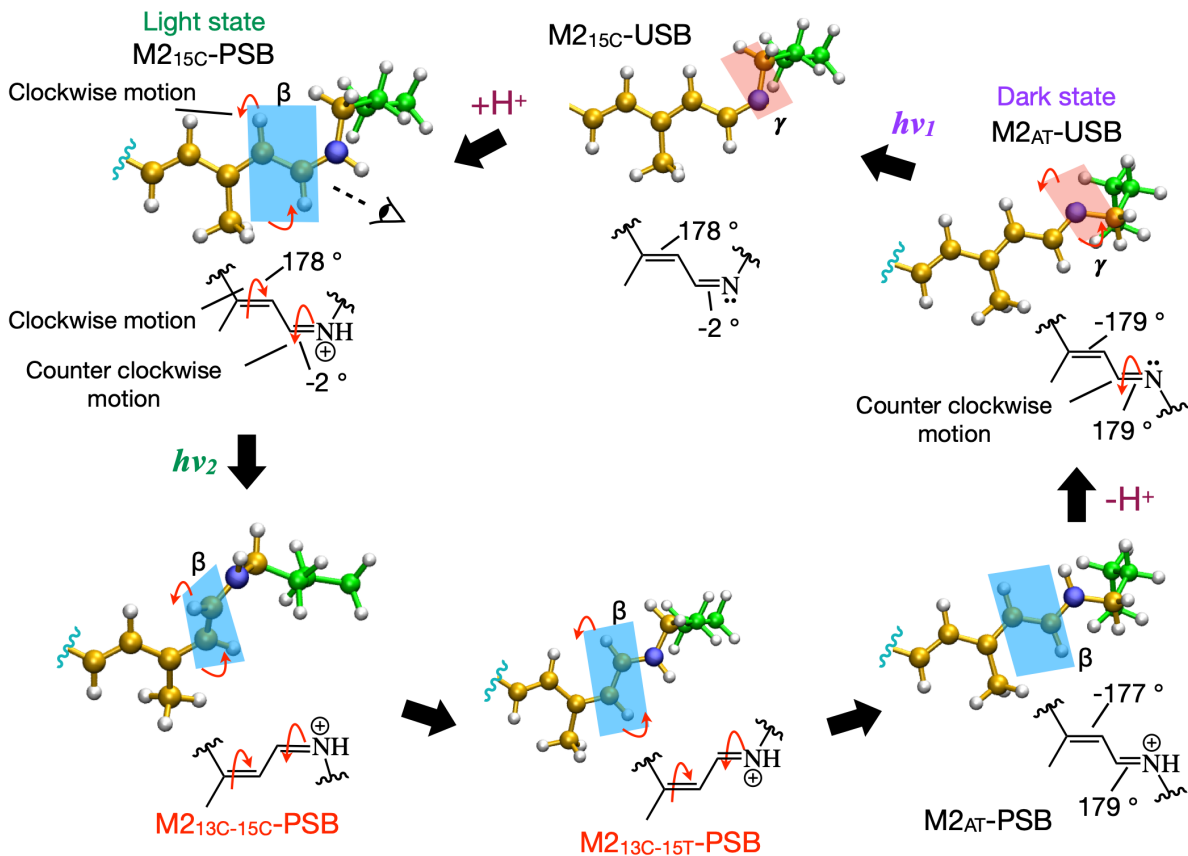


**Figure 10.10:** Proposed M2 Photocycle

Proposed mechanism for the M2 photocycle. Hypothetical models are labelled in red.

***Is M2 a good model system to study the factors effecting rhodopsin photoisomerization?***

The features of M2 that we have discussed above, especially in its rPSB bound form, are not too far from the isomerization of certain microbial rhodopsins. These include: 1) the primary photoisomerization of the rPSB occurring at the C13=C14 double bond, 2) the isomerization intermediates bear similarities for the ones proposed and documented for *Anabaena* sensory rhodopsin,<sup>344, 345</sup> 3) the presence on an ABP photoisomerization mechanism which has been shown in bacteriorhodopsin.<sup>326, 346</sup> In the present section we also report another feature of this system, namely electronic state mixing, that we have previously documented for animal and microbial

rhodopsin and rPSB in solution.<sup>341</sup> As discussed in ref. 341, electronic state mixing has been proposed to control the speed of rPSB photoisomerization by changing the electronic structure of a PES. In order to investigate the presence of such mixing in this system, we recomputed the energy profiles of a selected representative M2<sub>15C</sub>-PSB trajectory at the CASPT2 level. For both the CASSCF and CASPT2 energy profiles, the evolution of positive charge on a fraction of rPSB, which is an indication of the electronic structure, are reported in Figure A10.17. The results are discussed in detail in section A10.9: Impact of electronic state mixing on the photoisomerization of M2<sub>15C</sub>-PSB.. In summary, we find that electronic state mixing would also control the speed of the photoisomerization of M2<sub>15C</sub>-PSB consistently with natural systems. The fact that M2<sub>15C</sub>-PSB photoisomerization is similar to natural rhodopsins is, in many ways, an indication that it may be used as a model system to study the chromophore/protein interaction governing rhodopsin photocycles.

### ***Conclusions***

Above we have studied the photocycle of a man-made rhodopsin, M2, that can undergo reversible photoisomerization. The study has been carried out with a combination of theory and experiments. The results suggest that the photocycle involves several intermediates and two separate photoisomerization events that are initiated by the absorption of photons with very different wavelengths. More specifically, green light excites M2<sub>15C</sub>-PSB which produces 13-*cis*, 15-*cis* photoproduct which then isomerizes into 13-*cis*, 15-*trans* and, finally, an all-*trans* form. This process is associated with the ABP photoisomerization mechanism which has never been documented in an artificial rhodopsin before. Our results also reinforce the idea that the bicycle-



pedal isomerization mechanism does not necessarily occur inside a space confining environment and can be rather an intrinsic property of the chromophore.<sup>347, 348</sup>

The photoisomerization of rUSB takes place directly around C15=N double bond from 15-*trans* into 15-*cis* form. The consistency between our findings related to rUSB isomerization and Siberian hamster cone pigments suggest that the information we have documented above may be valid for other rhodopsins hosting rUSB chromophores. For instance, such information may be useful to investigate the UV pigments found in birds and fish.<sup>349</sup>

The observation that while a PSB gives a 13-*cis* photoproduct, the rUSB gives rise to photoisomerization of the C15=N bond is consistent with a recent study of a rhodopsin mimic variant of M2.<sup>350</sup> In this study, it was shown that an all-*trans* retinylidene can be photoisomerized to a stable 13-*cis*,15-*cis* product; but only in its PSB state. This illustrates the clear difference in photoproduct outcome between protonated and unprotonated systems, as predicted here. The production of the 13-*cis*,15-*cis* photoproduct suggests a similar ABP photoisomerization mechanism in this rhodopsin mimic as well.

Finally, our study suggests that M2 may be reengineered as a fluorescent sensor. In this context, introducing mutations or a locked artificial retinal chromophore in such a way to increase the electronic state mixing may be useful due to the resulting increase in excited state lifetime.<sup>351, 352</sup>

### *Associated Content*

#### *Supporting Information (pg. 385)*

The Supporting Information provides a discussion of the computational and experimental protocols as well as the cryokinetic spectra at every measured temperature accompanied by a table with explanations.

#### *Funding*

This work was supported in part by the Italian MIUR for funding (PRIN 2015) and, in part, by the National Science Foundation under grants no. CHE-1710191 and CHE-1413739 and National Institute of Health under grant no. R15GM126627.

#### *Acknowledgments*

M.O. is grateful to the Ohio Supercomputer Center for granted computer time. Dr. Jack Fuzell is acknowledged for assistance in the initial setting up of the M2<sub>AT</sub>-PSB cryokinetics and Dr. L Tyler Mix is acknowledged for consultation on ultrafast data collection and fitting. Dr. Mikas Vengis is also acknowledged for donating the global and target analysis software.

# Copyright Information

## Chapter 4.

Reprinted with permission from 59. Copyright 2018 American Chemical Society.

Copyright Clearance Center RightsLink®

Home ? Email Support Sign in Create Account

**ACS Publications**  
Most Trusted. Most Cited. Most Read.

**Ultrafast Spintronics: Dynamics of the Photoisomerization-Induced Spin-Charge Excited-State (PISCES) Mechanism in Spirooxazine-Based Photomagnetic Materials**

Author: Adam J. Jenkins, Ziliang Mao, Aiko Kurimoto, et al  
Publication: Journal of Physical Chemistry Letters  
Publisher: American Chemical Society  
Date: Sep 1, 2018  
Copyright © 2018, American Chemical Society

**PERMISSION/LICENSE IS GRANTED FOR YOUR ORDER AT NO CHARGE**

This type of permission/license, instead of the standard Terms & Conditions, is sent to you because no fee is being charged for your order. Please note the following:

- Permission is granted for your request in both print and electronic formats, and translations.
- If figures and/or tables were requested, they may be adapted or used in part.
- Please print this page for your records and send a copy of it to your publisher/graduate school.
- Appropriate credit for the requested material should be given as follows: "Reprinted (adapted) with permission from (COMPLETE REFERENCE CITATION). Copyright (YEAR) American Chemical Society." Insert appropriate information in place of the capitalized words.
- One-time permission is granted only for the use specified in your request. No additional uses are granted (such as derivative works or other editions). For any other uses, please submit a new request.

BACK CLOSE WINDOW

## Chapter 5.

Reproduced from Ref. 27 with permission from the European Society for Photobiology, the European Photochemistry Association, and The Royal Society of Chemistry.

## Chapter 6.

Reprinted with permission from 28. Copyright 2020 American Chemical Society.

Copyright Clearance Center RightsLink®

Home ? Email Support Sign in Create Account

**ACS Publications**  
Most Trusted. Most Cited. Most Read.

**Conservation and Diversity in the Primary Reverse Photodynamics of the Canonical Red/Green Cyanobacteriochrome Family**

Author: Adam J. Jenkins, Sean Marc Gottlieb, Che-Wei Chang, et al  
Publication: Biochemistry  
Publisher: American Chemical Society  
Date: Oct 1, 2020  
Copyright © 2020, American Chemical Society

**PERMISSION/LICENSE IS GRANTED FOR YOUR ORDER AT NO CHARGE**


This type of permission/license, instead of the standard Terms & Conditions, is sent to you because no fee is being charged for your order. Please note the following:


- Permission is granted for your request in both print and electronic formats, and translations.
- If figures and/or tables were requested, they may be adapted or used in part.
- Please print this page for your records and send a copy of it to your publisher/graduate school.
- Appropriate credit for the requested material should be given as follows: "Reprinted (adapted) with permission from (COMPLETE REFERENCE CITATION). Copyright (YEAR) American Chemical Society." Insert appropriate information in place of the capitalized words.
- One-time permission is granted only for the use specified in your request. No additional uses are granted (such as derivative works or other editions). For any other uses, please submit a new request.

BACK CLOSE WINDOW

## Chapter 10.

Reprinted with permission from 60. Copyright 2020 American Chemical Society.

Home Help Email Support Sign in Create Account



**Computational and Spectroscopic Characterization of the Photocycle of an Artificial Rhodopsin**  
**Author:** Madushanka Manathunga, Adam J. Jenkins, Yoelvis Orozco-Gonzalez, et al  
**Publication:** Journal of Physical Chemistry Letters  
**Publisher:** American Chemical Society  
**Date:** Jun 1, 2020  
*Copyright © 2020, American Chemical Society*

**PERMISSION/LICENSE IS GRANTED FOR YOUR ORDER AT NO CHARGE**

This type of permission/license, instead of the standard Terms & Conditions, is sent to you because no fee is being charged for your order. Please note the following:

- Permission is granted for your request in both print and electronic formats, and translations.
- If figures and/or tables were requested, they may be adapted or used in part.
- Please print this page for your records and send a copy of it to your publisher/graduate school.
- Appropriate credit for the requested material should be given as follows: "Reprinted (adapted) with permission from (COMPLETE REFERENCE CITATION). Copyright (YEAR) American Chemical Society." Insert appropriate information in place of the capitalized words.
- One-time permission is granted only for the use specified in your request. No additional uses are granted (such as derivative works or other editions). For any other uses, please submit a new request.

[BACK](#) [CLOSE WINDOW](#)

## Appendices

### *Chapter 4. Supporting Information for “Ultrafast Spintronics: Dynamics of the Photoisomerization-Induced Spin-Charge Excited State (PISCES) Mechanism in Spirooxazine-based Photomagnetic Materials”*

#### *A4.1: Experimental Procedures*

The excitation pulses were generated by an amplified Ti:Sapphire laser, a Spitfire Pro from Spectra Physics, which generated 800 nm light in 1 kHz pulses with 2.5 mJ of energy and a bandwidth of 40 nm. This light was then separated into a pump and probe beam by the use of a beam splitter. The 550 nm pump pulse was generated by a home-built non-collinear optical parametric amplifier (NOPA). The 800 nm fundamental was split into two different beams, a pump and a seed. The pump beam passed through a beta barium borate (BBO) crystal, resulting in sum harmonic generation and in 400 nm light being produced. The 800 nm fundamental of the other beam passes through an ND filter that allows for varying intensity of light being transmitted and then through a yttrium aluminum garnet (YAG) crystal, resulting in the formation of a supercontinuum of the seed. The seed beam was passed through a 540 nm filter with a 10nm bandwidth to minimize the extraneous wavelengths of the seed beam. In the case of this experiment the pump wavelength was 550 nm with a bandwidth of 15 nm at a power between 250 and 300 nJ at the sample. The pump pulses travelled through a chopper operating at 500 Hz to collect difference spectra between the pumped and un-pumped samples.

The probe pulses were generated by taking the 800 nm fundamental of the Spitfire and passing it through a slowly translating 2 mm CaF<sub>2</sub> window to generate white light. To temporally overlap the pump and probe beams at the sample as well as control the probe delay between -10 and 7.1

ns with respect to the pump light, the white light passed through a mechanical stage (Newport IMS 600) that varies the path length of the probe light. Once the pump and probe light were temporally and spatially overlapped at the sample, the probe light was then directed into a spectrograph (Oriel MS 127i) equipped with a 256-pixel photodiode array (Hamamatsu S3901 and C7884). The polarization of both the pump and probe were set at the magic angle,  $54.7^\circ$  to eliminate anisotropic effects associated with rotational dynamics.

#### A4.2: Sample Preparation

APSO and CoAPSO were dissolved in degassed toluene to a concentration of  $\sim 0.5$  OD/mm at the maximum absorbance in a UV-Vis absorption spectrum. The samples were prepared in a  $N_2$  glovebox and placed into 0.25-mm (APSO) and 0.5-mm (CoAPSO) quartz cuvettes and sealed with black wax to avoid exposure to atmospheric oxygen. The sample cuvettes were placed on a motorized stage that translated the cuvette in an oval so that fresh sample was being excited and probed at each set of pulses as well as to keep the sample at room temperature. Both samples were excited by 550 nm at between 250 and 300 nJ and probed in the UV-visible range (325-800 nm).

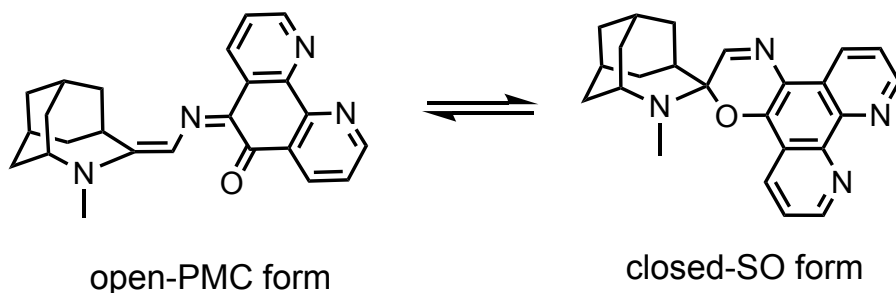


**Figure A4.1:** PMC and SO forms of APSO.

A4.3: Ultrafast Transient Spectra for APSO and CoAPSO

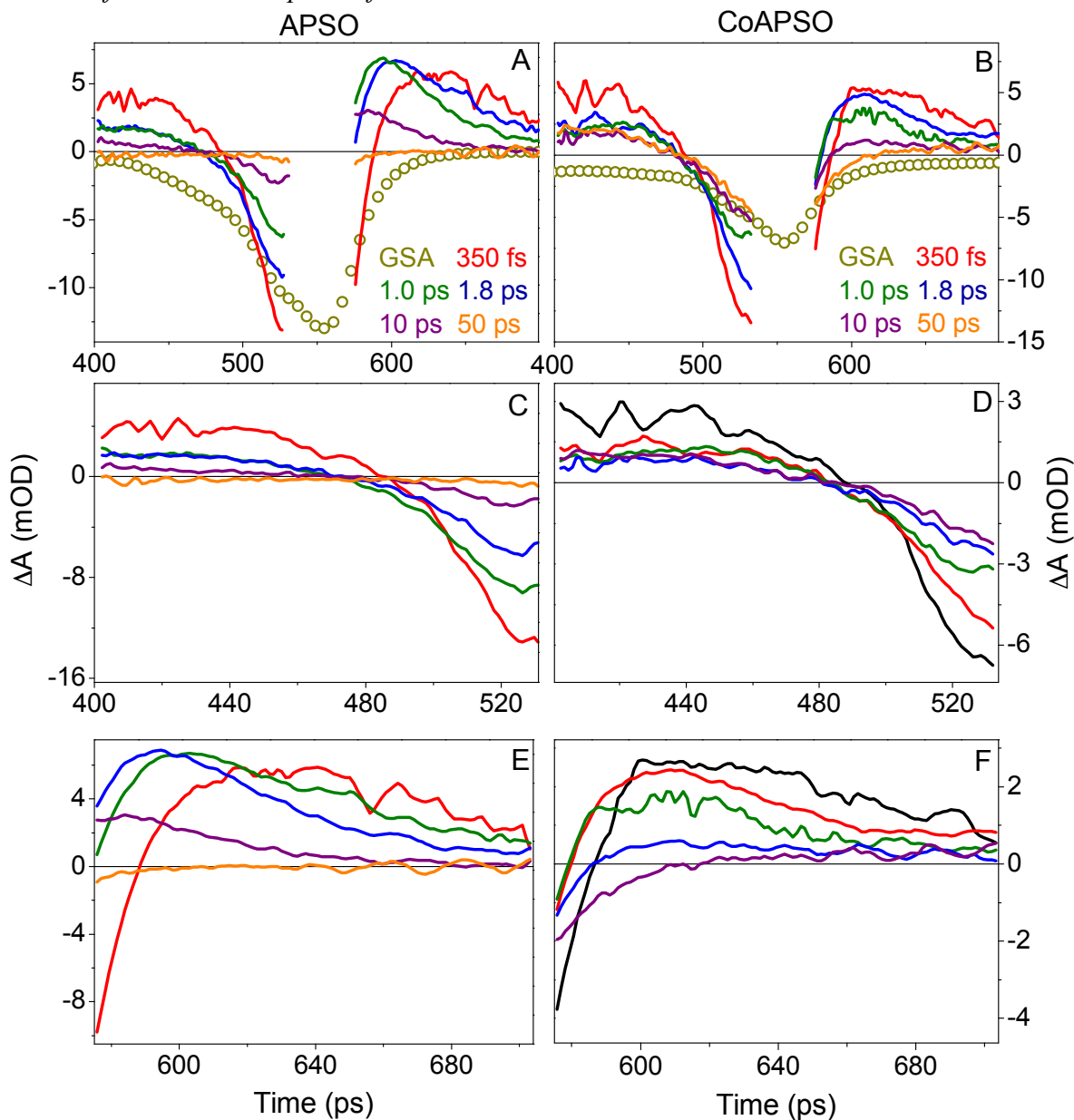


**Figure A4.2:** Transient Absorption of APSO and CoAPSO in the visible region

Transient absorption of APSO (2A) and CoAPSO (2B) in the visible region. Figures 2C, 2E and 2D, 2F show the transient absorption spectra on the left and right of the pump scatter for APSO and CoAPSO, respectively. The selected times for all panels are indicated in Panels A and B. APSO and CoAPSO were excited with 550 nm at 300 nJ.

#### A4.4: Possible Ring Closure Mechanisms.

The ground-state ring-closing mechanism has been proposed to proceed either via a “rotation” or an “inversion” pathway for 1,3,3-trimethylspiro[indoline-2,3'-naphtho[2,1-*b*][1,4]oxazine] (Figure A4.3).<sup>241, 242</sup> The inversion pathway involves a cis-to-trans isomerization step followed by inversion step at the central nitrogen and then C–O bond formation to give the SO form. The rotation pathways involve an isomerization about the C=N bond and then ring closure. Both mechanisms are multistep and involve an isomerized intermediate. Alternative pathways have been proposed based on computational studies but require higher activation energies or lead to high-energy isomers, and are therefore less likely to occur *in situ*.<sup>241, 242</sup>

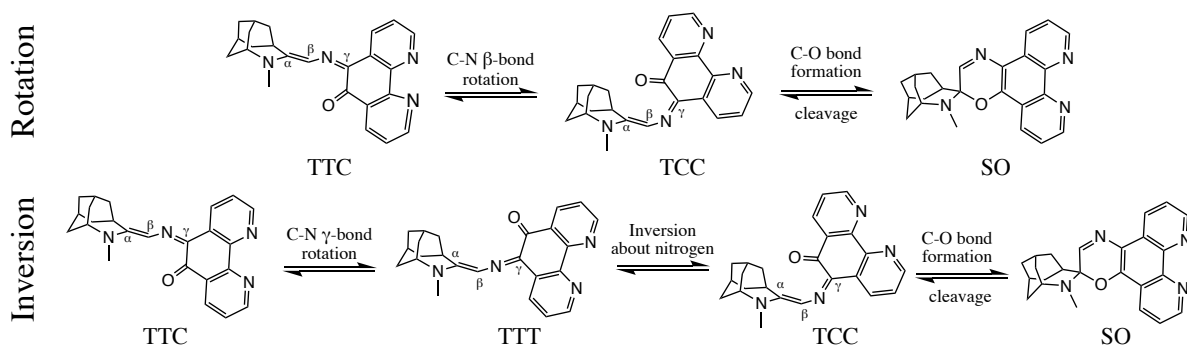


**Figure A4.3:** Possible Thermal Isomerization Pathways for SO to PMC Forms

Possible thermal isomerization pathways for SO to PMC for 1,3,3-trimethylspiro[indoline-2,3'-naphtho[2,1-*b*][1,4]oxazine].<sup>241, 242</sup> TCC is the structure of our cis-PMC.

#### A4.5: Quantum Yield Estimations for APSO and CoAPSO

Figure S2 compares the amplitude of EADS2 to amplitude of the scaled terminal EADS for both APSO and CoAPSO. As previously mentioned, there is no observed change in absorption in the final state. Comparing the amplitudes of the second and scaled final state EADS in Figure S2 the



QY appears to be 2.3% for APSO and 3.4% for CoAPSO, since the final EADS for APSO and CoAPSO had to be scaled by 43 and 29, respectively, to be on the same scale as EADS 2 at the clean bleach at 532 nm.

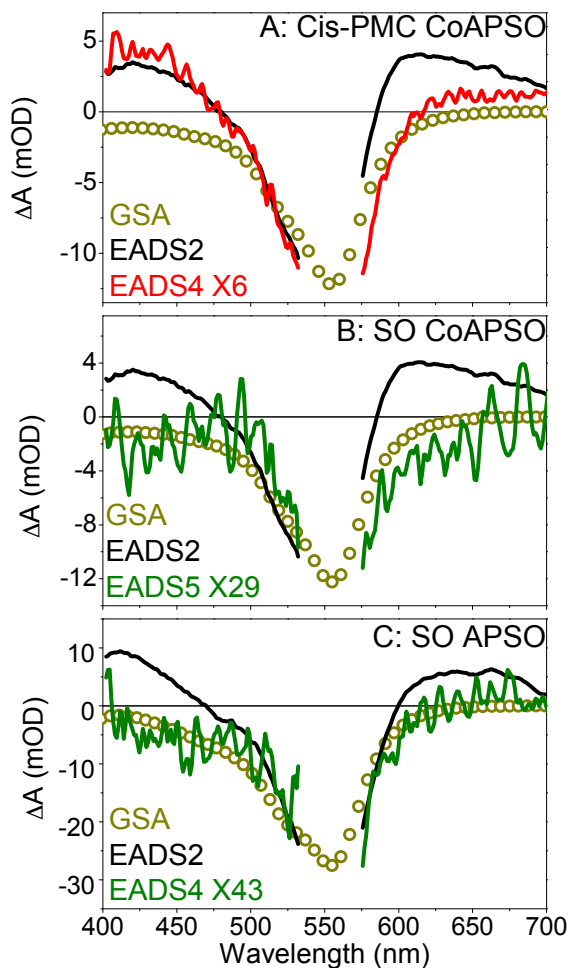


**Figure A4.4:** APSO and CoAPSO Quantum Yield Estimations

Overlap of initial and scaled cis PMC and final EADS for CoAPSO (Figure 3I and 3J) and initial and scaled final EADS for APSO (Figure 3E) from the analysis of the visible data (Figure 2). The GSA are represented by the open dark yellow circles. This scaling resulted in a QY of ~17% for Cis-PMC and ~4% SO for CoAPSO and ~2% for SO for APSO and ~4% for CoAPSO.

#### A4.6: APSO and CoAPSO Transient Green to UV Comparison

Figure S3 compares the UV-Vis spectra of APSO and CoAPSO between 325 and 500 nm. The APSO spectra exhibit a positive absorption around 415 nm, while the CoAPSO spectra exhibit a positive absorption around 450 nm. As with the visible region, CoAPSO exhibits slower kinetics. This region is the UV region in which the CoAPSO has two semiquinone ligands that contribute to absorption here, whereas in the APSO ligand, there is contribution from both the open PMC and closed SO form here, therefore the bleach is likely due to ground state bleach.

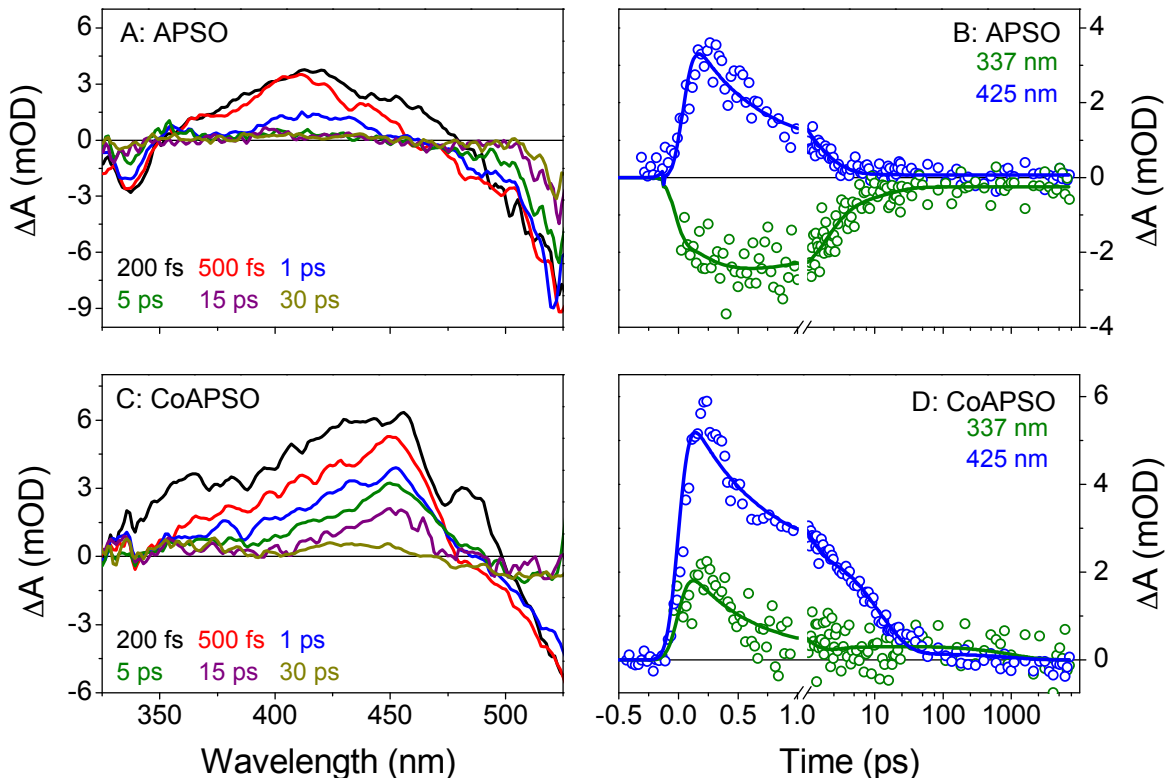
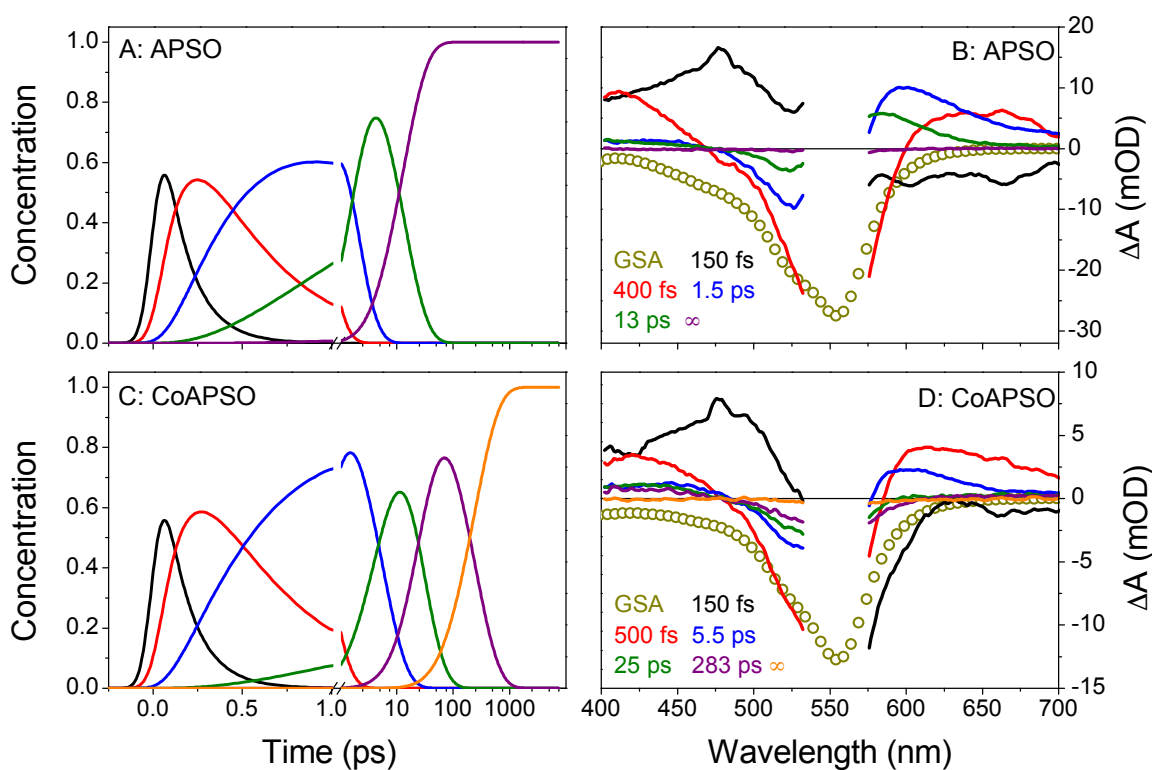


**Figure A4.5:** APSO and CoAPSO Green to UV Dynamics Comparison

Transient absorption and kinetics for APSO (3A and 3B) and CoAPSO (3C and 3D) in the UV-Vis region. APSO and CoAPSO were excited with 550 nm at 300 nJ.

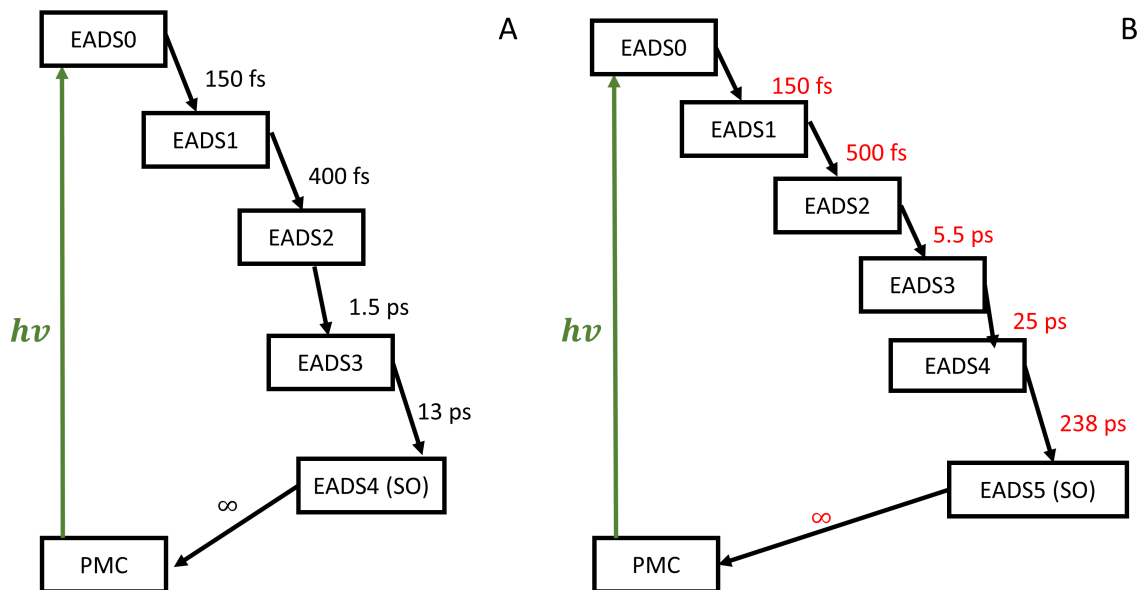
#### A4.7: Global Analysis of APSO and CoAPSO

Figure S4 compares the visible concentration profiles and EADS for APSO and CoAPSO. The TA data of APSO and CoAPSO were fitted using a five-compartment sequential model and a six-compartment sequential model, respectively. The second state for APSO and CoAPSO roughly match the inverted GSA (Figure S4B and S4D; unfilled circles). Figure S5 depict simple schematics for the sequential models used for APSO and CoAPSO, respectively.



**Figure A4.6:** APSO and CoAPSO Concentration Profiles and EADS

Concentration profiles and EADS of APSO (6A and 6B) and CoAPSO (6C and 6D) in the visible region. Where the EADS are color coded to match the concentration profiles. The GSA are also depicted in the EADS panels, represented by the unfilled gold circles.



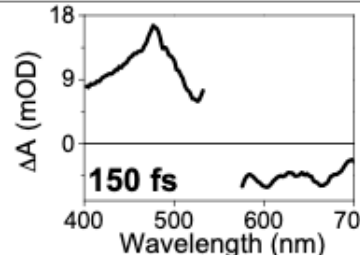
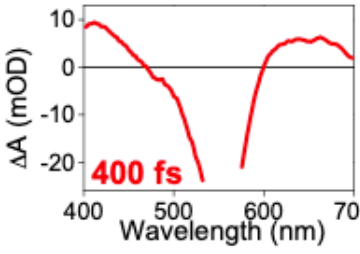
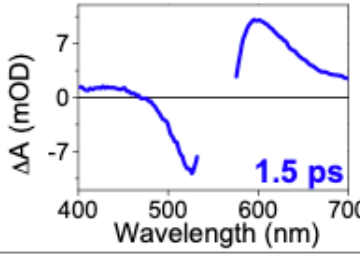
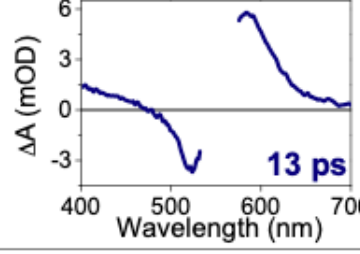
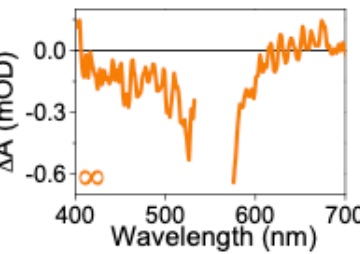
**Figure A4.7:** APSO and CoAPSO Sequential Models

Five-compartment (A) and six-component (B) sequential model used for APSO and CoAPSO, respectively.

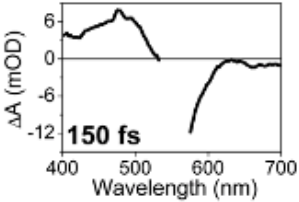
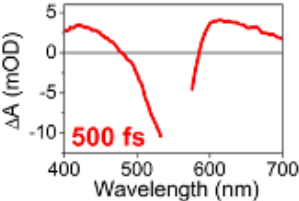
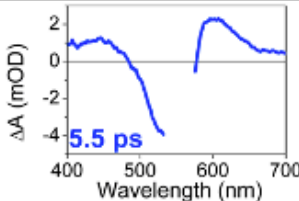
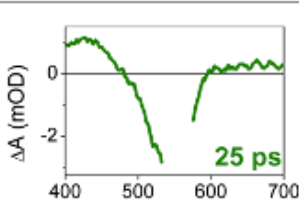
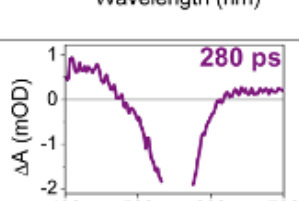
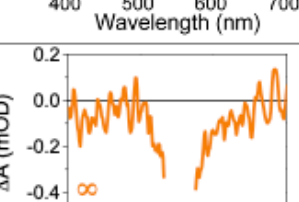
#### *A4.8: EADS Analysis of APSO and CoAPSO*

All of the EADS are depicted in Figures 3 and S4 for APSO (Figures 3A-E, S4B) and CoAPSO (Figures 3F-J, S4D), following the sequential models presented in Figure S5. The first three EADS for APSO and CoAPSO look qualitatively similar. After EADS2, APSO and CoAPSO split and have qualitatively different spectra, suggesting a slight divergence in mechanism for APSO and CoAPSO after the vibrational cooling and twisting.

**Table A4.1: APSO EADS Assignments**

 <p>150 fs</p>	<p>150 fs spectrum that has broad ESA between 400-525 nm and a mixture of ground state bleach and SE in the 575-700 nm regions. Given the short lifetime of this state,<sup>352, 353</sup> it was attributed to the relaxation of the Frank-Condon (FC) excited state (<math>S_3</math>) to a vibrationally excited <math>S_1</math> state. Given Castro et.al theoretical study, the FC state was assigned to the third excited singlet state (<math>S_3</math>), since it had the greatest oscillator strength.<sup>235</sup></p>
 <p>400 fs</p>	<p>400 fs spectrum that was attributed to the vibrationally excited <math>S_1</math> state relaxing to the ground vibrational state of <math>S_1</math> due to the lifetime of the state being a few hundred femtoseconds as well as the blue shift in the ESA between 580-700 nm (Figures 3B, 3C, S4B, (red and blue curves for <math>S_1</math> figures)).<sup>240, 241</sup></p>
 <p>1.5 ps</p>	<p>1.5 ps spectrum was attributed to a twisting of APSO in the <math>S_1</math> PES given the ~2-5 ps time constants and blue shift of the spectrum.<sup>354, 355</sup> Since the system is staying in the same electronic configuration and just relaxing, it made sense that this and the previous EADS for APSO were similar in shape with a decrease in the ESA (Figure S4B).</p>
 <p>13 ps</p>	<p>After vibrationally cooling and twisting, APSO and <u>CoAPSO</u> diverge. EADS3 for APSO (Figure 3D), had a 13 ps lifetime and signatures of ESA and was assigned to the relaxation from <math>S_1</math> to <math>S_0</math>.</p>
	<p>This terminal EADS for APSO persisted beyond the scope of this experiment and did not show any clear signs of positive absorption to indicate the presence of a long-lived photoproduct, but still had a weak bleach. This weak bleach indicated that not <u>all</u> of the sample excited has returned to the GS and that the photoproduct either did not absorb in this region or was so weak that it was hidden by noise. When scaling the bleaches of this terminal EADS to EADS1 (Figure S2C), there was indeed a small QY of photoproduct, ~2 %, assuming a clean bleach around 525 nm. The lack of SO generation was attributed to a parasitic CI, which was previously reported for the ring closure reaction of IPSO.<sup>37</sup></p>

**Table A4.2: CoAPSO EADS Assignments**

	<p>150 fs state that has broad ESA between 400-525 nm and a mixture of ground state bleach and SE in the 575-700 nm regions. Given the short lifetime of this state,<sup>352, 353</sup> it was attributed to the relaxation of the Frank-Condon (FC) excited state (<math>S_2</math>) to a vibrationally excited <math>S_1</math> state. Given Castro et.al theoretical study, the FC state was assigned to the third excited singlet state (<math>S_3</math>), since it had the greatest oscillator strength.<sup>235</sup></p>
	<p>500 fs state was attributed to the vibrationally excited <math>S_1</math> state relaxing to the ground vibrational state of <math>S_1</math> due to the lifetime of the state being a few hundred femtoseconds as well as the blue shift in the ESA between 580-700 nm (Figures 3G, 3H, S4D (red and blue curves for SI figures)).<sup>240, 241</sup></p>
	<p>The third and last set of quantitatively similar spectra for APSO and CoAPSO (Figure 3C, 3H and S4B, S4D). 5.5 ps state that exhibited blue shifted ESA. This state was attributed to a twisting of CoAPSO in the <math>S_1</math> PES given the ~2-5 ps time constants and blue shift in the spectrum.<sup>354, 355</sup></p>
	<p>The fourth spectrum had a longer lifetime than that of APSO (25 ps vs 13 ps) as well as evolves into a state that lives for 280 ps that was not observed in APSO. This 25 ps state was attributed to the relaxing from <math>S_1</math> to <math>S_0</math> (analogous to the 13 ps spectrum in APSO) which resulted in the formation of trans and cis-PMC formation (whereas APSO essentially only formed the trans-PMC configuration). This increase in lifetime of the <math>S_1</math> ground vibrational state corresponds to a higher QY for CoAPSO than APSO, which is why cis-PMC is observed for CoAPSO and not APSO. This state is a mixture of the previous and following states given the extra absorbance around 600 nm.</p>
	<p>Relaxation from the <math>S_1</math> state to the <math>S_0</math> state for CoAPSO showed the appearance of another state that absorbs at ~425 nm and was assigned to cis-PMC-<math>S_0</math>. This cis-PMC state then lived for 280 ps and decayed primarily back to the trans-PMC. When scaled to EADS1 it was estimated that this cis-PMC-<math>S_0</math> form with a QY of ~17%.</p>
	<p>Like with APSO, CoAPSO did not have clear evidence of positive absorption in the terminal EADS (Figures 3E, J), but it still had a non-zero bleach, indicating that not all of the excited CoAPSO relaxed back to the ground state. When scaling the bleaches, the QY for the photoproduct (assumed to be SO) was estimated to be ~4% for CoAPSO (Figure 2B), assuming a clean bleach around 525 nm.</p>

Chapter 5. Supporting information for “Conservation and Diversity in the Secondary Forward  
Photodynamics of Red/Green Cyanobacteriochromes”

A5.1: Supplemental Secondary Forward Dynamics of Red/Green CBCRs

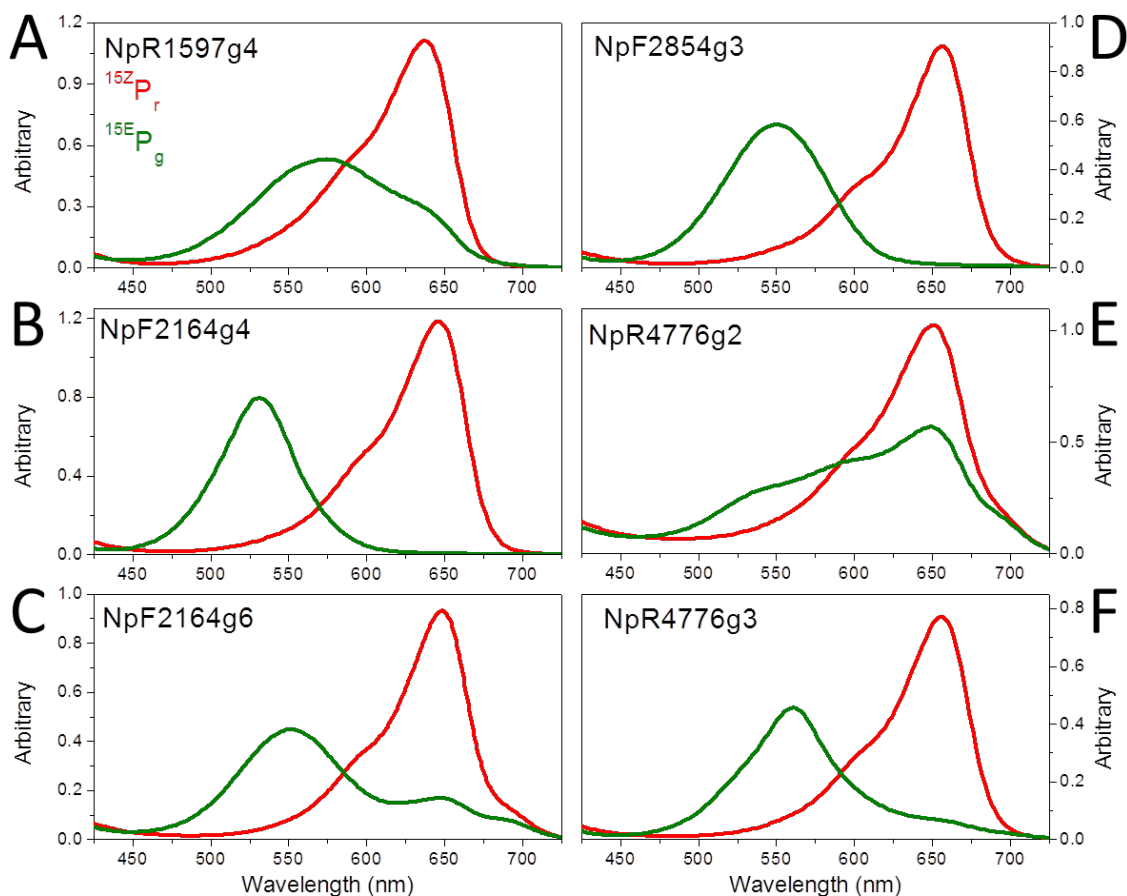


**Figure A5.1:** Red/Green CBCR Static Absorbance Spectra

Ground state  $^{15}ZP_r$  (red curves) and  $^{15}EP_g$  (green curves) absorption spectra for the remaining CBCRs in this study. Several CBCRs do not fully convert from the  $^{15}ZP_r$  to the  $^{15}EP_g$  state, as shown by the distorted  $^{15}EP_g$  spectra for NpR1597g4, NpR4776g2, and NpF2164g6.

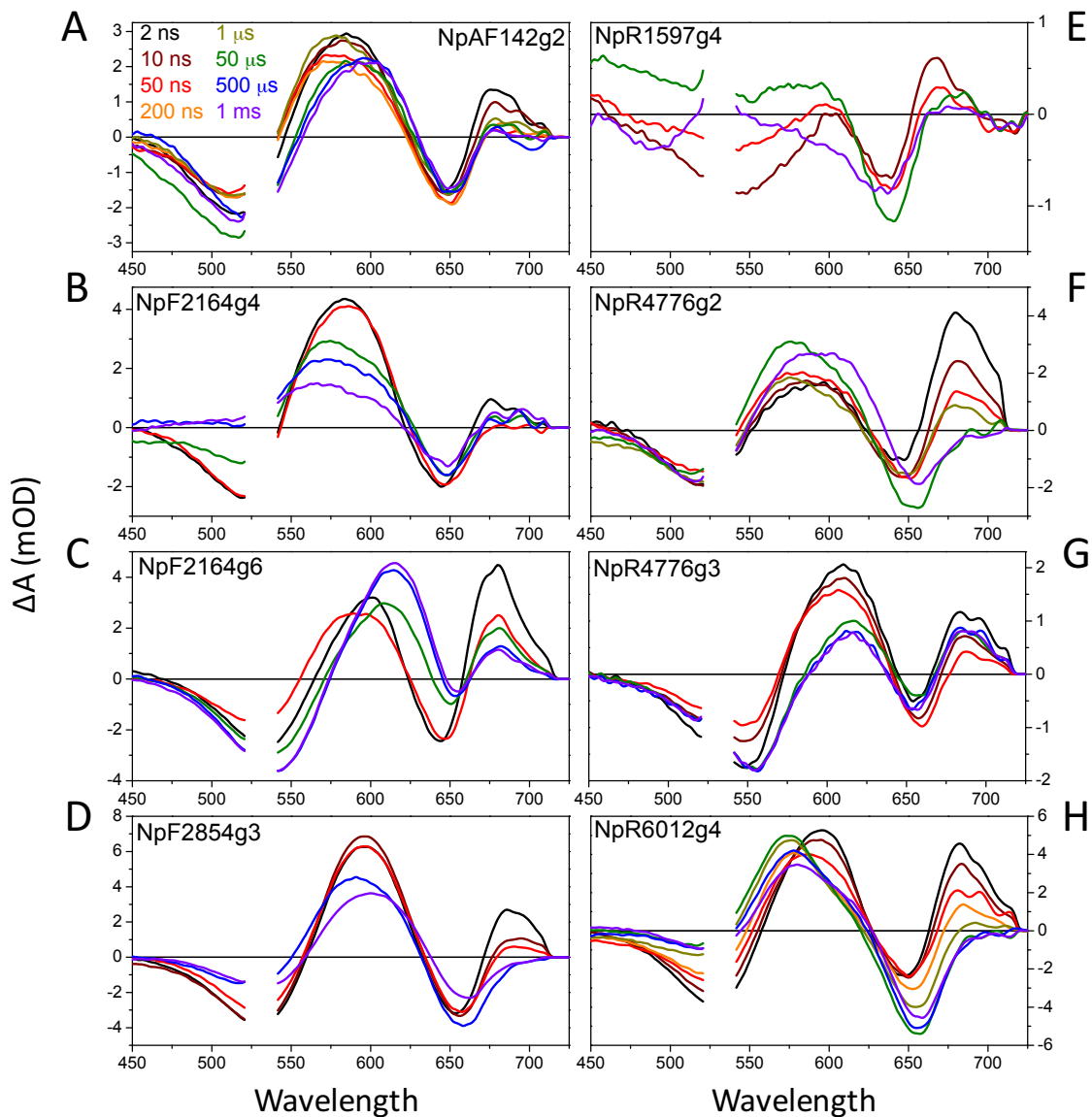


**Figure A5.2:** Red/Green CBCR Secondary Forward Transient Absorption Spectra  
 Raw (uncorrected) transient absorption spectra after 532-nm excitation for (A) NpAF142g2 (B) NpF2164g4, (C) NpF2164g6, (D) NpF2854g3, (E) NpR1597g4 (F) NpR4776g2, and (G) NpR4776g3 and (H) NpR6012g4. Signals exhibit signatures of forward and reverse reaction dynamics overlapping. Spectra are color-coded to the probe times specified in the legend in panel A. Note that not all probe times are represented for each CBCR.



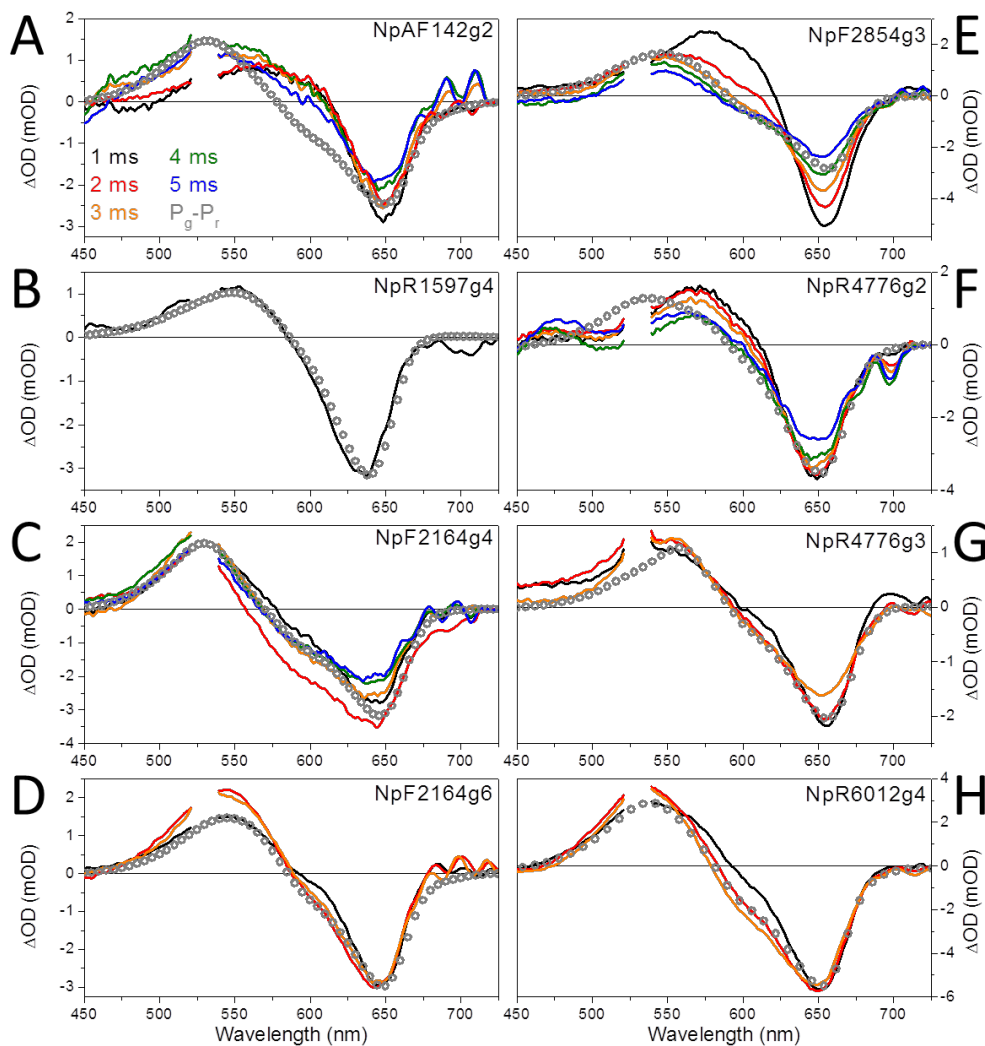


**Figure A5.3:** Primary and Secondary Forward 1 ms Transient Absorbance Spectra  
 Transient absorption difference spectra for the CBCRs past 1 ms. Signals for (B) NpR1597g4 were not collected past 1 ms. Signals for (D) NpF2164g6, (G) NpR4776g3 and (H) NpR6012g4 were not collected past 3 ms. The signals for the remaining CBCRs suffer from low S/N after 5 ms. This is especially true for (E) NpF2854g3. Spectra colors correspond to the probe times specified in the legend in panel A. Ground state difference spectra (gray circles) are shown to determine completeness of the photoreaction for each CBCR.

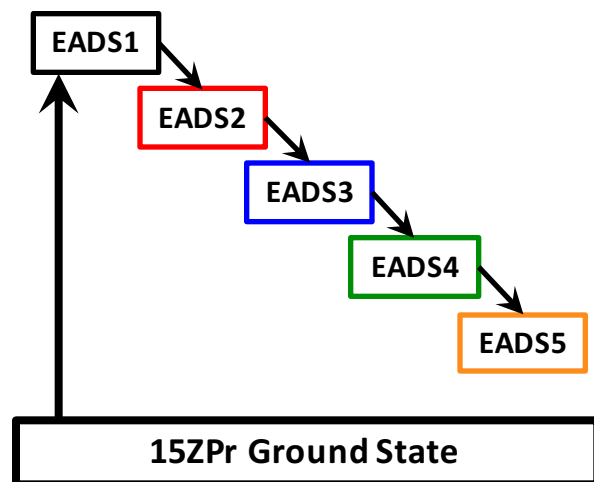


**Figure A5.4:** Sequential Model

Sequential model used to extract Evolution Associated Difference Spectra (EADS) for each CBCR.

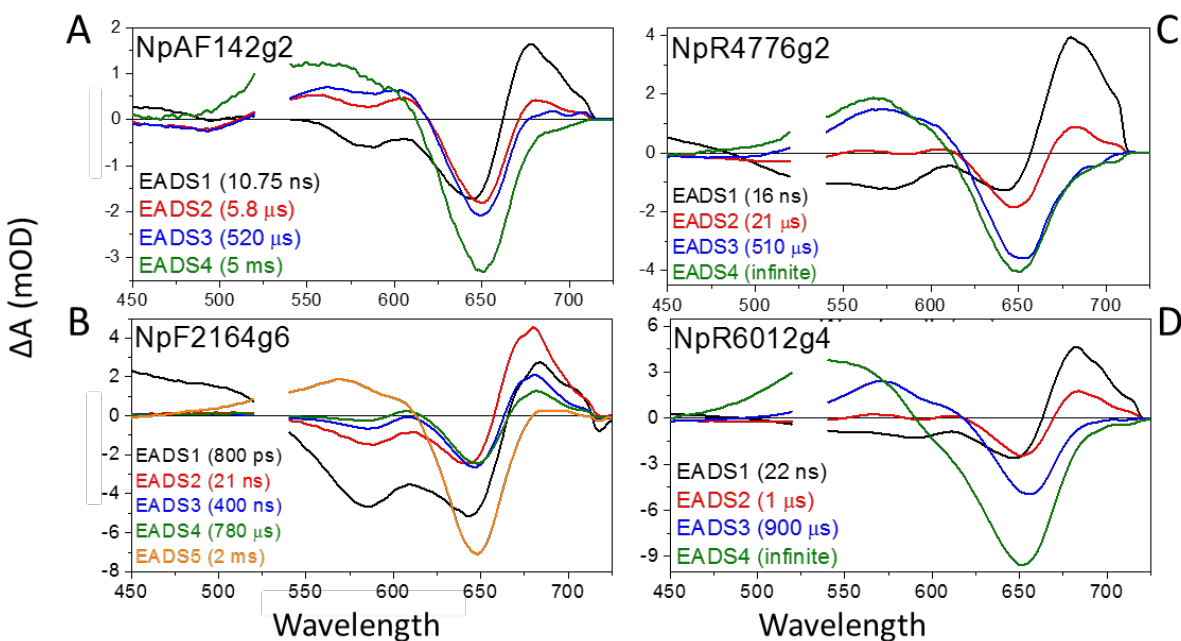


**Figure A5.5:** Secondary Forward Red/Green CBCR EADS

EADS (color coded to model in Figure S4) for the CBCRs that exhibit the unproductive Lumi-Of pathway using the sequential model presented in Figure S4: (A) NpAF142g2 (B) NpF2164g6 (C) NpR4776g2 and (D) NpR6012g4. The static 15EPg - 15ZPr difference spectrum (dashed grey curves) are shown for comparison. The EADS of the CBCRs that did not exhibit the unproductive Lumi-Of pathway can be found in Figure 6

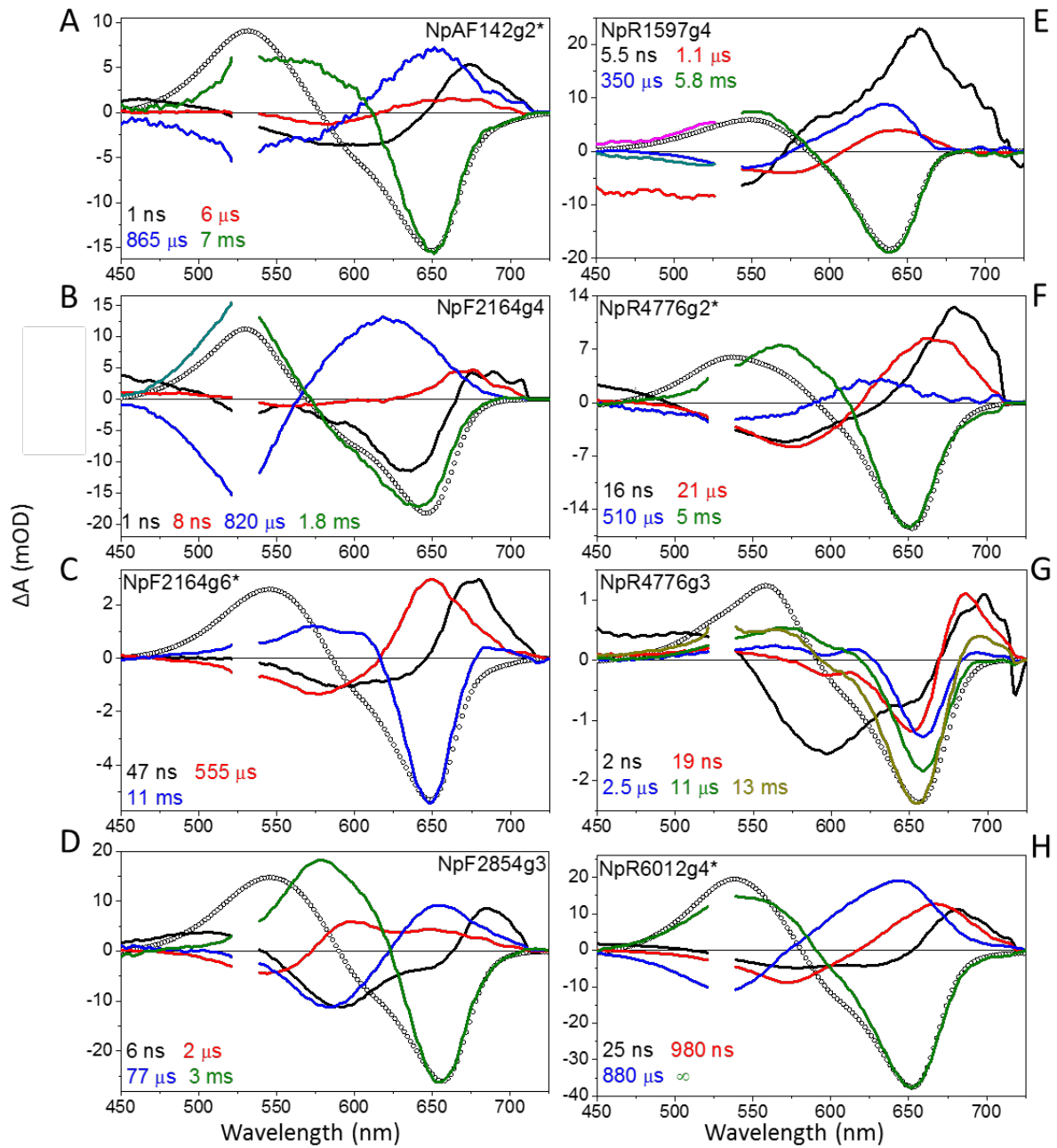


**Figure A5.6:** Secondary Forward Red/Green CBCR DADS

DADS of the various CBCR domains using a parallel model incorporating the same time constants as the EADS analysis (sequential model) given in Table 1.

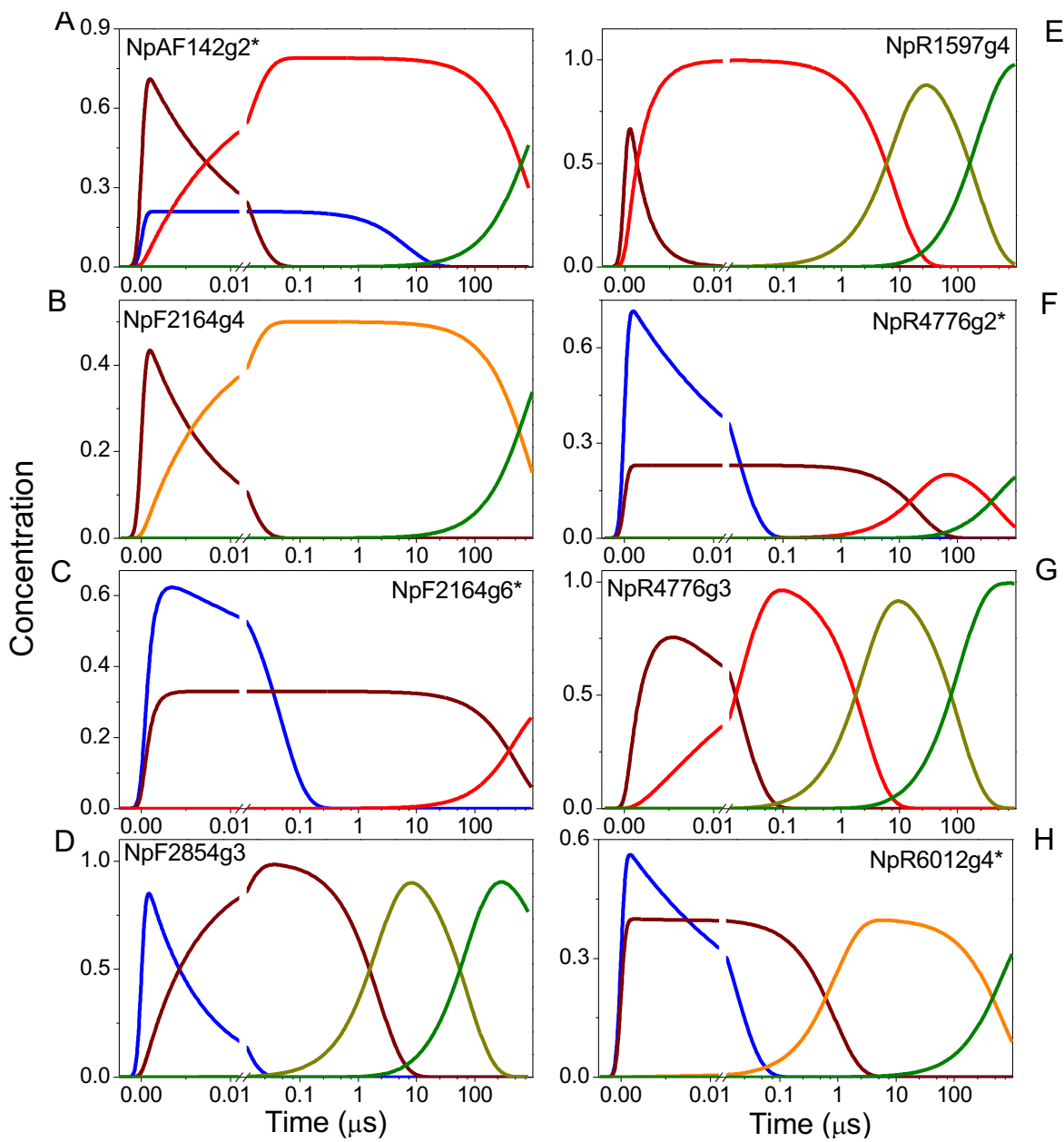


**Figure A5.7:** Secondary Forward Red/Green CBCR Concentration Profiles  
 Concentration profiles from the fitting of the various CBCR domains using the model presented in Figure 5. The curves are color coded to match the EADS in Figure 6.

## A5.2: Supplemental Abbreviated Red/Green CBCR Amino Acid Alignments

```
NpAF142g2: -----VGMVWDTYLQETQGGRYRNNETF
NpF2164g6: -----IRTIWEDEHLQQTQGGRYRNNETF
NpR4776g2:      NESEIGINTVWNDTYL
NpR6012g4: -----IKTVWEDTHLQETQGGRYAQGENF
NpF2164g4: -----IKTVWEDEHLQQTQGGRYRNNETL
NpF2854g3: -----KNLVWEDTHLQETKGGRYRNNENF
NpR1597g4: -----IVPVADDYLQETQGRNFANGKSI
NpR4776g3: -----TKTVWQDSYLQETQGGRYRHNETF
NpF2164g5*:----- IKTIWMDEHLQETQGGRYRNHETF
```

**Figure A5.8:** Red/Green CBCR Amino Acid Sequence Alignment Near the Asp Motif. Sequence alignment of the 7 out of 8 of these proteins, excluding NpR4776g2, were previously reported by Rockwell et al.<sup>69</sup> The proteins with names written in blue exhibited the unproductive Lumi-O<sub>f</sub> and those written in red did not. Given the protein sequence obtained for NpR6012g4 and the protein sequence alignment from Rockwell et. al,<sup>1</sup> the tryptophan (W) written in red was identified as W655 and the aspartic acid (D) written in blue was identified as D657. The orientation of these two specific amino acid residues were shown to be responsible for the spectral inhomogeneity in NpR6012g4 and the unproductive <sup>152</sup>P<sub>o</sub> subpopulation.<sup>108</sup> The corresponding residue in the 7 other proteins previously reported by Rockwell et. al. and NpR4776g2 were also highlighted.<sup>1</sup> Every protein studied had a W at this corresponding location (written in red), except for NpR1597g4 which incorporated a valine (V) at this location which is written in green. All the domains studied also incorporated Asp (blue) at the same location in the amino acid sequence as NpR6012g4. The sequence alignment for 4776g2 was obtained by performing a BLASTp search comparing the amino acid sequence for NpR6012g4 and NpR4776g2 obtained from a patent belonging to Dr. Lagarias.<sup>353</sup> \*NpF2164g5 secondary dynamics were not probed, hence not included in this study, because the primary dynamics revealed no measurable Lumi-R quantum yield,<sup>176</sup> but was added as a comparison for NpR159g4 that also exhibited a low Lumi-R quantum yield but replaced the conserved Trp with Val.

**Table A5.1: Amino Acids at Locations With Known Importance**

Amino acid present at key locations shown to effect CBCRs.<sup>197</sup> The domain names highlighted in orange displayed features consistent with the unproductive <sup>15</sup>ZP<sub>o</sub> subpopulations and the amino acid residues highlighted in red differ from the more consistently presented amino acid residues at the given positions.

Domain	B1 notch	B2 Phe	Lid Trp	Asp	Cys	His	Helix Phe
NpAF142g2	Ser	Phe	Trp	Asp	Cys	His	Phe
NpF2164g6	Ala	Phe	Trp	Asp	Cys	His	Phe
NpR4776g2	Ser	Phe	Trp	Asp	Cys	His	Phe
NpR6012g4	Ala	Phe	Trp	Asp	Cys	His	Phe
NpF2164g4	Ala	Phe	Trp	Asp	Cys	His	Phe
NpF2854g3	Gly	Phe	Trp	Asp	Cys	His	Phe
NpR1597g4	Thr	Phe	Val	Asp	Cys	His	Met
NpR4776g3	Ala	Tyr	Trp	Asp	Cys	His	Ile

```

AnPixJg2  DRVAVYRFNPD--WSGEFVAES--VGSGWVKLVGPD----IKTVWEDTHLQETQGGRYRHQESF-VVNDI-YEAGHFS
NpAF142g2  DRLSVYRFNAD--WSGEFVGDYETANPRWGRSIKLG----VGMVWDDTYLQETQGGRYRNNETF-VVDDI-HSQGFTQ
NpF2164g6  DRLAVYRFNPD--WSGEFIAES--VSREWVALVGPE----IRTIWEDEHLQQTQGGRYRNNETF-VINDV-YTAGHAQ
NpR4776g2  DRVSVYRFDSN--WSGEFVGDFEAASPYWSNESEIG----INTVWNDTYLQDTEGGRYRNNETF-AVDDI-YKMGFAK
NpR6012g4  DRVAVYRFNPN--WSGEFVAES--VAHTWVKLVGPD----IKTVWEDTHLQETQGGRY
                T631                H641                W655

NpF2164g4  DRLAIYRFNSD--WSGEFIAES--VGSDWVPLVGPD----IKTVWEDEHLQQTQGGRYRNNETL-AVNDI-YTVGYAQ
NpF2854g3  ERVGVYRFNED--WSGEFVSNFGMVEAQWDSINPFG----KNLVWEDTHLQETKGGRYRNNENF-AVEDI-YQAGHSR
NpR1597g4  DRVTIYRFRAD--WSGEFVAES--LAQGWTPVRE-----IVPVVADDYLQETQGRNFANGKSI-VIKDI-YSANYSI
NpR4776g3  DRVAVFQFQAD--WSGEYIAEF--VGDGWVKLVGSN----TKTVWQDSYLQETQGGRYRHNETF-AVDDI-YQVGHSQ

```

**Figure A5.9: Red/Green CBCR Parial Amino Acid Sequence**

Partial amino acid sequence of the Red/Green CBCRs presented here reported by Rockwell et al.<sup>69,197</sup> The domain names highlighted in orange displayed features consistent with the unproductive <sup>15</sup>ZP<sub>o</sub> subpopulations. The amino acids highlighted in red were consistent with the domains that possessed the <sup>15</sup>ZP<sub>o</sub> subpopulations and the amino acids highlighted in blue are consistent with the domains that did not have the <sup>15</sup>ZP<sub>o</sub> subpopulations. Interestingly, at the T631 position of NpR6012g4, all of the <sup>15</sup>ZP<sub>o</sub> subpopulations containing domains had a glycine residue (other than NpR6012g4) and all of the non <sup>15</sup>ZP<sub>o</sub> subpopulations containing domains had a serine residue.

NpAF142g2	WGGEFVGDYETANPRWGRSIKLG
NpF2164g6	WGGEFIAES
NpR4776g2	WGGEFVGDFEAASPYWSNESEIG
NpR6012g4	WTGEFVAES
All2699g2	WGGEFVGDFEATSPHWSNESKIS
AnpixJg3	WGGEFVAES
AnpixJg4	WGGEFVAES
NpF2164g4	WSGEFIAES
NpF2854g3	WSGEFVSNFGMVEAQWDSINPFG
NpR1597g4	WSGEFVAES
NpR4776g3	WSGEYIAEF
AnpixJg2	WSGEFVAES
NpF2164g5	WSVEFVAES
NpF2854g1	WSGSFINRFGFAEHPWDALTAFG
NpF2854g2	WSGEFVSQFGMLEPQWHRIHPFG
NpR5113g2	WSGNFVAES
NpR6012g3	WGGEFVAES
NpR6012g2	WSGEFVAES
slr1393g3	WSGEFIHES
NpF2164g7*	WSGEFVVES *Orange/Green CBCR

**Figure A5.10:** Red/Green CBCR Partial Amino Acid Sequence Near Selectively  $^{152}\text{P}_o$ .

#### Selectively Conserved Residue

Partial amino acid sequence around T631 (highlighted in purple) position of NpR6012g4 believed to be of importance of several Red/Green CBCRs reported by Rockwell et al.<sup>69, 197</sup> Multiple residues incorporated a serine residue (highlighted in blue) at this location, consistent with not having the unproductive  $^{152}\text{P}_o$  subpopulation and a few incorporated the glycine (highlighted in red) that was consistent with having the unproductive  $^{152}\text{P}_o$  subpopulation. The names written in red are the domain that were characterized and did not have the unproductive  $^{152}\text{P}_o$  subpopulations and the domains that did exhibit the unproductive  $^{152}\text{P}_o$  subpopulation are written in orange. If the serine/glycine residue is indicative of the presence of the unproductive  $^{152}\text{P}_o$  subpopulation then this suggest that a larger percentage of the Red/Green CBCRs presented in this list do not incorporate the unproductive  $^{152}\text{P}_o$  subpopulations than the 50% of samples whose secondary dynamics were reported here.

*Chapter 6. Supporting Information For “Conservation and Diversity in the Primary Reverse Photodynamics of the Canonical Red/Green Cyanobacteriochrome Family”*

**Includes: Supplemental Methods, Supplemental Discussion on Quantum Yield Estimations from Target Modeling, Supplemental Figures (S1-S14), Supplementary Discussion on Red/Green CBCR Structures (S15-S18), Supplemental Tables (S1-S4) and Supplemental References**

*A6.1: Supplemental Methods*

*A6.1.1 Estimating Quantum Yield by Comparing Raw Signals.*

For NpF2854g3, the excited-state  $P_g^*$  transient spectra were normalized to the initial amplitude of the ESA band for NpR6012g4. After normalization, it was observed that the scaled Lumi- $G_o$  spectrum at maximum amplitude for NpF2854g3 was approximately 88% the amplitude of that for NpR6012g4. Because these CBCRs demonstrate comparable photoproduct spectral features, it is assumed that the both CBCRs exhibit similar extinction coefficients.<sup>182</sup> Since the Lumi- $G_o$  spectrum for NpF2854g3 was then scaled by  $\sim 1.13$  to match the amplitude of NpR6012g4 spectrum, the Lumi- $G_o$  quantum yield in NpF2854g3 is estimated at  $\sim 50\%$  ( $0.88 \times 56$ ).

This same approach was taken for NpAF142g2. After normalization, the scaled Lumi- $G_o$  spectrum amplitude for NpAF142g2 was  $\sim 82\%$  of that for NpR6012g4. So, Lumi- $G_o$  for NpAF142g2 was further scaled by  $\sim 1.22$ , estimating the Lumi- $G_o$  quantum yield in NpAF142g2 at  $\sim 46\%$ . Finally, the same approach was also applied for NpR5113g2. The magnitude of the primary Lumi- $G_y$  spectrum of NpR5113g2 (Figure S6) after scaling is approximately 63% of that for NpR6012g4 and must be further scaled to roughly overlap with that for NpR6012g4. Using the same



assumption as described above for NpAF142g2, this method estimates ~35% quantum yield for the Lumi-G<sub>0</sub> species in NpR5113g2. With that in mind, the evolution from Lumi-G<sub>0</sub> to Lumi-G<sub>y</sub> in NpR5113g2 was assumed to be ~92% efficient to fit the long-time kinetics of the partially obscured bleach band.

Unfortunately, accurate estimation of the  $\Phi_{\text{Meta-Gr}}$  could not be achieved due to the absence of an existing standard for comparison. However, assumptions were made based on the long-time dynamics of the partial bleach band and the first two photoproduct species, and the relative amplitudes of the SADS to be discussed later. These factors assume a ~4.3% quantum yield of Meta-G<sub>r</sub> within the experimental probe window. The specifics regarding the modeling of the data is discussed in greater detail in the manuscript. Similar quantum yield estimations were done for the other CBCRs in this study (Table A6.3).

#### *A6.1.2 Target Model Construction.*

If the initial, unbiased sequential model did not extract the difference spectra of the real populations (Species Associated Difference Spectra or SADS), then more complicated multi-component target model analysis is required. To generate viable target models, features observed in the transient difference spectra (i.e. decay, growths, or shifts in the spectral signals; Figures 6.2, A6.2, and A6.3) and kinetics (i.e. non-monotonic behavior or synchronized growth and decay in signals; Figures 6.3, A6.4, and A6.) are used in correlation with the results of the sequential analysis (i.e. the Evolution Associated Difference Spectra or EADS and apparent lifetimes; Figure A6.7). Taking the differences of the EADS sequentially (EADS2-EADS1, EADS3-EADS2, etc.;

Figure A6.8) is useful in better visualizing the changes between sequential EADS. For example, the difference EADS2 and EADS1 of NpR5113g2 (Figure A6.8) matches EADS3, which indicates that there are at least two  $^{15}\text{EP}_g^*$  populations that populate a spectrally comparable Lumi-G<sub>0</sub> photointermediate. This is reflected in the target model of the reverse dynamics of NpR5113g2 (Figure A6.10). The resulting SADS (Figures 6.5 and A6.10) and concentration profiles (Figures 5 and Figure A6.11) of the target models in Figure A6.9 are compared in multiple figures.

### *A6.1.3 Quantum Yield Estimations from Target Modeling.*

Similar to the forward reaction dynamics,<sup>176</sup> the absolute quantum yield Lumi-G<sub>0</sub> photointermediate ( $\Phi_{\text{Lumi-G}_0}$ ) generation was difficult to estimate directly from the TA signals alone due to overlapping ESA decay, SE, or photointermediate signals. Since direct estimation of  $\Phi_{\text{Lumi-G}_0}$  is not available for these CBCRs,  $\Phi_{\text{Lumi-G}_0}$  was estimated using NpR6012g4 as a reference in a similar manner as that used for the forward reactions.<sup>176, 182, 183</sup> Unfortunately, the presence of overlapping Lumi-G<sub>0</sub> and Meta-G<sub>y</sub> photointermediates in several of the CBCRs confounds this approach (Figure A6.6). Therefore, these estimates provide a lower-limit for  $\Phi_{\text{Lumi-G}_0}$ . SADS for the excited-state and photoproduct populations extracted by the target analyses therefore provided alternative values for these estimates.

For the representative Class I<sub>R</sub> sensor NpF2164g6,  $^{15}\text{EP}_g^*\text{-I}$  exhibited a 1.86 ps lifetime, with 64% generating Lumi-G<sub>0</sub>.  $^{15}\text{EP}_g^*\text{-II}$  was longer living with a lifetime of ~13.7 ps, ~40% of which generating Lumi-G<sub>0</sub>. This inhomogeneous model predicts an overall  $\Phi_{\text{Lumi-G}_0}$  of ~36% (Table A6.3). As a Class I<sub>R</sub> sensor, Lumi-G<sub>0</sub> did not decay on the ultrafast timescale. With the SADS

method,  $\Phi_{\text{Lumi-G}_0}$  for NpF2164g6 (Figure A6.14A) was estimated to be 36%, which closely agrees with 34% estimated from the raw data comparison with NpR6012g4 (Figure A6.6).

For the representative Class II<sub>R</sub> sensor NpAF142g2,  $^{15E}P_g^*$ -I exhibited a 1.7 ps lifetime with ~57% forming Lumi-G<sub>0</sub>.  $^{15E}P_g^*$ -II was longer living with an 11.6 ps lifetime, ~65% of which produced the Lumi-G<sub>0</sub> population.  $^{15E}P_g^*$ -III population possessed a 75 ps lifetime and did not yield a resolvable photointermediate. The SADS comparison method for NpAF142g2 estimated  $\Phi_{\text{Lumi-G}_0}$  at 49% (Figure A6.14B) which was similar to 46% estimated using raw data (Figure A6.6). Similar to the conversion observed in NpR6012g4,<sup>183</sup> the efficiency of Lumi-G<sub>0</sub> conversion to Meta-G<sub>y</sub> for NpAF142g2 was nearly 100%. The Meta-G<sub>y</sub> population exhibited a lifetime of ~20 ns. Since there was no discernible photointermediate population formed after Meta-G<sub>y</sub>, its decay (at least partially) was modeled to refill the GSB on this timescale. Reverse dynamics also has been reported for the Class II<sub>R</sub> sensor NpR6012g4 that exhibited excitation wavelength dependence where the shorter wavelength excitation increased the quantum yield of photoisomerization from 45% with 575 nm excitation to 60% with 500 nm excitation.<sup>183</sup> A similar wavelength dependence also was observed for Slr1393g3.<sup>185</sup>

For the representative Class III<sub>R</sub> sensor NpR4776g3, two  $^{15E}P_g^*$  populations with lifetimes of ~13 ps and 162 ps were observed. In this case, 20% of the shorter lived  $^{15E}P_g^*$ -I population and ~5% of the longer lived  $^{15E}P_g^*$ -II population yielded Lumi-G<sub>0</sub> with ~9.3%  $\Phi_{\text{Lumi-G}_0}$  (Figure A6.10C). Absolute estimation of the yield of  $^{15Z}P_r$  and Meta-G<sub>r</sub> could not be made since there is no established standard of reference for estimating the Meta-G<sub>r</sub> quantum yield. However, to fit the

GSB recovery kinetics for NpR4776g3, Lumi-G<sub>o</sub> was assumed to bifurcate such that 4% yielded Meta-G<sub>r</sub> with the remaining 96% returning to the <sup>15E</sup>P<sub>g</sub> ground state.

For the Class III<sub>R</sub> sensor NpR5113g2, the SADS comparison method estimated a 39% Lumi-G<sub>o</sub> quantum yield (Figure A6.13), which was similar to the 35% estimate using raw data (Figure A6.6). NpR5113g2 was modeled such that 92% of the Lumi-G<sub>o</sub> population evolved to Meta-G<sub>y</sub> ( $\Phi_{\text{Meta-G}_y} \sim 36\%$ ) and that  $\sim 13\%$  of Meta-G<sub>y</sub> evolved to Meta-G<sub>o</sub> and Meta-G<sub>r</sub> ( $\Phi_{\text{Meta-G}_o} \sim 4.8\%$ ) in order to fit the GSB recovery kinetics. Although no resolvable decay of Meta-G<sub>o</sub> or Meta-G<sub>r</sub> was observed within the experimental probe delay, we assumed that Meta-G<sub>r</sub> continued to grow after  $\sim 8$ -ns. Quantum yield estimates for the other CBCRs can be found in Table A6.3.

#### A6.2: Supplemental Red/Green CBCR Primary Reverse Dynamics

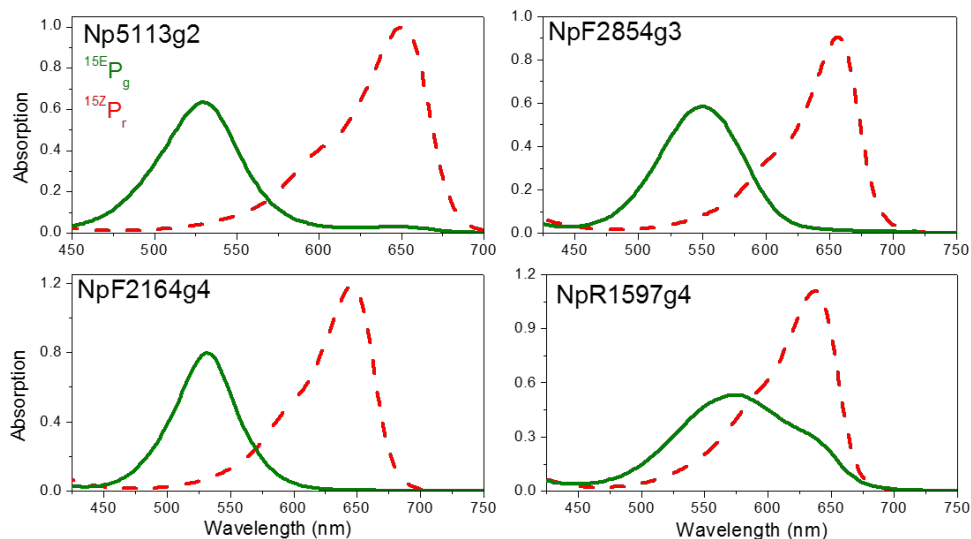


**Figure A6.1:** Remaining Red/Green CBCR Ground State Absorption Spectra

Ground-state absorption spectra for the remaining CBCRs investigated in this study, as indicated in the panels. <sup>15E</sup>P<sub>g</sub> spectra (solid green curves) are shown accompanied by their corresponding <sup>15Z</sup>P<sub>r</sub> spectra (dashed red curves).

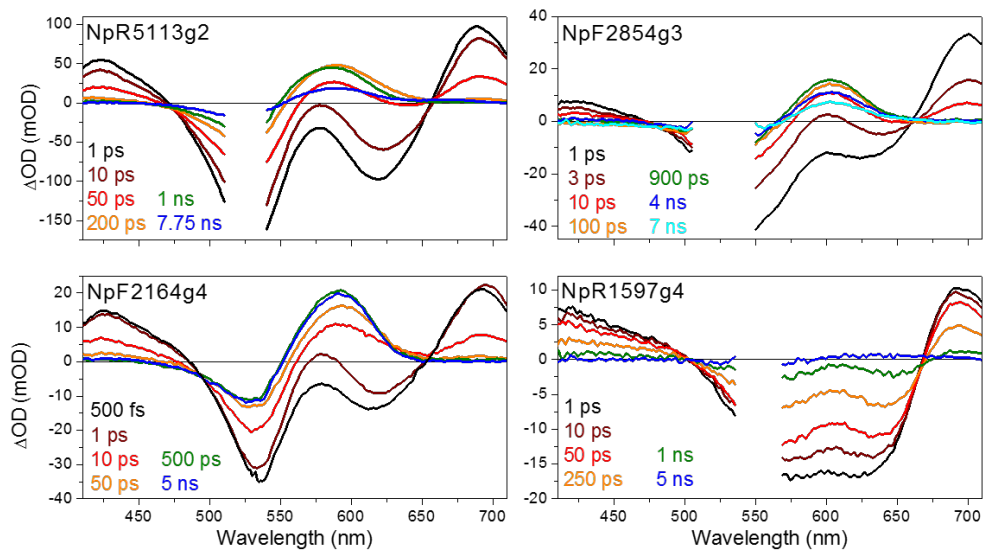


**Figure A6.2:** Remaining Red/Green CBCR Primary Reverse Transient Absorption Difference Spectra

Transient absorption difference spectra of the remaining CBCRs after excitation of the  $^{15}E_g$  ground state. All CBCRs in this study exhibit qualitatively similar excited-state spectra, though with differing kinetics, especially after the decay of the excited state.

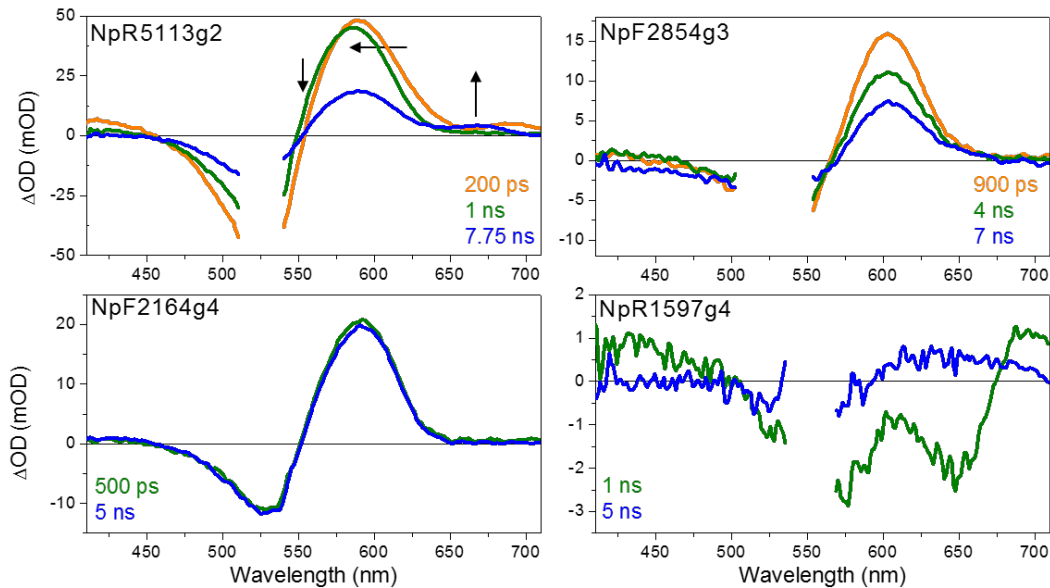


**Figure A6.3:** Remaining Red/Green CBCR Primary Reverse Transient Absorption Difference Spectra at Later Times

Later time reverse reaction transient absorption difference spectra for remaining CBCRs.

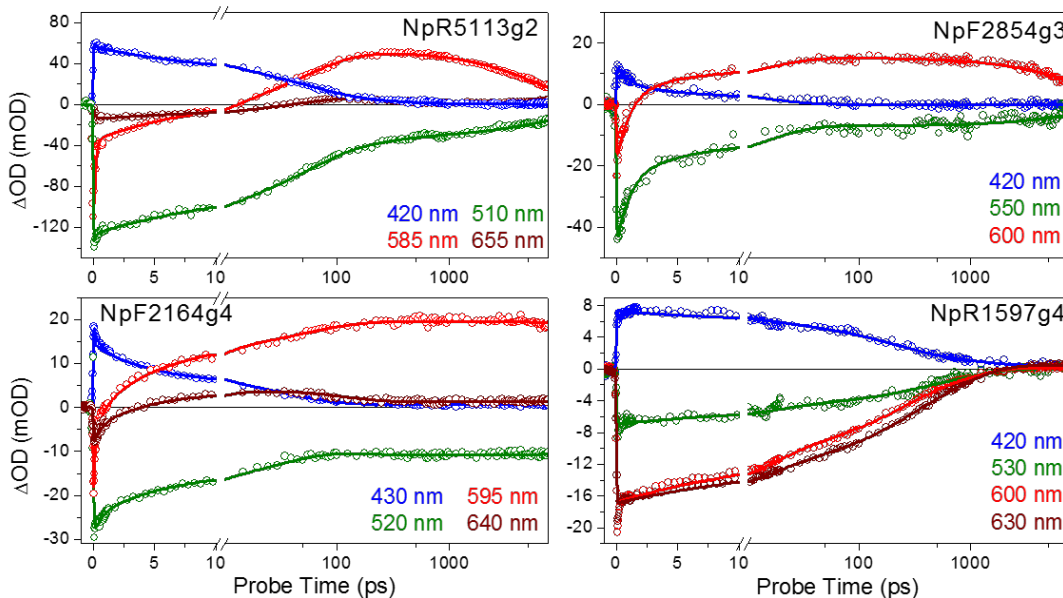


**Figure A6.4:** Remaining Red/Green CBCR Primary Reverse Kinetics

Kinetic traces for the remaining CBCRs at wavelengths specified in the legends. Wavelengths were chosen to represent regions of prominent dynamic signals (ESA, bleach, photoproduct(s), etc.). All kinetic data is overlaid with fit curves extracted using the target model for each CBCR.

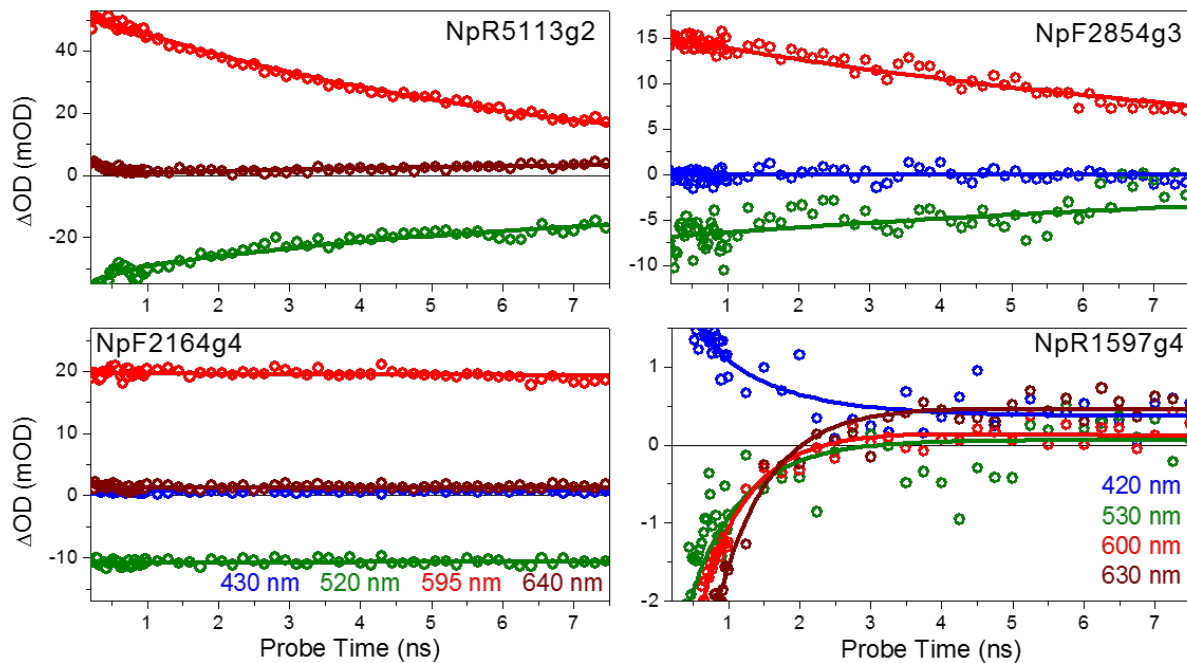


**Figure A6.5:** Remaining Red/Green CBCR Primary Reverse Kinetics Focused on Later Times  
 Kinetic traces for the remaining CBCRs at wavelengths specified in the legends, focusing on the longtime (>1 ns) dynamics of the photoproduct(s). All kinetic data is overlaid with fit curves extracted using the target model for each CBCR.

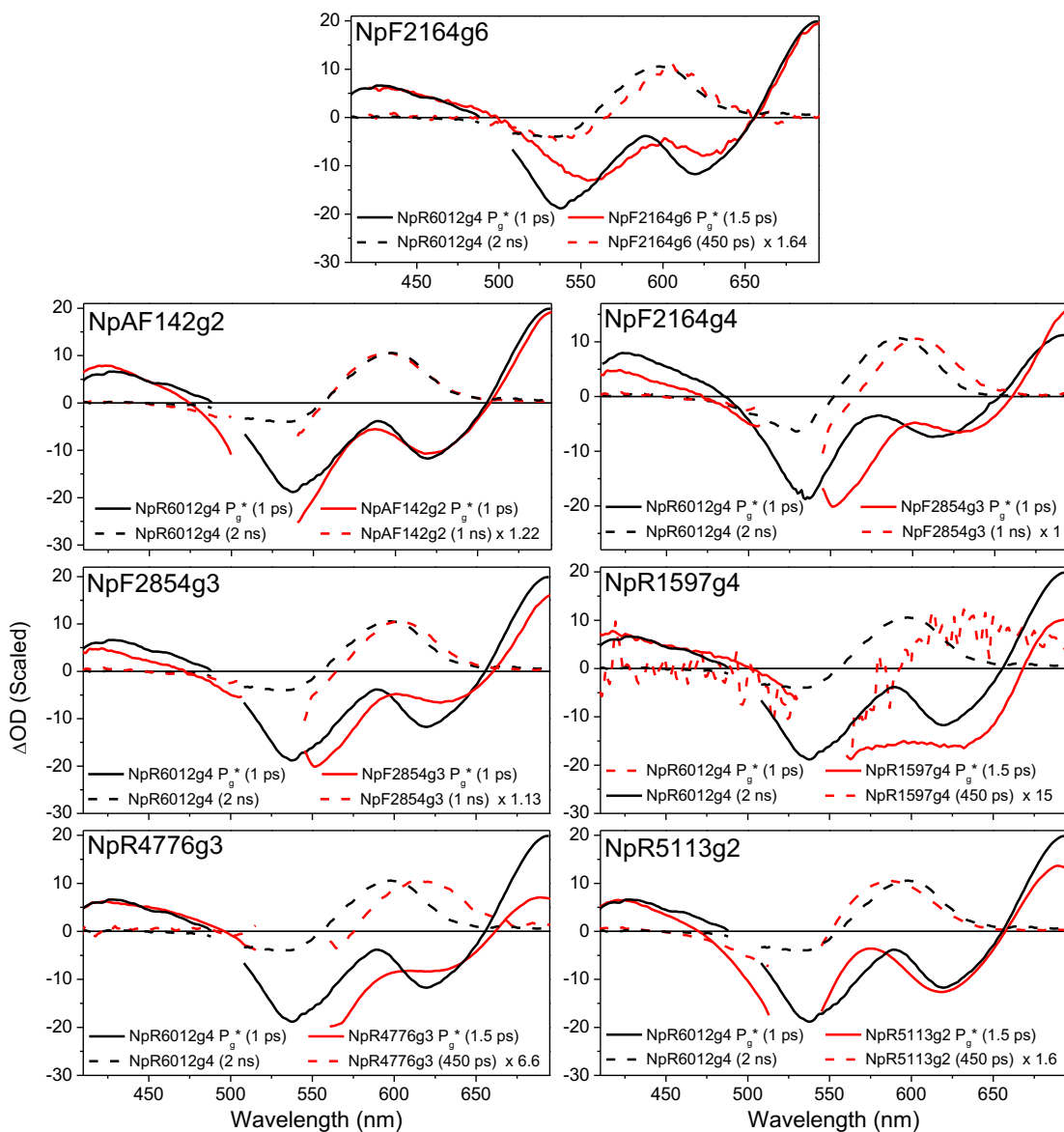


**Figure A6.6:** Red/Green CBR Lumi- $G_o$  Quantum Yield Estimation Using Raw Spectra  
 Photoproduct quantum yield estimations for the CBRs made using raw spectral data for the CBRs and NpR6012g4. Early excited-state spectra for the CBRs are scaled to that for NpR6012g4. Using the same scaling factor, scaled longtime Lumi- $G_o$  spectra for the CBRs are compared to those of NpR6012g4. Any further scaling needed to match the CBRs' photoproduct spectra to those of NpR6012g4 indicates a discrepancy in the quantum yields of the CBRs and NpR6012g4.



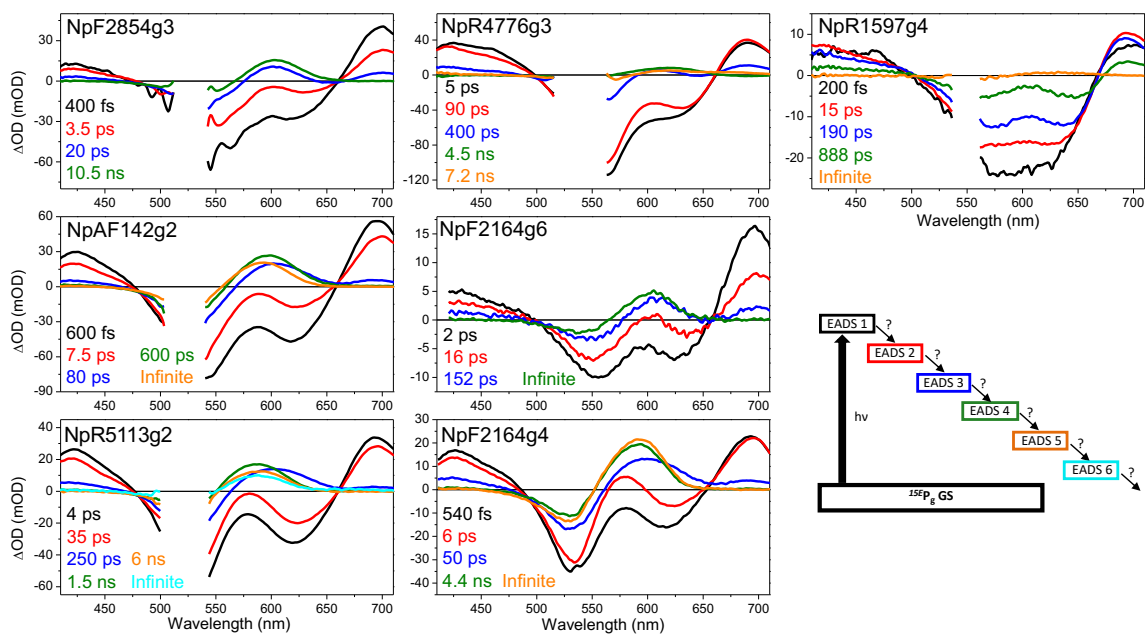


**Figure A6.7:** Red/Green CBCR Primary Reverse EADS

Results of the sequential EADS analysis for all eight CBCRs studied. All CBCRs were fit using the sequential model shown in the bottom right panel. Time constants associated with each EADS are displayed in the legends of the respective panels.

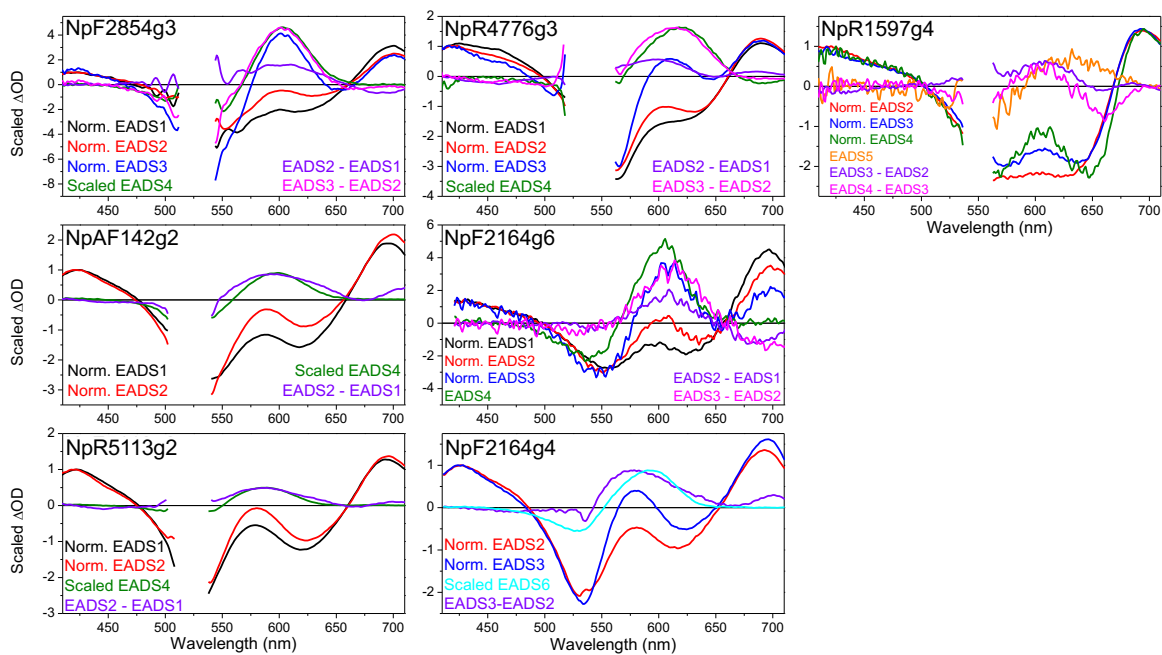


**Figure A6.8:** Red/Green CBCR Primary Reverse EADS Decomposition  
 EADS decomposition for each of the eight CBCRs studied. EADS representing primary excited-state signals were normalized and subtracted sequentially to reveal

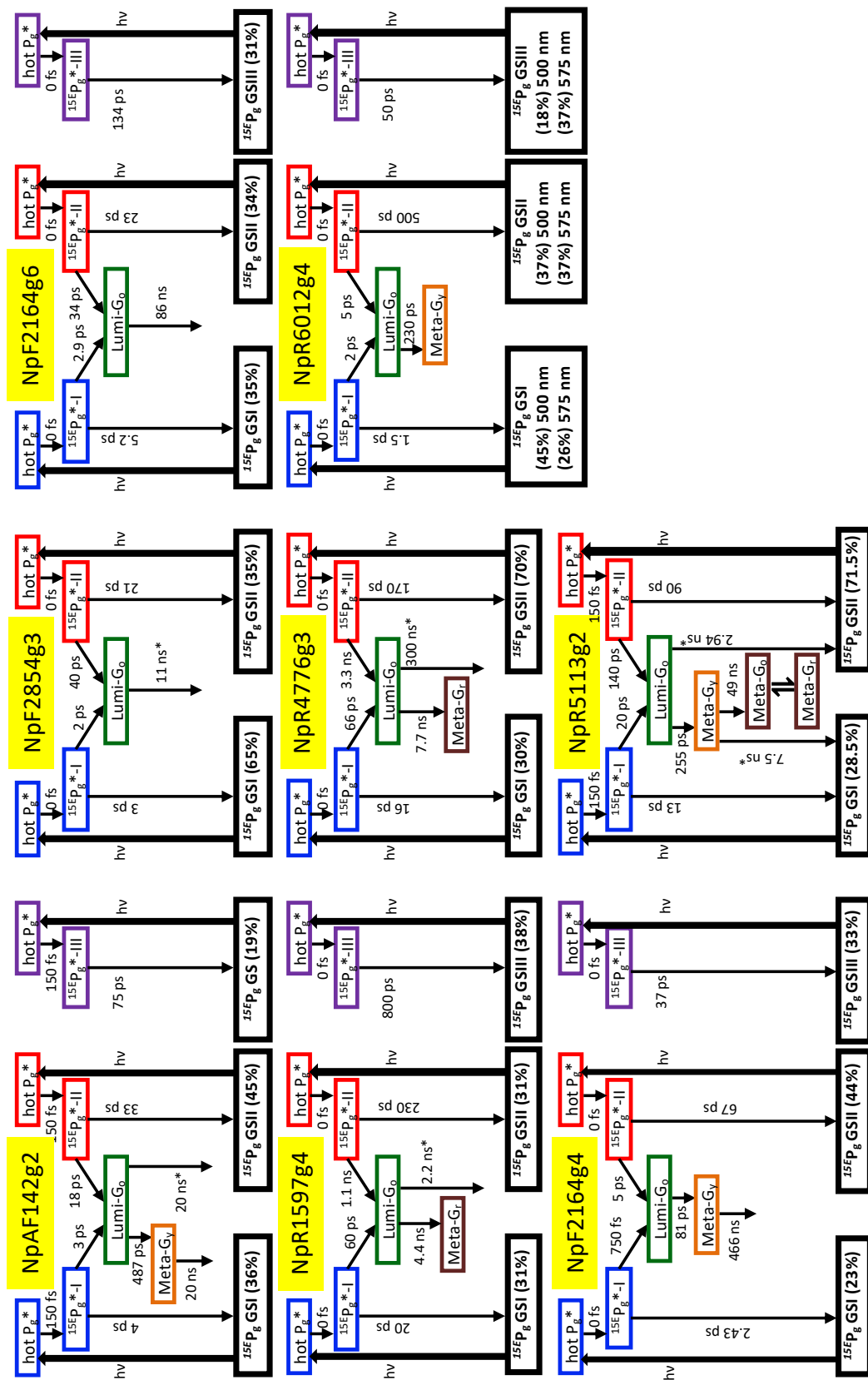
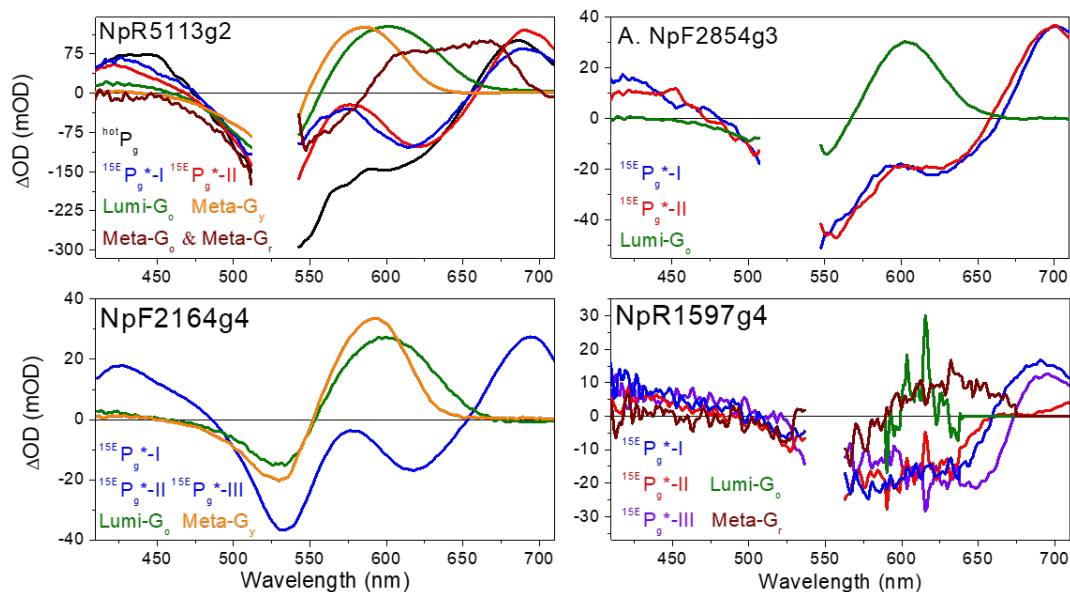


Figure A6.9: Red/Green CBCR Primary Reverse Target Models

Target models for every CBCR studied here



**Figure A6.10:** Remaining Red/Green CBCR Primary Reverse SADS

Species associated difference spectra (SADS) extracted from the target model(s) (Figure A6.9) for the specified CBCRs.

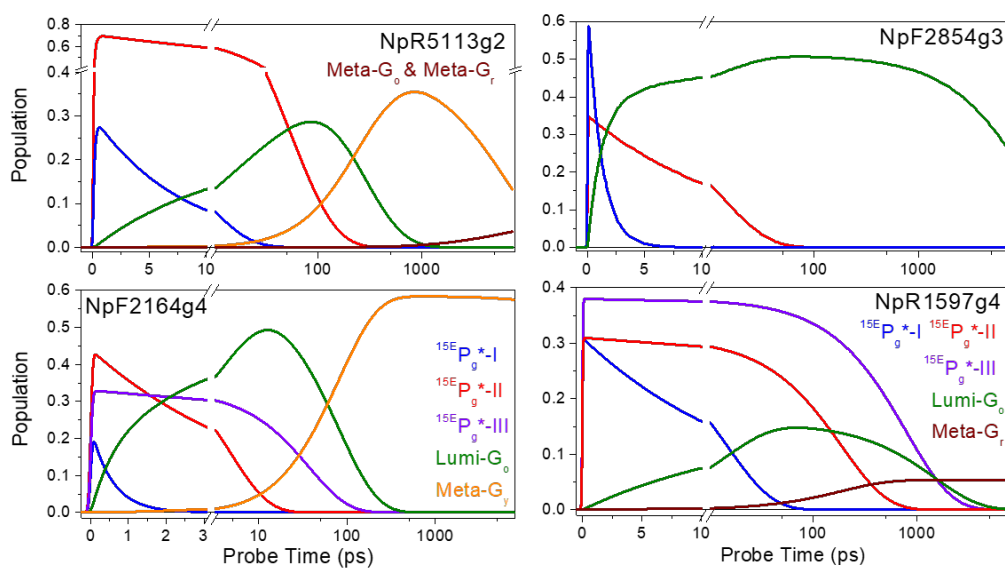


**Figure A6.11:** Remaining Red/Green CBCR Primary Reverse Concentration Curves

Concentration profiles from corresponding target model(s) show the flow of populations from one state to the next for the specified CBCRs. The concentration curves on the top row are color coded to match the legends found on the bottom row.

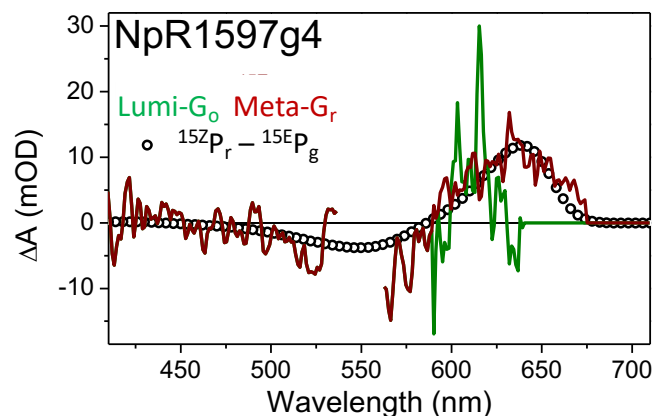


**Figure A6.12:** NpR1597g4 Photointermediate and Static Difference Spectra Comparison Comparison of the photointermediate spectra and  $^{15Z}P_r - ^{15E}P_g$  difference spectrum of NpR1597g4 which indicated that like NpR4776g3, NpR1597g4 generates a population on an ultrafast timescale with a structurally relaxed chromophore that is comparable to that of the  $^{15Z}P_r$  photoproduct.

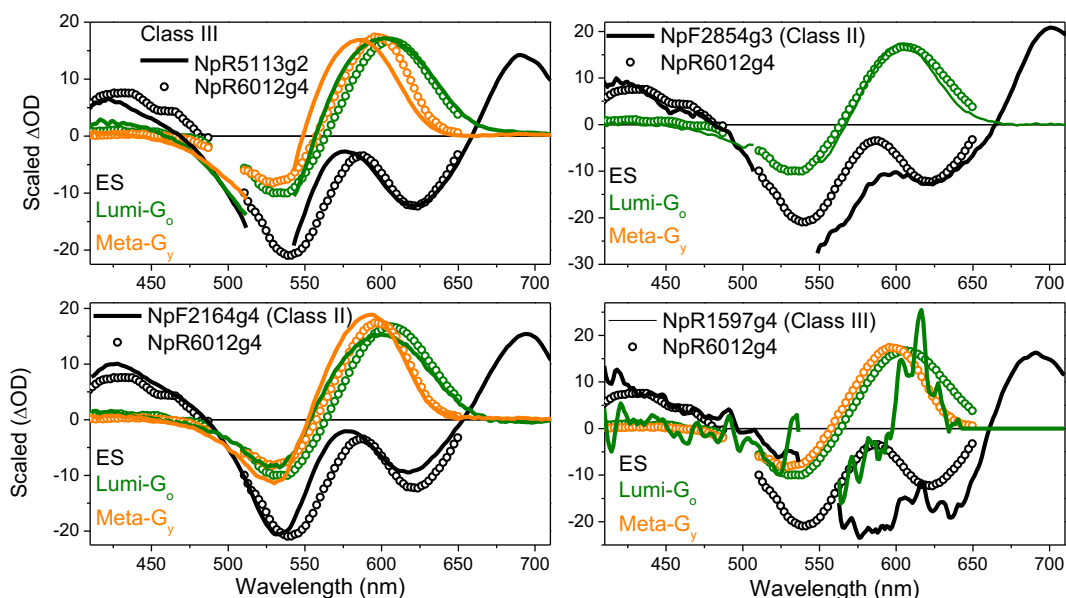


**Figure A6.13:** Remaining Red/Green CBCR SADS Lumi-G<sub>0</sub> Quantum Yield Estimates Photoproduct quantum yield estimations for the remaining four CBCRs as outlined in the manuscript. Excited-state ( $^{15E}P_g^*$ ), Lumi-G<sub>0</sub> and Meta-G<sub>γ</sub> SADS are represented by black, green, and orange curves, respectively. The SADS for each representative CBCR (solid lines) overlap well with those for NpR6012g4 (open circles), with near identical amplitudes and similar spectral shape.

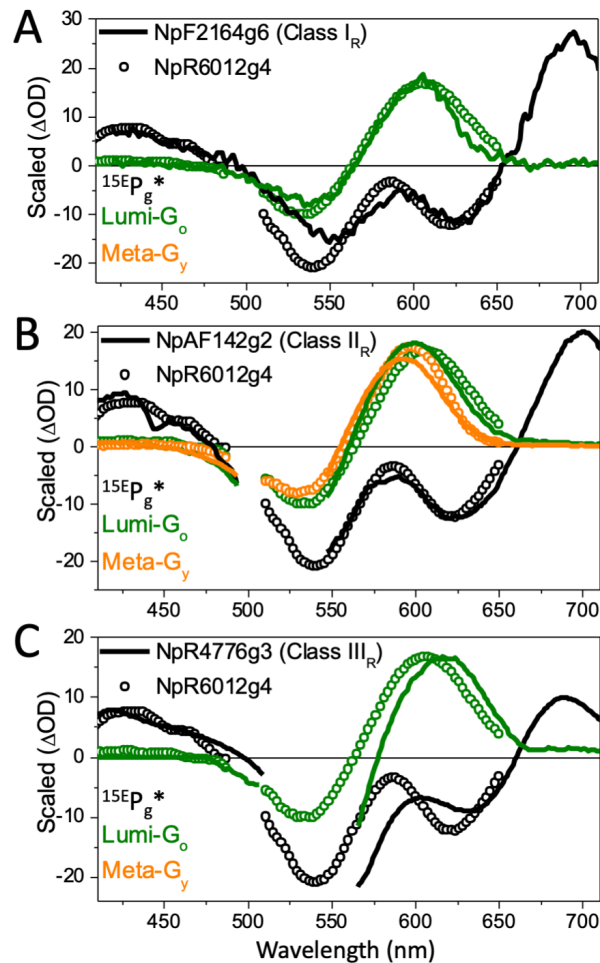


**Figure A6.14:** Representative Red/Green CBCR SADS Lumi- $G_o$  Quantum Yield Estimates

Estimation of the quantum yields for the reverse photoreaction of the representative domains. Excited-state ( $^{15}E_g^*$ ), Lumi- $G_o$  and Meta- $G_y$  SADS are represented by black, green, and orange curves, respectively. (A) NpF2854g3, (B) NpAF142g2, and (C) NpR5113g2 (solid curves) are overlaid with those for NpR6012g4 (open circles). The SADS for each representative CBCR overlap well with those for NpR6012g4, with near identical amplitudes and similar spectral shape.

### A6.3: Supplementary Discussion on Red/Green CBCR Structures

The Class III domains were the only ones to incorporate conserved, smaller alanine (A) residues at Columns A and B of Figure 6.9, which may give more room for the chromophore to planarize further. NpR6012g4 did not exhibit a red absorbing intermediate, but Slr1393g3 exhibited excitation wavelength dependent red absorbing transient population on an ultrafast timescale.<sup>185</sup> The structures of the signaling state of Slr1393g3 and NpR6012g4 had the corresponding Ile and Val (Figure 6.9, column B) facing the chromophore and were 4 Å and 10.5 Å from the D-ring, respectively (Figure A6.16B and A6.16D). In contrast, the corresponding Asp and Glu of Slr1393g3 and NpR6012g4 (Figure 6.9, column A) were pointing away from the chromophore and into the solvent (Figures A6.16B&D). It should be noted that the Asp and Ile residues in Slr1393g3 in Column A and B of Figure 6.9 were also present in the Class II domains. This suggest that these smaller Ala residues may not play a role and that the protein in general moves away from the D-ring, allowing for further planarization.

Overall, the <sup>15E</sup>P<sub>g</sub> signaling state structures of Slr1393g3 and NpR6012g4 were comparable (Figure A6.16), which is not surprising given that they have similar amino acid sequences (Figure 6.9 and S18). The distance between the residues and the chromophore differed slightly between the <sup>15E</sup>P<sub>g</sub> NpR6012g4 and Slr1393g3 structures. The Slr1393g3 <sup>15E</sup>P<sub>g</sub> structure had an additional “bulky” amino acid residue near the chromophore and a smaller average distance (~0.3 Å) of these larger residues from the D-ring of the chromophore (Figure A6.17 and Table A6.4). These residues being slightly closer to the chromophore may be associated with the observed longer excited state lifetimes and lower  $\Phi_{\text{Lumi-Go}}$  observed for Slr1393g3 by hindering the isomerization of the D-ring.<sup>185</sup> It should be noted that the structures of the signaling state of NpR6012g4 and Slr1393g3

were measured using different methods (solution NMR and X-ray crystallography), so the differences in the distances between the residues and the chromophore may be an artifact of the experiment or sample preparation.

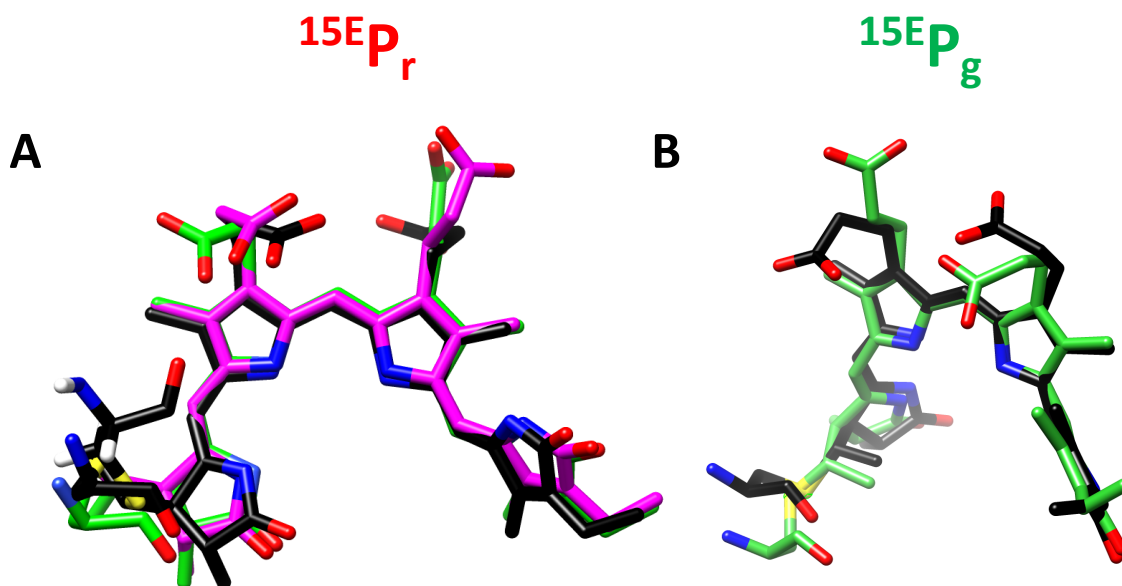


**Figure A6.15:** Resolved PCB Chromophore Conformation Comparison

(A) Overlap of the  $^{15}\text{ZP}_r$  dark adapted state chromophore structure of AnPixJg2 (magenta; 3W2Z), NpR6012g4 (black; 6BHN 1.10), and Slr1393g3 (green; 5DFX) showing that the C and D rings are at an angle and are not planar in all of the CBCRs. (B) Overlap of the  $^{15}\text{ZP}_g$  signaling state chromophore structure of NpR6012g4 (blue; 6GHO 1.1) and the Slr1393g3 (tan; 5M82). Both structures have the A to D rings arranged left to right.



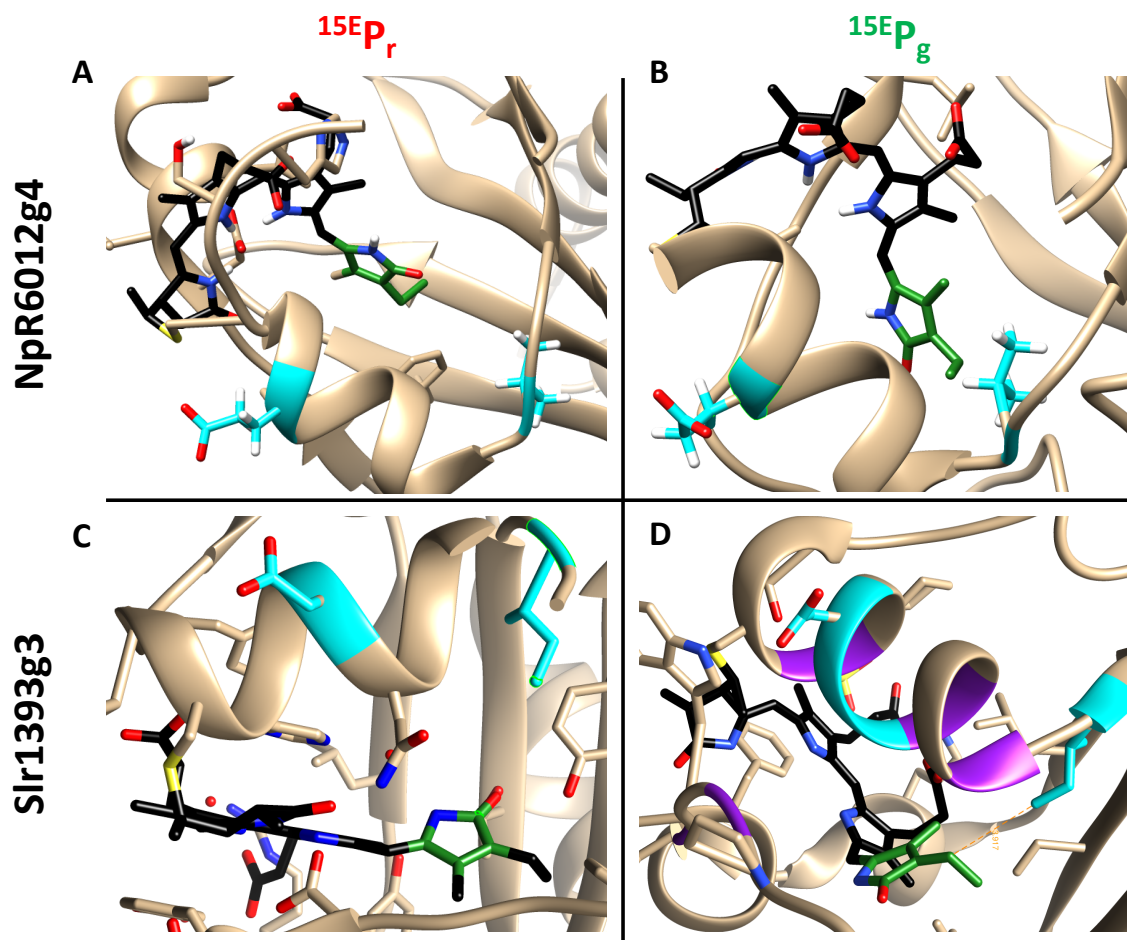


**Figure A6.16:** Resolved Positions of Analogous Alanine Residues in the Dark-Adapted and Signaling State Structures

Dark (A, C; 6BHN, 5DFX) and signaling (B, D; 6BHO, 5M82) state structures of NpR6012g4 and Slr1393g3. The amino acid residues that were aligned to the alanine residues in Figure 6.10 are colored in cyan here (Glu690 and Val697 for NpR6012g4 and Ile538 and Asp531 for Slr1393g3). The chromophore is colored black except for the D-ring which was colored green.

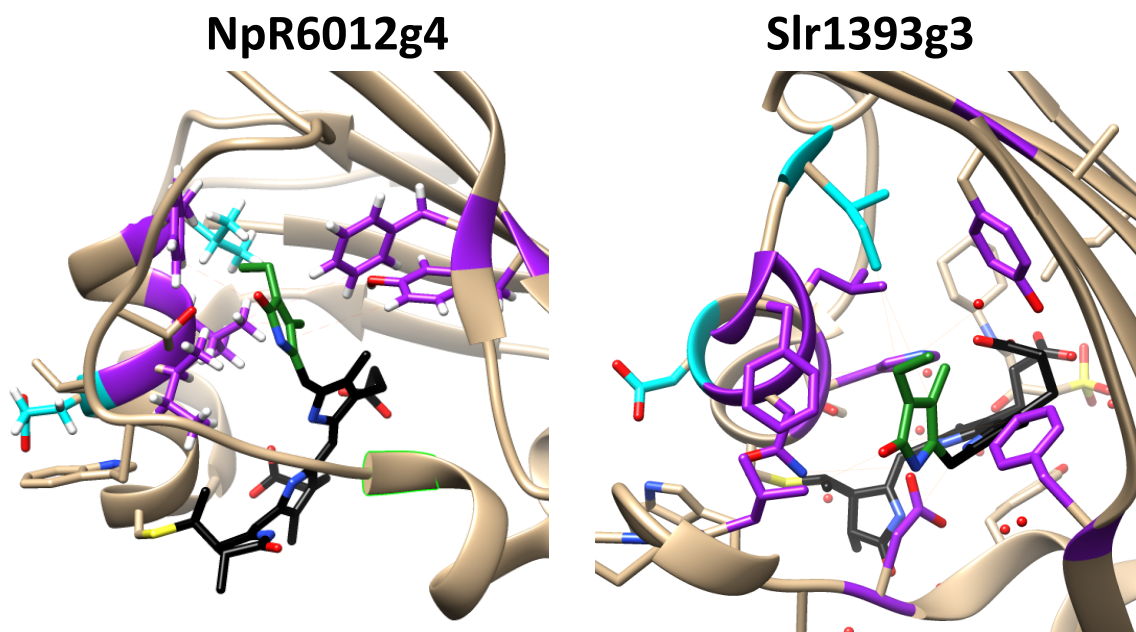


**Figure A6.17:** Resolved Signaling State Structures of Red/Green CBCRs Focusing on the Chromophore Pocket

Signaling state structures of NpR6012g4 (left; 6BHO) and Slr1393g3 (right; 5M82) with emphasis on the larger amino acid residues near the chromophore.

```

441 QNIFRATSDEVRHLLSCDRVLYVRFNPDWSGEFIHESVAQMWEPL--KDLQNNFPLWQDT 499
+ IF+ T+ EVR LL CDRV VYRFNP+W+GEF+ ESVA W L D++ +W+DT
602 EEIFKTTTQEVRQLLRCDRVAVYRFNPNWTGEFVAESVAHTWVKLVGPDIKT---VWEDT 658

500 YLQENEGGRYRNHESLAVGDVETAGFTDCHLDNLRRFEIRAFLTVPVFVGEQLWGLLGAY 559
+LQE +GGRY E+ V D+ G + CH++ L +FE++A++ VPVE GEQLWGLL AY
659 HLQETQGGRYAQQENFVVNDIYQVGHSPCHIEILEQFEVKAYVIVPVFEAGEQLWGLLAAY 718

560 QNGAPRHWQAREIHLLHQIANQLGVAVYQAQLLARFQ 596
QN R W E+ LL +I NQLG+A+ Q + L + Q
719 QNSGTRDWDESEVTLLARIGNQLGLALQCTEYLQQVQ 755

```

**Figure A6.18:** NpR6012g4 and Slr1393g3 Full Sequence Alignment

Protein sequence alignment of Slr1393g3 (top) and NpR6012g4 (bottom). Amino acids highlighted in green are the matches.

A6.4: Supplemental Tables for the Primary Reverse Dynamics of Red/Green CBCRs

**Table A6.1:** Global Analysis Excited State Parameters

Parameters associated with the excited-state populations for the target analysis of studied CBCRs. All time scales are in picoseconds (ps) unless otherwise labeled. Not all CBCRs exhibit three excited-state populations. The two different sets of initial populations for NpR6012g4 was the result of fitting two sets of data using different excitation wavelengths.<sup>182</sup>

Sample	Class	GS1/GS2/GS3 (%)	$^{hot}P_{g^*}$	ES1			ES2			ES3
				$\tau$	$\rightarrow$ GS	$\rightarrow$ Lumi-G <sub>0</sub>	$\tau$	$\rightarrow$ GS	$\rightarrow$ Lumi-G <sub>0</sub>	$\rightarrow$ GS
NpF2164g6	IR	35/34/31	-	1.86	5.2	2.9	13.7	23	34	134
AnPixJg2 <sup>166</sup>	II <sub>R</sub>	47/43/10	-	0.5	1.3	0.7	4	10	7	56
NpAF142g2	II <sub>R</sub>	36/45/19	0.15	1.71	4	3	11.6	33	18	75
NpF2164g4	II <sub>R</sub>	23/44/33	-	575 fs	2.43	750 fs	4.65	67	5	37
NpF2854g3	II <sub>R</sub>	65/35/-	-	1.2	3	2	13.8	21	40	-
NpR6012g4 <sup>174</sup>	II <sub>R</sub>	45/37/18 26 <sup>a</sup> /37/37 <sup>a</sup>	-	562 fs	0.9	1.5	4.95	500	5	50
NpR1597g4	III <sub>R</sub>	31/31/38	-	15	20	60	190	230	1100	800
NpR4776g3	III <sub>R</sub>	30/70/-	-	12.9	16	66	162	170	3300	-
NpR5113g2	III <sub>R</sub>	28.5/71.5/-	0.15	7.9	13	20	54.8	90	140	-

**Table A6.2:** Global Analysis Photointermediate Parameters

Parameters associated with the photoproduct dynamics for the target analysis of studied CBCRs. All time scales are in picoseconds unless otherwise labeled. Not all CBCRs exhibit three excited-state populations. \*No Meta-G<sub>g</sub> quantum yield since it overlaps the bleach.  
\*Yield is based on bleach recovery dynamics.

Sample	Class	Lumi-G <sub>o</sub>					Meta-G <sub>y</sub>				
		$\tau$	$\rightarrow$ GS	$\rightarrow$ Meta-G <sub>y</sub>	$\rightarrow$ Meta-G <sub>r</sub>	$\Phi_{\text{Lumi-Go}}$	$\tau$	$\rightarrow$ GS	$\rightarrow$ Meta-G <sub>r</sub>	$\Phi_{\text{Meta-G}_y}$	$\Phi_{\text{Meta-G}_r^*}$
NpF2164g6	I <sub>R</sub>	-	-	-	-	0.36	-	-	-	-	-
AnPixJg2 <sup>166</sup> *	II <sub>R</sub>	-	-	234	-	0.555	7.5 ns				
NpAF142g2	II <sub>R</sub>	475	2000	487	-	0.49	200 ns	20 ns	-	0.48	-
NpF2164g4	II <sub>R</sub>	81	-	81	-	0.585	466 ns	466 ns	-	0.585	-
NpF2854g3*	II <sub>R</sub>	1100	1100	-	-	0.51	-	-	-	-	-
NpR6012g4 <sup>1</sup> 74	II <sub>R</sub>	230	-	230	-	0.56, 0.48	-	-	-	0.56, 0.48 <sup>a</sup>	-
NpR1597g4	III <sub>R</sub>	1467	2200	-	4400	0.13	-	-	-	-	0.04
NpR4776g3	III <sub>R</sub>	7500	300 ns	-	7700	0.093	-	-	-	-	0.09
NpR5113g2	III <sub>R</sub>	235	2940	255	-	0.39	6.5 ns	7500	49 ns	0.36	0.04

**Table A6.3:** Photointermediate Quantum Yield Estimates and electronic absorption spectral properties

Photochemical quantum yield estimates and electronic absorption spectral properties. The two  $\Phi_{\text{Lumi-Go}}$  values for NpR6012g4 correspond to two different excitation wavelengths (a: 500 nm and b: 675 nm). \*  $\Phi_{\text{Lumi-Go}}$  for Slr1393g3 was estimated by comparing the initial ground state bleach and terminal ground state bleach in the EADS near 530 nm after 515 nm<sup>c</sup>, 540 nm<sup>d</sup>, and 560 nm<sup>e</sup> excitation.<sup>185</sup>

CBCR	Class	Abs. Peak ( <sup>152</sup> P <sub>r</sub> )	Abs. Peak ( <sup>15E</sup> P <sub>g</sub> )	$\Phi_{\text{Lumi-Go}}$	$\Phi_{\text{Lumi-165-Rf}}$	$\Phi_{\text{Meta-GO}}^*$	$\Phi_{\text{Meta-GO}}$
NpF2164g6	I <sub>R</sub>	649 nm	551 nm	0.36	0.3	-	-
AnPixJg2 <sup>166</sup>	II <sub>R</sub>	647 nm	543 nm	0.555	0.395	0.555	-
NpAF142g2	II <sub>R</sub>	650 nm	534 nm	0.49	0.3	0.48	-
NpF2164g4	II <sub>R</sub>	646 nm	532 nm	0.585	0.13	0.585	-
NpF2854g3	II <sub>R</sub>	656 nm	550 nm	0.51	0.36	-	-
NpR6012g4 <sup>175</sup>	II <sub>R</sub>	651 nm	540 nm	0.56 <sup>a</sup> 48 <sup>b</sup>	0.40	~0.52	-
NpR1597g4	III <sub>R</sub>	638 nm	574 nm	0.13	0.04	-	0.043
NpR4776g3	III <sub>R</sub>	656 nm	560 nm	0.093	0.18	-	0.091
NpR5113g2	III <sub>R</sub>	650 nm	530 nm	0.39	0.17	0.36	0.048
Slr1393g3* <sup>177</sup>	III <sub>R</sub>	648 nm	535 nm	<u>0.195<sup>c</sup></u> 0.14, <sup>d</sup> 0.15 <sup>e</sup>	NA	-	-

**Table A6.4:** Distances between the Chromophore and Adjacent Residues

Distances of residues near the Chromophore in the Signal State of NpR6012g4 (6BHO) and Slr1393g3 (5M82).

NpR6012g4		Slr1393g3	
3.779	Asp657 (HB)	3.345	Leu495
3.83	Ile691	3.702	Phe536
4.533	Phe695	3.917	Ile538
4.545	Phe634	4.131	Asp498 (HB)
4.769	Thr653 (HB)	4.543	Phe474
5.142	Val697	4.669	His529 (HB)
4.751	Leu692	5.058	Leu533
5.747	Tyr624 (HB)	5.374	Asn532 (HB)
		5.589	Tyr559
4.637	Avg All	4.48088889	Avg All
4.94166667	Avg Larger AA Residues	4.62575	Avg Larger AA Residues

*Chapter 7. Supporting Information for “Conservation and Diversity in the Secondary Reverse Photodynamics of the Canonical Red/Green Cyanobacteriochrome Family”*

**Includes: Supplemental Wild-Type Red/Green CBCRs (Figures S1-S8, Tables S1-S3), Supplemental Wild-Type Reverse Dynamics Non-Conserved Features (Figures S9-S11, Tables S4-S6), Supplemental Wild-Type Amino Acid Sequence Alignments (Figure S12-S13), Supplemental Wild-Type Red/Green CBCR Structures (Figures S14-S16, Tables S7-S9), Supplemental  $\beta$ 2FV NpR6012g4 (Figures S17-S24, Table S10), and Supplemental Forward  $\beta$ 2FV NpR6012g4 Dynamics Discussion.**

A7.1: Wild-Type Red/Green CBCRs Spectra and Dynamics

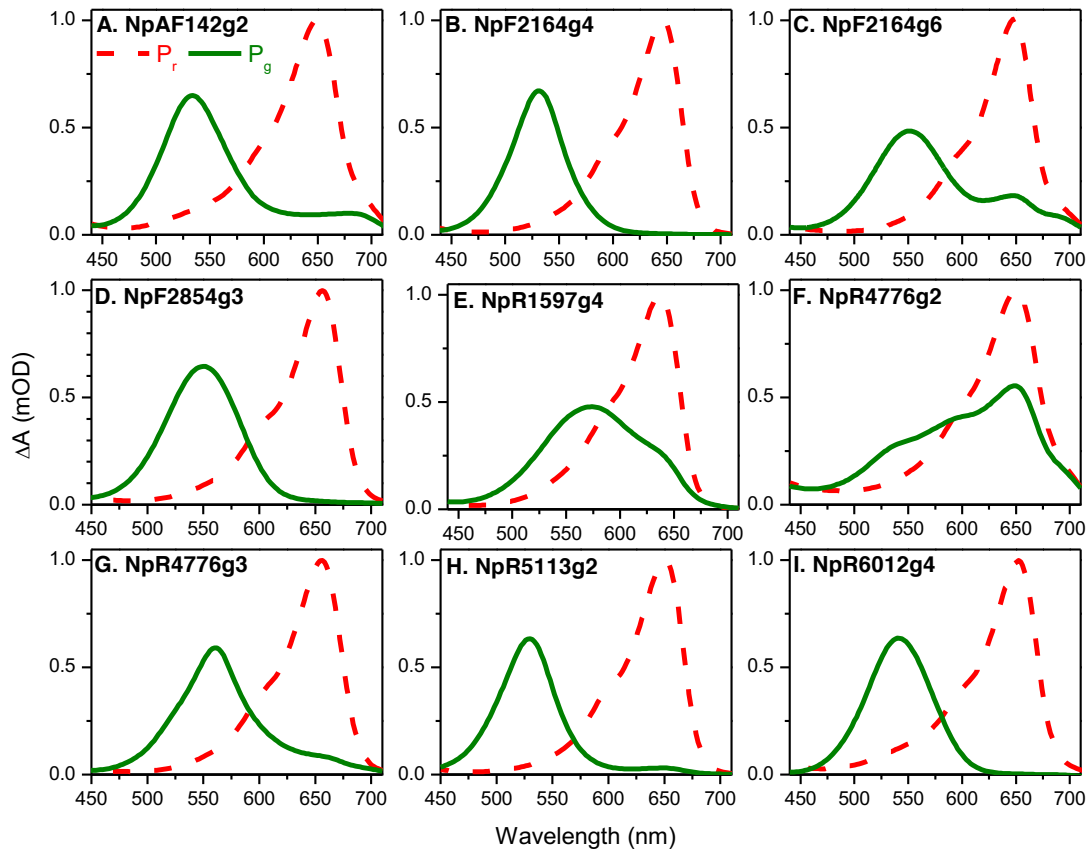
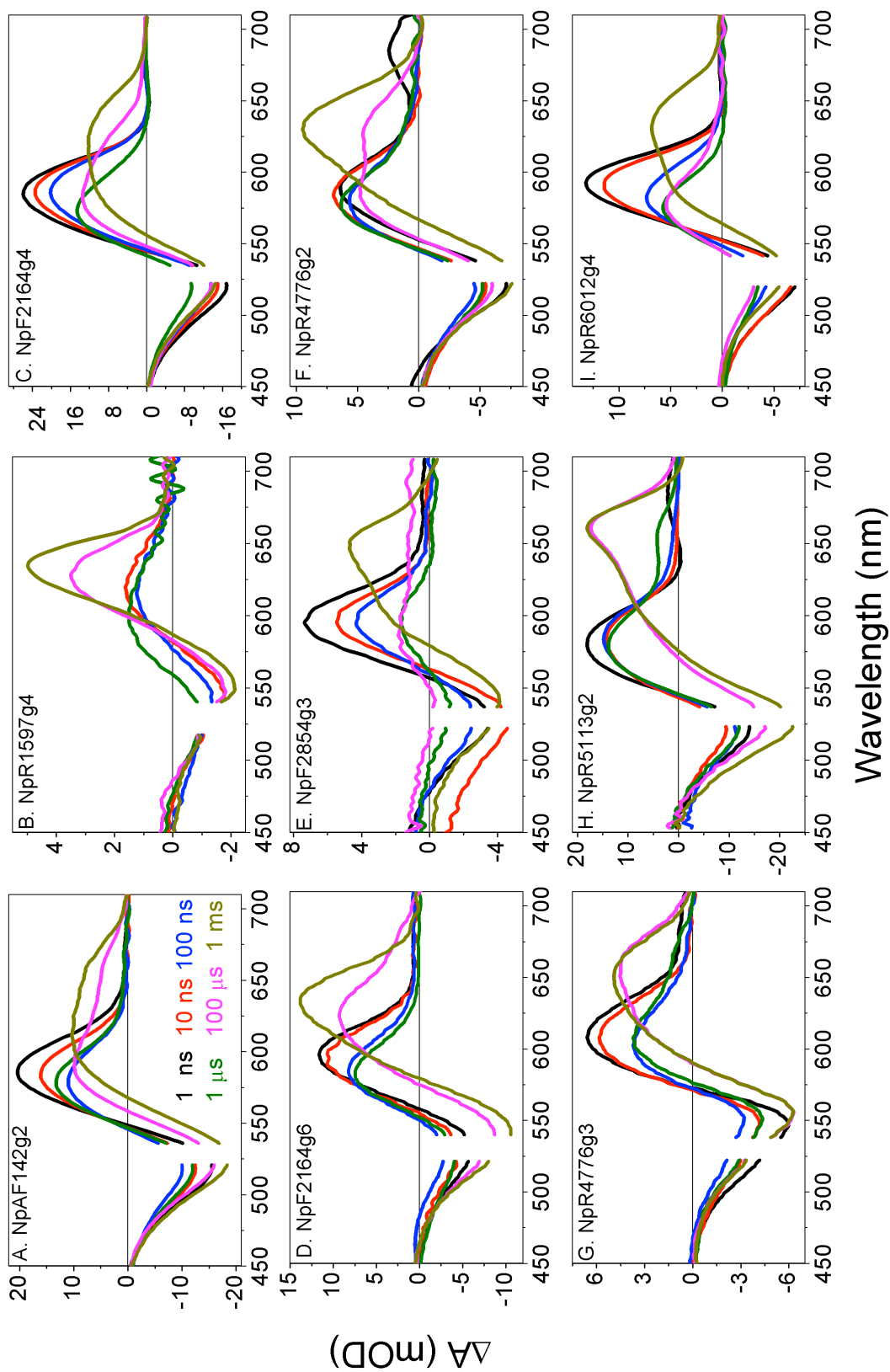


Figure A7.1: Red/Green CBCRs Ground State Absorption.

Dark-adapted and light-adapted spectra of the red/green CBCRs studied in the secondary reverse dynamics study.



**Figure A7.2:** Red/Green CBCR Secondary Reverse Transient Absorption Difference Spectra

Secondary reverse transient absorption difference spectra of all studied CBCR Domains.



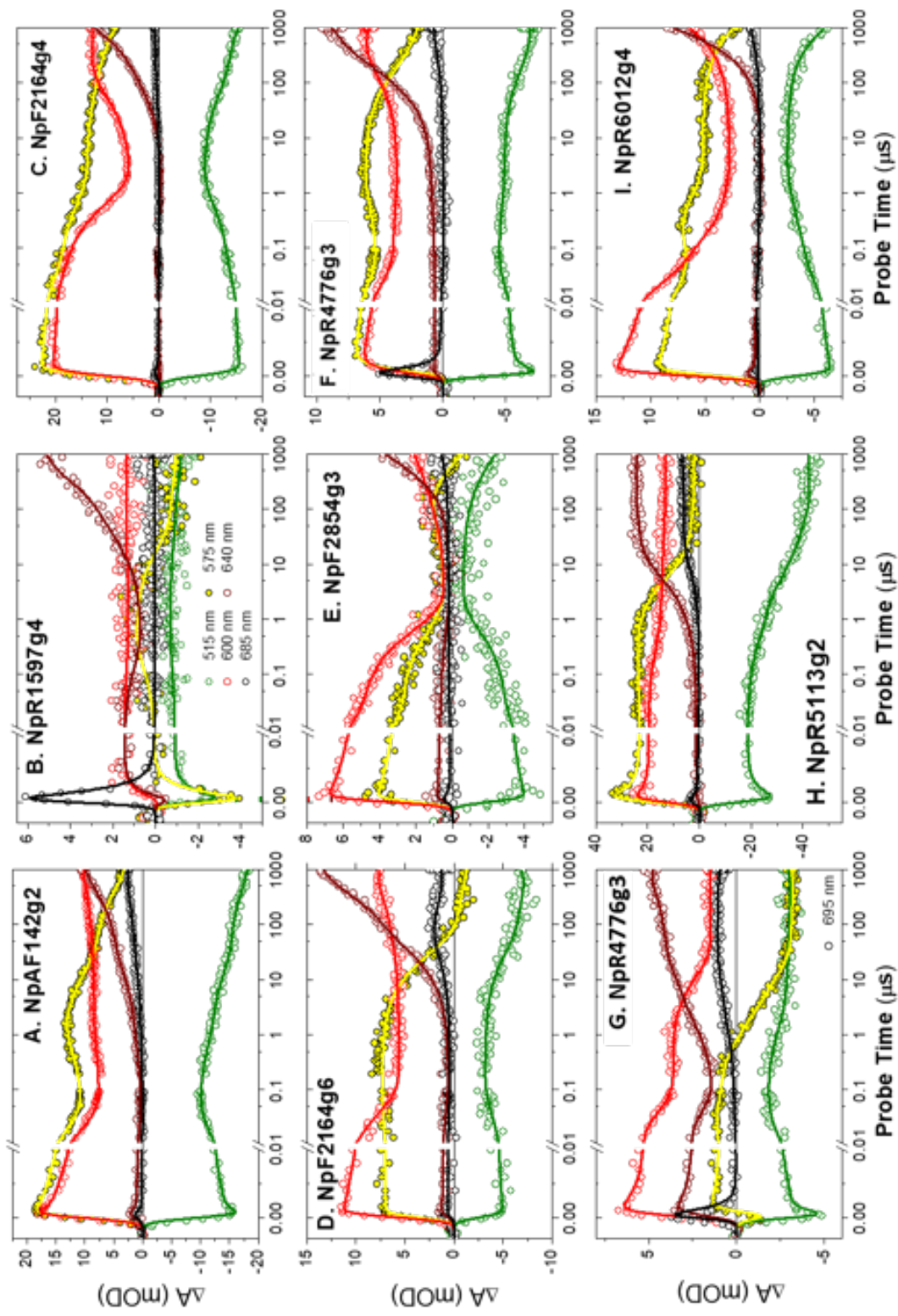


**Figure A7.3:** Red/Green CbCR Secondary Reverse Kinetic Traces

Select secondary reverse kinetic of all studied CbCR Domains. Fits to the data via a sequential model (solid curves) are shown.

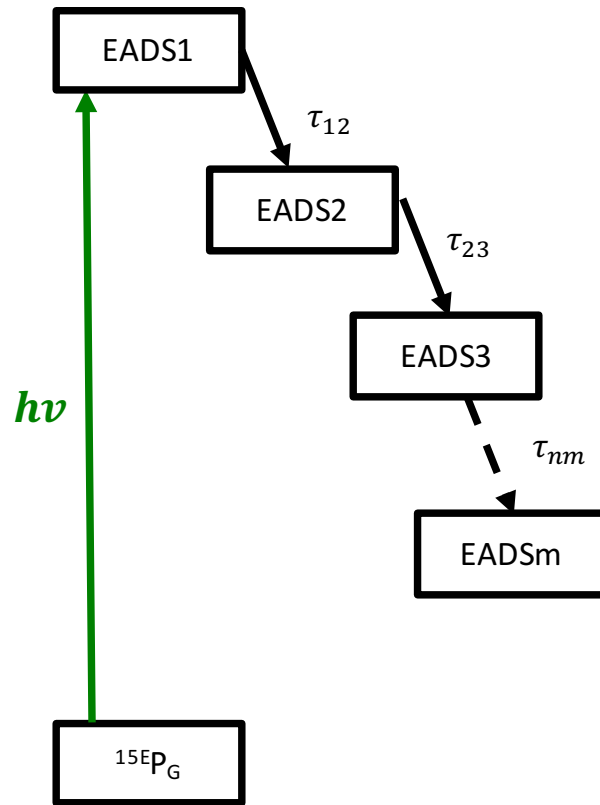


**Figure A7.4:** Sequential Model

Sequential model used in the global analysis of the secondary reverse dynamics of red/green CBCRs.

**Table A7.1:** Red/Green CBCR Secondary Reverse Global Analysis Parameters

Sequential EADS analysis of secondary reverse photoreaction dynamics. 2-4\*Initial spectra are contaminated with long living excited-state spectra. The only CBCRs to exhibit  $^{15}\text{P}_g^*$  absorbance in the secondary dynamics were the domains that had a Tyr residue near the bilin C10. Primary dynamics of NpR4776g2 were not collected, but this CBCR had this Tyr residue and  $^{15}\text{P}_g^*$  absorbance which supports the correlation reported in the primary reverse dynamics.<sup>28</sup>

Domain (UF Class)	Primary Dynamics Lumi apparent lifetime <sup>28</sup>	EADS1 ( $\tau/\lambda$ )	EADS2 ( $\tau/\lambda$ )	EADS3 ( $\tau/\lambda$ )	EADS4 ( $\tau/\lambda$ )	EADS5 ( $\tau/\lambda$ )	EADS6 ( $\tau/\lambda$ )	EADS7 ( $\tau/\lambda$ )
NpF2164g6 (Class-Ir)	NA, Lumi did not evolve on an UF timescale	35.5 ns 595 nm	31 $\mu\text{s}$ 582 nm	214 $\mu\text{s}$ 620 nm	2.7 ms 630 nm	Flow 650 nm		
NpF2854g3 (Class-IIr)	11 ns	0.9 ns (shunt) 596 nm	26.8 ns (shunt) 596 nm	693 ns 584 nm	84 $\mu\text{s}$ 596nm	2 ms 592	Flow 653 nm	
NpF2164g4 (Class-IIr)	81 ps	20.2 ns (shunt) 585 nm	524 ns 587 nm	65.2 $\mu\text{s}$ 570 nm	5 ms 590 nm	>Flow 642 nm		
NpR4776g2 (NA)	NA	800 ps* $^{15}\text{P}_g^*$	20 ns 586nm	617 ns 580 nm	143 $\mu\text{s}$ 577 nm	5 ms 622 nm	Flow 650 nm	
NpR6012g4 (Class-IIr)	230 ps	263 ps* 604 nm	18.5 ns (shunt) 595 nm	136 ns 593 nm	833 ns (shunt) 580 nm	884 $\mu\text{s}$ 578 nm	3 ms 632 nm	Flow 652 nm
NpAF142g2 (Class-IIr)	475 ps	500 ps* $^{15}\text{P}_g^*$	17.8 ns 586 nm	493 ns 578 nm	13.9 $\mu\text{s}$ 580 nm	220 $\mu\text{s}$ 588 nm	5 ms 604 nm	Flow 643 nm
NpR1597g4 (Class-IIIr)	1.47 ns	1.34 ns* $^{15}\text{P}_g^*$	126 ns 620 nm	40.8 $\mu\text{s}$ 632 nm	3 ms 612 nm	Flow 635 nm		
NpR4776g3 (Class-IIIr)	7.5 ns	1 ns* $^{15}\text{P}_g^*$	28.8 ns (shunt) 615 nm	1.11 $\mu\text{s}$ 607 nm	9.7 $\mu\text{s}$ 619 nm	4 ms 651 nm	Flow 657 nm	
NpR5113g2 (Class-IIIr)	235 ps	0.5 ns* $^{15}\text{P}_g^*$	2 ns (shunt) 578 nm	1.7 $\mu\text{s}$ 587 nm	8.2 $\mu\text{s}$ 659 nm	inf 664 nm		

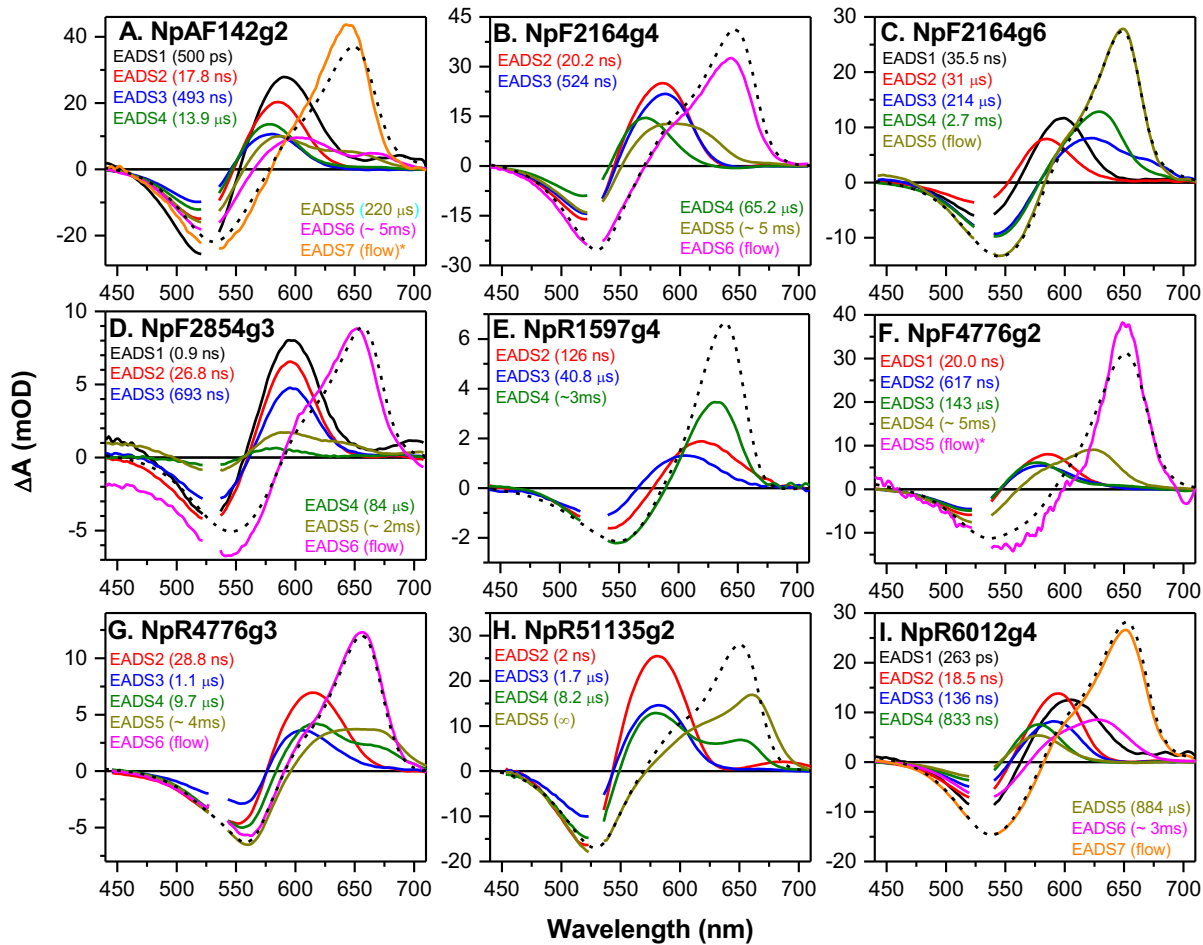


**Figure A7.5: Red/Green CBCR Secondary Reverse Dynamics EADS**

The Evolutionary Associated Difference Spectra (EADS) of all studies CBCR samples including the 1 to 10 ms flow region. Fits to the data are in Figure A7.3. The far-red absorbance in the 2 ns (red curve) of NpR5113g2 was attributed to an artifact.

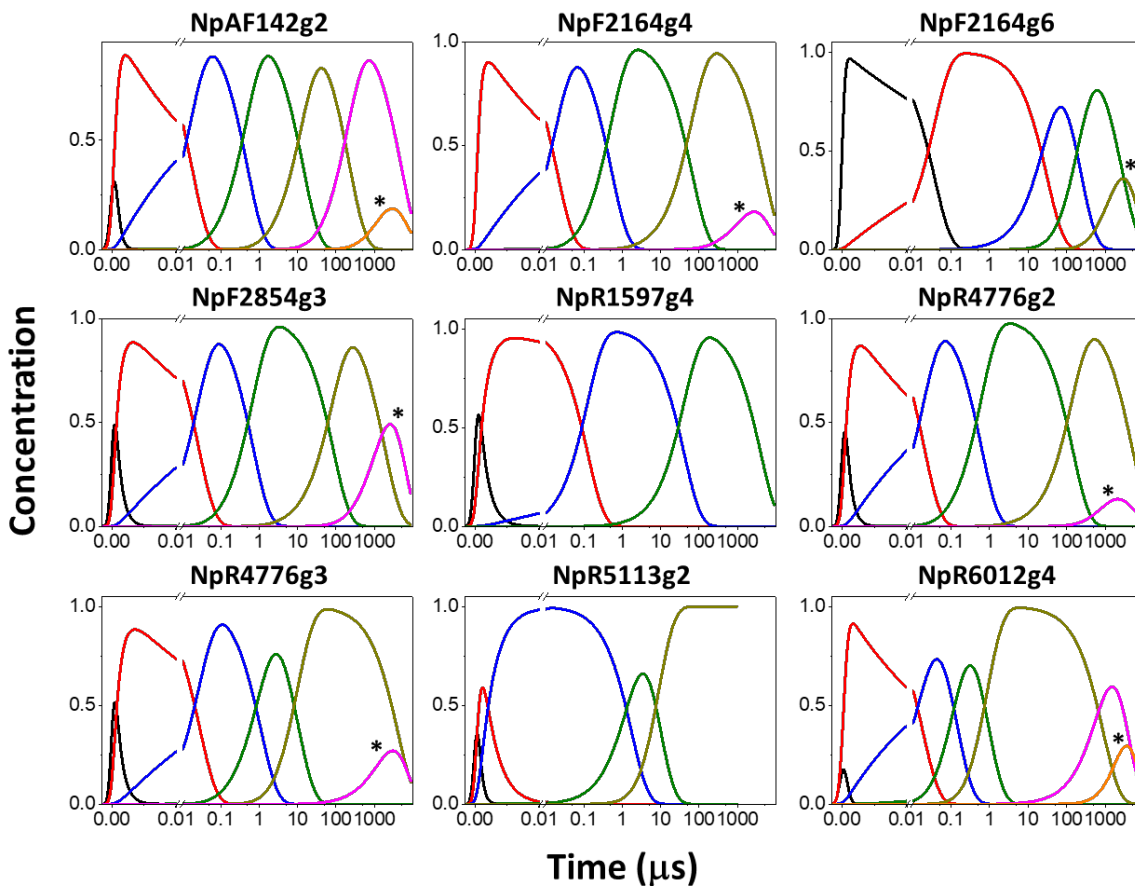


**Figure A7.6:** Red/Green CBR Secondary Reverse Dynamics Concentraiton Profiles

Concentration profiles from the sequential analysis of all studies CBR samples. The curves are color coordinated to the legend in Figure A7.5. Not all of the EADS associated with the black concentration curve are given due to ESA contamination (NpF2164g4, NpR1597g4, NpR4776g2, NpR4776g3, and NpR5113g2). If there is a black curve in the EADS then it was assigned as the Lumi-G<sub>0</sub> intermediate (Figure A7.8: NpAF142g2, NpF2164g6, NpF2854g3, NpR6012g4). Fits are shown to the data are given in Figure A7.3. \*Represents the flow region.

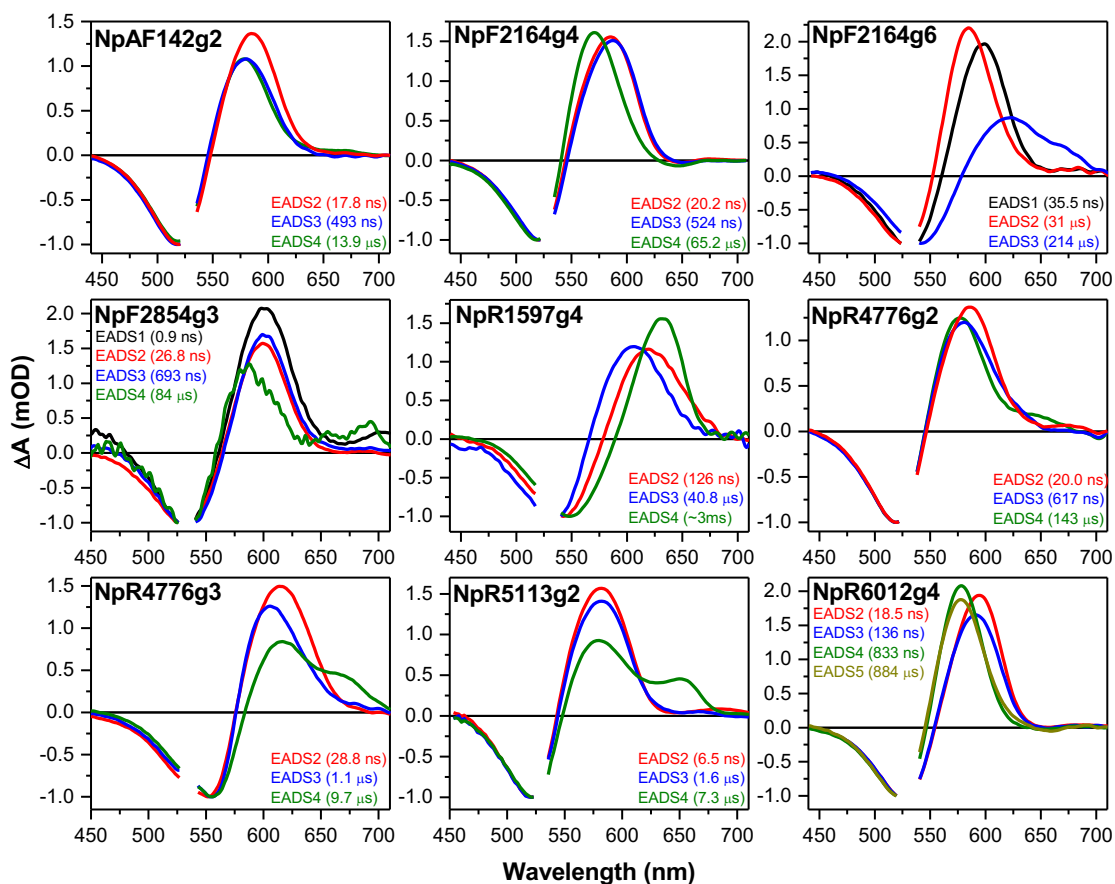


**Figure A7.7: Red/Green CBCR Secondary Reverse Dynamics Normalized EADS**

The normalized EADS of all studies CBCR samples to more readily observe spectral shifting trends and if ground state intermediate shunts were present. Fits are shown to the data on Figure A7.3.

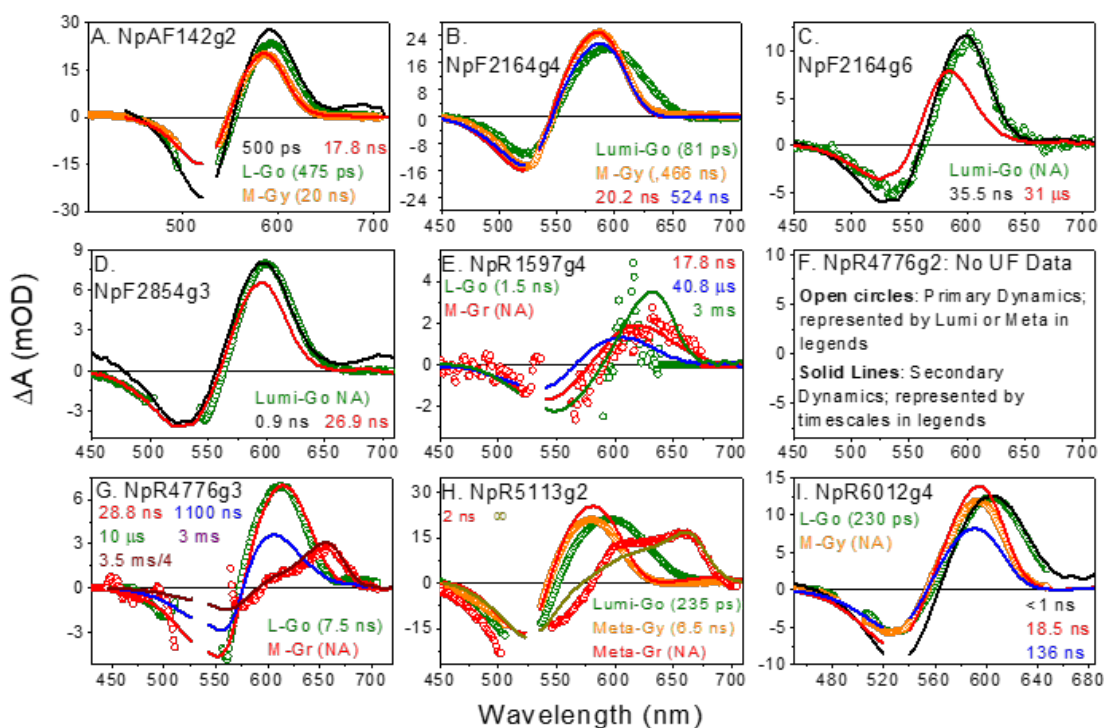


**Figure A7.8:** Red/Green CBCR Primary and Secondary Reverse Dynamics Comparison  
Overlap of long time (solid lines, sequential) and ultrafast (open circles, target) fittings.

**Table A7.2:** Primary and Secondary Reverse Dynamics Excitation Wavelengths

Excitation wavelengths used in the long-time and ultrafast experiments. The bandwidth of the excitation pulse determined by the wavelength excised for pump scatter is given for NpR4776g3 and NpR5113g2 given the discrepancies in the primary and secondary dynamics. The primary dynamics have wavelengths red-shifted of the isosbestic point resolved in the temperature dependent  $^{15}\text{E}_g$  spectra and could be preferentially exciting a subpopulation with different dynamics.

Sample	Primary Pump Wavelength (nm) <sup>28</sup>	Secondary Pump Wavelength (nm)
NpAF142g2	521	532
NpR1597g4	552	532
NpF2164g4	529	532
NpF2164g6	530	532
NoF2854g3	528	532
NpR4776g2	NA	532
NpR4776g3	536 (561 to 517 nm)	532 (538 to 522 nm)
NpR5113g2	526 (541 to 513 nm)	532 (535 to 523 nm)
NpR6012g4	500 and 675 <sup>183</sup>	532

**Table A7.3:** Comparison of the Primary and secondary Reverse Dynamics

Comparison of Ultrafast and Longtime spectra.

Sample	State (Lifetime)	
NpAF142g2	EADS1 (500 ps) ~ L-Go (475 ps) Perhaps: L-Go is red shifted but they have comparable lifetimes and EADS1 being blues shifted may be due to the fact state is in instrument response.	EADS2 (17.8 ns) == M-Gy (20 ns) Good spectral overlap, lifetimes are similar but UF has a lot of uncertainty due to 8 ns temporal ceiling.
NpR1597g4	EADS2 (17.8 ns) ~ M-Gr (NA) UF data extremely noisy. M-Gr bleach is slightly red shifted. Time constants are consistent (17.8 ns is beyond temporal ceiling of UF)	
NpF2164g4	EADS2 (20.2 ns) ~ M-Gy (466 ns) M-Gy slightly red shifted, may not have completed blue-shifting in 8-ns temporal ceiling of UF. Lifetimes are vastly different but UF lifetime has a lot of uncertainty due to 8 ns temporal ceiling	
NpF2164g6	EADS1 (35.5 ns) ~ L-Go (UF, NA) Perhaps: L-Go is red shifted of EADS1 and L-Go persist beyond 8 ns, and EADS lifetime is consistent (35.5 ns)	
NoF2854g3	EADS1 (900 ps) ~ L-Go (UF, NA) Unlikely: L-Go is red shifted of EADS1 and L-Go persist for 8 ns	
NpR4776g2	No UF Data	No UF Data
NpR4776g3	EADS2 (28.8 ns) == L-Go (487 ps) Spectra of essentially perfect overlap but they have significantly different lifetimes	M-Gr (UF, NA) is not observed in LT Time step too large; skipped over its evolution
NpR5113g2	EADS2 (6.5 ns) == M-Gy (6.5 ns); M-Gy slightly red-shifted since blue-shifting of the state isn't completed in the 8 ns temporal ceiling of UF. Or due to difference in excitation WLs ( 532 nm, 498 nm)s	M-Gr (UF, NA) is not observed in LT Time step too large; skipped over its evolution
NpR6012g4	EADS1 (<1 ns) == L-Go (230 ps)	EADS2 (13.8 ps) == M-Gy (NA)



A7.2: Wild-Type Reverse Dynamics Non-Conserved Feature

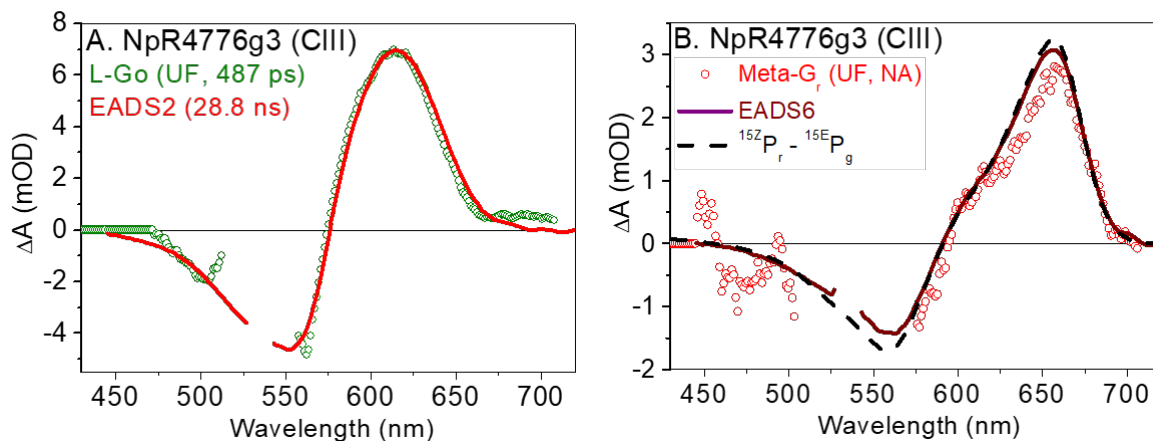


**Figure A7.9:** Primary and Secondary NpR4776g3 Meta-G<sub>r</sub> Comparison

Overlap of long time (solid lines, sequential) and ultrafast (open circles, target) fittings. Comparison of NpR4776g3 primary and secondary signals.

**Table A7.4:** Reverse Meta-G<sub>r/f</sub> and Forward Lumi-R<sub>f</sub> Comparison

Reverse Meta-G<sub>r/f</sub> and forward Lumi-R<sub>f</sub> peak absorbance

DOMAIN	Meta-G <sub>r/f</sub> Peak Absorbance	Lumi-R <sub>f</sub> Peak Absorbance
AnPixJg2	686 nm	678 nm
NpAF142g2	667 nm	692 nm
NpF2164g6	668 nm	685 nm
NpR4776g3	NA (Broad)	701 nm
NpR5113g2	660 nm	683 nm

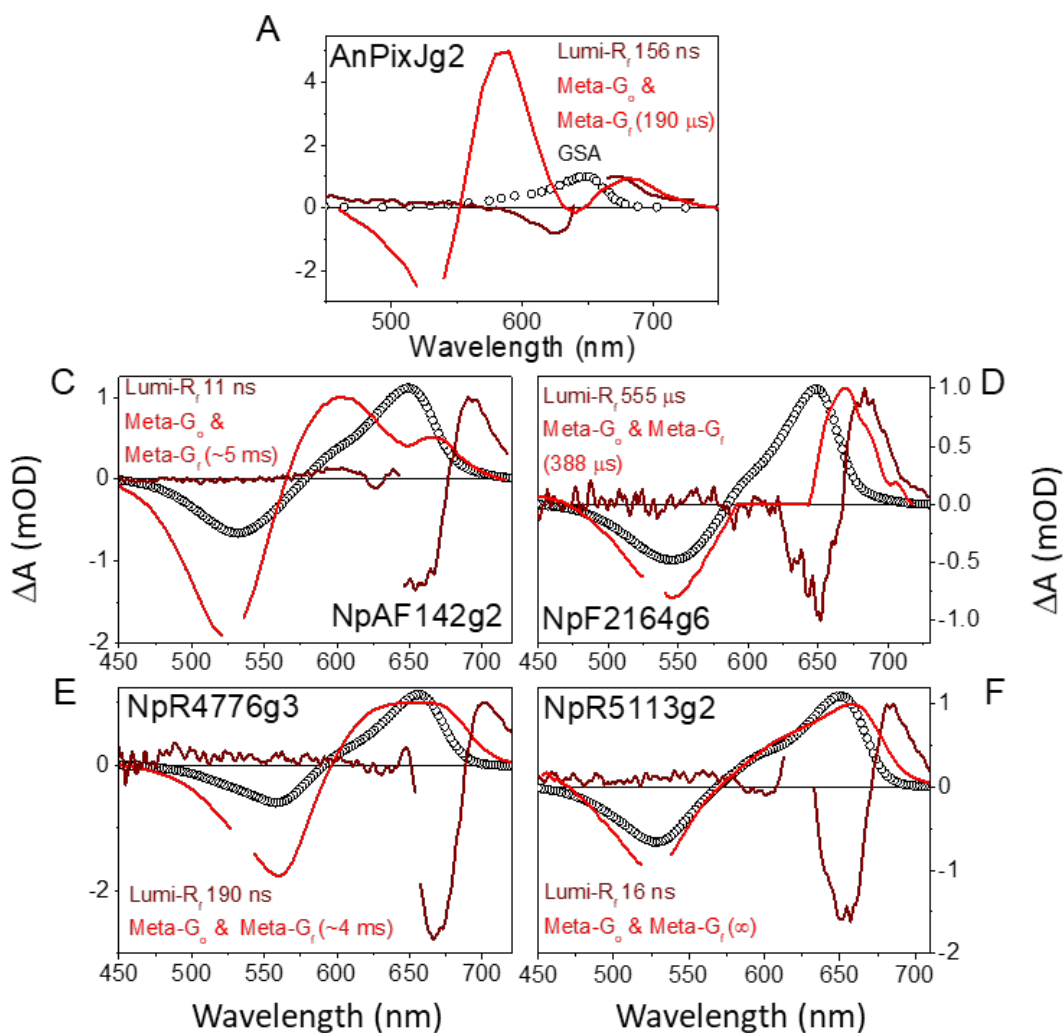


**Figure A7.10:** Reverse Meta-G<sub>r</sub> and Forward Lumi-R<sub>f</sub> Spectral Comparison

Overlap of the reverse dynamics Meta-G<sub>r/f</sub> and forward dynamics Lumi-R<sub>f</sub> to show their spectral similarities. Lifetimes of the Meta-G<sub>o</sub> and Meta-G<sub>r/f</sub> reverse dynamics photointermediate mixtures and forward dynamics Lumi-R<sub>f</sub> obtained through sequential and target global analysis are provided in the legends for further comparison of these photointermediates.

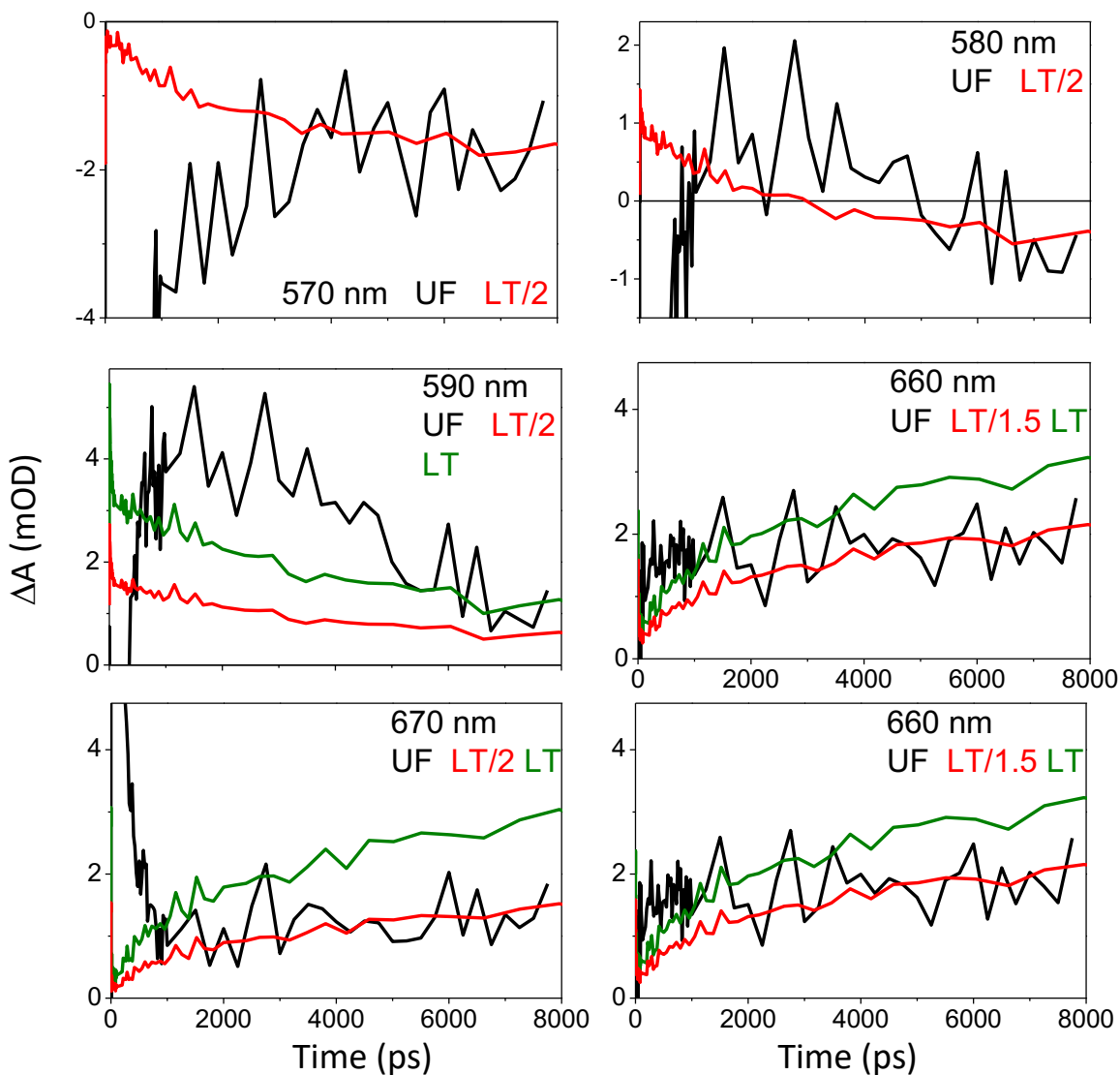


**Figure A7.11: Primary and Secondary Reverse Kinetics Comparison**

Overlap of long time (solid lines, sequential) and ultrafast (open circles, target) fittings. Comparison of NpR4776g3 primary and secondary dynamics kinetics at select wavelengths near  $^{15Z}P_r$  to emphasize the formation of a population with a chromophore environment similar to  $^{15Z}P_r$  on an ultrafast timescale.

**Table A7.5:** Comparison of Various Reverse Dynamics Features in canonical red/green CBCRs

Comparison of various reverse dynamics features of the canonical Red/Green CBCRs. It should be noted that ground state intermediate shunts were reported for all of the Class III<sub>R</sub> domains and NpAF142g2 in the primary dynamics.<sup>28</sup>

Domain	P <sub>g</sub> (nm)	P <sub>r</sub> (nm)	Pr-P <sub>g</sub>	Lumi-Go Lifetime (ns)	Meta-G1 (ns)	Shunt	Red Shifted Meta
NpR5113g2 (III)	530	648	118	NA	1700	YES	YES
NpF2164g4 (II)	532	646	114	NA	20.2	Maybe	NO
NpAF142g2 (II + Tyr)	534	650	116	0.5	20	Maybe	Maybe
NpF4776g2 (NA)	535	650	115	20	617	NO	NO
NpR6012g4 (II)	540	651	111	0.263	136	YES	NO
NpF2854g3 (II)	550	656	106	0.9	26.9	Maybe	NO
NpF2164g6 (I)	551	649	98	35.5	31000	NO	YES
NpF4776g3 (III)	560	656	96	28.8	1100	Maybe	YES
NpR1597g4 (III)	574	638	64	17.8	40800	NO	NO

**Table A7.6:** Comparison of Reverse EADS Absorption and Non-Conserved Features in canonical red/green CBCRs

Comparison of reverse EADS absorption and non-conserved features of the canonical Red/Green CBCRs reverse dynamics. The CBCR believed to have shunts are highlighted in yellow and green. This suggest that there is not a correlation between the photointermediate absorption and the presence of a shunt.

Domain	EADS1	Shunt	Red Shifted Meta	Domain	EADS2	Shunt	Red Shifted Meta
NpR5113g2 (III)	581	YES	YES	NpR4776g2 (NA)	581	NO	NO
NpF2164g4 (II)	585	Maybe	NO	NpR5113g2 (III)	581	YES	YES
NpR4776g2 (NA)	587	NO	NO	NpAF142g2 (II + Tyr)	584	Maybe	Maybe
NpAF142g2 (II + Tyr)	591	Maybe	Maybe	NpF2164g6 (I)	585	NO	YES
NpF2854g3 (II)	596	Maybe	NO	NpF2164g4 (II)	587	Maybe	NO
NpF2164g6 (I)	599	NO	YES	NpR6012g4 (II)	594	YES	NO
NpR6012g4 (II)	605	YES	NO	NpF2854g3 (II)	596	Maybe	NO
NpR4776g3 (III)	615	Maybe	YES	NpR4776g3 (III)	605	Maybe	YES
NpR1597g4 (III)	620	NO	NO	NpR1597g4 (III)	605	NO	NO
Domain	EADS3	Shunt	Red Shifted Meta	Domain	EADS4	Shunt	Red Shifted Meta
NpF2164g4 (II)	570	Maybe	NO	NpAF142g2 (II + Tyr)	578	Maybe	Maybe
NpR4776g2 (NA)	576	NO	NO	NpR6012g4 (II)	578	YES	NO
NpAF142g2 (II + Tyr)	578	Maybe	Maybe	NpF2854g3 (II)	581	Maybe	NO
NpR5113g2 (III)	581	YES	YES	NpF2164g4 (II)	595	Maybe	NO
NpR6012g4 (II)	590	YES	NO	NpR4776g2 (NA)	625	NO	NO
NpF2854g3 (II)	597	Maybe	NO	NpF2164g6 (I)	633	NO	NO
NpR4776g3 (III)	615	Maybe	YES	NpR4776g3 (III)	649.5	NO	YES
NpF2164g6 (I)	620	NO	YES	NpR5113g2 (III)	654	Maybe	YES
NpR1597g4 (III)	633	NO	NO	NpR1597g4 (III)	660	YES	YES



## Meta-Gf

AnPiXJg2  
 Npr216496  
 Npr477693  
 Npr511392  
**Npr216497B**  
 NpAF14292\*

KOAVSKMEKLRV-SNID---KIQGGGGRRQKCRRAVRNPVSEV--KSSKGSZVKVG-PDIKQVEEYVSGVGGRHQSRVAV  
 ERAITRISSEKIQV-QEED---TTRNALPDRSHECDAIAYRNPVCEET--ADSSREVAIVG-PEIRIMEEELQVGGVRRNDFPFI  
 QRVEIVAKVYKSLD---AQGGVGGVCKSOAQAFAFOQAQSEY--EFGDEVKVGSNTKQVQSQSEVGGVRRNDFPFI  
 DQVIAQVDRKIRSP-LDIE---TTRKEDVIRKQQAQAIFSNV--VPSFAESTPVVG---IQTIFTVQVGGVVDNDFPFI  
 YRLPSRLTE-MAOSHGNVL---EFTQFAEHLRQKVKVREPSEV--VPSFTGDPKVG---TSLAKVRVLYNCGVVRKSLR  
**QQAARLIANNRQSLDVT---TTRRGGVCCQECDAISRNAQSEVGDYFANPRGRSIK-LGVGMDDTSSVGGVRRNDFPFI**

Y59 B2 Phe W90

## No Meta-Gf

Slr139393  
 Npr216494  
 Npr285493  
 Npr159794  
 Npr477692  
 Npr601294

ERAITRISSEKIQV-QEED---NTRASDVRHISCDAIAYRNPVSEV--HPSKQOMEPKDIQNNFLLQVTVVENEVGGVRRNDFPFI  
 ENAIARVADRNNS-QQEF---TTRTDLARQFKCDAIAYRNPVSEV--ADSSREVAIVG-PEIRIMEEELQVGGVRRNDFPFI  
 ORATEVVGKIRSS-ENID---LTLKEDVIRKQQAQAIFSNV--VPSFAESTPVVG---IQTIFTVQVGGVVDNDFPFI  
 EKAATVVEKIQS-LDIG---TTRKEDVIRKQQAQAIFSNV--VPSFAESTPVVG---IQTIFTVQVGGVVDNDFPFI  
 FOAVKVIKIAERES-LDQTD---TTRKEDVIRKQQAQAIFSNV--VPSFAESTPVVG---IQTIFTVQVGGVVDNDFPFI  
 EKAVIKISNRQSLDVT---TTRRGGVCCQECDAISRNAQSEVGDYFANPRGRSIK-LGVGMDDTSSVGGVRRNDFPFI

F474 Y500 W655 H659

## Meta-Gf

AnPiXJg2  
 Npr216496  
 Npr477693  
 Npr511392  
**Npr216497B**  
 NpAF14292\*

GDITEA---GHFSRDELFQEFKATIVVAAEKAGLAVYONGTETEVEVSSFTQVGLPFI  
 GAVITA---GHQVDEKIQQRATITRFAANKAGLAVYONGTETEVEVSSFTQVGLPFI  
 DDTIQV---GHQVAVFQIQARAAAPITIQOAGLAVYONGTETEVEVSSFTQVGLPFI  
 GAVQA---GLTDVAVTQQAQAFATAIQDKAGLAVYONGTETEVEVSSFTQVGLPFI  
 DNTISV---GHDEVHIQFMMGFKAMSTIQENRAGLAVYONGTETEVEVSSFTQVGLPFI  
 DAVHSQ---GFCQVDELEIQEFQAVAVVQVQVAGLAVYONGTETEVEVSSFTQVGLPFI

122Bilin C528

## No Meta-Gf

Slr139393  
 Npr216494  
 Npr285493  
 Npr159794  
 Npr477692  
 Npr601294

GIVETA---GFTDVIDDNRRFERAELTIVVVEOAGLAVYONGTETEVEVSSFTQVGLPFI  
 GAVITA---GYQVDEKIQQRATITRFAANKAGLAVYONGTETEVEVSSFTQVGLPFI  
 EDIQV---GHQVAVFQIQARAAAPITIQOAGLAVYONGTETEVEVSSFTQVGLPFI  
 KAVSA---NYIIRHATAELMQARAVVAVIQEKAGLAVYONGTETEVEVSSFTQVGLPFI  
 DDTIKM---GFAKVIDNLEQVHAFVIAITVQKAGLAVYONGTETEVEVSSFTQVGLPFI  
 GAVQA---GHPVDELEIQEFQAVAVVQVQVAGLAVYONGTETEVEVSSFTQVGLPFI

Figure A7.13: Red/Green CBCR Amino Acid Sequence Alignment Separated by Meta-G<sub>r</sub> Red Shifted of <sup>152</sup>P<sub>r</sub>

Wild-type Amino acid sequence alignment separated by presence of Meta-G<sub>r</sub> red shifted of <sup>152</sup>P<sub>r</sub>.

#### A7.4: Wild-Type Red/Green CBCR Structures

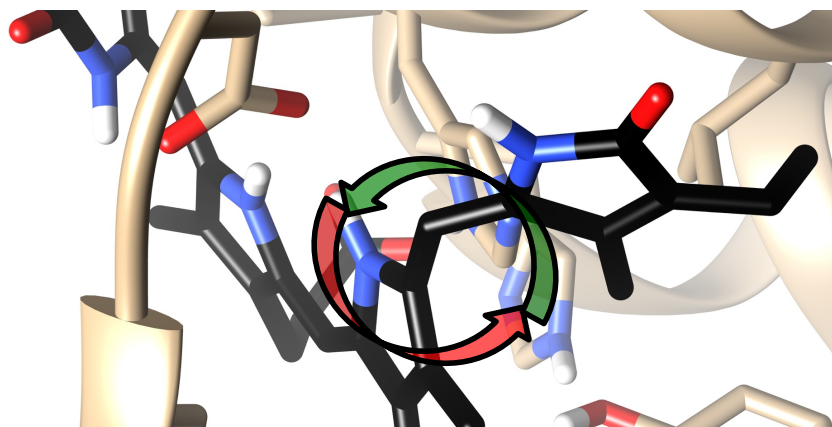


**Figure A7.14:** Proposed Chromophore Isomerization for Red/Green CBCRs.

Proposed rotation of the chromophore for forward and reverse cycle of canonical red/green CBCRs.

**Table A7.7:** Red/Green CBCR Chromophore Dihedral and Tilt Angles

Dihedral angles and tilt angles of C/D rings. Atoms are labeled in Figure 7.1A. The C/D ring tilt of AnPixJg2 was determined by measuring<sup>o</sup> the angle between two planes defined by the C and D rings using Chimera.<sup>292</sup>

Domain	Code	Nc-C14-C15-C16	C14-C15-C16-Nd	C/D Ring Tilt
Dark Adapted <sup>15Z</sup> P <sub>r</sub>				
AnPixJg2	3W2Z	-147.9°	27.0°	55.5°
NpR6012g4	6BHN	-132.4°±7.8°	359.4°±5.9°	49.0°±5.6°
Slr1393g3	5DFY	-155.6°	26.3°	48°
Light Adapted <sup>15E</sup> P <sub>g</sub>				
NpR6012g4	6BHO	-131.8°±14.3°	189.4°±17.6°	58.8°±4.8°
Slr1393g3	5M82	-109.8°	181.6°	62°

**Table A7.8:** Average Chromophore Dihedral and Tilt Angles in NpR6012g4

Average dihedral angles and tilt angles of all pyrrole rings for NpR6012g4 reported by Lim et al.<sup>108</sup> The m-n dihedral angle is analogous to Nx-Cm-Cn-Ny in Table A7.7. The atoms are labeled in Figure 7.1A. The  $\Delta$ Deplanarization is highlighted green if  $^{15E}P_g$  was more distorted and red if  $^{15Z}P_r$  was more distorted.

NpR6012g4	Pr	Pg	$\Delta$ Deplanarization
4-5 dihedral angle	-6.8	-10.4	-3.6
5-6 dihedral angle	25.9	-39.1	-13.2
9-10 dihedral angle	-6.8	-8	-14.8
10-11 dihedral angle	4.5	-0.3	4.2
14-15 dihedral angle	-132.4	-131.8	0.6
15-16 dihedral angle	-0.6	-170.6	-10
A/B ring tilt	23.2	46.3	-23.1
B/C ring tilt	7.8	10	-2.2
C/D ring tilt	49	58.8	-9.8

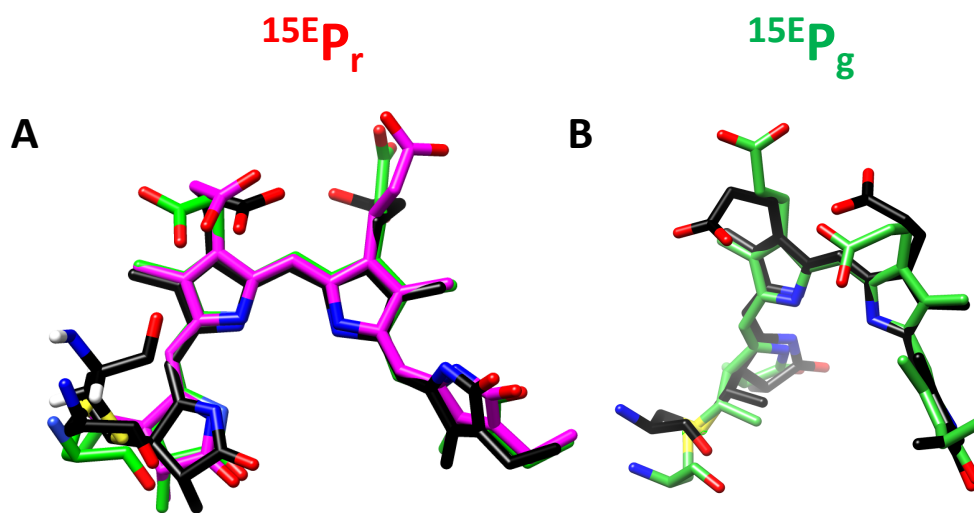


**Figure A7.15:** Chromophore Overlap of Red/Green CBCR with Resolved Structures.

(A) Overlap of the  $^{15Z}P_r$  dark adapted state chromophore structure of AnPixJg2 (magenta; 3W2Z), NpR6012g4 (black; 6BHN 1.10), and Slr1393g3 (green; 5DFX) showing that the C and D rings are at an angle and are not planar in both domains. (B) Overlap of the  $^{15Z}P_g$  signaling state chromophore structure of NpR6012g4 (blue; 6GHO 1.1) and the Slr1393g3 (tan; 5M82). Both structures have the A to D rings arranged left to right.



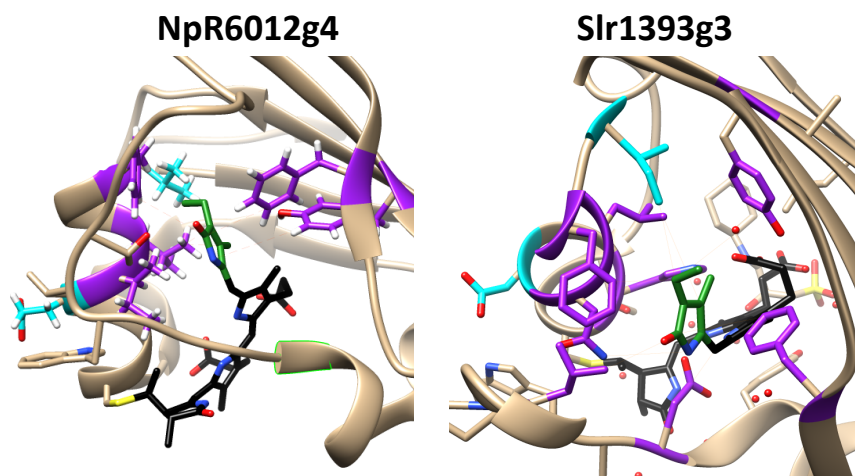


**Figure A7.16:** Signaling State Structural Comparison of NpR6012g4 and Slr1393g3.

Signaling state structures of NpR6012g4 (left; 6BHO) and Slr1393g3 (right; 5M82) with emphasis on the larger amino acid residues near the chromophore.

**Table A7.9:** Distances of Residues Closest to the Chromophore in the  $^{15E}P_g$  State  
Distances of residues near the Chromophore in the Signal State of NpR6012g4 (6BHO) and Slr1393g3 (5M82).

NpR6012g4		Slr1393g3	
3.779	Asp657 (HB)	3.345	Leu495
3.83	Ile691	3.702	Phe536
4.533	Phe695	3.917	Ile538
4.545	Phe634	4.131	Asp498 (HB)
4.769	Thr653 (HB)	4.543	Phe474
5.142	Val697	4.669	His529 (HB)
4.751	Leu692	5.058	Leu533
5.747	Tyr624 (HB)	5.374	Asn532 (HB)
		5.589	Tyr559
4.637	Avg All	4.481	Avg All
4.94166667	Avg Larger AA Residues	4.62575	Avg Larger AA Residues

A7.5:  $\beta 2FV$  NpR6012g4

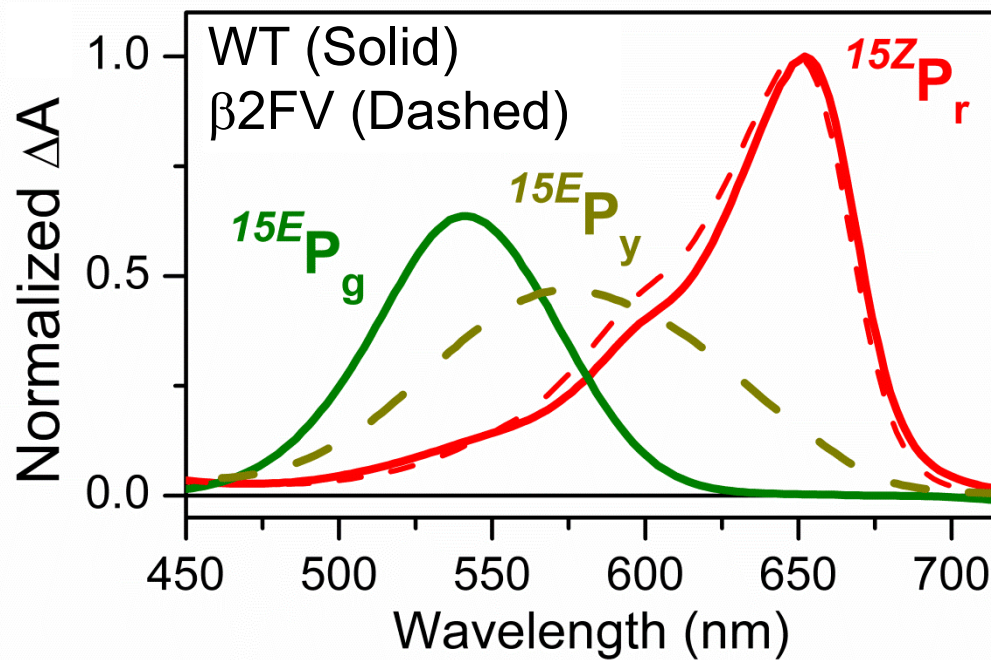


**Figure A7.17:** Ground State Absorption Comparison of NpR6012g4 and Slr13963g3.

Static absorption spectra of WT (solid) and  $\beta 2FV$  (dashed) NpR6012g4 are contrasted, revealing that the mutation resulted in a red shifting of the signaling state but did not affect the dark-adapted state. The spectra were scaled in manner to normalize the dark-adapted states ( $^{15}Z P_r$ ).

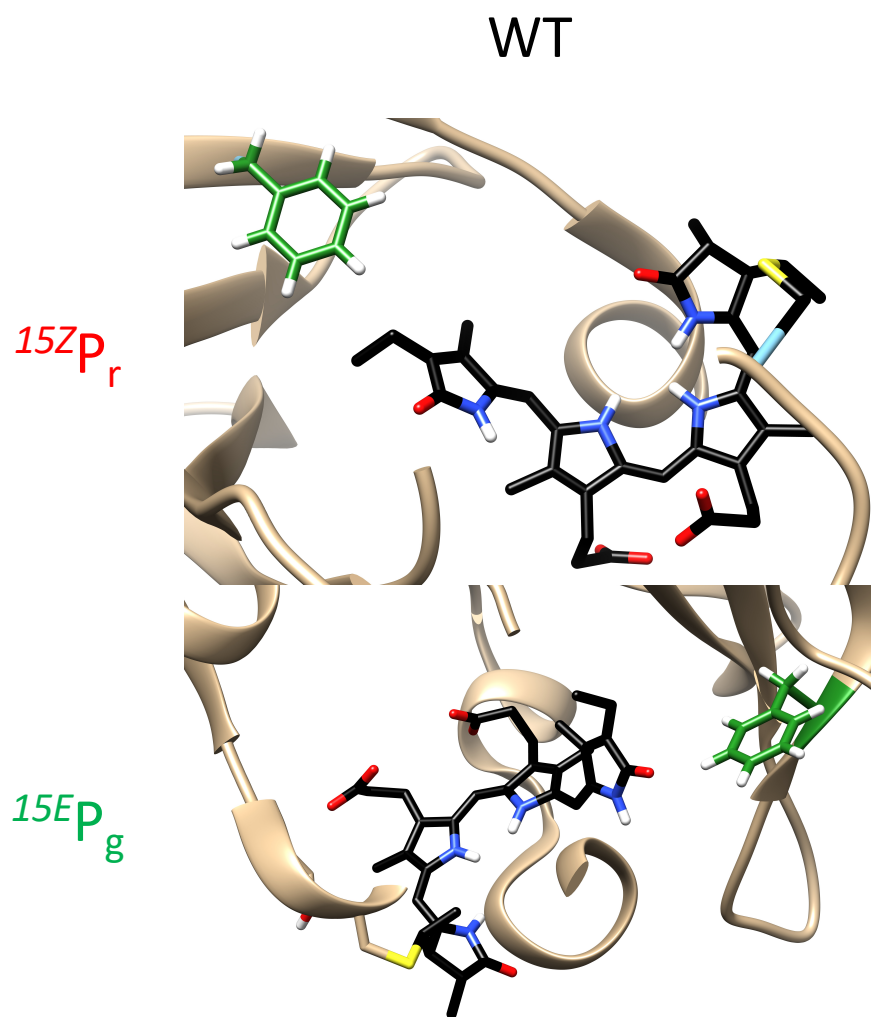


**Figure A7.18:** Location of  $\beta 2FV$  in NpR6012g4

Structure of WT NpR6012g4 in the  $^{15}ZP_r$  dark adapted state (6GHN) and  $^{15}EP_g$  signaling state (6GHO). The  $\beta 2F$  amino acid residue is colored green in each panel and the carbons of the chromophore are in black.

A7.5.1: Forward Dynamics

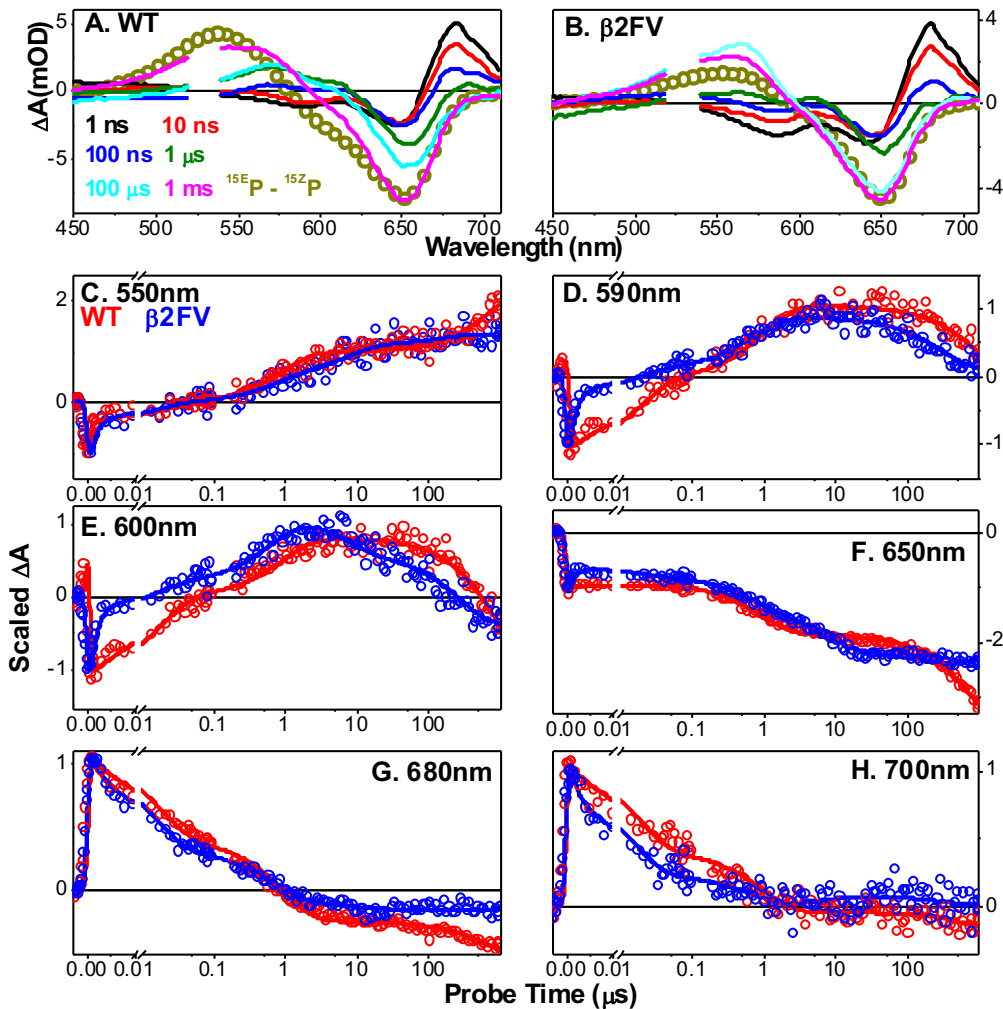


**Figure A7.19:** Secondary Forward Dynamics of WT and β2FV NpR6012g4

(A-B) Transient absorption spectra and (C-H) kinetic traces (up to 1 ms) of the secondary forward reaction ( $^{15Z}P_r \rightarrow ^{15E}P_g$ ) prior to subtracting the reverse dynamics to remove reverse dynamics contamination. (A-B). The transient absorption spectra at selected probe times. The ground-state  $^{15Z}P_g - ^{15E}P_r$  difference absorption spectra (unfilled circles) are added as a visual aid. The spectrum amplitude was scaled to be similar the ground-state bleach band of the 1-ms spectrum. (C-H) Kinetic traces at select wavelengths times for the WT (red) and the β2FV (blue) are contrasted. The fit (solid curves) for each kinetic trace (unfilled circles) was normalized at the signal minimum (or maximum) shortly after time zero.

**Table A7.10:** WT and  $\beta$ 2FV Forward Dynamics Sequential Model Parameters

Parameters extracted from the sequential EADS analysis of the secondary photoreaction dynamics. The initial spectra are contaminated with long living excited-state spectra.

\*Flow last for  $\sim 3$  ms.

		EADS 1	EADS 2	EADS 3	EAD S4	EADS5	EAD S6	EAD S7
$^{15}\text{ZP}_r \rightarrow ^{15}\text{EP}_g$ Forward	WT NpR6012g4	20 ns	970 $\mu\text{s}$	880 $\mu\text{s}$	$\infty^*$			
	$\beta$ 2FV NpR6012g4	1.3 ns	16 ns	700 ns	7.5 $\mu\text{s}$	300 $\mu\text{s}$	5 ms*	
$^{15}\text{EP}_g \rightarrow ^{15}\text{ZP}_r$ Reverse	WT NpR6012g4	260 ps	18 ns	140 ns	830 ns	880 $\mu\text{s}$	3 ms	> 3ms*
	$\beta$ 2FV NpR6012g4	600 ps	5.4 ns	1 $\mu\text{s}$	22 $\mu\text{s}$	240 $\mu\text{s}$	3 ms	> 3ms*

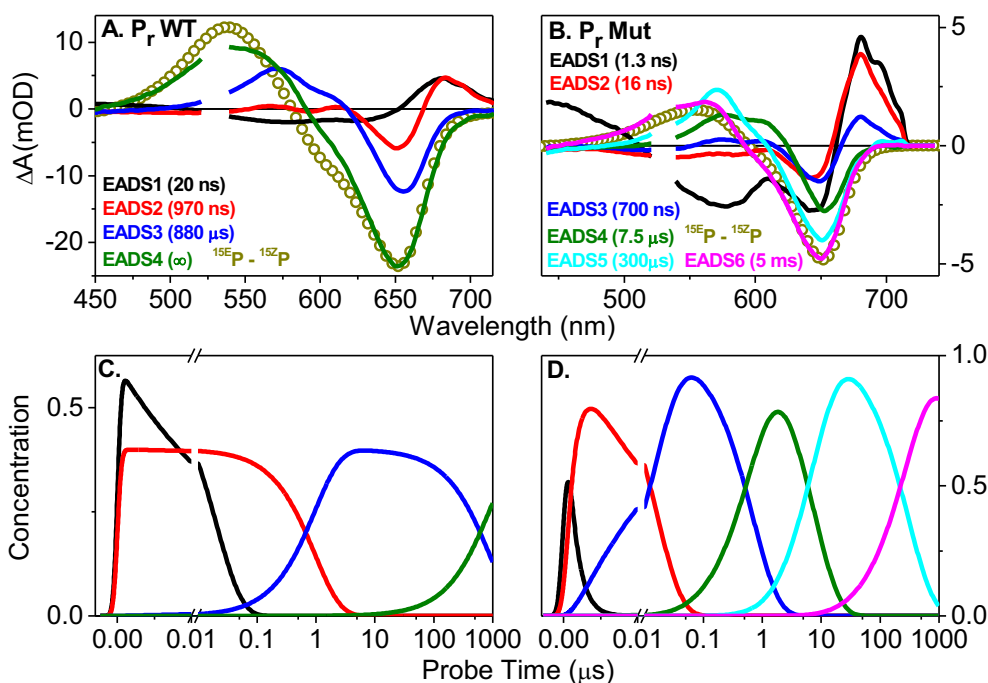


**Figure A7.20:** Secondary Forward Sequential Analysis of WT and  $\beta$ 2FV NpR6012g4  
Sequential-model analyses of the secondary forward reaction ( $^{15}\text{ZP}_r \rightarrow ^{15}\text{EP}_g$ ) dynamics of (A,C) WT and (B,D)  $\beta$ 2FV NpR6012g4 (prior to subtracting  $^{15}\text{EP}_g$ ). The decay times displayed in parenthesis next to the EADS legend. Concentration profiles of WT (C) and the  $\beta$ 2FV (D) NpR6012g4.

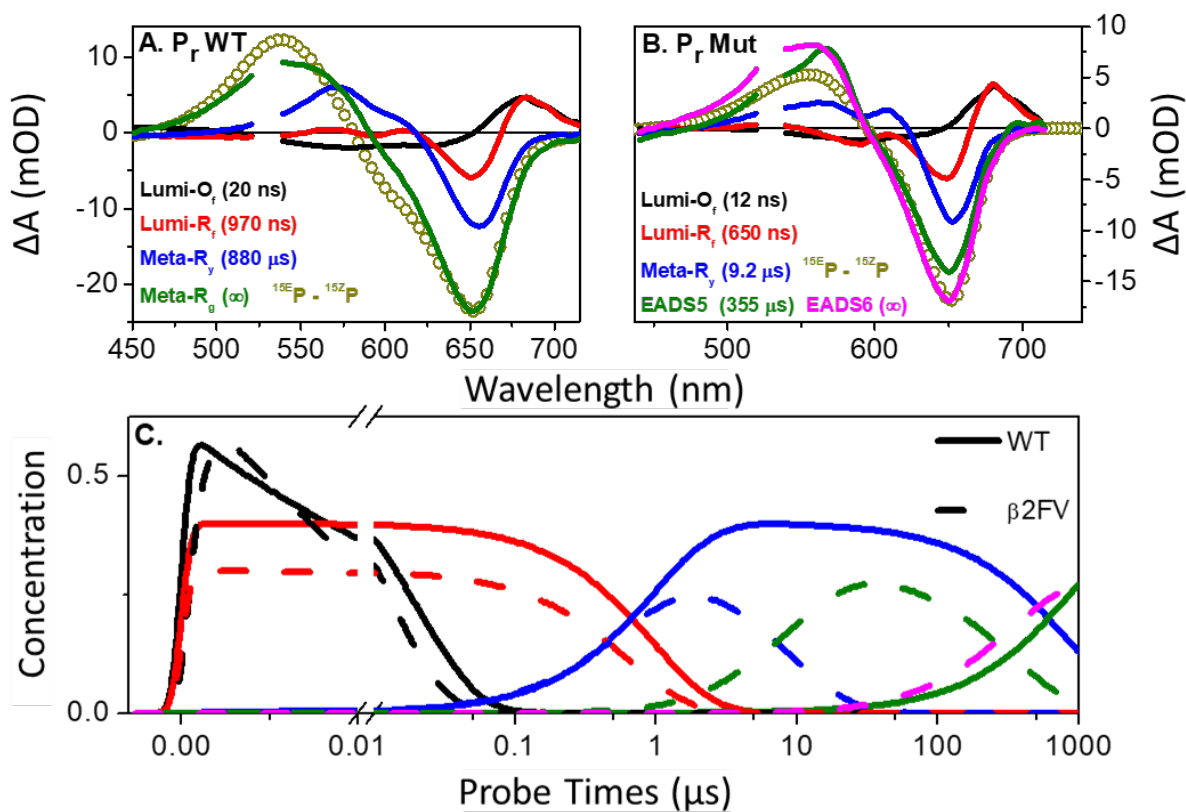


**Figure A7.21:** Secondary Forward Target Analysis of WT and  $\beta$ 2FV NpR6012g4

Target-model SADS analyses of the secondary forward reaction ( $^{15Z}P_r \rightarrow ^{15E}P_g$ ) dynamics of (A) WT and (B)  $\beta$ 2FV NpR6012g4. The decay times displayed in parenthesis next to the EADS legend. (C) Comparison of Concentration profiles of WT (solid curves) and the  $\beta$ 2FV (dashed curves) that shows that  $\beta$ 2FV evolves faster than WT.

A7.5.2: Reverse Dynamics

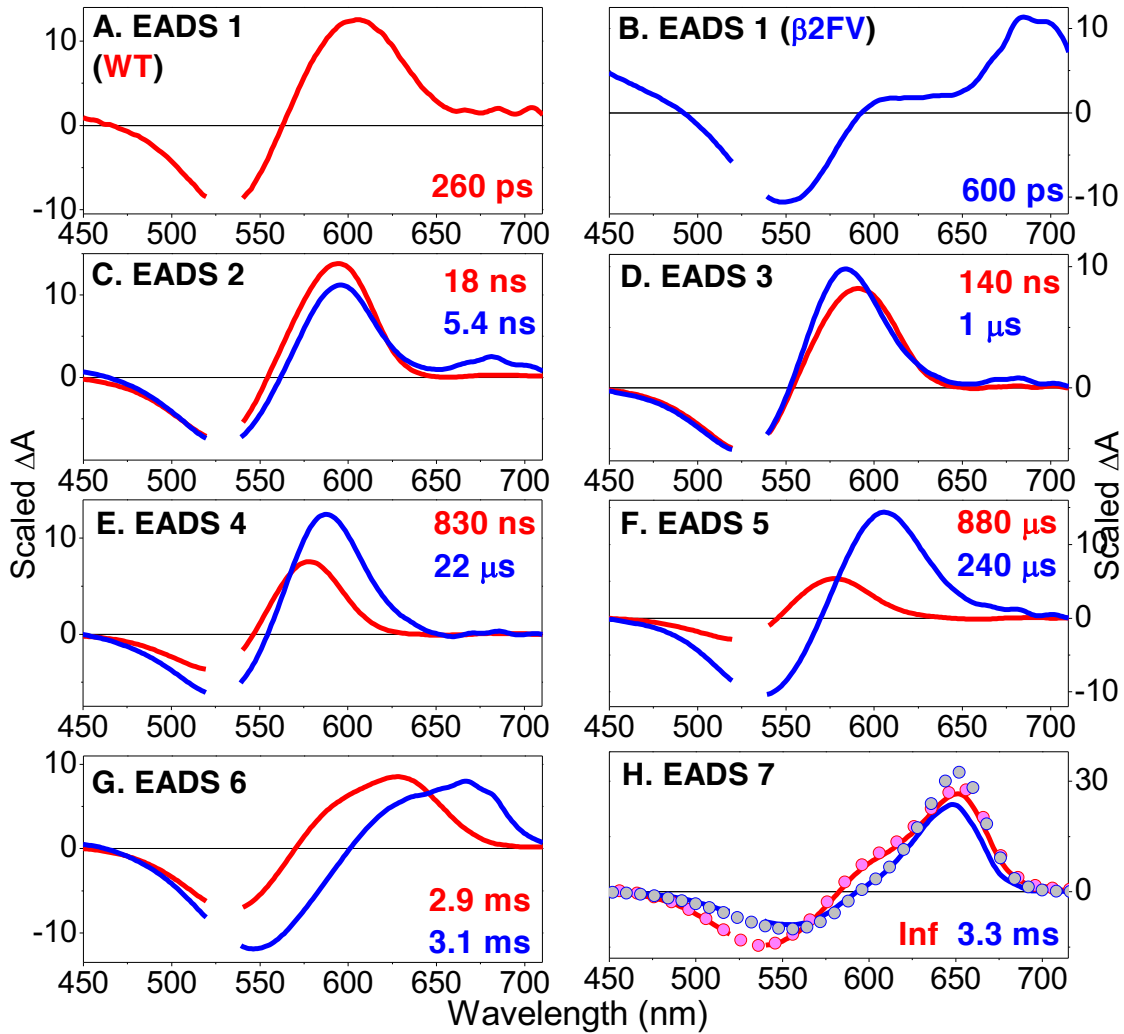


**Figure A7.22:** WT and  $\beta$ 2FV NpR6012g4 Secondary Reverse SADS Comparison

Comparison of the secondary reverse ( $^{15E}P_g \rightarrow ^{15Z}P_r$ ) dynamics for the WT (red curves) and the  $\beta$ 2FV (blue curves), with the lifetime of each compartment shown in each panel. The WT and  $\beta$ 2FV spectra in C-H were scaled at their ground state bleach 550nm for comparison. (H) The  $^{15Z}P_r - ^{15E}P_g$  difference spectra for the WT (red circles) and  $^{15Z}P_r - ^{15E}P_r$  the  $\beta$ 2FV (blue circles) are shown and were scaled to their respective GSB amplitudes. (I) Overlapped concentration profiles for the WT (solid curves) and the  $\beta$ 2FV (dashed curves) are displayed.

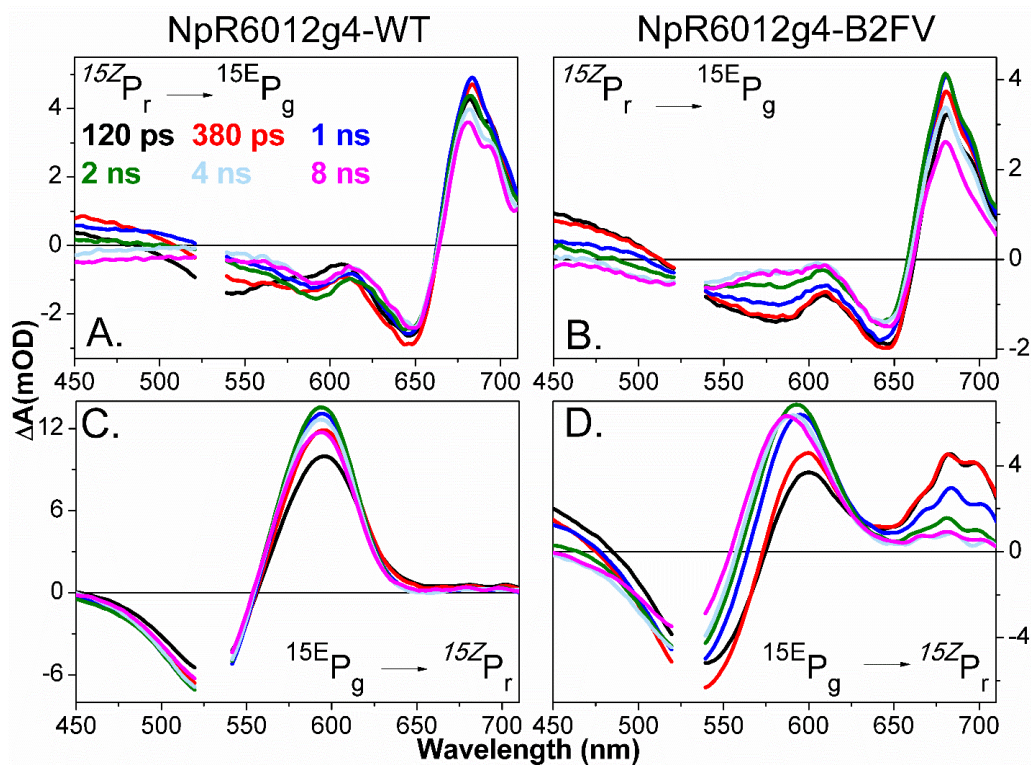


**Figure A7.23:** WT and  $\beta$ 2FV NpR6012g4 Secondary Forward and Reverse Transient Difference Spectra

Transient absorption spectra at selected probing times extracted from LTPP measurements of the forward ( $^{15}ZP_r \rightarrow ^{15}EP_g$ , A-B) and reverse ( $^{15}EP_g \rightarrow ^{15}ZP_r$ , C-D) dynamics for the WT NpR6012g4 (A and C) and the  $\beta$ 2FV NpR6012g4 (B and D). The forward reaction of  $\beta$ 2FV is prior to subtracting reverse dynamics.



### A7.5.3: WT and $\beta$ 2FV Photocycles

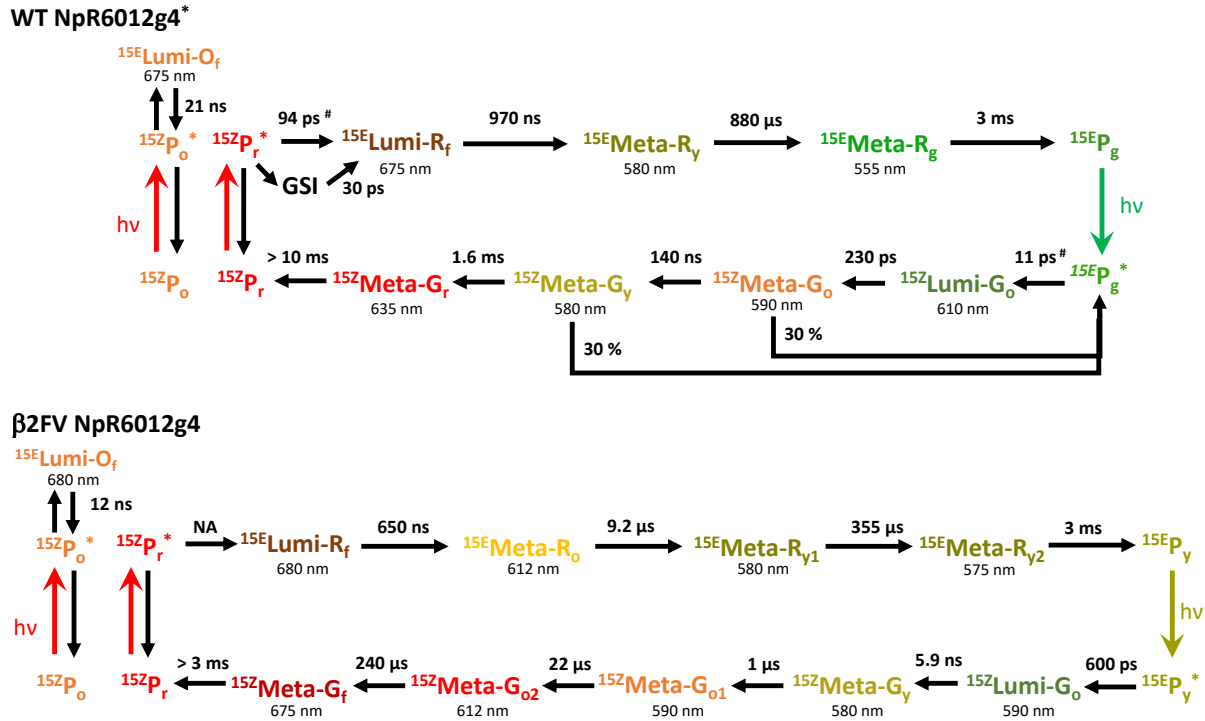


**Figure A7.24:** WT and  $\beta$ 2FV NpR6012g4 Photocycles

Comparison of WT and  $\beta$ 2FV photocycles, where  $\beta$ 2FV NpR6012g4, unlike WT did not incorporate shunts incorporated a Meta-G photointermediate with absorbance red shifted of  $^{15Z}P_r$  that was observed for several other Red/Green CBCRs.<sup>29, 179</sup> \*The forward photocycle for the WT was courtesy of Kirpich et al. and was slightly modified to include the photo-unproductive  $^{15Z}P_o$  subpopulation.<sup>29</sup>

### A7.5.4: Forward $\beta$ 2FV NpR6012g4 Dynamics Discussion

*Transient Signals.* Unlike the  $^{1EZ}P_g$  signaling state, the  $^{15Z}P_r$  dark adapted state spectra of WT and  $\beta$ 2FV NpR6012g4 were comparable (Figure A7.19). The secondary forward photodynamics of

$^{152}\text{P}_r$  for both samples are contrasted in Figure A7.21. Because of the short lifetime of the two  $^{152}\text{P}_r$  \* states,<sup>182</sup> the TA signals are composed primarily of a negative bleach signal arising from the loss of ground-state absorption and a positive absorption due to photointermediates. The transient spectra in Figure A7.21A and B exhibit qualitatively similar features with bleaches near 650 nm and an initial positive absorption at 675 nm (Lumi- $\text{R}_f$ ) that precedes a sequential blue shifting in absorbance as the delay time increased. The Lumi- $\text{R}_f$  photointermediate evolved faster in  $\beta 2\text{FV}$  than WT, and both have evolved by 1  $\mu\text{s}$ . In the 1 ns and 10 ns transient spectra (Figure A7.21A and B), the depression around 580 nm correspond to the bleach of the photo-unproductive orange absorbing subpopulation resolved for a few CBCR domains.<sup>27, 108</sup>. As expected from the differences in the light-adapted static spectra of the two samples (Figure A7.17), the 1-ms spectra differ appreciably with the WT absorbance being significantly blue shifted of  $\beta 2\text{FV}$ . Furthermore, after 100  $\mu\text{s}$ , the WT exhibited a  $\sim 10$  nm blue-shifting as well as a growth in absorption, whereas  $\beta 2\text{FV}$  NpR6012g4 exhibited a decay in absorbance and no further spectral shifting. Interestingly, the 1 ms spectra of  $\beta 2\text{FV}$  more closely resembled the static spectra difference spectra than the WT, suggesting that the forward photocycle of  $\beta 2\text{FV}$  is completed faster than the WT (Figure A7.21A and B).

The evolution of WT (red) and  $\beta 2\text{FV}$  (blue) NpR6012g4 signals are clearer in the kinetics compared in Figure A7.21C-H. The kinetic traces have been normalized at peaks near time 0 for comparison. Upon excitation, WT and  $\beta 2\text{FV}$  NpR6012g4 had positive absorption near 680 nm (Figure A7.19G). As this signal decayed, synchronized growth at 600 and 590 nm was observed, indicating evolution from a red shifted intermediate (Lumi- $\text{R}_f$ ) to a blue shifted intermediate

(Meta-R<sub>y</sub>). This was coupled with a revealing of the bleach at 650 nm (Figure A7.21F) that was due to Meta-R<sub>y</sub> having less overlap with the bleach than Lumi-R<sub>f</sub>. As the 590-600 nm signals decayed, a growth near 550 nm was observed (Figure A7.21C) that leveled off for β2FV near ~300 μs but continued to grow in for WT past 1 ms. This suggested the Meta-G<sub>g</sub> was being populated in the WT and perhaps that the <sup>15E</sup>P<sub>y</sub> photoproduct was being populated in β2FV NpR6012g4 given the similarities the difference static spectra and the 1 ms transient difference spectra (Figure A7.21B).

*Global Analysis.* Target model analysis with two subpopulations was used for the fitting of the β2FV NpR6012g4 as previously reported for WT NpR6012g4 and other red/green CBCRs (Table A7.10).<sup>27, 29, 108</sup> The results of the target analysis for WT and β2FV NpR6012g4 are compared in Figure A7.21. Just as with WT, β2FV NpR6012g4 had an unproductive orange absorbing subpopulation (<sup>15Z</sup>P<sub>o</sub>) that only populated Lumi-O<sub>f</sub> before decaying back to <sup>15Z</sup>P<sub>o</sub>. The Lumi-R<sub>f</sub> photointermediate persists until 970 ns for WT and 650 ns for β2FV. Similar to the WT, following Lumi-R<sub>f</sub>, there was a consistent blue shifting in photointermediates from Meta-R<sub>o</sub> and Meta-R<sub>y</sub> prior to populating the <sup>15E</sup>P<sub>y</sub> photoproduct.<sup>27, 29, 108</sup> Global analysis of the transient absorption spectra of β2FV had stronger evidence of an orange absorbing photointermediate after Lumi-R<sub>f</sub> that was resolved in the cryokinetics of WT NpR6012g4, but not the room temperature.<sup>27, 29, 73, 108</sup> The concentration curves are also compared in Figure A7.21C shows that β2FV mutation resulted in faster evolution through the photointermediates.

*Chapter 8. Supporting Information for “Comparative Secondary Photodynamics of the Red/Far-Red Phytochrome Cph1 and the Red/Green Cyanobacteriochrome NpR6012g4”*

**Includes: Supplemental Background Information (Figure S1), Photocycles (Schemes S1 and S2), Excitation Wavelength Parameters (Table S1), Room Temperature Forward and Reverse Dynamics (Figures S2-S6; Table S2), Supplemental Forward and Reverse Cryokinetics (Figures S7-S26, Tables S4-S6), Supplemental Cph1Δ Photocycle (Figure S27), and Supplemental References.**

*A8.1: Background Information*

```

Cph1Δ      NRLRQQANLRDFYDVIVEEVRRTMGFDRVMLYRFDENNHGDVIAEDKRDD----MEPYLG
NpR6012g4  NRIRQSSDVEEIEFKTTTQEVRLRCRDVAVYRFNPNWTGEFVAESVAHTWVKLVGPDIK

Cph1Δ      LHYPESDIPQPARRLFIHNPIRVIPDVYGVAVPLTPAVNPSTNRAVDLTESILRSAYHCH
NpR6012g4  TVWEDTHLQETQGGRYAQGENFVVNDIYQVG--HSP-----CH

Cph1Δ      LTYLKNMGV GASLTISLIKDGHLWGLIACHHQT
NpR6012g4  IEILEQFEVKAYVIVPVFAGEQLWGLLAAYQNS
  
```

**Figure A8.1:** Cph1Δ and NpR6012g4 Sequence Alignment.

Cph1Δ and NpR6012g4 Sequence Alignment. Highlight Color Code: Yellow: (22%) Conserved residues between Cph1Δ and NpR6012g4; Grey: (42%) Conservative substitutions. Pink: Bilin binding cysteine residue; Red (Cph1Δ Only): Aspartic acid residue (Cph1Δ Asp-207) of GAF domain involved in a salt bridge to the PHY domain in the dark-adapted state; Green (NpR6012g4 only): Phenylalanine residues associated with generating the green absorbing light adapted state

## Cph1

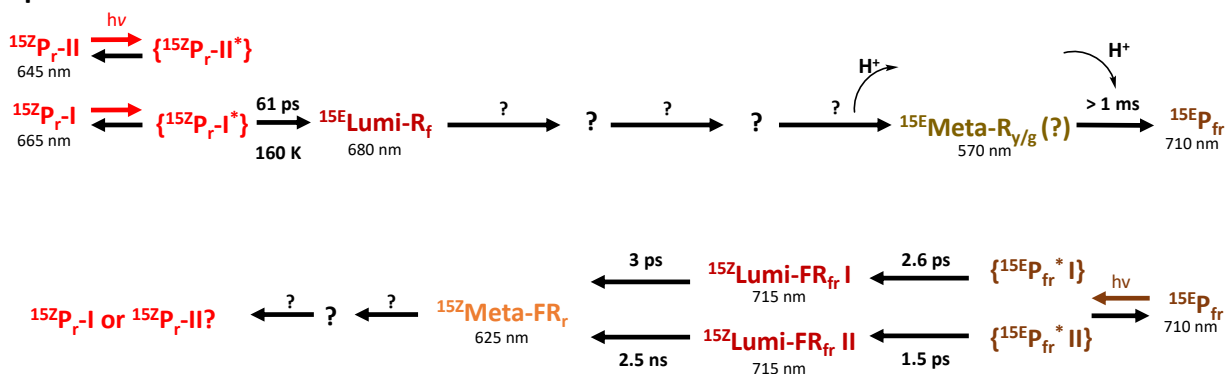


**Figure A8.2:** Current Model Mechanisms of the Forward and Reverse Reaction of Cph1Δ.

Current model (top) forward and (bottom) reverse mechanisms for Cph1Δ.<sup>101-104, 135</sup> Since it is not clear how the red absorbing cryo-trapped populations<sup>100, 101, 143</sup> are related to the yellow-red population resolved at room temperature, they are left out of this photocycle. The excited states were put into brackets to signify heterogeneity and the times represent the time constants extracted using global analysis methods.

### A8.1.1: Additional Background Information for Figure A8.1

A transient deprotonation event in Cph1 has been reported for the forward direction of Cph1Δ.<sup>135</sup> However, this hypothesis remains controversial.<sup>118, 128, 307-309</sup> Mizutani et al. have argued for a deprotonation step in the  $^{15}ZP_r \rightarrow ^{15}EP_{fr}$  reaction of phytochrome A isolated from peas using temperature resolved resonance Raman spectroscopy.<sup>128</sup> Conversely, Kneip et al. reported that this deprotonation did not occur using cryo-FTIR measurements on phytochrome A from etiolated seedlings.<sup>118</sup> Conflicting studies on deprotonation of phytochromes isolated from *Avena sativa* using low temperature FTIR and Raman spectroscopies also have been reported.<sup>307-309</sup> Other plant phytochrome photocycles appear not to incorporate deprotonation dynamics since transient

absorption spectroscopy and cryo-UV-Vis measurements did not exhibit significantly blue-shifted intermediates.<sup>116, 119, 120, 124-127, 130, 131, 134, 314, 354, 355</sup> Deprotonation dynamics reported for Agp1 from *Agrobacterium fabrum*,<sup>153, 312</sup> for Cph1 and Cph2 from *Synechocystis* sp. PCC6803,<sup>135, 171</sup> and for DrBphP from *Deinococcus radiodurans*<sup>311</sup> were dependent on highly conserved Asp and His residues.<sup>61, 311, 312</sup> Similar deprotonation of the pyrrole ring dynamics were reported for CphA from *Calothrix* PCC7601<sup>151</sup> and *Tolypothrix* PCC7601,<sup>124</sup> although these intermediates were not as extremely blue shifted and strongly overlapped the <sup>15</sup>ZP<sub>r</sub> dark-state bleach.

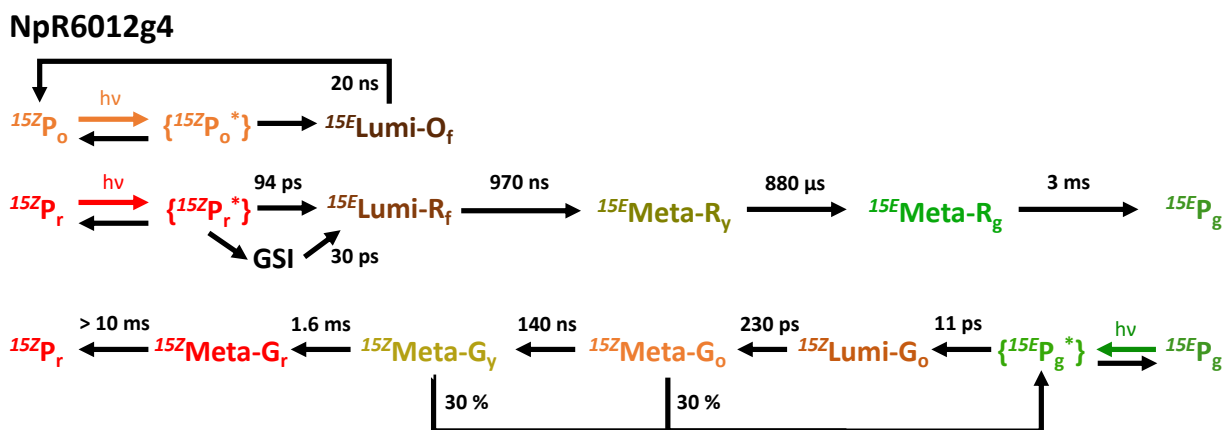


**Figure A8.3:** Current Model Mechanisms of the Forward and Reverse Reaction of NpR6012g4.

Current model (top) forward and (bottom) reverse mechanisms for NpR6012g4.<sup>29, 108, 182, 183, 356</sup> The excited states were put into brackets to signify heterogeneity and GSI is an abbreviation for ground state intermediate. The times represent the time constants extracted using global analysis methods.

**Table A8.1:** Experimental Parameters  
Excitation wavelengths used for various experiments in these investigations

Experiment	Cph1Δ Forward	Cph1Δ Reverse	NpR6012g4 Forward	NpR6012g4 Reverse
UFPP	600 nm and 670 nm	730 nm	~630-640 nm	500 nm and 575 nm
LTPP	532 nm	532 nm	532 nm	532 nm
Cryokinetics	650 nm	725 nm	653 nm	526 nm

*A8.2: Supplemental Cph1Δ and NpR6012g4 Room Temperature Dynamics*

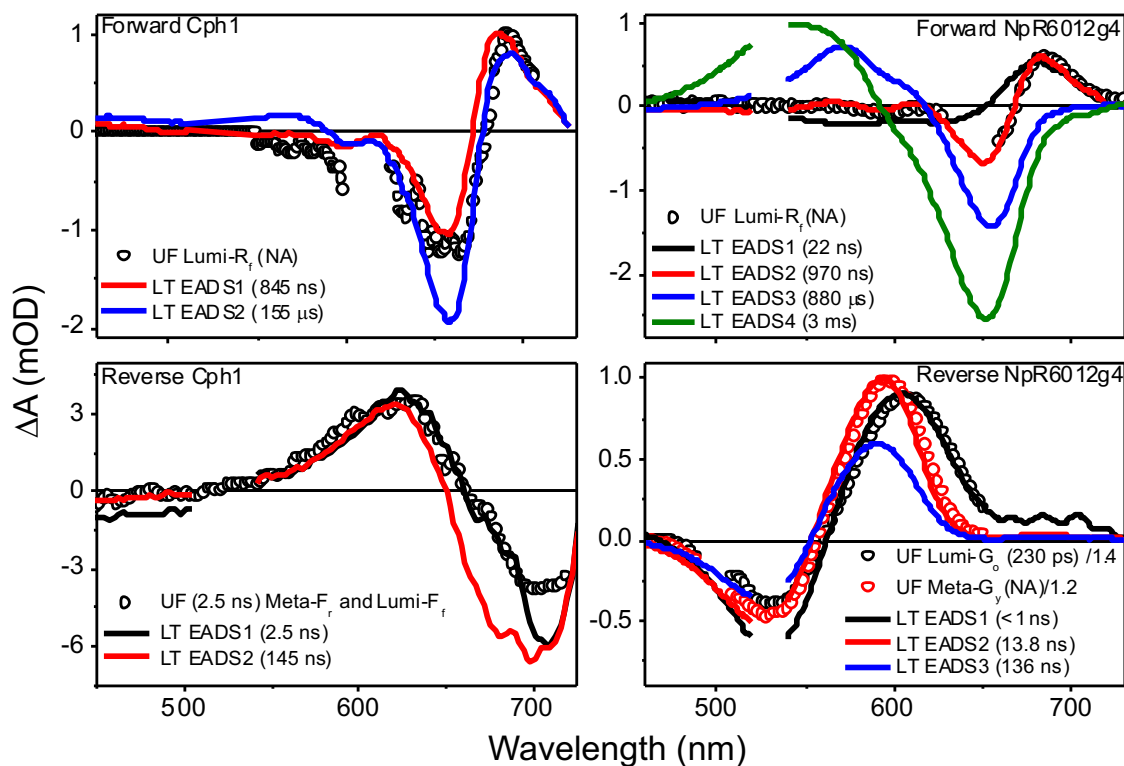


**Figure A8.4:** Forward and Reverse Reaction EADS of Cph1 and NpR6012g4

Forward (A and B) and reverse (C and D) evolution associated difference spectra (EADS) from ultrafast and longtime pump probe for Cph1Δ (A and C) and NpR6012g4 (B and D).<sup>27, 29, 100-104, 108, 182, 183</sup>

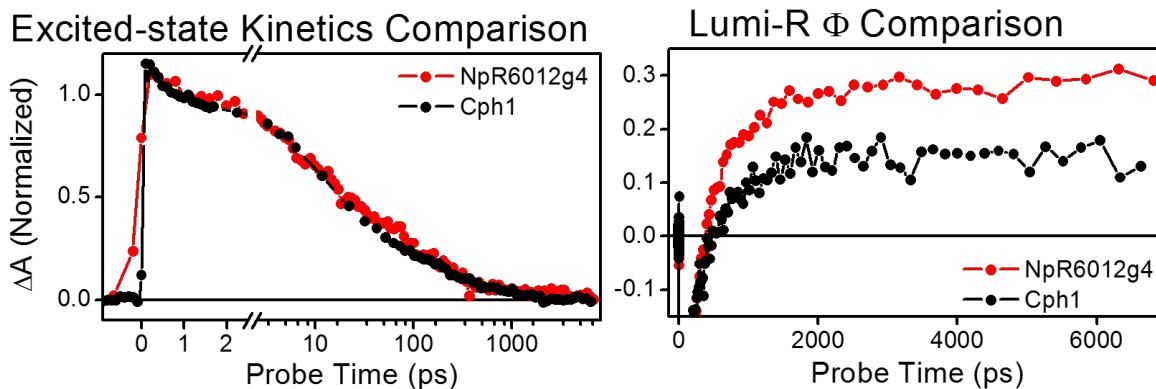


**Figure A8.5:** Cph1 $\Delta$  and NpR6012g4 Primary Forward Kinetics Comparison

Comparison of Cph1 $\Delta$  (black curves) and NpR6012g4 (red curves) forward excited-state kinetics (left) and Lumi-R<sub>f</sub> quantum yields.<sup>100, 101, 182, 183</sup>

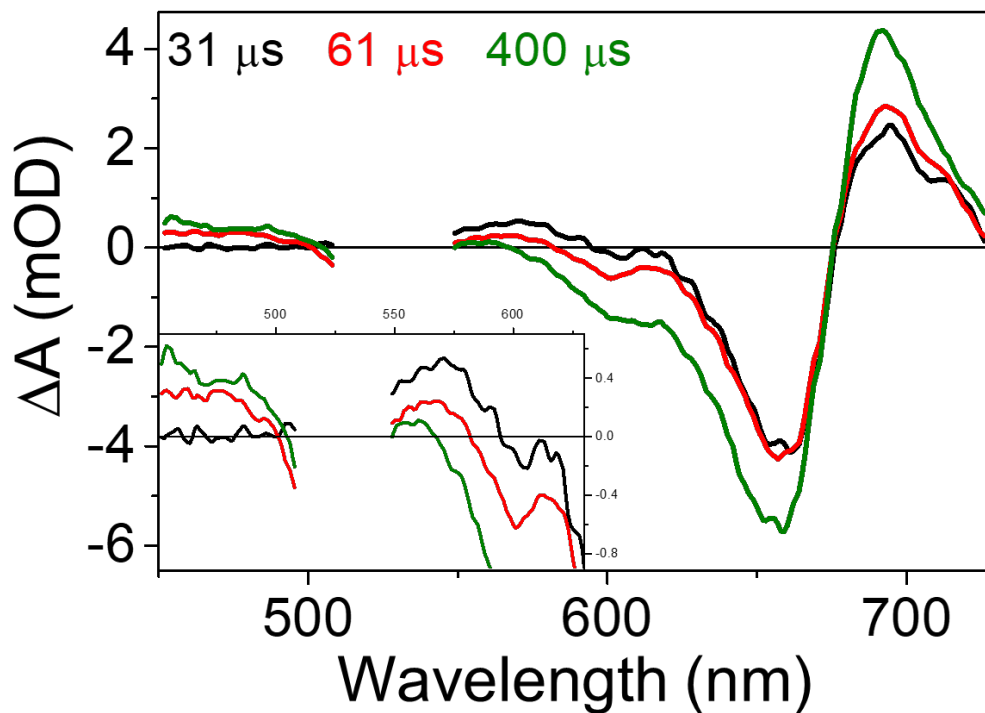


**Figure A8.6:** Secondary Forward Cph1 $\Delta$  TA Difference Spectra (20-40  $\mu$ s)

TA difference spectra emphasizing the presence of Meta-G<sub>g</sub> (575 nm) and Meta-G<sub>b</sub> (475 nm) intermediates in the forward dynamics of Cph1 $\Delta$



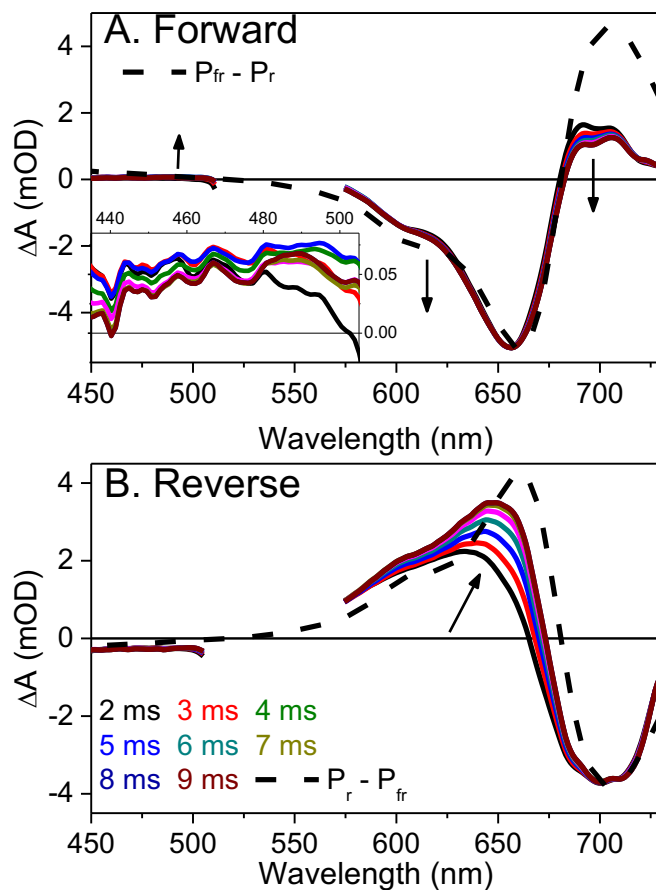


**Figure A8.7:** Secondary Forward and Reverse Cph1 $\Delta$  TA Difference Spectra (2-10 ms)

The bleach normalized Cph1 $\Delta$  transient difference spectra from 2 ms to 10 ms for the forward (A) and reverse (B) reaction dynamics. The arrow indicates the trend of increasing in the probe time. The forward dynamics spectra are normalized at 660 nm, and the reverse is normalized at 700 nm, and they are compared with the difference spectra of complete reaction (dashed curves) of  $P_{fr} - P_r$  and  $P_r - P_{fr}$  for forward and reverse reactions, respectively. These dynamics are in the flow region where the excited sample is flowing out of the probe region.

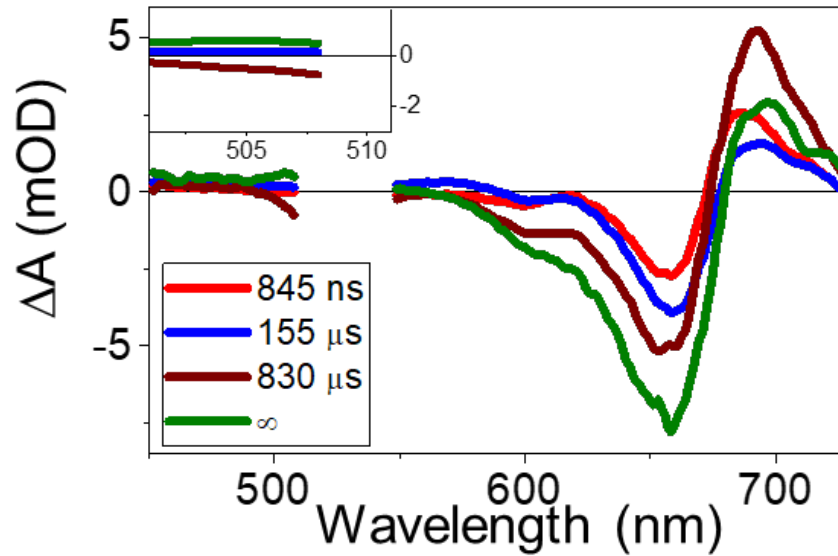


**Figure A8.8:** Secondary Forward Room Temperature TA EADS of Cph1Δ.

Secondary forward room temperature TA EADS of Cph1Δ which shows the population of two unique green absorbing intermediates.

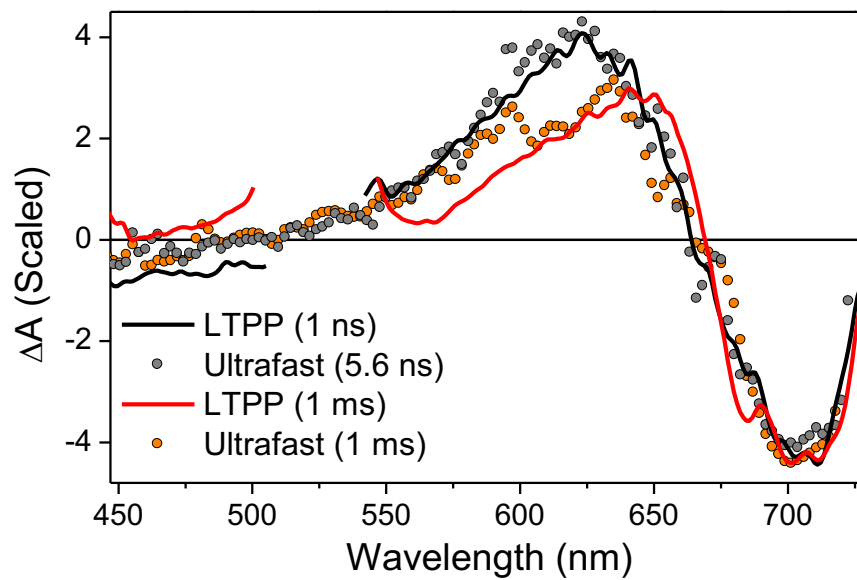


**Figure A8.9:** Primary and Secondary Forward Cph1Δ TA spectra Comparison

Overlap of Cph1Δ ultrafast and LTPP reverse spectra at two different delay times.<sup>100, 101</sup>

**Table A8.2:** Cph1Δ Forward and Reverse Room-Temp TA Observations

Time Constant	Description	Interpretation
$^{15Z}P_r \rightarrow ^{15E}P_{fr}$		
835 ns	<ul style="list-style-type: none"> <li>Loss of far-red absorption and growth of green absorption</li> <li>Orange absorption ~ constant</li> </ul>	<ul style="list-style-type: none"> <li>Lumi-R<sub>f</sub> is evolving to Meta-R<sub>o</sub> at a comparable rate as Meta-R<sub>o</sub> is evolving to Meta-R<sub>g</sub></li> </ul>
155 μs	<ul style="list-style-type: none"> <li>Loss in green absorption and growth of far-red absorption</li> </ul>	<ul style="list-style-type: none"> <li>Evolution of Meta-R<sub>g</sub> to Meta-R<sub>f</sub></li> </ul>
830 μs	<ul style="list-style-type: none"> <li>Loss of Meta-R<sub>f</sub> and a growth of a green absorbance blue shifted of Meta-R<sub>g</sub></li> </ul>	<ul style="list-style-type: none"> <li>Evolution of Meta-R<sub>f</sub> to Meta-R<sub>b</sub> which continued past the flow region</li> </ul>
$^{15E}P_{fr} \rightarrow ^{15Z}P_r$		
2.5 ns	<ul style="list-style-type: none"> <li>Loss of red shoulder absorption while maintaining max absorption wavelength position</li> <li>Same 2.5 ns time constant as Lumi-FR<sub>f</sub> II → Meta-FR<sub>r</sub> previously reported in an ultrafast study.<sup>103</sup></li> </ul>	<ul style="list-style-type: none"> <li>2.5 ns spectrum is a mixture of Lumi-FR<sub>f</sub> II and Meta-FR<sub>r</sub> I captured in the previously reported UF data</li> <li>The loss of the red shoulder and revealing of the bleach is due to the evolution of Lumi-FR<sub>f</sub> II to Meta-FR<sub>r1</sub></li> <li>Cryo 170 → 180 K</li> </ul>
145 ns	<ul style="list-style-type: none"> <li>Red shifting of the spectra</li> <li>The peak has some spectral similarities with that of P<sub>r-II</sub> – P<sub>fr</sub></li> <li>Does not have the shoulder of P<sub>r-II</sub> – P<sub>fr</sub>,</li> </ul>	<ul style="list-style-type: none"> <li>Evolution of Meta-FR<sub>r1</sub> to Meta-FR<sub>r2</sub> or <math>^{15Z}P_{r-II}</math></li> <li>Cryo 200 → 210 K</li> </ul>
375 μs	<ul style="list-style-type: none"> <li>Further (larger) red shifting of the spectra</li> <li>Blue shoulder similar to <math>^{Total}P_r - P_{fr}</math>,</li> <li>Peak is not as red shifted as <math>^{Total}P_r - P</math></li> </ul>	<ul style="list-style-type: none"> <li>Evolution of Meta-FR<sub>r</sub> II or <math>^{15Z}P_{r-II}</math>:  <math>Meta-FR_r II \rightarrow ^{15Z}P_{r-II} \rightleftharpoons ^{15Z}P_{r-I}</math>                      Or  <math>^{15Z}P_{r-II} \rightleftharpoons ^{15Z}P_{r-I}</math></li> <li>Cryo 210 K → 220 K</li> </ul>

A8.3: *Cph1*Δ Forward Cryokinetics

**Cyroknetics Experiment Procedure**

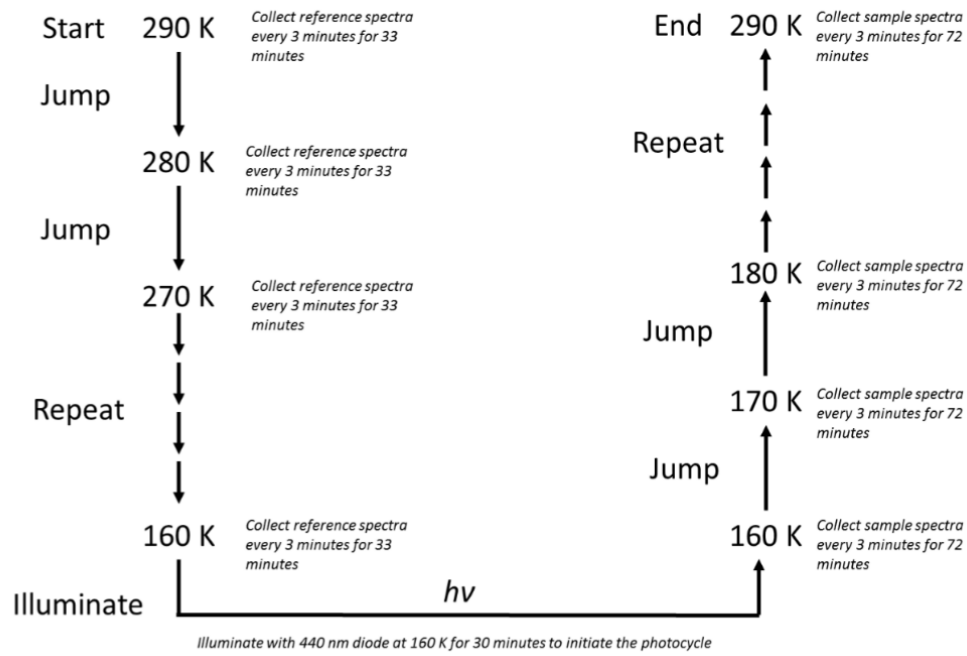


**Figure A8.10:** Cryokinetics Experiment Flowchart

Schematic depicting flow of an average cryokinetics experiment.

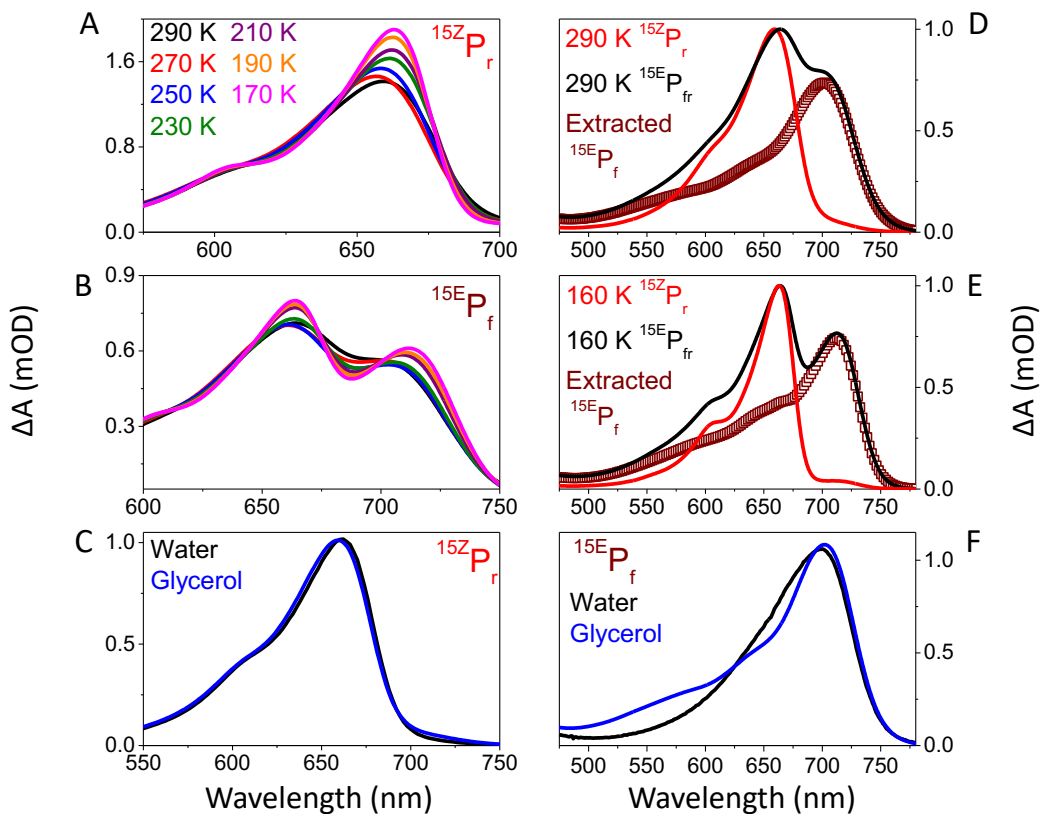


**Figure A8.11:** Temperature Dependence of the parental States of Cph1Δ

(A) Temperature dependence on the  $^{15Z}P_r$  absorption where there is an initial blue-shifting and increase in absorption with a decrease in temperature (290-260 K) followed by a red-shift (250-230 K) and a continuation of the increase in absorption (250-160 K) as the temperature is further decreased. (B) Temperature dependence on the  $^{15E}P_{fr}$  absorption (color coded to legend in (A)) where there is a red shifting and growth of the far-red absorbance due to the narrowing of the parental bands with the decrease in temperature. It should be noted that there is strong  $^{15Z}P_r$  contamination. (C) Comparison of the  $^{15Z}P_r$  absorption in H<sub>2</sub>O (UFPP and LTPP samples) and Glycerol (cryo sample), showing that the addition of glycerol did not affect the absorption of  $^{15Z}P_r$  much other than blue shifting the spectra by 2-3 nm. (D)  $^{15Z}P_r$  and  $^{15E}P_{fr}$  with  $^{15Z}P_r$  contamination spectra at 290 K (solid lines). The extracted spectra of  $^{15E}P_{fr}$  at 290 K (open burgundy boxes) was obtained by subtracting 57.5% of  $^{15Z}P_r$  at 290 K. (E)  $^{15Z}P_r$  and  $^{15E}P_{fr}$  with  $^{15Z}P_r$  contamination spectra at 160 K (solid lines). The extracted spectra of  $^{15E}P_{fr}$  at 160 K (open burgundy boxes) was obtained by subtracting 57.5% of  $^{15Z}P_r$  at 160 K. (F) Comparison of the extracted  $^{15E}P_{fr}$  absorption in H<sub>2</sub>O (UFPP and LTPP samples) and glycerol (cryo sample).

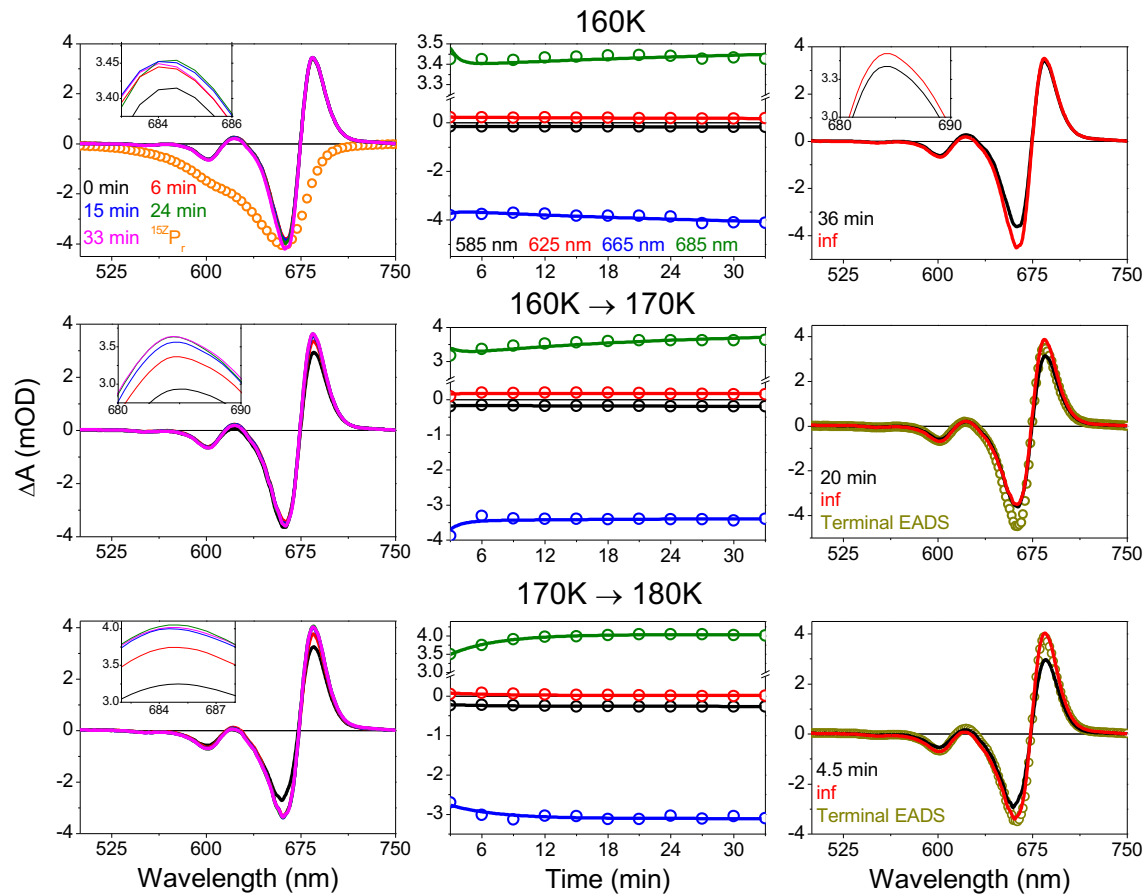


**Figure A8.12:** Forward Cryokinetics of Cph1 $\Delta$  from 160 K to 180 K.

Forward cryokinetics of Cph1 $\Delta$  from 160 K to 180 K. In the EADS figures, the preceding temperatures terminal EADS are represented by open golden circles.

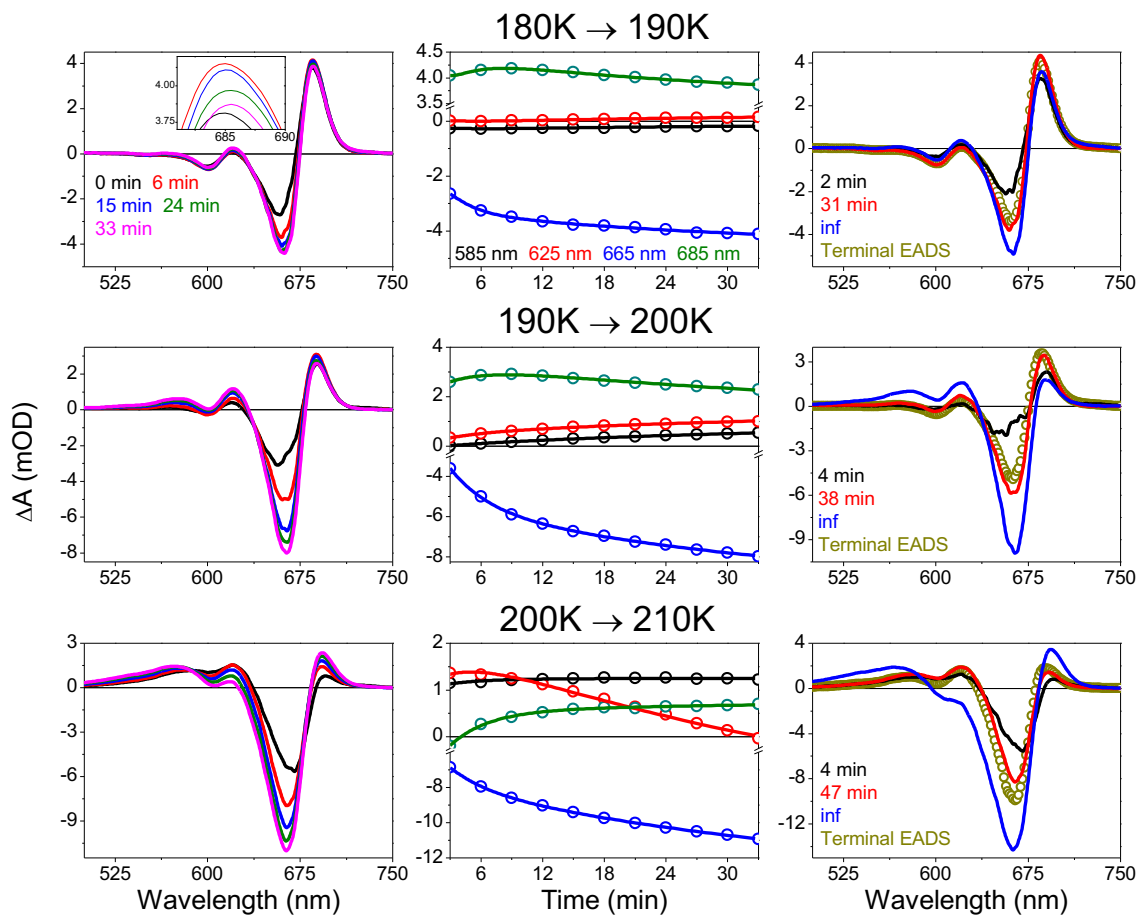


**Figure A8.13:** Forward Cryokinetics of Cph1 $\Delta$  from 190 K to 210 K.

Forward cryokinetics of Cph1 $\Delta$  from 190 K to 210 K. In the EADS figures, the preceding temperatures terminal EADS are represented by open golden circles.

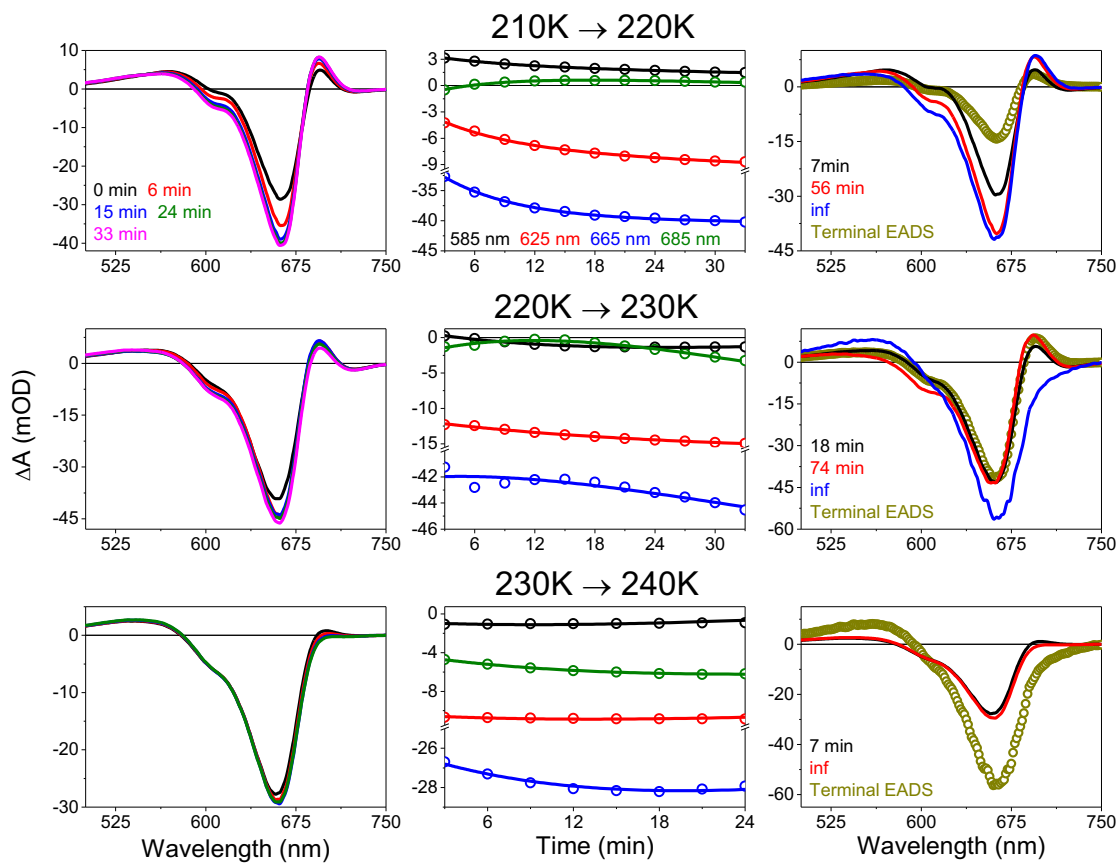


**Figure A8.14:** Forward Cryokinetics of Cph1 $\Delta$  from 220 K to 240 K.

Forward cryokinetics of Cph1 $\Delta$  from 220 K to 240 K. In the EADS figures, the preceding temperatures terminal EADS are represented by open golden circles.



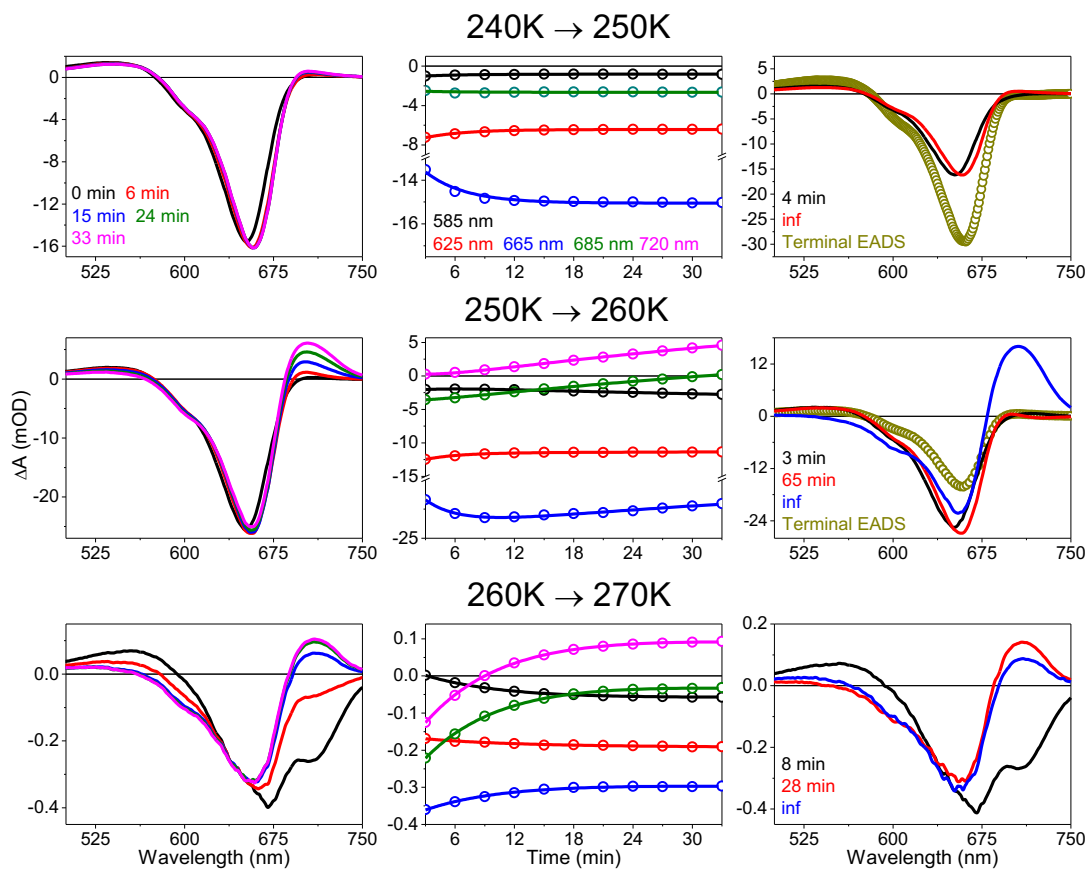


**Figure A8.15:** Forward Cryokinetics of Cph1Δ from 250 K to 270 K.

Forward cryokinetics of Cph1Δ from 250 K to 270 K. In the EADS figures, the preceding temperatures terminal EADS are represented by open golden circles.

**Table A8.3: Cph1Δ Forward Cryokinetics Observations**

Temperature Jump	Description	Interpretation
160 K	<ul style="list-style-type: none"> <li>(+) Abs ~ 685 nm &amp; ~ 623 nm</li> <li>(-) Abs ~663 nm &amp; ~ 600 nm</li> </ul>	<ul style="list-style-type: none"> <li>(+) @ 685 nm = Lumi-R<sub>f</sub> abs.</li> <li>(+) @ 623 nm = Meta-R<sub>o</sub></li> <li>(-) signals is described by GSB</li> </ul>
150 → 160 K	<ul style="list-style-type: none"> <li>Same as 160 K</li> </ul>	<ul style="list-style-type: none"> <li>Thermalization at early time</li> </ul>
170 → 180 K	<ul style="list-style-type: none"> <li>Same as 160 &amp; 170 K</li> <li>(-) signal @ 663 nm → 668 nm</li> </ul>	<ul style="list-style-type: none"> <li>Bleach red shifted due to increase in temp</li> </ul>
180 → 190 K	<ul style="list-style-type: none"> <li>(-) signal @ 668 → 663 nm</li> <li>Slight decrease in 685 nm (+) signal</li> <li>Slight increase in 621 nm (+) signal</li> <li>Decrease of 663 (-) signal</li> </ul>	<ul style="list-style-type: none"> <li>Perhaps previous shift was an error or due to increase in temp (<b>Figure S8</b>)</li> <li>Loss of Lumi-R<sub>f</sub> state</li> <li>Generation of Meta-R<sub>o</sub> state from Lumi-R<sub>f</sub></li> <li>Thermalization (663 (-) signal decrease)</li> </ul>
190 → 200 K	<ul style="list-style-type: none"> <li>(+) peak: 685 nm → 688 nm</li> <li>Loss of 688 nm peak</li> <li>Growth of 621nm (+) and 557 – 595 nm (+) signals</li> <li>Decrease of 663 (-) signal</li> </ul>	<ul style="list-style-type: none"> <li>Red shift due to increase in temp. (<b>Figure S8</b>)</li> <li>Lumi-R<sub>f</sub> → Meta-R<sub>o</sub> → Meta-R<sub>g</sub> evolution</li> <li>Revealing of the bleach due to loss of overlapping Lumi-R<sub>f</sub></li> </ul>
200 → 210 K	<ul style="list-style-type: none"> <li>(+) peak: 688 nm → 693 nm</li> <li>Growth of 693 nm (+) signal</li> <li>Loss of 621 nm (+) signal</li> <li>Slight growth b/w 500-580 nm</li> <li>Decrease of 663 (-) signal</li> </ul>	<ul style="list-style-type: none"> <li>Meta-R<sub>o</sub> → Meta-R<sub>g</sub> → Meta-R<sub>f</sub>. Meta-R<sub>g</sub> is being populated from Meta-R<sub>o</sub> faster than it is evolving</li> <li>Revealing of the bleach is due to loss of overlapping Meta-R<sub>o</sub></li> </ul>
210 → 220 K	<ul style="list-style-type: none"> <li>Growth of 695 nm (+) signal</li> <li>Decrease of 600 – 670 nm (-) signal</li> <li>Weak growth b/w 500 -545 nm (+)</li> </ul>	<ul style="list-style-type: none"> <li>Population of Lumi-R<sub>f</sub>/Meta-R<sub>f</sub> from Meta-R<sub>o</sub> or Meta-R<sub>g</sub>. At this temperature population and evolution of Meta-R<sub>g</sub> are nearly equal</li> </ul>
220 → 230 K	<ul style="list-style-type: none"> <li>Decay of 610 nm (-) signal (Thermalization)</li> <li>Decay of 693 nm (+) signal</li> </ul>	<ul style="list-style-type: none"> <li>Loss of overlapping Meta-R<sub>o</sub></li> <li>Evolution of Meta-R<sub>f</sub> to Meta-R<sub>b</sub></li> </ul>
230 → 240 K	<ul style="list-style-type: none"> <li>Decay of 693 nm (+) signal</li> <li>Growth of 500-575 nm (+) signal</li> </ul>	<ul style="list-style-type: none"> <li>Evolution of Meta-R<sub>f</sub> to Meta-R<sub>b</sub></li> </ul>
240 → 250 K	<ul style="list-style-type: none"> <li>Red shifting of bleach</li> <li>Weak growth of 703 nm (+) signal</li> <li>Weak decay of 520 nm (+) signal</li> </ul>	<ul style="list-style-type: none"> <li>Thermalization/Temp increase</li> <li>Evolution of Meta-R<sub>b</sub> to <sup>15E</sup>P<sub>fr</sub></li> </ul>
250 → 260 K	<ul style="list-style-type: none"> <li>Decay in green region</li> <li>Red shifting of the bleach with slight filling in</li> <li>Growth of 705 nm (+) signal</li> </ul>	<ul style="list-style-type: none"> <li>Meta-R<sub>b</sub> is evolving to <sup>15E</sup>P<sub>fr</sub> given the overlap with the difference of the static spectra. Population of <sup>15E</sup>P<sub>fr</sub> causes a slight filling in of the bleach. The red shifting of the bleach can be accounted by losing overlapping Meta-R<sub>b</sub></li> </ul>
260 → 270 K	<ul style="list-style-type: none"> <li>Decay in green region</li> <li>Growth of 705 nm (+) signal</li> </ul>	<ul style="list-style-type: none"> <li>Evolution of Meta-R<sub>b</sub> to <sup>15E</sup>P<sub>fr</sub></li> </ul>

A8.4: NpR6012g4 Forward Cryokinetics

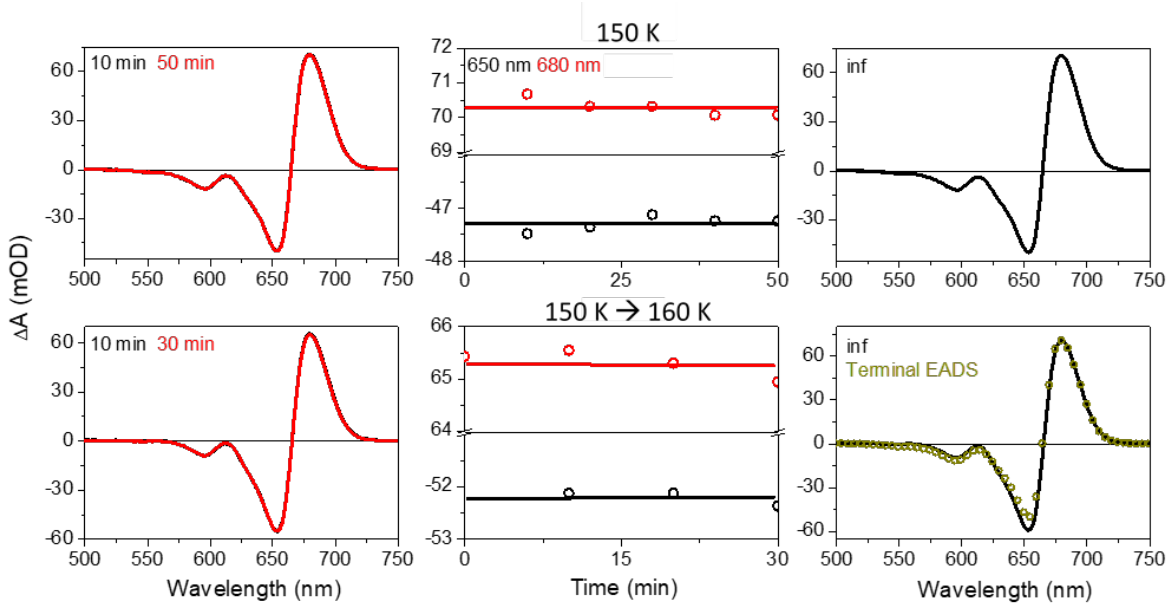


**Figure A8.16:** Forward Cryokinetics of NpR6012g4 from 150 K to 160 K.

Cryokinetics of NpR6012g4 from 150 K to 160 K. In the EADS figures, the preceding temperatures terminal EADS are represented by open grey circles.

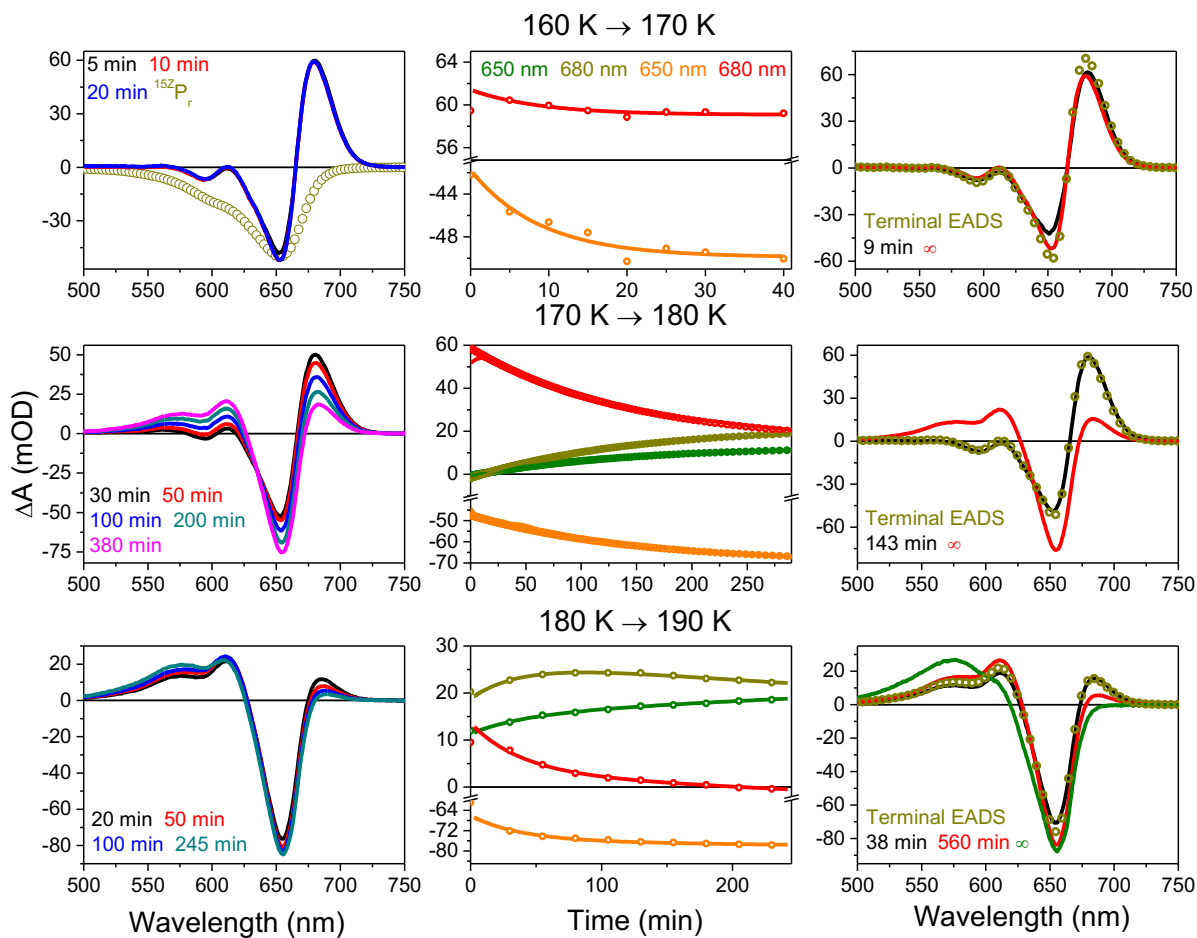


**Figure A8.17:** Forward Cryokinetics of NpR6012g4 from 170 K to 190 K.

Cryokinetics of NpR6012g4 from 170 K to 190 K. In the EADS figures, the preceding temperatures terminal EADS are represented by open grey circles.

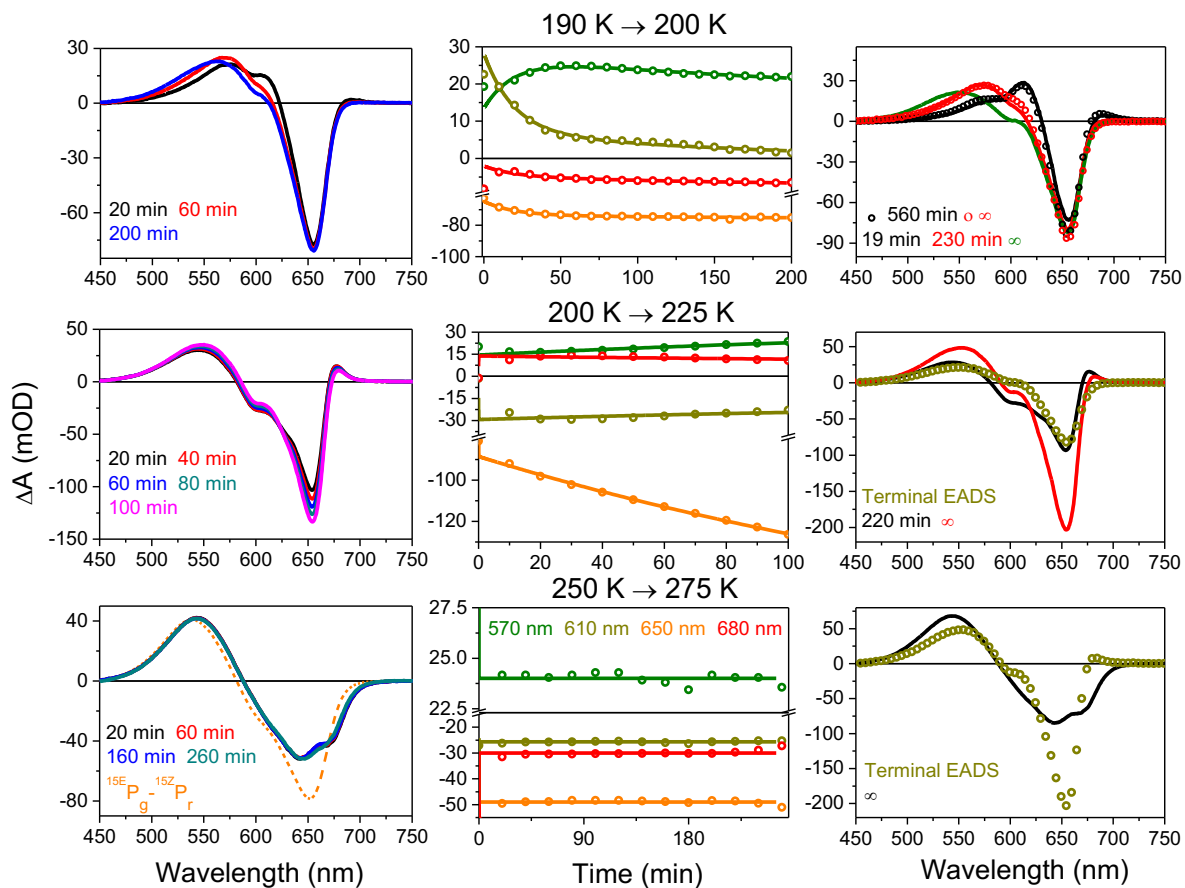


**Figure A8.18:** Forward Cryokinetics of NpR6012g4 from 200 K to 275 K.

Cryokinetics of NpR6012g4 at 200, 225, and 275 K. In the EADS figures, the preceding temperatures terminal EADS are represented by open grey circles. There was a resurgence in the far-red absorbance where Lumi-R<sub>f</sub> absorbs at 225 K. This was because this was a different experimental run that had a larger temperature jump and still had residual Lumi-R<sub>f</sub>.

**Table A8.4:** NpR6012g4 Forward Cryokinetics Observations

Temperature Jump	Description	Interpretation
150 K	<ul style="list-style-type: none"> <li>• Peak (+) Absorbance 680 nm</li> <li>• Peak (-) Absorbance 650 nm</li> <li>• Peak (-) Absorbance 595 nm</li> </ul>	<ul style="list-style-type: none"> <li>• Lumi-R<sub>f</sub> absorption</li> <li>• Ground State bleach</li> <li>• Meta-R<sub>o</sub> overlapping the GSB</li> </ul>
160 → 170 K	<ul style="list-style-type: none"> <li>• Peak (+) Absorbance 680 nm</li> <li>• Peak (-) Absorbance 650 nm</li> <li>• Peak (-) Absorbance 595 nm</li> </ul>	<ul style="list-style-type: none"> <li>• Lumi-R<sub>f</sub> absorption</li> <li>• Ground State bleach</li> <li>• Meta-R<sub>o</sub> overlapping the GSB</li> </ul>
160 → 170 K	<ul style="list-style-type: none"> <li>• Peak (+) Absorbance 680 nm</li> <li>• Peak (-) Absorbance 650 nm</li> <li>• Peak (-) Absorbance 595 nm</li> </ul>	<ul style="list-style-type: none"> <li>• Lumi-R<sub>f</sub> absorption</li> <li>• Ground State bleach</li> <li>• Meta-R<sub>o</sub> overlapping the GSB</li> </ul>
170 → 180 K	<ul style="list-style-type: none"> <li>• (+) decay @ 680 nm</li> <li>• (-) growth @ 650 nm</li> <li>• (+) growth @ 610 nm with a shoulder from 530-595 nm</li> </ul>	<ul style="list-style-type: none"> <li>• Loss of initial Lumi-R<sub>f</sub></li> <li>• Loss of overlapping Lumi-R<sub>f</sub></li> <li>• Population of Meta-R<sub>y</sub> and Meta-R<sub>o</sub> photointermediates.</li> </ul>
180 → 190 K	<ul style="list-style-type: none"> <li>• Decaying 680 nm (+) signal</li> <li>• Slightly growing 650 nm (-) signal</li> <li>• Growing 550-575 nm (+) signal</li> <li>• No Change at 610 nm (+) signal</li> </ul>	<ul style="list-style-type: none"> <li>• Lumi-R<sub>f</sub> is evolving to Meta-R<sub>y</sub>, resulting in the decaying @ 680 nm and revealing of the bleach at 650 nm. Meta-R<sub>y</sub> is evolving to Meta-R<sub>g</sub> as quickly as it is being generated, describing the growth of (+) signal between 550-575 nm and the absorbance at 610 nm being constant.</li> </ul>
190 → 200 K	<ul style="list-style-type: none"> <li>• Decay in 610 nm (+) abs by 60 min</li> <li>• Blue shift in spectra between 60 and 200 min</li> </ul>	<ul style="list-style-type: none"> <li>• Evolution of any residual Meta-R<sub>y</sub> to Meta-R<sub>g</sub></li> </ul>
200 → 225 K Start of a different run	<ul style="list-style-type: none"> <li>• Slight growth of 500-560 nm (+) signal</li> <li>• Growth of 653 nm (-) signal</li> <li>• Decay of 680 nm (+) signal</li> </ul>	<ul style="list-style-type: none"> <li>• Evolution to Meta-R<sub>g</sub></li> <li>• This is from a different run with a larger temperature jump, so the 680 nm (+) signal is residual Lumi-R<sub>f</sub></li> </ul>
250 → 275 K	<ul style="list-style-type: none"> <li>• No real change in spectra with time</li> </ul>	<ul style="list-style-type: none"> <li>• Population of <sup>15</sup>EP<sub>g</sub> (Given LTPP EADS overlap; Figure 5).</li> </ul>

A8.5: Cph1Δ Reverse Cryokinetics

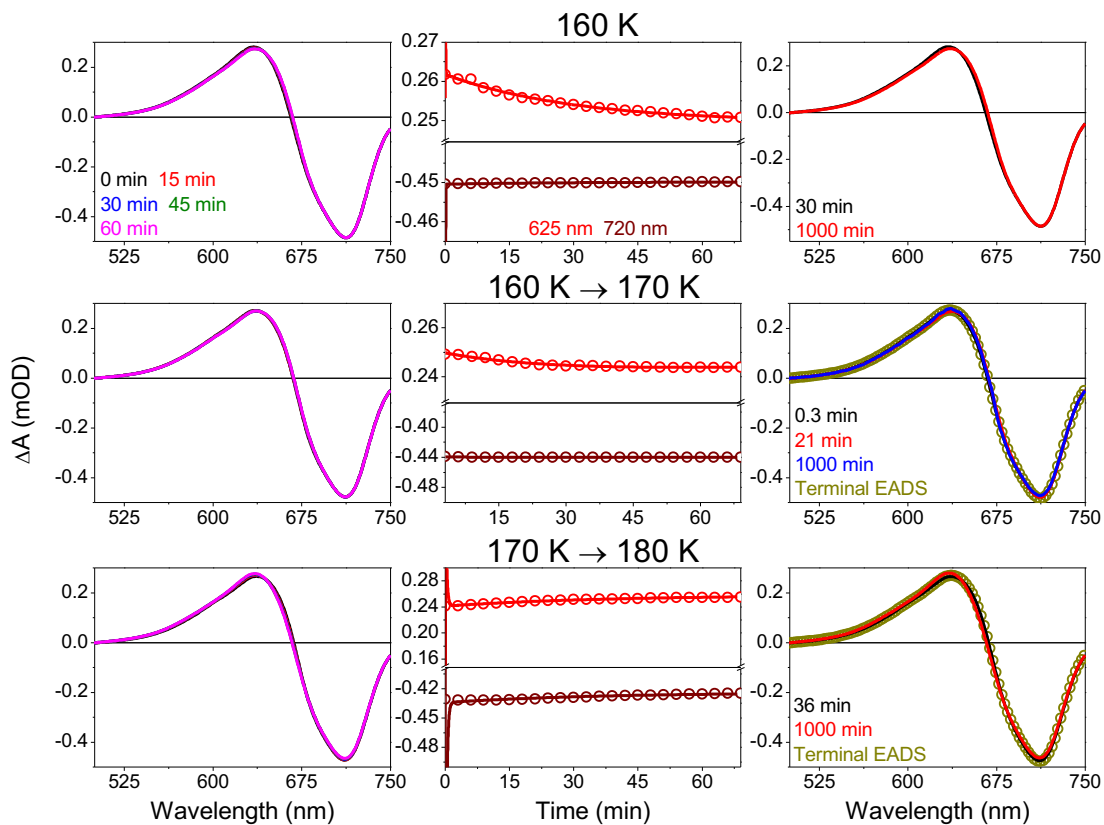


**Figure A8.19:** Reverse Cryokinetics of Cph1Δ from 160 K to 180 K.

Reverse cryokinetics of Cph1Δ from 160 K to 180 K. In the EADS figures, the preceding temperatures terminal EADS are represented by open golden circles.

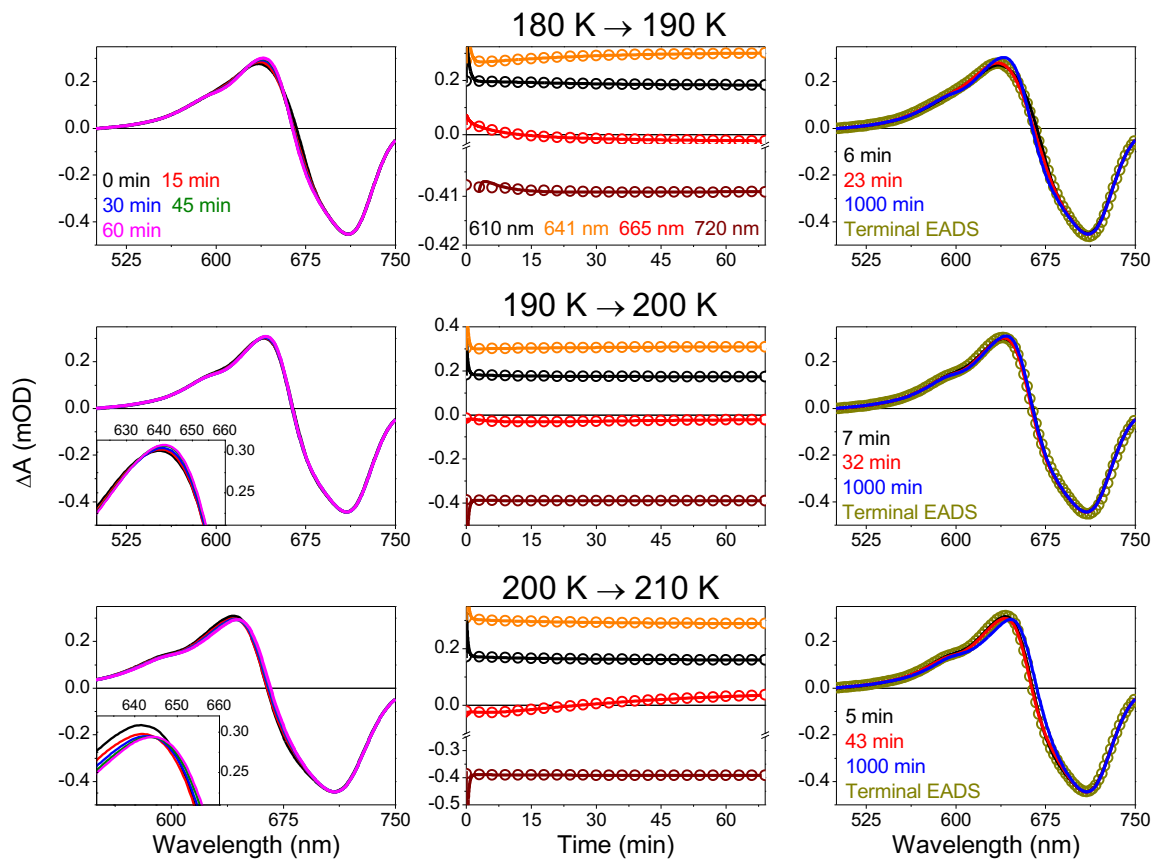


**Figure A8.20:** Reverse Cryokinetics of Cph1 $\Delta$  from 190 K to 210 K.

Reverse cryokinetics of Cph1 $\Delta$  from 190 K to 210 K. In the EADS figures, the preceding temperatures terminal EADS are represented by open golden circles.



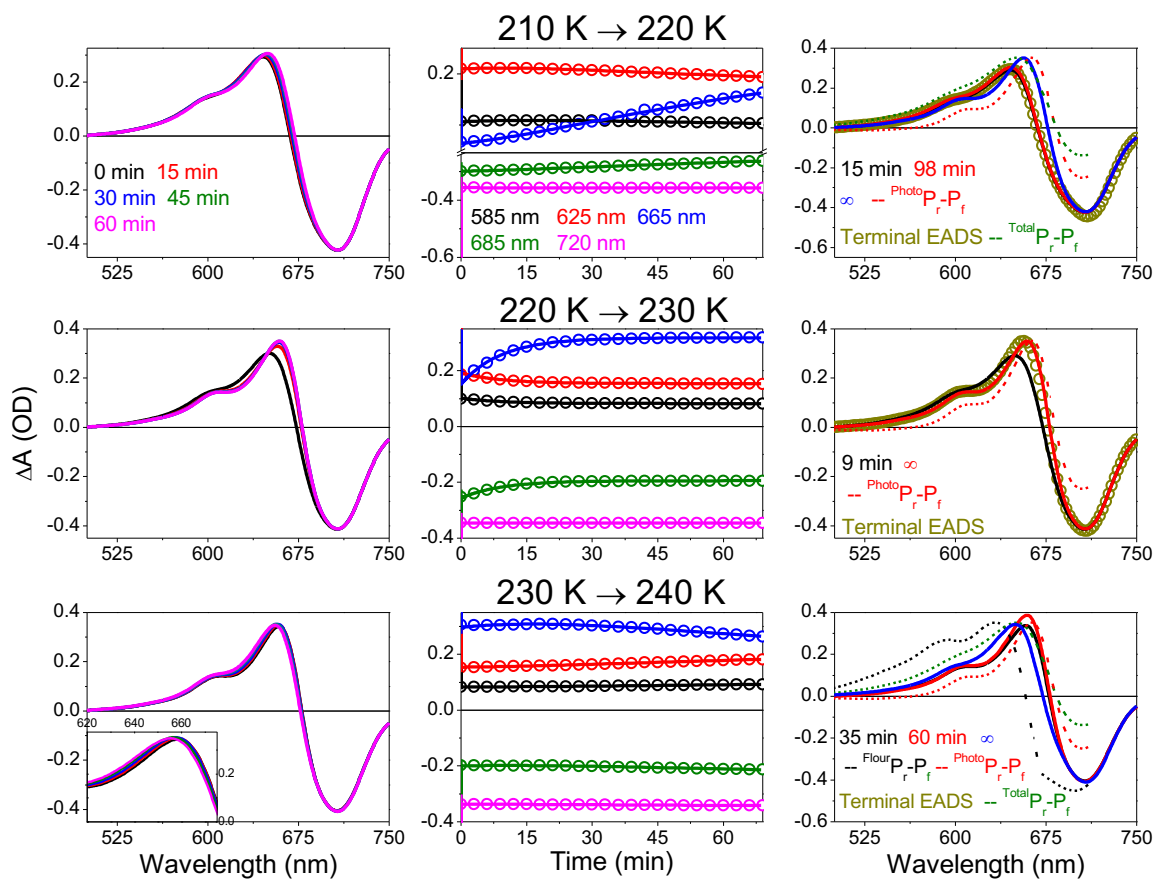


**Figure A8.21:** Reverse Cryokinetics of Cph1 $\Delta$  from 220 K to 240 K.

Reverse cryokinetics of Cph1 $\Delta$  from 220 K to 240 K. In the EADS figures, the preceding temperatures terminal EADS are represented by open golden circles.

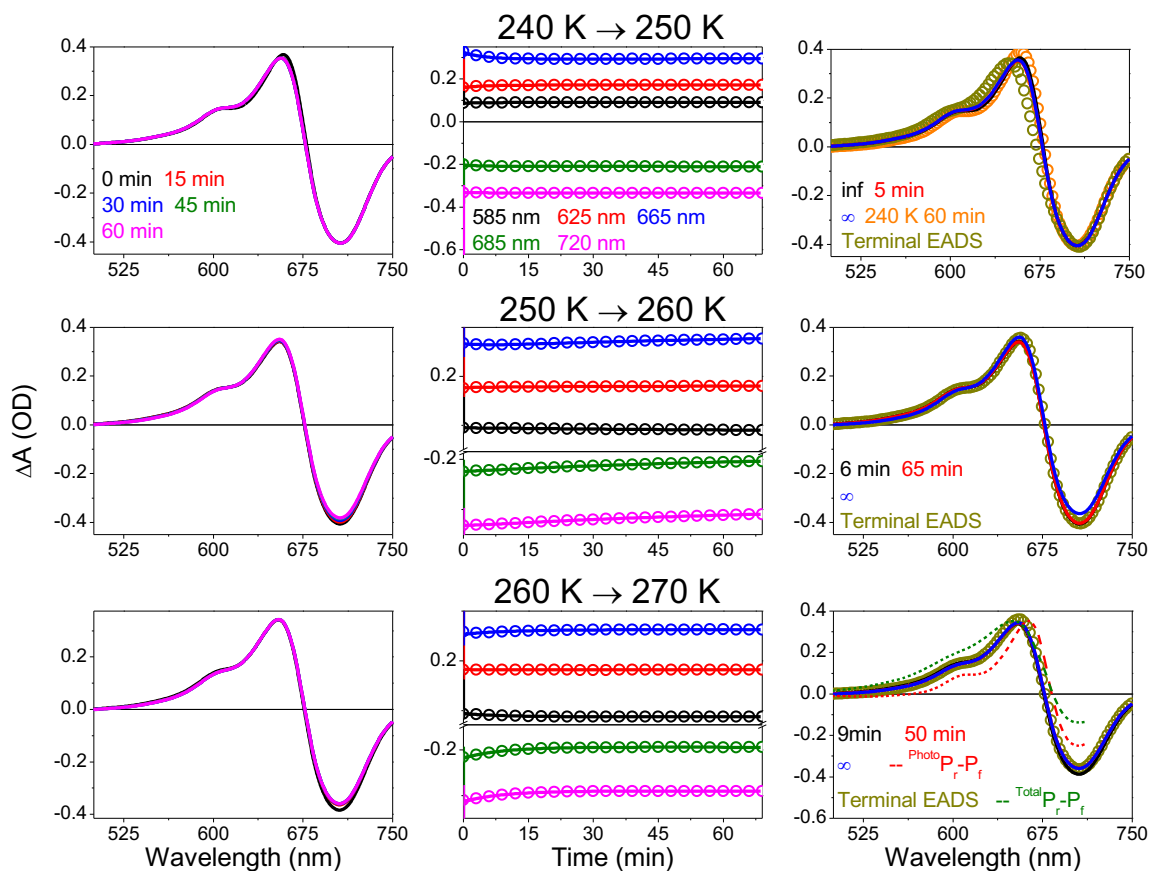


**Figure A8.22:** Reverse Cryokinetics of Cph1 $\Delta$  from 250 K to 270 K.

Reverse cryokinetics of Cph1 $\Delta$  from 250 K to 270 K. In the EADS figures, the preceding temperatures terminal EADS are represented by open golden circles.

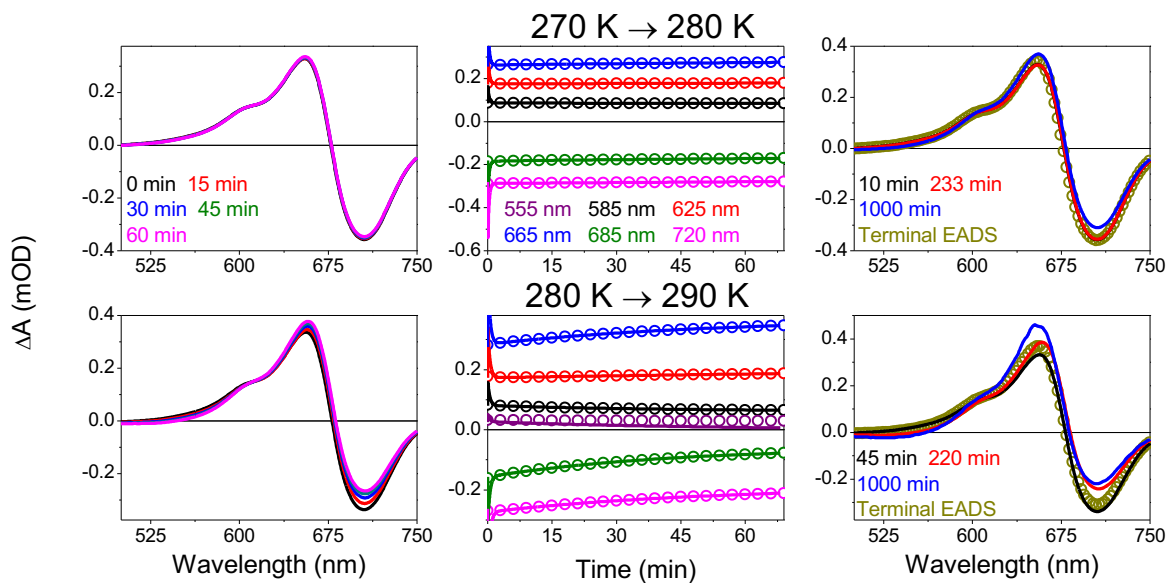


**Figure A8.23:** Reverse Cryokinetics of Cph1 $\Delta$  from 280 K to 290 K.

Reverse cryokinetics of Cph1 $\Delta$  at 280 K and 290 K. In the EADS figures, the preceding temperatures terminal EADS are represented by open golden circles.

**Table A8.5: Cph1Δ Reverse Cryokinetics Observations**

Temperature Jump	Description	Interpretation
160 K	<ul style="list-style-type: none"> <li>Negative signal @ 712 nm</li> <li>Positive Signal @ 635 nm</li> </ul>	<ul style="list-style-type: none"> <li>Ground state bleach</li> <li>Meta-FR<sub>r</sub> absorption</li> </ul>
160 → 170 K	<ul style="list-style-type: none"> <li>Same as 160 K</li> </ul>	<ul style="list-style-type: none"> <li>Preceding terminal EADS overlap confirms</li> </ul>
170 → 180 K	<ul style="list-style-type: none"> <li>Same as 170 K</li> <li>May be slight (negligible) blue shifting</li> </ul>	<ul style="list-style-type: none"> <li>Preceding terminal EADS overlap confirms</li> <li>Thermalization</li> </ul>
180 → 190 K	<ul style="list-style-type: none"> <li>Growth of 641 nm (+) signal</li> <li>Decay in shoulder (657 – 675 nm)</li> </ul>	<ul style="list-style-type: none"> <li>Spectra does not match dark state (no blue shifted shoulder). Evolution to secondary Meta-FR<sub>r</sub> state.</li> </ul>
190 → 200 K	<ul style="list-style-type: none"> <li>Same as 190 K</li> <li>Blue-side shoulder is more pronounced than at 190 K</li> </ul>	<ul style="list-style-type: none"> <li>Preceding terminal EADS overlap confirms</li> </ul>
200 → 210 K	<ul style="list-style-type: none"> <li>Red shifting of positive band (+2-4 nm)</li> </ul>	<ul style="list-style-type: none"> <li>Temperature affect</li> </ul>
210 → 220 K	<ul style="list-style-type: none"> <li>Further red shifting of the positive band (+2-4 nm)</li> </ul>	<ul style="list-style-type: none"> <li>Evolution to Fluorescent <sup>15Z</sup>P<sub>r</sub>-II</li> </ul>
220 → 230 K	<ul style="list-style-type: none"> <li>Further red shifting of the positive band (+ 2-4 nm)</li> </ul>	<ul style="list-style-type: none"> <li>Temperature affect</li> </ul>
230 → 240 K	<ul style="list-style-type: none"> <li>Blue shifting of positive band. More blue shifted than 220 K terminal EADS (- 2-3 nm)</li> <li>Growth on the blue sided shoulder</li> </ul>	<ul style="list-style-type: none"> <li>Population of Photoactive <sup>15Z</sup>P<sub>r</sub> -I</li> </ul>
240 → 250 K	<ul style="list-style-type: none"> <li>EADS are slightly red shifted from preceding temperature</li> </ul>	<ul style="list-style-type: none"> <li>Equilibration of <sup>15Z</sup>P<sub>r</sub>-II and <sup>15Z</sup>P<sub>r</sub>-I</li> </ul>
250 → 260 K	<ul style="list-style-type: none"> <li>Same as 250 K</li> <li>Small decay of (-) 700 nm signal</li> </ul>	<ul style="list-style-type: none"> <li>Too long (1 hr.) to be a temperature affect, no positive signal decay to indicate a shunt back to the <sup>15Z</sup>P<sub>r</sub> state.</li> <li>Equilibration of <sup>15Z</sup>P<sub>r</sub>-II and <sup>15Z</sup>P<sub>r</sub>-I</li> </ul>
260 → 270 K	<ul style="list-style-type: none"> <li>Same as 260 K</li> </ul>	<ul style="list-style-type: none"> <li>Same as 260 K</li> </ul>
270 → 280K	<ul style="list-style-type: none"> <li>Same as 270 K</li> </ul>	<ul style="list-style-type: none"> <li>Same as 270 K</li> </ul>
280 → 290K	<ul style="list-style-type: none"> <li>Growth of 655 nm (+) peak</li> <li>Decay of 710 nm (-) signal</li> <li>Decay of 550 nm (+) signal</li> </ul>	<ul style="list-style-type: none"> <li>Green-yellow (weakly) absorbing Meta-F<sub>r</sub> state transferring over to <sup>15Z</sup>P<sub>r</sub> state that overlaps the <sup>15E</sup>P<sub>fr</sub> state, resulting in the observation of the bleach filling in</li> <li>Equilibration of <sup>15Z</sup>P<sub>r</sub>-II and <sup>15Z</sup>P<sub>r</sub>-I</li> </ul>

A8.6: NpR6012g4 Reverse Cryokinetics

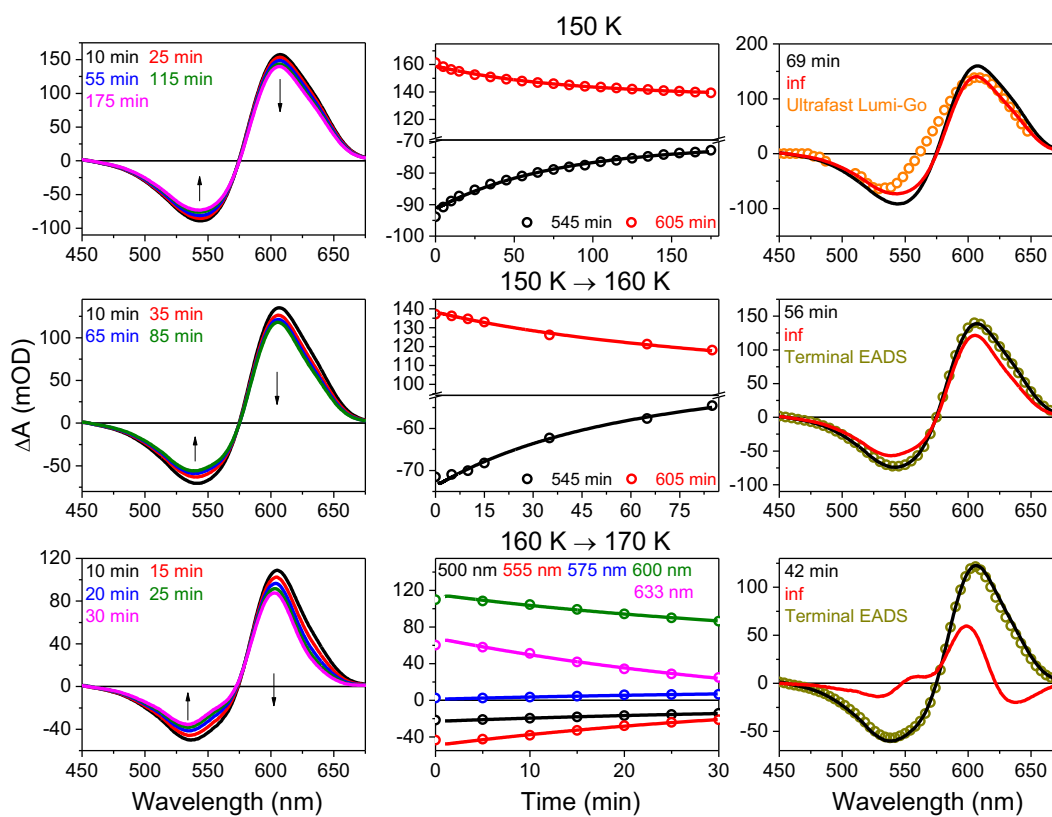


**Figure A8.24:** Reverse Cryokinetics of NpR6012g4 from 150 K to 170 K.

Reverse cryokinetics of NpR6012g4 from 150 K and 170 K. In the EADS figures, the preceding temperatures terminal EADS are represented by open golden circles.

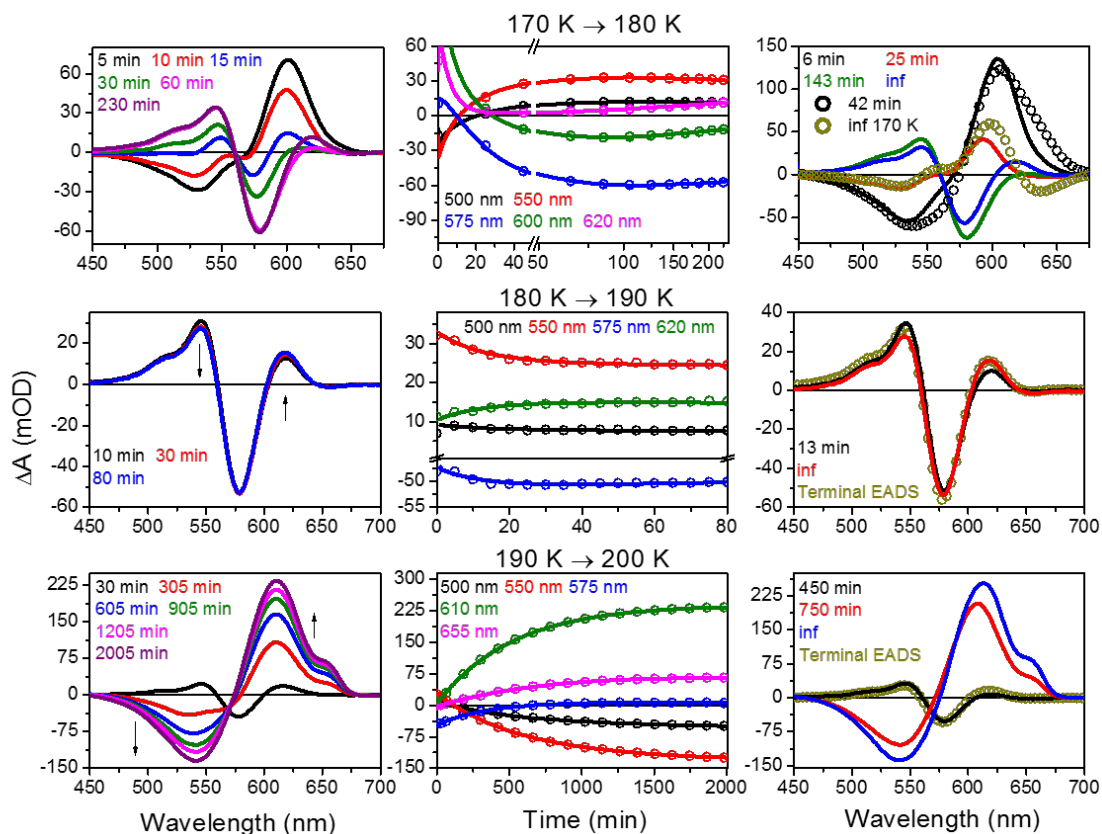


**Figure A8.25:** Reverse Cryokinetics of NpR6012g4 from 180 K to 200 K.

Reverse cryokinetics of NpR6012g4 from 180 K and 200 K. In the EADS figures, the preceding temperatures terminal EADS are represented by open golden circles.

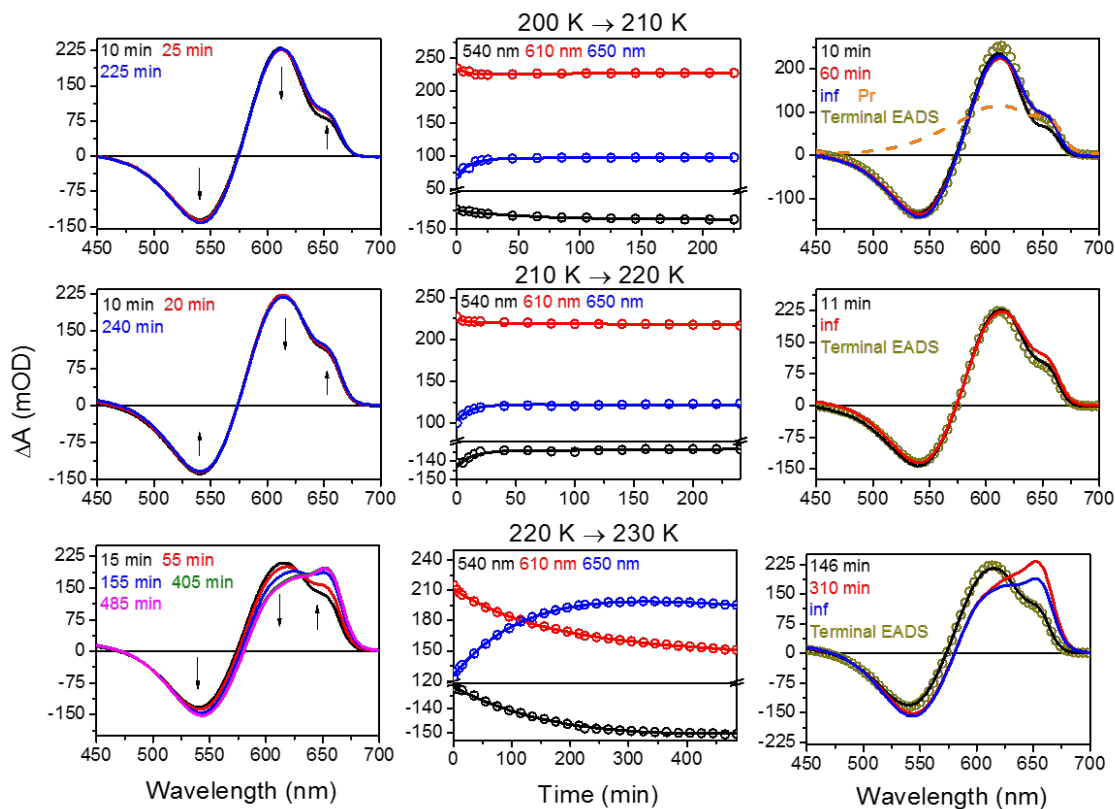


**Figure A8.26:** Reverse Cryokinetics of NpR6012g4 from 210 K to 230 K.

Reverse cryokinetics of NpR6012g4 from 210 K and 230 K. In the EADS figures, the preceding temperatures terminal EADS are represented by open golden circles.

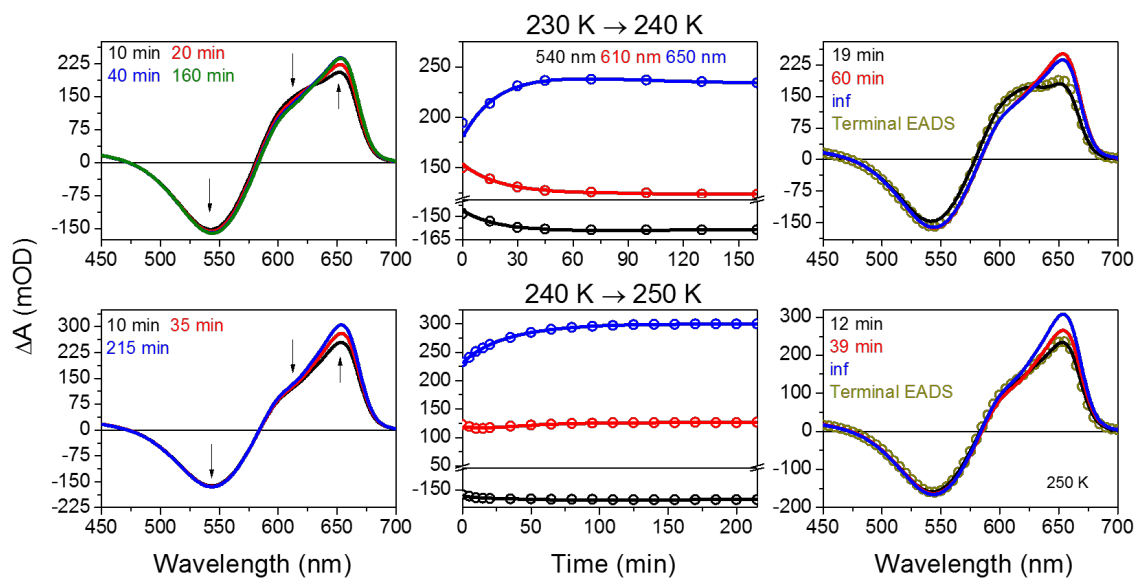


**Figure A8.27:** Reverse Cryokinetics of NpR6012g4 from 150 K to 170 K.

Reverse cryokinetics of NpR6012g4 at 240 K and 250 K. In the EADS figures, the preceding temperatures terminal EADS are represented by open golden circles.

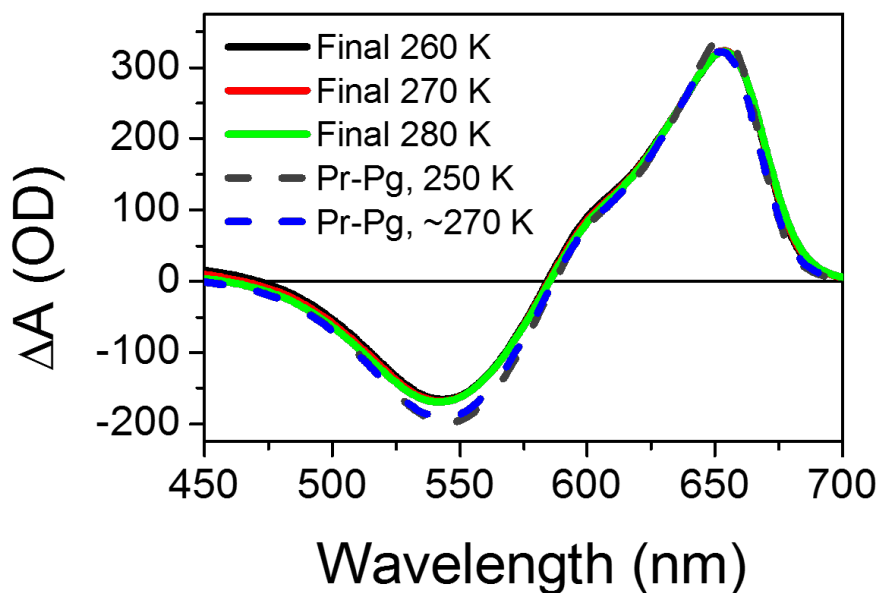


**Figure A8.28:** Terminal Reverse Cryokinetics of NpR6012g4 from 260 K to 280 K.

Terminal reverse cryokinetics (solid lines) between 260 K and 270 K overlapped with the Pr-P<sub>g</sub> spectra at 250 K and 270 K.



**Table A8.6: NpR6012g4 Reverse Cryokinetics Observations**

Temperature Jump	Description	Interpretation
150 K	<ul style="list-style-type: none"> <li>Decay of positive absorption @ 610 nm</li> <li>Decay of negative signal at 540 nm</li> <li>Decay of negative signal is faster than that of positive signal</li> </ul>	<ul style="list-style-type: none"> <li>Shunt back to the ground state</li> </ul>
150 → 160 K	<ul style="list-style-type: none"> <li>Same as 150 K</li> </ul>	<ul style="list-style-type: none"> <li>Same as 150 K</li> </ul>
160 → 170 K	<ul style="list-style-type: none"> <li>Same as 160 K</li> <li>EADS shows positive population and blue shifting of the spectra</li> </ul>	<ul style="list-style-type: none"> <li>Shunt coupled with evolution to Meta-G<sub>g</sub></li> </ul>
170 → 180 K	<ul style="list-style-type: none"> <li>Growth of (+) peak at 540 nm</li> <li>Long shoulder to 475 nm</li> <li>Growth of (-) signal at 575 nm</li> <li>Growth of (=) signal at 615 nm</li> </ul>	<ul style="list-style-type: none"> <li>Meta-G<sub>g</sub> being populated from Lumi-G<sub>r</sub>, revealing the GSB around 575 nm</li> <li>Evolution of Meta-G<sub>g</sub> to Meta-G<sub>r</sub> at later times</li> </ul>
180 → 190 K	<ul style="list-style-type: none"> <li>Small decay of 575 nm peak</li> <li>Small growth at 615 nm</li> </ul>	<ul style="list-style-type: none"> <li>Evolution of Meta-G<sub>g</sub> to Meta-G<sub>r</sub></li> </ul>
190 → 200 K	<ul style="list-style-type: none"> <li>Growth of (+) signal at 610 nm with shoulder at 650 nm</li> <li>Growth of (-) signal at 540 nm</li> </ul>	<ul style="list-style-type: none"> <li>Evolution of Meta-G<sub>g</sub> to Meta-G<sub>r</sub>, revealing the GSB around 540 nm</li> </ul>
200 → 210 K	<ul style="list-style-type: none"> <li>Small growth in the (+) 650 nm shoulder</li> <li>Small decay of the (+) 600 nm peak</li> <li>Small growth of the (-) 540 nm signal</li> <li>All occurring in the first 20 -25 min</li> </ul>	<ul style="list-style-type: none"> <li>Either: minuscule evolution of Meta-G<sub>r</sub> to <sup>152</sup>P<sub>r</sub> or thermalization</li> </ul>
210 → 220 K	<ul style="list-style-type: none"> <li>Same as 210 K</li> </ul>	<ul style="list-style-type: none"> <li>Same as 210 K</li> </ul>
220 → 230 K	<ul style="list-style-type: none"> <li>Decay of (+) 610 nm peak</li> <li>Growth of (+) 650 nm peak</li> <li>Slight growth of 550 nm (-) signal</li> </ul>	<ul style="list-style-type: none"> <li>Evolution of Meta-G<sub>r</sub> to <sup>152</sup>P<sub>r</sub>, revealing the GSB around 550 nm</li> </ul>
230 → 240 K	<ul style="list-style-type: none"> <li>Same as 230 K</li> </ul>	<ul style="list-style-type: none"> <li>Same as 230 K</li> </ul>
240 → 250 K	<ul style="list-style-type: none"> <li>Same as 240 K</li> </ul>	<ul style="list-style-type: none"> <li>Same as 240 K</li> </ul>
250 → 260 K	<ul style="list-style-type: none"> <li><sup>152</sup>Pr has been produced</li> </ul>	<ul style="list-style-type: none"> <li><sup>152</sup>P<sub>r</sub> has been produced</li> </ul>
260 → 270 K	<ul style="list-style-type: none"> <li>Same as 260 K</li> </ul>	<ul style="list-style-type: none"> <li>Same as 260 K</li> </ul>
270 → 280K	<ul style="list-style-type: none"> <li>Same as 270 K</li> </ul>	<ul style="list-style-type: none"> <li>Same as 270 K</li> </ul>

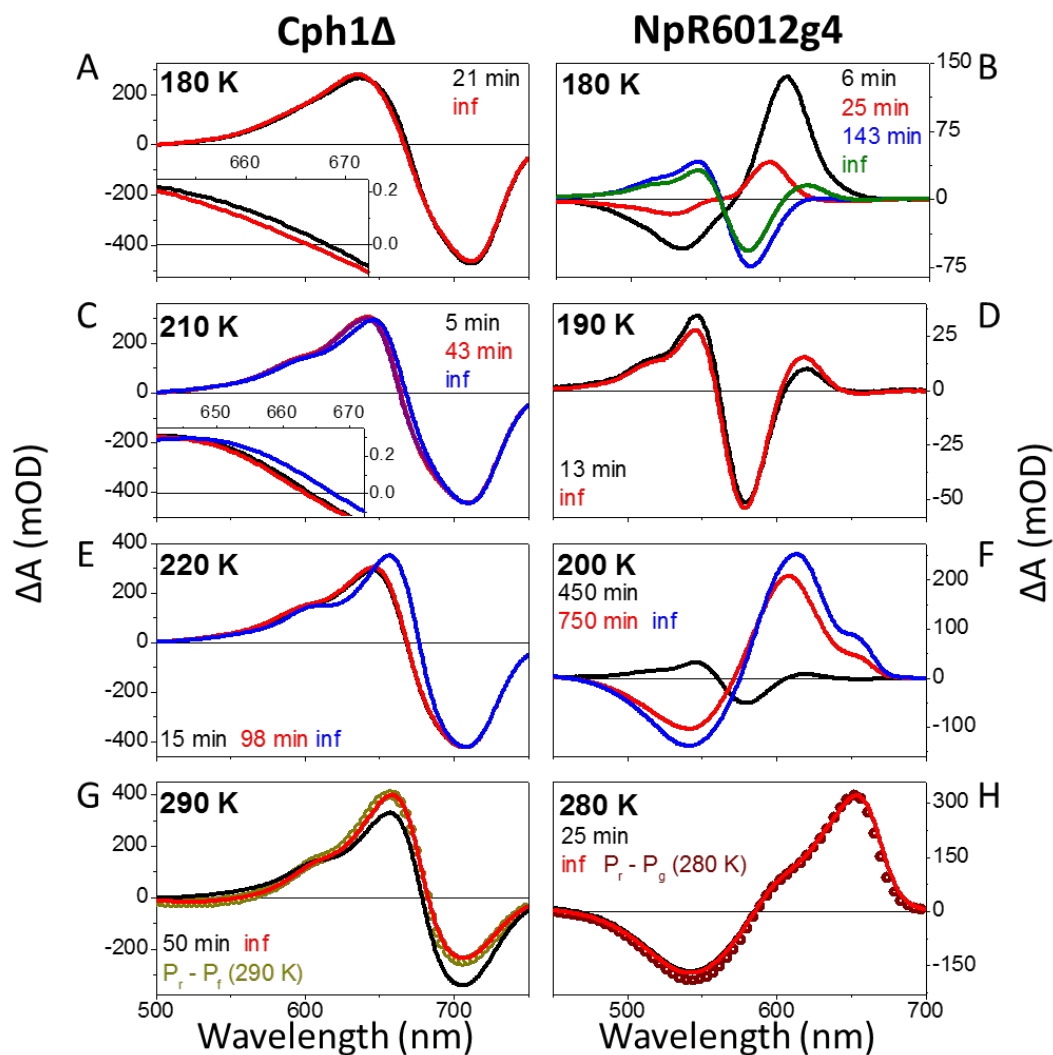


**Figure A8.29:** Comparison of the Reverse Cryokinetics of Cph1Δ and NpR6012g4

Comparison of the reverse cryokinetics EADS of Cph1Δ (left column) and NpR6012g4 (right column). Selected temperatures highlighted the comparison of the dynamics where there was an initial blue shifting of the spectra (1 for Cph1Δ and 2 for NpR6012g4; A, B) followed by a red shifted photointermediate (C, D) and finally a red shifting to the  $^{15Z}P_r$  dark state. At 180 K, NpR6012g4 has two blue shifting photointermediates, namely a Meta- $G_o$  and Meta- $G_g$  (B; red and blue curves). The following red shift was also observed at 180 K (B; green curve), but not for Cph1Δ. The reverse cryokinetics of Cph1Δ and NpR6012g4 further differ since between 220 K and 290 K there are equilibrations of the two parental subpopulations of Cph1Δ that is not present in NpR6012g4.

# Cph1Δ

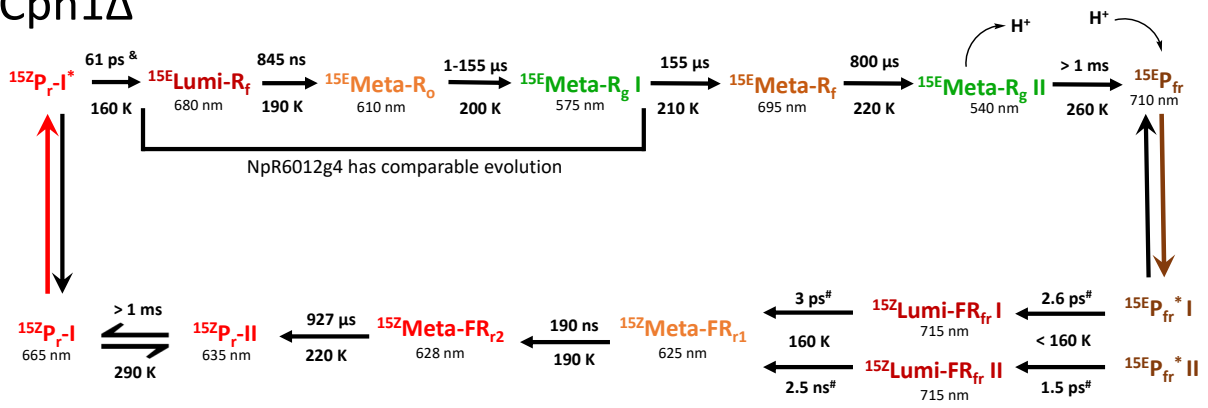


**Figure A8.30: Photocycle of Cph1Δ**

Complete photocycle for Cph1Δ (&<sup>100, 101, 104</sup> #<sup>102, 103</sup>), where the protonation events of the forward reaction are located at the chromophore.

*Chapter 9. Supporting Information for “Extending the Photoswitching Activity to the Far-red for Cyanobacteriochromes”*

**Includes: Supplemental Methods, Supplemental Structural Information, Supplemental Ultrafast Dynamics, Supplemental Sequential Analysis, Supplemental Target Model Construction, and Supplemental QM/MM Vertical Excitation Energies**

*A9.1: Supplemental Methods*

*A9.1.1 Sample Preparation.*

The WT and mutated CBCRs were prepared as previously described.<sup>63, 67</sup>

*A9.1.2 Dual Excitation Interweaved Spectroscopy.*

The experimental methods for DEWI spectroscopy have been previously reported,<sup>183</sup> but a brief summary is given below. The broadband probe and excitation pulses used in the DEWI experiment were generated from a Ti:Sapphire amplified laser (Spectra Physics Spitfire Pro) operating at 1 KHz. The broadband probe was generated by passing the 800 nm fundamental through a slowly translating 2 mm CaF<sub>2</sub> crystal. The excitation pulses used to initiate the forward dynamics were generated at the desired energies (~660 and 730 nm; Table A9.1) using two independent, homebuilt noncollinear optical parametric amplifiers (NOPAs). The three pulses were then spatially and temporally overlapped at the sample (Figure A9.1) and the excitation pulses were interweaved using two choppers synched to the laser and revolving at 500 Hz and 250 Hz so that the individual pump-probe spectra were measured sequentially. DEWI measurements were preferred over

separate pump-probe experiments to give a more direct comparison of the two excitation wavelengths by minimalizing the effects of sample degradation and light fluctuations.

To ensure a fresh sample enriched in the  $^{152}\text{P}_{\text{fr}}$  dark-adapted state for each excitation pulse, the samples were illuminated with a LED resonant with the light-adapted state absorbance and flowed continuously ( $\sim 20$  mL/min) in a closed circuit. The WT and S917P:Q918P Anacy\_2551g3 samples were prepared as previously described<sup>63,67</sup> and were flowed through a 2-mm thick quartz cuvette with an optical density of 0.3-0.4 of the dark-adapted state.

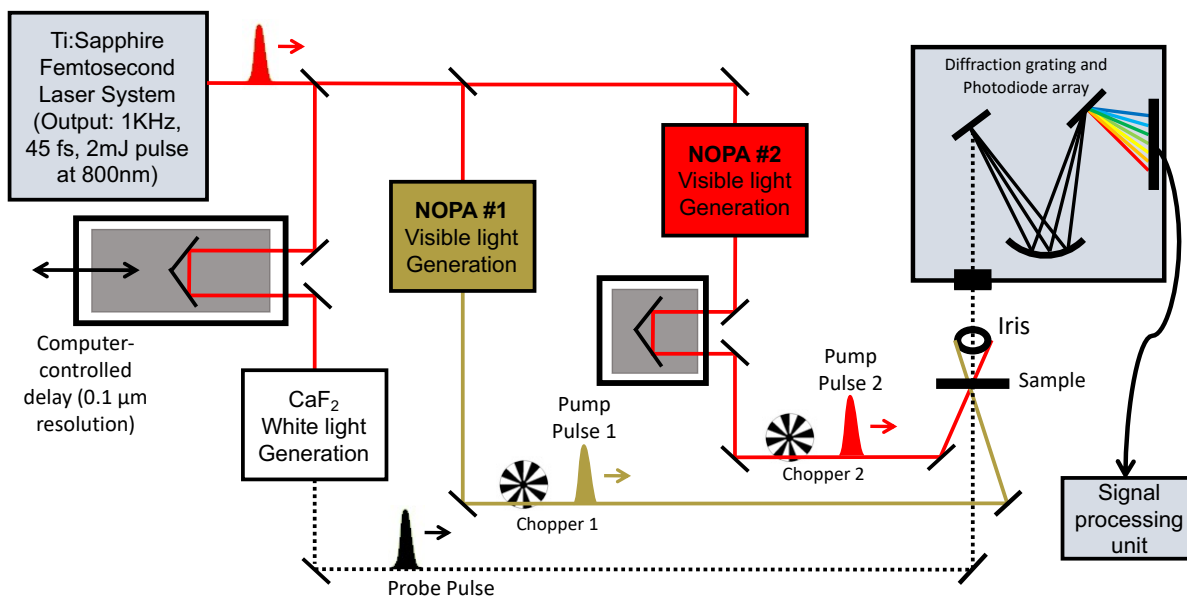


**Figure A9.1:** Dual Excitation Wavelength Interleaved (DEWI) Spectroscopy Schematic.

Dual Excitation Wavelength Interleaved (DEWI) spectroscopy schematic. The difference between DEWI and pump probe (PP) spectroscopies is that in PP spectroscopy there is only a single excitation wavelength instead of two that are interchanged by differing the frequencies of the choppers (500 and 250 Hz) for pump pulse 1 and 2.

**Table A9.1:** DEWI Experimental Parameters for the Forward Dynamics of WT and S917P:Q918P Anacy\_2551g3

Dark and light state peak absorption of WT and S917P:Q918P Anacy\_2551g3 and excitation wavelengths for the forward DEWI experiment.

Sample (Chromophore; Photocycle)	Dark-adapted State Peak Absorption	Light-adapted State Peak Absorption	Forward (Vis and NIR)
WT Anacy_2551g3 (PCB; F/O)	727 nm	590 nm	DEWI: 640 nm; 730 nm
S917P:Q918P Anacy_2551g3 (PCB; F/R)	726 nm	675 nm	DEWI: 660 nm; 730 nm

### *A9.1.3 Global Analysis.*

Ultrafast transient absorption difference spectra typically are a superposition of four signals: (i) negative ground state bleach (GSB) due to the loss of the starting population, (ii) negative stimulated emission (SE;  $S_1 \rightarrow S_0$ ), (iii) positive excited state absorption ( $^{15}ZP_{fr}^*$  absorbance;  $S_1 \rightarrow S_n$ ), and (iv) positive photointermediate absorption. Coupled with transient data, global analysis is a powerful tool that separates the time dependent spectra into a linear combination of time-independent spectra that are weighted by a time-dependent concentration profile.<sup>221, 243</sup> This is achieved by fitting the data with the numerical solutions of a linear combination of first order differential equations describing a postulated model:

$$\frac{dn_i}{dt} = A_i I(t) + \sum_{i,j} K_{i,j} n_j(t) \quad (1)$$

where  $n_i$  represents the  $i^{\text{th}}$  microscopic population of interest,  $A_i$  is the initial occupancy of the  $i^{\text{th}}$  population,  $I(t)$  is the pump pulse temporal envelope, and  $K_{i,j}$  is the connectivity matrix that is composed of the rate constants describing the flow from the  $i^{\text{th}}$  population into the  $j^{\text{th}}$  population.

Initially, the transient data were first fit to unbiased sequential models ( $A \rightarrow B \rightarrow C \rightarrow \dots$ ) with consistently increasing lifetimes (Table A9.4, Figures A9.10 -A9.13). If the postulated model extracted the spectra of the true subpopulations, then species associated difference spectra (SADS) and the associated lifetimes are obtained. If the true subpopulations were not extracted, then evolution associated difference spectra (EADS) and the associated apparent lifetimes are extracted. If EADS were obtained from the postulated model, then more complicated target models with coevolving subpopulations are required to extract the SADS.

#### *A9.1.4 Computational Methodology.*

The starting geometry of the protein was based on the far-red absorbing form ( $^{15Z}P_{fr}$ ) of the Anacy\_2551g3 crystal structure (PDB ID: 6UV8).<sup>67</sup> Missing hydrogen atoms were added to the crystal structure using the tleap program of AMBER 16.<sup>357</sup> The protonation states of all titratable residues were considered at the pH 7.0. The PCB chromophore was modelled in four different protonation states (Figures 9.2B-9.2 E) as suggested in the study by Bandara et al.<sup>67</sup> In all these models, the propionate chains attached to the B and C rings of PCB were modelled in the deprotonated form. The protein was solvated in a rectangular box of TIP3P water molecules using the solvatebox plugin of tleap, with a distance of at least 15 Å between the atoms and the boundaries of the box. The addions2 plugin of tleap was used to neutralize the system by adding Na<sup>+</sup> ions. In all simulations, the cut-off for non-bonded interactions was 12.0 Å and long-range interactions were treated using the Particle Mesh Ewald algorithm. VMD (Visual Molecular Dynamics)<sup>358</sup> was used for visualization. PCB was described using our own derived AMBER compatible parameters published elsewhere.<sup>359</sup>

At the beginning of the simulation, the solvent atoms were minimized in 10,000 steps with restraints of  $100 \text{ kcal mol}^{-1} \text{ \AA}^{-2}$  on all atoms of protein and PCB. This was followed by minimization of all atoms of the solvent and protein atoms in 10,000 steps with restraints of  $100 \text{ kcal mol}^{-1} \text{ \AA}^{-2}$  on all atoms of PCB. These classical minimizations were carried out using the AMBER16 program. The resulting system was then optimized on the ground state using hybrid QM/MM methodology. The QM region chosen for the optimizations was the truncated PCB chromophore without the propionate chain (66 atoms) and the MM region consisted of all atoms of the protein within  $5 \text{ \AA}$  of the chromophore. The QM region was described at B3LYP/def2-SVP level of theory with dispersion correction and Becke-Jonson damping. The MM region was described using the AMBERff14SB force field.<sup>360</sup> Further, excited state optimizations were carried for all the models at the CAM-B3LYP/def2-SVP level of theory. Excitation energies were computed for both ground and excited optimized geometries at the ADC(2)/def2-SVP<sup>361</sup> level of theory using the Turbomole 7.2 program.<sup>362</sup> The optimizations on both the ground and excited states were carried out using the ChemShell<sup>363, 364</sup> program interfaced to ORCA 4.0.<sup>365, 366</sup>



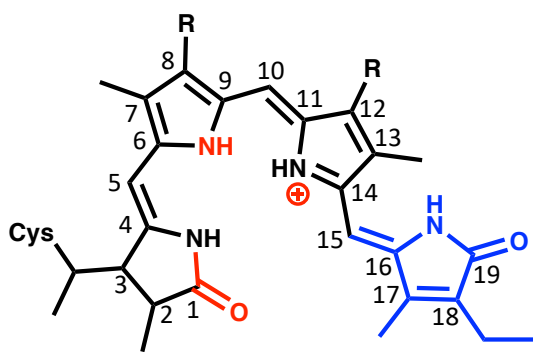
## A9.2: Structural Information

**Table A9.2:** Chromophore Structural Information for the  $^{15Z}P_{fr}$  Dark-Adapted State of Anacy\_2551g3.

Dihedral angles and ring tilts for the the dark  $^{15Z}P_{fr}$  dark-adapted state of Anacy\_2551g3.

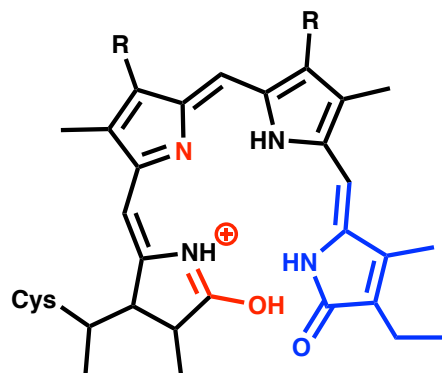
N <sub>A</sub> -C4-C5-C6	C4-C5-C6-N <sub>B</sub>	N <sub>B</sub> -C9-C10-C11	C9-C10-C11-N <sub>C</sub>	N <sub>C</sub> -C14-C15-C16	C14-C15-C16-N <sub>C</sub>
-1.385°	-57.479°	-4.253°	35.358°	-37.917°	44.491°
Ring Tilt	A/B	B/C	C/D		
	55.968°	35.234°	35.082°		

A: Typical red/green CBCR



15Z, 15-anti PCB Chromophore

B: Anacy\_2551g3



15Z, All-syn PCB Chromophore (di-A-protonated lactim)

**Figure A9.2:** PCB Chromophore Comparison of a Red/Green and Far-Red CBCR.

Comparison of the dark-adapted PCB chromophore conformation for red/green CBCRs<sup>108, 291</sup> and a preferred tautomer of a far-red CBCR.<sup>67</sup> The change in the syn/anti conformation is highlighted in blue and the differences in the protonation and charge distributions are highlighted in red.

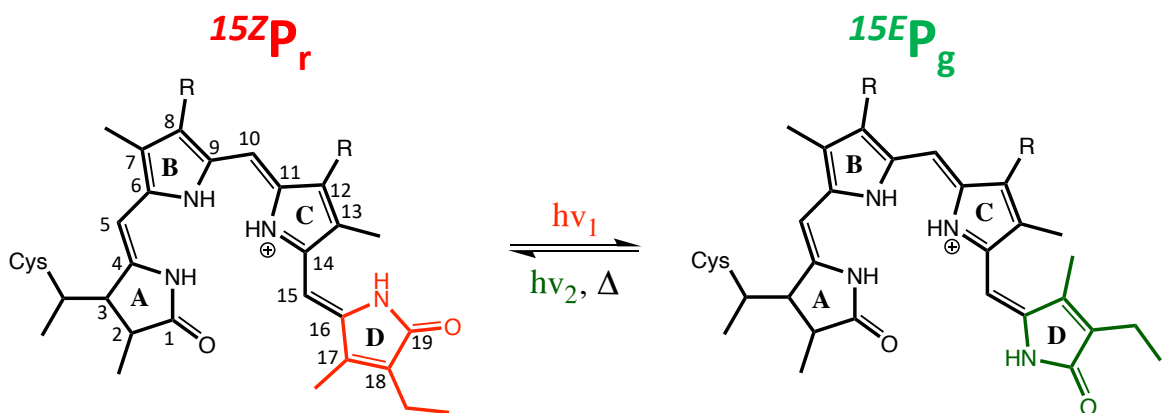


**Figure A9.3:** Classical Chromophore Photocycle

PCB dark adapted ( $^{15Z}P_r$ ) and signaling state ( $^{15E}P_g$ ) chromophore conformation structures for red/green CBCRs.<sup>108</sup>

### A9.3: Ultrafast Dynamics

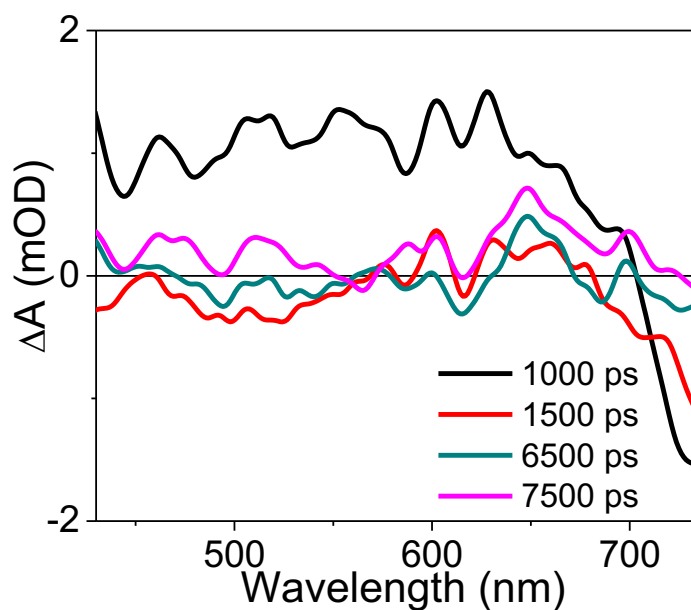


**Figure A9.4:** Anacy\_2551g3 Primary Forward Difference Spectra

WT Anacy\_2551g3 later time transient spectra that shows a growth in the 500-650 nm region after 800 ps and decayed by 1500 ps.

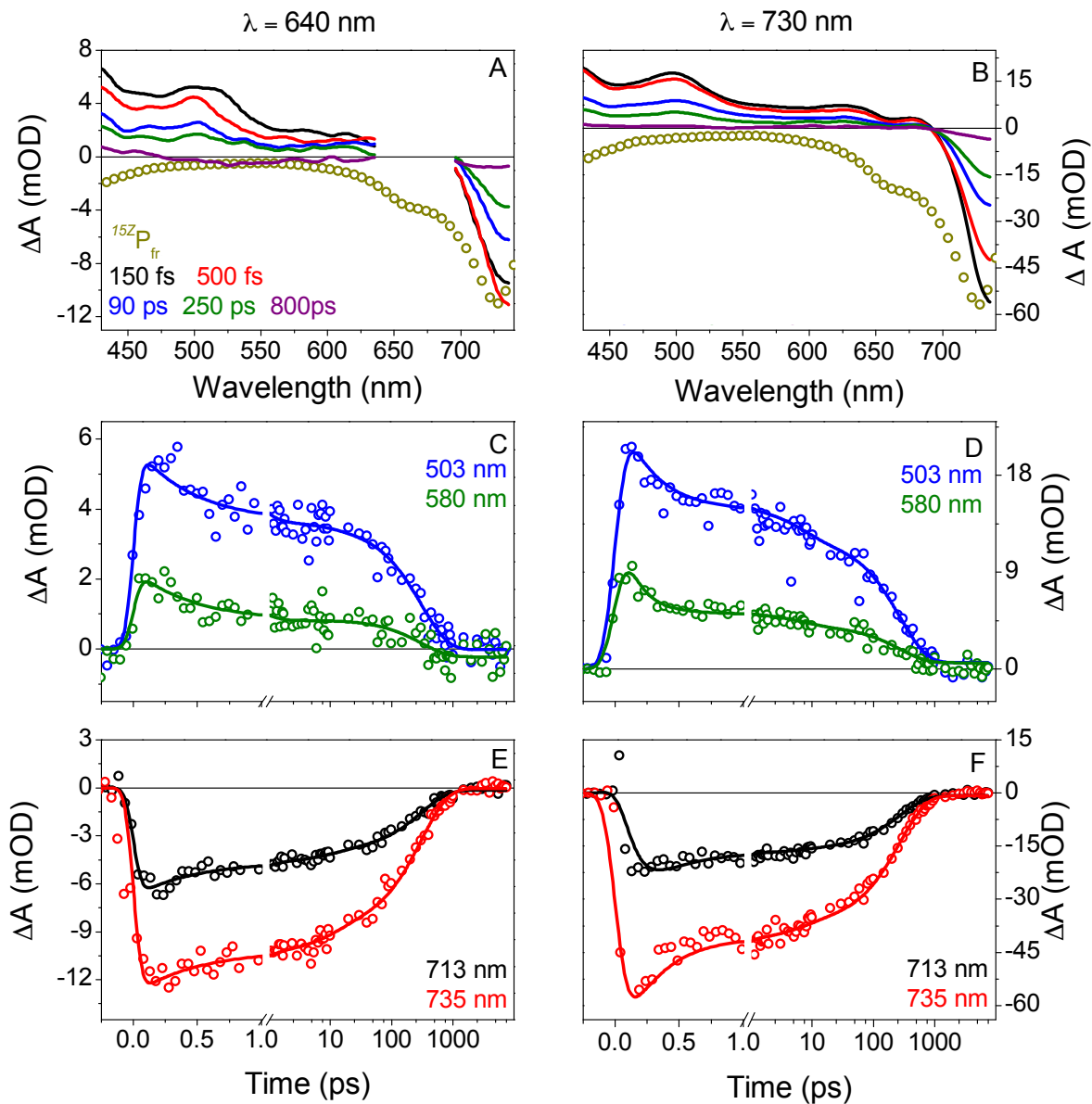


**Figure A9.5:** WT Anacy\_2551g3 Visible Probe DEWI Results

Forward dynamics of WT Anacy\_2551g3 in the visible region after either 660 (left column) or 730 (right column) excitations. Panel B is color coded to the legend in panel A. For the kinetics, open circles are data, and the solid lines are from the fit.

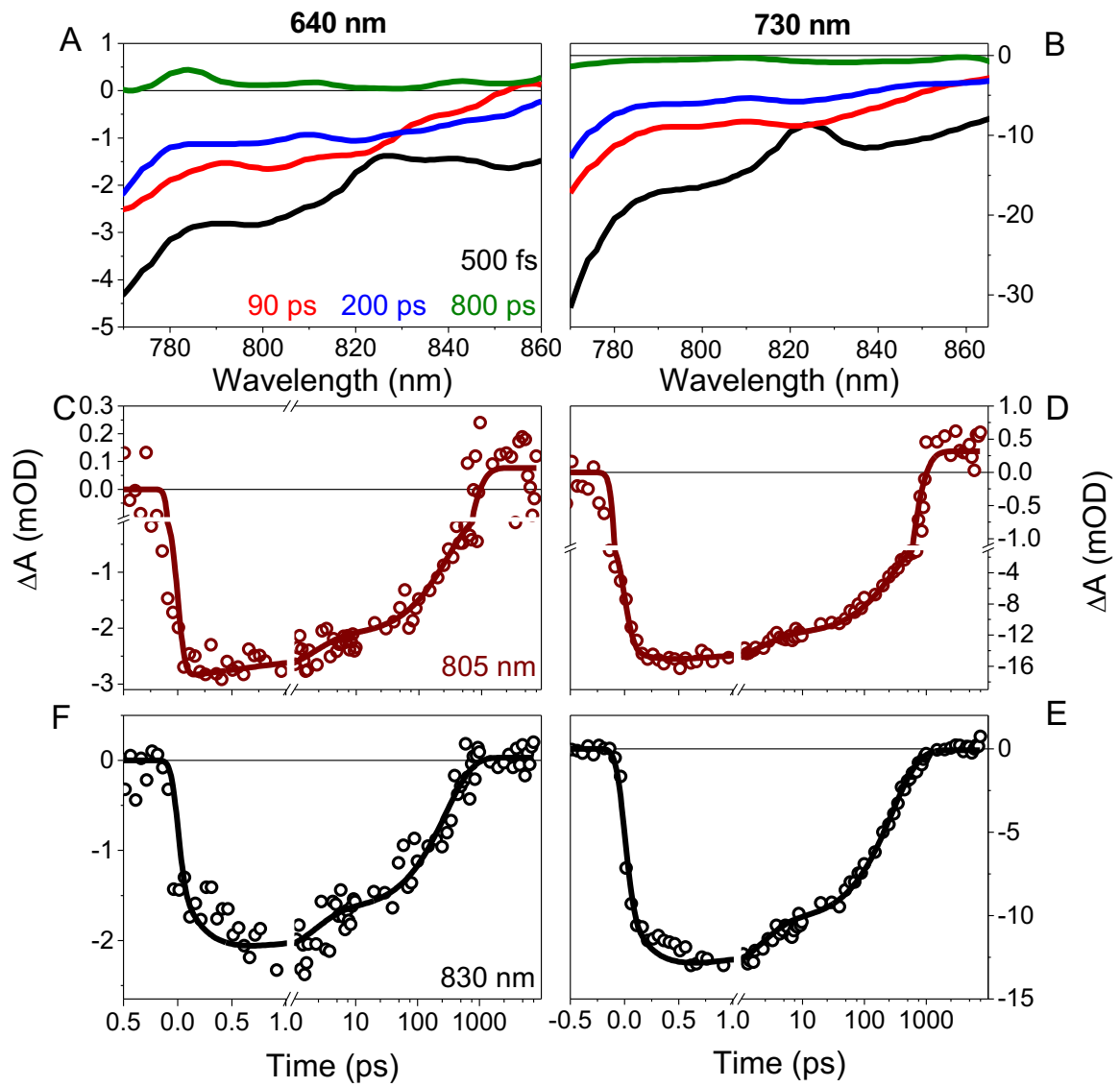


**Figure A9.6:** WT Anacy\_2551g3 NIR Probe DEWI Results

Forward dynamics of WT Anacy\_2551g3 in the NIR region after either 660 (left column) or 730 (right column) excitations. Panel B is color coded to the legend in panel A. For the kinetics, open circles are data, and the solid lines are from fit.

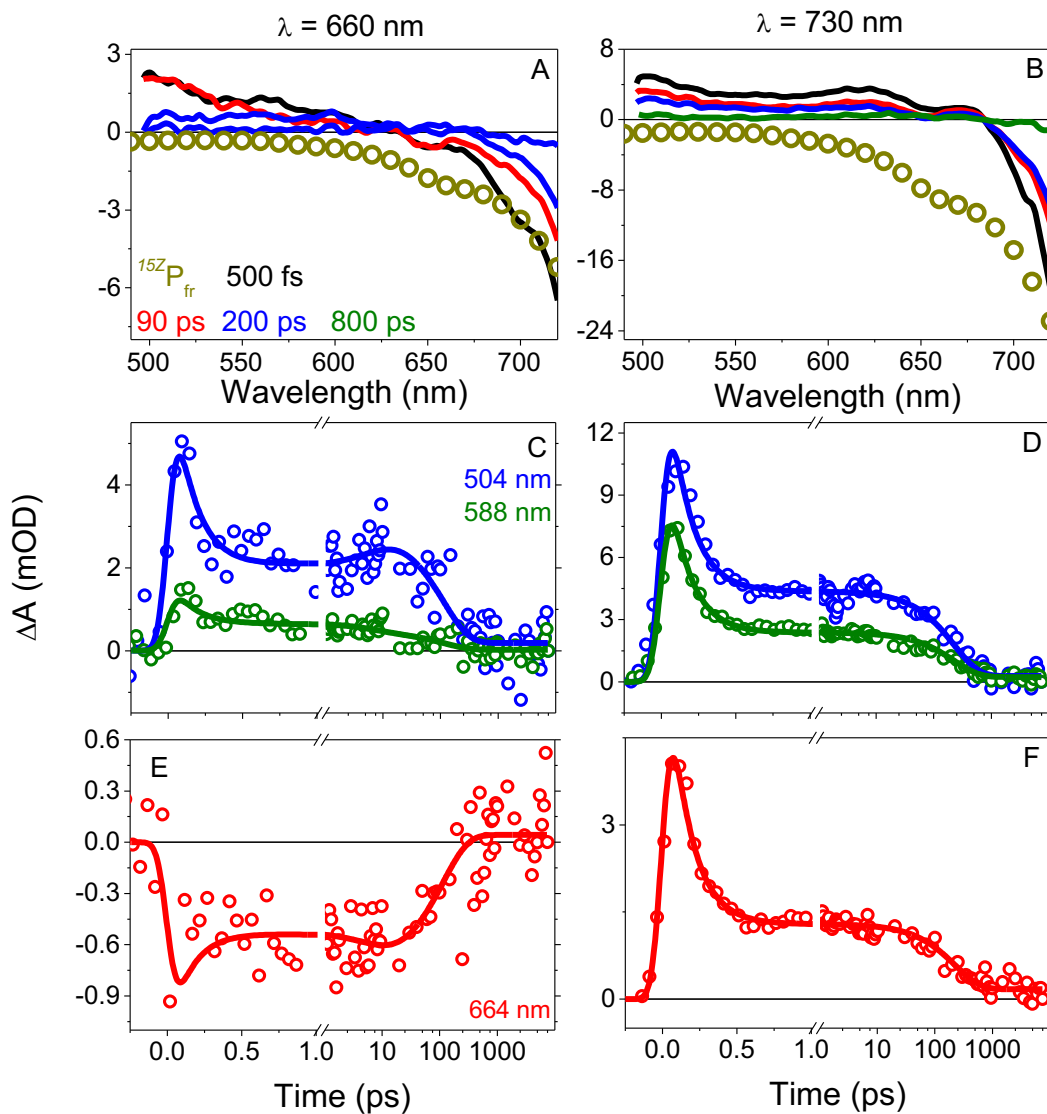


**Figure A9.7:** S917P:Q918P Anacy\_2551g3 Visible Probe DEWI Results

Forward dynamics of S917P:Q918P Anacy\_2551g3 in the visible region after either 660 (right column) or 730 (left column) excitations. Panel B is color coded to the legend in panel A. For the kinetics, open circles are data, and the solid lines are from the fit. The 730 nm excitation fit required a two-compartment sequential model to fit all of the kinetics. The peak that persists for 500 fs can be attributed to either an early time artifact or a  $^{hot}P_{fr}^*$ .

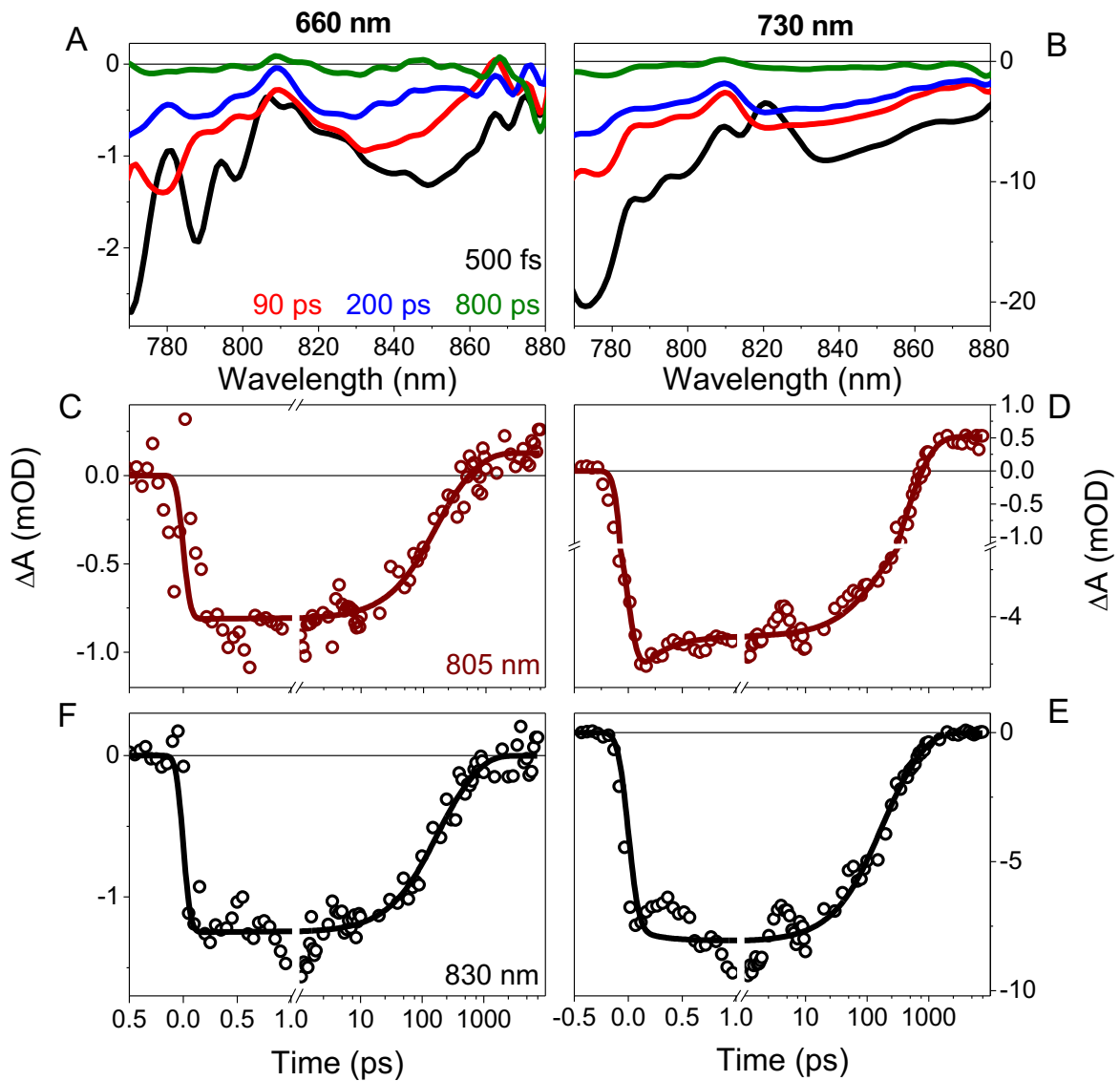


**Figure A9.8:** S917P:Q918P Anacy\_2551g3 NIR Probe DEWI Results

Forward dynamics of S917P:Q918P Anacy\_2551g3 in the NIR region after either 660 (right column) or 730 (left column) excitations. Panel B is color coded to the legend in panel A. For the kinetics, open circles are data, and the solid lines are from the fit.

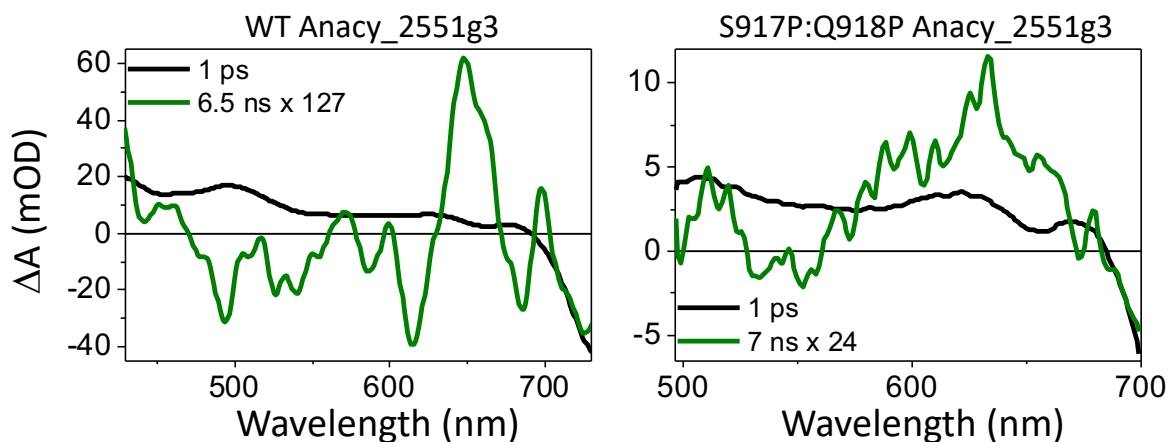


**Figure A9.9:** Forward Quantum Yield Estimation for WT and S917P:Q918P Anacy\_2551g3

Overlap of early and scaled late time transient difference spectra for (left) WT and (right) S917P:Q918P Anacy\_2551g3 after 730 nm excitation to estimate the forward efficiency of these far-red CBCRs.

**Table A9.3:** Lumi-FR QY estimation from scaling of the transient spectra in Figure A9.9.

WT Anacy_2551g3	S917P:Q918P Anacy_2551g3
0.8%	4.2%

#### A9.4: Sequential Global Analysis

WT and S917P:Q918P Anacy\_2551g3 were modelled in the same fashion, so the modeling for WT will only be discussed. Initially, a sequential model ( $A \rightarrow B \rightarrow C \dots$ ; Figure A9.10) was used and extracted three spectrally comparable  $^{15}ZP_{fr}^*$  EADS in the visible and NIR regions with unique apparent lifetimes (Figures A9.11 and A9.12, Table A9.4): 220 fs, 2.2 ps, and 270 ps. The 220 fs NIR EADS resolved the same positive peak on the SE band that was observed in the 500 fs transient difference spectra (Figures 9.3 and A9.11) and was attributed to second order diffraction of residual; 410 nm from the NOPA. Excitation of the Soret band and Raman scattering of a bending

mode of water were also considered, but ultimately rejected given the presence of this signal beyond the temporal overlap of pump and probe pulses (Figure A9.8). The terminal EADS for both the visible and NIR probes extracted long lived positive absorbance near ~650 nm and ~800 nm, respectively. These peaks were consistent with the kinetics (Figure 9.4) and were attributed to long-lived photointermediates.

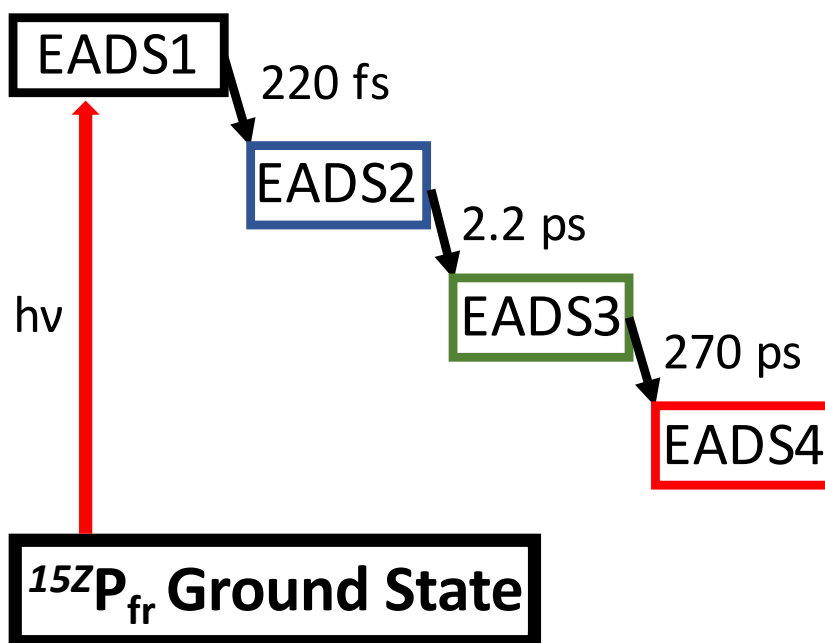


Figure A9.10: Sequential Model

Sequential model used in the initial global analysis fitting of WT and S917P:Q918P Anacy\_2551g3.



**Table A9.4:** Sequential Model Parameters for WT and S917P:Q918P Anacy\_2551g3  
 Sequential model parameters for WT and S917P:Q918P Anacy\_2551g3 where the visible and NIR data sets were modeled with the same time constants.

	WT 640 nm (Vis)	WT 730 nm (Vis)	WT 640 nm (NIR)	WT 730 nm (NIR)
$\tau_{01}$	0.220 ps	0.220 ps	0.220 ps	0.220 ps
$\tau_{12}$	2.2 ps	2.2 ps	2.2 ps	2.2 ps
$\tau_{23}$	270 ps	270 ps	270 ps	270 ps
	S917P:Q918P 660 nm (Vis)	S917P:Q918P 730 nm (Vis)	S917P:Q918P 660 nm (NIR)	S917P:Q918P 730 nm (NIR)
$\tau_{01}$	0.145 ps	0.145 ps	0.145 ps	0.145 ps
$\tau_{12}$	23 ps	23 ps	23 ps	23 ps
$\tau_{12}$	320 ps	320 ps	320 ps	320 ps

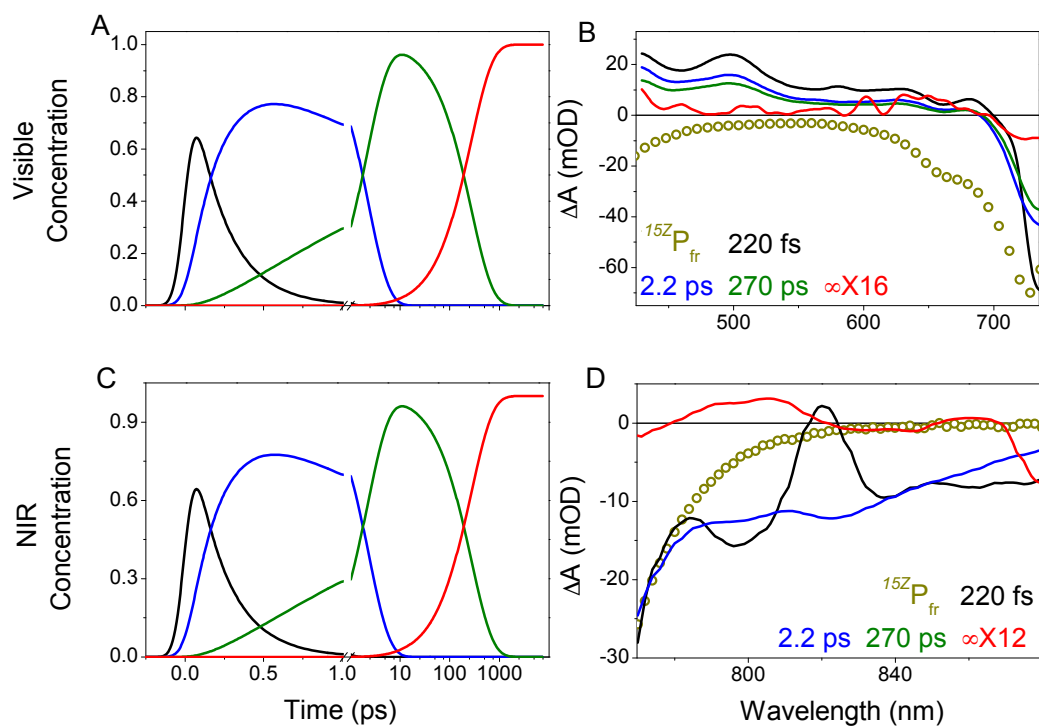


**Figure A9.11:** WT Anacy\_2551g3 EADS and Concentration Profiles

(A, C) Concentration profiles and EADS (B, D) from the sequential analysis of WT Anacy\_2551g3 after 730 nm excitation in the (A, B) visible and (C, D) NIR spectral regions. The positive absorbance at 820 nm (D; black curve) was attributed to second order diffraction of 410 nm from the NOPA. The GSA is represented by golden open circles.

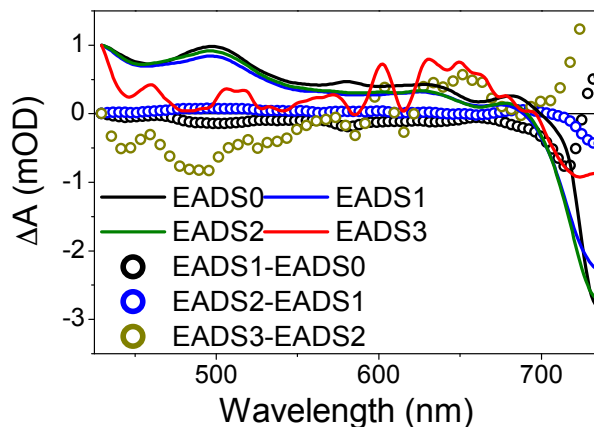


**Figure A9.12:** WT Anacy\_2551g3 Difference of EADS

Difference of the EADS extracted in the sequential model for WT Anacy\_2551g3 after 730 nm excitation. The fluctuations in the at wavelengths  $\geq \sim 715$  nm was attributed to overlapping pump scatter for EADS1-EADS0.

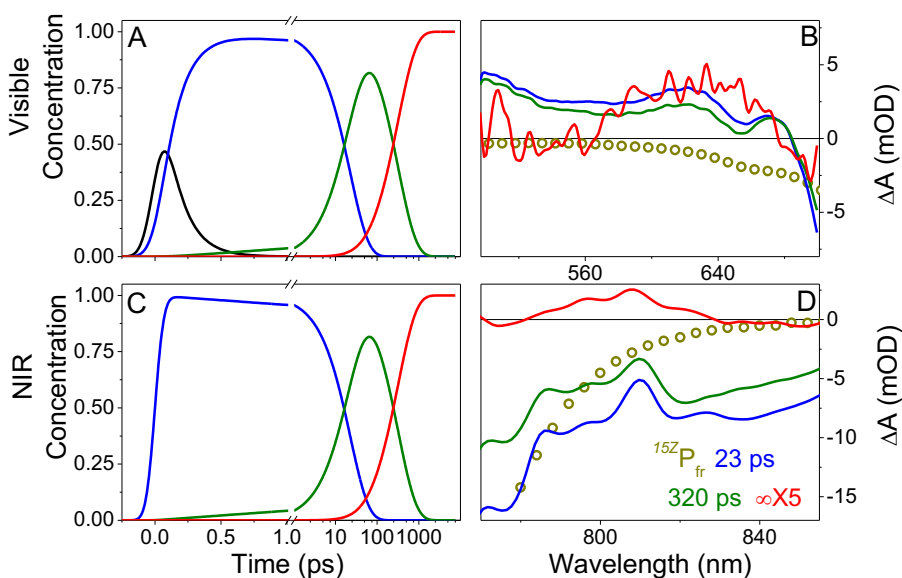


**Figure A9.13:** S917P:Q918P Anacy\_2551g3 EADS and Concentration Profiles

(A, C) Concentration profiles and (B, D) EADS from the sequential analysis of S917P:Q918P Anacy\_2551g3 after 730 nm excitation in the (A, B) visible and (C, D) NIR spectral regions. The positive absorbance at 820 nm (D; black curve) was attributed to second order diffraction of 410 nm from the NOPA. The GSA is represented by golden open circles.

#### A9.5: Target Model Construction

The features observed in the kinetics and transient difference spectra coupled with the EADS were used to generate more sophisticated target models (Figures 9.5A and A9.14) to extract SADS and lifetimes of the  $^{15Z}P_{fr}^*$  and photointermediate populations. Given that a bleach was not available in the NIR region at all time points, the visible data set was modeled first. Since there were three unique lifetimes for spectrally homogeneous  $^{15Z}P_{fr}^*$  populations (Figures A9.11 and A9.13), a target model consisting of three  $^{15Z}P_{fr}^*$  populations where only the longest lived  $^{15Z}P_{fr}^*$  population evolving into the red-absorbing photointermediate was used. The 220 fs compartment was attributed to an early time artifact and is not shown. For the longest lived  $^{15Z}P_{fr}^*$  population, the lifetimes for the  $^{15Z}P_{fr}^*$  decay and the red absorbing (~600-690) photointermediate population (Figure 9.5B) were optimized to overlap the bleach of  $^{15Z}P_{fr}^*$  and the photointermediate between ~690-730 nm while still fitting the data (Figure 9.4). Given the lack of a clean bleach in the  $^{15Z}P_{fr}^*$  and photointermediate spectra in the NIR spectral region as well as the similarities between the visible and NIR data sets (Figures 9.3, 9.4, A9.11, and A9.13), the same target model and  $^{15Z}P_{fr}^*$  lifetimes from the target analysis in the visible region were used to fit the NIR dynamics.

**Table A9.5:** Target Model Parameters for WT and S917P:Q918P Anacy\_2551g3

Rate constants from the target fitting of the forward isomerization reactions for WT and S917P:Q918P Anacy\_2551g3 obtained using the target model in Figure 9.5 and Figure A9.14. Note that these parameters were also used for both excitation wavelengths.

Population	Initial Occupancy (%)	$\tau_{\text{effective}}$	$\tau$	partitioning	Lumi-F QY (%)
WT $^{15Z}P_{\text{fr}}\text{-I}$	25	2.2 ps	2.2 ps (GS-I)	1.0 GS-I	0%
WT $^{15Z}P_{\text{fr}}\text{-II}$ (Vis)	75	270 ps	290 ps (GS-II) 15 ns (Meta-F <sub>r</sub> )	0.98 GS-II 0.02 Meta-F <sub>r</sub>	~1.4%
WT $^{15Z}P_{\text{fr}}\text{-II}$ (NIR)	75	270 ps	290 ps (GS-II) 15 ns (Lumi-F <sub>n</sub> )	0.98 GS-II 0.02 Lumi-F <sub>n</sub>	~1.4%
Lumi-F <sub>n</sub>	0	$\infty$	$\infty$	N/A	N/A
Meta-F <sub>r</sub>	0	$\infty$	$\infty$	N/A	N/A
S917P:Q918P $^{15Z}P_{\text{fr}}\text{-I}$	50	23 ps	115 ps (GS)	1.0 GS-I	0%
S917P:Q918P $^{15Z}P_{\text{fr}}\text{-II}$ (Vis)	50	320 ps	480 ps (GS) 7.3 ns (Meta-F <sub>r</sub> )	0.94 GS-II 0.06 Meta-F <sub>r</sub>	~3.1%
S917P:Q918P $^{15Z}P_{\text{fr}}\text{-II}$ (NIR)	50	320 ps	480 ps (GS) 7.3 ns (Lumi-F <sub>n</sub> )	0.94 GS-II 0.06 Lumi-F <sub>n</sub>	~3.1%
Lumi-F <sub>n</sub>	0	$\infty$	$\infty$	N/A	N/A
Meta-F <sub>r</sub>	0	$\infty$	$\infty$	N/A	N/A
Avg. $^{15Z}P_{\text{fr}}^*$ Lifetime (ps)			Area Under Concentration Curve (ps * [ $^{15Z}P_{\text{fr}}^*$ ])		
WT		213.92	WT		214
S917P:Q918P		282.69	S917P:Q918P		282
(S917P:Q918P-WT)/WT*100		32.15%	(S917P:Q918P-WT)/WT*100		31.77%

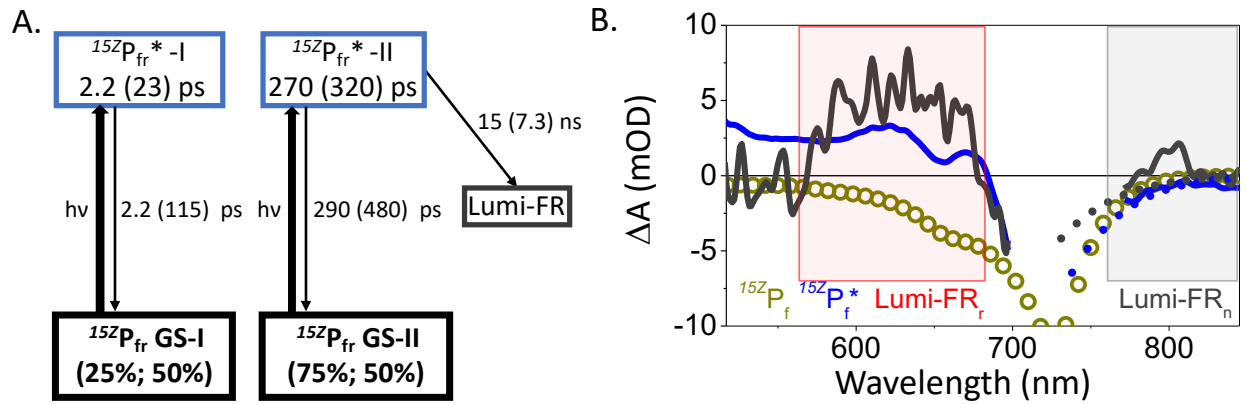


**Figure A9.14:** S917P:Q918P Anacy\_2551g3 SADS

Target analysis of S917P:Q918P Anacy\_2551g3 after 730 nm excitation. The time constants in parenthesis are for S917P:Q918P Anacy\_2551g3.

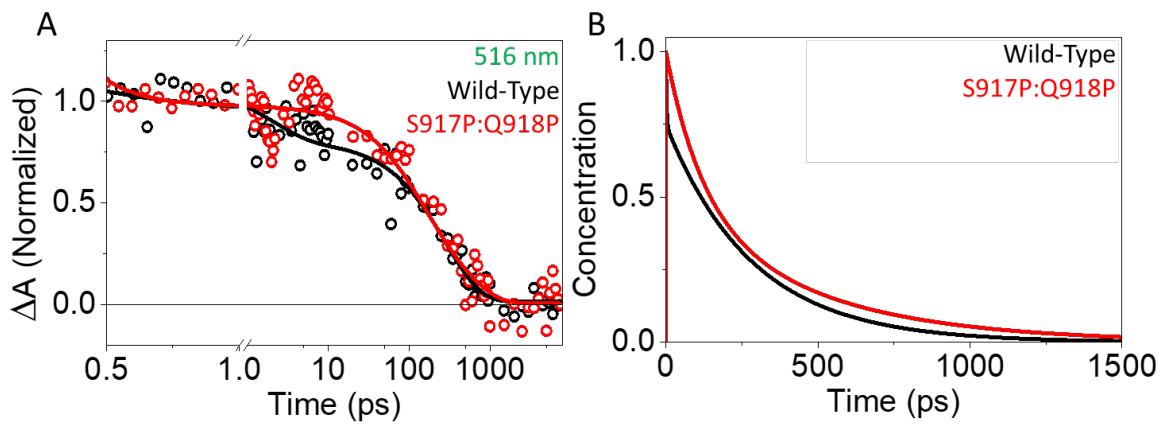


**Figure A9.15:** WT and S917PQ918P  $^{152}\text{P}_{\text{fr}}^*$  Lifetime Comparison

Comparison of the (A) normalized  $^{152}\text{P}_{\text{fr}}^*$  kinetics at 508 nm and (B) sum of the  $^{152}\text{P}_{\text{fr}}^*$  concentration profiles displaying an ~32% extension of the  $^{152}\text{P}_{\text{fr}}^*$  lifetime in S917P:Q918P Anacy\_2551g3 compared to the WT after 730 nm excitation. The first ~500 fs of S917P:Q918P was attributed to an early time artifact, so the WT and S917P:Q918P mutant kinetics at 508 nm were normalized near ~750 fs.

A9.6: QM/MM Vertical Excitation Energies

**Table A9.6:** QM/MM Ground State and Excited State Vertical Excitation Energies of Four Probable Chromophore Tautomers

(a) QM/MM vertical excitation energies ( $\lambda_{\text{exc}}$ ) based on ground state (GS) and excited state geometries of the chromophore conformations in Figure 9.1B-E. (b) Difference of the QM/MM vertical excitation energies ( $\Delta\lambda_{\text{exc}}$ ) in (a).

(a)

Long Name	Short Name	GS nm (eV)	ES (SE) nm (eV)
<b>Experimental</b>	Exp	727 (1.71)	NA
<b>Bislactam</b>	B	660 (1.88)	713 (1.74)
<b>A-Lactim</b>	A	675 (1.84)	729 (1.70)
<b>Diprotonated A-Lactim</b>	DA	566 (2.19)	623 (1.99)
<b>Diprotonated D-Lactim</b>	DB	571 (2.17)	634 (1.95)

(b).

\DeltaShort Name	\DeltaGS  nm (eV)	\DeltaES (SE)  nm (eV)
<b> B-A </b>	15 (0.04)	16 (0.04)
<b> B-DA </b>	94 (0.31)	90 (0.25)
<b> B-DB </b>	89 (0.29)	79 (0.21)
<b> A-DA </b>	109 (0.35)	106 (0.29)
<b> A-DB </b>	104 (0.33)	95 (0.25)
<b> DA-DB </b>	5 (0.02)	11 (0.04)

## ***Chapter 10. Supporting Information for “Computational and Spectroscopic Characterization of the Photocycle of an Artificial Rhodopsin”***

### *10.1: Computational Methods*

The construction of QM/MM models of M2<sub>15C</sub>-PSB and M2<sub>AT</sub>-USB were done following the ASEC-FEG protocol previously described<sup>338</sup> and summarized in section *A9.1*. The X-ray crystallographic structure of M2<sub>15C</sub>-PSB (PDB ID: 4YFP) was obtained from the protein databank, protonation of the amino acid residues were determined using PROPKA<sup>2</sup> consistent with our previous work,<sup>1,3</sup> and used as input to ASEC-FEG protocol. In QM/MM geometry optimization and energy computation, an active space comprising all  $\pi$ -electrons and  $\pi$ -orbitals (i.e. 12 electrons in 12  $\pi$ -orbitals) of the retinal chromophore was used. The QM/MM model of M2<sub>AT</sub>-USB was constructed in the same way using the corresponding crystallographic structure (PDB ID: 4YFQ).

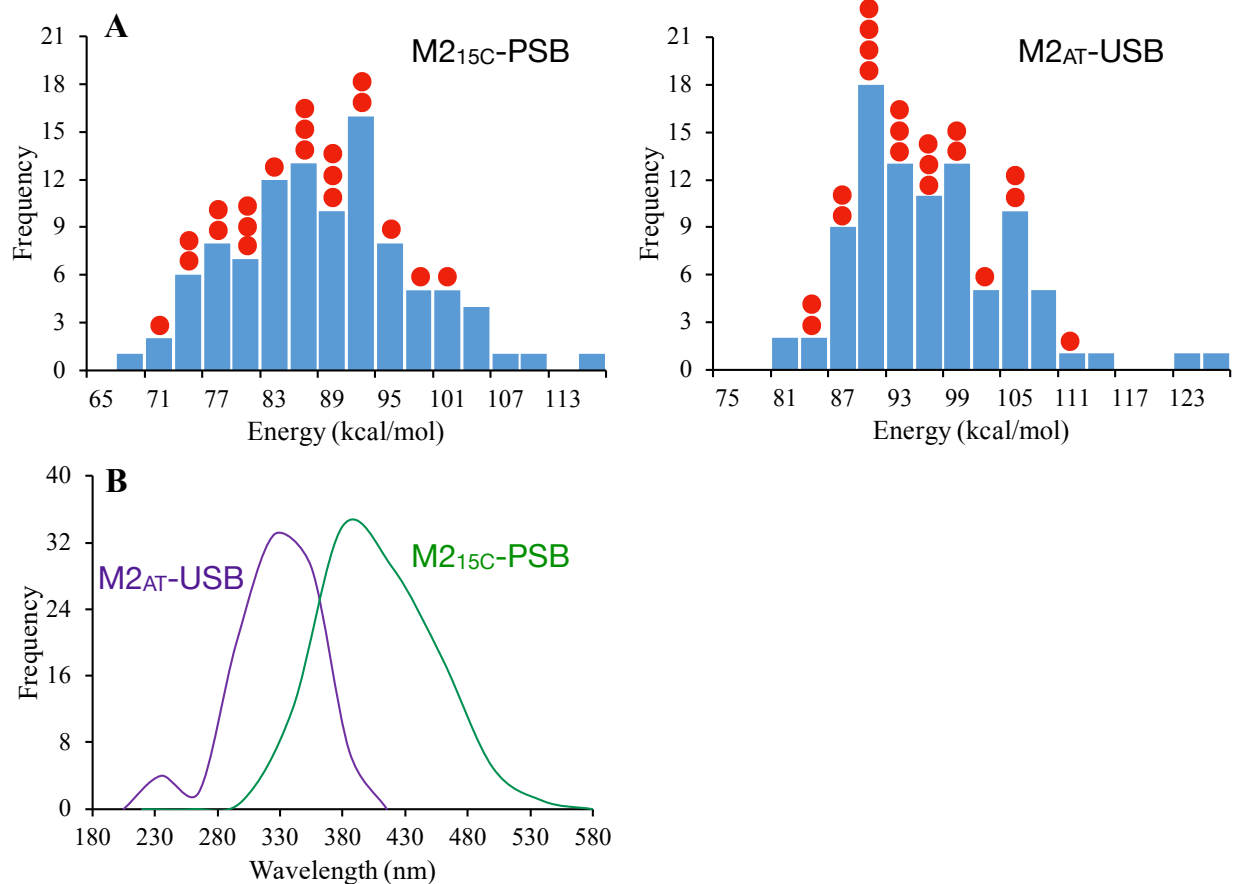
The initial conditions required to simulate M2<sub>15C</sub>-PSB and M2<sub>AT</sub>-USB photodynamics at room temperature were generated following the protocol described in section *A9.2*. A sample of 20 was selected from the generated initial conditions. This was done by constructing the absorption band (see

Figure **A10.1A**) and selecting 20 initial conditions that represents the full band. The M2<sub>15C</sub>-PSB trajectories were launched on S<sub>1</sub> or S<sub>2</sub> based on the computed oscillator strength and propagated at 3-root-state-average CASSCF/6-31G\*/AMBER level (meaning that we use CASSCF method<sup>4</sup> with 6-31G\* basis set for QM region and AMBER<sup>5</sup> molecular parameters for MM region) up to 0.8 ps. This was achieved using MOLCAS/TINKER computer packages.<sup>6,7</sup> Note that the same QM/MM setup used in the generation of initial conditions was used here (see Figure A10.3). When



a molecule reaches a CI, it is allowed to hop between the two PESs using Tully surface hop algorithm<sup>8,9</sup> implemented in MOLCAS 8.1.<sup>6</sup>

The launching of the M2<sub>AT</sub>-USB trajectories was done following the same procedure, however, at the 5-root-state-average CASSCF level. This is due to the fact that spectroscopic state of the M2<sub>AT</sub>-USB initial conditions was either S<sub>3</sub> or S<sub>4</sub>. The possible reaction paths for M2<sub>AT</sub>-USB photoisomerization around C11=C12, C13=C14 and C15=N bonds were also mapped using relaxed scans. For this purpose, a structure closest to the average was extracted from the 100 molecular structures that constructs M2<sub>AT</sub>-USB ASEC model. Such a single structure was optimized on its ground state and used as the starting point for subsequent relaxed scans. The reaction path mapping was performed at 6-root-state-average CASPT2//CASSCF /AMBER level with an active space comprising of 14 electrons in 13 orbitals to consider the possible involvement of the n- $\pi^*$  state.



**Figure A10.1:** Initial Conditions for M2<sub>15C</sub>-PSB and M2<sub>AT</sub>-USB

A. Distribution of the absorption energies of M2<sub>15C</sub>-PSB (left) and M2<sub>AT</sub>-USB (right) initial conditions. The selected initial conditions to simulate the photodynamics are represented by red spheres. B. Computed absorption bands using 100 initial conditions. Note that they qualitatively reproduce the peak positions and shapes of the experimentally observed absorption bands.

#### *A10.1.1: ASEC-FEG protocol.*

The ASEC-FEG protocol<sup>1</sup> requires an initial X-ray crystallographic structure or a homology model. First, the input protein structure is inspected for any missing amino acid residues or

abnormalities. If the structure does not contain any hydrogen atoms, as in X-ray crystallographic structures, the ionization states of charged amino acid residues are determined at physiological pH, hydrogens are added to all the residues of protein and an energy minimization is carried out following the methodology described in ref. <sup>3</sup>. Second, the ASEC cycle is started by embedding the protein structure in a 70 Å size cubic water box (see Figure A10.2A). The Na<sup>+</sup> or Cl<sup>-</sup> ions are added to the box, such that total charge of the system is neutralized. Then, a long classical (i.e. based on a molecular mechanics force field) molecular dynamics simulation (from now on MMMD) is carried out for about 5 ns until the system reaches the thermodynamic equilibrium, followed by 5 more ns to collect the data in such equilibrium conditions. This is performed using the GROMACS computer package.<sup>10</sup> During the simulation, the retinal chromophore and C<sub>ε</sub> atom of the covalently bound lysine (Ret-Lys subsystem hereafter) are geometrically kept fixed; but the rest of the system (protein and solvent molecules) is allowed to move. From the above MMMD simulation, 100 snapshots are extracted. A 30 Å shell, based on the distance from any Ret-Lys atom, is selected from each snapshot and are overlapped to construct the, so called, ASEC configuration (Figure A10.2B), a superposition of 100 configurations which mimics the thermal equilibrium. This means that the environment of the retinal chromophore is now a cloud of pseudo-atoms. In order to avoid over-estimation of the non-bonding interactions in the ASEC configuration, the charges and van der Waals parameters of each pseudo-atoms are scaled. Note that the interaction between retinal chromophore and the ASEC configuration is exactly the same as the time-average interaction between the chromophore and the environment along the MD.

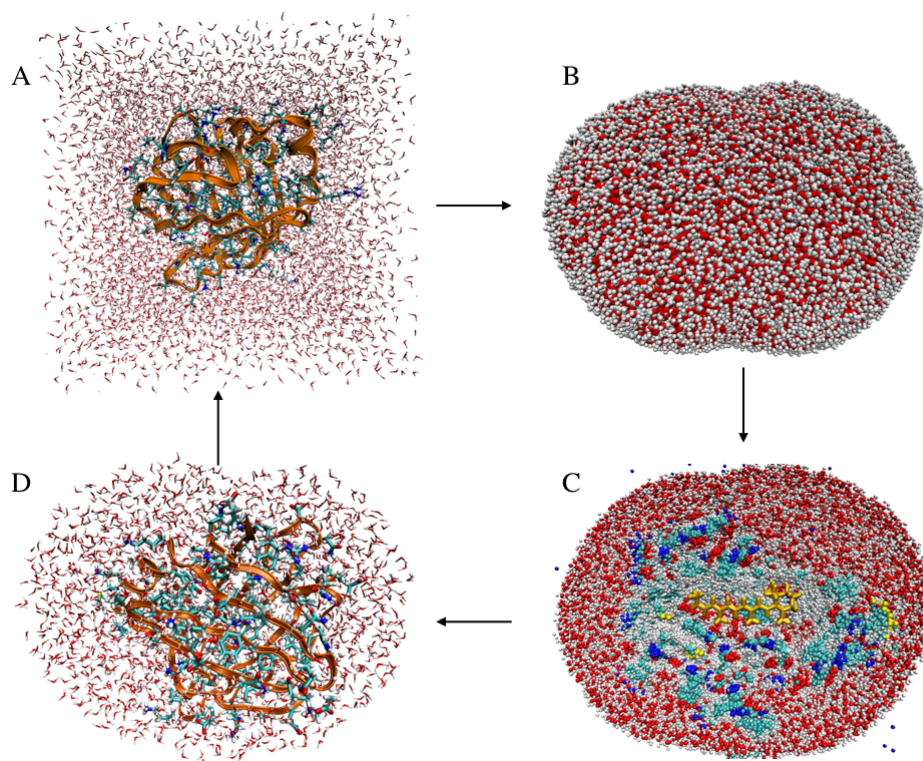


**Figure A10.2:** ASEC Protocol

The ASEC protocol. A. The protein is embedded in a 70 Å size cubic water box and a long MMMD simulation is carried out. B. A selected shell from each of the selected 100 configurations are overlapped to construct the ASEC configuration. C. The Ret-Lys subsystem (gold) is optimized inside ASEC environment at QM/MM level. Spheres of different colors represent overlapped protein atoms or pseudo-atoms that belong to ASEC environment. D. The structure closest to the average protein structure is selected from ASEC. This will be used as input to next ASEC iteration.

At this point, a QM/MM setup is defined; the Ret-Lys subsystem and ASEC configuration are treated at QM and MM levels respectively (Figure A10.2C) and a QM/MM geometry optimization and absorption energy computation is carried out. This is achieved by following a previously established CASPT2//CASSCF/6-31G\*/AMBER protocol<sup>11</sup> and the MOLCAS/TINKER

computer package.<sup>7,12</sup> A structure closest to the average is selected out of the 100 configurations (Figure A10.2D) and used to initiate another ASEC cycle (i.e. MD, ASEC configuration and QMMM calculations). In this way, the ASEC cycle is continued iteratively until the difference between absorption energy values from two consecutive iterations become less than 0.5 kcal/mol.

#### *A10.1.2: Generation of the initial conditions.*

Since the ASEC configurations represent an ensemble in thermodynamic equilibrium, they can be used to construct the absorption band. In this work, 100 protein structures that are used to construct the ASEC model were selected to generate initial conditions. For each configuration, a cavity containing amino acid residues or water molecules located within 4 Å distance of any chromophore atom was defined. Then a 300 ps long MMMD simulation was performed on chromophore and cavity residues. The rest of the environment was kept frozen during this simulation. The molecular geometries and velocities corresponding to the last step of each MMMD simulation were extracted and a QM/MM setup was defined (see Figure A10.2). Starting from these geometries and velocities, 200 fs long QM/MM ground state dynamics were performed at single-root CASSCF/6-31G\*/AMBER level. The geometries and velocities of the final step of these QM/MM ground state dynamics simulations are the initial conditions required to launch excited state dynamics. The quality of such initial conditions were checked by computing absorption wavelength for each geometry at CASPT2 level<sup>13</sup> and constructing the absorption band.

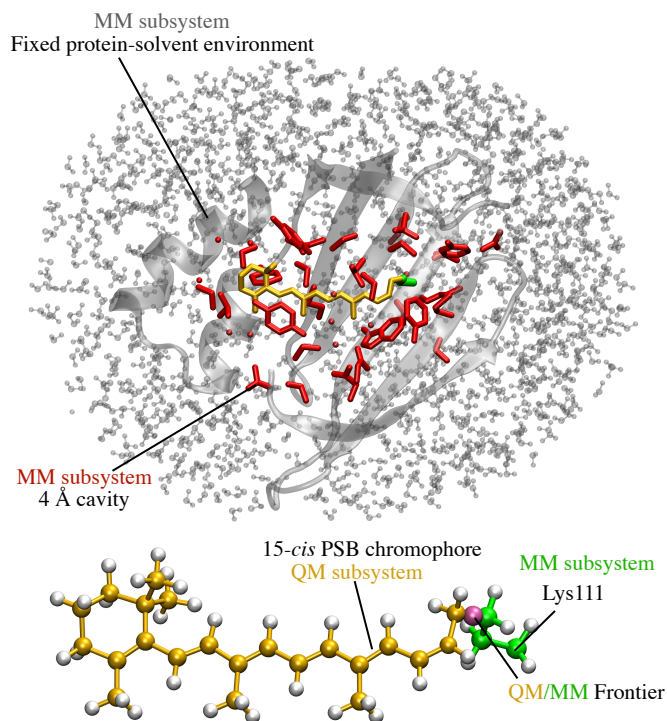


**Figure A10.3:** QM/MM setup

The QM/MM setup used trajectory computations taking M215C-PSB as an example. The 15-cis rPSB chromophore (gold), treated at QM level, is bound to a specific lysine residue (green) treated at MM level via a link atom introduced at the QM/MM frontier. The residues within 4 Å distance of any QM atom (red) are allowed to move at MM level, while the remaining protein-solvent environment (grey) is kept frozen at MM level during simulations. Note that for a clear representation, hydrogen atoms of chromophore and cavity residues in the upper illustration are not shown.

#### *A10.1.3: Comparison of M215C-PSB model against crystallographic structure.*

Upon the comparison of ASEC generated M215C-PSB model against crystallographic structure, we noted that the backbone loop 55-60 of the former is significantly different from the latter (see overlapped red and green molecular structures in top). Further investigations revealed that such a backbone movement in the computed model occurs during the molecular dynamics simulations.

More specifically, the TYR59 residue which is originally pointing away from the rPSB flips over and aligns with the rPSB forming a pi stacking. In order to facilitate this residue movement, the backbone loop change in residue 55-60 occurs. To find out the impact of this residue flip on C13=C14 isomerization path, we selected a representative from M2<sub>15C</sub>-PSB initial conditions, optimized it on the ground state, and mapped reaction path using a relaxed scan (Figure A10.4). We then flipped the TYR59 residue of this model away from the rPSB, reoptimized the system on its ground state, and recomputed the reaction path (Figure A10.4). The results suggest that this residue flip/loop change has no significant impact on the C13=C14 isomerization path.

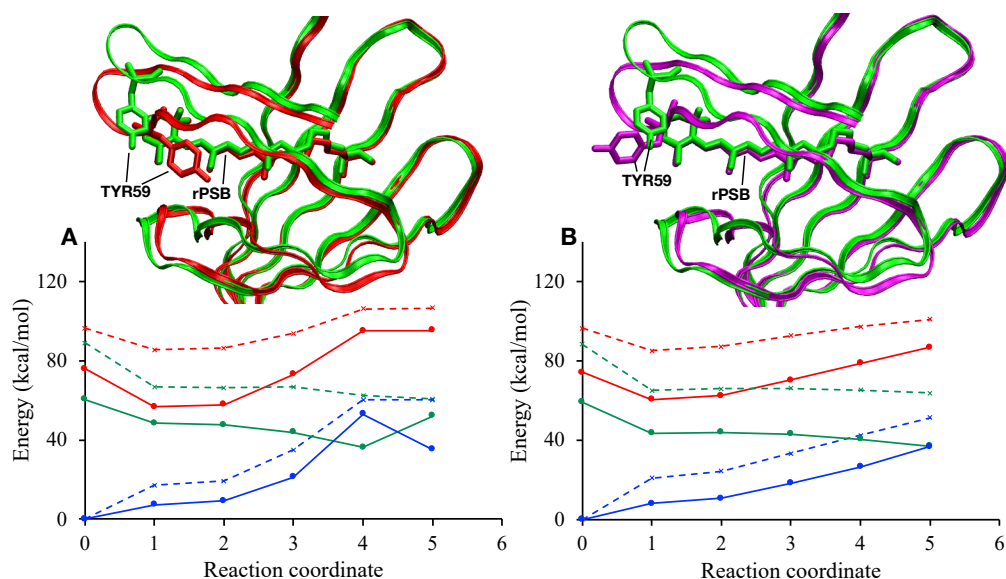


**Figure A10.4:** Evolution of CASSCF (dashed) and CASPT2 energies (solid) along the isomerization of M2<sub>15C</sub>-PSB around C13=C14 double bond

Evolution of CASSCF (dashed) and CASPT2 energies (solid) along the isomerization of M2<sub>15C</sub>-PSB around C13=C14 double bond (A) and the same computed for a model containing reoriented TYR59 (B). Points 0-5 of the reaction coordinate correspond to ground state optimized, S1 optimized and S1 constrained optimized structures at 150, 130, 120 and 110 degree respectively. The molecular structures shown on top compare the loops formed by residues 55-60 of crystallographic structure (PDB ID: 4YFR, green) against computed M215C-PSB (red) and the model with reoriented TYR59 (magenta).

## *A10.2: Experimental Methods*

### *A10.2.1: Sample Preparation.*

The samples were prepared as previously described (Chapter 2),<sup>14</sup> and were concentrated to 0.5 OD for the given pathlengths. The cryokinetic sample buffer deviated slightly from the previously published work where M2 was solvated in 66% glycerol and 33% buffer.

### *A10.2.2: Ultrafast Transient Broadband Absorption Spectroscopy.*

The details of the apparatus used to measure the primary (100 fs to ~8 ns) photodynamics of both the M2<sub>15C</sub>-PSB and M2<sub>AT</sub>-USB reactions have been published previously.<sup>15</sup> The features relevant to the data reported here are briefly discussed below. An 800-nm Ti:Sapphire amplified laser (SpectraPhysics Spitfire Pro) pumped a homebuilt non-collinear optical parametric amplifiers (NOPA) to generate the excitation pulses used for initiating the PSB (565 nm at 330 nJ). The excitation pulse for the SB photodynamics bypassed the NOPA and the second harmonic of the fundamental 800 nm output (400 nm at 400 nJ). These wavelengths were selected to be near the peaks of the static absorption spectra of M2<sub>15C</sub>-PSB and M2<sub>AT</sub>-USB (Figure 10.1). The instrument response functions for both directions were estimated at ~150 fs from the signal rise times of the excited-state absorption (ESA) bands.

The sample was flowed continuously (~20 mL/min) in a closed circuit to ensure a fresh sample for each excitation pulse. The sample was flowed through a 2-mm thick quartz cuvette. For the M2<sub>15C</sub>-PSB and M2<sub>AT</sub>-USB reactions measurements, the sample was continuously illuminated with either a UV or green CW laser diode to populate the desired state.



### *A10.2.3: Cryokinetic UV-Vis Spectroscopy.*

The low-temperature cryokinetic measurements were performed using an Oxford Instruments Optistat DN liquid nitrogen cryostat placed in the beam path of a Shimadzu UV-vis spectrometer. The cryokinetic measurements were performed from 170 to 260 K, by steps of 10 K for the M2<sub>AT</sub>-USB reaction. Given the thermal dark conversion of the M2<sub>15C</sub>-PSB state, the reverse reaction was limited to studying from 170 to 240 K. Prior to data collection, the sample was illuminated with 366 or 532 nm light, for the M2<sub>15C</sub>-PSB and M2<sub>AT</sub>-USB dynamics, respectively, to shift most of the population to the desired state. Reference spectra were then recorded every 3 min for 27 min to capture a true reference spectrum at each temperature. At 170 K, the sample was then illuminated to initiate the photocycle. After illumination, spectra were collected every 3 min for 72 min at each temperature. At these lower temperatures, photointermediates are thermally trapped and as the temperature increased, the photocycle proceeds through the multiple intermediates to the photoproduct state. The differences between the terminal reference spectrum and each illuminated spectrum at the same temperature were calculated to eliminate the influence of thermal equilibration and create spectra that resemble ultrafast transient absorption spectra for ease of interpretation. A flowchart depicting the cryokinetic measurement process is available in Figure A10.5.

### *A10.2.4: Protein Expression, Purification, and Characterization.*

The BL21 (DE3) pLysE E. coli competent cells (50  $\mu$ L) were used for gene transformation. The sample was held 30 minutes in ice. After heat-shock at 42 °C for 45 seconds, 950  $\mu$ L of LB was added to the sample. The sample and agar plate containing ampicillin (100  $\mu$ g/mL) were kept at

37°C for 30 minutes. Then 100 μL of the solution was streaked on LB agar plate and incubated at 37°C overnight. To inoculate 1 L of LB with ampicillin (100 μg/mL) a single colony was used. After the cell culture was grown at 37°C while shaking for 8 h, (OD~0.9) the overexpression was started by adding 1 mL of 1M IPTG solution into 1 L cell culture (overall concentration 1.0 mM of IPTG). The solution was shaken at 19°C for 36 hours.<sup>14,16</sup> The cells were collected by centrifuging for 20 min at 5,000 rpm (4°C). The supernatant was discarded, and the cells were resuspended in 60 mL of Tris buffer (10 mM Tris•HCl, pH=8.0). Then ultrasonication was used to lyse the cells (Power 60%, 1 min x 3), and the sonicated mixture centrifuged at 16°C (10,000 rpm, 20 min).

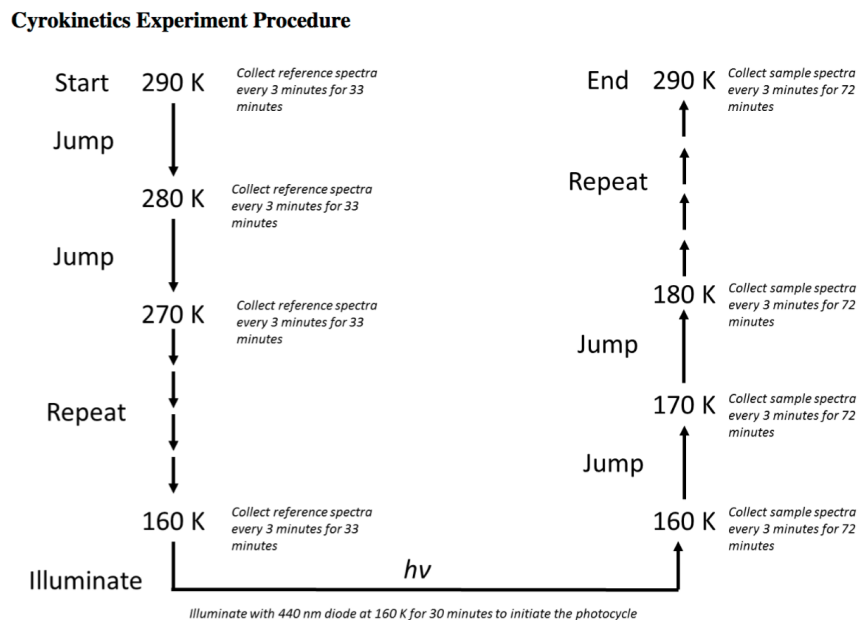


**Figure A10.5:** Cryokinetic Experimental Schematic  
Schematic depicting flow of an average cryokinetics experiment.

Next the purification was performed at 4°C by Ion exchange chromatography using Q Sepharose™, Fast Flow resin. The protein was bound to the column by gravity flow, the column washed with 50 mL of 10 mM Tris-HCl buffer. The bound protein was then eluted with 10 mM Tris, 150 mM NaCl, pH = 8.0, the pure fractions desalted using EMD Millipore centrprep centrifugal units (cutoffs:10 KDa) with 10 mM Tris pH=8.0 buffer, three times, and loaded on a second anion exchange column (15Q, GE Health Sciences, BioLogic DuoFlow system). The same Source Q program as mentioned previously,<sup>14,16</sup> was used for the purification.

The samples were prepared in 150 mM NaCl, 10 mM Tris-HCl (pH=8.0). For both ultrafast and cryokinetic experiment, the concentration of retinal kept at 0.5 equivalent of protein concentration in all experiments. The concentrations of proteins were calculated according to the extinction coefficient reported previously for M2.<sup>14,16</sup> The concentration of samples was calculated with regards to meet the optimal OD for ultrafast (0.5 in 0.2mm cuvette) and cryokinetics (OD=0.5 in 1mm cuvette) experiments measured by Cary 100 Bio Win UV-Vis spectrophotometer (Varian Instruments).

The PSB has absorptions corresponding to  $\lambda_{\max} > 450$  nm, while deprotonated imine peaks (USB) appear at  $\lambda_{\max} \sim 368$  nm. The unbound retinal absorbs at  $\lambda_{\max} \sim 380$  nm. All-trans retinal extinction coefficient in ethanol is  $48,000 \text{ M}^{-1}\text{cm}^{-1}$  at 380 nm.

A10.4: Supporting experimental results for  $M2_{15C}$ -PSB isomerization

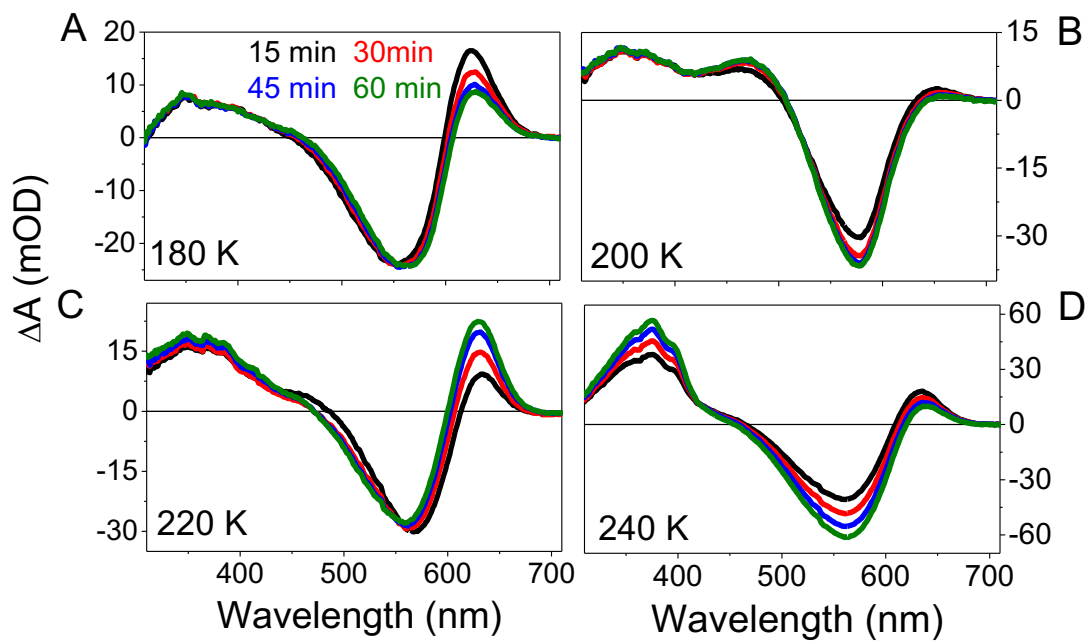


**Figure A10.6:**  $M2_{15C}$ -PSB Cryokinetics at Select Temperatures

Cryokinetic difference spectra at selected temperatures that isolate the photointermediates associated with the  $M2_{15C}$ -PSB  $\rightarrow$   $M2_{AT}$ -USB dynamics. All spectra are color coded to the legend found in panel A.

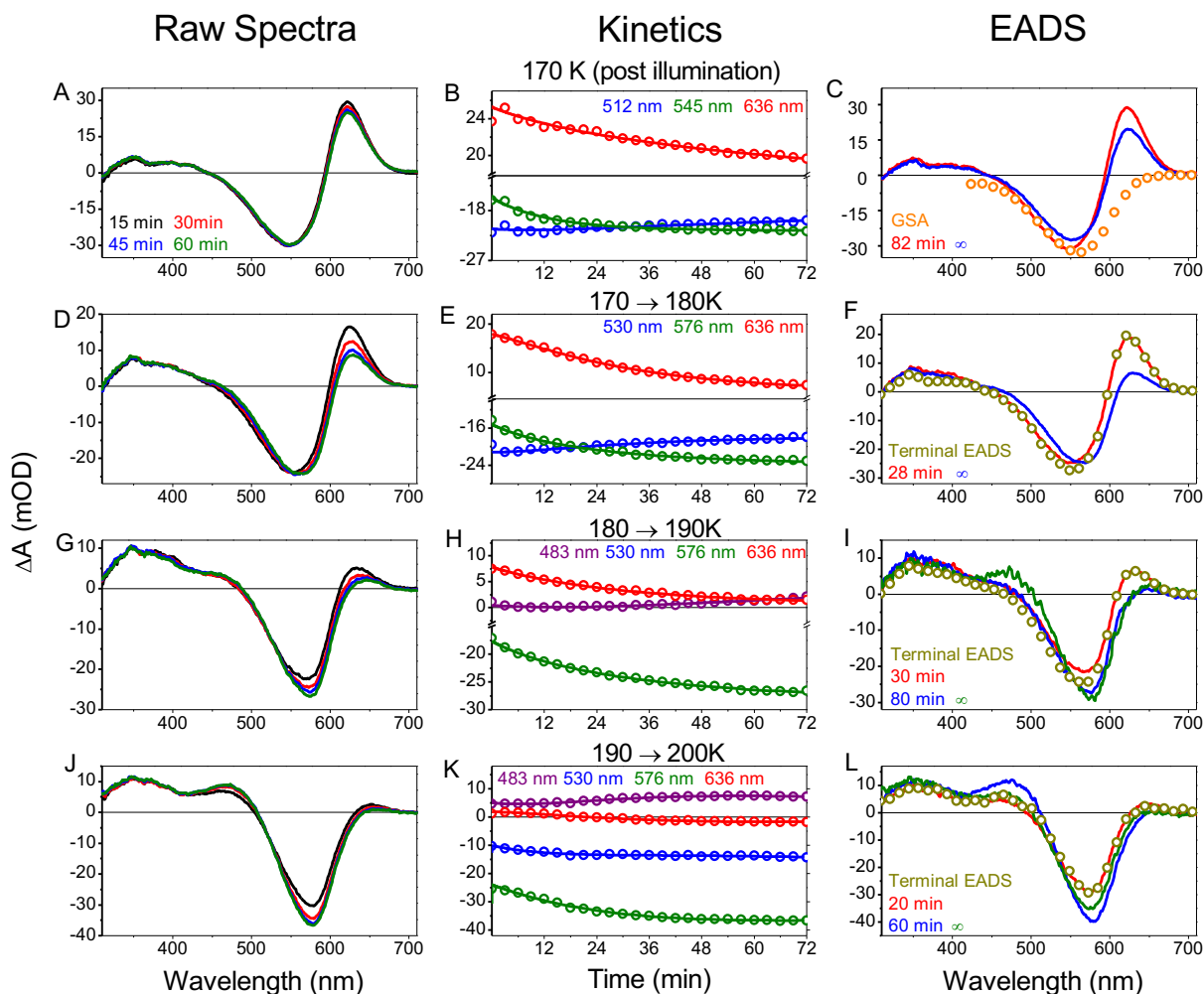


**Figure A10.7:** M2<sub>15C</sub>-PSB Cryokinetics Between 170 and 200 K

M2<sub>15C</sub>-PSB cryokinetics between 170 and 200 K and corresponding global analysis of M2. The raw spectra are color coded to match and are at the same time. In the EADS, the terminal EADS from the previous temperature is represented as open golden circles (F, I, L) and the post 366 nm illumination absorbance at 240 K is represented by orange open circles (C). For each temperature jump EADS, an initial EADS ascribed to an 8-10 min. thermalization of the sample/cryostat is not shown. See Table A10.1 for a detailed explanation of the figures.

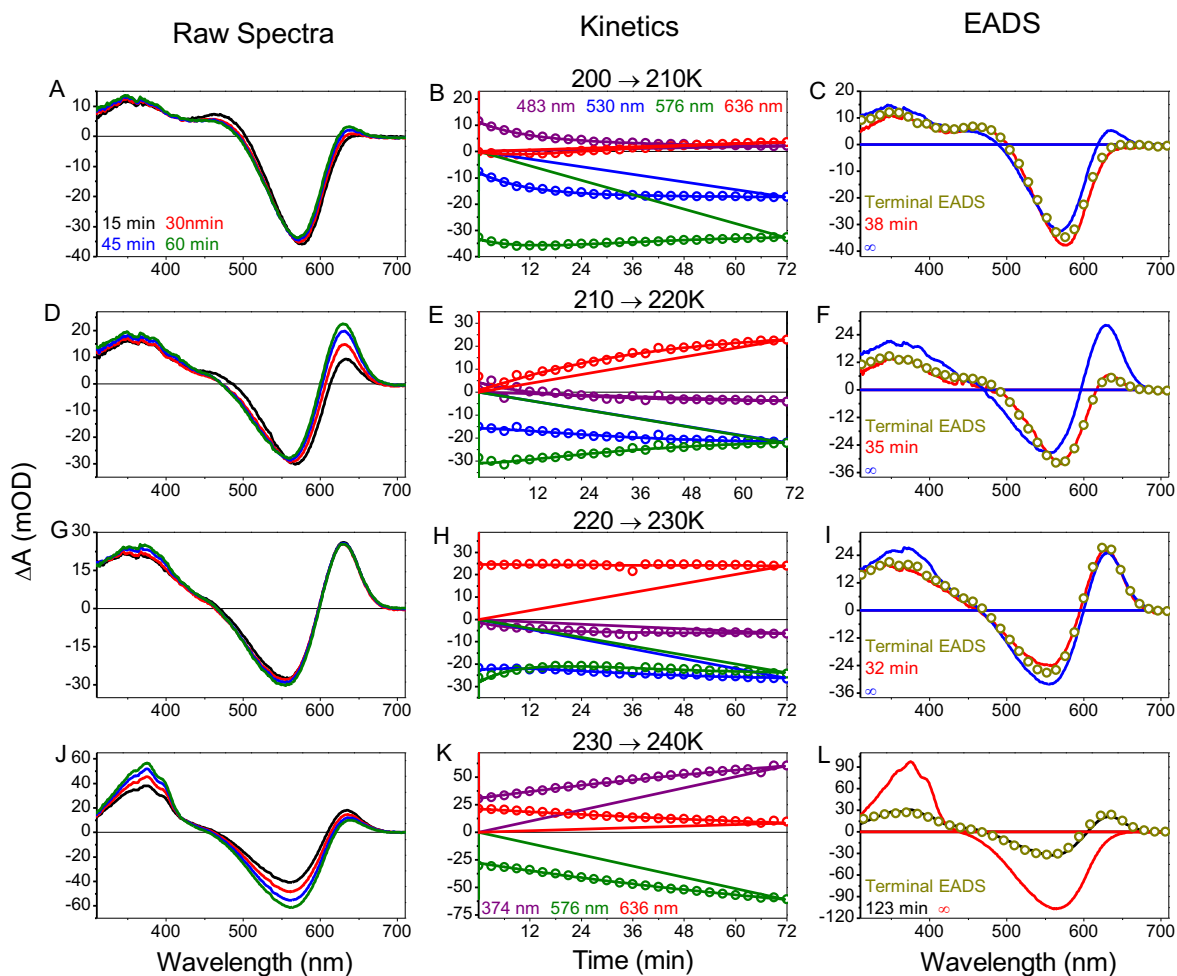


**Figure A10.8:** M2<sub>15C</sub>-PSB Cryokinetics Between 210 and 240 K

M2<sub>15C</sub>-PSB cryokinetics between 210 and 240 K and corresponding global analysis of M2. The raw spectra and kinetics are color coded to match and are at the same times and wavelengths (unless another legend is indicated). In the EADS, the terminal EADS from the previous temperature is represented as open golden circles. For each temperature jump EADS, an initial EADS ascribed to an 8-10 min thermalization of the sample/cryostat is not shown. See Table A10.1 for a detailed explanation of the figures.

**Table A10.1.** Cryokinetic observations and interpretations for the M2<sub>15C</sub>-PSB Reaction

Observations and interpretations of the cryokinetics data for the M2<sub>15C</sub>-PSB reaction (Figures A10.6 and A10.7).

Temperature Jump	Description	Interpretation
170 K	<ul style="list-style-type: none"> <li>625 nm decay</li> </ul>	<ul style="list-style-type: none"> <li>Loss of initial 625 nm photoproduct</li> </ul>
170 → 180 K	<ul style="list-style-type: none"> <li>625 nm decay (faster than 170 K)</li> <li>Red shift of 625 nm +absorbance and 575 nm bleach</li> </ul>	<ul style="list-style-type: none"> <li>Loss of initial 625 nm photoproduct</li> </ul>
180 → 190 K	<ul style="list-style-type: none"> <li>625 nm decay (slower than 180K)</li> <li>Growth of 575 nm bleach</li> <li>Red shift of 625 nm +absorbance and 575 nm bleach</li> <li>483 nm +absorbance growth (small, kinetic trace)</li> </ul>	<ul style="list-style-type: none"> <li>Beginning to have no initial 625 nm photoproduct</li> <li>Loss of rPSB</li> <li>Production of new photoproduct</li> </ul>
190 → 200 K	<ul style="list-style-type: none"> <li>625 nm no more decay</li> <li>Growth of 575 nm bleach</li> <li>No more red shifting of 575/625 nm</li> </ul>	<ul style="list-style-type: none"> <li>No more initial 625 nm photoproduct</li> <li>Continued loss of rPSB</li> <li>Thermal equilibrium of states?</li> </ul>
200 → 210 K	<ul style="list-style-type: none"> <li>Growth and blue shift at 575 nm (bleach region)</li> <li>Growth of + absorbance at ~625 nm</li> <li>Decay of 483 nm + absorbance</li> </ul>	<ul style="list-style-type: none"> <li>Photoproduct absorption fighting against bleach probably same as new 625 nm + absorbance?</li> <li>New 625 nm photoproduct absorption spectrum different than lower temperature (<b>Fig. S5</b>). If comparable to 240 K the photoproduct abs in bleach region as well (<b>Fig. S6</b>).</li> <li>Loss of photoproduct</li> </ul>
210 → 220 K	<ul style="list-style-type: none"> <li>Continued growth and blue shift at 575 nm (bleach region)</li> <li>Blues shift of 575 nm bleach and new 625 nm + absorbance</li> </ul>	<ul style="list-style-type: none"> <li>Photoproduct absorption fighting against bleach, probably same as new 625 nm + absorbance</li> </ul>
220 → 230 K	<ul style="list-style-type: none"> <li>No new 625 nm change</li> <li>Growth (very small) of 575 nm bleach</li> </ul>	<ul style="list-style-type: none"> <li>Reached equilibrium</li> <li>Loss of rPSB and no more new 625 nm photoproduct growth to fight it</li> </ul>
230 → 240 K	<ul style="list-style-type: none"> <li>Decay of 625 nm + absorbance</li> <li>Growth of 575 nm bleach</li> <li>Growth of + absorbance between 340-410 nm</li> </ul>	<ul style="list-style-type: none"> <li>Loss of new 625 nm photoproduct to rUSB (final photoproduct)</li> <li>Loss of rPSB &amp; new 625 nm photoproduct</li> <li>Production of rUSB from new 625 nm photoproduct</li> </ul>

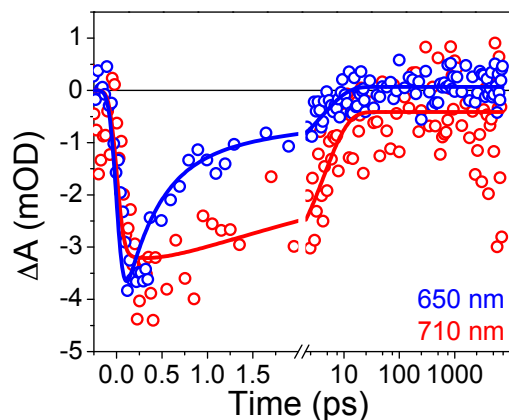


**Figure A10.9:** Comparison of the 650 and 710 nm kinetics of M2<sub>15C</sub>-PSB

Comparison of the 650 and 710 nm kinetics of M2<sub>15C</sub>-PSB after 565 nm excitation.

*A10.5: Supporting experimental results for M2<sub>AT</sub>-USB isomerization*

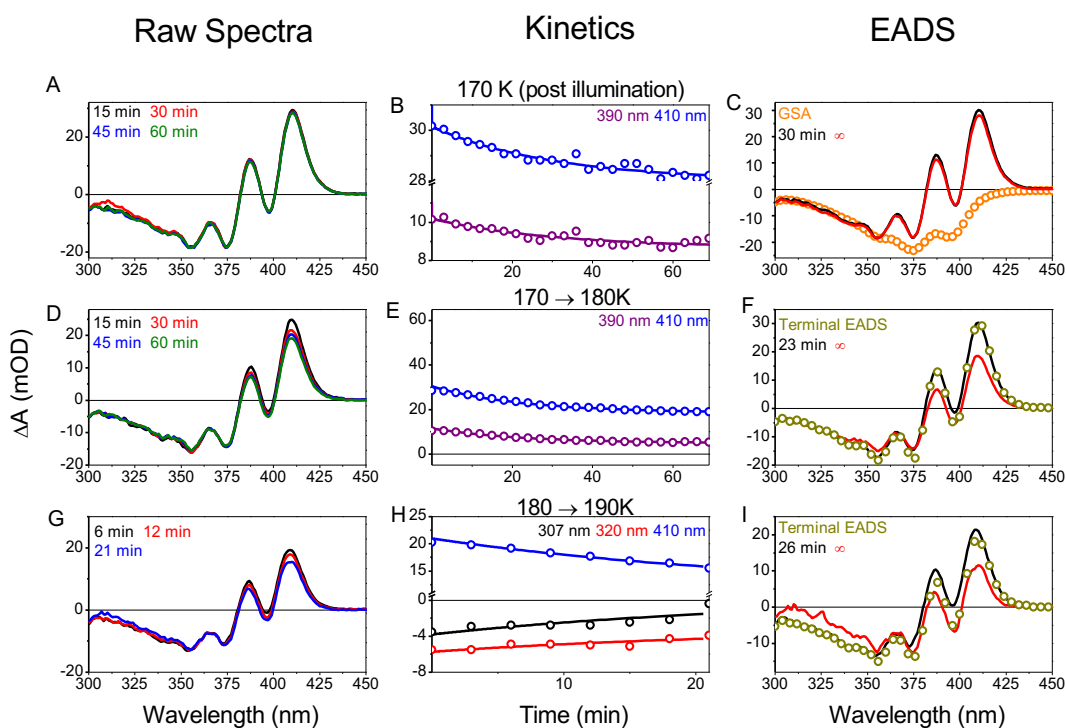


**Figure A10.10:** M2<sub>AT</sub>-USB Cryokinetics Between 170 and 190 K

M2<sub>AT</sub>-USB isomerization cryokinetics between 170 and 190 K and corresponding global analysis of M2. In the EADS, the terminal EADS from the previous temperature is represented as open golden circles (F, I) and the post 532 nm illumination absorbance at 240 K is represented by orange open circles (C). See Table A10.2 for a detailed explanation of the figures.



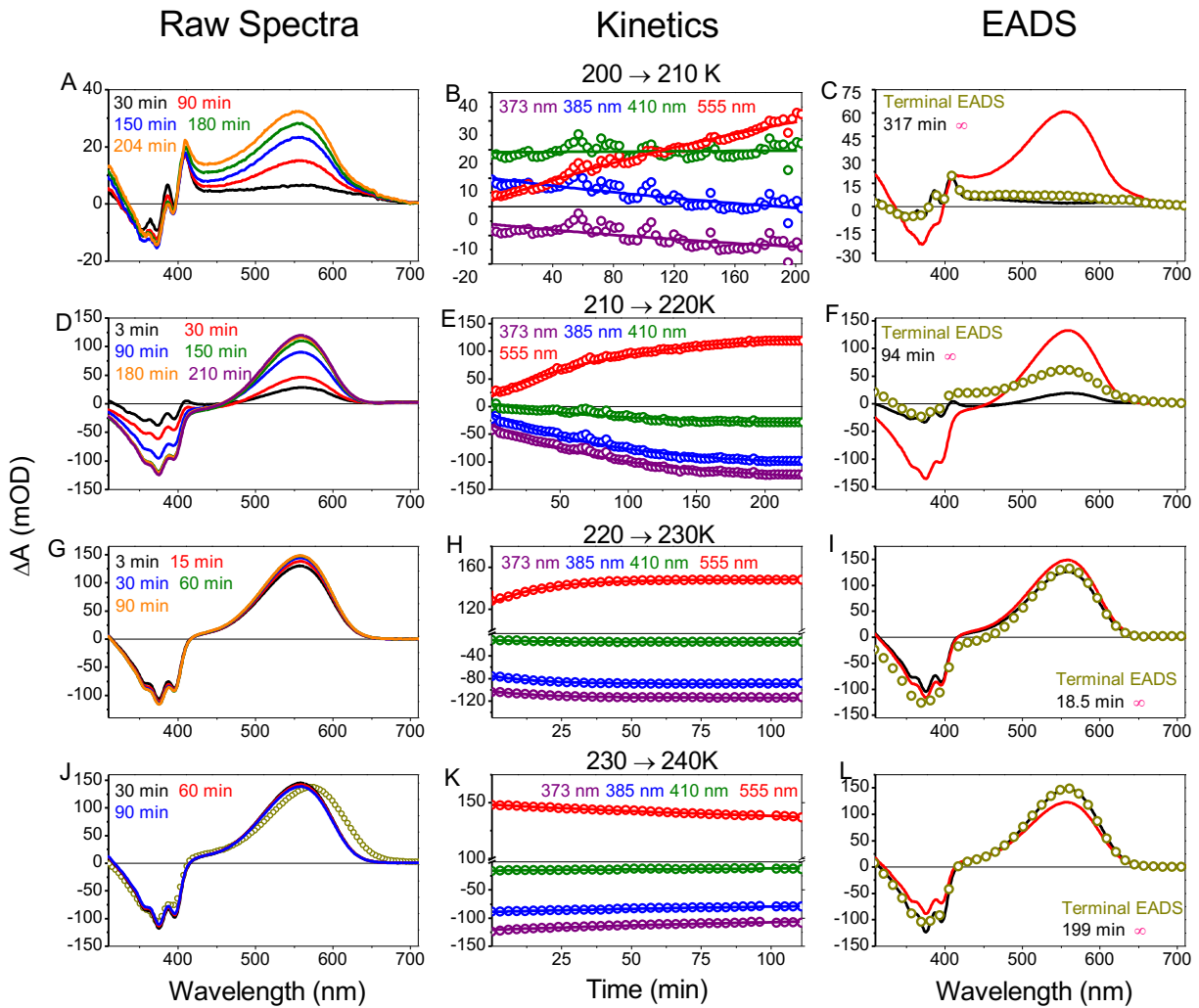


**Figure A10.11: M2<sub>AT</sub>-USB Cryokinetics Between 200 and 240 K**

M2<sub>AT</sub>-USB isomerization cryokinetics between 210 and 240 K and corresponding global analysis of M2. In the EADS, the terminal EADS from the previous temperature is represented as open golden circles (C, F, I, L). See Table A10.2 for a detailed explanation of the figures.

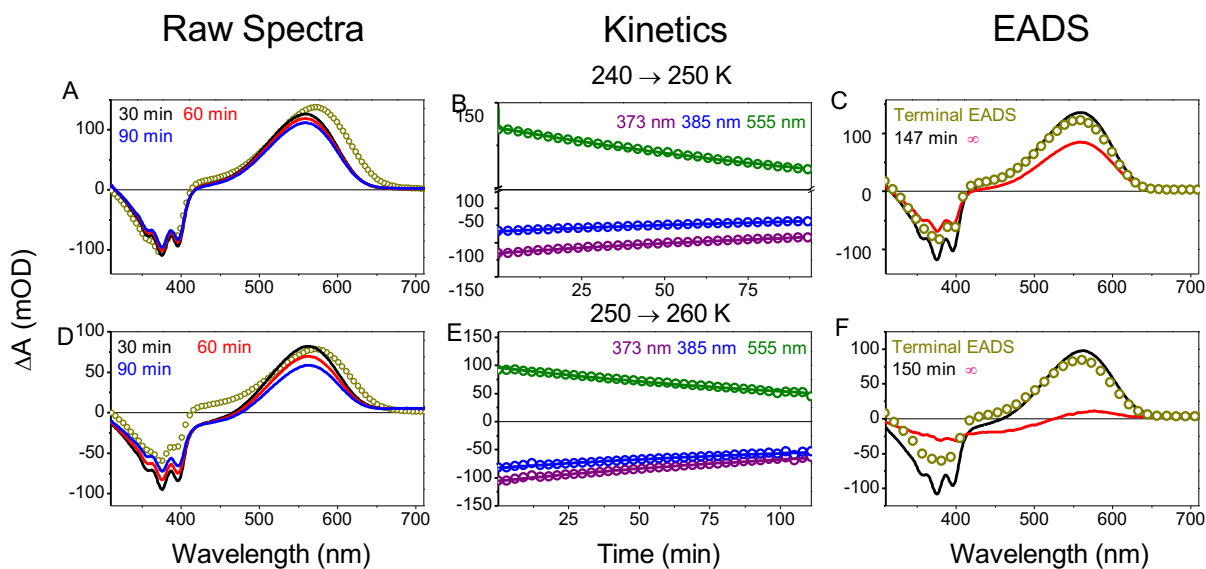


**Figure A10.12:** M2<sub>AT</sub>-USB Cryokinetics at 250 and 260 K

M2AT-USB isomerization cryokinetics between 250 and 260 K and corresponding global analysis of M2. In the EADS, the terminal EADS from the previous temperature is represented as open golden circles (C, F, I). See Table A10.2 for a detailed explanation of the figures.

**Table A10.2.** Cryokinetic observations and interpretations for the M2<sub>AT</sub>-PUSB Reaction

Temperature Jump	Description	Interpretation	Reference Spectra
170 K	<ul style="list-style-type: none"> <li>+Absorbance at 390 and 410 nm</li> <li>Peak at 365 nm</li> <li>-Absorbance in the 300-350 nm range</li> <li>No real change in the spectra with time</li> </ul>	<ul style="list-style-type: none"> <li>Primary photoproduct(s) absorbance.</li> <li>rUSB bleach</li> <li>The sample is at too low temperature that there is not enough energy to get over any energy barriers</li> </ul>	<ul style="list-style-type: none"> <li>Continued increase in absorbance at 373 and 396 nm</li> <li>396 nm abs close to 230 K</li> <li>373 and 396 nm are close to 180 K</li> <li>355 nm absorbance seem to not increase w/ continued decrease in T.</li> <li>Maxima at 361 and 384 nm</li> </ul>
170 → 180 K	<ul style="list-style-type: none"> <li>Small 390 and 410 nm decay</li> </ul>	<ul style="list-style-type: none"> <li>Loss of initial 390/410 nm photoproduct</li> <li>No apparent photoproduct. Maybe fighting 300-350 nm bleach or abs in deeper UV?</li> </ul>	<ul style="list-style-type: none"> <li>Continued increase in absorbance at 373, 396, 361, and 384 nm</li> <li>396 nm close in absorbance to 230 K</li> </ul>
180 → 190 K	<ul style="list-style-type: none"> <li>Small 390 and 410 nm decay</li> </ul>	<ul style="list-style-type: none"> <li>Loss of initial 390/410 nm photoproduct</li> <li>No apparent photoproduct. Maybe fighting 300-350 nm bleach</li> </ul>	<ul style="list-style-type: none"> <li>Continued increase in absorbance at 373, 396, 361, and 384 nm</li> </ul>
190 → 200 K	<ul style="list-style-type: none"> <li>NA</li> </ul>	<ul style="list-style-type: none"> <li>NA</li> </ul>	<ul style="list-style-type: none"> <li>Continued increase in absorbance at 373, 396, 361, and 384 nm</li> </ul>
200 → 210 K	<ul style="list-style-type: none"> <li>+Absorbance at 550 nm</li> <li>loss of signal at 373, 385, and 410 nm</li> </ul>	<ul style="list-style-type: none"> <li>First appearance of final photoproduct (rPSB)</li> <li>Loss of primary photoproduct</li> </ul>	<ul style="list-style-type: none"> <li>All wavelength of interest reaches a min (except 384 min at 220 K)</li> <li>355 nm essentially plateaus at this temperature (very small raise w/ further decrease in T)</li> </ul>
210 → 220 K	<ul style="list-style-type: none"> <li>555 nm + Absorbance growth</li> <li>Decrease in 385 and 410 nm peaks</li> </ul>	<ul style="list-style-type: none"> <li>Formation of final photoproduct (rPSB)</li> <li>Loss of initial photoproduct</li> </ul>	<ul style="list-style-type: none"> <li>All wavelengths decrease in absorbance; albeit as a much slower rate</li> <li>Minimum reached for 384 nm</li> </ul>
220 → 230 K	<ul style="list-style-type: none"> <li>Very small/slow growth of 555 nm</li> <li>Very small/slow decay 385 and 410 nm peaks</li> </ul>	<ul style="list-style-type: none"> <li>Loss of initial photoproduct</li> <li>Formation of rPSB from photoproduct beginning to fight loss of rPSB to rUSB, rPSB slightly wining.</li> </ul>	<ul style="list-style-type: none"> <li>All wavelengths of interest decrease in intensity</li> </ul>
230 → 240 K	<ul style="list-style-type: none"> <li>Abs spectra essentially overlapped</li> <li>Very small/slow decay of 555 nm (seen in kinetics)</li> <li>Very small/slow growth 385 and 410 nm peaks (seen in kinetics)</li> </ul>	<ul style="list-style-type: none"> <li>High enough temperature for spontaneous decay of rPSB to rUSB ground state</li> <li>Formation of PSB from photoproduct fighting loss of rPSB to rUSB, rUSB slightly wining.</li> </ul>	<ul style="list-style-type: none"> <li>All wavelengths of interest decrease in intensity</li> </ul>
240 → 250 K	<ul style="list-style-type: none"> <li>Faster decay of 555 nm signal</li> <li>Growth of 200-350 nm region</li> </ul>	<ul style="list-style-type: none"> <li>Faster loss of rPSB to rUSB.</li> <li>Return of rUSB state</li> </ul>	<ul style="list-style-type: none"> <li>NA</li> </ul>
250 → 260 K	<ul style="list-style-type: none"> <li>Same as 250 K</li> </ul>	<ul style="list-style-type: none"> <li>Same as 250 K</li> </ul>	<ul style="list-style-type: none"> <li>NA</li> </ul>

A10.6: Energy profiles along the reaction paths leading to Kink CIs.

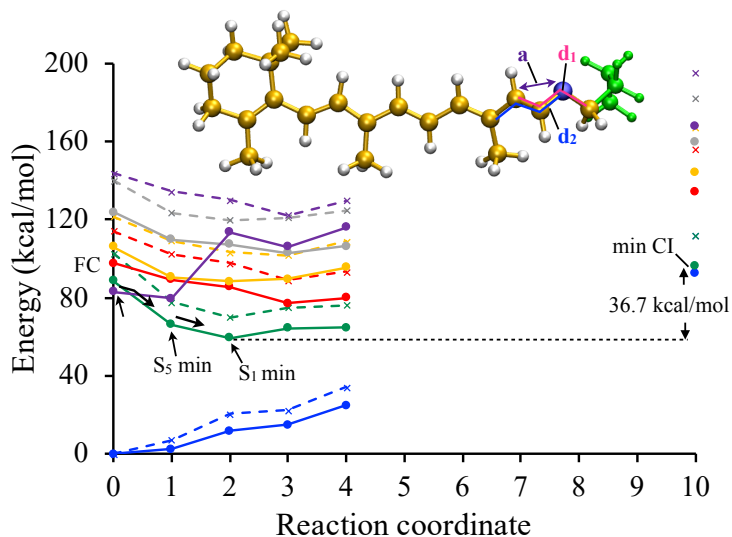


**Figure A10.13:** Evolution of CASSCF (dashed) and CASPT2 energies (solid) along the isomerization of M<sub>2</sub><sub>AT</sub>-USB around C15=N double bond

Evolution of CASSCF (dashed) and CASPT2 energies (solid) along the isomerization of M<sub>2</sub><sub>AT</sub>-USB around C15=N double bond. S<sub>0</sub> to S<sub>5</sub> states are denoted by blue, green, red, yellow, grey and violet colors respectively. The points 3 and 4 of the reaction coordinate were obtained by optimizing the geometry while keeping the value of the dihedral d<sub>1</sub> constrained at 160, 140 degrees. The geometric parameters of interest are highlighted in the rUSB structure shown on top. A near CI structure was obtained by carrying out a geometry optimization while constraining dihedrals d<sub>1</sub>, d<sub>2</sub> and distance a at 120, 150 degrees and 2.0 Å respectively. Such a structure was then used to start a CI optimization which resulted in Point 10 of the reaction coordinate.

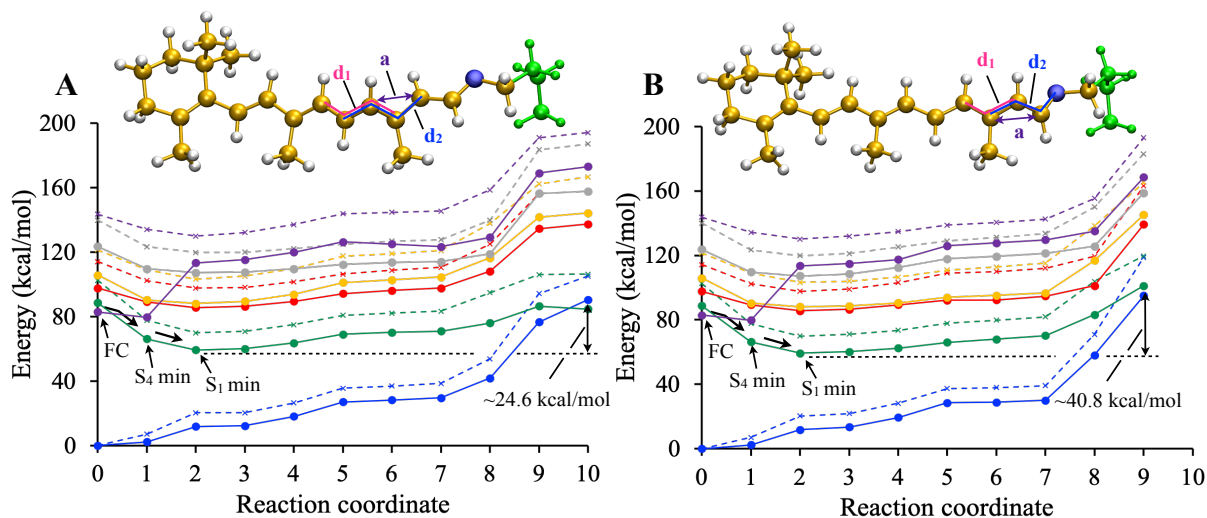


**Figure A10.14:** Evolution of CASSCF (dashed) and CASPT2 energies (solid) along the isomerization of M2<sub>AT</sub>-USB around C11=C12 and C13=C14 double bonds

Evolution of CASSCF (dashed) and CASPT2 energies (solid) along the isomerization of M2<sub>AT</sub>-USB around C11=C12 and C13=C14 double bonds (A and B respectively). S<sub>0</sub> to S<sub>5</sub> states are denoted by blue, green, red, yellow, grey and violet colors respectively. The points 3 to 9 of the reaction coordinate were obtained from a series of constraint geometry optimizations. The geometric parameters of interest are highlighted in the rUSB structure shown on top. Points 3 to 5 are obtained by optimizing the geometry while keeping the value of the dihedral d<sub>1</sub> constrained at 160, 140 and 120 degrees. Points 6 and 7 are obtained by constraining d<sub>2</sub> at 160 and 150 degrees while fixing d<sub>1</sub> at 120 degrees. Finally, in order to obtain points 8 and 9, the bond length a is constrained at 2.2 and 2.0 Å with d<sub>1</sub> and d<sub>2</sub> set to 120 and 150 degrees respectively. Point 10 represents the minimum conical intersection which was only located for C11=C12 isomerization.

A10.7: Geometric parameters of excited state optimized  $M2_{AT}$ -USB structures.

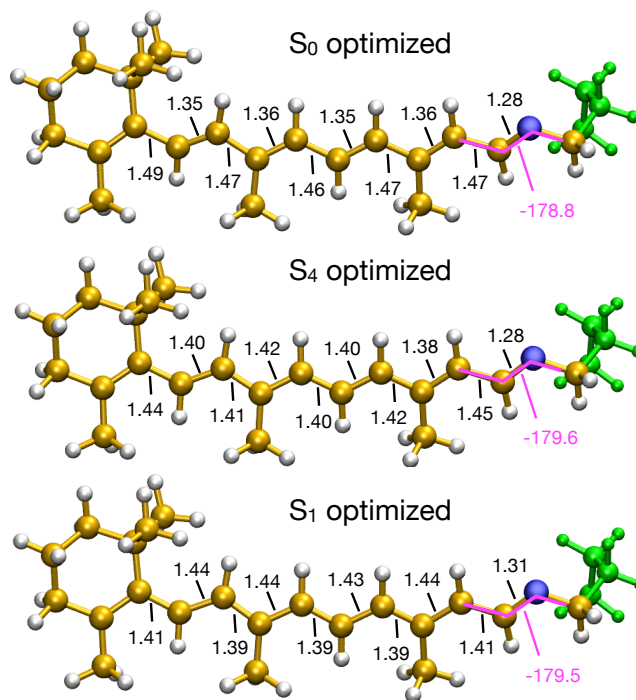


**Figure A10.15:**  $M2_{AT}$ -USB Optimized Geometric Parameters

Geometric parameters of S<sub>0</sub>, S<sub>4</sub> and S<sub>1</sub> optimized  $M2_{AT}$ -USB molecular structures. Bond lengths are in angstrom and dihedrals are in degrees.

A10.8: Proposed proton transfer mechanisms.

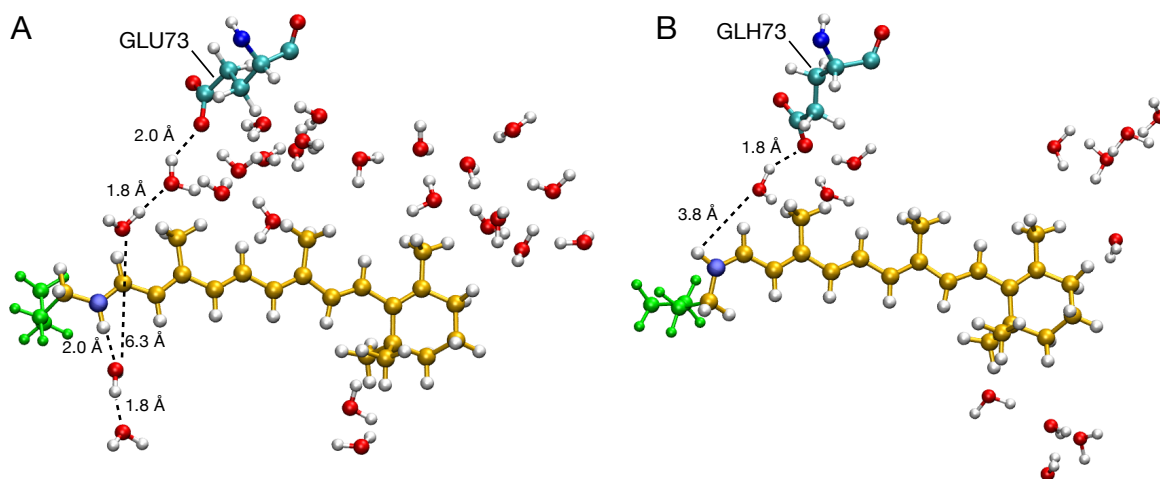


**Figure A10.16:** Proposed Deprotonation Pathways for M2

(A) Proposed pathway for the deprotonation of rPSB during M2<sub>15C</sub>-PSB to M2<sub>AT</sub>-USB conversion. The hydrogen bond network is represented by black dashed lines. (B) The same for M2<sub>15C</sub>-USB to M2<sub>15C</sub>-PSB conversion. Note that the acidic proton on GLH73 has been transferred to Schiff base through the H bond network.

A10.9: Impact of electronic state mixing on the photoisomerization of M2<sub>15C</sub>-PSB.

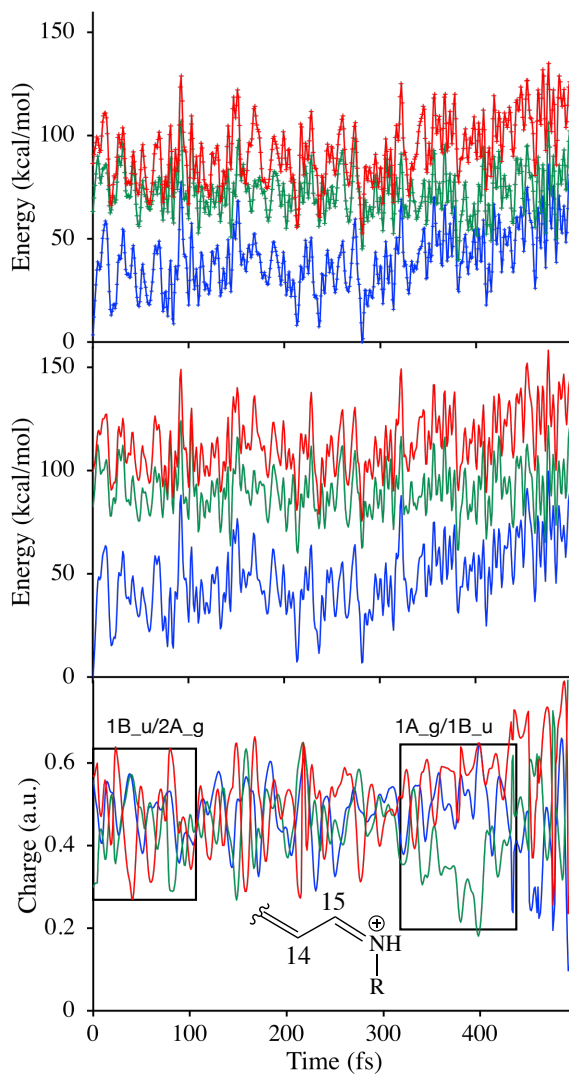


**Figure A10.17:** CASPT2 and CASSCF Energies and Mulliken charges along a representative M2<sub>15C</sub>-PSB trajectory

Evolution of CASPT2 (top) and CASSCF energies (middle) and Mulliken charges on a fraction of rPSB (bottom) along a representative M2<sub>15C</sub>-PSB trajectory. The charges shown in the bottom panel are the total charge on the fraction of molecular shown.

As discussed in ref. <sup>341</sup> electronic state mixing has been proposed to control the speed of rPSB photoisomerization by changing the electronic structure of a PES. In order to investigate the



presence of such mixing in this system, we recomputed the energy profiles of a selective representative M2<sub>15C</sub>-PSB trajectory at the CASPT2 level. For both the CASSCF and CASPT2 energy profiles, the evolution of positive charge on a fraction of rPSB, which is an indication of the electronic structure, are reported in Figure A9.17. In order to interpret these results, we must recall three important pieces of information that we have documented in ref. <sup>341</sup> using a model retinal chromophore in the gas phase. These include: 1) CASPT2 and CASSCF energy topologies are similar, 2) a trajectory initiated from the Frank-Condon region may reach 3 conical intersections: a crossing between two PESs associated with 1Ag and 1Bu electronic structures/characters (1Ag/1Bu CI), a crossing between two canonical intersections associated with 1Ag and 2Ag characters (1Ag/2Ag CI), and a crossing between two PESs with 1Bu and 2Ag characters (1Bu/2Ag CI), 3) one can use the total charge computed on a fraction of rPSB to learn about the character of the PES. Based on the oscillator strengths, we launched the selected trajectory on S<sub>1</sub> which is associated with reactive 1Bu character. Note that the 1Bu character of the S<sub>1</sub> PES is indicated by the ca. 3 positive charge (see framed region between 0-100 fs in Figure A9.17, bottom panel) remaining in the nitrogen containing chromophore fragment. However, as the molecule progresses on S<sub>1</sub>, the character of the PES varies from reactive 1Bu to nonreactive 2Ag, which delays the photoisomerization of the molecule. This can be interpreted using the coupling between the states. For example, as apparent in Figure A9.17 bottom panel, the green and red lines in framed region between 0-100 fs displays an out of phase oscillatory relationship. This suggest that during such periods, the molecule remains in the vicinity of a 1Bu/2Ag CI where the electronic wavefunction of the S<sub>1</sub> and S<sub>2</sub> states may exchange their characters. This is also evident in the CASPT2 energy profiles where S<sub>1</sub> and S<sub>2</sub> PESs approach each other. Such an oscillatory

relationship is often maintained (except during the periods where  $S_1$  couples with a state higher than  $S_2$ ) until 330 fs. After 330 fs, one can observe the coupling between  $S_1$  and  $S_0$  ( $1A_g/1B_u$  coupling) and the molecule reaches a  $1A_g/1B_u$  CI and decays to  $S_0$ . This suggests that electronic state mixing controls the speed of the photoisomerization of  $M2_{15C}$ -PSB similar to natural systems.

## References

1. Gaffney, K. J., Capturing photochemical and photophysical transformations in iron complexes with ultrafast X-ray spectroscopy and scattering. *Chem. Sci.* **2021**, *12*, 8010-8025.
2. Sato, M., Photodissociation of Simple Molecules in the Gas Phase. *Chem. Sci.* **2001**, *101*, 2678-2725.
3. Kostko, O.; Bandyopadhyay, B.; Ahmed, M., Vacuum Ultraviolet Photoionization of Complex Chemical Systems. *Annu Rev Phys Chem* **2016**, *67* (1), 19-40.
4. Fujitsuka, M.; Kim, S. S.; Lu, C.; Tojo, S.; Majima, T., Intermolecular and Intramolecular Electron Transfer Processes from Excited Naphthalene Diimide Radical Anions. *J. Phys. Chem. B* **2014**, *119* (24), 7275-7282.
5. Xiao, Z.; Cai, S.; Sahi, Y.; Yang, B.; Gaio, S., A photo-induced C–O bond formation methodology to construct tetrahydroxanthones. *Chem. Commun.* **2014**, *50*, 5254-5257.
6. Heinz, B.; Malkmus, S.; Laimgruber, S.; Dietrich, S.; Schulz, C.; Rück-Braun, K.; Braun, M.; Zinth, W.; Gilch, P., Comparing a Photoinduced Pericyclic Ring Opening and Closure: Differences in the Excited State Pathways. *J. Am. Chem. Soc.* **2007**, *129* (27), 8577-8584.
7. Poplata, S.; Tröster, A.; Zou, Y.-Q.; Bach, T., Recent Advances in the Synthesis of Cyclobutanes by Olefin [2 + 2] Photocycloaddition Reactions. *Chem. Rev.* **2016**, *116* (17), 9748-9815.
8. Henzl, J.; Mehlhorn, M.; Gawronski, H.; Rieder, K.-H.; Morgenstern, K., Reversible cis-trans-Isomerisierung eines einzelnen Azobenzol-Moleküls. *Angewandte Chemie* **2006**, *118* (4), 617-621.
9. Lubbe, A. S.; Szymanski, W.; Feringa, B. L., Recent developments in reversible photoregulation of oligonucleotide structure and function. *Chemical Society Reviews* **2017**, *46* (4), 1052-1079.
10. Harris, J. D.; Moran, M. J.; Aprahamian, I., New molecular switch architectures. *Proceedings of the National Academy of Sciences* **2018**, *115* (38), 9414-9422.
11. Jørgensen, K., Photochemical Oxidative Cyclisation of Stilbenes and Stilbenoids—The Mallory-Reaction. *Molecules* **2010**, *15* (6), 4334-4358.
12. Paramonov, S. V.; Lokshin, V.; Fedorova, O. A., Spiropyran, chromene or spirooxazine ligands: Insights into mutual relations between complexing and photochromic properties. *Journal of Photochemistry and Photobiology C: Photochemistry Reviews* **2011**, *12* (3), 209-236.
13. Jiang, M.; Paul, N.; Bieniek, N.; Backup, T.; NHampp, N.; Motzkus, M., Photocleavage of coumarin dimers studied by femtosecond UV transient absorption spectroscopy. *Physical chemistry chemical physics : PCCP* **2017**, *19*, 4597-4606.
14. Xia, H.; Xie, K.; Zou, G., Advances in Spiroyrans/Spirooxazines and Applications Based on Fluorescence Resonance Energy Transfer (FRET) with Fluorescent Materials. *Molecules* **2017**, *22* (12), 2236.
15. Barachevsky, V. A., Photochromic Quinones. In *Organic Photochromic and Thermochemical Compounds: Volume 1: Main Photochromic Families*, Crano, J. C.; Guglielmetti, R. J., Eds. Springer US: Boston, MA, 2002; pp 267-314.
16. Tian, H.; Zhang, J., *Photochromic materials: Preparation, properties and applications*. 2016; p 1-421.

17. Zhang, F.; Kurokawa, K.; Lassoued, A.; Crowell, J. A.; Miller, D. T., Cone photoreceptor classification in the living human eye from photostimulation-induced phase dynamics. *Proc. Natl. Acad. Sci.* **2019**, *116* (16), 7951-7956.
18. Dechaine, J. M.; Gardner, G.; Weinig, C., Phytochromes differentially regulate seed germination responses to light quality and temperature cues during seed maturation. *Plant, Cell & Environment* **2009**, *32* (10), 1297-1309.
19. Franklin, K. A.; Whitelam, G. C., Phytochromes and shade-avoidance responses in plants. *Ann Bot* **2005**, *96* (2), 169-175.
20. Casal, J. J., Photoreceptor Signaling Networks in Plant Responses to Shade. *Annu. Rev. Plant Biol.* **2013**, *64* (1), 403-427.
21. Sage, L., *Pigment of the Imagination: A History of Phytochrome Research*. Academic Press, Inc: San Diego, 1992; p 562.
22. Campbell, E. L.; Hagen, K. D.; Chen, R.; Risser, D. D.; Ferreira, D. P.; Meeks, J. C., Genetic analysis reveals the identity of the photoreceptor for phototaxis in hormogonium filaments of *Nostoc punctiforme*. *J Bacteriol* **2015**, *197* (4), 782-791.
23. Song, J.-Y.; Cho, H. S.; Cho, J.-I.; Jeon, J.-S.; Lagarias, J. C.; Park, Y.-I., Near-UV cyanobacteriochrome signaling system elicits negative phototaxis in the cyanobacterium *Synechocystis* sp. PCC 6803. *Proceedings of the National Academy of Sciences* **2011**, *108* (26), 10780.
24. Yoshihara, S.; Suzuki, F.; Fujita, H.; Geng, X. X.; Ikeuchi, M., Novel Putative Photoreceptor and Regulatory Genes Required for the Positive Phototactic Movement of the Unicellular Motile Cyanobacterium *Synechocystis* sp. PCC 6803. *Plant and Cell Physiology* **2000**, *41* (12), 1299-1304.
25. Hirose, Y.; Chihong, S.; Mai, W.; Yonekawa, C.; Murata, K.; Ikeuchi, M.; Eki, T., Diverse Chromatic Acclimation Processes Regulating Phycoerythrocyanin and Rod-Shaped Phycobilisome in Cyanobacteria. *Mol Plant* **2019**, *12*, 715-725.
26. Sanfilippo, J. E.; Garczarek, L.; Partensky, F.; Kehoe, D. M., Chromatic Acclimation in Cyanobacteria: A Diverse and Widespread Process for Optimizing Photosynthesis. *Annu. Rev. Microbiol* **2019**, *73*, 407-433
27. Jenkins, A. J.; Gottlieb, S. M.; Chang, C.-W.; Hayer, R. J.; Martin, S. S.; Lagarias, J. C.; Larsen, D. S., Conservation and Diversity in the Secondary Forward Photodynamics of Red/Green Cyanobacteriochromes. *Photochem. Photobiol. Sci.* **2019**, *18*, 2539-2552.
28. Jenkins, A. J.; Gottlieb, S. M.; Chang, C.-W.; Kim, P. W.; Hayer, R. J.; Hanke, S. J.; Martin, S. S.; Lagarias, J. C.; Larsen, D. S., Conservation and Diversity in the Primary Reverse Photodynamics of Red/Green Cyanobacteriochromes. *Biochemistry* **2020**, *59* (41), 4015-4028.
29. Kirpich, J. S.; Chang, C.-W.; Franse, J.; Yu, Q.; Escobar, F. V.; Jenkins, A. J.; Martin, S. S.; Narikawa, R.; Rockwell, N. C.; Ames, J. B.; Lagarias, J. C.; Larsen, D. S., Comparison of the Forward and Reverse Photocycle Dynamics of Two Highly Similar Canonical Red/Green CBCRs Reveals Unexpected Differences. *Biochemistry* **2021**, *60* (4), 274-288.
30. Montgomery, B. L., Sensing the light: photoreceptive systems and signal transduction in cyanobacteria. *Molecular Microbiology* **2007**, *64* (1), 16-27.
31. Van Der Horst, M. A.; Hellingwerf, K. J., Photoreceptor proteins, "star actors of modern times": A review of the functional dynamics in the structure of representative members of six different photoreceptor families. *Accounts of Chemical Research* **2004**, *37*, 13-20.

32. Barachevsky, V. A., Photochromic spirocompounds and chromenes for sensing metal ions. *Review Journal of Chemistry* **2013**, *3* (1), 52-94.
33. Lerch, M. M.; Szymański, W.; Feringa, B. L., The (photo)chemistry of Stenhouse photoswitches: guiding principles and system design. *Chemical Society Reviews* **2018**, *47* (6), 1910-1937.
34. Irie, M., Diarylethenes for Memories and Switches. *Chemical Reviews* **2000**, *100* (5), 1685-1716.
35. Petersen, A. U.; Hofmann, A. I.; Fillols, M.; Mansø, M.; Jevric, M.; Wang, Z.; Sumbly, C. J.; Müller, C.; Moth-Poulsen, K., Solar Energy Storage by Molecular Norbornadiene–Quadricyclane Photoswitches: Polymer Film Devices. *Advanced Science* **2019**, *6* (12), 1900367.
36. Dreos, A.; Wang, Z.; Udmark, J.; Ström, A.; Erhart, P.; Börjesson, K.; Nielsen, M. B.; Moth-Poulsen, K., Liquid Norbornadiene Photoswitches for Solar Energy Storage. *Advanced Energy Materials* **2018**, *8* (18), 1703401.
37. Mansø, M.; Petersen, A. U.; Wang, Z.; Erhart, P.; Nielsen, M. B.; Moth-Poulsen, K., Molecular solar thermal energy storage in photoswitch oligomers increases energy densities and storage times. *Nature Communications* **2018**, *9* (1), 1945.
38. Gromov, S. P.; Vedernikov, A. I.; Lobova, N. A.; Kuz'mina, L. G.; Dmitrieva, S. N.; Strelenko, Y. A.; Howard, J. A. K., Synthesis, Structure, and Properties of Supramolecular Photoswitches Based on Ammonioalkyl Derivatives of Crown Ether Styryl Dyes. *The Journal of Organic Chemistry* **2014**, *79* (23), 11416-11430.
39. Fredy, J. W.; Méndez-Ardoy, A.; Kwangmettatom, S.; Bochicchio, D.; Matt, B.; Stuart, M. C. A.; Huskens, J.; Katsonis, N.; Pavan, G. M.; Kudernac, T., Molecular photoswitches mediating the strain-driven disassembly of supramolecular tubules. *Proceedings of the National Academy of Sciences* **2017**, *114* (45), 11850.
40. Li, Y.; Zhang, H.; Qi, C.; Guo, X., Light-driven photochromism-induced reversible switching in P3HT–spiropyran hybrid transistors. *Journal of Materials Chemistry* **2012**, *22* (10), 4261-4265.
41. Frolova, L. A.; Troshin, P. A.; Susarova, D. K.; Kulikov, A. V.; Sanina, N. A.; Aldoshin, S. M., Photoswitchable organic field-effect transistors and memory elements comprising an interfacial photochromic layer. *Chemical Communications* **2015**, *51* (28), 6130-6132.
42. Barman, S.; Das, J.; Biswas, S.; Maiti, T. K.; Pradeep, S., A spiropyran–coumarin platform: an environment sensitive photoresponsive drug delivery system for efficient cancer therapy. *J. Mater. Chem. B* **2017**, *5*, 3940-3944.
43. Feringa, B. L., The Art of Building Small: From Molecular Switches to Motors *Angew. Chem. Int.* **2017**, *59* (37), 11060-11078.
44. Chernov, K. G.; Redchuk, T. A.; Omelina, E. S.; Verkhusha, V. V., Near-Infrared Fluorescent Proteins, Biosensors, and Optogenetic Tools Engineered from Phytochromes. *Chemical Reviews* **2017**, *117* (9), 6423-6446.
45. Oliinyk, O. S.; Chernov, K. G.; Verkhusha, V. V., Bacterial Phytochromes, Cyanobacteriochromes and Allophycocyanins as a Source of Near-Infrared Fluorescent Probes. *Int J Mol Sci* **2017**, *18* (8), 1691-1692.
46. Piatkevich, K. D.; Subach, F. V.; Verkhusha, V. V., Far-red light photoactivatable near-infrared fluorescent proteins engineered from a bacterial phytochrome. *Nature Communications* **2013**, *4*, 2153.

47. Shcherbakova, D. M.; Shemetov, A. A.; Kaberniuk, A. A.; Verkhusha, V. V., Natural photoreceptors as a source of fluorescent proteins, biosensors, and optogenetic tools. *Annu Rev Biochem* **2015**, *84*, 519-550.
48. Paquette, M. M.; Plaul, D.; Kurimoto, A.; Patrick, B. O.; Frank, N. L., Opto-Spintronics: Photoisomerization-Induced Spin State Switching at 300 K in Photochrome Cobalt–Dioxolene Thin Films. *J. Am. Chem. Soc.* **2018**, *44*, 14990–15000.
49. Aldoshin, S. M., Heading to photoswitchable magnets. *Journal of Photochemistry and Photobiology A: Chemistry* **2008**, *200* (1), 19-33.
50. Drepper, T.; Krauss, U.; Meyer zu Berstenhorst, S.; Pietruszka, J.; Jaeger, K.-E., Lights on and action! Controlling microbial gene expression by light. *Appl. Microbiol. Biotechnol.* **2011**, *90* (1), 23-40.
51. Kyweriga, M.; Mohajerani, M. H., Optogenetic Approaches for Mesoscopic Brain Mapping. In *Optogenetics: Methods and Protocols*, Kianianmomeni, A., Ed. Springer New York: New York, NY, 2016; pp 251-265.
52. Mahmoudi, P.; Veladi, H.; Pakdel, F. G., Optogenetics, Tools and Applications in Neurobiology. *J Med Signals Sens* **2017**, *7* (2), 71-79.
53. O’Shea, D. J.; Kalanithi, P.; Ferenczi, E. A.; Hsueh, B.; Chandrasekaran, C.; Goo, W.; Diester, I.; Ramakrishnan, C.; Kaufman, M. T.; Ryu, S. I.; Yeom, K. W.; Deisseroth, K.; Shenoy, K. V., Development of an optogenetic toolkit for neural circuit dissection in squirrel monkeys. *Scientific Reports* **2018**, *8* (1), 6775.
54. G, N.; Tan, A.; Farhatnia, Y.; Rajadas, J.; Hamblin, M. R.; Khaw, P. T.; Seifalian, A. M., Channelrhodopsins: visual regeneration and neural activation by a light switch. *N Biotechnol* **2013**, *30* (5), 461-474.
55. Zhang, F.; Wang, L.-P.; Brauner, M.; Liewald, J. F.; Kay, K.; Watzke, N.; Wood, P. G.; Bamberg, E.; Nagel, G.; Gottschalk, A.; Deisseroth, K., Multimodal fast optical interrogation of neural circuitry. *Nature* **2007**, *446*, 633-639.
56. Schröder-Lang, S.; Schwärzel, M.; Seifert, R.; Strünker, T.; Kateriya, S.; Looser, J.; Watanabe, M.; Kaupp, U. B.; Hegemann, P.; Nagel, G., Fast manipulation of cellular cAMP level by light in vivo. *Nature Methods* **2006**, *4*, 39.
57. Fan, H. Y.; Morgan, S.-A.; Brechun, K. E.; Chen, Y.-Y.; Jaikaran, A. S. I.; Woolley, G. A., Improving a Designed Photocontrolled DNA-Binding Protein. *Biochemistry* **2011**, *50* (7), 1226-1237.
58. Venkataramani, S.; Jana, U.; Dommaschk, M.; Sonnichsen, F. D.; Tucek, F.; Herges, R., Magnetic Bistability of Molecules in Homogeneous Solution at Room Temperature. *Science* **2011**, *331* (6016), 445-448.
59. Jenkins, A. J.; Ziliang, M.; Kurimoto, A.; Mix, L. T.; Frank, N.; Larsen, D. S., Ultrafast Spintronics: Dynamics of the Photoisomerization-Induced Spin–Charge Excited-State (PISCES) Mechanism in Spirooxazine- Based Photomagnetic Materials. *J. Phys. Chem. Lett.* **2018**, *9*, 5351-5357.
60. Manathunga, M.; Jenkins, A. J.; Orozco-Gonzalez, Y.; Ghanbarpour, A.; Borhan, B.; Geiger, J. H.; Larsen, D. S.; Olivucci, M., Computational and Spectroscopic Characterization of the Photocycle of an Artificial Rhodopsin. *J. Phys. Chem. Lett.* **2020**, *22*, 4245-4252.
61. Essen, L.-O.; Mailliet, J.; Hughes, J., The structure of a complete phytochrome sensory module in the Pr ground state. *Proc. Nati. Acad. Sci.* **2008**, *105* (38), 14709.

62. Borthwick, H. A.; Hendricks, S.; Parker, M.; Toole, E.; Toole, V. K., A reversible photoreaction controlling seed germination. *Proc. Natl. Acad. Sci. USA* **1952**, *38*, 662.
63. Rockwell, N. C.; Martin, S. S.; Lagarias, J. C., Identification of Cyanobacteriochromes Detecting Far-Red Light. *Biochemistry* **2016**, *55* (28), 3907-3919.
64. Rockwell, N. C.; Martin, S. S.; Gulevich, A. G.; Lagarias, J. C., Phycoviolobilin Formation and Spectral Tuning in the DXCF Cyanobacteriochrome Subfamily. *Biochemistry* **2012**, *51* (7), 1449-1463.
65. Moreno, M. V.; Rockwell, N. C.; Mora, M.; Fisher, A. J.; Lagarias, C. J., A far-red cyanobacteriochrome lineage specific for verdins. *Proc. Natl. Acad. Sci.* **2020**, *Under Review*.
66. Rockwell, N. C.; Martin, S. S.; Lagarias, C. J., Identification of DXCF cyanobacteriochrome lineages with predictable photocycles. *Photochem. Photobiol. Sci.* **2015**, *14* (5), 929-941.
67. Bandara, S.; Rockwell, N. C.; Zeng, X.; Ren, Z.; Wang, C.; Shin, H.; Martin, S. S.; Moreno, M. V.; Lagarias, C. J.; Yang, X., Crystal Structure of a Far-Red-Sensing Cyanobacteriochrome Reveals an Atypical Bilin Conformation and Spectral Tuning Mechanism. *Proc. Natl. Acad. Sci. USA* **2020**, *118* (12), e2025094118.
68. Rockwell, N. C.; Martin, S. S.; Feoktistova, K.; Lagarias, J. C., Diverse two-cysteine photocycles in phytochromes and cyanobacteriochromes. *Proc. Natl. Acad. Sci.* **2011**, *108* (29), 11854-11859.
69. Rockwell, N. C.; Martin, S. S.; Lagarias, J. C., Red/Green Cyanobacteriochromes: Sensors of Color and Power. *Biochemistry* **2012**, *51* (48), 9667-9677.
70. Rockwell, N. C.; Martin, S. S.; Gan, F.; Bryant, D. A.; Lagarias, J. C., NpR3784 is the prototype for a distinctive group of red/green cyanobacteriochromes using alternative Phe residues for photoproduct tuning. *Photochem. Photobiol. Sci.* **2015**, *14* (2), 258-269.
71. Kehoe, D. M.; Grossman, A. R., Similarity of a Chromatic Adaptation Sensor to Phytochrome and Ethylene Receptors. *Science* **1996**, *273* (5280), 1409.
72. Rockwell, N. C.; Njuguna, S. L.; Roberts, L.; Castillo, E.; Parson, V. L.; Dwojak, S.; Lagarias, J. C.; Spiller, S. C., A Second Conserved GAF Domain Cysteine Is Required for the Blue/Green Photoreversibility of Cyanobacteriochrome Tlr0924 from *Thermosynechococcus elongatus*. *Biochemistry* **2008**, *47* (27), 7304-7316.
73. Jenkins, A. J.; Chang, C.-W.; Gregory, J.; Kim, P. W.; Agnew, H.; Martin, S. S.; Rockwell, N. C.; Lagarias, J. C.; Larsen, D. S., Comparison of the Forward and Reverse Secondary Photocycle Dynamics of the Cyanobacterial Phytochrome Cph1 and the Canonical Red/Green Cyanobacteriochrome NpR6012g4 Reveals Unexpected Similarities. *Biochemistry* **xxx**, *Submitted*.
74. Nosrati, M.; Berbasova, T.; Vasileiou, C.; Borhan, B.; Geiger, J. H., A Photoisomerizing Rhodopsin Mimic Observed at Atomic Resolution. *Journal of the American Chemical Society* **2016**, *138* (28), 8802-8808.
75. Berbasova, T.; Nosrati, M.; Vasileiou, C.; Wang, W.; Lee, K. S. S.; Yapici, I.; Geiger, J. H.; Borhan, B., Rational Design of a Colorimetric pH Sensor from a Soluble Retinoic Acid Chaperone. *Journal of the American Chemical Society* **2013**, *135* (43), 16111-16119.
76. Vasileiou, C.; Vaezslami, S.; Crist, R. M.; Montserrat, R.-S.; Geiger, J. H.; Borhan, B., Protein Design: Reengineering Cellular Retinoic Acid Binding Protein II into a Rhodopsin Protein Mimic. *J. Am. Chem. Soc.* **2007**, *129* (19), 6140-6148.

77. Lokshin, V.; Samat, A.; Metelitsa, A. V., Spirooxazines: synthesis, structure, spectral and photochromic properties. *Russian Chemical Reviews* **2002**, *71* (11), 893-916.
78. Klajn, R., Spiropyran-based dynamic materials. *Chemical Society Reviews* **2014**, *43* (1), 148-184.
79. Buback, J.; Kullmann, M.; Langhojer, F.; Nuernberger, P.; Schmidt, R.; Würthner, F.; Brixner, T., Ultrafast Bidirectional Photoswitching of a Spiropyran. *Journal of the American Chemical Society* **2010**, *132* (46), 16510-16519.
80. Hobley, J.; Pfeifer-Fukumura, U.; Bletz, M.; Asahi, T.; Masuhara, H.; Fukumura, H., Ultrafast Photo-Dynamics of a Reversible Photochromic Spiropyran. *The Journal of Physical Chemistry A* **2002**, *106* (10), 2265-2270.
81. Kohl-Landgraf, J.; Braun, M.; Özçoban, C.; Gonçalves, D. P. N.; Heckel, A.; Wachtveitl, J., Ultrafast Dynamics of a Spiropyran in Water. *Journal of the American Chemical Society* **2012**, *134* (34), 14070-14077.
82. Takeda, J.; Ikeda, Y.; Mihara, D.; Kurita, S.; Sawada, A.; Yokoyama, Y., Transient Absorption Spectroscopy for Photochemical Reactions of a Negative Photochromic Spiropyran. *Molecular Crystals and Liquid Crystals Science and Technology. Section A. Molecular Crystals and Liquid Crystals* **2000**, *345* (1), 191-196.
83. Asahi, T.; Masuhara, H., Photocoloration of Spironaphthoxazine Microcrystalline Powder by Femtosecond Laser Pulse Excitation. *Chemistry Letters* **1997**, *26* (11), 1165-1166.
84. Suzuki, M.; Asahi, T.; Masuhara, H., Temperature dependence of ultrafast photoinduced ring-opening and -closure reactions of spironaphthooxazine in crystalline phase. *Journal of Photochemistry and Photobiology A: Chemistry* **2006**, *178* (2), 170-176.
85. Tamai, N.; Masuhara, H., Femtosecond transient absorption spectroscopy of a spirooxazine photochromic reaction. *Chemical Physics Letters* **1992**, *191* (1), 189-194.
86. Suzuki, M.; Asahi, T.; Masuhara, H., Cooperative Photochemical Reaction Mechanism of Femtosecond Laser-Induced Photocoloration in Spirooxazine Microcrystals. *ChemPhysChem* **2005**, *6* (11), 2396-2403.
87. Siddiqui, K. M.; Corthey, G.; Hayes, S. A.; Rossos, A.; Badali, D. S.; Xian, R.; Murphy, R. S.; Whitaker, B. J.; Miller, R. J. D., Synchronised photoreversion of spirooxazine ring opening in thin crystals to uncover ultrafast dynamics. *CrystEngComm* **2016**, *18* (38), 7212-7216.
88. Aramaki, S.; Atkinson, G. H., Spirooxazine photochromism: picosecond time-resolved Raman and absorption spectroscopy. *Chemical Physics Letters* **1990**, *170* (2), 181-186.
89. Suzuki, M.; Asahi, T.; Takahashi, K.; Masuhara, H., Ultrafast dynamics of photoinduced ring-opening and the subsequent ring-closure reactions of spirooxazines in crystalline state. *Chemical Physics Letters* **2003**, *368* (3), 384-392.
90. Buntinx, G.; Foley, S.; Lefumeux, C.; Lokshin, V.; Poizat, O.; Samat, A., Evidence for a photophysical deactivation pathway competing with the photochromic transformation in a cyano-substituted spironaphthoxazine. *Chemical Physics Letters* **2004**, *391* (1), 33-37.
91. Poisson, L.; Raffael, K. D.; Soep, B.; Mestdagh, J.-M.; Buntinx, G., Gas-Phase Dynamics of Spiropyran and Spirooxazine Molecules. *Journal of the American Chemical Society* **2006**, *128* (10), 3169-3178.
92. Antipin, S. A.; Petrukhin, A. N.; Gostev, F. E.; Marevtsev, V. S.; Titov, A. A.; Barachevsky, V. A.; Strokach, Y. P.; Sarkisov, O. M., Femtosecond transient absorption



- spectroscopy of non-substituted photochromic spirocompounds. *Chemical Physics Letters* **2000**, *331* (5), 378-386.
93. di Nunzio, M. R.; Danilov, E. O.; Rodgers, M. A. J.; Favaro, G., Ultrafast excited-state dynamics in some spirooxazines and chromenes. Evidence for a dual relaxation pathway. *Photochemical & Photobiological Sciences* **2010**, *9* (10), 1391-1399.
94. Tamai, N.; Miyasaka, H., Ultrafast Dynamics of Photochromic Systems. *Chemical Reviews* **2000**, *100* (5), 1875-1890.
95. Asahi, T.; Suzuki, M.; Masuhara, H., Cooperative Photochemical Reaction in Molecular Crystal Induced by Intense Femtosecond Laser Excitation: Photochromism of Spiroanthoxazine. *The Journal of Physical Chemistry A* **2002**, *106* (10), 2335-2340.
96. Wilkinson, F.; Worrall, D. R.; Hopley, J.; Jansen, L.; Williams, S. L.; Langley, A. J.; Matousek, P., Picosecond time-resolved spectroscopy of the photocolouration reaction of photochromic naphthoxazine-spiro-indolines. *Journal of the Chemical Society, Faraday Transactions* **1996**, *92* (8), 1331-1336.
97. Kumar, R. S. S.; Luer, L.; Polli, D.; Garbugli, M.; Lanzani, G., Primary photo-events in a metastable photomerocyanine of spirooxazines. *Opt. Mater. Express* **2011**, *1* (2), 293-304.
98. Patel, D. G.; Paquette, M. M.; Kopelman, R. A.; Kaminsky, K.; Ferguson, M. J.; Frank, N. L., A Solution- and Solid-State Investigation of Medium Effects on Charge Separation in Metastable Photomerocyanines. *J. Am. Chem. Soc.* **2012**, *132*, 12568-12586.
99. Stojković, E. A.; Toh, K. C.; Alexandre, M. T. A.; Baclayon, M.; Moffat, K.; Kennis, J. T. M., FTIR Spectroscopy Revealing Light-Dependent Refolding of the Conserved Tongue Region of Bacteriophytochrome. *J. Phys. Chem. Lett.* **2014**, *5* (15), 2512-2515.
100. Kirpich, J. S.; Mix, L. T.; Martin, S. S.; Rockwell, N. C.; Lagarias, J. C.; Larsen, D. S., Protonation Heterogeneity Modulates the Ultrafast Photocycle Initiation Dynamics of Phytochrome Cph1. *J. Phys. Chem. Lett.* **2018**, *9* (12), 3454-3462.
101. Kim, P. W.; Rockwell, N. C.; Martin, S. S.; Lagarias, J. C.; Larsen, D. S., Dynamic inhomogeneity in the photodynamics of cyanobacterial phytochrome Cph1. *Biochemistry* **2014**, *53* (17), 2818-2826.
102. Kim, P. W.; Rockwell, N. C.; Martin, S. S.; Lagarias, J. C.; Larsen, D. S., Heterogeneous Photodynamics of the Pfr State in the Cyanobacterial Phytochrome Cph1. *Biochemistry* **2014**, *53* (28), 4601-4611.
103. Kim, P. W.; Pan, J.; Rockwell, N. C.; Chang, C.-W.; Taylor, K. C.; Lagarias, J. C.; Larsen, D. S., Ultrafast E to Z Photoisomerization Dynamics of the Cph1 Phytochrome. *Chem. Phys. Lett.* **2012**, *549*, 86-92.
104. Kim, P. W.; Rockwell, N. C.; Freer, L. H.; Chang, C.-W.; Martin, S. S.; Lagarias, J. C.; Larsen, D. S., Unraveling the Primary Isomerization Dynamics in Cyanobacterial Phytochrome Cph1 with Multipulse Manipulations. *J. Phys. Chem. Lett.* **2013**, *4* (16), 2605-2609.
105. Burgie, E. S.; Wang, T.; Bussell, A. N.; Walker, J. M.; Li, H.; Vierstra, R. D., Crystallographic and Electron Microscopic Analyses of a Bacterial Phytochrome Reveal Local and Global Rearrangements during Photoconversion. *J. Biol. Chem.* **2014**, *289*, 24573-24587.
106. Burgie, E. S.; Vierstra, R. D., Phytochromes: An Atomic Perspective on Photoactivation and Signaling. *Plant Cell* **2014**, *26* (12), 4568-4583.

107. Anders, K.; Daminelli-Widany, G.; Mroginski, M. A.; von Stetten, D.; Essen, L. O., Structure of the cyanobacterial phytochrome 2 photosensor implies a tryptophan switch for phytochrome signaling. *The Journal of biological chemistry* **2013**, *288* (50), 35714-25.
108. Lim, S.; Yu, Q.; Gottlieb, S. M.; Chang, C.-W.; Rockwell, N. C.; Martin, S. S.; Madsen, D.; Lagarias, J. C.; Larsen, D. S.; Ames, J. B., Correlating structural and photochemical heterogeneity in cyanobacteriochrome NpR6012g4. *Proc. Natl. Acad. Sci.* **2018**, *115* (17), 4387-4392.
109. Nagae, T.; Unno, M.; Koizumi, T.; Miyanoiri, Y.; Fujisawa, T.; Masui, K.; Kamo, T.; Wada, K.; Eki, T.; Ito, Y.; Hirose, Y.; Mishima, M., Structural basis of the protochromic green/red photocycle of the chromatic acclimation sensor RcaE. *Proc. Natl. Acad. Sci.* **2021**, *118* (20), e2024583118.
110. Rockwell, N. C.; Martin, S. S.; Lagarias, J. C., Mechanistic Insight into the Photosensory Versatility of DXCF Cyanobacteriochromes. *Biochemistry* **2012**, *51* (17), 3576-3585.
111. Gottlieb, S. M.; Kim, P. W.; Corley, S. C.; Madsen, D.; Hanke, S. J.; Chang, C.-W.; Rockwell, N. C.; Martin, S. S.; Lagarias, J. C.; Larsen, D. S., Primary and Secondary Photodynamics of the Violet/Orange Dual-Cysteine NpF2164g3 Cyanobacteriochrome Domain from *Nostoc punctiforme*. *Biochemistry* **2014**, *53* (6), 1029-1040.
112. Toh, K. C.; Stojković, E. A.; van Stokkum, I. H. M.; Moffat, K.; Kennis, J. T. M., Proton-transfer and hydrogen-bond interactions determine fluorescence quantum yield and photochemical efficiency of bacteriophytochrome. *Proc. Natl. Acad. Sci.* **2010**, *107* (20), 9170-9175.
113. van Thor, J. J.; Ronayne, K. L.; Towrie, M., Formation of the early photoproduct Lumi-R of cyanobacterial phytochrome Cph1 observed by ultrafast mid-infrared spectroscopy. *J. Am. Chem. Soc.* **2007**, *129* (1), 126-132.
114. Aramendia, P. F.; Ruzsicska, B. P.; Braslavsky, S. E.; Schaffner, K., Laser flash photolysis of 124-kilodalton oat phytochrome in water and deuterium oxide solutions: formation and decay of the I700 intermediates. *Biochemistry* **1987**, *26* (5), 1418-1422.
115. Andel III, F.; Hasson, K. C.; Gai, F.; Anfinrud, P. A.; Mathies, R. A., Femtosecond time-resolved spectroscopy of the primary photochemistry of phytochrome. *Biospectroscopy* **1997**, *3* (6), 421-433.
116. Kendrick, R. E.; de Kok, J., Intermediates in phytochrome phototransformation. *Science Progress (1933-)* **1983**, *68* (272), 475-486.
117. Müller, M. G.; Lindner, I.; Martin, I.; Gärtner, W.; Holzwarth, A. R., Femtosecond Kinetics of Photoconversion of the Higher Plant Photoreceptor Phytochrome Carrying Native and Modified Chromophores. *Biophys. J.* **2008**, *94* (11), 4370-4382.
118. Kneip, C.; Hildebrandt, P.; Schlamann, W.; Braslavsky, S. E.; Mark, F.; Schaffner, K., Protonation State and Structural Changes of the Tetrapyrrole Chromophore during the Pr → Pfr Phototransformation of Phytochrome: A Resonance Raman Spectroscopic Study. *Biochemistry* **1999**, *38* (46), 15185-15192.
119. Schmidt, P.; Gertsch, T.; Remberg, A.; Gärtner, W.; Braslavsky, S. E.; Schaffner, K., The Complexity of the Pr to Pfr Phototransformation Kinetics Is an Intrinsic Property of Native Phytochrome\*. *Photochemistry and Photobiology* **1998**, *68* (5), 754-761.
120. Ruzsicska, B. P.; Braslavsky, S. E.; Schaffner, K., The Kinetics of the Early Stages of the Phytochrome Phototransformation Pr → Pfr. A Comparative Study of Small (60 Kdalton) and

- Native (124 Kdalton) Phytochromes from Oat. *Photochemistry and Photobiology* **1985**, *41* (6), 681-688.
121. Holzwarth, A. R.; Venuti, E.; Braslavsky, S. E.; Schaffner, K., The phototransformation process in phytochrome. I. Ultrafast fluorescence component and kinetic models for the initial Pr → Pfr transformation steps in native phytochrome. *Biochimica et Biophysica Acta (BBA) - Bioenergetics* **1992**, *1140* (1), 59-68.
122. Bischoff, M.; Hermann, G.; Rentsch, S.; Strehlow, D., Ultrashort Processes of Native Phytochrome: Femtosecond Kinetics of the Far-Red-Absorbing Form Pfr. *The Journal of Physical Chemistry A* **1998**, *102* (23), 4399-4404.
123. Bischoff, M.; Hermann, G.; Rentsch, S.; Strehlow, D., First Steps in the Phytochrome Phototransformation: A Comparative Femtosecond Study on the Forward (Pr → Pfr) and Back Reaction (Pfr → Pr). *Biochemistry* **2001**, *40* (1), 181-186.
124. Chizhov, I.; Zorn, B.; Manstein, Dietmar J.; Gärtner, W., Kinetic and Thermodynamic Analysis of the Light-induced Processes in Plant and Cyanobacterial Phytochromes. *Biophys. J.* **2013**, *105* (9), 2210-2220.
125. Schmidt, P.; Westphal, U. H.; Worm, K.; Braslavsky, S. E.; Gärtner, W.; Schaffner, K., Chromophore-protein interaction controls the complexity of the phytochrome photocycle. *Journal of Photochemistry and Photobiology B-Biology* **1996**, *34* (1), 73-77.
126. Sineshchekov, V. A.; Akhobadze, V. V., Phytochrome States in Etiolated Pea Seedlings: Fluorescence and Primary Photoreactions at Low Temperatures. *Photochemistry and Photobiology* **1992**, *56* (5), 743-749.
127. Kendrick, R. E.; Spruit, C. J. P., Phytochrome Intermediates in vivo – III Kinetic Analysis of Intermediate Reactions at Low Temperature. *Photochemistry and Photobiology* **1973**, *18* (2), 153-159.
128. Mizutani, Y.; Tokutomi, S.; Kitagawa, T., Resonance Raman spectra of the intermediates in phototransformation of large phytochrome: deprotonation of the chromophore in the bleached intermediate. *Biochemistry* **1994**, *33* (1), 153-8.
129. Spruit, C. J. P.; Kendrick, R. E., Phototransformations of Phytochrome: The Characterization of Lumi-F and Meta-Fa. *Photochemistry and Photobiology* **1977**, *26* (2), 133-138.
130. Pratt, L. H.; Inoue, Y.; Furuya, M., Photoactivity of Transient Intermediates in the Pathway From the Red-Absorbing to the Far-Red-Absorbing Form of Avena Phytochrome as Observed by a Double-Flash Transient-Spectrum Analyzer. *Photochemistry and Photobiology* **1984**, *39* (2), 241-246.
131. Pratt, L. H.; Smmazakit, Y.; Inoue, Y.; Furuya, M., Analysis of Phototransformation Intermediates in the Pathway from the Red-Absorbing to the Far-Red-Absorbing Form of Avena Phytochrome by a Multichannel Transient Spectrum Analyzer. *Photochemistry and Photobiology* **1982**, *36* (4), 471-477.
132. Sineshchekov, V. A., Fluorescence and Photochemical Investigations of Phytochrome in Higher Plants. *Journal of Botany* **2010**, *2010*.
133. Sineshchekov, V. A., Evidence for the existence of two phytochrome A populations. *Journal of Photochemistry and Photobiology B: Biology* **1995**, *28* (1), 53-55.

134. Ruddat, A.; Schmidt, P.; Gatz, C.; Braslavsky, S. E.; Gärtner, W.; Schaffner, K., Recombinant Type A and B Phytochromes from Potato. Transient Absorption Spectroscopy. *Biochemistry* **1997**, *36* (1), 103-111.
135. van Thor, J. J.; Borucki, B.; Crielaard, W.; Otto, H.; Lamparter, T.; Hughes, J.; Hellingwerf, K. J.; Heyne, M. P., Light-induced proton release and proton uptake reactions in the cyanobacterial phytochrome Cph1. *Biochemistry* **2001**, *40* (38), 11460-11471.
136. Kaminski, S.; Mroginski, M. A., Molecular Dynamics of Phycocyanobilin Binding Bacteriophytochromes: A Detailed Study of Structural and Dynamic Properties. *Journal of Physical Chemistry B* **2010**, *114* (50), 16677-16686.
137. Heyne, K.; Herbst, J.; Stehlik, D.; Esteban, B.; Lamparter, T.; Hughes, J.; Diller, R., Ultrafast dynamics of phytochrome from the cyanobacterium *Synechocystis*, reconstituted with phycocyanobilin and phycoerythrobilin. *Biophys. J.* **2002**, *82* (2), 1004-1016.
138. van Wilderen, L. J.; Clark, I. P.; Towrie, M.; van Thor, J. J., Mid-infrared picosecond pump-dump-probe and pump-repump-probe experiments to resolve a ground-state intermediate in cyanobacterial phytochrome Cph1. *The journal of physical chemistry. B* **2009**, *113* (51), 16354-64.
139. Fitzpatrick, A. E.; Lincoln, C. N.; van Wilderen, L. J.; van Thor, J. J., Pump-dump-probe and pump-repump-probe ultrafast spectroscopy resolves cross section of an early ground state intermediate and stimulated emission in the photoreactions of the Pr ground state of the cyanobacterial phytochrome Cph1. *The journal of physical chemistry. B* **2012**, *116* (3), 1077-88.
140. Dasgupta, J.; Frontiera, R. R.; Taylor, K. C.; Lagarias, J. C.; Mathies, R. A., Ultrafast excited-state isomerization in phytochrome revealed by femtosecond stimulated Raman spectroscopy. *Proc. Natl. Acad. Sci.* **2009**, *106* (6), 1784-1789.
141. Mroginski, M. A.; von Stetten, D.; Escobar, F. V.; Strauss, H. M.; Kaminski, S.; Scheerer, P.; Gunther, M.; Murgida, D. H.; Schmieder, P.; Bongards, C.; Gärtner, W.; Mailliet, J.; Hughes, J.; Essen, L. O.; Hildebrandt, P., Chromophore Structure of Cyanobacterial Phytochrome Cph1 in the Pr State: Reconciling Structural and Spectroscopic Data by QM/MM Calculations. *Biophys. J.* **2009**, *96* (10), 4153-4163.
142. Yang, Y.; Linke, M.; von Haimberger, T.; Hahn, J.; Matute, R.; González, L.; Schmieder, P.; Heyne, K., Real-Time Tracking of Phytochrome's Orientational Changes During Pr Photoisomerization. *J. Am. Chem. Soc.* **2012**, *134* (3), 1408-1411.
143. Foerstendorf, H.; Lamparter, T.; Hughes, J.; Gärtner, W.; Siebert, F., The Photoreactions of Recombinant Phytochrome from the Cyanobacterium *Synechocystis*: A Low-Temperature UV-Vis and FT-IR Spectroscopic Study. *Photochem. Photobiol.* **2000**, *71* (5), 655-661.
144. Yang, Y.; Linke, M.; Haimberger, T. v.; Matute, R.; González, L.; Schmieder, P.; Heyne, K., Active and silent chromophore isoforms for phytochrome Pr photoisomerization: An alternative evolutionary strategy to optimize photoreaction quantum yields. *Structural Dynamics* **2014**, *1* (1), 014701.
145. Sineshchekov, V.; Koppel, L.; Esteban, B.; Hughes, J.; Lamparter, T., Fluorescence investigation of the recombinant cyanobacterial phytochrome (Cph1) and its C-terminally truncated monomeric species (Cph1Δ2): implication for holoprotein assembly, chromophore-apoprotein interaction and photochemistry. *Journal of Photochemistry and Photobiology B: Biology* **2002**, *67* (1), 39-50.

146. Otto, H.; Lamparter, T.; Borucki, B.; Hughes, J.; Heyn, M. P., Dimerization and Inter-Chromophore Distance of Cph1 Phytochrome from *Synechocystis*, as Monitored by Fluorescence Homo and Hetero Energy Transfer. *Biochemistry* **2003**, *42* (19), 5885-5895.
147. Frontiera, R. R.; Fang, C.; Dasgupta, J.; Mathies, R. A., Probing structural evolution along multidimensional reaction coordinates with femtosecond stimulated Raman spectroscopy. *Physical Chemistry Chemical Physics* **2012**, *14* (2), 405-414.
148. Bizimana, L. A.; Epstein, J.; Brazard, J.; Turner, D. B., Conformational Homogeneity in the Pr Isomer of Phytochrome Cph1. *The Journal of Physical Chemistry B* **2017**, *121* (12), 2622-2630.
149. Stensitzki, T.; Yang, Y.; Wolke, A. L.; Knapp, E. W.; Hughes, J.; Mroginski, M. A.; Heyne, K., Influence of Heterogeneity on the Ultrafast Photoisomerization Dynamics of Pfr in Cph1 Phytochrome. *Photochem Photobiol* **2017**, *93* (3), 703-712.
150. Rohmer, T.; Lang, C.; Bongards, C.; Gupta, K.; Neugebauer, J.; Hughes, J.; Gartner, W.; Matysik, J., Phytochrome as Molecular Machine: Revealing Chromophore Action during the Pfr → Pr Photoconversion by Magic-Angle Spinning NMR Spectroscopy (vol 132, pg 4431, 2010). *Journal of the American Chemical Society* **2010**, *132* (26), 9219-9219.
151. Schwinté, P.; Gärtner, W.; Sharda, S.; Mroginski, M. A.; Hildebrandt, P.; Siebert, F., The Photoreactions of Recombinant Phytochrome CphA from the Cyanobacterium *Calothrix* PCC7601: A Low-Temperature UV-Vis and FTIR Study. *Photochem. Photobiol.* **2009**, *85* (1), 239-249.
152. Jorissen, H. J.; Quest, B.; Remberg, A.; Coursin, T.; Braslavsky, S. E.; Schaffner, K.; de Marsac, N. T.; Gartner, W., Two independent, light-sensing two-component systems in a filamentous cyanobacterium. *European journal of biochemistry* **2002**, *269* (11), 2662-71.
153. Borucki, B.; von Stetten, D.; Seibeck, S.; Lamparter, T.; Michael, N.; Mroginski, M. A.; Otto, H.; Murgida, D. H.; Heyn, M. P.; Hildebrandt, P., Light-induced proton release of phytochrome is coupled to the transient deprotonation of the tetrapyrrole chromophore. *The Journal of biological chemistry* **2005**, *280* (40), 34358-64.
154. Borucki, B.; Seibeck, S.; Heyn, M. P.; Lamparter, T., Characterization of the Covalent and Noncovalent Adducts of Agp1 Phytochrome Assembled with Biliverdin and Phycocyanobilin by Circular Dichroism and Flash Photolysis. *Biochemistry* **2009**, *48* (27), 6305-6317.
155. Schumann, C.; Groß, R.; Wolf, M. M. N.; Diller, R.; Michael, N.; Lamparter, T., Subpicosecond Midinfrared Spectroscopy of the Pfr Reaction of Phytochrome Agp1 from *Agrobacterium tumefaciens*. *Biophys. J.* **2008**, *94* (8), 3189-3197.
156. Linke, M.; Yang, Y.; Zienicke, B.; Hammam, M. A.; von Haimberger, T.; Zacarias, A.; Inomata, K.; Lamparter, T.; Heyne, K., Electronic transitions and heterogeneity of the bacteriophytochrome Pr absorption band: An angle balanced polarization resolved femtosecond VIS pump-IR probe study. *Biophys J* **2013**, *105* (8), 1756-66.
157. Singer, P.; Wörner, S.; Lamparter, T.; Diller, R., Spectroscopic Investigation on the Primary Photoreaction of Bathy Phytochrome Agp2-Pr of *Agrobacterium fabrum*: Isomerization in a pH-dependent H-bond Network. *ChemPhysChem* **2016**, *17* (9), 1288-1297.
158. Takala, H.; Niebling, S.; Berntsson, O.; Björling, A.; Lehtivuori, H.; Häkkänen, H.; Panman, M.; Gustavsson, E.; Hoernke, M.; Newby, G.; Zontone, F.; Wulff, M.; Menzel, A.; Ihalainen, J. A.; Westenhoff, S., Light-induced structural changes in a monomeric bacteriophytochrome. *Structural Dynamics* **2016**, *3* (5), 054701.

159. Falklöf, O.; Durbeej, B., Steric Effects Govern the Photoactivation of Phytochromes. *ChemPhysChem* **2016**, *17* (7), 954-957.
160. Kaminski, S.; Daminelli, G.; Mroginski, M. A., Molecular Dynamics Simulations of the Chromophore Binding Site of *Deinococcus radiodurans* Bacteriophytochrome Using New Force Field Parameters for the Phytychromobilin Chromophore. *Journal of Physical Chemistry B* **2009**, *113* (4), 945-958.
161. Feliks, M.; Lafaye, C.; Shu, X.; Royant, A.; Field, M., Structural Determinants of Improved Fluorescence in a Family of Bacteriophytochrome-Based Infrared Fluorescent Proteins: Insights from Continuum Electrostatic Calculations and Molecular Dynamics Simulations. *Biochemistry* **2016**, *55* (31), 4263-74.
162. Hontani, Y.; Shcherbakova, D. M.; Baloban, M.; Zhu, J.; Verkhusha, V. V.; Kennis, J. T. M., Bright blue-shifted fluorescent proteins with Cys in the GAF domain engineered from bacterial phytochromes: fluorescence mechanisms and excited-state dynamics. *Scientific Reports* **2016**, *6*, 37362.
163. Mathes, T.; Ravensbergen, J.; Kloz, M.; Gleichmann, T.; Gallagher, K. D.; Woitowich, N. C.; Peter, R. S.; Kovaleva, S. E.; Stojković, E. A.; Kennis, J. T. M., Femto- to Microsecond Photodynamics of an Unusual Bacteriophytochrome. *J. Phys. Chem. Lett.* **2014**, *6* (2), 239-243.
164. Zhu, J.; Shcherbakova, D. M.; Hontani, Y.; Verkhusha, V. V.; Kennis, J. T. M., Ultrafast excited-state dynamics and fluorescence deactivation of near-infrared fluorescent proteins engineered from bacteriophytochromes. *Scientific Reports* **2015**, *5*, 12840.
165. Wang, C.; Flanagan, Moira L.; McGillicuddy, Ryan D.; Zheng, H.; Ginzburg, Alan R.; Yang, X.; Moffat, K.; Engel, Gregory S., Bacteriophytochrome Photoisomerization Proceeds Homogeneously Despite Heterogeneity in Ground State. *Biophys. J.* **2016**, *111* (10), 2125-2134.
166. Velazquez Escobar, F.; Hildebrandt, T.; Utesch, T.; Schmitt, F. J.; Seuffert, I.; Michael, N.; Schulz, C.; Mroginski, M. A.; Friedrich, T.; Hildebrandt, P., Structural Parameters Controlling the Fluorescence Properties of Phytochromes. *Biochemistry* **2014**, *53* (1), 20-29.
167. Toh, K. C.; Stojkovic, E. A.; Rupenyan, A. B.; van Stokkum, I. H.; Salumbides, M.; Groot, M. L.; Moffat, K.; Kennis, J. T., Primary reactions of bacteriophytochrome observed with ultrafast mid-infrared spectroscopy. *The journal of physical chemistry. A* **2011**, *115* (16), 3778-86.
168. Toh, K. C.; Stojkovic, E. A.; van Stokkum, I. H.; Moffat, K.; Kennis, J. T., Fluorescence quantum yield and photochemistry of bacteriophytochrome constructs. *Physical chemistry chemical physics : PCCP* **2011**, *13* (25), 11985-97.
169. Yang, X.; Ren, Z.; Kuk, J.; Moffat, K., Temperature-scan cryocrystallography reveals reaction intermediates in bacteriophytochrome. *Nature* **2011**, *479*, 428.
170. Velazquez Escobar, F.; Piwowarski, P.; Salewski, J.; Michael, N.; Fernandez Lopez, M.; Rupp, A.; Qureshi, B. M.; Scheerer, P.; Bartl, F.; Frankenberg-Dinkel, N.; Siebert, F.; Andrea Mroginski, M.; Hildebrandt, P., A protonation-coupled feedback mechanism controls the signalling process in bathy phytochromes. *Nature Chemistry* **2015**, *7*, 423.
171. Anders, K.; Gutt, A.; Gärtner, W.; Essen, L.-O., Phototransformation of the Red Light Sensor Cyanobacterial Phytochrome 2 from *Synechocystis* Species Depends on Its Tongue Motifs. *The Journal of biological chemistry* **2014**, *289* (37), 25590-25600.
172. Wu, S. H.; Lagarias, J. C., Defining the bilin lyase domain: Lessons from the extended phytochrome superfamily. *Biochemistry* **2000**, *39* (44), 13487-13495.

173. Park, C.-M.; Kim, J.-I.; Yang, S.-S.; Kang, J.-G.; Kang, J.-H.; Shim, J.-Y.; Chung, Y.-H.; Park, Y.-M.; Song, P.-S., A Second Photochromic Bacteriophytochrome from *Synechocystis* sp. PCC 6803: Spectral Analysis and Down-Regulation by Light. *Biochemistry* **2000**, *39* (35), 10840-10847.
174. Vierstra, R. D.; Zhang, J., Phytochrome signaling: solving the Gordian knot with microbial relatives. *Trends in plant science* **2011**, *16* (8), 417-26.
175. Ulijasz, A. T.; Cornilescu, G.; von Stetten, D.; Kaminski, S.; Mroginski, M. A.; Zhang, J.; Bhaya, D.; Hildebrandt, P.; Vierstra, R. D., Characterization of Two Thermostable Cyanobacterial Phytochromes Reveals Global Movements in the Chromophore-binding Domain during Photoconversion. *Journal of Biological Chemistry* **2008**, *283* (30), 21251-21266.
176. Gottlieb, S. M.; Kim, P. W.; Chang, C.-W.; Hanke, S. J.; Hayer, R. J.; Rockwell, N. C.; Martin, S. S.; Lagarias, J. C.; Larsen, D. S., Conservation and Diversity in the Primary Forward Photodynamics of Red/Green Cyanobacteriochromes. *Biochemistry* **2015**, *54* (4), 1028-1042.
177. Fukushima, Y.; Iwaki, M.; Narikawa, R.; Ikeuchi, M.; Tomita, Y.; Itoh, S., Photoconversion Mechanism of a Green/Red Photosensory Cyanobacteriochrome AnPixJ: Time-Resolved Optical Spectroscopy and FTIR Analysis of the AnPixJ-GAF2 Domain. *Biochemistry* **2011**, *50* (29), 6328-6339.
178. Tachibana, S. R.; Tang, L.; Zhu, L.; Takeda, Y.; Fushimi, K.; Ueda, Y.; Nakajima, T.; Kuwasaki, Y.; Sato, M.; Narikawa, R.; Fang, C., An Engineered Biliverdin-Compatible Cyanobacteriochrome Enables a Unique Ultrafast Reversible Photoswitching Pathway. *Int. J. Mol. Sci.* **2021**, 5252.
179. Jenkins, A. J.; Chang, C.-W.; Madsen, D.; Gottlieb, S. M.; Hayer, R. J.; Lee, H.; Martin, S. S.; Lagarias, J. C.; Larsen, D. S., Conservation and Diversity in the Secondary Reverse Photodynamics of Red/Green Cyanobacteriochromes. *in preparation xxx*.
180. Chang, C.-W.; Gottlieb, S. M.; Kim, P. W.; Rockwell, N. C.; Lagarias, J. C.; Larsen, D. S., Reactive Ground-State Pathways Are Not Ubiquitous in Red/Green Cyanobacteriochromes. *J. Phys. Chem. B* **2013**, *117* (38), 11229-11238.
181. Jenkins, A.; Agnew, H.; Chang, C. W.; Kirpich, J. S.; Mix, L. T.; Martin, S. S.; Lagarias, C. J.; Larsen, D. S., Cryokinetics of the Subclasses of Cyanobacteriochromes. *in preparation xxx*.
182. Kim, P. W.; Freer, L. H.; Rockwell, N. C.; Martin, S. S.; Lagarias, J. C.; Larsen, D. S., Femtosecond Photodynamics of the Red/Green Cyanobacteriochrome NpR6012g4 from *Nostoc punctiforme*. 1. Forward Dynamics. *Biochemistry* **2012**, *51* (2), 608-618.
183. Kim, P. W.; Freer, L. H.; Rockwell, N. C.; Martin, S. S.; Lagarias, J. C.; Larsen, D. S., Femtosecond Photodynamics of the Red/Green Cyanobacteriochrome NpR6012g4 from *Nostoc punctiforme*. 2. Reverse Dynamics. *Biochemistry* **2012**, *51* (2), 619-630.
184. Kim, P. W.; Freer, L. H.; Rockwell, N. C.; Martin, S. S.; Lagarias, C. J.; Larsen, D. S., Second-Chance Forward Isomerization Dynamics of the Red/Green Cyanobacteriochrome NpR6012g4 from *Nostoc punctiforme*. *J. Am. Chem. Soc.* **2012**, *134* (1), 130-133.
185. Slavov, C.; Xu, X.; Zhao, K.-h.; Gärtner, W.; Wachtveitl, J., Detailed insight into the ultrafast photoconversion of the cyanobacteriochrome Slr1393 from *Synechocystis* sp. *Biochim. Biophys. Acta* **2015**, *1847* (10), 1335-1344.
186. Xu, X. L.; Gutt, A.; Mechelke, J.; Raffelberg, S.; Tang, K.; Miao, D.; Valle, L.; Borsarelli, C. D.; Zhao, K. H.; Gartner, W., Combined mutagenesis and kinetics characterization

- of the bilin-binding GAF domain of the protein Slr1393 from the Cyanobacterium *Synechocystis* PCC6803. *ChemBiochem : a European journal of chemical biology* **2014**, *15* (8), 1190-9.
187. Kirpich, J. S.; Chang, C. W.; Madsen, D.; Gottlieb, S. M.; Martin, S. S.; Rockwell, N. C.; Lagarias, J. C.; Larsen, D. S., Noncanonical Photodynamics of the Orange/Green Cyanobacteriochrome Power Sensor NpF2164g7 from the PtxD Phototaxis Regulator of *Nostoc punctiforme*. *Biochemistry* **2018**, *57* (18), 2636-2648.
  188. Kirpich, J. S.; Gottlieb, S. M.; Chang, C. W.; Kim, P. W.; Martin, S. S.; Lagarias, J. C.; Larsen, D. S., Forward Photodynamics of the Noncanonical Red/Green NpR3784 Cyanobacteriochrome from *Nostoc punctiforme*. *Biochemistry* **2019**, *58* (18), 2297-2306.
  189. Kirpich, J. S.; Gottlieb, S. M.; Chang, C.-W.; Kim, P. W.; Martin, S. S.; Lagarias, J. C.; Larsen, D. S., Reverse Photodynamics of the Noncanonical Red/Green NpR3784 Cyanobacteriochrome from *Nostoc punctiforme*. *Biochemistry* **2019**, *58* (18), 2307-2317.
  190. Gottlieb, S. M.; Chang, C. W.; Martin, S. S.; Rockwell, N. C.; Lagarias, J. C.; Larsen, D. S., Optically Guided Photoactivity: Coordinating Tautomerization, Photoisomerization, Inhomogeneity, and Reactive Intermediates within the RcaE Cyanobacteriochrome. *J. Phys. Chem. Lett.* **2014**, *5* (9), 1527-1533.
  191. Gottlieb, S. M.; Kim, P. W.; Rockwell, N. C.; Hirose, Y.; Ikeuchi, M.; Lagarias, J. C.; Larsen, D. S., Primary photodynamics of the green/red-absorbing photoswitching regulator of the chromatic adaptation E domain from *Fremyella diplosiphon*. *Biochemistry* **2013**, *52* (46), 8198-208.
  192. Chang, C.-W.; Gottlieb, S. M.; Rockwell, N. C.; Martin, S. S.; Lagarias, J. C.; Larsen, D. S., Tracking the secondary photodynamics of the green/red cyanobacteriochrome RcaE from *Fremyella diplosiphon*. *Chemical Physics Letters* **2016**, *644*, 225-230.
  193. Hardman, S. J. O.; Hauck, A. F. E.; Clark, I. P.; Heyes, D. J.; Scrutton, N. S., Comprehensive analysis of the green-to-blue photoconversion of full-length Cyanobacteriochrome Tlr0924. *Biophys. J.* **2014**, *107* (9), 2195-2203.
  194. Hauck, A. F.; Hardman, S. J.; Kutta, R. J.; Greetham, G. M.; Heyes, D. J.; Scrutton, N. S., The photoinitiated reaction pathway of full-length cyanobacteriochrome Tlr0924 monitored over 12 orders of magnitude. *The Journal of biological chemistry* **2014**, *289* (25), 17747-57.
  195. Freer, L. H.; Kim, P. W.; Corley, S. C.; Rockwell, N. C.; Zhao, L.; Thibert, A. J.; Lagarias, J. C.; Larsen, D. S., Chemical Inhomogeneity in the Ultrafast Dynamics of the DXCF Cyanobacteriochrome Tlr0924. *J. Phys. Chem. B* **2012**, *116* (35), 10571-10581.
  196. Sato, T.; Kikukawa, T.; Miyoshi, R.; Kajimoto, K.; Yonekawa, C.; Fujisawa, T.; Unno, M.; Eki, T.; Hirose, Y., Protochromic absorption changes in the two-cysteine photocycle of a blue/orange cyanobacteriochrome. *Journal of Biological Chemistry* **2019**, *294*, 18909-18922.
  197. Rockwell, N. C.; Martin, S. S.; Gulevich, A. G.; Lagarias, J. C., Conserved Phenylalanine Residues Are Required for Blue-Shifting of Cyanobacteriochrome Photoproducts. *Biochemistry* **2014**, *53* (19), 3118-3130.
  198. Zhang, f.; Vierock, J.; Yizhar, O.; Fenno, L. E.; Tsunoda, S.; Kianianmomeni, A.; Prigge, M.; Berndt, A.; Cushman, J.; Polle, J.; Magnuson, J.; Hegemann, P.; Deisseroth, K., The Microbial Opsin Family as Optogenetic Tools. *Cell* **2011**, *147* (7), 1446-1457.
  199. Terakita, A., The opsins. *Genome Biol* **2005**, *6* (3), 213.
  200. Senova, S.; Poupon, C.; Dauguet, J.; Stewart, H. J.; Dugué, G. P.; Jan, C.; Hosomi, K.; Ralph, G. S.; Barnes, L.; Drouot, X.; Pouzat, C.; Mangin, J. F.; Pain, F.; Doignon, I.; Aron-



- Badin, R.; Brouillet, E.; Boyden, E. S.; Mitrophanous, K. A.; Hantraye, P.; Palfi, S., Optogenetic Tractography for anatomo-functional characterization of cortico-subcortical neural circuits in non-human primates. *Scientific Reports* **2018**, *8* (1), 3362.
201. Boyden, E. S.; Zhang, F.; Bamberg, E.; Nagel, G.; Deisseroth, K., Millisecond-timescale, genetically targeted optical control of neural activity. *Nat. Neurosci.* **2005**, *8* (9), 1263-1268.
202. LaLumiere, R. T., A new technique for controlling the brain: optogenetics and its potential for use in research and the clinic. *Brain Stimul.* **2011**, *4* (1), 1-6.
203. Arenkiel, B. R.; Peca, J.; Davison, I. G.; Feliciano, C.; Deisseroth, K.; Augustine, G. J.; Ehlers, M.; Feng, G., In vivo light-induced activation of neural circuitry in transgenic mice expressing channelrhodopsin-2. *Neuron* **2013**, *54* (2), 205-218.
204. Lee, J. H.; Kreitzer, A. C.; Singer, A. C.; Schiff, N. D., Illuminating Neural Circuits: From Molecules to MRI. *The Journal of Neuroscience* **2017**, *37* (45), 10817.
205. Ernst, O. P.; Lodowski, D. T.; M., E.; Hegemann, P.; Berown, L. S., Microbial and Animal Rhodopsins: Structures, Functions, and Molecular Mechanism. *Chem. Rev.* **2014**, *114*, 126-163.
206. Kiser, P. D.; Golczak, M.; Palczewski, K., Chemistry of the Retinoid (Visual) Cycle. *Chem. Rev.* **2014**, *114* (1), 194-232.
207. Karasuyama, M.; Inoue, K.; Nakamura, R.; al., e., Understanding Colour Tuning Rules and Predicting Absorption Wavelengths of Microbial Rhodopsins by Data-Driven Machine-Learning Approach. *Sci. Rep.* **2018**, *8*, 15580.
208. Wang, W.; Geiger, J. H.; Borhan, B., The photochemical determinants of color vision: Revealing how opsins tune their chromophore's absorption wavelength. *Bioessays* **2014**, *36* (1), 65-74.
209. Huntress, M. H.; Gozem, S.; Malley, K. R.; Jailaubekov, A. E.; Vasileiou, C.; Vengris, M.; Geiger, J. H.; Borhan, B.; Schapiro, I.; Larsen, D. S.; Olivucci, M., Toward an Understanding of the Retinal Chromophore in Rhodopsin Mimics. *The journal of physical chemistry. B* **2013**, *117*, 10053-10070.
210. Hirose, Y.; Shimada, T.; Narikawa, R.; Katayama, M.; Ikeuchi, M., Cyanobacteriochrome CcaS is the green light receptor that induces the expression of phycobilisome linker protein. *Proc. Natl. Acad. Sci.* **2008**, *105*, 9528-9533.
211. Rockwell, N. C.; Martin, S. S.; Lagarias, J. C., There and Back Again: Loss and Reacquisition of Two-Cys Photocycles in Cyanobacteriochromes. *Photochemistry and Photobiology* **2017**, *93* (3), 741-754.
212. Rockwell, N. C.; Martin, S. S.; Lim, S.; Lagarias, J. C.; Ames, J. B., Characterization of Red/Green Cyanobacteriochrome NpR6012g4 by Solution Nuclear Magnetic Resonance Spectroscopy: A Hydrophobic Pocket for the C15-E,anti Chromophore in the Photoproduct. *Biochemistry* **2015**, *54* (24), 3772-3783.
213. Rockwell, N. C.; Shang, L.; Martin, S. S.; Lagarias, J. C., Distinct classes of red/far-red photochemistry within the phytochrome superfamily. *Proceedings of the National Academy of Sciences of the United States of America* **2009**, *106* (15), 6123-6127.
214. Gambetta, G. A.; Lagarias, J. C., Genetic engineering of phytochrome biosynthesis in bacteria. *Proc. Natl. Acad. Sci. USA* **2001**, *98* (19), 10566-10571.
215. Gaeta, A. L., Catastrophic Collapse of Ultrashort Pulses. *Phys. Rev. Lett.* **2000**, *84*, 3582.

216. Ahmed, J.; Siyal, M. Y.; Adeel, F.; Hussain, A., Supercontinuum Generation by Nonlinear Optics. In *Optical Signal Processing by Silicon Photonics*, Singer: Singapore, 2013.
217. Polson, R. C.; Vardeny, Z. V., nanomaterials. In *Nanomaterials*, 2011.
218. Bonifacio, R.; Lugiato, L. A., Cooperative radiation processes in two-level systems: Superfluorescence. *Physical Review A* **1975**, *11* (5), 1507-1521.
219. Manzoni, C.; Cerullo, G., Design criteria for ultrafast optical parametric amplifiers. *J. Opt.* **2016**, *18*, 103501.
220. A., K. D., Theory of Optical Parametric Noise. *Physical Review* **1968**, *174* (3), 1027-1041.
221. van Stokkum, I. H. M.; Larsen, D. S.; van Grondelle, R., Global and target analysis of time-resolved spectra. *Biochimica et Biophysica Acta (BBA) - Bioenergetics* **2004**, *1657* (2), 82-104.
222. Stajic, J., The Future of Quantum Information Processing. *Science* **2013**, *339* (6124), 1163-1163.
223. Kaufman, A. M.; Lester, B. J.; Reynolds, C. M.; Wall, M. L.; Foss-Feig, M.; Hazzard, K. R. A.; Rey, A. M.; Regal, C. A., Two-particle quantum interference in tunnel-coupled optical tweezers. *Science* **2014**, *345* (6194), 306-309.
224. Bobbert, P. A., Manipulating spin in organic spintronics. *Science* **2014**, *345* (6203), 1450-1451.
225. Sato, O.; Iyoda, T.; Fujishima, A.; Hashimoto, K., Photoinduced magnetization of a cobalt-iron cyanide. *Science* **1996**, *272* (5262), 704-705.
226. Poganiuch, P.; Decurtins, S.; Gutlich, P., Thermal-Induced And Light-Induced Spin Transition In Fe(Mtz)6 (Bf4)2 - 1st Successful Formation Of A Metastable Low-Spin State By Irradiation With Light At Low-Temperatures. *Journal of the American Chemical Society* **1990**, *112* (9), 3270-3278.
227. Matsumoto, T.; Newton, G. N.; Shiga, T.; Hayami, S.; Matsui, Y.; Okamoto, H.; Kumai, R.; Murakami, Y.; Oshio, H., Programmable spin-state switching in a mixed-valence spin-crossover iron grid. *Nature Communications* **2014**, *5*.
228. Talham, D. R.; Meisel, M. W., Thin films of coordination polymer magnets. *Chemical Society Reviews* **2011**, *40* (6), 3356-3365.
229. Bousseksou, A.; Molnar, G.; Salmon, L.; Nicolazzi, W., Molecular spin crossover phenomenon: recent achievements and prospects. *Chemical Society Reviews* **2011**, *40* (6), 3313-3335.
230. Ababei, R.; Pichon, C.; Roubeau, O.; Li, Y. G.; Brefuel, N.; Buisson, L.; Guionneau, P.; Mathoniere, C.; Clerac, R., Rational Design of a Photomagnetic Chain: Bridging Single-Molecule Magnets with a Spin-Crossover Complex. *Journal of the American Chemical Society* **2013**, *135* (39), 14840-14853.
231. Cafun, J. D.; Lejeune, J.; Baudelet, F.; Dumas, P.; Itie, J. P.; Bleuzen, A., Room-Temperature Photoinduced Electron Transfer in a Prussian Blue Analogue under Hydrostatic Pressure. *Angewandte Chemie-International Edition* **2012**, *51* (36), 9146-9148.
232. Ohkoshi, S. I.; Tokoro, H., Photomagnetism in Cyano-Bridged Bimetal Assemblies. *Accounts of Chemical Research* **2012**, *45* (10), 1749-1758.
233. Hoshino, N.; Iijima, F.; Newton, G. N.; Yoshida, N.; Shiga, T.; Nojiri, H.; Nakao, A.; Kumai, R.; Murakami, Y.; Oshio, H., Three-way switching in a cyanide-bridged CoFe chain. *Nature Chemistry* **2012**, *4* (11), 921-926.

234. Gros, C. R.; Peprah, M. K.; Hosterman, B. D.; Brinzari, T. V.; Quintero, P. A.; Sendova, M.; Meisel, M. W.; Talham, D. R., Light-Induced Magnetization Changes in a Coordination Polymer Heterostructure of a Prussian Blue Analogue and a Hofmann-like Fe(II) Spin Crossover Compound. *Journal of the American Chemical Society* **2014**, *136* (28), 9846-9849.
235. Michelle M. Paquette, D. P., Aiko Kurimoto, Brian O. Patrick, and Natia L. Frank, Photoswitchable Molecular Magnets for Nonvolatile Memory Applications.
236. Paquette, M. M.; Patrick, B. O.; Frank, N. L., Determining the Magnitude and Direction of Photoinduced Ligand Field Switching in Photochromic Metal–Organic Complexes: Molybdenum–Tetracarbonyl Spirooxazine Complexes. *Journal of the American Chemical Society* **2011**, *133* (26), 10081-10093.
237. Adams, D. M.; Dei, A.; Rheingold, A. L.; Hendrickson, D. N., Bistability in the [CoII(semiquinonate)<sub>2</sub>] to [CoIII(catecholate)(semiquinonate)] valence-tautomeric conversion. *Journal of the American Chemical Society* **1993**, *115* (18), 8221-8229.
238. Adams, D. M.; Hendrickson, D. N., Pulsed Laser Photolysis and Thermodynamics Studies of Intramolecular Electron Transfer in Valence Tautomeric Cobalt o-Quinone Complexes. *Journal of the American Chemical Society* **1996**, *118* (46), 11515-11528.
239. Castro, P. J.; Gómez, I.; Cossi, M.; Reguero, M., Computational Study of the Mechanism of the Photochemical and Thermal Ring-Opening/Closure Reactions and Solvent Dependence in Spirooxazines. *The Journal of Physical Chemistry A* **2012**, *116* (31), 8148-8158.
240. Gómez, I.; Reguero, M.; Robb, M. A., Efficient Photochemical Merocyanine-to-Spiropyran Ring Closure Mechanism through an Extended Conical Intersection Seam. A Model CASSCF/CASPT2 Study. *The Journal of Physical Chemistry A* **2006**, *110* (11), 3986-3991.
241. Sheng, Y.; Leszczynski, J.; Garcia, A. A.; Rosario, R.; Gust, D.; Springer, J., Comprehensive Theoretical Study of the Conversion Reactions of Spiropyrans: Substituent and Solvent Effects. *The Journal of Physical Chemistry B* **2004**, *108* (41), 16233-16243.
242. Maurel, F.; Aubard, J.; Rajzmann, M.; Guglielmetti, R.; Samat, A., A quantum chemical study of the ground state ring opening/closing of photochromic 1,3,3-trimethylspiro[indoline-2,3[prime or minute]-naphtho[2,1-b][1,4]oxazine]. *Journal of the Chemical Society, Perkin Transactions 2* **2002**, (7), 1307-1315.
243. Holzwarth, A. R., Data Analysis of Time-Resolved Measurements. In *Biophysical Techniques in Photosynthesis*, Amesz, J.; Hoff, A. J., Eds. Springer Netherlands: Dordrecht, 1996; pp 75-92.
244. de Weerd, F. L.; van Stokkum, I. H. M.; van Grondelle, R., Subpicosecond dynamics in the excited state absorption of all-trans- $\beta$ -Carotene. *Chemical Physics Letters* **2002**, *354* (1), 38-43.
245. Larsen, D. S.; Papagiannakis, E.; van Stokkum, I. H. M.; Vengris, M.; Kennis, J. T. M.; van Grondelle, R., Excited state dynamics of  $\beta$ -carotene explored with dispersed multi-pulse transient absorption. *Chemical Physics Letters* **2003**, *381* (5), 733-742.
246. Rockwell, N. C.; Lagarias, J. C., A Brief History of Phytochromes. *ChemPhysChem* **2010**, *11* (6), 1172-1180.
247. Möglich, A.; Yang, X. J.; Ayers, R. A.; Moffat, K., Structure and Function of Plant Photoreceptors. *Annu. Rev. Plant Biol.* **2010**, *61*, 21-47.
248. Briggs, W. R.; Spudich, J. L., *Handbook of Photosensory Receptors*. Wiley-VCH: Weinheim, Germany, 2005; p 473.

249. Rockwell, N. C.; Su, Y.-S.; Lagarias, C. J., Phytochrome Structure and Signaling Mechanisms. *Annu Rev Plant Biol.* **2006**, *57*, 837-858.
250. Franklin, K. A.; Quail, P. H., Phytochrome functions in Arabidopsis development. *J. Exp. Bot.* **2010**, *61* (1), 11-24.
251. Quail, P. H., Phytochrome photosensory signalling networks. *Nat. Rev. Mol. Cell Biol.* **2002**, *3* (2), 85-93.
252. De Riso, V.; Raniello, R.; Maumus, F.; Rogato, A.; Bowler, C.; Falciatore, A., Gene silencing in the marine diatom *Phaeodactylum tricorutum*. *Nucleic Acids Res.* **2009**, *37* (14).
253. Blumenstein, A.; Vienken, K.; Tasler, R.; Purschwitz, J.; Veith, D.; Frankenberg-Dinkel, N.; Fischer, R., The *Aspergillus nidulans* phytochrome FphA represses sexual development in red light. *Current biology : CB* **2005**, *15* (20), 1833-8.
254. Froehlich, A. C.; Noh, B.; Vierstra, R. D.; Loros, J.; Dunlap, J. C., Genetic and molecular analysis of phytochromes from the filamentous fungus *Neurospora crassa*. *Eukaryot. Cell* **2005**, *4* (12), 2140-2152.
255. Rockwell, N. C.; Lagarias, J. C., The structure of phytochrome: A picture is worth a thousand spectra. *Plant Cell* **2006**, *18*, 4-14.
256. Narikawa, R.; Fukushima, Y.; Ishizuka, T.; Itoh, S.; Ikeuchi, M., A novel photoactive GAF domain of cyanobacteriochrome AnPixJ that shows reversible green/red photoconversion. *J. Mol. Biol.* **2008**, *380* (5), 844-55.
257. Narikawa, R.; Ishizuka, T.; Muraki, N.; Shiba, T.; Kurisu, G.; Ikeuchi, M., Structures of cyanobacteriochromes from phototaxis regulators AnPixJ and TePixJ reveal general and specific photoconversion mechanism. *Proc. Natl. Acad. Sci.* **2013**, *110* (3), 918-923.
258. Yoshihara, S.; Ikeuchi, M., Phototactic motility in the unicellular cyanobacterium *Synechocystis* sp. PCC 6803. *Photochem. Photobiol. Sci.* **2004**, *3* (6), 512-8.
259. Kehoe, D. M.; Gutu, A., Responding to color: The regulation of complementary chromatic adaptation. *Annu. Rev. Plant Biol.* **2006**, *57*, 127-150.
260. Pennacchietti, F.; Losi, A.; Xu, X. L.; Zhao, K. H.; Gartner, W.; Viappiani, C.; Cella, F.; Diaspro, A.; Abbruzzetti, S., Photochromic conversion in a red/green cyanobacteriochrome from *Synechocystis* PCC6803: quantum yields in solution and photoswitching dynamics in living *E. coli* cells. *Photochemical & photobiological sciences : Official journal of the European Photochemistry Association and the European Society for Photobiology* **2015**, *14* (2), 229-37.
261. Edgar, R. C., MUSCLE: multiple sequence alignment with high accuracy and high throughput. *Nucleic Acids Res.* **2004**, *32* (5), 1792-1797.
262. Carroll, E. C.; Compton, O. C.; Madsen, D.; Osterloh, F. E.; Larsen, D. S., Ultrafast carrier dynamics in exfoliated and functionalized calcium niobate nanosheets in water and methanol. *J. Phys. Chem. C* **2008**, *112* (7), 2394-2403.
263. Spillane, K. M.; Dasgupta, J.; Lagarias, J. C.; Mathies, R. A., Homogeneity of Phytochrome Cph1 Vibronic Absorption Revealed by Resonance Raman Intensity Analysis. *J. Am. Chem. Soc.* **2009**, *131* (39), 13946-13948.
264. Velazquez Escobar, F.; Utesch, T.; Narikawa, R.; Ikeuchi, M.; Mroginski, M. A.; Gärtner, W.; Hildebrandt, P., Photoconversion Mechanism of the Second GAF Domain of Cyanobacteriochrome AnPixJ and the Cofactor Structure of Its Green-Absorbing State. *Biochemistry* **2013**, *52* (29), 4871-4880.

265. Schroeder, T., Imaging stem-cell-driven regeneration in mammals. *Nature* **2008**, *453*, 345-351.
266. Shu, X.; Royant, A.; Lin, M. Z.; Aguilera, T. A.; Lev-Ram, V.; Steinbach, P. A.; Tsien, R. Y., Mammalian Expression of Infrared Fluorescent Proteins Engineered from a Bacterial Phytochrome. *Science* **2009**, *324* (5928), 804-807.
267. Weissleder, R.; Pittet, M. J., Imaging in the era of molecular oncology. *Nature* **2008**, *452*, 580-589.
268. Kobayashi, H.; Ogawa, M.; Alford, R.; Choyke, P. L.; Urano, Y., New Strategies for Fluorescent Probe Design in Medical Diagnostic Imaging. *Chem. Rev.* **2010**, *110* (5), 2620-2640.
269. Möglich, A.; Moffat, K., Engineered photoreceptors as novel optogenetic tools. *Photochem. Photobiol. Sci.* **2010**, *9* (10), 1286-1300.
270. Gourinchas, G.; Etzl, S.; Winkler, A., Bacteriophytochromes - from informative model systems of phytochrome function to powerful tools in cell biology. *Curr Opin Struct Biol* **2019**, *57*, 72-83.
271. Blain-Hartung, M.; Rockwell, N. C.; Moreno, M. V.; Martin, S. S.; Gan, F.; Bryant, D. A.; Lagarias, C. J., Cyanobacteriochrome-based photoswitchable adenylyl cyclases (cPACs) for broad spectrum light regulation of cAMP levels in cells. *J. Biol. Chem.* **2018**, *293* (22), 8473-8483.
272. Fernandez-Rodriguez, J.; Moser, F.; Song, M.; Voigt, C. A., Engineering RGB color vision into *Escherichia coli*. *Nat. Chem. Biol.* **2017**, *13*, 706-708.
273. Ramakrishnan, P.; Tabor, J. J., Repurposing *Synechocystis* PCC6803 UirS-UirR as a UV-violet/green photoreversible transcriptional regulatory tool in *E. coli*. *ACS Synth Biol.* **2016**, *5* (7), 733-740.
274. Beyer, H. M.; Juillot, S.; Herbst, K.; Samodelov, S. L.; Müller, K.; Schamel, W. W.; Römer, W.; Schaffner, E.; Nagy, F.; Strähle, U.; Weber, W.; Zurbriggen, M. D., Red light-regulated reversible nuclear localization of proteins in mammalian cells and zebrafish. *ACS Synth. Biol.* **2015**, *4* (9), 951-958.
275. Ryu, M.-H.; Kang, I.-H.; Nelson, M. D.; Jensen, T. M.; Lyuksyutova, A. I.; Siltberg-Liberles, J.; Raizen, D. M.; Gomelsk, M., Engineering adenylate cyclases regulated by near-infrared window light. *Proc. Natl. Acad. Sci.* **2014**, *111* (28), 10167-10172.
276. Müller, K.; Weber, W., Optogenetic tools for mammalian systems. *Mol Biosyst.* **2013**, *9*(4), 596-608.
277. Tabor, J. J.; Levskaya, A.; Voigt, C. A., Multichromatic control of gene expression in *Escherichia coli*. *J Mol Biol.* **2011**, *405*(2), 315-324.
278. Shimizu-Sato, S.; Huq, E.; Tepperman, J. M.; Quail, P. e. H., A light-switchable gene promoter system. *Nat. Biotech.* **2002**, *20*, 1041-1044.
279. Rockwell, N. C.; Lagarias, J. C., Phytochrome diversification in cyanobacteria and eukaryotic algae. *Curr. Opin. Plant Biol.* **2017**, *37*, 87-93.
280. Auldridge, M. A.; Forest, K. T., Bacterial phytochromes: More than meets the light. *Crit Rev Biochem Mol Biol.* **2011**, *46* (1), 67-88.
281. Fushimi, K.; Narikawa, R., Cyanobacteriochromes: photoreceptors covering the entire UV-to-visible spectrum. *Curr Opin Struct Biol* **2019**, *57*, 39-46.
282. Fushimi, K.; Ikeuchi, M.; Narikawa, R., The expanded red/green cyanobacteriochrome lineage: An evolutionary hot spot. *Photochem. Photobiol.* **2017**, *93* (3), 903-906.

283. Ikeuchi, M.; Ishizuka, T., Cyanobacteriochromes: a new superfamily of tetrapyrrole-binding photoreceptors in cyanobacteria. *Photochem. Photobiol. Sci.* **2008**, *7* (10), 1159-1167.
284. Cho, S. M.; Jeoung, S. C.; Song, J.-Y.; Song, J.-J.; Park, Y.-I., Hydrophobic Residues near the Bilin Chromophore-Binding Pocket Modulate Spectral Tuning of Insert-Cys Subfamily Cyanobacteriochromes. *Sci. Rep.* **2017**, *7*, 40576.
285. Hirose, Y.; Rockwell, N. C.; Nishiyama, K.; Narikawa, R.; Ukaji, Y.; Inomata, K.; Lagarias, J. C.; Ikeuchi, M., Green/red cyanobacteriochromes regulate complementary chromatic acclimation via a protochromic photocycle. *Proc. Natl. Acad. Sci.* **2013**, *110* (13), 4974-4979.
286. Holzwarth, A. R.; Wendler, J.; Schaffner, K.; Sundstrom, V.; Sandstrom, A.; Gillbro, T., Phytochrome Models. 8. Picosecond Kinetics of Excited-State Relaxation in Biliverdin Dimethyl Ester. *Isr. J. Chem.* **1983**, *23* (2), 223-231.
287. Kim, J. E.; Tauber, M. J.; Mathies, R. A., Wavelength dependent cis-trans isomerization in vision. *Biochemistry* **2001**, *40* (46), 13774-8.
288. Vanbrederode, M. E.; Gensch, T.; Hoff, W. D.; Hellingwerf, K. J.; Braslavsky, S. E., Photoinduced Volume Change and Energy-Storage Associated with the Early Transformations of the Photoactive Yellow Protein from *Ectothiorhodospira-halophila*. *Biophys. J.* **1995**, *68* (3), 1101-1109.
289. Song, L.; El-Sayed, M. A.; Lanyi, J. K., Protein catalysis of the retinal subpicosecond photoisomerization in the primary process of bacteriorhodopsin photosynthesis. *Science* **1993**, *261* (5123), 891-4.
290. Fushimi, K.; Enomoto, G.; Ikeuchi, M.; Narikawa, R., Distinctive Properties of Dark Reversion Kinetics between Two Red/Green-Type Cyanobacteriochromes and their Application in the Photoregulation of cAMP Synthesis. *Photochem. Photobiol.* **2017**, *93* (3), 681-691.
291. Xu, X.; Höppner, A.; Wiebeler, C.; Zhao, K.-H.; Schapiro, I.; Gärtner, W., Structural elements regulating the photochromicity in a cyanobacteriochrome. *Proc. Natl. Acad. Sci.* **2020**, *117* (5), 2432-2440.
292. Pettersen, E. F.; Goddard, T. D.; Huang, C. C.; Couch, G. S.; Greenblatt, D. M.; Meng, E. C.; Ferrin, T. E., UCSF Chimera--a Visualization System for Exploratory Research and Analysis. *J Comput Chem.* **2004**, *25* (13), 1605-1612.
293. Buhrke, D.; Kuhlmann, U.; Michael, N.; Hildebrandt, P., The Photoconversion of Phytochrome Includes an Unproductive Shunt Reaction Pathway. *Chemphyschem* **2018**, *19* (5), 566-570.
294. Zienicke, B.; Molina, I.; Glenz, R.; Singer, P.; Ehmer, D.; Velazquez Escobar, F.; Hildebrandt, P.; Diller, R.; Lamparter, T., Unusual Spectral Properties of Bacteriophytochrome Agp2 Result from a Deprotonation of the Chromophore in the Red-absorbing Form Pr. *J. Biol. Chem.* **2013**, *288*, 31738-31751.
295. Ordaz, J. D.; Wu, W.; Xu, X.-M., Optogenetics and its application in neural degeneration and regeneration. *Neural Regen Res* **2017**, *12* (8), 1197-1209.
296. Wiltbank, L. B.; Kehoe, D. M., Two Cyanobacterial Photoreceptors Regulate Photosynthetic Light Harvesting by Sensing Teal, Green, Yellow, and Red Light. *mBio* **2016**, *7* (1), e02130-15.
297. Li, J.; Li, G.; Wang, H.; Deng, X. W., Phytochrome Signaling Mechanisms. *The Arabidopsis Book* **2011**, *2011* (9).

298. Fushimi, K.; Miyazaki, T.; Kuwasaki, Y.; Nakajima, T.; Yamamoto, T.; Suzuki, K.; Ueda, Y.; Miyake, K.; Takeda, Y.; Choi, J.-H.; Kawagishi, H.; Park, E. Y.; Ikeuchi, M.; Sato, M.; Narikawa, R., Rational conversion of chromophore selectivity of cyanobacteriochromes to accept mammalian intrinsic biliverdin. *Proceedings of the National Academy of Sciences* **2019**, *116* (17), 8301.
299. Rumyantsev, K. A.; Shcherbakova, D. M.; Zakharova, N. I.; Emelyanov, A. V.; Turoverov, K. K.; Verkhusha, V. V., Minimal domain of bacterial phytochrome required for chromophore binding and fluorescence. *Scientific Reports* **2015**, *5*, 18348.
300. Jang, J.; McDonald, S.; Uppalapati, M.; Woolley, G. A., Green, orange, red, and far-red optogenetic tools derived from cyanobacteriochromes. *bioRxiv* **2019**, 769422.
301. Oliinyk, O. S.; Shemetov, A. A.; Pletnev, S.; Shcherbakova, D. M.; Verkhusha, V. V., Smallest near-infrared fluorescent protein evolved from cyanobacteriochrome as versatile tag for spectral multiplexing. *Nature Communications* **2019**, *10* (1), 279.
302. Escobar, F. V.; Lang, C.; Takiden, A.; Schneider, C.; Balke, J.; Hughes, J.; Alexiev, U.; Hildebrandt, P.; Mroginski, M. A., Protonation-Dependent Structural Heterogeneity in the Chromophore Binding Site of Cyanobacterial Phytochrome Cph1. *J. Phys. Chem. B* **2017**, *121* (1), 47-57.
303. Heyes, D. J.; Khara, B.; Sakuma, M.; Hardman, S. J. O.; O'Cualain, R.; Rigby, S. E. J.; Scrutton, N. S., Ultrafast red light activation of *Synechocystis* phytochrome Cph1 triggers major structural change to form the Pfr signalling-competent state. *PLoS One* **2012**, *7* (12), e52418-e52418.
304. Heyes, D. J.; Hardman, S. J. O.; Pedersen, M. N.; Woodhouse, J.; De La Mora, E.; Wulff, M.; Weik, M.; Cammarata, M.; Scrutton, N. S.; Schirò, G., Light-induced structural changes in a full-length cyanobacterial phytochrome probed by time-resolved X-ray scattering. *Commun. Biol* **2019**, *2* (1), 1.
305. Remberg, A.; Lindner, I.; Lamparter, T.; Hughes, J.; Kneip, C.; Hildebrandt, P.; Braslavsky, S. E.; Gärtner, W.; Schaffner, K., Raman Spectroscopic and Light-Induced Kinetic Characterization of a Recombinant Phytochrome of the Cyanobacterium *Synechocystis*. *Biochemistry* **1997**, *36* (43), 13389-13395.
306. Mroginski, M. A.; Murgida, D. H.; Hildebrandt, P., The Chromophore Structural Changes during the Photocycle of Phytochrome: A Combined Resonance Raman and Quantum Chemical Approach. *Acc. Chem. Res* **2007**, *40* (4), 258-266.
307. Matysik, J.; Hildebrandt, P.; Schlamann, W.; Braslavsky, S. E.; Schaffner, K., Fourier-Transform Resonance Raman Spectroscopy of Intermediates of the Phytochrome Photocycle. *Biochemistry* **1995**, *34*, 10497-10507.
308. Foerstendorf, H.; Benda, C.; Gärtner, W.; Storf, M.; Scheer, H.; Siebert, F., FTIR Studies of Phytochrome Photoreactions Reveal the CO Bands of the Chromophore: Consequences for Its Protonation States, Conformation, and Protein Interaction†. *Biochemistry* **2001**, *40* (49), 14952-14959.
309. Hildebrandt, P.; Hoffmann, A.; Lindemann, P.; Heibel, G.; Braslavsky, S. E.; Schaffner, K.; Schrader, B., Fourier Transform Resonance Raman Spectroscopy of Phytochrome\*. *Biochemistry* **1992**, *31*, 7957-7962.

310. Collette, F.; Renger, T.; Schmidt am Busch, M., Revealing the Functional States in the Active Site of BLUF Photoreceptors from Electrochromic Shift Calculations. *The journal of physical chemistry. B* **2014**, *118* (38), 11109-11119.
311. Wagner, J. R.; Zhang, J.; von Stetten, D.; Mina, G.; Murgida, D. H.; Mroginski, M. A.; Walker, J. M.; Forest, K. T.; Hildebrandt, P.; Vierstra, R. D., Mutational Analysis of Deinococcus radiodurans Bacteriophytochrome Reveals Key Amino Acids Necessary for the Photochromicity and Proton Exchange Cycle of Phytochromes. *The Journal of biological chemistry* **2008**, *283*, 12212-12226.
312. Stetten, D. v.; Seibeck, S.; Michael, N.; Scheerer, P.; Mroginski, M. A.; Murgida, D. H.; Krauss, N.; Heyn, M. P.; Hildebrandt, P.; Borucki, B.; Lamparter, T., Highly Conserved Residues Asp-197 and His-250 in Agp1 Phytochrome Control the Proton Affinity of the Chromophore and Pfr Formation. *The Journal of biological chemistry* **2006**, *282*, 2116-2123.
313. Björling, A.; Berntsson, O.; Lehtivuori, H.; Takala, H.; Hughes, A. J.; Panman, M.; Hoernke, M.; Niebling, S.; Henry, L.; Henning, R.; Kosheleva, I.; Chukharev, V.; Tkachenko, N. V.; Menzel, A.; Newby, G.; Khakhulin, D.; Wulff, M.; Ihalainen, J. A.; Westenhoff, S., Structural photoactivation of a full-length bacterial phytochrome. *Sci Adv* **2016**, *2* (8), e1600920-e1600920.
314. Eilfeld, P.; Rüdiger, W., Absorption Spectra of Phytochrome Intermediates. In *Zeitschrift für Naturforschung C*, 1985; Vol. 40, p 109.
315. Seibeck, S.; Borucki, B.; Otto, H.; Inomata, K.; Khawn, H.; Kinoshita, H.; Michael, N.; Lamparter, T.; Heyn, M. P., Locked 5Zs-biliverdin blocks the Meta-RA to Meta-RC transition in the functional cycle of bacteriophytochrome Agp1. *FEBS Letters* **2007**, *581* (28), 5425-5429.
316. Müller, M. G.; Lindner, I.; Martin, I.; Gärtner, W.; Holzwarth, A. R., Femtosecond Kinetics of Photoconversion of the Higher Plant Photoreceptor Phytochrome Carrying Native and Modified Chromophores. *Biophys. J.* **2008**, *94*, 4370-4382.
317. Jenkins, A.; Kirpich, J. S.; Mix, L. T.; Martin, S. S.; Lagarias, C. J.; Larsen, D. S., Primary Dynamics of Far-Red Cyanobacteriochromes. *in preparation xxx*.
318. Spudich, J. L.; Yang, C. S.; Jung, K. H.; Spudich, E. N., Retinylidene Proteins: Structures and Functions from Archaea to Humans. *Annu. Rev. Cell Dev. Biol.* **2000**, *16*, 365-392.
319. Kandori, H.; Shichida, Y.; Yoshizawa, T., Photoisomerization in Rhodopsin. *Biochemistry* **2001**, *66*, 1197-1209.
320. Schoenlein, R. W.; Peteanu, L. A.; Mathies, R. A.; Shank, C. V., The First Step in Vision: Femtosecond Isomerization of Rhodopsin. *Science* **1991**, *254*, 412-415.
321. Peteanu, L. A.; Schoenlein, R. W.; Wang, Q.; Mathies, R. A.; Shank, C. V., The First Step in Vision Occurs in Femtoseconds: Complete Blue and Red Spectral Studies. *Proc. Natl. Acad. Sci.* **1993**, *90*, 11762-11766.
322. Warshel, A., Bicycle-Pedal Model for the First Step in the Vision Process. *Nature* **1976**, *260*, 679-683.
323. Warshel, A.; Barboy, N., Energy Storage and Reaction Pathways in the First Step of the Vision Process. *J. Am. Chem. Soc.* **1982**, *104*, 1469-1476.
324. Warshel, A.; Chu, Z. T.; Hwang, K., K., The Dynamics of the Primary Event in Rhodopsins Revisited. *Chem. Phys.* **1991**, *158*, 303-314.



325. Dormans, G. J.; Groeneboom, G. C.; van Dorst, W. C. A.; Buck, H. M., A Quantum Chemical Study on the Mechanism of Cis-Trans Isomerization in Retinal-like Protonated Schiff Base. *J. Am. Chem. Soc.* **1988**, *110*, 1406-1415.
326. Yu, J. K.; Liang, R.; Liu, F.; Martinez, T. J., First-Principles Characterization of the Elusive I Fluorescent State and the Structural Evolution of Retinal Protonated Schiff Base in Bacteriorhodopsin. *J. Am. Chem. Soc.* **2019**, *141*, 18193-18203.
327. Crist, R. M.; Vasileiou, C.; Rabago-Smith, M.; Geiger, J. H.; Borhan, B., Engineering a Rhodopsin Protein Mimic. *J. Am. Chem. Soc.* **2006**, *128*, 4522-4523.
328. Berbasova, T.; Santos, E. M.; Norsati, M.; Vasileiou, C.; Geiger, J. H.; Borhan, B., Light-Activated Reversible Imine Isomerization: Towards a Photochromic Protein Switch. *Chembiochem : a European journal of chemical biology* **2016**, *17*, 407-414.
329. Schapiro, I.; Ruhman, S., Ultrafast Photochemistry of Anabaena Sensory Rhodopsin: Experiment and Theory. *Biochimica et biophysica acta* **2014**, *1837*, 589-597.
330. Matsuyama, T.; Yamashita, T.; Imamoto, Y.; Shichida, Y., Photochemical Properties of Mammalian Melanopsin. *Biochemistry* **2012**, *51*, 5454-5462.
331. Ehrenberg, D.; Varma, N.; Deupi, X.; Koyanagi, M.; Terakita, A.; Schertler, G. F. X.; Heberle, J.; Lesca, E., The Two-Photon Reversible Reaction of the Bistable Jumping Spider Rhodopsin-1. *Biophys. J.* **2019**, *116*, 1248-1258.
332. Melloni, A.; Rossi Paccani, R.; Donati, D.; Zanirato, V.; Sinicropi, A.; Parisi, M. L.; Martin, E.; Ryazantsev, M.; Ding, W. J.; Frutos, L. M., Modeling, Preparation, and Characterization of a Dipole Moment Switch Driven by Z / E Photoisomerization. *J. Am. Chem. Soc.* **2010**, *132*, 9310-9319.
333. Gozem, S.; Melaccio, F.; Luk, H. L.; Rinaldi, S.; Olivucci, M., Learning from Photobiology How to Design Molecular Devices Using a Comput. *Chem. Soc. Rev.* **2014**, *43*, 4019-4036.
334. Sinicropi, A.; Martin, E.; Ryazantsev, M.; Helbing, J.; Briand, J.; Sharma, D.; Leonard, J.; Haacke, S.; Cannizzo, A.; Chergui, M., An Artificial Molecular Switch That Mimics the Visual Pigment and Completes Its Photocycle in Picoseconds. *Proc. Natl. Acad. Sci.* **2008**, *105*, 17642-17647.
335. Gueye, M.; Manathunga, M.; Agathangelou, D.; Orozco, Y.; Paolino, M.; Fusi, S.; Haacke, S.; Olivucci, M.; Leonard, J., Engineering the Vibrational Coherence of Vision into a Synthetic Molecular Device. *Nat. Commun.* **2018**, *9*, 313.
336. McIsaac, R. S.; Bedbrook, C. N.; Arnold, F. H., Recent Advances in Engineering Microbial Rhodopsin for Optogenetics. *Curr Opin Struct Biol* **2015**, *33*, 8-15.
337. Frutos, L. M.; Andruniow, T.; Santoro, F.; Ferre, N.; Olivucci, M., Tracking the Excited-State Time Evolution of the Visual Pigment with Multiconfigurational Quantum Chemistry. *Proc. Natl. Acad. Sci.* **2007**, *104*, 7764-7769.
338. Orozco-Gonzalez, Y.; Manathunga, M.; Marin, M. D. C.; Agathangelou, D.; Jung, K. H.; Melaccio, F.; Ferre, N.; Haacke, S.; Continho, K.; Canuto, S., An Average Solvent Electrostatic Configuration Protocol for QM/MM Free Energy Optimization: Implementation and Application to Rhodopsin Systems. *J. Chem. Theory. Comput.* **2017**, *13*, 6391-6404.
339. Mix, L. T.; Kirpich, J. S.; Kumauchi, M.; Ren, J.; Vengris, M.; Hoff, W. D.; Larsen, D. S., Bifurcation in the Ultrafast Dynamics of the Photoactive Yellow Proteins from *Leptospira biflexa* and *Halorhodospira halophila*. *Biochemistry* **2016**, *55* (44), 6138-6149.

340. Gozem, S.; Luk, H. L.; Schapiro, I.; Olivucci, M., Theory and Simulation of the Ultrafast Double-Bond Isomerization of Biological Chromophores. *Chem. Rev.* **2017**, *117*, 13502-13565.
341. Manathunga, M.; Yang, X.; Orozco-Gonzalez, Y.; Olivucci, M., Impact of Electronic State Mixing on the Photoisomerization Time Scale of the Retinal Chromophore. *J. Phys. Chem. Lett.* **2017**, *2017* (8).
342. Sampedro Ruiz, D.; Cembran, A.; Garavelli, M.; Olivucci, M.; Fub, W., Structure of the Conical Intersections Driving the Cis-Trans Photoisomerization of Conjugated Molecules. *Photochem. Photobiol.* **2007**, *76*, 622-633.
343. Bonovicini, A.; Demoulin, B.; Altavilla, S. F.; Nenov, A.; El-Tahawy, M. M. T.; Segarra-Marti, J.; Giussani, A.; Batista, V. S.; Garavelli, M.; Rivalta, I., Ultraviolet Vision: Photophysical Properties of the Unprotonated Retinyl Schiff Base in the Siberian Hamster Cone Pigment. *Theor. Chem. Acc.* **2016**, *135*, 110.
344. Strambi, A.; Durbeej, B.; Ferre, N.; Olivucci, M., Anabaena Sensory Rhodopsin Is a Light-Driven Unidirectional Rotor. *Proc. Natl. Acad. Sci.* **2010**, *107*, 21322-21326.
345. Kawanabe, A.; Furutani, Y.; Jung, K. H.; Kandori, H., Photochromism of Anabaena Sensory Rhodopsin. *J. Am. Chem. Soc.* **2007**, *129*, 8644-8649.
346. Altoe, O.; Cembran, A.; Olivucci, M.; Garavelli, M., Aborted Double Bicycle-Pedal Isomerization with Hydrogen Bond Breaking Is the Primary Event of Bacteriorhodopsin Proton Pumping. *Proc. Natl. Acad. Sci.* **2010**, *107*, 20172-20177.
347. Schapiro, I.; Weingart, O.; Buss, V., Bicycle-Pedal Isomerization in a Rhodopsin Chromophore Model. *J. Am. Chem. Soc.* **2008**, *131*, 16-17.
348. Weingart, O., The Twisted C11C12 Bond of the Rhodopsin ChromophoreA Photochemical Hot Spot. *J. Am. Chem. Soc.* **2007**, *129*, 10618-10619.
349. Jacobs, G. H., Ultraviolet Vision in Vertebrates. *Am. Zool.* **1992**, *32*, 544-554.
350. Ghanbarpour, A.; Nairat, M.; Nosrati, M.; Santos, E. M.; Vasileiou, C.; Dantus, M.; Borhan, B.; Geiger, J. H., Mimicking Microbial Rhodopsin Isomerization in a Single Crystal. *J. Am. Chem. Soc.* **2019**, *141*, 1735-1741.
351. Manathunga, M.; Yang, X.; Olivucci, M., Electronic State Mixing Controls the Photoreactivity of a Rhodopsin with All- Trans Chromophore Analogues. *J. Phys. Chem. Lett.* **2018**, *9*, 6350-6355.
352. Marin, M. D. C.; Agathangelou, D.; Orozco-Gonzalez, Y.; Valentini, A.; Kato, Y.; Abe-Yoshizumi, R.; Kandori, H.; Choi, A.; Jung, K. H.; Haacke, S., Fluorescence Enhancement of a Microbial Rhodopsin via Electronic Reprogramming. *J. Am. Chem. Soc.* **2019**, *141*, 262-271.
353. Lagarias, J. C.; Rockwell, N. C.; Martin, S. S. Cyanobacteriochromes as color-fast or color -switching food additives. May 5, 2016.
354. Zhang, C.-F.; Farrens, D. L.; Björling, S. C.; Song, P.-S.; Kilger, D. S., Time-Resolved Absorption Studies of Native Etiolated Oat Phytochrome. *J. Am. Chem. Soc.* **1992**, *114*, 4569-4580.
355. Braslavsky, S. E.; Matthews, J. I.; Herbert, H. J.; de Kok, J.; Spruit, C. J. P.; Schaffner, K., CHARACTERIZATION OF A MICROSECOND INTERMEDIATE IN THE LASER FLASH PHOTOLYSIS OF SMALL PHYTOCHROME FROM OAT. *Photochem. Photobiol.* **1979**, *31*, 417-420.

356. Gottlieb, S. M.; Corley, S. C.; Madsen, D.; Larsen, D. S., Note: A flexible light emitting diode-based broadband transient-absorption spectrometer. *Review of Scientific Instruments* **2012**, *83* (5), 056107.
357. Case, D. A.; Betz, R. M.; Cerutti, D. S.; Cheatham, T. E.; Darden, T. A.; Duke, R. E.; Giese, T. J.; Gohlke, H.; Goetz, A. W.; Homeyer, N.; Izadi, S.; Janowski, P.; Kaus, J.; Kovalenko, A.; Lee, T. S.; LeGrand, S.; Li, P.; Lin, C.; Luchko, T.; Luo, R.; Madej, B.; Mermelstein, D.; Merz, K. M.; Monard, G.; Nguyen, H.; Nguyen, H. T.; Omelyan, I.; Onufriev, A.; Roe, D. R.; Roitberg, A.; Sagui, C.; Simmering, C. L.; Botello-Smith, W. M.; Swails, J.; Walker, R. C.; Wang, J.; Wolf, R. M.; Wu, X.; Xiao, L.; Kollman, P. A., AMBER. **2016**.
358. Humphrey, W.; Dalke, A.; Schulten, K., VMD: Visual Molecular Dynamics. *J. Mol. Graph.* **1996**, *14*, 33-38.
359. Rao, A. G.; Wiebeler, C.; Sen, S.; Cerutti, D. S.; Schapiro, I., Histidine protonation controls structural heterogeneity in the cyanobacteriochrome AnPixJg2. *Phys. Chem. Chem. Phys.* **2021**, *23*, 7359-7367.
360. Maier, J. A.; Martinez, C.; Kasavajhala, K.; Wickstrom, L.; Hauser, K. E.; Simmerling, C., ff14SB: Improving the Accuracy of Protein Side Chain and Backbone Parameters from ff99SB. *J. Chem. Theory. Comput.* **2015**, *11*, 39.
361. Schirmer, J., A new approximation scheme for the polarization propagator. *Phys. Rev. A.* **1982**, *26*, 2395-2416.
362. Furche, F.; Ahlrichs, R.; Hättig, C.; Klopper, W.; Sierka, M.; Weigend, F., Turbomole. *Wiley Interdiscip. Rev. Comput. Mol. Sci.* **2014**, *4*, 91-100.
363. Kästner, J.; Carr, J. M.; Keal, T. W.; Thiel, W.; Wander, A.; Sherwood, P., An open-source geometry optimizer for atomistic simulations. *J. Phys. Chem. A* **2009**, *113*, 11856-11865.
364. Mertz, S.; Kästner, J.; Sokol, A. A.; Keal, T. W.; Thiel, W.; Wander, A.; Sherwood, P., ChemShell-a modular software package for QM/MM simulations. *Wiley Interdiscip. Rev. Comput. Mol. Sci.* **2014**, *4*, 101-110.
365. Neese, F., The ORCA program system. *WIREs Comput. Mol. Sci.* **2012**, *2*, 72-78.
366. Neese, F., Software update: the ORCA program system, version 4.0. *Wiley Interdiscip. Rev. Comput. Mol. Sci.* **2018**, *8*, e1327.